

Lecture Notes in Electrical Engineering 721

Rajeev Agrawal
Chandramani Kishore Singh
Ayush Goyal *Editors*

Advances in Smart Communication and Imaging Systems

Select Proceedings of MedCom 2020

 Springer

Lecture Notes in Electrical Engineering

Volume 721

Series Editors

Leopoldo Angrisani, Department of Electrical and Information Technologies Engineering, University of Napoli Federico II, Naples, Italy

Marco Arteaga, Departament de Control y Robótica, Universidad Nacional Autónoma de México, Coyoacán, Mexico

Bijaya Ketan Panigrahi, Electrical Engineering, Indian Institute of Technology Delhi, New Delhi, Delhi, India

Samarjit Chakraborty, Fakultät für Elektrotechnik und Informationstechnik, TU München, Munich, Germany

Jiming Chen, Zhejiang University, Hangzhou, Zhejiang, China

Shanben Chen, Materials Science and Engineering, Shanghai Jiao Tong University, Shanghai, China

Tan Kay Chen, Department of Electrical and Computer Engineering, National University of Singapore, Singapore, Singapore

Rüdiger Dillmann, Humanoids and Intelligent Systems Laboratory, Karlsruhe Institute for Technology, Karlsruhe, Germany

Haibin Duan, Beijing University of Aeronautics and Astronautics, Beijing, China

Gianluigi Ferrari, Università di Parma, Parma, Italy

Manuel Ferre, Centre for Automation and Robotics CAR (UPM-CSIC), Universidad Politécnica de Madrid, Madrid, Spain

Sandra Hirche, Department of Electrical Engineering and Information Science, Technische Universität München, Munich, Germany

Faryar Jabbari, Department of Mechanical and Aerospace Engineering, University of California, Irvine, CA, USA

Limin Jia, State Key Laboratory of Rail Traffic Control and Safety, Beijing Jiaotong University, Beijing, China

Janusz Kacprzyk, Systems Research Institute, Polish Academy of Sciences, Warsaw, Poland

Alaa Khamis, German University in Egypt El Tagamoa El Khames, New Cairo City, Egypt

Torsten Kroeger, Stanford University, Stanford, CA, USA

Qilian Liang, Department of Electrical Engineering, University of Texas at Arlington, Arlington, TX, USA

Ferran Martín, Departament d'Enginyeria Electrònica, Universitat Autònoma de Barcelona, Bellaterra, Barcelona, Spain

Tan Cher Ming, College of Engineering, Nanyang Technological University, Singapore, Singapore

Wolfgang Minker, Institute of Information Technology, University of Ulm, Ulm, Germany

Pradeep Misra, Department of Electrical Engineering, Wright State University, Dayton, OH, USA

Sebastian Möller, Quality and Usability Laboratory, TU Berlin, Berlin, Germany

Subhas Mukhopadhyay, School of Engineering & Advanced Technology, Massey University, Palmerston North, Manawatu-Wanganui, New Zealand

Cun-Zheng Ning, Electrical Engineering, Arizona State University, Tempe, AZ, USA

Toyoaki Nishida, Graduate School of Informatics, Kyoto University, Kyoto, Japan

Federica Pascucci, Dipartimento di Ingegneria, Università degli Studi "Roma Tre", Rome, Italy

Yong Qin, State Key Laboratory of Rail Traffic Control and Safety, Beijing Jiaotong University, Beijing, China

Gan Woon Seng, School of Electrical & Electronic Engineering, Nanyang Technological University, Singapore, Singapore

Joachim Speidel, Institute of Telecommunications, Universität Stuttgart, Stuttgart, Germany

Germano Veiga, Campus da FEUP, INESC Porto, Porto, Portugal

Haitao Wu, Academy of Opto-electronics, Chinese Academy of Sciences, Beijing, China

Junjie James Zhang, Charlotte, NC, USA

The book series *Lecture Notes in Electrical Engineering* (LNEE) publishes the latest developments in Electrical Engineering - quickly, informally and in high quality. While original research reported in proceedings and monographs has traditionally formed the core of LNEE, we also encourage authors to submit books devoted to supporting student education and professional training in the various fields and applications areas of electrical engineering. The series cover classical and emerging topics concerning:

- Communication Engineering, Information Theory and Networks
- Electronics Engineering and Microelectronics
- Signal, Image and Speech Processing
- Wireless and Mobile Communication
- Circuits and Systems
- Energy Systems, Power Electronics and Electrical Machines
- Electro-optical Engineering
- Instrumentation Engineering
- Avionics Engineering
- Control Systems
- Internet-of-Things and Cybersecurity
- Biomedical Devices, MEMS and NEMS

For general information about this book series, comments or suggestions, please contact leontina.dicecco@springer.com.

To submit a proposal or request further information, please contact the Publishing Editor in your country:

China

Jasmine Dou, Editor (jasmine.dou@springer.com)

India, Japan, Rest of Asia

Swati Meherishi, Editorial Director (Swati.Meherishi@springer.com)

Southeast Asia, Australia, New Zealand

Ramesh Nath Premnath, Editor (ramesh.premnath@springernature.com)

USA, Canada:

Michael Luby, Senior Editor (michael.luby@springer.com)

All other Countries:

Leontina Di Cecco, Senior Editor (leontina.dicecco@springer.com)

**** This series is indexed by EI Compendex and Scopus databases. ****

More information about this series at <http://www.springer.com/series/7818>

Rajeev Agrawal · Chandramani Kishore Singh ·
Ayush Goyal
Editors

Advances in Smart Communication and Imaging Systems

Select Proceedings of MedCom 2020

 Springer

Editors

Rajeev Agrawal
G. L. Bajaj Institute of Technology
and Management
Greater Noida, India

Chandramani Kishore Singh
Indian Institute of Science Bangalore
Bengaluru, India

Ayush Goyal
Department of Electrical Engineering
and Computer Science
Texas A&M University – Kingsville
Kingsville, TX, USA

ISSN 1876-1100

ISSN 1876-1119 (electronic)

Lecture Notes in Electrical Engineering

ISBN 978-981-15-9937-8

ISBN 978-981-15-9938-5 (eBook)

<https://doi.org/10.1007/978-981-15-9938-5>

© Springer Nature Singapore Pte Ltd. 2021

This work is subject to copyright. All rights are reserved by the Publisher, whether the whole or part of the material is concerned, specifically the rights of translation, reprinting, reuse of illustrations, recitation, broadcasting, reproduction on microfilms or in any other physical way, and transmission or information storage and retrieval, electronic adaptation, computer software, or by similar or dissimilar methodology now known or hereafter developed.

The use of general descriptive names, registered names, trademarks, service marks, etc. in this publication does not imply, even in the absence of a specific statement, that such names are exempt from the relevant protective laws and regulations and therefore free for general use.

The publisher, the authors and the editors are safe to assume that the advice and information in this book are believed to be true and accurate at the date of publication. Neither the publisher nor the authors or the editors give a warranty, expressed or implied, with respect to the material contained herein or for any errors or omissions that may have been made. The publisher remains neutral with regard to jurisdictional claims in published maps and institutional affiliations.

This Springer imprint is published by the registered company Springer Nature Singapore Pte Ltd. The registered company address is: 152 Beach Road, #21-01/04 Gateway East, Singapore 189721, Singapore

Preface

Recent advances in different domains like sensor technologies, wireless communications, computer vision medical image, data processing and globalization of digital society across various social areas have intensified the growth of remote healthcare services. However, several socioeconomic aspects and integration of these services with classical healthcare system remain as a challenging issue. In today's context, smart systems are emerging from the integration of embedded computing devices, smart objects, imaging techniques, people and physical environments, which are normally tied by a communication infrastructure. These include systems like smart cities, smart grids, smart factories, smart buildings, smart houses and smart cars where every object is connected to every other object. They are aimed to provide an adaptive, resilient, efficient and cost-effective scenario.

This book presents the selected proceedings of the International Conference on Smart Communication and Imaging Systems (MedCom 2020). It explores the recent technological advances in the field of next-generation communication systems and latest techniques for image processing, analysis and its related applications. The topics include design and development of smart, secure and reliable future communication networks; satellite, radar and microwave techniques for intelligent communication. The book also covers methods and applications of GIS and remote sensing; medical image analysis and its applications in smart health; and other real-life applications of imaging and smart communication. This book can be a valuable resource for academicians, researchers and professionals working in the field of smart communication systems and image processing including artificial intelligence, machine learning and their applications in building smart systems. It will contribute to foster integration of latest and future communication technologies with imaging systems and services, suggesting solutions to various social and techno-commercial issues of global significance.

Greater Noida, India
Bengaluru, India
Kingsville, USA

Rajeev Agrawal
Chandramani Kishore Singh
Ayush Goyal

Contents

Benign–Malignant Mass Characterization Based on Multi-gradient Quinary Patterns	1
Rinku Rabidas, Romesh Laishram, and Amarjit Roy	
Improved Switching Vector Median Filter for Removal of Impulse Noise from Color Images	11
Amarjit Roy, Snehal Chandra, and Rinku Rabidas	
Optimal Orientation Controller Design for F-16/MATV Using Robust and Discrete Linear–Quadrature–Gaussian (LQG) Controller	21
G. Kassahun Berisha and Parvendra Kumar	
BER Analysis of FRFT-OFDM System Over α-μ Fading Channel Under CFO	35
Ashish Mishra, Anushka Singh, Aditi Verma, S. Pratap Singh, and M. Lakshmanan	
An Overview of FTTH for Optical Network	41
S. Sugumaran, Durga Naga Lakshmi, and Shilpa Choudhary	
Comparison of Various Classification Techniques on Brain Tumor Detection	53
Ravi Prakash Chaturvedi and Udayan Ghose	
Fake News Detection Based on Machine Learning	67
Pushpa Choudhary, Suchita Pandey, Sakshi Tripathi, and Shubham Chaurasiya	
Design of Octagonal-Shaped CP Antenna for RFID Handheld Reader Applications	77
Niraj Agrawal, A. K. Gautam, Rajesh Mishra, and S. D. Choudhary	
Speed Optimization of Multipliers	85
Amit Gupta, Chiranjeev Singhal, Priya Singh, Satyam Dubey, Saurabh Sharma, and Waris Quraishi	

Upgradation of Assurance Based on Revealing Quality of Healthcare Domain Around the Globe Using Internet of Things	97
Sandeep Srivastava, Pramod Kumar Srivastava, Deepak Gupta, and Dinesh Kumar Yadav	
Wideband Sub-6 GHz Micro-strip Antenna: Design and Fabrication	109
Pankaj Jha, Shailendra Singh, and Ram Lal Yadava	
Performance Analysis of Deep Transfer Learning for Manifestation of COVID-19 Using Chest X-ray	117
Manish Arya, Amit Sehgal, and Rajeev Agrawal	
Design of Single-Fed Dual-Polarized Planar Antenna for Dual-Band Automotive Applications	131
Niraj Agrawal, A. K. Gautam, Rajesh Mishra, and S. D. Choudhary	
SCSZB: Sensor Congregate Stable Zonal-Based Routing Protocol Designed for Optimal WSN	139
Anshu Kumar Dwivedi, A. K. Sharma, Manju, Samayveer Singh, and P. S. Mehra	
Web Object Ranking for Location-Based Web Object Search	151
K. N. Anjan Kumar, T. Satish Kumar, R. Krishna Prasad, and S. G. Ravi Kumar	
OCHEP: An Optimized Cluster Head Election Protocol for Heterogeneous WSNs	167
Samayveer Singh, Piyush Yadav, Aruna Malik, and Rajeev Agrawal	
Internet of Things: Architecture, Applications and Future Aspects	183
Anu Priya, Amrita Rai, and R. P. Singh	
Demand Response-Based Congestion Management Considering Wind Energy Source in Competitive Power Market	191
Anjali Agrawal, Seema N. Pandey, and Laxmi Srivastava	
Power Transfer Loadability Enhancement of Congested Transmission Network Using DG	201
Divya Asija and Pallavi Choudekar	
Performance Analysis of Free Space Optical Communication System Over Double Generalized Gamma Distribution with Polarization Shift Keying Modulation	211
Tanmay Singh, Sandhya, Rupali Srivastava, Sunil Yadav, M. Lakshmanan, Saurabh Katiyar, and Piyush Jain	
Binary Differential Evolution-Based Feature Selection for Hand Gesture Classification	221
Anamika, Rinki Gupta, and Ghanapriya Singh	

LoRa-Based Wireless Automation and Monitoring System 233
 Mayank Tiwari, Kumar Abhishek Ranjan, Amit Sehgal, Akash Kumar,
 and Saurabh Srivastava

**Novel Approach to Denoise Electrocardiogram Signal Using
 LabVIEW Techniques** 247
 Shivam Pandey, Rajat Mehrotra, M. A. Ansari, and Pragati Tripathi

**Convolution Based Multilevel DWT Architecture Using Distributed
 Arithmetic and FIR Bi-orthogonal Filter for Two-Dimensional
 Data Analysis** 261
 Maram Anantha Guptha, Surampudi Srinivasa Rao,
 and Ravindrakumar Selvaraj

**Closed-Form Expressions of BER and Capacity
 for Co-operative NOMA** 271
 Simran Sethi, Soumil Tripathi, Shreya Srivastava, Saurabh Katiyar,
 S. Pratap Singh, and M. Lakshmanan

Real Time Physical Fitness Monitoring App: BeTough 281
 Pushpa Choudhary, Akhilesh Kumar Choudhary, Arun Kumar Singh,
 and Ashish Tripathi

**A Novel Scheme for Medical Image Compression Using Huffman
 and DCT Techniques** 289
 Ankit Kumar Chaudhary, Rajat Mehrotra, M. A. Ansari,
 and Pragati Tripathi

Review on Next Step Home Automation Using Wi-Fi Module 301
 Himanshu Kumar Patel, Vishvapriya Gaur, Shivam Kumar,
 Ayush Kumar Singh, and Sudhanshu Mittal

Literature Review: Predicting Faults in Object-Oriented Software 309
 Ankush Joon, Rajesh Kumar Tyagi, and Krishan Chillar

**Tunable Transmittance Using Temperature Dependence ZnS-Based
 ID Photonic Crystals** 325
 Sanjeev Sharma, Vipin Kumar, and Shradha Gupta

**Design and Analysis of UWB-Multiband Notch Antenna Loaded
 with CSRR and U-Shaped Slot for Wireless Applications** 331
 Madan Kumar Sharma, Suryadeep Singh, Tanishq Thakur,
 Syed Md. Moazzam Sajjad Razi, and Shubham Tiwari

**Gray-Version Invariant Reversible Data Hiding Scheme Based on 2D
 Histogram Modification for Color Images** 343
 Aruna Malik, Samayveer Singh, Shashank Awasthi, and Piyush Yadav

Resonant Frequency Prediction of Patch Antenna in the Presence of Inserted Airgap Using Machine Learning	353
Mahima Soni, Kanhaiya Sharma, Ganga Prasad Pandey, and Surendra K Gupta	
Impact of K-Nearest Neighbour on Classification Accuracy in KNN Algorithm Using Machine Learning	363
Abhishek Srivastava	
Low-Energy-Based Multi-hop Cluster Head Selection for IoT Applications Using Super Nodes	375
Hardika Raman and B. Mohapatra	
Dynamic Wireless Charging for Electrical Vehicles	387
Harsh Agarwal, Vikrant Vashistha, Shohrab Alam, Pallavi Choudekar, and Ruchira	
Economic Benefits of Implementing Demand Response in Congested Network of Deregulated Power Market	395
Anjali Agrawal, Ragini Malviya, Seema N. Pandey, and Laxmi Srivastava	
An Overview of the Intelligent Control-Based Optimization Methods for Integrated Renewable Energy Sources	405
Akanksha Sharma, H. P. Singh, R. K. Viral, and Naqui Anwer	
Bit Error Rate Analysis for Indoor Optical Wireless Communication System	423
Mansi Gupta, Gagan Agrawal, Namrata Kumari, and Rekha Rani	
An Automatic Self-sufficient Irrigation System Using Microcontrollers	433
Varun Singh Chauhan, Ruchira Singla, and Pallavi Choudekar	
Performance Analysis of Smart PMSM Drive Using SVM Based 3-Level Neutral Point Clamped Inverter	441
Ratan Raju Ravela, Dharmendra Kumar Singh, and Jay Singh	
Performance Analysis of Indoor Visible Light Communication System Using NRZ-OOK Modulation Technique	453
Mohd Faheem, Indra Kumar Verma, Prakhar Nag, Shivam Goswami, and Vinay Singh	
A 73% PAE, Highly Gain Inverse Class-F Power Amplifier for S-Band Applications	467
Jathoth Deepak Naik, Pradeep Gorre, Rajesh Kumar, Sandeep Kumar, and Hanjung Song	

Performance Analysis of Stationary and Moving V2V Communications Using NS3	475
Divyanshu Gupta, Aditi Uppal, Ayushi Walani, Devanshi Singh, and Amanpreet Singh Saini	
COVID-19 Pandemic and Post-pandemic: Impact and Technical Threats in India	485
Aastha Tyagi and Madhu Sharma Gaur	
IoT-Based Automation Irrigation System	501
Rahul Thakur and Jay Singh	
Leaky Wave Antenna for Wide Angle Beam Scanning and High Directivity	511
Ruchi Agarwal, Prakhar Pratap Singh, Suresh Kumar, Umang Singh, and Vipul Agarwal	
Modelling and Simulation of Advance Charging for Electric and Solar Assisted Vehicles	523
Pushpendra Kumar Singh, M. A. Ansari, Nidhi Singh Pal, Jay Singh, and Nivedita Singh	
Design and Performance Analysis of the Ghost-Shaped Antenna for Extremely High-Frequency Applications	533
Madan Kumar Sharma, Nitin Kumar Gautam, Gagan Walia, Ankit Sharma, Nikhil Sachan, and Deepak Kumar	
Design and Comparative Analysis of Photovoltaic Battery Charge Control Techniques in Simulink Environment	545
Santosh Kumar Yadav, Nidhi Singh, M. A. Ansari, and Rohit Kumar	
High Impedance Fault Analysis of Distributed Power System Network Using Discrete Wavelet Transform	561
Abrar Ul Qadir Bhat, Anupama Prakash, Vijay Kumar Tayal, and Pallavi Choudekar	
Implementation of Secured Wired and WLAN Network Using eNSP	577
Amanpreet Singh Saini, Pallavi Gupta, and Harshita Gupta	
Performance of X-Band CMOS LNA with Broadband Approach for 5G Wireless Networks	591
Srihith Kumar Pottam, Raghavendra D. Kabade, T. N. Nikith, Saptarshi Mondal, and Sandeep Kumar	
Design and Analysis of Pattern Reconfigurable MIMO Antenna Using PIFA Structure	603
Ranjana Kumari, Archit Kumar Jha, Anuj Sachan, Aryan Kishan, and Milkey Jain	

Three-Phase Fault Analysis of Distributed Power System Using Fuzzy Logic System (FLS)	615
Abrar Ul Qadir Bhat, Anupama Prakash, Vijay Kumar Tayal, and Pallavi Choudekar	
Design and Analysis of Reconfigurable MIMO Antenna for Wireless Applications	625
Chirag Agrawal, Akshay Pratap Singh, Bisma Ashraf, and Ranjana kumari	
Implementation of Cyclic Reed–Muller Code for Molecular Communication	637
Ruchi Rai, S. Pratap Singh, M. Lakshmanan, and V. K. Pandey	
Design of Cascaded H-Bridge Multilevel Inverter	645
Nitin Pawar, Vijay Kumar Tayal, and Pallavi Choudekar	
Reliability and Energy Efficiency of Ring Frame Machine in Textile Industries: Secure, Smart, and Reliable Network	657
Saurabh Kumar Rajput, Sulochana Wadhvani, and Jay Singh	
Economic Load Dispatch Using Evolutionary Technique	665
Rohit Kumar, Nidhi Singh, M. A. Ansari, and Santosh Kumar Yadav	
VLSI Implementation of Hamming Code for Molecular Communication	685
Ruchi Rai, S. Pratap Singh, M. Lakshmanan, and V. K. Pandey	
Power Analyses in AMBA AHB Protocol and Synthesis Over Xilinx ISE	693
Abhishek Deshwal, Aman Singh, Ashutosh Gupta, P. C. Joshi, and Chiranjeev Singhal	
SPICE Based Design and Implementation of Digital Circuits Using GALEOR Technique	703
Puneet Kumar Mishra, Amrita Rai, Mayank Rai, and Amiya Prakash	
Efficient Energy Allocation Strategies for Various Cooperative Communication Schemes	713
Vivek K. Dethe, Om Prakash, and C. V. Ghule	
Steganography Using Block Pattern Detection in AMBTC Image	723
Neeraj Kumar and Dinesh Kumar Singh	
Analysis of Smart Electricity Grid Framework Unified with Renewably Distributed Generation	735
Vivek Saxena, Narendra Kumar, Uma Nangia, and Jay Singh	

About the Editors

Dr. Rajeev Agrawal is currently working as professor and director at G. L. Bajaj Institute of Technology and Management, Greater Noida, India. He has an illustrated experience of more than 25 years in teaching and research, holds a B.E. degree in Electronics Engineering and M. Tech. degree in System Engineering. He received Ph.D. in the area of Wireless Communication Channels from School of computer & System sciences, JNU, New Delhi. He was visiting professor at Kennesaw State University, Georgia, USA under a joint research projects in the area of Remote Patient Monitoring & Medical Imaging in the year 2010 and 2011. His research areas include planning and performance analysis of wireless networks and medical image analysis for automated diagnosis. He has more than 60 publications in international journals and proceedings. He has been awarded by various state and national agencies for his contribution to research and academics. He is also serving as reviewer for several reputed international journals.

Dr. Chandramani Kishore Singh is currently an assistant professor with the department of electronic systems engineering, Indian Institute of Science, Bengaluru. He received M.E. and Ph.D. degrees in electrical communication engineering from the Indian Institute of Science, Bengaluru, India, in 2005 and 2012, respectively. He worked as a wireless communications engineer in ESQUBE Communications Solutions Pvt. Ltd., Bengaluru, from 2005 to 2006. He was a post-doctoral researcher with TREC, a joint research team between INRIA Rocquencourt and ENS Paris from 2012 to 2013, and with the Coordinated Science Laboratory, University of Illinois at Urbana Champaign, USA, from 2013 to 2014. His research interests include communication networks, data centers, and smart grids. He has published more than 30 papers in respected international journals and conferences. Dr. Chandramani has also received the Microsoft Research India Rising Star Award in 2011.

Dr. Ayush Goyal is working as assistant professor in the department of electrical engineering and computer science at Texas A&M University, Kingsville, Texas. He completed his B.S. in electrical engineering from Boise State University (BSU),

Boise, USA and Ph.D. in computer Science from Oxford University, Oxford, UK. He was a postdoctoral research fellow in the department of computer science, Tulane University, New Orleans, USA. His areas of research interest are neurological disease prediction, brain MRI image analysis and bio-informatics for connected healthcare. He has more than 40 publications in international journals and proceedings. He was awarded Clarendon scholarship to pursue Ph.D. at Oxford University.

Benign–Malignant Mass Characterization Based on Multi-gradient Quinary Patterns



Rinku Rabidas, Romesh Laishram, and Amarjit Roy

Abstract This paper introduces a new descriptor, multi-gradient quinary pattern (M-GQP), for the categorization of breast masses as malignant or benign. The proposed attributes measure local information via local quinary pattern (LQP) based on a five-level encoding scheme from the gradient images obtained using Sobel operator having eight distinct masks at different directions. The gradient magnitude and angle image features provide better consistency and stability in high texture regions like edges and micro-information in different orientations, respectively. The assessment is performed using the mammographic images of the mini-MIAS dataset. A group of salient discriminators are opted via stepwise logistic regression technique, and a cross-validation method with tenfold is leveraged along with Fishers linear discriminant analysis as a classifier to avoid any bias. An A_z value of 0.97 with an accuracy of 90.26% is achieved as the best outcome which is further compared with some of the competing methods in the literature.

Keywords Breast cancer · Mammogram · Mass · Classification · Multi- gradient pattern

R. Rabidas (✉)

Department of Electronics and Communication Engineering, Assam University, Silchar, India

e-mail: rabidas.rinku@gmail.com

R. Laishram

Department of Electronics and Communication Engineering, Manipur Institute of Technology, Takyelpat, India

e-mail: romeshlaishram@gmail.com

A. Roy

Department of Electronics and Communication Engineering, BML Munjal University, Gurgaon, India

e-mail: royamarjit90@gmail.com

© Springer Nature Singapore Pte Ltd. 2021

R. Agrawal et al. (eds.), *Advances in Smart Communication and Imaging Systems*,

Lecture Notes in Electrical Engineering 721,

https://doi.org/10.1007/978-981-15-9938-5_1

1 Introduction

Though rare in male, breast cancer is the most common cancer cases among women worldwide and the second most common type of cancer overall. According to the latest report, new instances of breast cancer registered in the year 2018 were over 2 million [1]. Identification and diagnosis of breast cancer at the preliminary stage is the sole way to improve the survival rate. Although different imaging modalities are available at present, the most preferred method of screening breast cancer is X-ray mammography because other imaging methods like magnetic resonance imaging (MRI) and computed tomography (CT) have their own limitations of being expensive and high radiations, respectively. Several abnormalities which include bilateral asymmetry, architectural distortion, calcification, and mass are the usual symptoms of breast cancer at their early stages. Among these, the identification and characterization of masses are always a tough task because of the variations in size, shape, and margin. In addition to it, the fatigue caused to the radiologists due to the continuous examinations of mammograms, there may be a possibility of human error which can affect severely. Thus, computer-aided detection (CADe) and computer-aided diagnosis (CADx) systems are evolved to support the radiologists as an alternative evaluator.

In general, a mass is determined as malignant or benign based on the shape, margin, and texture information. A round/oval-shaped, smooth edge, and less fatty tissues are considered as benign case in contrast to the malignant ones having undefined margin, non-uniform shape, and high-fat tissues. This hypothesis is exploited by the researchers to introduce different shape-, margin-, and texture-based features for mass classification [2–5]. Though shape [4] and margin information [5] renders significant efficiency, it suffers from the limitation of precise segmentation of masses which is difficult to achieve in case of automatic systems. Therefore, mostly texture-based attributes [2, 6, 7] are preferred in the CADx systems. A comparative study of various attributes based on local textural information for mass categorization is presented in [8]. Haralick's texture measures generated from gray-level co-occurrence matrix (GLCM) of the rubber band straightening transform (RBST) images, proposed by Sahiner et al. [7], reported an area under the receiver operating characteristic (ROC) curve (A_z value) of 0.94 utilizing 160 mammographic images. The oriented patterns are investigated via radial local ternary pattern (RLTP), proposed by Muramatsu et al., and observed an A_z value of 0.90 [9]. Multi-resolution analysis of angular patterns is evaluated for the classification and observed an A_z value of 0.86 with 433 DDSM images [6]. Local binary pattern (LBP) with Zernike moments has also been successfully evaluated on mass classification of 160 mammograms having an efficiency of 0.96 [10]. Rabidas et al. analyzed the discontinuities by Ripplet-II transform and observed an A_z value of 0.91 [11]. Local descriptor-based curvelet transform are also inspected to diagnose the masses which delivered an efficiency of 0.95 with 200 mammograms [3]. Though various methods of mass characterization are reported in the literature, none assures complete success. Hence, in this paper, a new texture feature, multi-gradient quinary pattern (M-GQP), is proposed where

local measures are computed from the gradient images using LQP which offers more consistency in measuring gradient information from uniform and near-uniform areas. In addition, the extracted descriptors are also robust to illuminations. The gradient images, in both magnitude and angle, are obtained using Sobel operator having eight distinct masks at different directions as of result it provides better resolution in edge regions in addition to the micro-information at different orientations.

The paper is arranged as follows: The introduction of the mini-MIAS database is briefly provided in Sect. 2 followed by the methodology for mass classification in Sect. 3. The details about the experimental setup and the assessment of the result are discussed in Sect. 4. Lastly, the paper is concluded with the future scope of work in Sect. 5.

2 Database

To assess the proficiency of the introduced attributes, several experiments are performed utilizing the mammographic screenings of the mini-MIAS database—a widely used database by the researchers. This database is collected and managed by the Mammographic Image Analysis Society, London, UK [12]. The size of the mammograms is 1024×1024 and is digitized at $200 \mu\text{m}/\text{pixel}$ with 8 and 16 bits/pixel as gray-level resolution. Excluding the other anomalies, out of 59 mass cases, 20 malignant and 38 benign cases are selected in the present work. The annotations of the anomalies are attached along with the database.

3 Methodology

Since the texture of malignant and benign masses varies remarkably, in this paper, the discriminating textural information is measured via the proposed attributes, multi-gradient quinary patterns, for the determination of mammographic masses as malignant or benign. From the extracted descriptors, a subset of optimal features is opted out using a feature selection technique followed by a classifier for evaluation of the introduced attributes. The schematic layout of the proposed approach for benign–malignant mass categorization is demonstrated in Fig. 1.

3.1 Selection of ROIs

The distance between text and figure should be about 8 mm, and the distance between figure and caption about 6 mm. The annotations defining the mass lesions are provided along with the mini-MIAS database where the anomalies are marked by a circle with

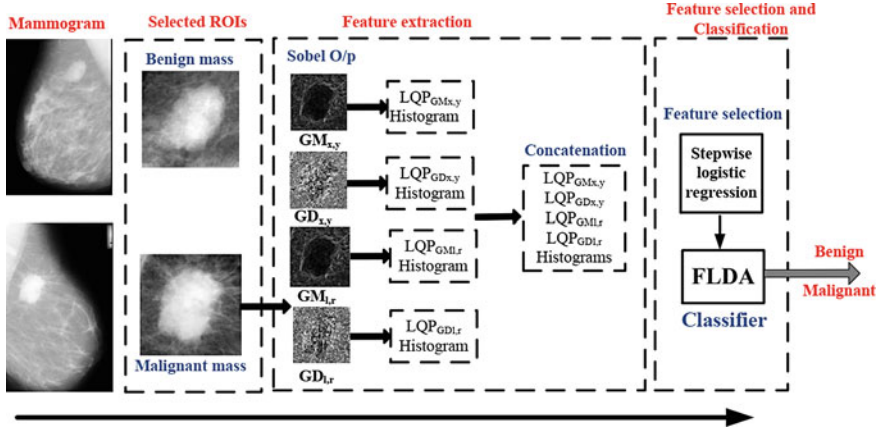


Fig. 1 Schematic layout of the introduced approach for benign-malignant mass classification

a predefined radius that encloses the mass lesion with its center at the middle. Considering 10 pixels more to the predefined radius, a region in square shape, covering the complete mass region, is chosen and termed as region of interests (ROIs). The sample images of the selected ROIs for both the malignant and benign masses are shown in selected ROIs section of Fig. 1.

3.2 Feature Extraction

Since features perform a key role in CADx systems, computation of salient attributes is also a challenging task. Considering the fact that the texture of malignant and benign masses varies remarkably, thus, in this study, a new descriptor, multi-gradient quinary pattern (M-GQP), is proposed where local information based on a five-level encoding scheme is measured from the gradient images. The gradient magnitude image measures render high consistency and stability in high texture regions like edges against the normal texture images in contrast to the gradient angle image which provides micro-information in different orientations. Moreover, the attributes extracted from gradient images are also robust to illuminations. Being simple, effective, and computationally efficient, Sobel operator is preferred with eight different masks at distinct directions (see Fig. 2) to obtain the two types of gradient images in lr and xy directions [13].

The convolution operation of an image patch with the east (e) and north (n) Sobel masks gives gradient relations of magnitude and angle along xy direction of the center pixel.

$$\begin{aligned}
 G_x(e) &= (p_o + 2p_1 + P_2) - (p_6 + 2p_7 + p_8) \\
 G_y(n) &= (p_o + 2p_3 + P_6) - (p_2 + 2p_5 + p_8)
 \end{aligned} \tag{1}$$

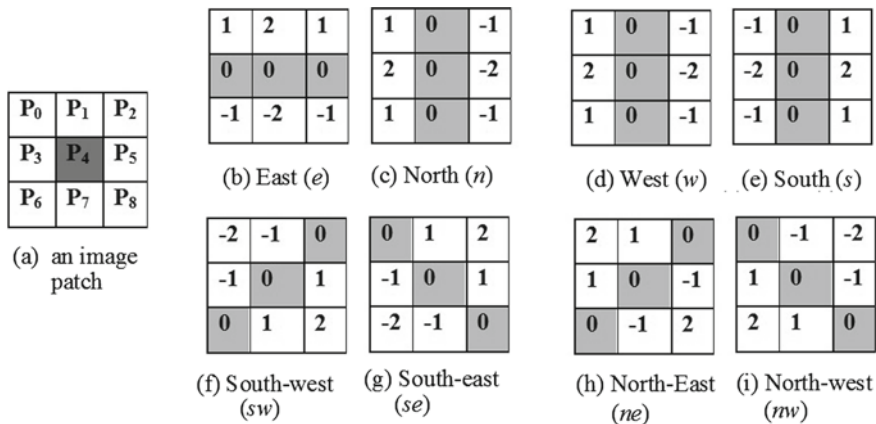


Fig. 2 Demonstration of different masks in different orientations

where $G_x(e)$ and $G_y(n)$ denote the gradient of the center pixel P_4 in horizontal and vertical directions, respectively. The gradient magnitude (GM_{xy}) and angle ($\theta_1(x, y) \in [0, \pi]$) components of the pixel P_4 along the north and east direction are calculated as follows:

$$GM_{xy}(e_n) = |G_x(e)| + |G_y(n)|; \quad \theta_1(x, y) = GD_{xy}(e_n) = \tan^{-1}\left(\frac{G_y(n)}{G_x(e)}\right) \quad (2)$$

The two other gradients using west (*w*) and south (*s*) Sobel masks can be obtained as:

$$G_x(w) = -G_x(e); \quad G_y(s) = -G_y(n) \quad (3)$$

Similarly, the gradient magnitude and angular components in the *lr* direction can be obtained through convolution of the image patch with southeast (*se*) and southwest (*sw*) Sobel masks as follows:

$$\begin{aligned} G_l(se) &= (p_1 + 2p_2 + P_5) - (p_3 + 2p_6 + p_7) \\ G_r(sw) &= (p_5 + 2p_8 + P_7) - (2p_0 + p_1 + p_3) \end{aligned} \quad (4)$$

where $G_l(se)$ and $G_r(sw)$ represent the gradient of the pixel P_4 along the left diagonal mask direction and right diagonal mask direction, respectively. In the similar way, by convolving with the northeast (*ne*) and northwest (*nw*) Sobel masks, we can calculate the other two gradients in the *lr* direction, but due to mirror symmetry it can be obtained as follows:

$$G_l(nw) = -G_l(se); \quad G_l(ne) = -G_l(sw) \quad (5)$$

Then, the gradient magnitude (GM_{lr}) and angle ($\theta_2(l, r) \in [0, \pi]$) of the pixel P_4 in the southwest and southeast direction are calculated as follows:

$$GM_{lr}(se_sw) = |G_l(se)| + |G_r(sw)|; \quad \theta_2(l, r) = GD_{lr}(se_sw) = \tan^{-1} \left(\frac{G_l(se)}{G_r(sw)} \right) \quad (6)$$

The different illustrations of malignant and benign masses in terms of gradient magnitude and angle representations are shown in Fig. 4.

These gradient images are further utilized to extract local measures via local quinary pattern (LQP) which offers consistency in near-uniform as well as uniform regions. Due to the five-level encoding scheme of LQP, it overcomes the limitations of LBP and its extended version local ternary pattern (LTP) [14]. The expression for five-level encoding of the texture image along with its splitting in different LBPs is given below:

$$d(I_p, I_c, T_1, T_2) = \begin{cases} +2, & I_p \geq (I_c + T_2) \\ +1, & (I_c + T_1) \leq I_p < (I_c + T_2) \\ 0, & (I_c - T_1) \leq I_p < (I_c + T_1) \\ -1, & (I_c - T_2) \leq I_p < (I_c - T_1) \\ -2, & \text{otherwise} \end{cases}$$

$$d_l(x) = \begin{cases} 1, & x = l, \quad l \in [-2, -1, 0, +1, +2] \\ 0, & \text{otherwise} \end{cases} \quad (7)$$

where I_c represents the intensity of the center pixel with I_p as its neighboring pixels. T_1 and T_2 are the thresholds for five-level quantization of the neighboring pixels which is further decomposed to observe LBPs as shown in Fig. 3. The histogram of LBPs obtained from the different gradient images (both angle and magnitude) at various orientations is concatenated to configure the final set of features of that image

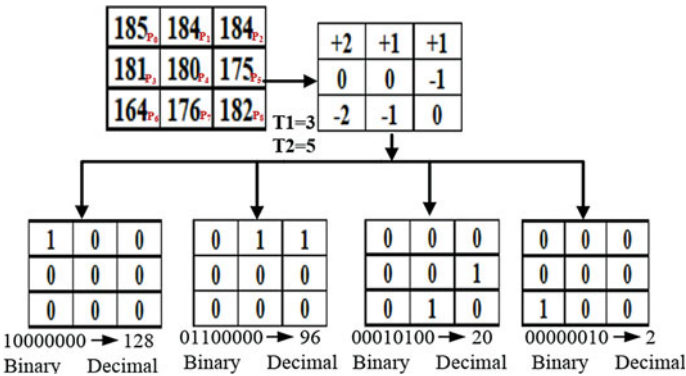


Fig. 3 Illustration of five-level code generation for LQP

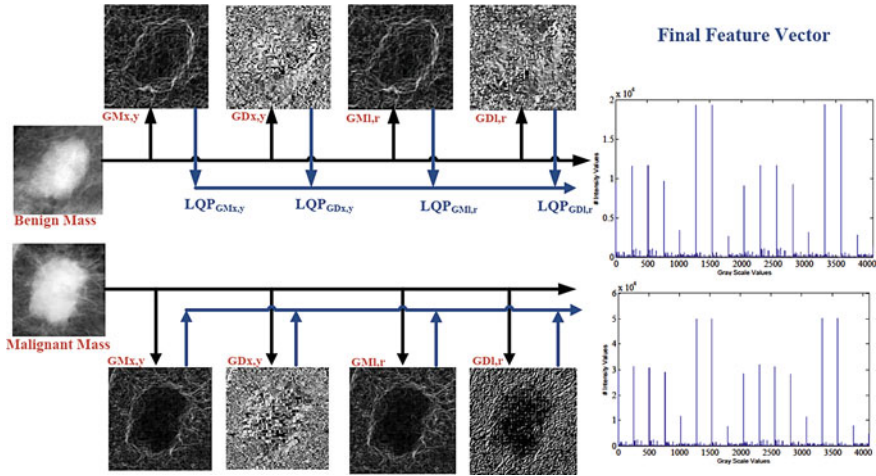


Fig. 4 Different illustrations of malignant and benign masses

(see Fig. 4) having length as 16×2^P where P defines the number of neighboring pixels. The distance between text and figure should be about 8 mm.

3.3 Selection of Features and Categorization

A large number of attributes are measured from the feature extraction step where all the computed measures do not carry remarkable discriminating potential for the determination of masses as malignant or benign. Moreover, it may lead to over-fitting problem. Hence, to filter the significant features, stepwise logistic regression technique [15] is employed. Being simple and effective, Fisher's linear discriminant analysis (FLDA) [16] is utilized as a classifier for decision making.

4 Experimental Setup, Results, and Discussion

The assessment of the introduced CADx system is carried out using MATLAB software on a personal computer. It comprises Intel(R) Core™ i3 processor with 2.27 GHz frequency and 4 GB RAM. The performance evaluation matrix includes accuracy (A_{cc}) in percentage and A_z value to examine the efficiency of the proposed features. To avoid bias, if any, in the CADx system, cross-validation technique with tenfold is incorporated along with FLDA which is repeated for ten times and finally, the average of all the runs is reported as the outcome of the system.

Table 1 Average of accuracy (A_{cc}) and A_z value for proposed feature set having different values of thresholds— T_1 and T_2

Feature set (T_1, T_2)	A_z	A_{cc} (%)	#FS*
M-GQP _{1,3}	0.97 ± 0.02	90.26 ± 0.02	5
M-GQP _{1,4}	0.90 ± 0.01	80.96 ± 0.01	6
M-GQP _{1,5}	0.93 ± 0.01	88.90 ± 0.01	5
M-GQP _{2,4}	0.96 ± 0.01	87.83 ± 0.02	5
M-GQP _{2,5}	0.81 ± 0.02	78.90 ± 0.03	6
M-GQP _{3,5}	0.91 ± 0.01	85.93 ± 0.02	6
M-GQP _{3,6}	0.89 ± 0.01	84.40 ± 0.02	7

*# FS indicates number of features selected

Bold indicates the best results in the table

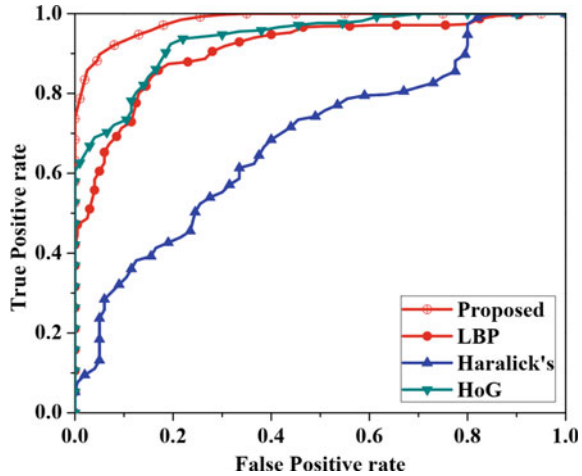
The performance evaluation is conducted by varying the thresholds— T_1 and T_2 while keeping the parameters, R and P , constant with values 1 and 8, respectively, to avoid larger feature set. The final outcome of the proposed features with all the variations is provided in Table 1 where it can be noticed that unit difference in threshold values offers better efficiency and an A_z value of 0.97 with an accuracy of 90.26% is achieved as the best result. This optimum output is further compared with other competing methods reported in the literature as listed in Table 2 where it clearly establishes its supremacy over other techniques. Moreover, a comparison of the ROC curves with the proposed attributes against LBP [17], Haralick's [18], and histogram of oriented (HoG) [19] pattern features having an efficiency of 0.91, 0.68, and 0.93, respectively, is also illustrated in Fig. 5 which effectively demonstrates the superiority of the introduced descriptors.

Table 2 Proposed approach is compared with other recently developed competing schemes in terms of A_z value

Methods	A_z
M-GQP _{1,3} (proposed)	0.97
Nascimento et al. [20]	0.96
Rabidas et al. [11]	0.91
Muramatsu et al. [9]	0.90
Serifovic-Trbalic et al. [21]	0.89
Midya and Chakraborty [6]	0.86

Bold indicates the best results in the table

Fig. 5 Illustration of different ROC curves observed with various feature sets



5 Conclusion

In the present work, a new texture attribute, M-GQP, is introduced for the determination of breast masses as malignant or benign. Gradient images obtained after employing eight different masks of Sobel operator in various directions provide microscopic information along with better consistency in the high texture lesions like edges due to which it possesses significant categorizing potential in benign–malignant mass classification and outperforms some of the competing technique in the literature. The larger feature set is the limitation of this methodology which can be mitigated by using efficient feature selection technique. Hence, the authors are in a process to examine a suitable combination of feature selection technique and classifier on other larger databases.

References

1. Fund WCR (2019) Breast cancer statistics. <https://www.wcrf.org/dietandcancer/cancertrends/breast-cancer-statistics>. Accessed on Apr 2019
2. Rabidas R, Midya A, Chakraborty J (2018) Neighborhood structural similarity mapping for the classification of masses in mammograms. *IEEE J Biomed Health Inform* 22:826–834
3. Rabidas R, Midya A, Chakraborty J, Sadhu A, Arif W (2018) Multi-resolution analysis using integrated microscopic configuration with local patterns for benign malignant mass classification. In: *Proceedings of SPIE medical imaging*, p 105752N
4. Tahmasbi A, Saki F, Shokouhi SB (2011) Classification of benign and malignant masses based on Zernike moments. *Comput Biol Med* 41:726–735
5. Wei CH, Chen SY, Liu X (2012) Mammogram retrieval on similar mass lesions. *Comput Methods Programs Biomed* 106:234–248

6. Midya A, Chakraborty J (2015) Classification of benign and malignant masses in mammograms using multi-resolution analysis of oriented patterns. In: 12th international symposium on biomedical imaging (ISBI), Apr 2015, pp 411–414
7. Sahiner BS, Chan HP, Petrick N, Helvie MA, Goodsitt MM (1998) Computerized characterization of masses on mammograms: the rubber band straightening transform and texture analysis. *Med Phys* 24:516–526
8. Rabidas R, Midya A, Chakraborty J, Arif W (2016) A study of different texture features based on local operator for benign-malignant mass classification. *Procedia Comput Sci* 93:389–395 (2016) (Proceedings of the 6th International Conference on Advances in Computing and Communications)
9. Muramatsu C, Hara T, Endo T, Fujita H (2016) Breast mass classification on mammograms using radial local ternary patterns. *Comput Biol Med* 72:43–53
10. Laroussi M, Ben Ayed N, Masmoudi A, Masmoudi D (2013) Diagnosis of masses in mammographic images based on Zernike moments and Local binary attributes. In: World congress on computer and information technology (WCCIT), pp 1–6
11. Rabidas R, Chakraborty J, Midya A (2016) Analysis of 2D singularities for mammographic mass classification. *IET Comput Vis* 11(1):22–32
12. Suckling J (1994) The mammographic image analysis society digital mammogram database *exerpta medica*. *Int Congr Ser* 1069:375–378
13. Al-Sumaidae S, Abdullah M, Al-Nima R, Dlay S, Chambers JA (2017) Multigradient features and elongated quinary pattern encoding for image-based facial expression recognition. *Pattern Recogn* 71:249–263
14. Nanni L, Lumini A, Brahnam S (2012) Survey on LBP based texture descriptors for image classification. *Expert Syst Appl* 39:3634–3641
15. Ramsey FL, Schafer DW (1997) *The statistical sleuth: a course in methods of data analysis*. Duxbury Press, CA
16. Duda RO, PH, Stork GD (2001) *Pattern classification*, 2nd edn. Wiley Interscience, New York
17. Ojala T, Pietikainen M, Maenpaa T (2002) Multiresolution gray-scale and rotation invariant texture classification with local binary patterns. *IEEE Trans Pattern Anal Mach Intell* 24:971–987
18. Haralick R, Shanmugam K, Dinstein I (1973) Textural features for image classification. *IEEE Trans Syst Man Cybern* 3:610–621
19. Pomponiu V, Hariharan H, Zheng B, Gur D (2014) Improving breast mass detection using histogram of oriented gradients. In: *SPIE medical imaging—2014: computer aided diagnosis*, vol 9035, Mar 2014, pp 90351R–90351R
20. do Nascimento MZ, Martins AS, Neves LA, Ramos RP, Flores EL, Carrijo GA (2013) Classification of masses in mammographic image using wavelet domain features and polynomial classifier. *Expert Syst Appl* 40:6213–6221
21. Serifovic-Trbalic A, Trbalic A, Demirovic D, Prljaca N, Cattin P (2014) Classification of benign and malignant masses in breast mammograms. In: *37th international convention on information and communication technology, electronics and microelectronics (MIPRO)*, May 2014, pp 228–233

Improved Switching Vector Median Filter for Removal of Impulse Noise from Color Images



Amarjit Roy, Snehal Chandra, and Rinku Rabidas

Abstract Image noise is defined as the random variation of color information or intensity in images. It is recognized as a type of electronic noise. Impulse noise is a “high level-low level” noise that affects an image abruptly. A filtering technique defined as an improved switching vector median filter (ISVMF) is proposed for removing impulse noise from color images in this manuscript. The performance analysis has been done for varied noise densities. Though performance has been shown in terms of Lena images, it delivers improved results irrespective of variation of images. The performance comparison has been done on the basis of standard metrics like peak signal to noise ratio (PSNR) and structural similarity index (SSIM), etc. It is observed that the proposed improved switching vector median filter (ISVMF) provides better results both visually and statistically as compared to the other conventional filtering techniques. This better performance may be due to the fact that the threshold has been localized rather than generalized in the filter resulting in better homogeneity across the various sections of the image.

Keywords Image noise · Impulse noise · Vector median filter · ISVMF · PSNR · SSIM

A. Roy (✉) · S. Chandra

Department of Electronics and Communication, BML Munjal University, Gurgaon, Haryana, India
e-mail: royamarjit90@gmail.com

S. Chandra

e-mail: snehalchandra31@gmail.com

R. Rabidas

Department of Electronics and Communication, Assam University, Silchar, Assam, India
e-mail: rabidas.rinku@gmail.com

© Springer Nature Singapore Pte Ltd. 2021

R. Agrawal et al. (eds.), *Advances in Smart Communication and Imaging Systems*,
Lecture Notes in Electrical Engineering 721,
https://doi.org/10.1007/978-981-15-9938-5_2

1 Introduction

An image is a visual representation that has been stored and created in an electronic form. For image processing, different types of filtering techniques are used depending upon the requirements. The most traditional approach in this regard is considered as the application of median filter. This filter is a single-step filtering technique. It is applied on every pixel of a gray image irrespective of whether it is corrupt or not. The median of a given kernel is found out and the pixel under operation gets substituted by the calculated median. The principle of VMF filter is discussed in this section that is applicable for R-G-B images in which the pixel comprises of three components namely red (R), green (G), and blue (B). This filtering technique determines the vector distance between the corrupt pixels with each pixel in a given kernel and then replaces the corrupt pixel with the least vector distance. This is done in order to maintain the homogeneity of an image. The vector distance is calculated by the following general formula given as:

$$d = \sqrt{(XR^* - XR)^2 + (XB^* - XB)^2 + (XG^* - XG)^2} \quad (1)$$

where, the pixel to be operated is defined by: X^* and using the pixel X , the vector distance is being determined. The major drawback of the conventional VMF filtering technique that it operates on every pixel irrespective of whether it is corrupt or not which results in unnecessary wastage of time and machine cycles.

A lot of image denoising algorithms are available in the literature for removing impulses from corrupted images. An adaptive switching median (ASWM) filter [1] works on a localized threshold value which delivers improved results considering parameters like MAE and PSNR in comparison with median filtering algorithms. A SVM-based fuzzy filter [2] showed a great improvement in PSNR for the images corrupted by high density noise. An advanced technique for removing impulse noise with adaptive dual thresholds [3] has been further improved by the introduction of an adaptive support vector-based classification filter (ASVC) [4]. It is suggested to revise the existing techniques by implementation of new methodology in them [5]. A mathematical tool derived using robust estimation theory is used to develop nonlinear filters to provide excellent robustness properties [6]. In center weighted median (CWM), more weight is being provided at the central pixel so as to achieve superior performance. It is observed that more image information is restored with better visual perception [7]. A filter having switching procedure based on the local measurements of impulses yielded better results [8]. In another technique, using Laplacian operator, minimum value from the obtained convolutions is calculated in one-dimensional way [9]. Noise ranking switching filter (NRSF) outperforms several advanced filtering techniques that preserves more textural information with more edge details [10]. The switching bilateral filter (SBF) incorporates an improved noise detector that is utilized to detect both impulse as well as Gaussian noise [11]. In boundary discriminative noise detection (BDND), two different noise detection

techniques have been incorporated which in turn improves the performance not only in detection but also in noise removing capability [12]. A superior technique for removal of impulses from gray images is based on SVM classification has been proposed by Roy et al. [13]. Region adaptive fuzzy filter that utilizes the channel difference information for re-construction of channel information has been proposed in the paper [14]. This filtering technique is very useful for random valued impulse noise.

This research paper proposes a dynamic and robust image filtering technique for getting the image of optimum quality. The section organization is as follows; Sect. 2 comprises of the proposed filtering technique implementation, Sect. 3 elaborates results and discussions, and Sect. 4 concludes the chapter.

2 Improved Switching Median Filter (ISVMF)

The proposed methodology has incorporated the switching scheme of adaptive switching median (ASWM) filter [1] with vector median filter. First, detection is done according to ASWM and after that a VMF is processed on each pixels so as to remove the noise. At low density impulse noise, VMF with (5×5) is applicable. In contrast, at high density impulse noise, VMF with (7×7) window offers enhanced performance irrespective of images.

Detection of noise [1] is started with the calculation of the weighted standard deviation and weighted mean in the current kernel. The weights are in an inverse relation with the distance between weighted mean of pixels in the given kernel and pixel under operation. In each kernel, in an iterative manner the weighted mean is calculated. Then, by calculating the weighted standard deviation, the localized threshold is determined. This algorithm is explained in the following steps:-

Initial Stage: Consider a window W of size $[(2Q + 1) \times (2Q + 1)]$ whose weighted mean.

M_w is calculated for the pixels around the pixel under operation.

$$M_w(i,j) = \frac{\sum_{k,l} W_{k,l} X_{i+k,j+l}}{\sum_{k,l} W_{k,l}} \quad (2)$$

where $X_{i,j}$ is the pixel value and $W_{k,l}$ the weights. All these weights are equal to 1 at initial stage. The variation of index k and l is in the range of $[-Q, Q]$.

Step 1: The required weights are calculated as

$$W_{k,l} = \frac{1}{|X_{i+k,j+l} - M_w(i,j) + \delta|} \quad (3)$$

\square is a pre-determined small value, which is used by the denominator to avoid a possible indeterminate form. Then, a new weighted mean is determined by using (1).

Step 2: If, $|M_w(i, j)^t - M_w(i, j)^{t-1}| < \varepsilon$ where ε is an experimentally determined value, then the iteration is stopped, otherwise, start again from the first step.

($M_w(i, j)^t$ is the calculated weighted mean at any given iterative stage).

Next, the weighted standard deviation $\sigma_w(i, j)$ is given as:

$$\sigma_w(i, j) = \sqrt{\frac{\sum_{k,l} W_{k,l} (X_{i+k, j+l} - M_w(i, j))^2}{\sum_{k,l} W_{k,l}}} \quad (4)$$

The above steps are performed separately for each of the three components (red, blue, and green) of a pixel in a color image. Finally, ISVMF can be summarized in the following way:

1. Determine $\sigma_w(i, j)$ and $M_w(i, j)$, which are the weighted standard deviation and weighted mean respectively of the kernel comprising of the pixel under operation for each component of red, green, and blue.
2. The following rule is used for each of the RGB component of each pixel:

$$Y_{i,j} = \begin{cases} m_{i,j}, & \text{if } |X_{i,j} - M_{i,j}| > \alpha \times \sigma_w(i, j) \\ X_{i,j}, & \text{otherwise} \end{cases} \quad (5)$$

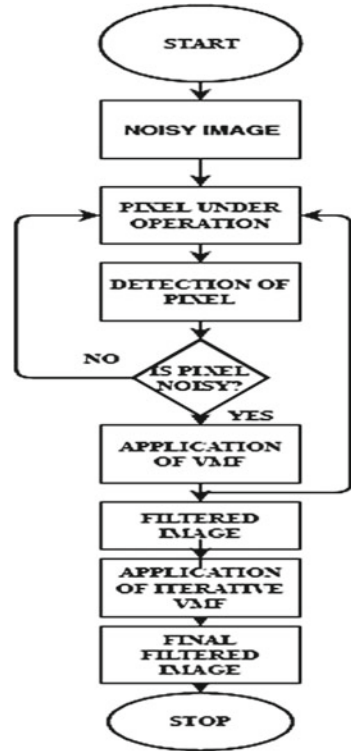
where $m_{i,j}$ is median of the kernel, α a given parameter and $\alpha \times \sigma_w(i, j)$ represents the localized threshold value. ISVMF is applied in a repetitive fashion. During each iteration stage in a given window, the threshold gets decreased. This is achieved by varying α value. Simulations performed on various standard images showed that the following strategy gives optimum results, which is given as:

$$\alpha_0 = 20; \alpha_{n+1} = \alpha_n \times 0.8 (n \geq 0) \quad (6)$$

where α_0 is the α parameter at initial stage and α_n the parameter in the n th step.

After detection of noise (Eqs. 2–6), VMF is processed over the image. An experiment has been performed for the selection of window size. Up to 40% of impulse noise VMF with 5×5 window is applicable, whereas beyond this a 7×7 window is applied. After completion of this stage, VMF is again applied so as to achieve final filtered image. This is done because some noisy pixels have not been detected in the earlier stage (Fig. 1).

Fig. 1 Flowchart for the proposed filtering technique (ISVMF)



3 Results and Discussion

Under this section, we are doing a comparison of the performance of conventional VMF and ISVMF on the basis of the following standard parameters:

1. Mean square error (MSE)
2. Structural similarity index (SSIM)
3. Peak signal to noise ratio (PSNR).

Among these parameters, PSNR should be high, MSE should be low, whereas the values of SSIM should be more and nearer to 1 (Figs. 2, 3 and Tables 1, 2, 3, 4, 5).

After analyzing the mathematical and visual results, it was observed that a bigger window size performed because of the presence of more number of non-corrupt pixels due to which the noise density becomes less, resulting in a clearer image. It has been observed that Fig. 4b provides more improved performance in comparison with Fig. 4a with less blurring effect also. This was proved as the various standard parameters of image processing like PSNR, MSE, and SSIM were found to be better in those cases. Hence, the proposed ISVMF was found to be more efficient than the conventional VMF technique for filtering of impulse noise from color images.

Fig. 2 **a** Original “Lena” image, **b** original “Lena” image



Fig. 3 **a** Image with 50% noise, **b** image with 50% noise

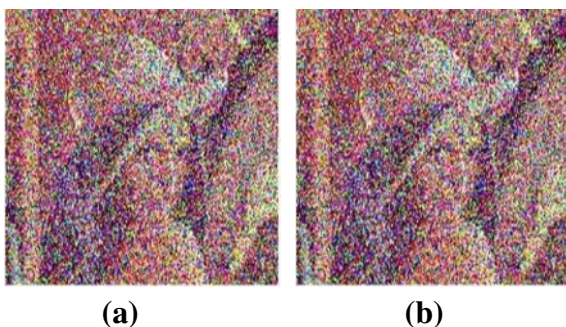


Table 1 Observation table for kernel size 5 * 5 of PSNR

Noise density	PSNR	
	VMF	ISVMF
20	17.6212	36.6632
30	16.6092	34.1920
40	13.5764	31.3951
50	11.6432	26.2427
60	9.7941	24.1143
70	8.2878	20.1392
80	7.1054	18.7065

4 Conclusion

After going through the different tables, observations, and the related parameters, we can conclude that if the noise density is low then a smaller window would provide us with an optimum quality image and if noise density is high, then in that case a larger window would provide with an optimum quality image. A better filter can be developed if a localized threshold is used rather than a generalized threshold in a

Table 2 Observation table for kernel size $5 * 5$ of SSIM

Noise density	SSIM	
	VMF	ISVMF
20	0.5920	0.9133
30	0.5709	0.8939
40	0.5501	0.8594
50	0.5411	0.8102
60	0.5301	0.7820
70	0.5127	0.7403
80	0.5502	0.7119

Table 3 Observation table for kernel size $7 * 7$ of PSNR

Noise density	PSNR	
	VMF	ISVMF
20	15.5785	35.5507
30	14.8831	33.0157
40	14.5314	30.0015
50	12.2565	28.2363
60	10.2948	26.4176
70	8.5232	24.0463
80	7.1490	21.5625

Table 4 Observation table for kernel size $7 * 7$ of SSIM

Noise density	SSIM	
	VMF	ISVMF
20	0.6621	0.9433
30	0.6421	0.9311
40	0.6312	0.89010
50	0.6210	0.8533
60	0.6101	0.8013
70	0.4952	0.7817
80	0.4872	0.7511

filtering technique. The maximum value of SSIM can be 1 which is possible only when two identical sets of data are compared.

As a future scope, the performance of this filter can further be enhanced by making it adaptive in nature as the randomness of the impulse noise varies from region to region. This will involve determining the noise density in a given image and then

Table 5 Comparison of performance of various filtering techniques in removing impulse noise from Lena image

Filters	Noise density			
	20	40	60	80
SBF	25.3293	20.9587	19.3982	16.4921
BDNDF	30.1956	28.1822	26.0291	21.2204
SVMCF	34.7142	28.0857	23.9013	20.2054
VMF	17.6212	14.5314	10.2948	7.1490
ISVMF	36.5507	31.3951	26.4176	21.5625

Fig. 4 **a** VMF filtered image, **b** ISVMF filtered image

selecting a suitable kernel size and other parameters for the filtering of the image justifying the adaptive approach of the filter developed.

References

1. Akkoul S, Lédée R, Leconge R, Harba R (2010) A new adaptive switching median filter. *IEEE Sig Process Lett* 17:587–590
2. Roy A, Singha J, Devi SS, Laskar RH (2016) Impulse noise removal using SVM classification based fuzzy filter from grayscale images. *Sig Process* 128:262–273
3. Gupta V, Chaurasia V, Shandilya M (2015) Random-valued impulse noise removal using adaptive dual threshold median filter. *J Vis Commun Image R* 262:96–304
4. Lin T, Yeh CT, Liu MK (2010) Application of SVM-based filter using LMS learning algorithm for image denoising. *Lecture Notes in Computer Science*, vol 6444. Springer, Berlin
5. Tukey JW (1997) *Exploratory data analysis*, 1st edn. Addison-Wesley, Menlo Park
6. Pitas I, Venetsanopoulos AN (1992) Order statistics in digital image processing. *Proc IEEE* 80(12):1893–1921
7. Ko SJ, Lee YH (1991) Center weighted median filters and their applications to image enhancement. *IEEE Trans Circuits Syst* 38:984–993
8. Sun T, Neuvo Y (1994) Detail preserving median based filters in image processing. *Pattern Recognit Lett* 15(4):341–347
9. Shuqun A, Karim MA (2002) A new impulse detector for switching median filters. *IEEE Signal Process Lett* 9(11):360–363

10. Chou HH, Hsu LY (2015) A noise-ranking switching filter for images with general fixed-value impulse noises. *IEEE Signal Process* 106:198–208
11. Jia-Shiuan CHL (2010) Switching bilateral filter with a texture noise detector for universal noise removal. *IEEE Trans Image Process* 19(9):2307–2320
12. Iyad F, Rami AL (2013) Efficient improvements on the BDND filtering algorithm for the removal of high-density impulse noise. *IEEE Trans Image Proc* 22:1223–1232
13. Roy A, Laskar RH (2015) Impulse noise removal based on SVM classification. In: *Proceedings of IEEE TENCON*, pp 1–5
14. Roy A, Manam L, Laskar RH (2018) Region adaptive fuzzy filter: an approach for removal of random-valued impulse noise. *IEEE Trans Ind Electron* 65:7268–7278

Optimal Orientation Controller Design for F-16/MATV Using Robust and Discrete Linear–Quadrature–Gaussian (LQG) Controller



G. Kassahun Berisha and Parvendra Kumar

Abstract A novel approach presents here robust orientation controller design for nonlinear F-16/MATV flight control system. A nonlinear flight system is linearized by feedback linearization with Taylor series expansion. An optimal LQG controller is designed to obtain the favorable steady state flight condition. The comparison between continuous and discrete LQG is fully discussed for the flight control system. First, the continuous LQG controllers with optimal parameters are designed for continuous time state space which represents the flight dynamic system based on separation principle. Secondly, the designed optimal LQG controller requires a very large controller gain to obtain the design objective, which generate deficiencies in term of high sensitivity and leads to the highly cost system. This leads to design a controller for discrete time state space by the discrete LQG controller and represents the flight control system. After implementing this controller into the system in MATLAB Simulink environment, using a singular value decomposition technique, it is founded that the performance and robustness of the design objective are satisfied.

Keywords Robust controller · Optimal LQG · Discrete LQG · Robustness · Sensitivity · Performance · Feedback linearization

Nomenclature

AFFTC Air-Force-Flight-Test-Center
AOA Angle-of-Attack
GE General Electric
LFWC Lockheed Fort Worth Company
LQE Linear–Quadratic Estimator

G. Kassahun Berisha · P. Kumar (✉)
Electrical and Computer Engineering Department, Wolaita Sodo University, Sodo, Ethiopia
e-mail: parvendraitr@gmail.com

G. Kassahun Berisha
e-mail: kassahunberisha@gmail.com

© Springer Nature Singapore Pte Ltd. 2021
R. Agrawal et al. (eds.), *Advances in Smart Communication and Imaging Systems*,
Lecture Notes in Electrical Engineering 721,
https://doi.org/10.1007/978-981-15-9938-5_3

LQG	Linear–Quadratic–Gaussian
LQR	Linear–Quadratic Regulator
MATV	Multi Axis Thrust Vectoring
TES	Test and Evaluation Squadron
VISTA	Variable Stability In-flight Simulator Test Aircraft
WL	Wright Laboratory

1 Introduction

To design the control rule for the aerospace system and deliberating applications has developed an illustrious investigation area in past years with its extensive applicability in industries and the academic world [1]. The paper presents here, a novel control scheme which is designed and discovered for F-16/MATV. The MATV program has been a joint effort by LFWC, AFFTC, Wright Laboratory, General Electric, and the 422nd TES. This program consists of incorporating a MATV nozzle system with VISTA/F-16 aircraft [2]. To validate envelope of flight, development beyond the normal F-16 AOA bounds, and to estimate possible planned well-being grown by using vectoring of thrust in air-2-air battle, an incorporated scheme is used in aircraft test [3–5].

A LQG control problem is a common fundamental control problem in control engineering [6]. An indeterminate linear system with white Gaussian noise is concern here, which having incomplete state evidence and undertaking control ingredient to quadratic costs. Additionally, the matchless solution establishes control law by linear dynamic feedback for easily calculated and employed. Thus, the LQG controller also works as fundamental to disturbed nonlinear systems of optimal control [7]. The combination of Kalman filter and the LQR makes a controller in the form of LQG. The separation principle can give the guarantees for independently design and computation. Applications of LQG control are in LTI system as well as in LTV systems. The applications for the LTI system are most common and for LTV systems allow the design of controllers with linear feedback by nonlinear indeterminate schemes [8].

Fine robustness properties cannot ensure automatically by optimal LGQ. After designing the LQG controller, by the close loop, property stability in a robust way must be checked separately. To encourage robustness, few system parameters may be predictable stochastic instead of deterministic [9]. A similar optimal controller may be used for more complicated control problem with the different controller parameters. Intentionally, the closed loop transfer function of the system should be close to that of the model [10]. Consequently, for a nonlinear F-16/MATV fighter aircraft, a new controller came into the picture to enhance the problem of classical control method [11]. The controller employs the LQG with LQE and optimal regulator. It was applied to minimize the mean-squared estimation error and for achievement of

better performance. The good robustness characteristic of the LQG controller was checked [12].

To designing an optimal dynamic regulator, the LQG control is a recent time domain technique. It provides the direct control for control effort, regulation performance, and to consider the process as well as measurement noise. Similar to the pole placement method, the state space model of a plant is necessary for LQG design. Researchers do a lot of efforts to design a well-organized control scheme for the flight control system, as stated in [13–15] using the LQG controller.

2 System Dynamics and Controller Design

System dynamics are explained by the following parts, which are given as below.

2.1 F-16/MATV Dynamics

Dynamics of aircraft motions are shown in Fig. 1.

An orientation vector describes the aircraft dynamics by $\Phi = (\varphi, \theta, \psi)^T$, where, φ , θ and ψ are the roll, pitch, and yaw angle correspondingly in an earth-fixed coordinate system. An equation of motion (Newton’s second law) for the aircraft is of three scalars with first-order differential equation of orientation control dynamics.

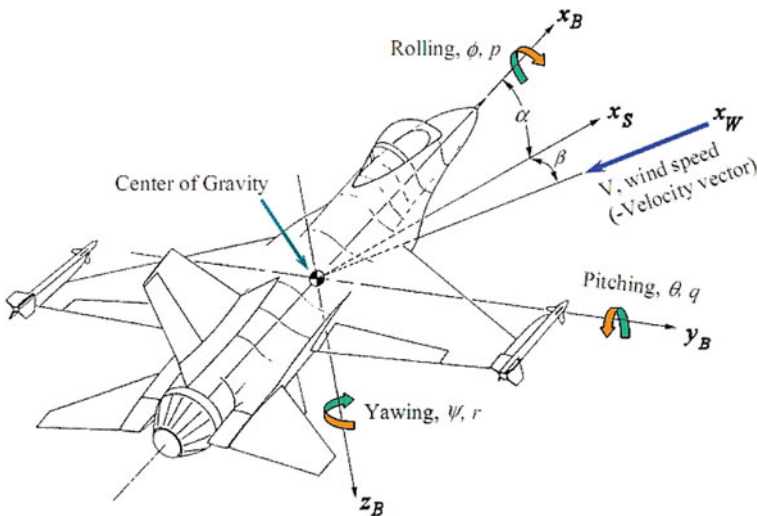


Fig. 1 Aerodynamic angles α and β , angles of aircraft orientation φ , θ , and ψ with angular charges p , q , and r

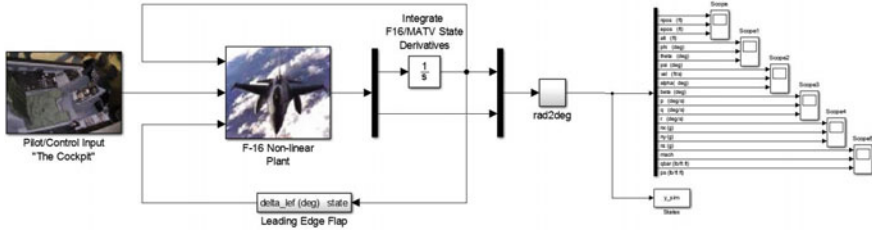


Fig. 2 General structure of nonlinear F-16/MATV dynamics

The orientation vector is given by $\Phi = (\varphi, \theta, \psi)^T$, where, φ , θ , and ψ are the roll, pitch, and the yaw angle, respectively [16].

$$\dot{\phi} = p + \tan \theta (q \sin \phi + r \cos \phi) \quad (1)$$

$$\dot{\theta} = q \cos \phi - r \sin \phi \quad (2)$$

$$\dot{\psi} = \frac{q \sin \phi + r \cos \phi}{\cos \theta} \quad (3)$$

The foremost edge flap is expected to glance with agreeing the transfer function well-defined in reference [17].

$$\delta_{lef} = 1.38 \frac{2s + 7.25}{s + 7.25} \alpha - 9.05 \frac{\bar{q}}{p_s} + 1.45 \quad (4)$$

where δ_{lef} , \bar{q} , and p_s are the foremost deflection of edge flap, dynamic, and the static pressure correspondingly.

The nonlinear F-16/MATV flight dynamics is implemented in MATLAB. Figure 2 shows the overall structures of nonlinear F-16/MATV flight dynamics.

2.2 System Linearization

The system linearization is a procedure to convert a nonlinear equation's set into partially or fully linearized algebraically set [18]. The linearized equation can be written as

$$\begin{aligned} \dot{x} &= Ax + Bu \\ y &= Cx + Du \end{aligned} \quad (5)$$

For linearization of a system, steady state conditions are as follows:

$$\beta, \phi, p, q, r \equiv 0$$

All the derivatives $\equiv 0$

$$\beta, \phi, p, q, r \equiv 0$$

$$VT = V_{Te}, \alpha = \alpha_e, \theta = \theta_e, \psi \equiv 0, \gamma_e \equiv 0$$

By some features of the steady states, the algebraic equations can be further reduced, and when the differentiating terms have $\cos \beta$ and $\cos \phi$, all the resultant $\sin \beta$ and $\sin \phi$ will be disappeared due to applied steady state conditions $\beta = 0$ and $\alpha = 0$. From this, it is possible to replace every $\cos \beta$ and $\cos \phi$ term in the conventional differential equation by a unity before applying some differentiation [19].

At the steady state condition with trimming total velocity of 500 ft/s and at orientation 15,000 fits and with the surface disturbance of elevator disturbance deflection of 5° , the general state space representation is obtained from MATLAB by using *ss()* function.

2.3 Optimal LQG Controller Design for Continuous Time System

The general optimal problem of LQG is to discover out the optimum $u(t)$ that diminishes the average cost function also called quadratic objective function [20]. It is given as

$$J = \lim_{T \rightarrow \infty} \frac{1}{2T} E \left[\int_{-T}^T [X(t)^T Q X(t) + U(t)^T R U(t)] dt \right] \quad (6)$$

2.4 Design of Optimal Linear-Quadratic Regulator

Redefining control variable as

$$\begin{aligned} \dot{x}(t) &= Ax(t) + Bu(t) + \Gamma w(t) \\ u(t) &= -Kx(t) \end{aligned} \quad (7)$$

where A , B , and C are the system, control, and the output matrix, respectively. The theory of LQR determines an optimal gain K (matrix) in such a way that the state-feedback rule $u = -Kx$ matters to minimize the quadratic cost function

$$J = \int_0^{\infty} [x^T(t)Q(t)x(t) + u^T(t)R(t)u(t)]dt \quad (8)$$

where Q and R are the weight matrix. The corresponding optimal control is assumed as

$$\begin{aligned} u &= -Kx = R^{-1}B^T Px \\ K &= -R^{-1}B^T P \end{aligned} \quad (9)$$

Here, K is optimal feedback gain matrix (controller gain), and it is obtained from the Riccati matrix (P). To obtain Riccati matrix, the solution is needed of the subsequent steady state Riccati equation [21].

$$AP + A^T P - PBR^{-1}B^T P + C^T QC = 0 \quad (10)$$

MATLAB function `lqg()` is used here to obtain the following optimal regulator gain matrix.

2.5 Design of Optimal Linear-Quadratic Estimator

The new estimated state equation can be defined as

$$\begin{aligned} \dot{\hat{x}}(t) &= A\hat{x}(t) + Bu(t) + L(y(t) - C\hat{x}(t)) \\ \dot{\hat{x}}(t) &= (A - LC)\hat{x}(t) + Bu(t) + L(y(t)) \end{aligned} \quad (11)$$

From Fig. 3 optimal regulator, the control problem is now defined as

$$u(t) = -K\hat{x}(t) \quad (12)$$

where Kalman gain is denoted by L (or optimal observer gain matrix), which is defined by the continuous filter Riccati equation (algebraic),

$$L = K^T = PeCV^{-1} \quad (13)$$

where covariance of approximation error is Pe , $\varepsilon_o(t)$ is obtained from algebraic Riccati equation by replacing A by A^T , B by C^T , Q by W , and R by V given as

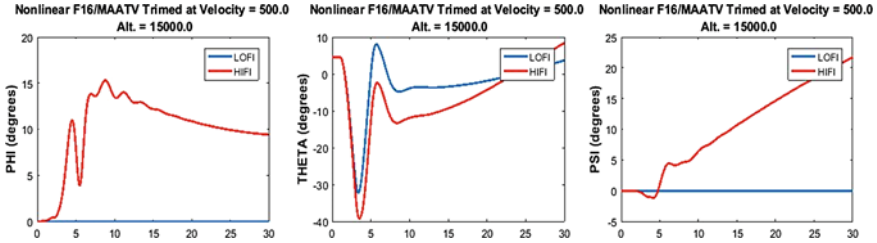


Fig. 4 Nonlinear F-16/MATV flight system response of the orientation flight condition

3 Simulation Results and Discussion

The obtained results shown here are the results achieved from MATLAB/Simulink environment when the F16/MATV is trimmed at steady state conditions with total velocity of 500 ft/s and orientation of 15,000 fts.

3.1 Nonlinear F16/MATV Flight Response

The following nonlinear response is obtained from MATLAB Simulation environment when the F-16/MATV flight dynamics are trimmed at a steady wing level, flight state conditions with inclusion of surface disturbance of the elevator disturbance deflection of 5°.

From Fig. 4, it is clear that obtained results of nonlinear flight responses are unstable and the system responses at the steady state do not attain the steady state condition.

3.2 Linearized F16/MATV Flight Response

Figure 5 linearized F-16/MATV system responses shows that the steady state condition is attained and since system is not applied to any controller so that the steady state time is so larger and the system response looks like unstable system.

3.3 The Continuous Time LQG Controller Response

At the same trimming steady state condition, the continuous linear–quadrature–Gaussian controller response is given in Fig. 6.

The obtained results require a controller with larger controller gain which is very expensive relatively.

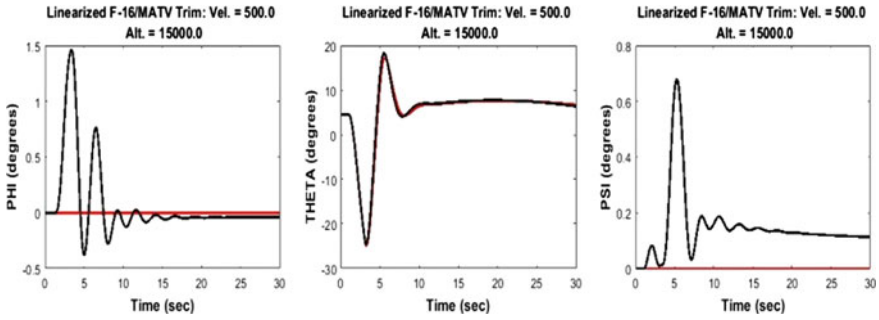


Fig. 5 Linearized F-16/MATV response of orientation dynamics

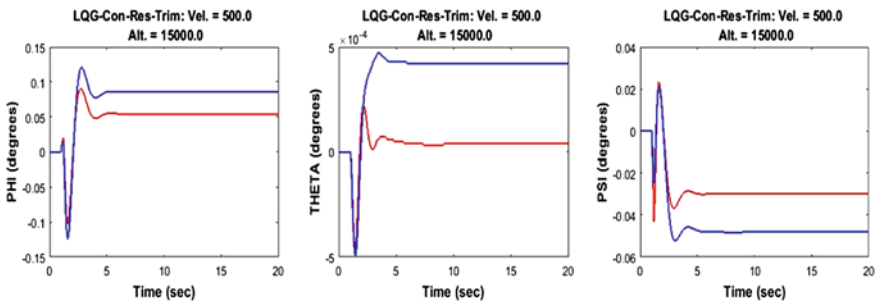


Fig. 6 LQG controller response for F-16/MATV orientation dynamics

3.4 The Discrete Linearized F-16/MATV Flight System Response

In the case of discrete system, compared to that of linearized continues time system for the system to attain its steady state condition, it requires less time, and the following results are obtained for the same flight condition as shown in Fig. 7.

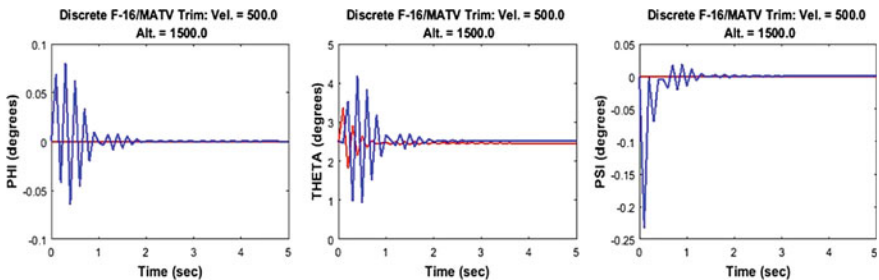


Fig. 7 Linearized discrete time F-16/MATV flight system response to orientation dynamics

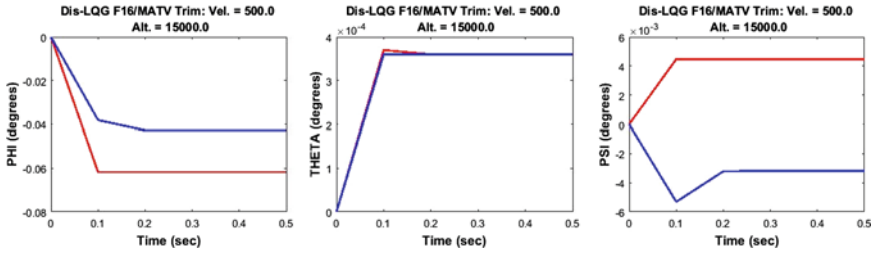


Fig. 8 Discrete LQG controller response to F-16/MATV flight system with orientation dynamics

3.5 The Discrete LQG Controller Response to F-16/MATV Flight System Dynamics

The discrete time linear–quadratic–Gaussian controller is the one which have high efficiency, stability, sensitivity and robustness property. The following simulation results obtained from the MATLAB Simulink have the same flight condition as shown in Fig. 8.

3.6 Comparison of Continuous LQG and Discrete LQG Controller

A comparison of continuous and discrete LQG with transient and the steady state value is shown in Table 1, are the data taken for the low fidelity flight condition (steady wings level). This clearly shows that the discrete LQG controller is having a high performance and stability characteristics compared with the continuous LQG controller. Since the design objectives set here are settling time, rise time, peak amplitude and steady state values. These are fully achieved with high robustness property by the discrete LQG controller. The LQG controller almost gives the same performance as that of when all states are available for measurement and the model is perfectly known. Therefore, the designed controller is acceptable.

3.7 SVD Robustness Checking Result

The result obtained when checking robustness using singular value decomposition for LQG controller shows in Fig. 9, those for the frequency lower than that 100 Hz, the singularity value of LQR response and LQG controller response are almost the same. Which shows the LQG controller is almost robust to external disturbance, and after this frequency, there is the big gap in between them, but roll-off (which is approximately 50 dB/decade) is very high. Therefore, at a high frequency, the

Table 1 Comparison of continuous LQG and discrete LQG controller

S. No.	State variable	Controller									
		Continuous LQG controller					Discrete LQG controller				
		Settling time (s)	Rise time (s)	Peak Amp	SS value		Settling time (s)	Rise time (s)	Peak Amp	SS value	
1	Roll angle (°)	7	1.5	-0.05831	0.05305	0.1	0.1	-0.06179	-0.06179		
2	Pitch angle (°)	8.4	1.4	-0.00538	0.00004	0.2	0.1	0.00037	0.00036		
3	Yaw angle (°)	4.6	1.2	-0.02478	-0.02939	0.1	0.1	0.00447	0.00447		

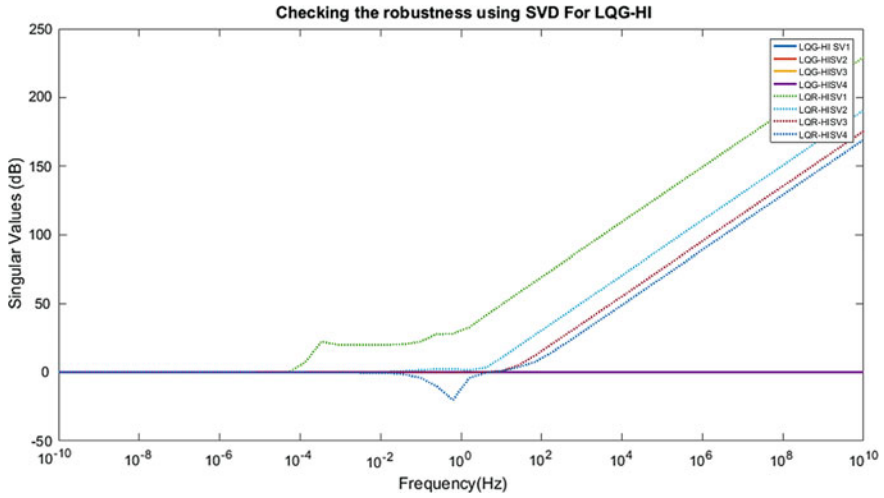


Fig. 9 Robustness checking using SVD for LQG

amplitude of unwanted signals is highly degraded. This makes the designed controller is robust to un-modeled dynamics.

4 Conclusions and Recommendations

The conclusion for the obtained result and recommendation is

4.1 Conclusions

This paper presents optimal control approach, linear–quadratic–Gaussian for the flight control system of F-16 fighter jet with MATV by applying both continuous time as well as discrete time control system.

All the essential design objectives (frequency and time specifications) are met by smearing both continuous and discrete time LQG controllers. Thus, LQG controller, which is based on the separation principle, is designed to stabilize the flight condition of F-16/MATV in steady state condition. Initially, the LQR controller is deliberate centered on the assumptions that all the states are available for measurement and the model is perfectly known. However, some states are not available for measurement, and in addition to this, the model is not perfect. So, these unmeasured states are estimated optimally in the presence of process and measurement noises, which come from linearization and inaccuracy of sensors. This observer is designed using Kalman filter.

The continuous LQG controller response predicted that even if the controller is having a good performance, stability, and robustness property, it takes a large settling time with some neglected harmonic response (i.e., the peak amplitude is very small for all response), which is a good characteristic of the LQG controller.

The discrete linear–quadratic–Gaussian controller as compared with continuous LQG is shown excellent property of robustness, stability, and performance. These properties make the controller more selectable for the efficient flight control system. For existence of large noise in the system, the controller response is very quickly (i.e., the settling time is very small) stabilized, and thus, the discrete LQG is highly recommended for the flight control system.

The controllers considered satisfied the transient design objectives, including robustness. Robustness of LQG is checked and found to be close to that of LQR, which is an ideal robust optimal regulator, until 100 Hz. Beyond this frequency, there is the big gap in between them. Nevertheless, roll-off (which is approximately 0 dB/decade) is very high which degrades the amplitude of high frequency components. Below 100 Hz, the roll-off is greater than 0 dB/decade. Therefore, the larger the bandwidth, the smaller would be the range of frequencies over which high noise attenuation is provided by the compensator, since the roll-off is below 0 db/decade in this range. Therefore, the selected controller with the given bandwidth is acceptable.

4.2 Recommendations

This controller is also applicable to the systems that have nonlinear nature, imperfect model, and for systems that are affected by unmeasured states.

Even though the LQG controller in this is recommended to control the flight system in steady state condition, there are controllers that are more robust than the proposed controller, since robustness is something comparative. The performance and robustness of the LQG controller can be measured by adjusting the noise covariance matrix and state-weighting matrix using trial and error, which is something tedious. So, it is recommended to design a controller that directly addresses the problem of robustness and performance regardless of the presence of noise in the system. These controllers are the H-infinity optimal controller, nonlinear controller, or input shaping which are beyond the scope of study.

References

1. Yang S (1996) Analysis of optimal midcourse guidance law. IEE Trans Aerosp Electron Syst 32(1):419–425
2. Dozwerneman W, Eller BG (1994) VISTA/F-16 multi axis thrust vectoring (MATV) control law design and evaluation. Lockheed Fort Worth Company, 13 July 1994
3. Wikipedia, Linear-quadratic-gaussian-control (online). Available http://en.wikipedia.org/wiki/Linearquadratic-Gaussian_control. Accessed 3 1 2018

4. Labane C, Zemalache MK (2014) Aircraft control system using LQG and LQR controller with optimal estimation-Kalman filter design. In: 3rd international symposium on aircraft airworthiness, ISAA 2013, no 80, pp 245–257
5. Sonneveldt L, Chu QP, Mulder JA (2007) Nonlinear flight control design using constrained adaptive backstepping. *J Guid Control Dyn* 324–325
6. McLean D (1990) Automatic flight control system. Prentice Hall International, Southampton
7. Slotine J, Li W (1991) Applied nonlinear control. Prentice-Hall, Upper Saddle River
8. Isidori A (1995) Nonlinear control systems. Springer, New York
9. Littleboy DM, Smith PR (1998) Using bifurcation methods to aid nonlinear dynamic inversion control law design. *J Guid Control Dyn* 21:632–638
10. Lavretsky E, Hovakimyan N (2005) Positive μ -modification for stable adaptation in dynamic inversion based adaptive control with input saturation. In: Proceedings of the American control conference
11. Kalman R, Bertram E (1960) Control system analysis and design via the ‘second method’ of Lyapunov, Part I: continuous time systems. *J Basic Eng Trans ASME Ser D* 82:371–393
12. Parks PC (1966) Liapunov redesign of model reference adaptive control systems. *IEEE Trans Autom Control* 11:362–367
13. Winsqr CA, Roy RJ (1968) Design of model—reference adaptive control systems by Liapunov’s second method. *IEEE Trans Autom Control* 13
14. Ki-Seok K, Keum-Jin L, Youdan K (2003) Reconfigurable flight control system design using direct adaptive method. *J Guid Control Dyn* 46
15. Ki-Seok K, Keum-Jin L, Youdan K (2002) Model following reconfigurable flight control system design using direct adaptive scheme. In: AIAA guidance, orientation, and control conference and exhibit, 5–8 Aug 2002, pp 151–742
16. Hyung KS, Youdan (2005) Reconfigurable flight control system design using discrete model reference adaptive control. In: AIAA guidance, orientation, and control conference and exhibit, 15–18 Aug 2005
17. Shaji J, Aswin BR (2015) Pitch control of aircraft using LQR & LQG control. *Int J Adv Res Electr Electron Instrum Eng* 4(8):2320–3765
18. Das S, Halder K (2016) Missile attitude control via a hybrid LQG-LTR-LQI control scheme with optimum weight selection. *J Guid Control*
19. Sonneveldt L (2010) Adaptive backstepping flight control for modern fighter aircraft. Wohrmann Print Service, Zutphen
20. Mulder JA, Staveren WHJJV, Vaart JCVD, Weerdt ED (2006) Flight dynamics, lecture notes AE3-302 technical report. Delft University of Technology
21. Nguyen L, Ogburn M, Gilbert W, Kibler K, Brown P, Deal P (1979) Technical paper 1538: simulator study of stall/post-stall characteristics of a fighter airplane with relaxed longitudinal static stability. NASA
22. Oort EV, Chu Q, Mulder J, Boom TVD (2006) Robust model predictive control of a feedback linearized nonlinear F-16/MATV aircraft model. In: AIAA guidance, orientation, and control conference and exhibit, Keystone, Colorado, 21–24 Aug 2006
23. Ferreira A, Barreiros J, Barra W Jr, Brito-de-Souza JR (2007) A robust adaptive LQG/LTR TCSC controller applied to damp power system oscillations. *Electr Power Syst Res* 77:956–964

BER Analysis of FrFT-OFDM System Over α - μ Fading Channel Under CFO



Ashish Mishra, Anushka Singh, Aditi Verma, S. Pratap Singh, and M. Lakshmanan

Abstract For the 5G mobile wireless system, the orthogonal frequency-division multiplexing (OFDM) is being unique sought-after techniques. But in OFDM-based system “Carrier Frequency Offset” (CFO) is one out of various impairments, which gives rise to “Inter-Carrier Interference” (ICI). In this paper, mitigation of CFO has been analyzed for FrFT-OFDM-based model under α - μ fading distribution. The outcome of CFO mitigation has been presented in terms of BER. α - μ distribution contains Rayleigh, Nakagami-m and Weibull channel distribution for dissimilar values of α and μ . Therefore, it is worthy to mention that the proposed analysis is the generalization of results available (Kumari et al. in Electron Lett 49(20):1299–1301, 2013 [1]), in which BER of the FrFT-OFDM scheme has been presented over a Rayleigh channel distribution. Numerical analysis has been carried out in MATLAB-14.

Keywords OFDM · Fading channel · Carrier-frequency offset · Bit error rate · Fractional Fourier transform

A. Mishra · A. Singh · A. Verma · S. Pratap Singh · M. Lakshmanan (✉)
Galgotias College of Engineering and Technology, Greater Noida, India
e-mail: tmlakshmanan@gmail.com

A. Mishra
e-mail: mishraashish966@gmail.com

A. Singh
e-mail: singhanu2612@gmail.com

A. Verma
e-mail: aditiverma166@gmail.com

S. Pratap Singh
e-mail: drsprataps@gmail.com

1 Introduction

In wireless communication system, BER analysis in transmission is the critical issue [1]. On the other hand, higher and higher data rates have been demanded in the development 1G to 5G communication system. Multi-carrier modulation technique; namely, OFDM has been suggested as one of the techniques in 5G. In OFDM system PAPR, CFO and ICI are major issues. Also, ICI which mainly arises due to CFO is of major impact. Drawbacks mentioned above have been overcome with the use of FrFT-OFDM in place of conventional FFT-OFDM system [1–3]. In [4] expression for BER of the BPSK modulation system has been derived over Rayleigh fading channel for the FRFT-OFDM in the presence of CFO. It is noticeable that due to Doppler frequency shift or phase noise [1, 2], there is disparity between transmitter and receiver in carrier frequency which causes “Carrier Frequency Offset” (CFO) and “Orthogonal Frequency-Division Multiplexing” (OFDM) is highly sensitive towards CFO. Also, CFO vanishes the orthogonality between the subcarriers. BER analysis for Rayleigh channel under DQPSK technique for FrFT-OFDM scheme shows better response for $\alpha = 0.9$ value than other values of α [3]. ICI can be also reduced at receiver side by receiver windowing, ICI self-termination and usage of IDFRFT/DFRFT or IFFT/FFT in the OFDM scheme [2, 3]. Authors in [4] claims that FrFT-OFDM can reduce ICI significantly. Also, effect of time offset under FFrFT-OFDM is analyzed in [5]. But by using FrFT in the OFDM system Also [3, 5] claims that that ICI can be reduced significantly. However, the comparison of bit error rate (BER) is more promising than the comparison of ICI.

Further, in the wireless communication, a medium between the transmitter and receiver that is channel has always been a predominant issue. As per the authors, best knowledge BER analysis for FrFT-OFDM-based system under CFO has been found over Rayleigh [6–9], Nakagami [10], Rician [11] fading channel models. Several publications have proposed for discrete form of FrFT [9–12]. In addition, [12–14] presents different performance measures for FRFT-OFDM system. In [13] a closed analytical expression of discrete fractional Fourier transform is presented. Analysis shows that the consequence of fractional order plays a prominent role in any analysis related to this field. Also, order optimization can be used to choose optimal fractional order. In [14], authors presented an algorithm for selecting the optimal fractional value for FrFT-OFDM system and impact of system parameters on optimal order. In [15], optimal order is obtained in FrFT to design an equalizer for decreasing “ICI” in MIMO OFDM system.

With literature, it is observed that none of the above work has presented any investigation by taking different modulations and channels. Also, it is worthy to mention that Alpha-mu fading channel includes various channel models which are Rayleigh, Nakagami-m, and Weibull as a special case. Therefore, BER analysis for the FrFT-OFDM-based system under CFO over α - μ fading channel has been found as a research gap. Therefore, this paper presents BER analysis over “ α - μ fading channel” under CFO. Consequence of different optimal orders has been analyzed in the numerical analysis.

Further, the remaining of paper is structured as follows: The overview is provided in segment 1, while the Channel model is delineated in segment 2. The numerical analysis of the findings is expanded in segment 3, and finally, conclusion of the paper is given in segment 4.

2 Channel Model

Fading models are used to describe the fading pattern in addition to the impact of “Electromagnetic Transmission” of any statistics over dissimilar parameters and different conditions. α - μ fading channel is the most general fading channel from which, other known fading channels which includes Rayleigh, Rician, Nakagami-m, etc. Fading channels may be derived as its special case.

Probability distribution function (PDF) of “ α - μ fading channel” [15]:

$$p(r) = \frac{\alpha \mu^\mu r^{\alpha\mu-1}}{\hat{\Gamma}(\mu)} e\left(\frac{-\mu r^\alpha}{\hat{r}^\alpha}\right) \quad (1)$$

where “ α ” and “ μ ” both are fading limitations, whose values are “2” and “1,” respectively. “ r ” is the wrapper of “ α - μ fading channel”:

$$r = \left[\sum_{i=1}^N (x_i^2 + y_i^2) \right]^{1/\alpha} \quad (2)$$

where x_i and y_i are “in-phase and the quadrature” component of the α - μ fading channel.

By converting the “in-phase and quadrature” component into discrete-time domain we get:

$$x_i(t) = \left(\frac{2}{L}\right)^{\frac{1}{\alpha}} \sum_{n=1}^L \cos \cos(w_d t \cos \alpha_n + \phi_n) \quad (3)$$

$$y_i(t) = \left(\frac{2}{L}\right)^{\frac{1}{\alpha}} \sum_{n=1}^L \cos \cos(w_d t \sin \alpha_n + \varphi_n) \quad (4)$$

where

$$\alpha_n = \frac{(2\pi n - \pi + \theta)}{4L} \quad (5)$$

where θ_n , φ_n and θ are statistically independent and uniformly disseminated over for all values of n .

3 Results and Discussion

In this segment, numerical examination has been presented for FFT/FrFT-OFDM-based system under CFO over “ α - μ fading channel.” BER of various modulation systems such as BASK, QPSK, and QAM have analyzed for the system under consideration with different code rates. For all numerical analysis $\alpha = 2$ and $\mu = 2$, respectively.

Figure 1 epitomizes the BER under FFT over the “Alpha-mu fading channel” for a given value of CFO at 6. Here, it can be seen that the BER of BASK is minimum which is followed by the BER of QPSK-1/2, QPSK-3/4, and 16QAM-3/4 code rate. BER of BASK is minimum, i.e., below 0.0001 for code rate 1/2, and maximum BER is shown by QAM, i.e., 0.1 for code rate 3/4. BER of QPSK is less for code rate 1/2, i.e., ~ 0.0001 and high for code rate 3/4, i.e., ~ 0.001 .

Figure 2 epitomizes the bit error rate under FFT over the “ α - μ fading channel” for a given cost of CFO at 10. Here, it can be seen that the BER of BASK is minimum which is followed by the BER of QPSK-1/2 and QPSK-3/4 code rate. Among the

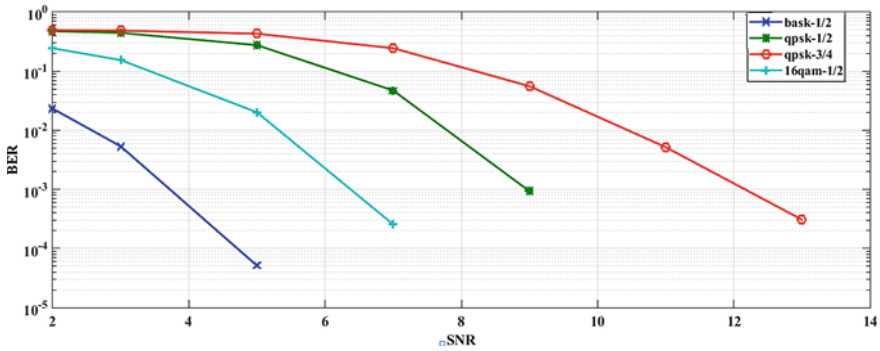


Fig. 1 BER of different modulation scheme under FFT for CFO of 10

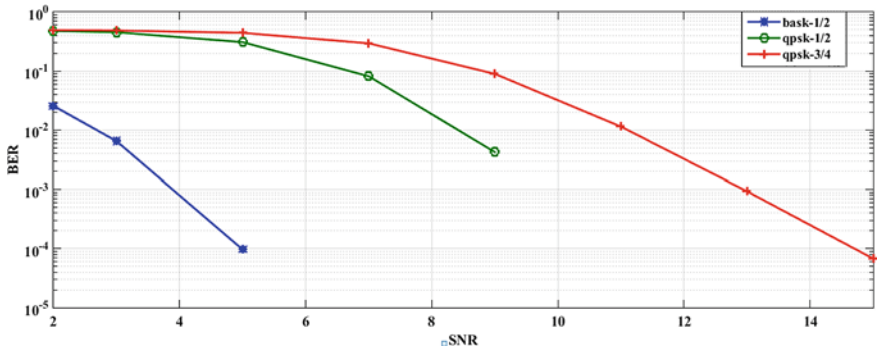


Fig. 2 BER of different modulation scheme under FFT for CFO of 6

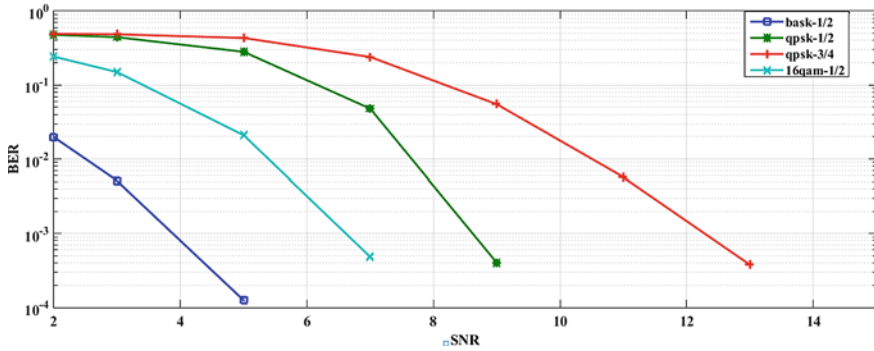


Fig. 3 BER of different modulation scheme under FrFT for CFO of 6

three graphs, the minimum value of BER is shown by BASK, i.e., ~ 0.0001 at $1/2$ code rate. Further, BER of QPSK is higher for code rate $1/2$, i.e., ~ 0.001 and highest for QPSK at code rate $3/4$, i.e., ~ 0.1 .

From Figs. 1 and 2, it can be determined that even on using the same modulation systems, i.e., BASK, QPSK, and QAM the bit error rate depends on the values of CFO in addition to that of type of modulation schemes.

Finally, Fig. 3, presents the BER under FrFT over the Alpha-mu fading channel for a given value of CFO at 6 from Fig. 3, it is observed that irrespective of modulation scheme BER is lowest for given values of SNR and CFO. Hence, it is concluded that under given scenario and given value of CFO FrFT outperform over FFT.

4 Conclusion

In OFDM-based system carrier frequency offset (CFO) is one out of various impairments, which gives rise to inter-carrier interference (ICI). This paper presents CFO mitigation using FrFT in OFDM-based system. BER has been evaluated over α - μ for FFT/FrFT-OFDM-based model. As α - μ channel distribution is the generalization of various channels distribution available in the literature. Therefore, the proposed analysis may be taken as the generalization of the similar results available in the literature. Also, it is found that using FrFT in OFDM-based system improves the BER significantly (by mitigating the effect of CFO) as compared to that of the FFT-based OFDM scheme. In addition, it may be noticed that the consequence of FrFT depends on the type and order of modulation techniques. The proposed results may be extended in various dimension, e.g., effect of the order of FrFT can be presented, different special cases of " α - μ fading channel" may be used to deduce the results available in literature.

References

1. Kumari S, Rai SK, Kumar A, Joshi HD, Singh, Saxena R (2013) Exact BER analysis of FRFT-OFDM system over frequency selective Rayleigh fading channel with CFO. *Electron Lett* 49(20):1299–1301
2. Kumar A, Magarini M, Joshi HD, Saxena R (2016) Exact SER analysis of DFrFt-based QPSK OFDM system over frequency selective Rayleigh fading channel with CFO. *J Comput Netw Commun*
3. Saxena R, Joshi HD (2013) Performance improvement in an OFDM system with MBH combinational pulse shape. *Digit Signal Proc* 23(1):314–321
4. Beaulieu NC, Tan P (2015) Effect of transmitter Nyquist shaping on ICI reduction in OFDM systems with carrier frequency offset. *Electron Lett* 41(13):746–748
5. Zheng J, Wang Z (2010) ICI analysis for FRFT-OFDM systems to frequency offset in time frequency selective fading channels. *IEEE Commun Lett* 14(10):888–890
6. Mallik RK (2003) On multivariate Rayleigh and exponential distributions, *IEEE Trans Inf Theory* 49(6)
7. Simon MK, Alouini MS (2005) *Digital communication over fading channels*, vol 95. Wiley, New York
8. Zheng YR, Xiao C (2003) Simulation models with correct statistical properties for Rayleigh fading channels. *IEEE Trans Commun* 51(6):920–928
9. Karagiannidis GK, Zogas DA, Kotsopoulos SA (2003) On the multivariate Nakagami-m distribution with exponential correlation. *IEEE Trans Commun* 51(8):1240–1244
10. Pimentel C, Falk TH, Lisboa L (2004) Finite-state Markov modeling of correlated Rician-fading channels. *IEEE Trans Veh Technol* 53(5):1491–1501
11. Kansal A, Singh K, Saxena R (2015) Bit error rate analysis of FrFT appended OFDM systems. *Optik* 126(7–8):715–718
12. Kansal A, Singh K, Saxena R (2017) Performance analysis of FrFT based OFDM system with 1024-PSK and 1024-QAM modulation under various wireless fading channels. *Int J Syst Assur Eng Manage* 8(1):137–145
13. Singh D, Kumar A, Joshi HD, Magarini M, Saxena R (2019) Symbol error rate analysis of OFDM system with CFO over TWDP fading channel. *Wireless Pers Commun* 109(4):2187–2198
14. Kansal A, Singh K, Saxena R (2015) Performance analysis of $\pi/4$ DQPSK for FrFT-OFDM system with carrier frequency offset. *Appl Math Inf Sci* 9(3):1383
15. Sood N, Sharma AK, Uddin M (2010) On channel estimation of OFDM—BPSK and QPSK over generalized Alpha-Mu fading distribution. *IJCNS* 3(4):380–384

An Overview of FTTH for Optical Network



S. Sugumaran, Durga Naga Lakshmi, and Shilpa Choudhary

Abstract This paper represents the work of optical fiber and how it is beneficial for human being. Optical fiber communication is fastest communication as compare to others. The speed of optical fiber communication is just same as speed of light. The loss is minimum in optical fiber communication so that we can transmit the data as far as we want. In this paper, we discuss about the fiber to the home (FTTH) and its parameters. This network provides very high internet speed for particular user approximately 256 Kbps to 100 Mbps. To provide broadband services to end-consumers through fiber, fiber to the home linkages are premeditated. To permit circulation of the communication services, a reflexive fiber arrangement and an active apparatus are provided in the network. The presentation of elementary constituents of the network is done and thereby ended by addressing the role of respective components to the design of the fiber to the home.

Keywords PON · Central unit · Fiber cable · FTTH

1 Introduction

FTTH was first introduced in 1999. It was launched the first commercial FTTH plan in 2001. Firstly, Japan was launched first FTTH plan throughout whole world. Fiber to the home (FTTH) is different expertise which is firstly cast-off by BSNL in India. The advantage of an optical fiber is based on the fact that it provides more than enough

S. Sugumaran (✉) · D. N. Lakshmi
Department of Electronics and Communication Engineering, Vishnu Institute of Technology,
Kovvada, AP, India
e-mail: sugudeep@gmail.com

D. N. Lakshmi
e-mail: durganagalakshmi.namburi@gmail.com

S. Choudhary
Department of Electronics and Communication Engineering, G. L. Bajaj Institute of Technology
& Management, Greater Noida, India
e-mail: shilpadchoudhary@gmail.com

bandwidth, and it acts as a perfect platform to deliver many services to the customers such as very high speed internet having ranges from 256 Kbps to 100 Mbps, high end video conferences with delegates and future coming technologies such as 3D motion capturing and also IPTV obligating diverse category of innards like HDTV. The crucial carter for the recent access technologies is internet having high speed which assists in undergoing factual broadband. For a protracted term objective, fiber to the home (FTTH) gives the impression to be the supreme appropriate option: It will be at ease to upsurge the bandwidth in the forthcoming days, if the consumers are exclusively obliged using optical fibers [1]. It provides very good quality of videos, conference calls, good quality of audio, all the amenities that exist on the internet boards, and very fast downloading speed. By creating consumption of this connectivity to the home devices using fiber, bandwidth on ultimatum can be brought to the user. Customer find customer premises equipment (CPE) called home.

2 What Is FTTH?

Communication using optical fiber is established by using the study of light in the glass medium. This fiber can cart a large amount of data, and it is completely independent with respect to distance. Electrical information can be transported through coaxial medium or copper cable, and it is completely dependent on distance. Glass fiber that is used currently has improved structure of electronics, enabled fiber to communicate light signal that is digitized thriving beyond the 100 km (60 miles) without amplification but it have some amount of transmission loss, minimal interference, and high potential with respect to bandwidth. Optical fiber cable is a more or less perfect medium for transmission (Fig. 1).

The exaltation capability of all former transmission media is surpassed by the FTTH network. In FTTH, firstly, we'll send the data through centre office (CO) and optical line transmission (OLT) in optical access network (OAN) to optical network

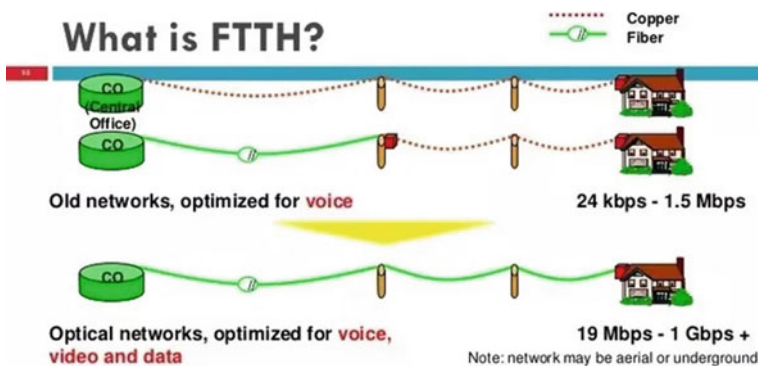


Fig. 1 FTTH

terminal (ONT) for single subscriber or optical network unit (ONU) for multiple subscribers.

3 Function of the Optical Fiber Cable

A bendable, see-through fiber prepared out of glass (silica) or plastic by producing them to a diameter, a touch denser when compared to that of a hair strand is called an optical fiber [2]. Optical fibers are mostly cast-off to diffuse the light information from one termination to another and authorize broadcast over extended distances particularly at advanced bandwidths (data rates) better than those provided by copper wire cables to discover extensive norm in communication systems. In order to make signals travel along them with slighter expanses of loss in toting, fibers are handed down instead of metal wires. Fibers are unrestricted to interference caused by electromagnetic waves, but this difficulty is undergone extremely in copper cables [3, 4].

4 Architecture of FTTH Network

A network that employs cables made up of fiber and turned out to be as optical electronics as a substitute of copper wire electronics is referred to as fiber to the premises (FTTP). It is used to associate with a client on the preferred linkage. To diminish the cost of installing high bandwidth services to the home, novel architectures of networking have been utilized. A new term FTTX which refers to the “FIBER TO THE X” is considered. Based on the area of coverage, it is classified into many sub portions called FTTC/FTTN for fiber to the curb or fiber to the node, FTTH/FTTP for fiber to the home or fiber to the premises, the term “premises” is used to indicate houses, flats, sites of small businesses, etc. Of late, a new branch called FTTW which stands for fiber to wireless is also added (Fig. 2).

According to the position of the termination of the fiber, various optical fiber conveyance procedures are categorized, and all are collectively termed as fiber to the X (FTTX). Optical fiber is previously cast-off for long-range communication, whereas metal cabling has conventionally been utilized for the connectivity from the telecom amenities to the customer. FTTX deployments cover varying amounts of that last distance [5].

1. *FTTN*: In a breakfront which may be at a distance of a few miles from the location of the customer, the optical fiber terminates. Then, from the middle breakfront to the central office, the cabling is generally copper in this configuration [6].
2. *FTTC*: This configuration is quite similar to the above one mentioned but what makes it different from the previous one is the distance of the optical fiber that

FTTX Fiber Architecture

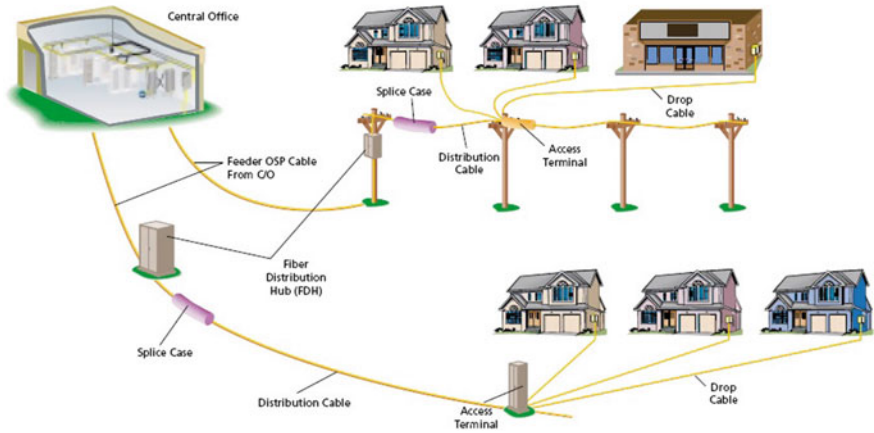


Fig. 2 FTTX fiber architecture

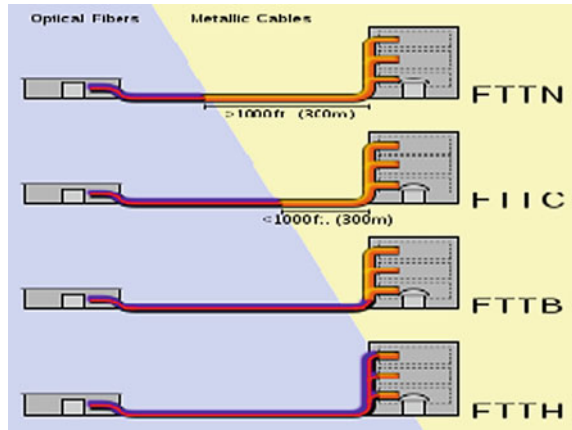
is spread between customer location to the intermediate node which is generally said be close to 300 yards [7].

3. *FTTB*: In this configuration, the cabling of fiber dismisses at the site of the building, which is stereotypically a multi stair unit. Distribution of facility to each and every unit may be done through any of a number of methods from the central office [8].
4. *FTTH*: In this type of configuration deployment, optical cabling at the distinct home or business.
5. *FTTP*: It is a combination of both FTTH and FTTB configurations or is sometimes used to indicate that a particular fiber network takes account of both homes and businesses (Fig. 3).

5 How It Works?

Fiber optics cables are the collection of glass cables which are of size close to a thin hair strand. At speeds and capacities far beyond present time’s copper-cable system, audio, video, and data signals are communicated through the fiber as pulses of light which are generated by the Laser. It works on very high speed and carry more amount of data which is very useful for user according to the diagram it will set up the PON which has control station send the data and then with the help of optical transmission line (OLT). PON works just like a splitter and many fibers are connected with PON, which transfers the data in form of light and at the receiver side photo diode is present which convert the light in the form of signal. It is served firstly in domestic and business users of small scale and medium scale enterprises;

Fig. 3 FTTX configurations



FTTP offers audio services and many other related features and gives contribution of nearly unlimited bandwidth for many applications such as surfing the internet at high speed, etc. It also offers some services which are not possible with the existing network [9].

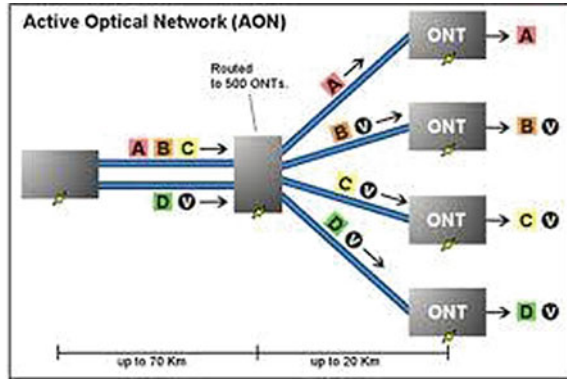
6 Optical Distribution of the Network

A plain fiber is the pretentious optical architecture with a good distribution network, because we have a dedicated configuration where one fiber for one customer goes from the central office. These sorts of networks are more expensive due to the machinery including fiber and the central office but the advantage is based on the fact that it can offer very large bandwidth [10]. A plain fiber is commonly preferential because of novel applicants and viable operators. Any form of regulatory remedy is possible using this topology [4]. To make fiber broadband links conceivable, two dissimilar network proposals are proposed one is active optical network and the other is passive optical network [11].

6.1 Active Optical Network (AON)

Having a fiber connection joining each house to the switches of phone enterprise, either to a local active switch or to a central office (CO) nearby is the meekest means to get homes connected to fiber. To accomplish distribution of information and course to the accurate end handlers, an active optical network (AON) utilizes routers or a switch aggregators which are basically switching apparatus motorized by electricity. Each switching breakfront can knob greater than a thousand clients, although four

Fig. 4 Active optical network (AON)

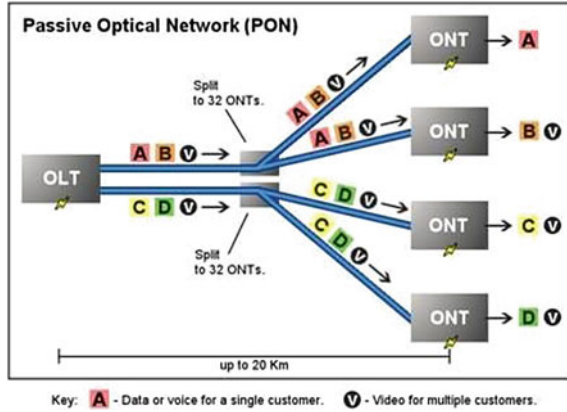


to five hundred is more emblematic [12]. This kind of apparatus performs switching and routing in two layers and three layers depending on the requirement and carries information from or to the central office. To carry estimated transmission using full duplex configuration with range of 100 Mbit/s over one optical fiber which is single mode FTTP, the IEEE 802.3ah standard empower facility providers. Speeds of 1 Gbit/s are becoming commercially available. Subscribers possess a one on one end fiber optic component. And also to accomplish distribution of information components that are active like amplifiers, repeaters, or shaping circuits are cast-off in AON networks with a covering range of about a hundred kilometer (Fig. 4).

6.2 *Passive Optical Network (AON)*

PON are used in telecommunication purpose. In which, we'll device architecture of point-to-multipoint using fiber optic splitters that are not motorized by power. Splitters are used to facilitate a single optical fiber for helping numerous customers, keeping in individual fibers between the hub and customer without obligating to delivery. At the facility provider's central office (hub), PONs require an optical line terminal (OLT) and adjoining end handlers, a numerous optical network units (ONUs) or optical network terminals (ONTs) are present. To lessen the quantity of fiber and equipment related to the hub that is necessary compared to that of one to one type of architectures, a PON is used [13]. According to the recommendation cited in ITU-T G.652, we use on wavelength for regulating traffic upstream and another wavelength for downstream in a single mode fiber in a PON which is generally termed as WDM multiplexing. There are some of the typical standards of PON such as APON/BPON, EPON, GEAPON, and GPON, and generally, we utilize the 1310 nm wavelength for upstream traffic and 1490 nm (nm) wavelengths for downstream traffic, and 1550 nm is used exclusively for elective overlay facilities such as radio frequency video, i.e., analog signal (Fig. 5).

Fig. 5 Passive optical network (PON)



Passive optical network further classified in two parts which is TDM PON, WDM-PON.

1. TDM passive optical network

Some of the configurations have been consistently developed for time division multiplexing TDM PON machineries for organization of FTTH. Out of them, some of the frequently used standards are summarized in Table 1 with their significant parameters [14–17]. In TDM PON, it is not likely for diverse operators to substantially stake the same fiber which is the biggest disadvantage. So, to overcome this problem, a multi-fiber distribution is essential [14]. Some of the configurations that are widely deployed are APON/BPON, EPON, and GPON. Among these, EPON stands first in deployment having roughly 40 million deployed ports followed by GPON whose growth is also substantial, but not more than 2 million connected to the port.

The typical signal transmission in upstream is initiated by ONU or ONT transmitting data for a fixed time period only. That means more than one ONT or ONU will not be able to transmit data simultaneously; i.e., time division multiplexing is undergone whereas in downstream direction the ONUs and ONTs receive data through the address that is specified in the data signal and will get directed to the prescribed destination that is provided in the data that is sent from an OLT. According to the information that is mentioned in Table 1, GPON mode of configuration contributes

Table 1 Classification of different configurations in a TDM PON

Parameter	BPON	EPON	GPON	XGPON	10G-EPON
Standard	ITU-T G.983	IEEE 802.3ah	ITU-T G.984	ITU-T G.987	IEEE 802.3av
Downstream data rate	622 Mbps	1.25 Gbps	2.5 Gbps	10 Gbps	10 Gbps
Upstream data rate	155 Mbps	1.25 Gbps	1.25 Gbps	2.5 Gbps	10 Gbps/Symmetric 1 Gbps/Asymmetric

compressed signal and audio services at a high speed of 2.5 Gbps. Other higher versions like XGPON and 10G-EPON can be operated at rates even higher than that of GPON. GPON reclaims many purposes of BPON in order to permit informal changeover from BPON to GPON. What makes GPON superior from other configurations is that it uses a protocol called generic framing procedure (GFP). This protocol interfaces all network packets enabled by GFP and to all major services provided and also supports both audio and data related services. The ITU-T recommendations G.984.1 through G.984.5 is considered to be GPON standard [16, 18]. The voice component can be represented as VOIP service (voice over IP, packet-switched protocol) and can be combined with data component in physical layer simulations. As a final point, the video module can be characterized as IPTV signal or as an RF video signal (traditional CATV). The price related with FTTH architectures are deliberated in obtainability demonstrating of the architectures are discussed in [2, 9, 19–21] talk over concerns and encounters that are associated with the coming generation PONs.

2. WDM Passive Optical Network

TDM-based multiplexing is the most frequently used standard technique. However, a non-standard sort of PON is currently established by a limited number of companies called as wavelength division multiplexing PON, or WDM-PON. It is the coming generation's access network. There is no particular standard or no particular definition for this WDM-PON which is universally approved by one and all. However, by some characterizations WDM-PON has committed and a separate wavelength for respective ONU wavelength division multiplexing passive optical networks. In WDM-PON, since multiple wavelengths are used, they can be cast-off to isolate each ONU into many number of unreal passive optical networks lying on the same physical configuration. The wavelengths when used collectively deliver effective consumption of wavelength and subordinate delays practiced by the ONUs [22].

This WDM-PON is further classified into two configurations as per the citation in SG15 of ITU-T [23]. The first one is time and wavelength division multiplexing PON (TWDM-PON), and the second category is AWG-based WDM-PON. In TDM PON, large number of users has to be supported and data need to be transmitted at a very faster speed and also more than one person should be able to access the fiber simultaneously. For this, different wavelengths can be transmitted on the same fiber and operators can access them at any point of time [23]. Whereas, in second category that is arrayed waveguide grating (AWG)-based WDM-PON each operator is delivered with a committed wavelength. Also, this WDM-PON since it uses a separate wavelength for different subscribers, it is said to have higher security and better privacy. It supports a transmission speed of 1.25 giga bits per second in both ways, i.e., up and down streams.

7 Advantages

1. Fiber to the home is the solitary expertise that will provide enough bandwidth.
2. It provides reliability and is afforded at a low enough cost, to meet the prerequisites of the user of the subsequent decade.
3. It is the only technology that is inexpensive these days, because of this reason number of corporations using wide variety of dissimilar business cases internationally are competing to install it in many number of locations.
4. FTTH is by now providing services at high profile and eventually users are finding it more advantageous than the “cable TV.”

8 Applications

1. Social applications custom the infrastructure of optical fiber to develop an intellect of civic. These include various communal social networking sites that are aimed at maintaining social relations, some sites introducing local news and events, i.e., intranets, and some video channels which are web based.
2. Arts and educational applications which include sophisticated online video conferencing in communal canthers, open-air pitches or kids’ play canthers to fetch live performances, educational apps, online music tutorials, e-book studying, and many more collaborating events into the civic.

9 Disadvantages of FTTH

The detriment with this technology is the price that is accompanied with FTTH cable and all other related infrastructure so that it is becoming a way too expensive to manage to pay for a typical house hold. Anyway, to get rid of this problem, there are some advanced resources that individuals can implement. Creating custom of an FTTP; i.e., fiber to the premises is one of the protuberant ways of doing so where the fiber optic technology is got into the premises instead of being paid it to individual homes. So, in this manner, both the purposes can be served; i.e., high speed is achieved, and cost factor is reduced instead of going for a compromise. It is pretty obvious that with the flow of time, innovative traditions will be developed for making groundbreaking consumption of fiber optic technology.

10 Limitations of FTTH

The limitation of optical fiber cables is based on the fact that they undergo some bending losses called scattering losses, and so, they should have restricted bend radius

(about 30 mm), and if that limitation is crossed, it is more likely that some information will be lost. So, in recent times, bend resistant fibers have been familiarized which have higher forbearance to bending.

Other limitation is that unlike copper UTP cables, optical cables can carry only data and they cannot carry power. Some POE enabled IP devices like internet protocol phones, wireless access points, etc., are motorized straight by using the unshielded twisted pair (UTP) cables which is not assisted by fiber as they carry only data.

References

1. Malik D, Dung S, Walia R (2012) Quality of service in two-stages EPON for fiber-to-the-home. *Int J Soft Comput Eng (IJSCE)* 2(2):387–390
2. Smith S (2006) Business class services over a GPON network. National Fiber Optic Engineers Conference. Optical Society of America
3. Kocher D, Kaler RS, Randhawa R (2013) Simulation of fiber to the home triple play services at 2 Gbit/s using GE-PON architecture for 56 ONUs. *Optik* 124(21):5007–5010
4. Chardy M, Costa M-C, Faye A, Trampont M (2012) Optimizing splitter and fiber location in a multilevel optical FTTH network. *Eur J Oper Res* 222(3):430–440
5. Effenberger F, Cleary D, Haran O, Kramer G, Li RD, Oron M, Pfeiffer T (2007) An introduction to PON technologies [Topics in Optical Communications]. *IEEE Commun Mag* 45(3):S17–S25
6. Malhotra JS, Kumar M, Sharma AK (2014) Low cost solution to high capacity 32×32 channel FTTH duplex link employing triple play services. *Optik* 125(1):93–96
7. Ab-Rahman MS, Aziz ANA, Khairuddin AA, Aziz SAC, Jumari K (2012) New optical splitter design for application in fibre-to-the-home passive optical network using virtual lab platform. *J Comput Sci* 8(6):864
8. Rodrigues C, Gamelas A, Carvalho F, Cartaxo A (2011) Evolution of FTTH networks based on radio-over-fibre. In: 2011 13th international conference on transparent optical networks. IEEE, pp 1–4
9. Al-Quzwini MM (2014) Design and implementation of a fiber to the home FTTH access network based on GPON. *Int J Comput Appl* 92(6)
10. Lange C, Gladisch A (2009) On the energy consumption of FTTH access networks. In: 2009 conference on optical fiber communication-incudes post deadline papers. IEEE, pp 1–3
11. Kim B, Lee W, Han J (2010) Outside plant architecture of fiber-based access network. In: Digest of the 9th international conference on optical Internet (COIN 2010). IEEE, pp 1–3
12. Kaler R, Kaler RS (2011) Simulation of fiber to the home at 10 Gbit/s using GE-PON architecture. *Optik* 122(15):1362–1366
13. Breuer D, Geilhardt F, Hülsermann R, Kind M, Lange C, Monath T, Weis E (2011) Opportunities for next-generation optical access. *IEEE Commun Mag* 49(2):s16–s24
14. Katla S, Balagoni A (2013) Technological and cost based analysis of future-proof fiber access passive networks: GPON and WDM PON. arXiv preprint arXiv:1308.5356
15. Senior JM, Yousif Jamro M (2009) Optical fiber communications: principles and practice. Pearson Education
16. Peng D, Zhang P (2011) Design of optical integrated access network based on EPON. In: Proceedings of 2011 international conference on electronics and optoelectronics (ICEOE 2011), pp 65–68
17. Qiu Y (2011) Availability estimation of FTTH architectures based on GPON. In: Proceedings of IEEE 2011 7th international conference on wireless communications, networking and mobile computing, pp 1–4
18. Ab-Rahman MS, Aziz SAC, Jumari K (2011) Ideal and non ideal condition analysis based on protection scheme in distribution fiber for immediate split FTTH-PON. *JApSc* 11(6):1026–1032

19. Bonetto E, Mellia M, Meo M (2012) Energy profiling of ISP points of presence. In: 2012 IEEE international conference on communications (ICC). IEEE, pp 5973–5977
20. Al-Chalabi S (2012) Optically powered telephone system over optical fiber with high service availability and low risk of investment in FTTH infrastructure. *IEEE Commun Mag* 50(8):102–109
21. Heard IB (2008) Availability and cost estimation of secured FTTH architectures. In: 2008 international conference on optical network design and modeling. IEEE, pp 1–6
22. Schneir JR, Xiong Y (2013) Economic implications of a co-investment scheme for FTTH/PON architectures. *Telecommun Policy* 37(10):849–860
23. James O (2011) High speed data to the home—an update, in proc. In: 2011 IEEE international conference on consumer electronics (ICCE), pp 663–664

Comparison of Various Classification Techniques on Brain Tumor Detection



Ravi Prakash Chaturvedi and Udayan Ghose

Abstract Brain tumor is world's most severe disease, and death rate has gradually increases. In this paper, we detect the brain different types of tumor via segmentation using neural network and classification using curvelet transform with unsupervised learning method. For that consideration, the process of new cells is replaced by old cells because of old cells are died first, but sometimes the old cells do not died and new cells are not able to replace other side; the new cells are often form a huge tissue and this called a tumor. We proposed the dynamic neural network with feed forwarded dynamic neurons for automatic image segmentation. The method, involvement of multiple neural layer architectures that particularly focus on extracting image features from image-related regions, besides having a positive effect against over fitting segmentation of MRI images by given the fewer number of weights in the network. Next, curvelet-based unsupervised learning technique for image classification, which is based on multistage and multidirectional transform that capturing the edge point in brain images. The edge pointes in an image are the significant information caring points, which are used to demonstrate better visual configuration of the image. Our approach achieved better results in brain tumor segmentation challenges on dataset by comparing with other existing methods. Our approach achieved better results in brain tumor segmentation challenges on BRATS 2019 dataset by comparing with other existing methods.

Keywords Component · Tumor · Neural network · SVM · PSO

R. P. Chaturvedi (✉) · U. Ghose
School of Information, Communication and Technology, Guru Gobind Singh Indraprastha
University, New Delhi, India
e-mail: rpchaturvedi51@gmail.com

U. Ghose
e-mail: udayan@ipu.ac.in

1 Introduction

Tumor in brain is a sort of strange cell conglomeration which is sure cerebrum areas. Because of the event of mind tumor, it very well may be ordered into essential and metastatic. Cerebrum tumors influence the people seriously, on account of the unusual development of cells inside the mind. It can upset appropriate cerebrum work and be hazardous. Two kinds of mind tumors have been distinguished as amiable tumors and dangerous tumors. Threatening mind tumor spread to different locales of the cerebrum and spine quickly. A fine point-by-point arrangement partitions the tumor into four evaluations and the higher evaluation tumors will be progressively dangerous. In grown-ups [1], the general sort of fundamental cerebrum tumor is accepted as gliomas. From the evaluations of I to IV seriousness, gliomas are grouped so as to reviewing arrangement of World Health Organization (WHO). The tumors are threatening and hurtful when the smoothness with destructive. The classification of the images in the dependent on the concepts like magnetic resonance imaging computed tomography filter, ultrasound, and X-beam.

The spinal string and cerebrum are secured by meninges and play as defender. As it increases in a moderate way, they are exceptionally expected as favorable tumors and it has low likelihood to spread. The tumor that happens at pituitary organ are known as pituitary tumors, and it is significant reason for about 14% of intracerebral tumors, with few are a result of deformities in acquired hereditary qualities [2] with some are a result of consistent transformation.

Separating second rate and high-grade glioma utilizing perfusion MRI has been fit for understanding couple of inconveniences in biopsy. The PC supported framework suggestion is useful for location. In earlier phases of tumor development, an effective and programmed framework for arranging cerebrum tumor underpins doctors to decipher the therapeutic pictures and helps in master's choice. Through investing diminished energy, the reviewing of cerebrum tumor is performed in this investigation and it gives improved precision. Moreover, the whole grouping system is noninvasive. For breaking down the medicinal pictures, enough centers had been given to analyze. The enthusiasm for the space of wellbeing-related systems and themes are developing now as the nearness of current ML methods have demonstrated its adequacy in settling distinctive issues [3]. A few examinations have been directed in various tumor characterization utilizing MRI, principally developmental calculations, MR mind pictures and fake neural systems (ANN) [4], bolster vector machine (SVM) and half and half-wise procedures are the shallow ML calculations that are utilized to separate the unusual and typical classes of pictures in cerebrum MR that are meant through existing works.

The classification of the cerebrum tumor is holding the picture data from the database which is utilizing in segments and creating the divisions. The strategy, association of little bits, incorporated different neural layer structures that especially centers on extricating picture highlights from picture-related districts, other than having a constructive outcome against over fitting division of MRI pictures by given the less number of loads in the system.

2 Literature Survey

Saleck et al. [5] presented another methodology utilizing FCM calculation, so as to extricate the mass from area of intrigued (ROI). The concept of the strategic distance with FCM is by maintaining the arrangement of pixels which will give you the data as such. The pixel-level arrangement is spread over the surface which is occupied with the GLCM mass limit precision. The proposed method is ideally affected the precision. Navjot Kaur [3] tumor perceived therapeutically as a dangerous disease which is bunch of infections and affected the cell development.

Swetha and KrishnaMohan [6] automatic brain tumor tissue detection is identified in the segmentation in pixel images through and evaluating tumor

Kumar and Kumar [7] as part of brain tumor the classification of the segmentation and classification will arranging the separation and save the life with some treatment which need to take against the disease. The focus of the personality that pictures perfect images and anisotropic filtering and uproar in SVM classifier will improve the image from the structure which are noticed some important showed procedure. The cerebrum will accomplish the MRI photographs in the framework and done the part of activities. The solicitation pixels are more powered in the framework.

Acharya and Choubey [8] the present paper proposed that we have used division, highlight extraction and arrangement method for discovery of tumors. Brain tumor detection and segmentation are a standout among the most difficult and tedious assignment: PCA is utilized for division, GLCM is utilized for include extraction, and neural system is utilized for arrangement of tumors.

Kaur and Gill [9] division has illustrated satisfactorily in this particular research district. Remedial picture getting ready is a dynamic and rapidly creating field. Psyche tumor division frameworks have shown it in recognizing; moreover, separating tumors in clinical pictures and it will continue into what's to come. Brain tumor detection is using canny edge detection with operators.

Li et al. [10] the structure of the framework utilizes neighborhood twofold models (LBPs) to evacuate in closer picture highlights, for example, edges, corners, and spots. The classification of the blend is highest level blend and choice-level blend which are used for Gabor activities and normal formations, and there will be sportive idea and organize the pattern. The union results from the classifier and decision-level mix performs on possibility in yields. The uses of the machine learning structure are mainly utilized in the classifier.

Dhanaseely et al. [11]. There are two models which have taken for the discussion, and the names of the models are CASNN and FFNN. The mentioned levels are involved in the investigation of the process. The extraction part of the system is done the computational weight losses. As mentioned in the database, features are removed from the PCA. The part of system is moving toward the getting ready stage and testing stage but the planning of the segment will be occupied in both stages.

Liu and Liu [12] declare a calculation of HV tiny picture join extraction and attestation utilizing faint-level co-event structure (GLCM) so as to appropriately segregate the segment data of human ailments (HV) minute pictures. Initial start

with 20 bits of picture of with the utilization of GLCM and after four parameters like entropy and centrality are evacuated using GLCM and some time for HV picture insistence is done.

Praveen and Singh [13] define another method to improve support vector machine using c means for tumor class know as cerebrum. He defined framework on different pad. In this, he use twofold and morphological operation by using FCM on MRI images and extract the dull feature using GLCM after that he use SVM and correctly define the this class of tumor.

Amasyali and Ersoy [14] classified the exactness and execution time in terms of improving the system and precision making with execution time are the huge factors into estimate the course of system. There are more datasets involved in this to improve the courses which is correctness test and time. The result of the course is focused on the estimation of the random forest and random committees and both are significant decision on the system.

3 Proposed System

The demise rate of diminish is centered brain tumor of ID and recognizable cerebrum tumor occupied in utilizing classifiers. The final work will be idealized different phases. Utilization of separating segments by calculation including gray-level event matrix (GLCM). The mentioned phase is combiner procedure of gathering classifier by programmed artificial neural network.

The identification of the pattern will be occupied with calculation of brain reverberation imaging which is contained with the restoring process. An ensemble classifier defines the neural system with machine learning system and support vector machine (Fig. 1) [3].

3.1 *Compilation Processing Step*

The compilation process is to handle the image that evacuates the data from the picture and is main constraint of the process. Based on the evacuation of the process, the image has to be improved well enough and handling will be much improved with the whole process. In the processing of the grayscale image will participate with the picture remaking process. At the filter stage, the noise will be arrest and evacuate [6].

The middle filter is clearly utilized for the commotion disposal in a shifting system. The system is evacuating the noise from the images like salt and pepper from the grayscale picture. The identified channel is collapsed with high pixels which is impact in terms of diminishing salt-and-pepper commotion also possibility will be reduced [15].

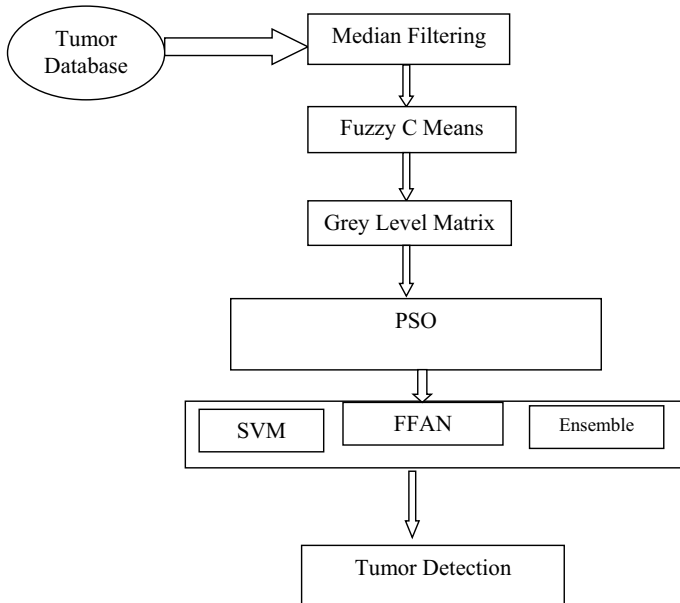


Fig. 1 Flowchart of the proposed system

3.2 Image Segmentation

The sort of images is critical as monumental quantities of pictures are created throughout the results and it is connected for clinical sort of physically separated these images in a really good time. The image participation is mentioned isolated the non-covering districts [16]. The isolated portion does contain with the pixels which is easier to separation on its way of investigation. The concept is really helpful to understand the bounds. [6]. The calculations of the mentioned area among the images are occupied in likeness and brokenness [17, 18].

The separation of vital half in clinical identification and may be valuable in pre-cautious concepts and promoted the concepts. Therefore, most of the accessible division is occupied parting and mixing techniques and edge-based bunching ways [19].

The process of bunching is ideally covering the images, and pre-handling stages are keen with the running the chosen bunches. At this while, we will utilize the bunching concept for locating the tumor zone in our images [20].

3.3 Features Extraction

The significant concept of the feature extraction is advanced in the development of grouping and separation of the important data for every class. The method of highlights is cleared from the concepts and arranges the vectors [21, 22]. The whole process is utilized by the classifiers to realize the data with focused unit [23].

The simplest way to winds up the concept will be highlighted with the characterization of the classes by arranging the permits and the feature extraction to recover the data from the crude data [24].

3.4 Classification

Arrangement is the way toward ordering the things as per its sort and example. Choosing the appropriate classifier brings about exactness and improved execution for different datasets. Here, the tumors are named benevolent and harmful tumor [6]. So the proposed framework joins CART characterization and troupe SVM-based arrangement to make the procedure more proficient than the current procedure. It is a discrete half-breed technique. Arrangement tree and relapse tree are joined and named as CART. Grouping tree predicts the class to which the information has a place with and the relapse tree will anticipate the exact values in genuine numbers [25, 21]. SVM helps in bunching the information into gatherings. So this has expanded the exactness in recognizing the precise tumor influenced territory [26]; another approach using deep neural network we precede the image segmentation using fuzzy-C mean and after applying PCA and DWT for feature extraction, then we use features optimization technique. Then we classify the brain tumor using feedforward neural network, SVM, ensemble classifier [27, 28].

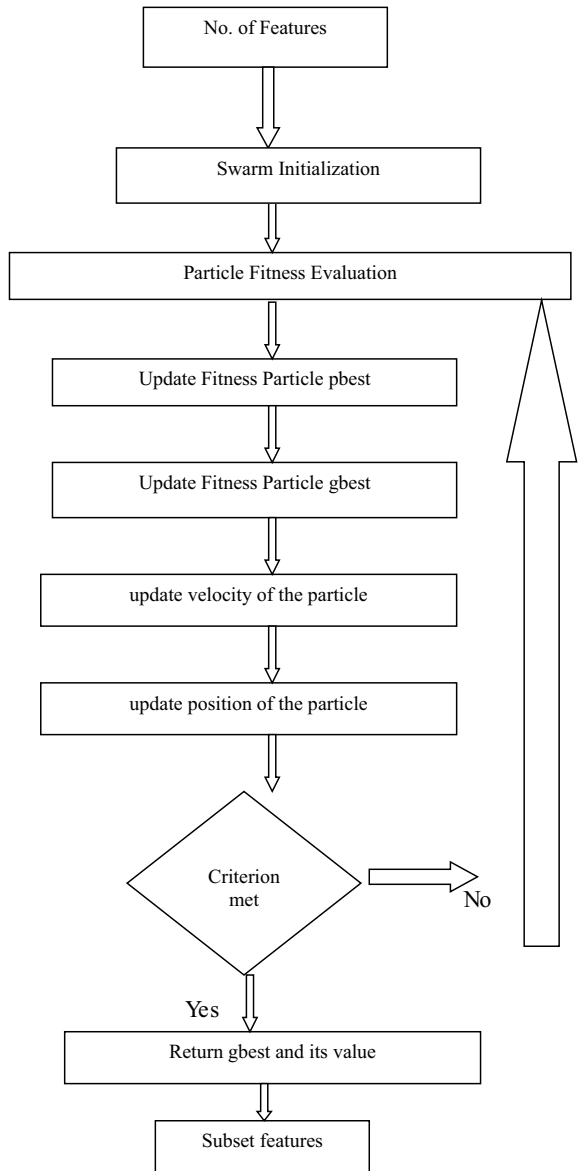
Ensemble support vector machine (SVM) is utilized for order process. It deals with straight information. It is additionally used to order numerous ongoing issues like content classification, face acknowledgment, malignancy finding, and many. It uses isolate and vanquishes technique. Based models are joined with high prescient execution in gathering SVM. It is powerful in high-dimensional areas and orders the picture [5, 29] (Fig. 2).

A supported vector machine based on statistical theory and a given data set is trained and try to map on y_i to function $f(x_i)$ for given sample set information this mapping is described as [30]:

$$P(l) = \text{Sign}\left(\sum x Q_i y_i K(Z, S_i) + b\right) \quad (1)$$

As a vectors of Q_s are the set of coefficients, are the function vectors, sx are the support vectors, z is the input vector, $K(z, sx)$ is the chosen kernel function, and b is the bias.

Fig. 2 Flowchart of PSO



$$\text{Linear : } Kx(xi, zi) = xi \bullet zi, \tag{2}$$

$$\text{Polynomial : } K(xi, zi) = ((xi \bullet zi) + 1)dx, dx > 0, \tag{3}$$

$$\text{RBF : } K(xi, zi) = \exp(-||xi - zi||^2/(2\sigma^2)). \tag{4}$$

And via this we find the accuracy through SVM using different kernel like linear, RBF, and polynomial [19].

4 Result and Discussion

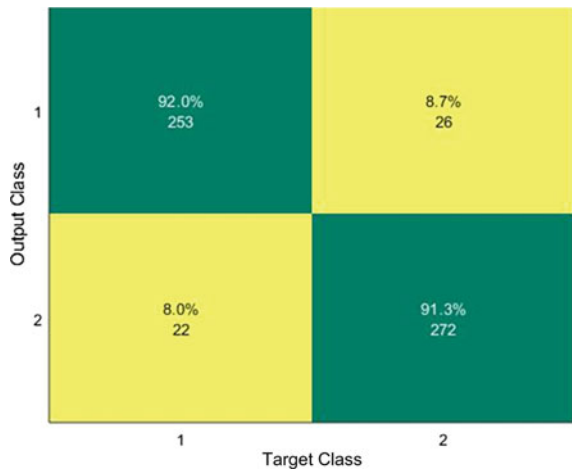
The presentation of the framework will be utilized the network, and the results could be following way Correct Positive (CP), False Positive (FP), False Negative (FN), and Correct Negative (CN), collectively says correct negative and correct positive. In various analysis, the concept will be figured out with the no tumor on this; at the point, it is false positive. 49 images were tried utilizing this disarray lattice. The exhibition of the twofold arrangement test has two significant factual measures in restorative field, and they are affectability and explicitness. Positive qualities accurately recognized are given in rate by affectability. Negative qualities accurately recognized are given in rate by explicitness.

So observing Table 1 and Fig. 3, the comparison is focus on accuracy and using FFANN and SVM and ELM give accuracy 99.78, 91.3, 99.43 using 25,000 pixel value the highest accuracy given by FFNN (Figs. 4, 5, 6, and 7).

Table 1 Comparison table accuracy

Classifier technique	Accuracy (%) existing	Accuracy (%) proposed
FFA neural network	89.33	99.78
Support vector machine	90.47	90.5
Ensemble classifier	94.01	94.43

Fig. 3 SVM proposed result



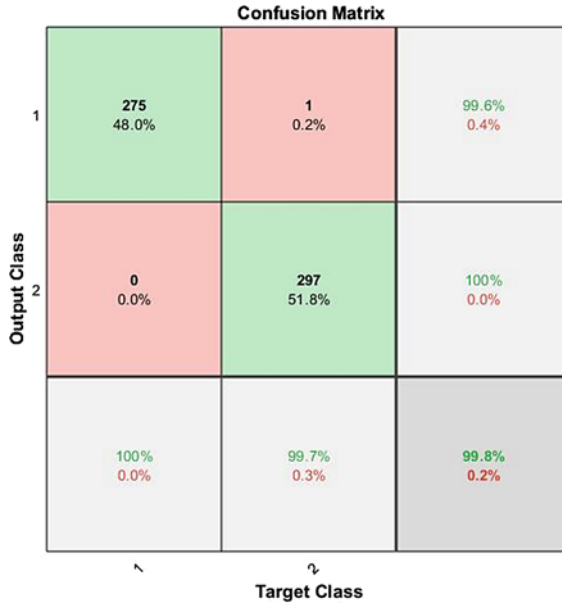


Fig. 4 FFA neural network result

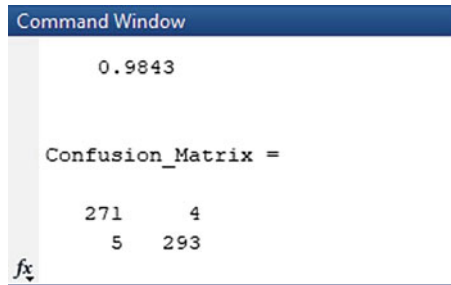


Fig. 5 Ensemble classifier result

Again we found from Table 2a, accuracy level via optimizing the features using swarm optimization is 99.68, 90.68, 99.54 for FFANN, SVM, Ensemble so again Ensemble give highest accuracy when contrasted (Fig. 8).

The comparison Table 3 differentiates ideal sensitivity existing and ideal sensitivity proposed classifier technique; the value of the FFA neural network will be 93.94 in existing and 99.67 in proposed method. The IDEAL support vector machine ideal sensitivity is 90.33 and 90.68 is proposed method.

As per the table, the classifier will maintain the FFA neural network, SVM, ELM that our proposed full ensemble classifier and ideal sensitivity.

The features of the system are given in Table 4.

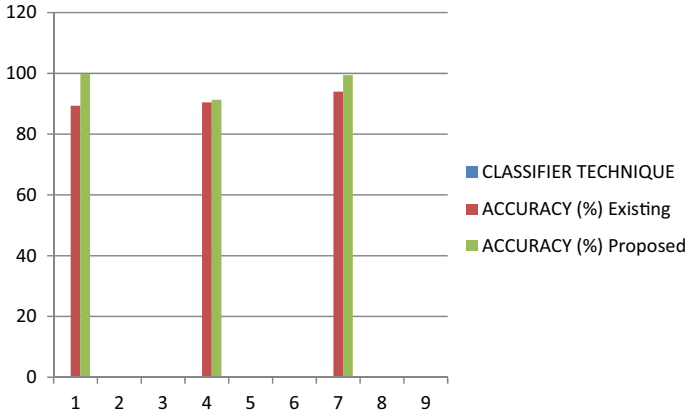


Fig. 6 Comparison of accuracy

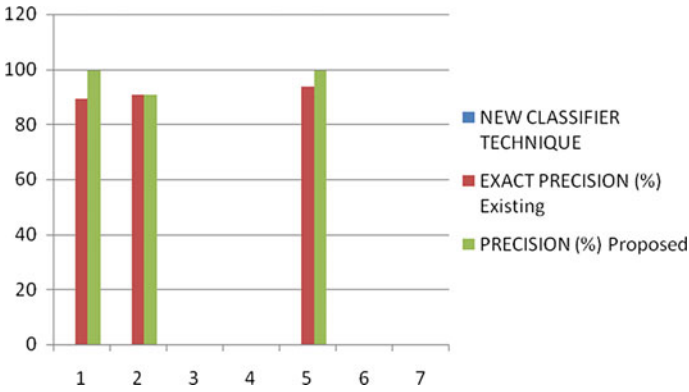


Fig. 7 Comparison of precision

Table 2 Comparison table precision

New ideal classifier technique	Exact precision (%) existing	Precision (%) proposed
FFA neural network	89.41	99.88
FULL support vector machine	90.59	91.3
IDEAL ensemble classifier	93.57	98.43

5 Conclusion

As per the results, the brain tumor will recognized by an image area preparing strategies. This method required different procedures like preparing utilizing channel

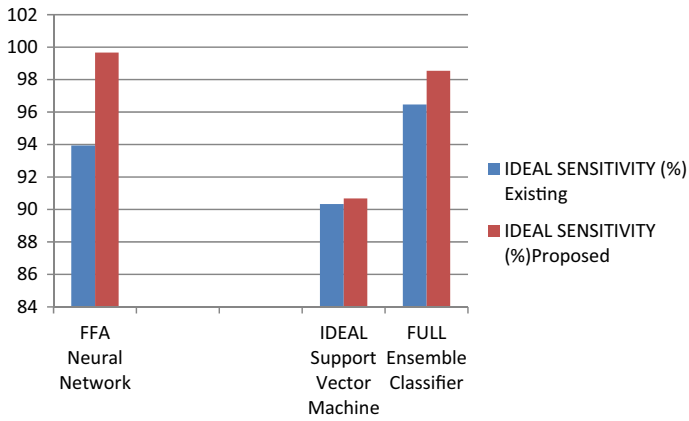


Fig. 8 Comparison of sensitivity

Table 3 Comparison table sensitivity

Exact classifier technique	Ideal sensitivity (%) existing	Ideal sensitivity (%) proposed
FFA neural network	93.94	99.67
IDEAL support vector machine	90.33	90.68
FULL ensemble classifier	96.47	98.54

Table 4 SVM feature results

Feature value	Image 1	Image 2	Image 3
Mean	0.00319	0.002749	0.001512
Standard deviation	0.0944	0.0897726	0.0898
Entropy	3.36	3.12	0.00806
RMS	0.094	0.089	0.84991
Variance	0.082	0.0085	7.78334
Smoothness	0.91	0.91	0.8499
Kurtosis	5.51	6.91	7.783
Skewness	0.4839	0.4507	0.6817
IDM	1.066	-0.76	1.14
Contrast	0.2322	0.24277	0.281148
correlation	0.09959	0.09684	0.096983
Energy	0.73098	0.7502	0.754603
Homogeneity	0.9248	0.0930284	0.929408

calculation, division utilizing bunching calculation, include extraction utilizing gray-level co-event framework and group order. The group of classifier is at long ordered the tumor or non-tumor area. The group classifier confirms a significant idea in our job. Group classifier is the blend of different individual classifiers. The classifiers are compressed with neural system, and full support vector machine, ideal ELM, classifier. The group of high exactness and less process time, and it is fully contrasted with all other classifier system. The identification results are appeared in reasoned that the group classifier is different angles.

References

1. HARalick RM, Shanmugam K (1973) Its 'hakDinstein: textural features for image classification. *IEEE Trans Syst Man Cybern* 3(6)
2. Materka A, Strzelecki M (1998) Texture analysis methods a review. Technical University of Lodz, Institute of Electronics, COST B11 report. Brussels
3. Song Y, Zhang C, Lee J, Wang F, Xiang S, Zang D (2008) Semi supervised discriminative classification with application to tumorous tissues segmentation of MR brain images. Springer, London
4. Rajendran S, Madheswaram M (2009) An improved image mining techniques for brain tumor classification using efficient classifier. *Int J Comput Sci Inf Secur (IJCSIS)* 6(3)
5. Tu C-J, Chuang L-Y, Chang J-Y, Yang C-H (2007) Member, IAENG. Feature selection using PSO-SVM. *Int J Comput Sci* 33:1 *IJCS_33_1_18*
6. Swetha G (2017) Automatic brain tumor tissue detection based on marker controlled watershed segmentation in MRI images. *IJAERS conference paper*
7. Al-amri S, Kalyankar NV, Khamitkar SD (2010) Image segmentation by using edge detection. *Int J Comput Sci Eng (IJCSSE)* 2(3)
8. Mutukrishnan R, Radha M (2011) Edge detection techniques for image segmentation. *Int J Comput Sci Inf Technol (IJCSIT)* 3(6)
9. Chandra E, Kanganalakshmi K (2011) Noise elimination in fingerprint image using median filter. *Int J Adv Network Appl* 2(6):950–955
10. Li W, Chen C, Su L, Du Q (2015) Local binary patterns and extreme learning machine for hyperspectral imagery classification. *IEEE Trans Geosci Remote Sens* 53(7):3681–3693
11. Dhanaseely AJ, Himavathi S, Srinivasan E (2012) Performance comparison of cascade and feed forward neural network for face recognition system. In: *Proceedings of international conference on software engineering mobile application modeling development (ICSEMA)*
12. Liu Q, Liu X (2013) Feature extraction of human viruses microscopic images using gray level co-occurrence matrix. In: *2013 internal conference on computer science and application (CSA)*. IEEE, pp 619–622
13. Parveen AS (2015) Detection of brain tumor in MRI images, using combination of fuzzy c-means and SVM. In: *2nd international conference, Computer Science*. <https://doi.org/10.1109/spin.2015.7095308>
14. Amasyali E (2014) Classifier ensembles with extended space of forest. *IEEE Trans Knowl Data Eng*
15. Subashini MM, Sahoo SK (2013) Brain MR image segmentation for tumour detection using artificial neural networks. *Int J Recent Technol Eng* 5(2). ISSN: 0975-4024
16. Kumar G, Bhatia PK (2014) A detailed review of feature extraction in image processing systems. In: *Fourth international conference on advanced computing & feature extraction in image processing systems. Advanced computing & communication technologies (ACCT)*. IEEE, pp 5–12

17. Quratulaina M, Jaffar A, Tae-Sunchoic (2014) Fuzzy anisotropic diffusion based segmentation and texture based ensemble classification of brain tumor. *Appl Soft Comput* 21:330–340
18. Acharya J, Gadhya S, Raviya (2013) Segmentation techniques for image analysis: a review. *Int J Comput Sci Manage Res* 2(4)
19. Bramer M (2013) Ensemble classification principles of data mining, pp 209–220
20. Seeraha GK, Kaur R (2013) Review on recent image segmentation techniques. *Int J Comput Sci Eng* 5(2)
21. Chandrashekhara SC (2014) Modified PSO based feature selection for classification of lung CT images. *Int J Comput Sci Inf Technol* 5(2)
22. Khairat KD, Turukmane AV (2014) Classification of brain tumor by feature vector using cart and C5.0 algorithms. *JAAST. Mater Sci (Special Issue)* 1(2):173–178
23. Mandloi G (2014) A survey of feature extraction technique for colour images. *Int J Comput Sci Inf Technol (IJCSIT)* 5(3)
24. Ahmad I (2015) Feature selection using particle swarm optimization in intrusion detection. *Int J Distrib Sens Netw*. Hindawi Publishing Corporation
25. Lashari SA, Ibrahim R (2013) A framework for medical image classification using soft-set. In: *The fourth international conference on electrical engineering and informatics, ICEEI*. Elsevier
26. Nagori M, Joshi M (2013) Methods and algorithm for extracting values from MRS Graph for brain tumor detection. In: *International conference on electrical engineering and computer science*. Elsevier
27. Janani V, Meena P (2013) Image segmentation for tumor detection using fuzzy inference system. *Int J Comput Sci Mobikle Comput* 2(5)
28. Canny J (1986) A computational approach to edge detection. *IEEE Trans Pattern Anal Mach Intell PAMI* 8(6):679–698
29. Panda M, Patra MR (2008) Some clustering algorithms to enhance the performance of the network intrusion detection system. *J Theor Appl Inf Technol* 4(8)
30. Sachdeva J, Kumar V, Gupta I, Khandelwal N, Ahuj CK (2011) Multiclass brain tumor classification using GA-SVM. *IEEE*. 978-0-7695-4593-6/611\$26.00@2011. <https://doi.org/10.1109/dese.2011.31>
31. Luts J, Heerschap A, Suykens JAK, Van Huffel S (2007) A combined MRI and MRI based multiclass system for brain tumor recognition using LS-SVMs with class probabilities and feature selection. *Artif Intell Med* 40:87–102

Fake News Detection Based on Machine Learning



Pushpa Choudhary, Suchita Pandey, Sakshi Tripathi,
and Shubham Chaurasiya

Abstract Mob lynchings, misrepresentation of government policies, manipulated history, and communal disharmony are some of the events that recently occurred due to fake news propagation. Hence, fake news detection model will help to spread awareness and harmony among individuals. According to BBC Report, 72% Indians fail to distinguish between ‘real’ and ‘fake’ news. Hence, in this paper a model is proposed in which natural language processing has been used for rectification of the text along with machine learning algorithms. The model predicted fake and real news successfully with 90.2% accuracy.

Keywords Fake news detection (FND) · Natural language toolkit (NLTK) · Convolutional neural networks (CNN) · Recurrent neural networks (RNN)

1 Introduction

News has been the provider of information since centuries. In traditional times, there were news agencies which were the source of news, and hence, reliability and confidentiality remained with the official organizations itself. In recent times, Internet grew rapidly from rural to urban areas. With the growth of internet, more users from all over the world got access to Internet and to spread the information in their way [1].

P. Choudhary (✉) · S. Pandey · S. Tripathi · S. Chaurasiya
Department of Information Technology, G. L. Bajaj Institute of Technology and Management,
Greater Noida, India
e-mail: pushpak2728@gmail.com

S. Pandey
e-mail: suchita.pandey28dec@gmail.com

S. Tripathi
e-mail: sakshi.tripathi498@gmail.com

S. Chaurasiya
e-mail: shubham06344sk@gmail.com

According to Economic Times report of 2019, there are 627 million internet users in India which means world’s second largest Internet user is available in India [2]. As the population of India is higher obviously number of user is also more who is using social media, in that case procreation of fake news is also high. A research by BBC shows that nearly 72% Indians struggled to distinguish between fake and real news [3]. Websites like The Onion [4], News Thump [5], The Poke News [6], and The Mash News [7] are among the top rankers of ‘Fake’ or ‘misleading’ news propagator [8]. Hence, many online fact checking resources like Snopes [9], FactCheck.org [10], Factmata.com [11], PolitiFact.com [12], and many more grew rapidly. Social networking sites such as Facebook, Whatsapp, and Google addressed this particular concern but the efforts hardly contributed in solving the issue.

Approaches to detect Fake News:

1. **Detection Approaches Based on Machine Learning:** Following are the algorithms which were used in the detection of fake news based on machine learning: support vector machines (SVMs), random forests, logistic regression models, conditional random field (CRF) classifiers, hidden Markov models (HMMs) [13].
2. **Detection approaches based on deep learning:** In this approach, following are the algorithms which were used for fake news detection by modern artificial neural networks, which is further classified into two methods, i.e., recurrent neural networks (RNN) and convolutional neural networks (CNN) [13].

This model will detect fake news which is provided by the news provider, comment sentiment analysis, and content of the provided news. In this paper, natural language processing is used for preprocessing of the dataset and machine learning approach to fight fake news (Fig. 1).

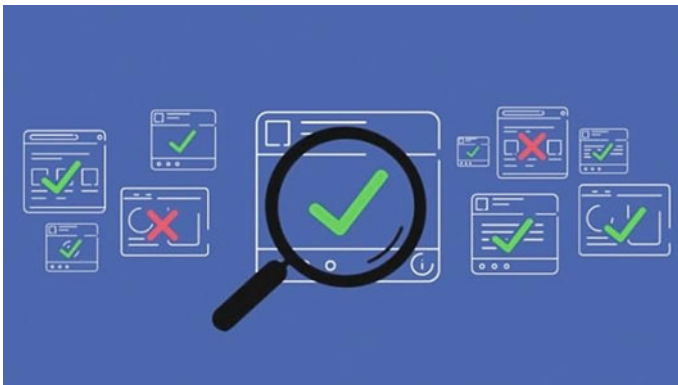


Fig. 1 Fact checker [14]

2 Literature Survey

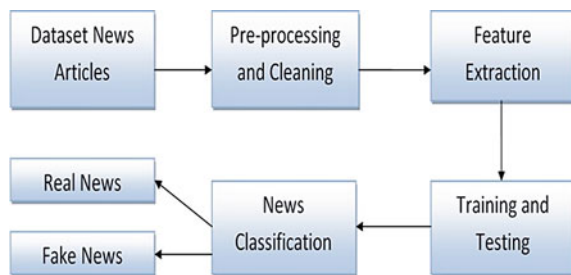
There are many models for fact checking and detecting fake news. PolitiFact [12]—A fact-checking website operated by Poynter Institute in St. Petersburg, Florida, which uses Truth-O-Meter to determine truthfulness of a statement/article/event/Image/video. But the fact checking is limited to political news and hence fails to cover broad spectrum of news. According to a survey paper, Facebook fake news sources can be encountered using BS Detector [15]. Another fact checking website, Factmata [11] provides platform to get better understanding of the content which is based on scores content on nine signals, the content includes about hate speech and political bias things, which is available on web for deep understanding of credibility and safety. Messenger for businesses flock has launched fake news detector that aims to stop false and misleading information from being introduced in their environment [16].

In India, fact checker has recently been launched by India Today, Times of India, and AFP India but these resources do not provide platform for users to check whether the news article they are viewing is fake or real. AltNews [17] has been successful in India to provide platform for user to clear their doubt, though it is yet to get more efficient and reliable.

3 Proposed Work

In this paper, a model is build based on preprocessing data with the use of Natural language Toolkit (NLTK) Library, removing all the stopwords such as—the||, —is||, and —are|| and only using those words which are unique, and it provides a relevant information. In these punctuations, numbers are also removed and then collected dataset converted into lowercase letters. Count Vectorizer or TF-IDF matrix algorithm has been used which will tallies to how often the word in used in a given article in the dataset. The process of methodology of fake news detection is shown in Fig. 2. Since the problem concerns with text classification and information extraction, for that naïve Bayes classifier has been used for text-based classification. For training and testing of dataset, multinomial NB and passive aggressive classifier have been

Fig. 2 Process flow diagram



used. In this, 33% training dataset and 67% test dataset. With the help of Count Vectorizer [18–20], rare words occurring in corpus also removed.

Objective of this paper is to make a website and app for user so that whenever he/she selects a text, the application reflects with floating window and provides user with the percentage of fake and real news of the selected text. The advantage with the application or Web site is that without opening or uploading any content in the application, the application will detect fake news.

4 Methodology

In this section, methodology of proposed model has been described. Figure 3 represents work flow of methods involved in creating the model. The major steps involved in building the model are:

1. Corpus of Text Document
2. Then preprocessing is done on corpus text
3. In the third step, analysis is done on Parsing and Basic Exploratory Data
4. Text representation using relevant feature engineering techniques
5. Modeling
6. Evaluation and Deployment.

4.1 Scraping News Articles for Data Retrieval

Currently, the model has been trained using dataset from Kaggle [21] with 6335 rows and 4 columns. News articles will be scraped from, in shorts [22], with the help of python libraries along with NLTK and spacy. A typical news article is also in the HTML section as shown in Fig. 4.

The specific HTML tags can also be used which contain the textual content [24]. Hence, with the help of libraries such as BeautifulSoup and requests, useful content will be scraped.

Collected dataset contains 6335 rows and 4 columns; the head of the dataset has been depicted in Fig. 5.



Fig. 3 Methodology of proposed model

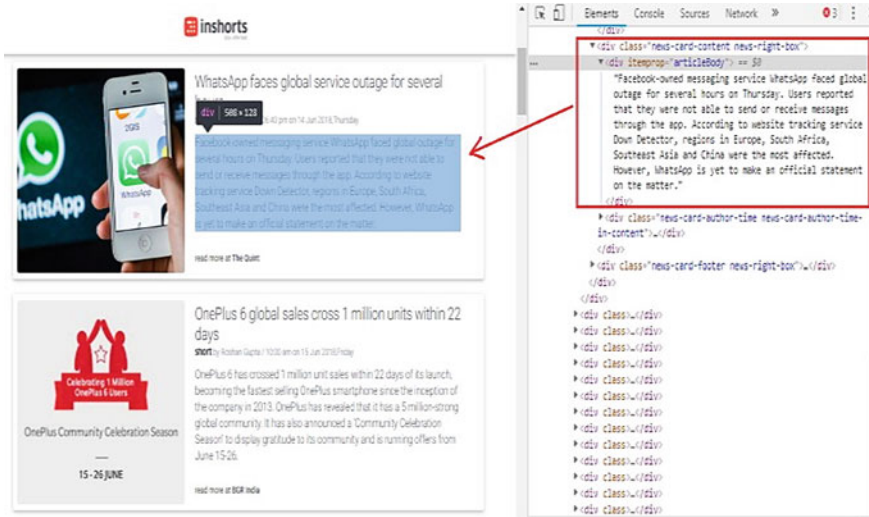


Fig. 4 Landing page for technology news articles and its corresponding HTML structure [23]

Unnamed: 0			title
0	8476		You Can Smell Hillary's Fea
1	10294	Watch The Exact Moment Paul Ryan Committed Pol.	
2	3608	Kerry to go to Paris in gesture of sympathy	
3	10142	Bernie supporters on Twitter erupt in anger ag..	
4	875	The Battle of New York: Why This Primary Matters	

Fig. 5 Dataset of real and fake news articles

4.2 Text Wrangling, Cleaning and Preprocessing

Here, the NLTK and spacy packages both have been leveraged to process the data. Stopwords can be used to process data and remove the most common words used in our dataset such as —and||, —the|| and —is||. Along with stopwords, HTML tags, accented text, expand contractions, punctuations, numbers, and special characters are also needed to be removed since they do not provide relevant information. Lemmatizing and stemming text are done with the help of functions such as `lemmatize_text()` and `simple_stemmer()`, respectively. With the help of TF-IDF vectorizer, word importance in a given article in the entire corpus is determined [25].

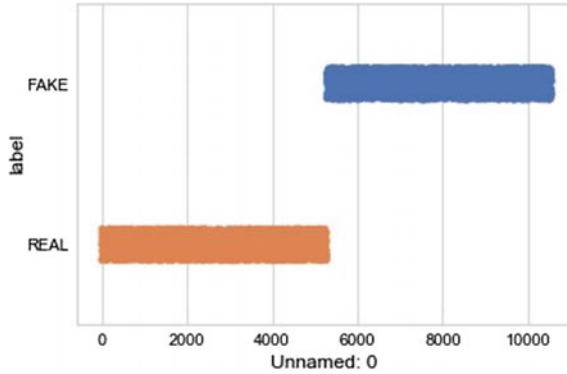


Fig. 6 Dataset visualization of fake news and real news using Seaborn X-axis represents label (fake or real), y-axis represents Index

4.3 Data Visualization and Feature Extraction

For better understanding of the dataset, matplotlib and seaborn libraries for visualization and plotting graphs are used. Using stripplot() method, present in seaborn library statistical plot as shown in Fig. 6 was formed which shows 0–5000, datasets are REAL while from 5000 to 10,000, datasets are FAKE. CountVectorizer library to remove the rare words was imported.

4.4 Modeling and Grid Search

With the help of multinomial NB and passive aggressive classifier, 33% of the dataset was trained and remaining set of data used as testing, i.e., 67%. Using confusion matrix, highest accuracy model will be achieved [26].

5 Result Analysis

Let us assume that given news as a positive, and classifier classifies given news as a fake:

- First case can be the number of True Positives is the number of news articles, correctly classified as Fake News.
- Second case can be the number of False Positives is the number of news articles, incorrectly classified as Fake News.
- Third case can be the number of True Negatives is the number of news articles, correctly classified as True News.

- Fourth case can be the number of True Positives is the number of news articles, incorrectly classified as True News.

For all the cases, precision of a classifier is calculated as follows:

$$\text{Precision} = \text{TP}/(\text{TP} + \text{FP})$$

where TP—Number of True Positive, FP—Number of False Positive.

The recall of a classifier is calculated as follows:

$$\text{Recall} = \text{TP}/(\text{TP} + \text{FN})$$

where FN is a Number of False Negative.

Four confusion matrixes are depicted in Fig. 7, which help in evaluating the quality of the output of a classifier. In this, multinomial NB and passive aggressive classifier are used on the fake or real news dataset. Diagonal elements of the matrix represent number of points which represents predicted label value is equal to true label value, whereas off-diagonal matrix represents number of points where prediction value fails.

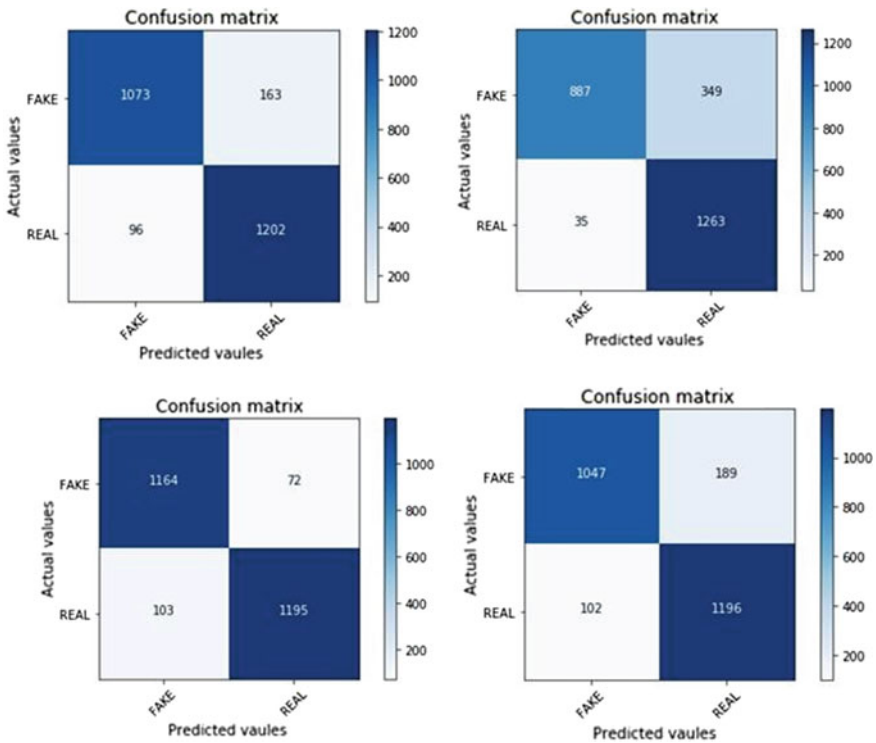


Fig. 7 Confusion matrix, without normalization

The following matrix shows the fake news detection without normalization. As in Fig. 7 depicted, the results of the matrix changes as the classification models or vectorizers are changed.

In Matrix 1, combination of Multinomial NB and TF-IDF vectorizer algorithm has been used.

In Matrix 2, combination of Multinomial NB and Count Vectorizer algorithm has been used.

In Matrix 3, combination of Passive Aggressive Classifier and TF-IDF vectorizer algorithm has been used.

In Matrix 4, combination of Passive Aggressive Classifier and Hashing Vectorizer algorithm has been used.

The precision for the given classifying model is 90.2%; recall on the other hand is 48.6%.

The positive predictive value (precision) of the model represents the relevant text documents among the retrieved text documents, whereas sensitivity (recall) is the fraction of total amount of relevant text documents that were actually retrieved.

6 Conclusion and Future Scope

In this paper, the proposed model is Fake News Detection which differentiates the text by text classification algorithms to tell whether the news is `_fake` 'or' `_real`'. For training, 33% dataset has been used, and 67% data has been used for testing the Fake News Detection model. The model predicted fake and real news successfully with 90.2% accuracy.

In future, VADER for sentiment analysis can be used which is more efficient algorithm and a text classification model that provides us with highest accuracy. Also, existing Fake News Detection models have worked for news and politics only, scope in Stock Markets, where shares rise and fall very frequently, still persists.

References

1. Hamdi T, Slimi H, Bounhas I, Slimani Y (2020) A hybrid approach for fake news detection in Twitter based on user features and graph embedding. In: International conference on distributed computing and internet technology, 9 Jan 2020. Springer, Cham, pp 266–280
2. Silva RM et al (2020) Towards automatically filtering fake news in Portuguese. *Expert Syst Appl* 146:113199
3. Ozbay FA, Alatas B (2020) Fake news detection within online social media using supervised artificial intelligence algorithms. *Phys A: Stat Mech Appl* 540:123174
4. Zhou X, Zafarani R, Shu K, Liu H (2019) Fake news: fundamental theories, detection strategies and challenges. In: Proceedings of the twelfth ACM international conference on web search and data mining, 30 Jan 2019, pp 836–837
5. Shu K et al (2020) FakeNewsNet: a data repository with news content, social context, and spatiotemporal information for studying fake news on social media. *Big Data* 8(3):171–188

6. Pennycook G, Rand DG (2020) Who falls for fake news? The roles of bullshit receptivity, overclaiming, familiarity, and analytic thinking. *J Pers* 88(2):185–200
7. Nguyen HH, Yamagishi J, Echizen I (2019) Use of a capsule network to detect fake images and videos. *arXiv preprint arXiv: 1910.12467*
8. Shu K et al (2017) Fake news detection on social media: a data mining perspective. *ACM SIGKDD Explor Newslett* 19(1):22–36
9. Tacchini E, Ballarin G, Della Vedova ML, Moret S, de Alfaro L (2017) Some like it hoax: Automated fake news detection in social networks. *arXiv preprint arXiv: 1704.07506*
10. Granik M, Mesyura V (2017) Fake news detection using naive bayes classifier. In: 2017 IEEE first Ukraine conference on electrical and computer engineering (UKRCON) 29 May 2017. IEEE, pp 900–903
11. FACTMATA – factmata.com [Online]. Available: <https://factmata.com/>
12. Fact Checking U.S. Politics | PolitiFact – politifact.com [Online]. Available: <https://politifact.com/>
13. Bondielli A, Marcelloni F (2019) A survey on fake news and rumour detection techniques. *Inf Sci* 497:38–55
14. Protecting the EU elections from misinformation and expanding our fact-checking program to new languages – aboutfb.com [Online]. Available: <https://about.fb.com/news>
15. B.S. Detector - Browser extension to identify fake news sites, Bsdetector.tech (2018) [Online]. Available: <http://bsdetector.tech/>
16. Messenger platform Flock launches feature to identify fake news, *economictimes.com* (2019) [Online]. Available: <https://m.economictimes.com/small-biz>
17. Alt News, *altnews.com* [Online]. Available: <https://www.altnews.in/>
18. Conroy NJ, Rubin VL, Chen Y (2015) Automatic deception detection: methods for finding fake news. In: *Proceedings of the association for information science and technology*, vol 52, no 1, pp 1–4
19. Feng S, Banerjee R, Choi Y (2012) Syntactic stylometry for deception detection. In: *Proceedings of the 50th annual meeting of the association for computational linguistics: short papers-volume 2*, Association for Computational Linguistics, 2012, pp 171–175
20. Gilda S (2017) Department of computer engineering, Evaluating machine learning algorithms for fake news detection. In: 2017 IEEE 15th Student Conference on Research and Development (SCoReD)
21. Pagliardini M, Gupta P, Jaggi M (2017) Unsupervised learning of sentence embeddings using compositional n-gram features. *arXiv preprint arXiv:1703.02507*
22. Rashkin H, Choi E, Jang JY, Volkova S, Choi Y, Allen PG (2017) Truth of varying shades: analyzing language in fake news and political fact-checking. In: *Proceedings of the 2017 conference on empirical methods in natural language processing*, pp 2931–2937
23. Balmas M (2014) When fake news becomes real: combined exposure to multiple news sources and political attitudes of inefficacy, alienation, and cynicism. *Communic Res* 41(3):430–454
24. Conroy NJ, Rubin VL, Chen Y (2015) Automatic deception detection: Methods for finding fake news. In: *Proceedings of the association for information science and technology* 52(1):1–4
25. Feng S, Banerjee R, Choi Y (2012) Syntactic stylometry for deception detection. In: *Proceedings of the 50th annual meeting of the association for computational linguistics: short papers-volume 2*, Association for Computational Linguistics, pp 171–175
26. Gottfried J, Shearer E (2016) News use across social media platforms 2016. In: *Pew research center reports*. <http://www.journalism.org/2016/05/26/news-use-across.com>

Design of Octagonal-Shaped CP Antenna for RFID Handheld Reader Applications



Niraj Agrawal, A. K. Gautam, Rajesh Mishra, and S. D. Choudhary

Abstract In this article, a circularly polarized octagonal-shaped slot antenna is proposed for radio frequency identification (RFID) reader application. The bandwidth and circulation polarization of proposed design are improved by changing the size of corner truncation and the octagonal-shaped slot. With an overall size of $65 \times 65 \times 1.6 \text{ mm}^3$, the designed antenna achieves measured return loss bandwidth of around 35 MHz (897–932 MHz) and axial ratio of bandwidth 10 MHz (913–923 MHz). The printed antenna agrees a good promise between simulate and measured values. The antenna exhibits a wide beam-width characteristic, around 113° in the upper hemisphere. The proposed antenna is suitable for RFID short-range reading applications.

Keywords Axial ratio (AR) · Radio frequency identification (RFID) · RHCP

1 Introduction

UHF RFID frequencies ranges and standards are regularized by an organizations such as the ISO (organization for international standardization), EPC Global and ASTM international. The frequency spectrum allocated for UHF RFID is 865–868 MHz

N. Agrawal (✉) · R. Mishra
Department of Electronics and Communication Engineering,
School of ICT, Gautam Buddha University, Greater Noida, India
e-mail: nirajagrawal@gmail.com

R. Mishra
e-mail: raj25mis@gmail.com

A. K. Gautam
Department of Electronics and Communication Engineering,
GBPIT Uttarakhand, Uttarakhand, India
e-mail: gautam1575@yahoo.co.in

S. D. Choudhary
Department of Electronics and Communication Engineering, NIET, Greater Noida, India
e-mail: suryadeo.bit@gmail.com

and 902–928 MHz. RFID technology has enormous application such as localization, monitoring and identification of object and also in health care, shops, supermarkets, shops and tracking and security in different operations for railways and airports. Practically, the efficiency of the RFID decreases due to the random orientation of the items. The efficiency of the RFID reader can be increased by using a orientation independent circularly polarized (CP) transmitter antenna [1, 3, 5, 8–10]. Thus, these antennas are effective for unpredictable orientation of the system.

In [10], a pair of slot loaded shorted patches and three-step impedance sections RFID chip is presented for UHF RFID tag application. In [9], the compactness is achieved by implanting four symmetric-slits, and circular-shaped asymmetric slots are used to generate CP radiation. A broadband CP patch antenna is presented a two side corner truncated patch with open-circuited microstrip line for universal UHF RFID applications [3]. Further, two orthogonally T-shaped slots are introduced on the square patch for achieving CP radiation [8]. In [12], a passive UHF RFID tag with variable impedance tuning range is used to match different RFID chips. A RFID tag antenna with Vivaldi-shaped aperture is presented to tune 915 MHz frequency [11], and a platform immune antenna solution for RFID tags is presented [6]. An inverted PIFA structure at a resonant frequency 920 MHz for a dongle-type RFID reader module is proposed [7]. Aforesaid antennas are either larger in size or show smaller operational bandwidth.

Therefore, in this article, a compact circularly polarized octagonal-shaped slot antenna for ISM radio frequency identification reader is designed and experimentally studied. The bandwidth and circulation polarization of proposed design are improved by changing the size of corner truncation and the octagonal-shaped slot. An intended RFID design reveals a wide 3-dB beam-width characteristic and excellent cross-polar discrimination (XPD) in the upper hemisphere. The prototype is printed on lossy substrate and practically measured. The optimized values of displayed antenna are obtained by CST simulator [4].

2 Antenna Design and Configurations

The radiating patch used in the proposed antenna is an unequal truncated corner with an octagonal-shaped in diagonal of first quadrant. The compactness in the antenna nourishes by using octagonal-shaped which consequently increases the total electrical length of the antenna, and circular polarization is nourished by unequal truncation of all four corners of the radiator. The unequal truncations on the corners are accountable to excite two orthogonal components as illustrated in Fig. 1. The compact design with a overall volume of $65 \times 65 \times 1.6 \text{ mm}^3$ is fabricated on FR4 material for UHF-RFID reader applications. The intended structure is simulated and optimized using the CST MW commercial simulator [4], and optimized value of parameters is scheduled in Table 1.

Fig. 1 Configuration of the designed antenna. **a** Perspective view and **b** Front view

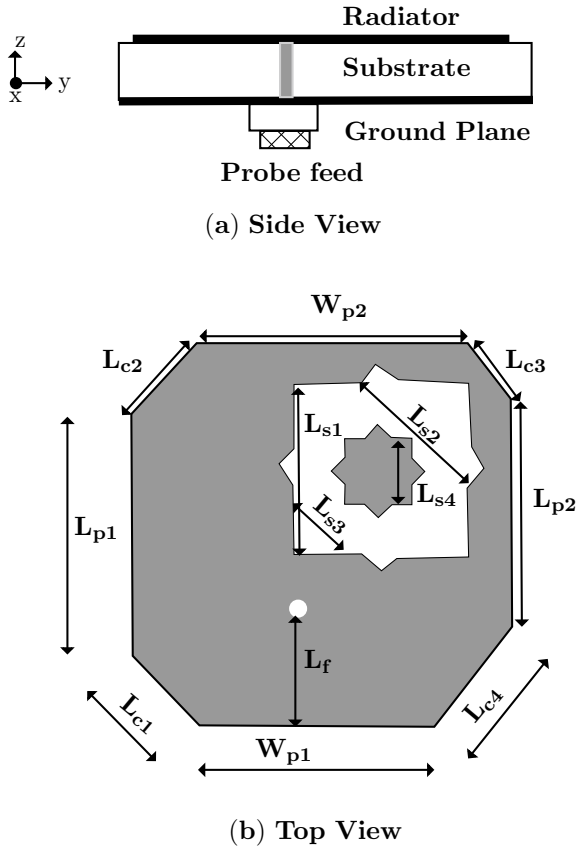


Table 1 Marked parameters in Fig. 1b

Parameters	Unit (mm)
L_{p1}	31.00
L_{p2}	36.00
L_{c1}	24.00
L_{c2}	24.04
L_{c3}	15.55
L_{c4}	25.45
L_{s1}	34.00
L_{s2}	28.20
L_{s3}	11.30
L_{s4}	12.00
W_{p1}	30.00
W_{p2}	37.00
L_f	16.50

2.1 CP Mechanism

For circular polarization, the magnitude of axial ratio must be unity, whereas the phase between degenerated orthogonal modes must be $\pm 90^\circ$. Two degenerated modes in the intended antenna excited due to the currents at 0° time phase and 90° time phase, respectively, are shown in Fig. 2. The length of the slots responsible for currents at 0° time phase and 90° time phase can be calculated as

$$L_1 = \frac{2L_{c2}}{3} + 2W_{p2} + L_{c3} + \frac{L_{p2}}{3} \quad (1)$$

$$L_2 = L_{c3} + L_{p2} + L_{c4} \quad (2)$$

The resonant frequencies due to these slots can be derived based on following equation,

$$f_{ri} = \frac{c}{2L_i \sqrt{\epsilon_{\text{reff}}}} \quad \text{where } i = 1, 2 \quad (3)$$

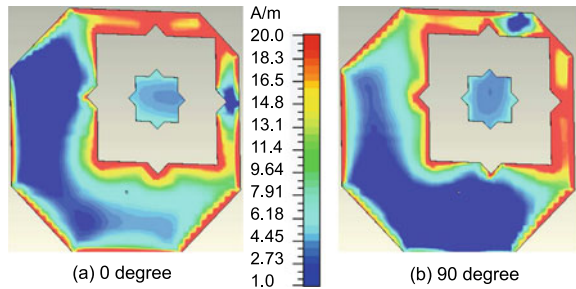
The evaluated dielectric constant is [2]

$$\epsilon_{\text{reff}} = \frac{\epsilon_r + 1}{2} + \frac{\epsilon_r - 1}{2} \left(1 + \frac{12h}{W} \right)^{-1/2} \quad (4)$$

By using listed data, $L_1 = 80.57$ mm and $L_2 = 77$ mm. Meanwhile, the tune frequencies computed based on Eqs. (1) and (2) are $f_{r1} = 899.9$ MHz and $f_{r2} = 953.7$ MHz, respectively.

Therefore, the mid-frequency f_o calculated for these two frequencies will be 926.8 GHz which is approximately equal to the centre frequency of simulated RFID resonance, and the variation of evaluated frequency is less than 2.5%. In the present case, degenerated orthogonal mode at $f_{r1} = 899.9$ MHz is leading by 45° , and second degenerated orthogonal mode at $f_{r2} = 953.7$ MHz GHz is leading by 45° , respectively, to the mid-frequency f_{r0} . Therefore, the phase relation between the frequencies is 90° . Hence, it radiates circular polarization at the center frequency of the operation 918 MHz and is shown in Fig. 2a, b.

Fig. 2 Simulated current distributions at 918 MHz: **a** $t = 0^\circ$ and **b** $t = 90^\circ$



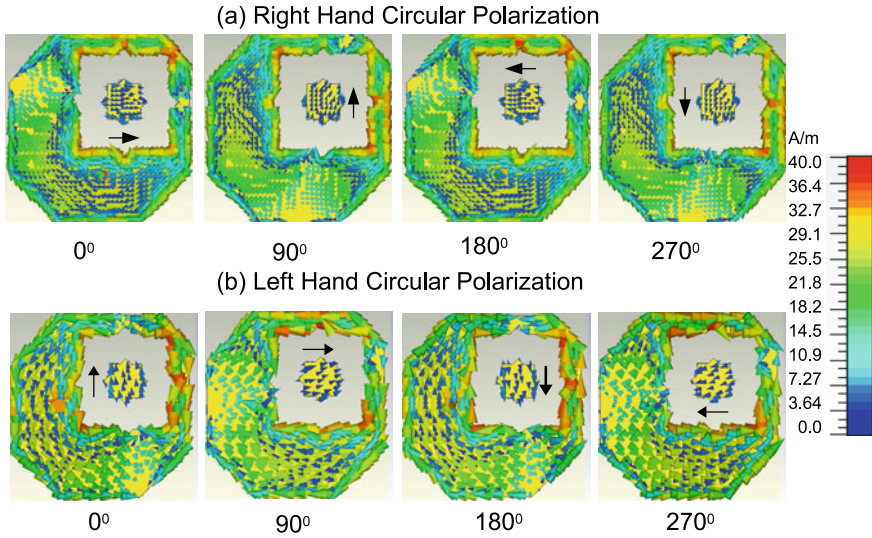


Fig. 3 Simulated current distributions at centre frequency (911 MHz) for different time phases **a** RHCP radiation. **b** LHCP radiation

The simulated current distributions at 918MHz are displayed in Fig. 3a, b to realize the sense of CP radiation. The current is distributed from 0° to 270°, with an interval of 90°. It is concluded from Fig. 3a that the current rotates in counter-clockwise direction to produce RHCP radiation with change in time phase. The sense of polarization can be changed to LHCP by altering the feed coordinate to *x*-axis. It can be observed from the Fig. 3b, the clockwise rotation of current with change in time phase revealed a LHCP radiation .

3 Measured Results and Discussion

The RFID antenna is printed on lossy substrate and experimentally verified. It is observed from Fig. 4 that good agreement of impedance bandwidth between simulated and experimental values. The intended antenna efficaciously shows the large impedance bandwidth of 35 MHz (897–932 MHz) and axial ratio of bandwidth 10 MHz (913–923 MHz).

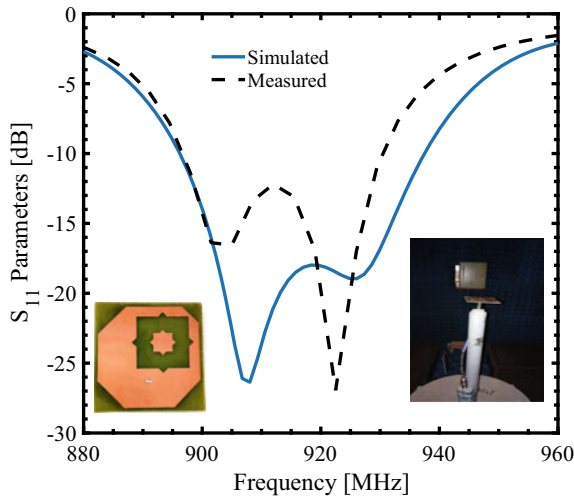


Fig. 4 S-parameters for the presented CP antenna

The simulated and measured 2-D radiation polar pattern at the centre frequencies 918 MHz has been represented in Fig. 5. Figure 5 reveals that the respective bore-sight gain is about 3.2 dBic. Through reference to Fig. 5a, b, the RHCP field (co-polar) in the xz and yz plane at 918 MHz is more effective than the LHCP field (cross-polar) by 26.5 dB. It is notoriously demonstrated that cross polarization rejection (XPD) is good.

The simulated and measured axial ratio arrangement of the designed structure is around 10 MHz (913–923 MHz) is illustrated in Fig. 6.

4 Conclusion

A octagonal-shaped circular polarized antenna for RFID application has been proposed in this letter. To achieve circulation polarization, unequal corner truncation and the octagonal-shaped slot were used. The simulated results of printed antenna agree well with measured once. The antenna displays a wide beam-width of about 113° in the upper hemisphere, ARBW (bore-side) 10 and 35 MHz wide impedance bandwidth. The proposed antenna is suitable for RFID short-range reading applications.

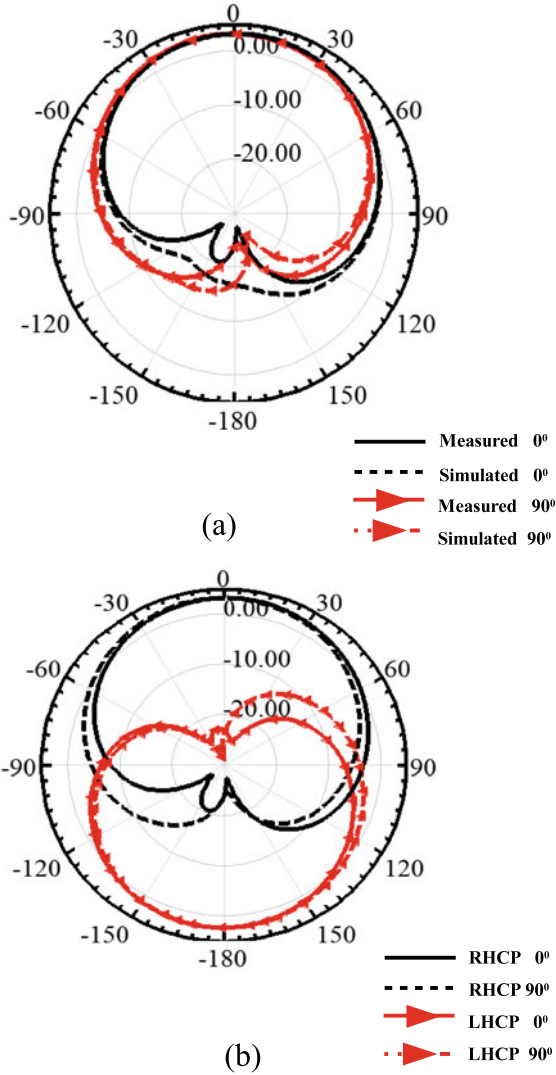
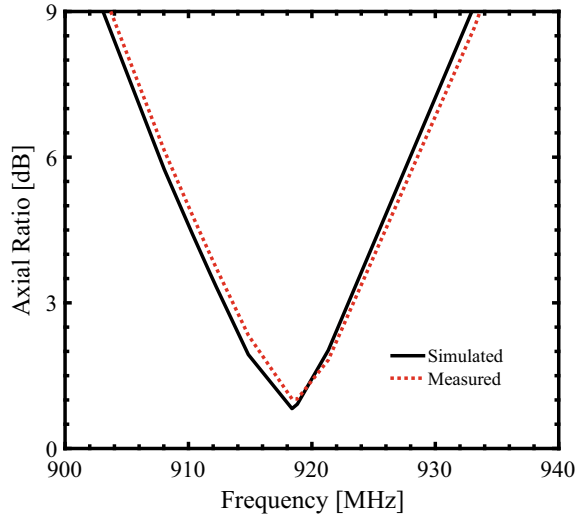


Fig. 5 Radiation polar patterns at frequency 918 MHz **a** Bore-sight gain **b** Cross polarization

Fig. 6 Axial ratio response of designed antenna



References

1. Agrawal N, Gautam AK, Rambabu K (2019) Design and packaging of multi-polarized triple-band antenna for automotive applications. *Int J Electron Commun AEU* 113
2. Balanis CA (2005) *Antenna theory analysis and design*. 3rd edn. Wiley
3. Chen ZN, Qing X, Chung HL (2009) A universal UHF RFID reader antenna. *IEEE Trans Microwave Theo Tech* 57(5):1275–1282
4. Computer simulation technology microwave studio (CST MWS)
5. Gautam AK, Farhan M, Agrawal N, Rambabu K (2019) Design and packaging of a compact circularly polarised planar antenna for 2.45-GHz RFID mobile readers. *IET Microwaves, Antennas and Propag* 13(13):2303–2309
6. Hirvonen M, Pursula P, Jaakkola K, Laukkanen K (2004) Planar inverted-F antenna for radio frequency identification. *Electron Lett* 40(14):848–850
7. Kim KT, Ko JH, Choi K, Kim HS (2011) Robust optimum design of PIFA for RFID mobile dongle applications. *IEEE Trans Magnet* 47(5):962–965
8. Lin YF, Lee CH, Pan SC, Chen HM (2013) Proximity-fed circularly polarized slotted patch antenna for RFID handheld reader. *IEEE Trans Antennas Propag* 61(10):5283–5286
9. Nasimuddin, Chen ZN, Qing X (2010) Asymmetric-circular shaped slotted microstrip antennas for circular polarization and RFID applications. *IEEE Trans Antennas Propag* 58(12):3821–3828
10. Polivka M, Svanda M (2015) Stepped impedance coupled-patches tag antenna for platform-tolerant UHF RFID applications. *IEEE Trans Antennas Propag* 63(9):3791–3797
11. Soliman EA, Sallam MO, Raedt WD, Vandenbosch GAE (2012) Miniaturized RFID tag antenna operating at 915 MHz. *IEEE Antennas Wireless Propag Lett* 11:1068–1071
12. Wang S, Tao Y, Wang G (2011) UHF RFID tag for integration into a cigarette pack. *IEEE Antennas Wireless Propag Lett* 10:1433–1436

Speed Optimization of Multipliers



Amit Gupta, Chiranjeev Singhal, Priya Singh, Satyam Dubey,
Saurabh Sharma, and Waris Quraishi

Abstract Multipliers play a vital role in DSP applications. The present development in processor design aims at a high-speed multiplier circuit. Generally, the computational power of any system is affected by its multiplier performance in terms of processing speed. The paper describes the parametrical comparison between different multipliers such as booth multiplier, Wallace multiplier, Wallace using compressor technique and modified booth multiplier in terms of processing speed. The delay of the critical path in Wallace multiplier using the compressor technique is minimized. The circuit is synthesized, and high speed is achieved by reducing the delay of the multiplier circuit. Optimizing the speed of the multiplier is the major design issue. However, improving the speed of multiplier may result in a larger area of the circuit.

Keywords Processing speed · Area · Delay

1 Introduction

Multiplication is the basic of almost all digital signal processing units, and it is important for those applications which are highly multiplication intensive. Also, algorithm used in the implementation of the multiplication operation plays a vital role in describing the overall speed of the system. Therefore, there has been much work on advanced high-speed multiplication and designing architecture in past few years. Procedural multiplication algorithm consists of mainly three steps [1]. For first step, the partial products are produced. For second step, the partial products are

A. Gupta (✉) · P. Singh · S. Dubey · S. Sharma · W. Quraishi
Department of Electronics and Communication, Galgotias College of Engineering and
Technology, Greater Noida, India
e-mail: amit.gupta@galgotiacollege.edu

P. Singh
e-mail: priyapsingh20@gmail.com

C. Singhal
DKOP Labs Private Limited, Noida, India

© Springer Nature Singapore Pte Ltd. 2021
R. Agrawal et al. (eds.), *Advances in Smart Communication and Imaging Systems*,
Lecture Notes in Electrical Engineering 721,
https://doi.org/10.1007/978-981-15-9938-5_10

minimized to the single row of final sum and the single row of carry. For the third step, carry and sum are summed up together that produce the result. The four multiplication algorithms have been covered, namely booth multiplier, Wallace multiplier, Wallace using compressor technique, modified booth multiplier and evaluating their performance in terms of delay parameter with resources like LUTs, I/O blocks, flipflops and later finding out which of the above-mentioned multiplier provides the high performance. Here, the major focus on the first step which consists of forming the partial product array, and a design of multiplication algorithm in which the compressor can add more than three bit and hence reduces the full adder operation time.

2 Booth Multiplier

Arithmetic shifting operation will perform on F, Q and p by one bit. In booth's multiplication algorithm, multiplication of two signed binary numbers is evaluated in two's complement notation [2]. It works shifting and adding efficiently according to the bits received which helps in increasing the speed. Booth's algorithm is of great need in the field of computer architecture [3].

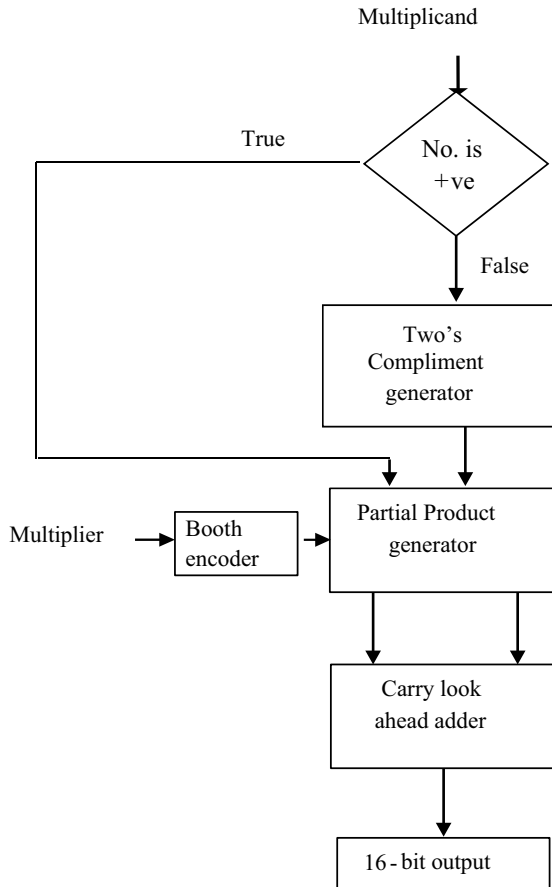
Algorithm:

1. Initialize value register F and p with zeroes.
2. Result will be stored in F and Q (multiplier) register.
3. If the least significant bit of Q and p is same, then F, Q and p register shifted arithmetic right by one bit.
4. If the least significant bit of Q and p is 0 and 1, respectively, then multiplicand is added with F. After addition, arithmetic right shifting operation will be performed on F, Q and p by one bit.
5. If the least significant bit of Q and p is 1 and 0, respectively, then multiplicand is subtracted with F. After subtraction, arithmetic right shifting operation will be performed on F, Q and p by one bit (Fig. 1).

3 Wallace Multiplier Algorithm

A Wallace tree is a powerful hardware function, used to multiply two integers in the digital circuit that is used in digital circuit [4]. Wallace multiplier requires a lot of hardware. In this method, the partial product matrix is reduced into a two-row matrix by various adders such as half adder, carry save adder, full adder, and these two rows are sum and by using a fast carry propagate adder and hence produce the output product [5]. For higher order of multiplicands, i.e., more than 8-bits, this advantage is highly beneficial, because of the addition of partial products is low in the Wallace tree and therefore the speed is increased [6].

Fig. 1 Booth algorithm



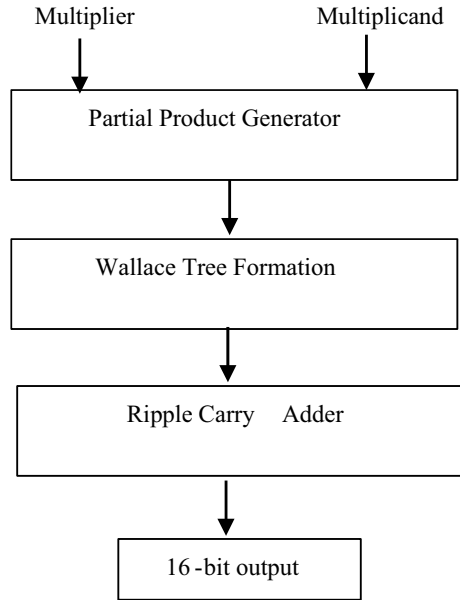
Algorithm:

1. Calculate the partial products by multiplying each bit of one argument by each bit of other, yielding N results.
2. Reduce the partial product by taking three rows at a time which results in two where one is for sum and other for carry.
3. Group the wires and add them with a ripple carry adder (Fig. 2).

4 Wallace Using Compressor Technique

The Wallace algorithm using compressor reduces the path delays during synthesis. It works the same as the Wallace multiplier algorithm [7]. In addition, it uses an additive compressor. Here, the compressors 4:3, 5:3, 6:3, 7:3, 8:4 are used in order

Fig. 2 Wallace algorithm



to simulate and synthesize [1, 4, 8]. It enhances the speed of the overall operation by reducing the delay of critical path [9].

1. Calculate the partial product, yielding N result.
2. Add each column bits using different compressor (4:3, 5:3, 6:3, 7:3, 8:4).
3. Repeat step 2 until each column has 3 or less than 3 bits.
4. Add them together using carry look ahead adder (Fig. 3).

5 Modified Booth Algorithms

Modified booth algorithm enhances the speed of multiplier and also helps in reducing the area of the multiplier circuit by reducing the partial products [3, 10].

Algorithm:

1. An array is formed by the multiplicand and multiplies.
2. Calculate the partial product by multiplying each bit of multiplicand with each bit of multiplies.
3. The resultant partial products are added along with generated carry (Fig. 4).

Fig. 3 Wallace using compressors

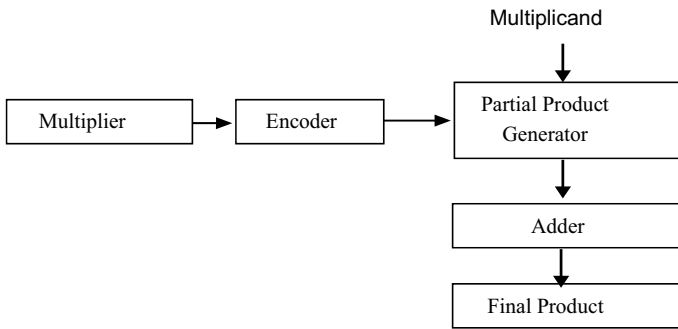
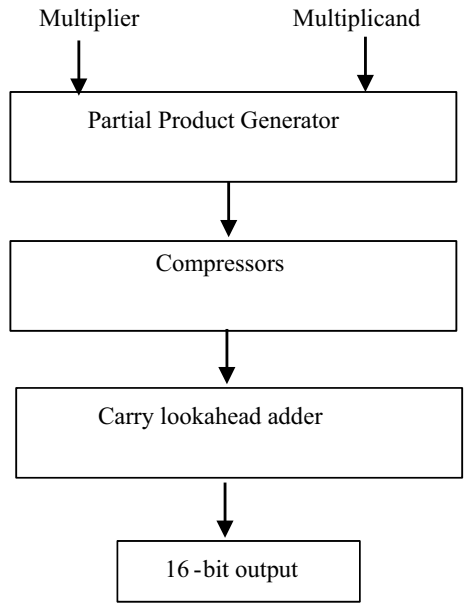


Fig. 4 Modified booth algorithm

6 Simulation Results

The architecture of booth multiplier, Wallace multiplier, Wallace using compressor technique, modified booth algorithm is coded in Verilog language, and reports of synthesis are taken using Xilinx ISE 14.6 simulator. Target device is Zynq, XC7Z010 (Figs. 5, 6, 7 and 8).

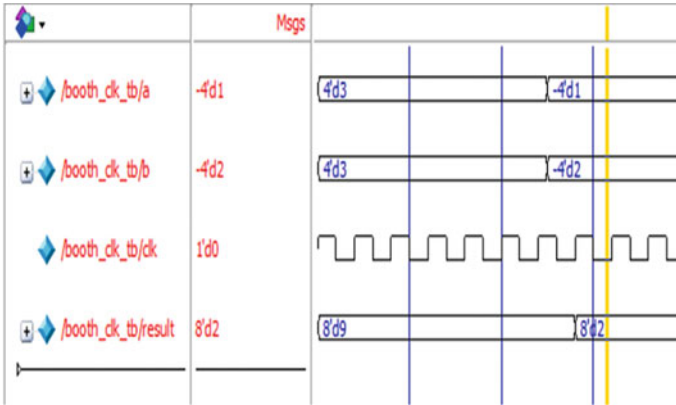


Fig. 5 Simulation waveform of booth multiplier

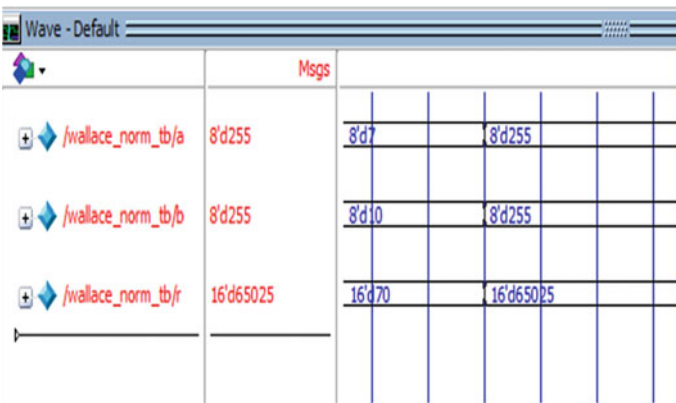


Fig. 6 Simulation waveform of Wallace multiplier

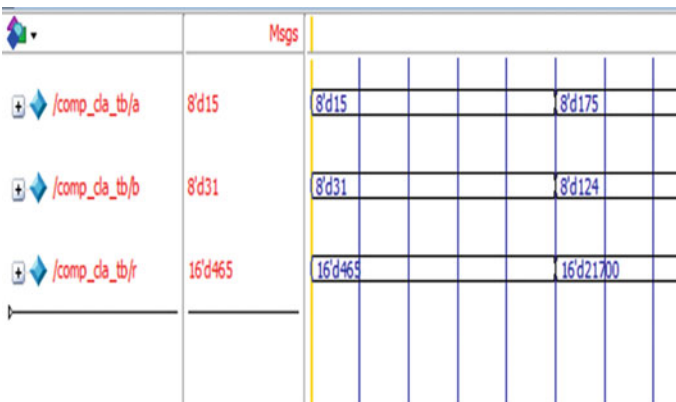


Fig. 7 Simulation waveform of Wallace using compressor

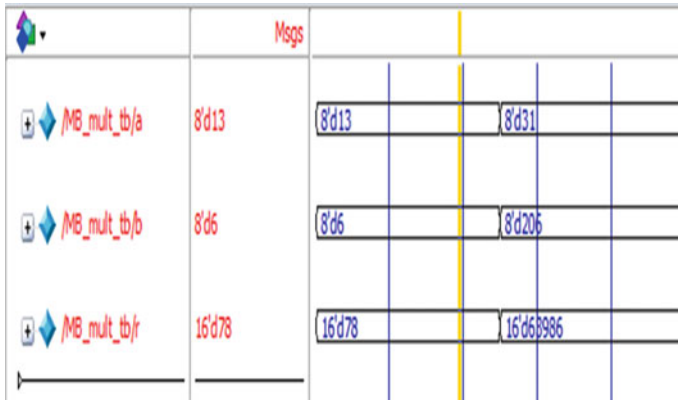


Fig. 8 Simulation waveform of modified multiplier

7 RTL Schematic

After synthesis of different multipliers reported in the literature [2, 3, 6], the HDL code is translated into RTL schematic shown in Figs. 9, 10, 11 and 12. The schematic shows data flow between different LUTs and registers.

8 Results

Obtained results are represented in a tabular form for each and every algorithm studied (Tables 1 and 2).

9 Conclusion

The design, simulation and synthesis of different types of multipliers (booth multiplier, modified booth multiplier, Wallace multiplier, Wallace multiplier using compressor) are performed. Analysis of their delays and power is recorded, and the results show that the booth multiplier takes the largest delays among these multipliers, and Wallace multiplier using the compressors has less delay. Here, 4:3, 5:3, 6:3, 7:3 and 8:4 compressors have been used that increase the speed of partial addition in the multiplier. 8:4-bit compressor has a maximum delay compared to other compressors, and this compressor has a large contribution of delay in the multiplier.

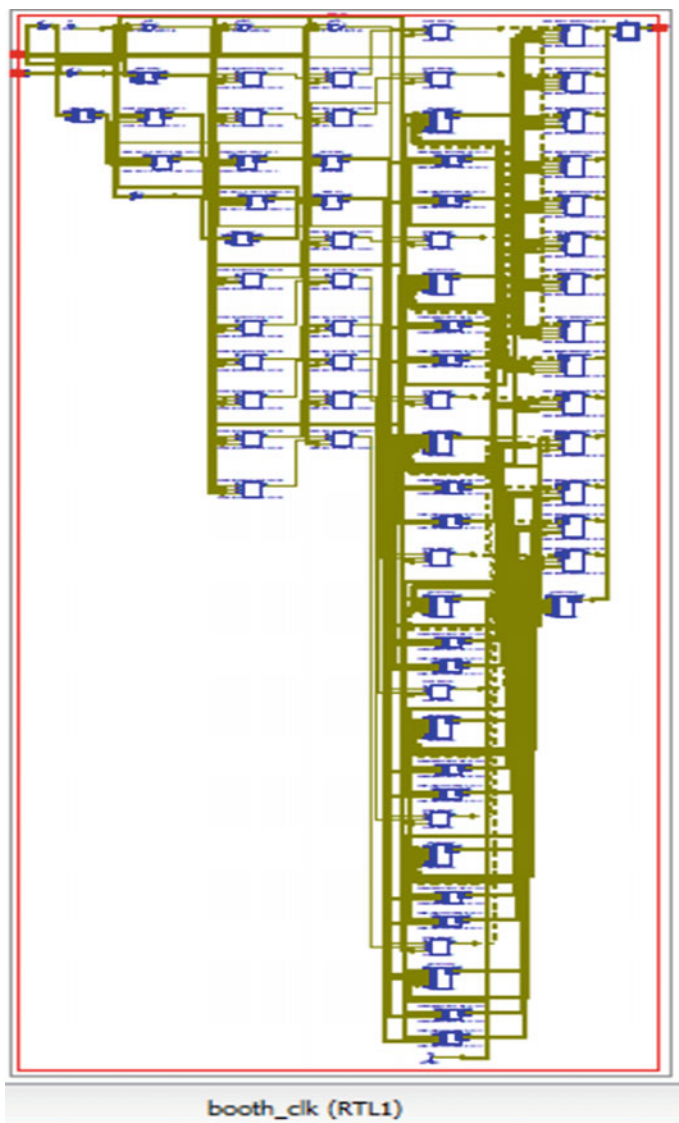


Fig. 9 RTL of booth multiplier

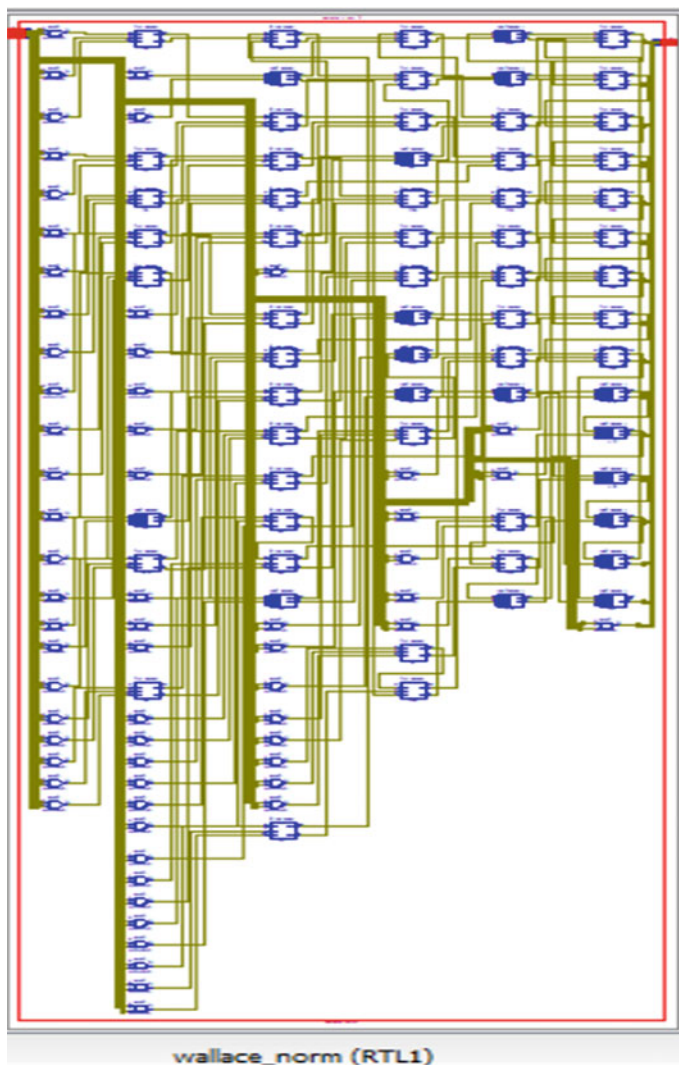


Fig. 10 RTL of Wallace multiplier

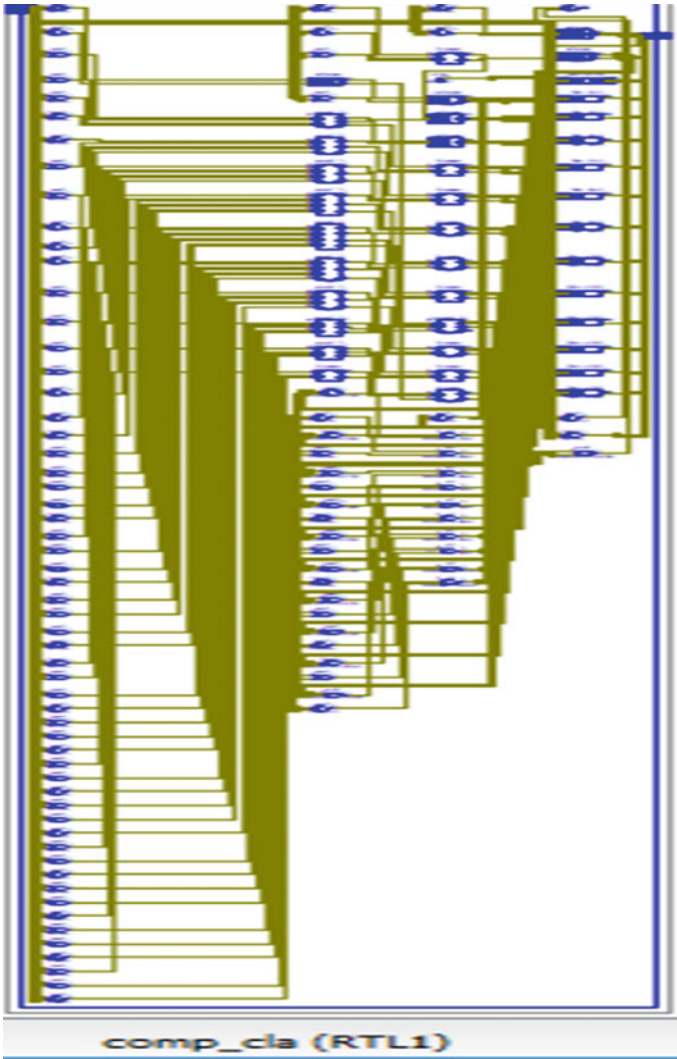


Fig. 11 RTL of Wallace using compressor

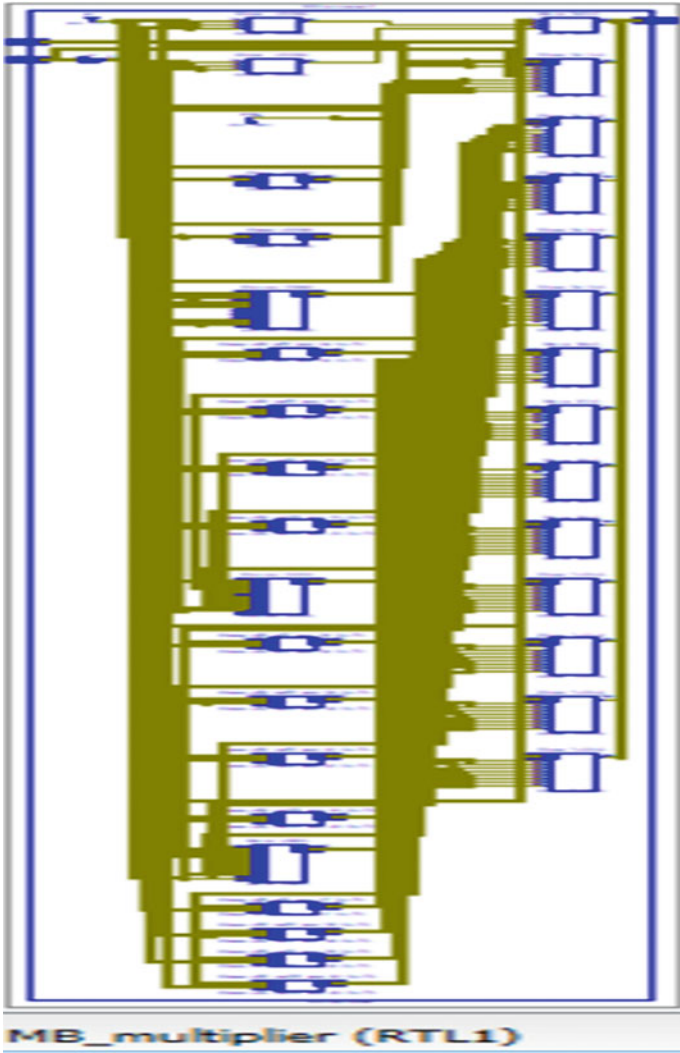


Fig. 12 RTL of modified booth multiplier

Table 1 Resource utilization summary

Resources	Booth multiplier	Wallace multiplier	Wallace using compressor	Modified booth multiplier
No. of slice LUTs	296	111	119	194
No. of Flipflops	0	0	0	0
No. of I/O blocks	33	32	32	32

Table 2 Parameter utilization comparison and summary

Parameter	Booth multiplier	Wallace multiplier	Wallace using compressor	Modified booth multiplier
Delay (ns)	13.156	7.323	5.500	7.604
Power (w)	0.10	0.10	0.10	0.10

References

1. Asif S, Kong Y (2015) Analysis of different architectures of counter based Wallace multipliers. In: 2015 tenth international conference on computer engineering & systems (ICCES). IEEE, pp 139–144
2. Vijetha K, Bhaskar SCV, Performance analysis of different multipliers for embedded and DSP applications
3. Sonal Prajapati (2018) Different multipliers and its performance analysis in VLSI using VHDL. *Int J Innov Res Technol* 2028–2033
4. Marimuthu CN, Thangaraj P (2010) Transmission gate based high performance low power multiplier. *J Appl Sci (Faisalabad)* 10(23):3051–3059
5. Asif S, Kong Y (2015) Design of an algorithmic Wallace multiplier using high speed counters. In: 2015 tenth international conference on computer engineering & systems (ICCES). IEEE, pp 133–138
6. Bansal H, Sharma KG, Sharma T (2014) Wallace tree multiplier designs: a performance comparison. *Innov Syst Des Eng* 5(5)
7. Robinson ME, Swartzlander E (1998) A reduction scheme to optimize the Wallace multiplier. In: Proceedings international conference on computer design. VLSI in Computers and Processors (Cat. No. 98CB36273). IEEE, pp 122–127
8. Rao EJ, Kumar KJ, Prasad TV (2018) Design of high speed Wallace tree multiplier using 8-2 and 4-2 adder compressors. *Int J Eng Technol* 7(4):2386–2390
9. Kang JY, Gaudiot JL (2006) A simple high-speed multiplier design. *IEEE Trans Comput* 55(10):1253–1258
10. Tomar GS, George ML (2018) Modified binary multiplier architecture to achieve reduced latency and hardware utilization. *Wireless Pers Commun* 98(4):3549–3561

Upgradation of Assurance Based on Revealing Quality of Healthcare Domain Around the Globe Using Internet of Things



Sandeep Srivastava, Pramod Kumar Srivastava, Deepak Gupta,
and Dinesh Kumar Yadav

Abstract The Internet of things (IoT) refers to a network of interconnected hi-end wireless sensors that are capable of collecting audio, video, mechanical, electronic and physical type of data. These mechanical and digital devices are all connected by a robust network to transfer the real-time data to a cloud where the information are processed to position, trace, monitor, administer and manage the desired change. In doing so, the parameters get tuned, and once the guidelines are added in these smart devices, the human reliance is eliminated for the subsequent guidance. The IoT infra is a combination of multiple technologies, using machine learning real-time analytics, commodity sensors and embedded systems using radio frequency identification (RFID). IoT exploits the discoveries and innovations in the area of networking, artificial intelligence, big data and data networking to achieve functionality, flexibility and efficiency in almost all day today fields. IoT enhances the digital experience; artificial intelligence algorithm and interconnected networks power it. In this paper, we discussed the origin, structure, applications and shortcomings of IoT in healthcare domain. We also discussed the endless possibilities that coming of age blend of new and old innovations using IoT. Finally, we demonstrated how the customization and modulation of our present knowledge about the IoT can enhance the quality of life providing medicines and drugs around us.

S. Srivastava (✉) · D. Gupta

Department of Master of Computer Application, GL Bajaj Institute of Technology and Management, Greater Noida, India

e-mail: sandeep.srivastava@glbitm.org

D. Gupta

e-mail: deepak.gupta@glbitm.org

P. K. Srivastava

Department of Mathematics, Rajkiya Engineering College, Azamgarh, India

e-mail: pramodksrivastava24042004@gmail.com

D. K. Yadav

Department of Electronics and Communications Engineering, IIMT College of Engineering, Greater Noida, India

e-mail: dinesh.vlsi.mod@gmail.com

© Springer Nature Singapore Pte Ltd. 2021

R. Agrawal et al. (eds.), *Advances in Smart Communication and Imaging Systems*,

Lecture Notes in Electrical Engineering 721,

https://doi.org/10.1007/978-981-15-9938-5_11

Keywords Wireless sensor · RFID · Real-time analytics · Health care · Medicines and drugs · IoT

1 Introduction

IoT, as the name suggests is the complex and interactive system of devices and machines, connected in an array, collecting data and analyzing it as per the prescribed parameters and taking predefined decisions and steps to make our lives easier. The existing technologies of sensing and data collection are teamed up in a dynamic setup, which is connected by various wireless networks [1–8]. The information thus gathered is sent to a cloud that facilitates data accumulation and analysis to interpret different results. The decisions thus arrived at are then communicated to other devices, and required changes are made. IoT aims at more in-depth automation and integrations of various mechanical, digital and computing machines. The machines and every such unit are given a unique identifier (UID). The applications of the IoT are endless, and the once distant dream is turning into the here—present reality. IoT is the convergence of modern technologies like embedded sensors, real-time computation and data storage, integrated systems, networking and artificial intelligence and robotics

The concept of such smart systems has been as old as the need for automation in machines. The idea goes back to 1982 when a coke vending machine in Carnegie Mellon University [9] became the first appliance to be connected to the Internet. This machine was programmed to sense and report the temperature and balance quantity of its inventory. The term using IoT was discovered by Kevin Ashton, in 1999, while working for Proctor and Gamble. He was working on (RIFD), radio frequency identification, as he believed that RIFD would be instrumental in providing the desired automation to computers and such devices. It was only after the concept of ubiquitous computing and the demand to integrate the present technology grew that the initial steps toward the IoT were taken [10–12].

1.1 *Basic Components for Required Architecture and Infrastructure of the IoT System*

The essential components of IoT can be understood in terms of components of IoT: hardware and software. The hardware: it is the underlying architecture and infrastructure of the IoT system. In Fig. 1, the IoT systems hardware has a remote component for control and monitoring of activity, servers, network channel and sensors. It consists of the primary sensors and embedded piece of equipment that have to ability to collect data related to the desired parameter like temperature, speed, light, weight, footfall, air quality, pressure, electricity, etc. [5]. The sensors collect the real-time data and serve as the eyes, ears and perception gatherers of the IoT

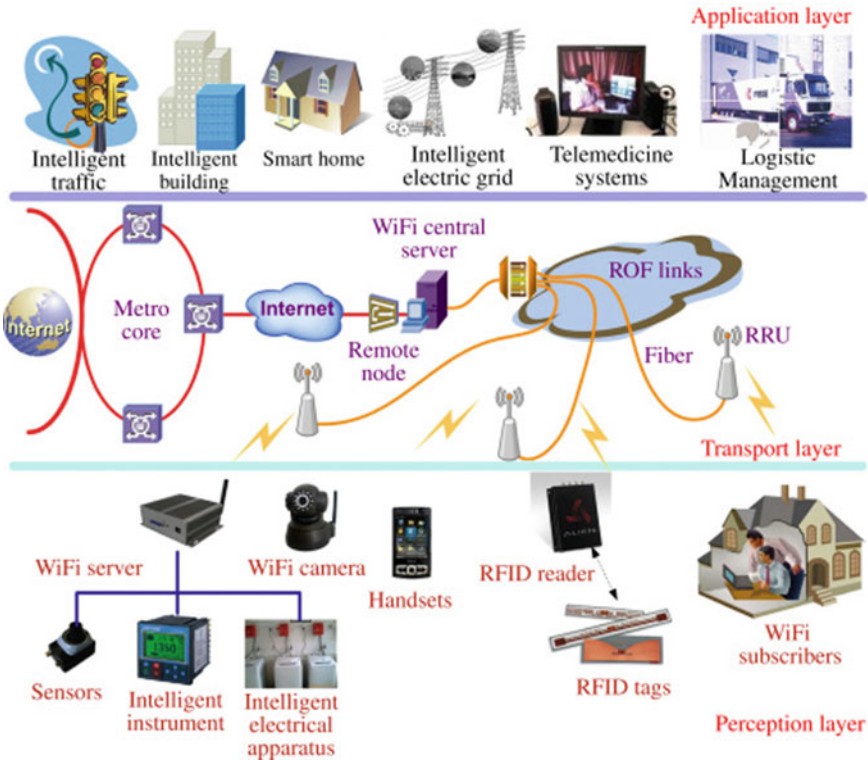


Fig. 1 IoT architecture

framework. These sensors can be of a wide range as magnetic sensors, acoustic sensors, proximity sensors and flow and shape sensors, etc. A bundle of such smart sensors can be used to collect an array of information for an IoT setup. For example, a Fitbit measures heart rate, sleep pattern, steps walked and stationary time spent. Thus, a smart IoT device can use sensors for body monitoring and GPS to collect the relevant information. A smart home can use a smoke detector, air quality monitor, intruder alert, electricity sensor, noise cancelation and remote monitoring of the house at the same time. These sensors can build to have some memory if the need arises, unable to store some data, if and when required. These sensors can be using a wide array of devices like routers and switches and modern technologies like GPS, RIFD, infrared, biochemical markers, mechanical receptors or photoelectric receptors to gather the desired information as per the set parameters.

1.2 *The Software for IoT Connection*

The IoT software uses partner systems, embedded systems and middleware to enable networking. The information collected by the smart sensors is relayed over a varied distance using a network like LAN, WAN, Ethernet, Bluetooth, Wi-Fi, multilayer frameworks like Weave, IoTivity, etc., are used to relay the massive volume of data collected. The various wireless networks that can be used also include Cat M1, Zigbee, Lo-Ra and NB-IoT7 [12]. Many customary and proprietary networks are also used in an organization's legacy systems, and the IoT integration is done as per the customized need of the business [13].

1.3 *The Networks Used Can Be*

- (a) Short-range wireless networks like Wi-Fi, ZigBee, Z-Wave, near-field communication (NFC), radio frequency identification (RIFD), light fidelity (Li-Fi) Bluetooth, etc.
- (b) Medium range wireless networks like LTE-Advances and high speed communication for mobile networks.
- (c) Long-range wireless networks like VSAT (tiny aperture terminal) relaying narrowband and broadband data and LPWAN (low-power extensive area network like RPMA, weightless, NB-IoT, LoRaWan).
- (d) Wired networks like Ethernet using fiber optics with switches and uses hubs and power line communication (PLC) which not only transports data but also carries power over long distances.

The software collects not only data but also filters, sort, save and analyze it to convert it to understandable and quantifiable results that can be used to take some viable actions. With the help of Fig. 2, showing the mechanism of intelligent RFID tag support decision making without the direct involvement of human beings takes the effort for automation to the next step. IoT can be defined in terms of the two ends it connects [14].

In terms of connectivity, it offers people to people, people to machines and machines to machines.

People to people connectivity: When everything is given unique identities, the devices can use the interconnected network to communicate among themselves and relay the relevant data, hence, enriching the people to people connectivity over an IP network. Earlier the communication was restricted to some specific exchange only. However, now the people can connect over the automatically processed useful information regarding the environment and surroundings, giving a more in-depth and more informative people to people connectivity [15].

People to machines: This is the mostly the data one needs to be captured and saved for later comparisons, say a device that monitors and records the sleep patterns, eating behaviors, or gait analysis of an individual and sends it over to a cloud that computes

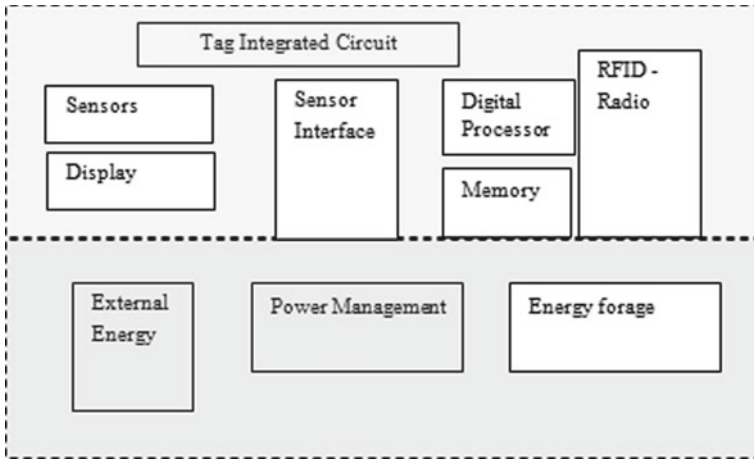


Fig. 2 Intelligent RFID tag

and analyzes the patterns and habits thus formed. This is where IoT smartly blends the sensors of varying types with the automation and make the need for human command redundant.

Machine to people: After the information is gathered and processed, a specific chain of commands need to be executed and that can be done by IoT facilitating the felids of inventory control and emergency response. This information can be shared and communicated over the wide-area connectivity systems such as GSM, GPRS, 3G and LTE. The commands can be scheduled for the right time and can thus help in the logistics and planning activities to a large extent [14].

2 Implementation Idea of IoT in Health Care and Life Enhancing

Using IoT, it helps widen access and improve the quality of education and health, as need of healthcare doubles [10]. Smart devices can help remotely monitor fatally ill patients having communicable diseases. A deadly communicative disease’s spreading pattern can be understood by an IoT-enabled smart sensors and all existing network that can help collection and processing of relevant information in real time. Even the idea of remote monitoring and remote controlling of functions can help scale the geographical barriers and increase the penetration of health care to remote and distant places. Health parameter detectors like heart rate monitor, blood sugar and blood pressure monitors can be smartly imbibed with the IoT networks to collect, store, analyze and transfer the parameter readings [16, 17].

Smart homes can have sophisticated fall detection mechanisms for elderly care and can monitor and manage the environment of the residence customizing it to the

needs of the occupants. IoT-enabled systems to allow health caregivers to capture the vitals and required parameter data and process it accordingly. These systems are patient-centered and thus can help in providing customized healthcare service to the needy and dependent patients [18].

2.1 Maintain Container Temperature Against Environment

In Fig. 3, a concern related to the IoT technologies to be connected with the environmental impacts of the medicine manufacture, use and eventual disposal of the entire semiconductor-rich devices. Environmental well-being is defined by numerous parameters like the temperature of the earth, the health of ozone layer, the condition of polar caps, the count of animals in the wild and overall forest thickness and quality of green cover on land. A lot of these variables are to be regularly monitored to form a conclusion about the condition of our environments [16–18]. Thus, many smart devices with embedded sensors are used to monitor and assess the condition of the environment around us. Internet of things can be used to assess the damage done to the environment till date. Internet of things can be used to assess the damage done to the environment till date with its use as a feeder for data to the strategic planning divisions which make the policy decisions. Picking of early signs of an imminent volcanic eruption or a tsunami can help save so many lives. IoT is the future as we enter a safe world and that takes proactive steps to regulate and improve its environment. The smart technology can be used to manage forest fires, to check air pollution levels and to check the water quality. Smart GPS/GSM-enabled trackers can be used in GPS collars to locate and monitor endangered species to study animal behavior. Environmental health indicators need an ongoing observation, and Internet of things can be instrumental in remote surveillance that smartly depicts patterns and trends as any major or minor change happens [19].

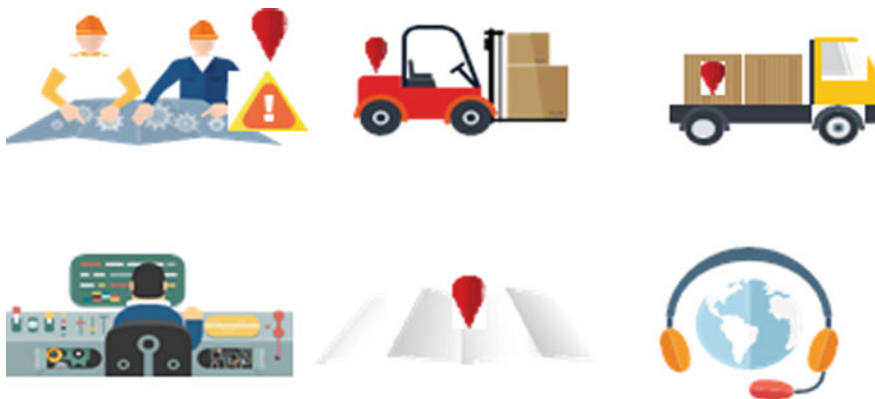


Fig. 3 Layout of IoT in pharma manufacturing and supply chain management

2.2 Security and Safety

We already have the GPS, and speed sensing enables applications that can direct us to the destinations by the shortest route. These IoT devices can enable functions as fire control, public announcements and crowd control. The automated smart and dynamic systems enable building smart traffic control systems. Internet of things can be used to create a network of intelligent highways that alerts drivers about landslides, or any accident or blockage on the way. The GPS-enabled disaster management technology can suggest new routes in case of an emergency. The interrelated well-connected sensors can make a safe and secure traffic management system having smart parking, smart toll collection systems (fast tag) and prompt and efficient road assistance system. Smart devices can be embedded in street lights and can thus automate the lighting systems that auto-regulate and adapt to the time of the day or the weather in a particular place. Mechanical strength sensors can catch the early signs of wear or stress in dam infrastructure, saving hundreds of lives in time. IoT, with its smart sensors, can identify toxicity levels without jeopardizing human lives. Smart night vision can enable navigation on roads during poor visibility. Precious human lives can be saved in case of gas leaks or nuclear incident. Timely intervention and scheduling of maintenance activity can save resource and lives in case a major/crucial component wears down. Smart IoT sensors can thus analyze the limiting factor and assess the apt repair and replacement schedules facilitating safety and security activities [9].

2.3 Smart Living Style

IoT is a part of the broader concept of home automation, which can include lighting, heating, air conditioning, media and security systems. Sixteen many such platforms like Amazon Echo, Google Home, Samsung's Smart Things Hub and Apple's Home Pod have brought automated home technologies to our lives. Also some non-proprietary, open-source ecosystems like Home Assistance, OpenHAB and Domoticz are also available alongside the customized commercial versions in the market. These devices can have the device providers' applications, for example, Apple's Siri, without the need of a Wi-Fi bridge or by open-source ecosystems. A smart home can save energy and allow remote monitoring of household for the users. A smart refrigerator can sense and alert about the freshness of eatables. The homes can have remotely monitored and controlled intruder alert systems. Internet of things can sense and regulate the use of electronics and lights that are not in use of saving energy. IoT can be actively used to monitor occupant behaviors and to understand the patterns that can help in saving energy or building emergency response plans.

2.4 Smart Agriculture for Herbal Medicine Information System

The IoT networks and sensors can collect and process data on soil content, humidity, pest infestation, microbial contamination, rainfall seed quality and temperature. The data can help in making informed decisions and to take proactive steps in calamity control. This can significantly enhance quality, increase productivity, minimize wastage and aid in better cost realization of crops. The allied agriculture activities like animal husbandry, pisciculture, sericulture, etc., have great potential for the introduction of IoT-enabled systems [13]. Soil and crop patterns synchronized with weather and climate condition studies can help in intelligent planning of crops to ensure a good crop and good demand for all the farmers. IoT can help with animal husbandry in remote surveillance and location of animals grazing in open pastures. The IoT can help smartly control and monitor the conditions like ventilation and temperature around the livestock

The offspring health and survival rate can be significantly enhanced by a smart system that monitors and schedules the vaccination schedules for all the animals on a farm [16].

3 Comparison Table of Various IoT-Based Application Use in Healthcare Domain

S. No.	Application name	IoT device used	Cloud computing-enabled	Sub-domain of health care where it is used.	Assurance of quality result
1.	Remote patient monitoring	Wearable devices with embedded sensors	Yes	Hospitals, patients, doctors	90–100%
2.	Hospital operations management	Embedded sensors	Yes	Hospital management	90–100%
3.	Glucose monitoring system	Wearable or embedded body sensors, transmitters	Yes	Patient/doctors	Depends on various factors—fasting, etc. Never 100%
4.	Automatic blood testing	Sensors, Bluetooth	Yes	Patient/doctors	Approx. 100%
5.	Automatic sanitization devices	Embedded sensors	No	Public domain	Approx. 100%

(continued)

(continued)

S. No.	Application name	IoT device used	Cloud computing-enabled	Sub-domain of health care where it is used.	Assurance of quality result
6.	Drug management	RFID	Yes	Hospitals, patients, doctors	90–100%
7.	Medical waste management systems	Embedded sensors, IoT-enabled robots	Yes	Hospitals	Approx. 100%

4 Shortcomings and Challenges of IoT

It is a significant concern with IoT as the information can pertain to a financial or a personal aspect of an individual. The terms of privacy should be not violated, and the trust and secrecy functions must be adequately dealt with. The data collected by the applications and devices should only use specific, the data must be aptly coded and protected against data theft, the cloud must receive and handle data securely, and the information accumulated on an individual should never be compromised. After the Snowden incident, people are apprehensive of any technology that is invasive of their private information. A survey revealed that “lack of the customer’s awareness, if hacker attacks and try to owning or planning to make clone of IoT devices in the next coming five years, 25% peoples decided to going terminated the use of the services and related services until they do not get safety guarantees.” The technology must be simplified for use and must not be confusing (including the confusing terminology) to the end-user. “If users need to learn different interfaces for their vacuums, their locks their sprinklers, their lights and their coffee makers, it is tough to say that their lives have been made any easier” [20, 21].

5 Conclusion

In this paper, we have presented a critical review that presents the role and application of IoT in healthcare field. Although it covers a wide variety of areas, and thus the applications serve different uses. The beneficiaries of IoT can be the individuals or the community (health care) or the enterprises (using the smart technology in manufacturing different kinds of medicines). Starting with its architecture, we have discussed in-depth the role and its application in the healthcare field. But notwithstanding the target beneficiaries, the IoT promises to revolutionize the field of data collection and data applications with the connectivity to help communication of the

information over distant places. The future holds a mindboggling array of possibilities of how the IoT can increase productivity, accuracy and efficiency. IoT is already making tremendous changes in the arena of health care by enabling self-monitored and efficient ecosystems. It is enhancing the quality of life, enriching the experience in the day to day lives. The home-oriented IoT systems are assisting by providing comfort and care of patient. The traceable and sensing devices are enabling real-time data capturing and are increasing by every innovation. The need of the hour is for the healthcare domain in respective areas to collaborate to push the IoT into the realm of easy accessibility and deeper integration in our worlds. Though there is much ground for improvement and much work needs to be done to address the issues of privacy, secrecy, device interoperability and cost-efficiency. However, the constant work in the right direction will eradicate the present issues. The future will be ready to embrace the change the IoT will bring to all our lives.

References

1. Janhunen J, Mikhaylov K, Petäjäjärvi J, Sonkki M (2019) Wireless energy transfer powered wireless sensor node for green IoT: design, implementation and evaluation. *Sensors* 19(1):e90
2. Kumar R, Singh A (2018) Throughput optimization for wireless information and power transfer in communication network. In: *Signal processing and communication engineering systems (SPACES)*. IEEE, pp 1–5
3. Yadav P, Agrawal R, Kashish K (2018) Protocols performance investigation using Ad Hoc WLAN for healthcare applications. *Pertanika J Sci Technol (JST)* 26(3):1333–1354
4. Singh M, Sachan S, Singh A, Singh KK (2019) Internet of Things in pharma industry: possibilities and challenges. In: *Emergence of pharmaceutical industry growth with industrial IoT approach*. Elsevier. <https://doi.org/10.1016/C2019-0-00219-1>
5. Sharma S, Kumar R, Singh A, Singh J (2020) Wireless information and power transfer using single and multiple path relay. *Int J Commun Syst*:e4464
6. Skiadopoulos K, Tsipis A, Giannakis K, Koufoudakis G, Christopoulou E, Oikonomou K, Kormentzas G, Stavrakakis I (2019) Synchronization of data measurements in wireless sensor networks for IoT applications. *Ad Hoc Netw* 89:47–57
7. Sharma S, Singh J, Kumar R, Singh A (2017) Throughput-save ratio optimization in wireless powered communication systems. In: *2017 International conference on information, communication, instrumentation and control (ICICIC)*, Aug. IEEE, pp 1–6
8. Dubey SD, Singh P, Yadav P, Singh KK (2020) Household waste management system using IoT and machine learning. *Procedia Comput Sci* 167:1950–1959
9. Lindquist W, Helal S, Khaled A, Hutchinson W (2019) IoTility: architectural requirements for enabling health IoT ecosystems. *IEEE Trans Emerg Topics Comput*
10. Rai A, Karatangi SV, Agarwal R, Prakash O (2018) Smart sensors transforms healthcare system. In: *Recent paradigms of deep learning and IoT in healthcare systems*. Apple Academic Press, Distribution by CRC Press, A Taylor Francis Group. <https://www.appleacademicpress.com/deep-learning-and-iot-in-healthcare-systems-paradigms-and-applications/9781771889322>
11. Parthasarathy P, Vivekanandan S (2020) A typical IoT architecture-based regular monitoring of arthritis disease using time wrapping algorithm. *Int J Comput Appl* 42(3):222–232
12. Shahinzadeh H, Moradi J, Gharehpetian GB, Nafisi H, Abedi M (2019) Iot architecture for smart grids. In: *International conference on protection and automation of power system (IPAPS)*. IEEE, pp 22–30
13. Addabbo T, Fort A, Mugnaini M, Panzardi E, Pozzebon A, Vignoli V (2019) A city-scale IoT architecture for monumental structures monitoring. *Measurement* 349–357

14. Conti M, Kaliyar P, Lal C (2019) CENSOR: Cloud-enabled secure IoT architecture over SDN paradigm. *Concurrency Comput: Prac Exp* 31(8):e4978
15. Chien WC, Lai CF, Hossain MS, Muhammad G (2019) Heterogeneous space and terrestrial integrated networks for IoT: architecture and challenges. *IEEE Netw* 33(1):15–21
16. Khanna A, Arora S, Chhabra A, Bhardwaj KK, Sharma DK (2019) IoT architecture for preventive energy conservation of smart buildings. In: *Energy conservation for IoT devices*. Springer, Singapore, pp 179–208
17. Subramaniaswamy V, Manogaran G, Logesh R, Vijayakumar V, Chilamkurti N, Malathi D, Senthilselvan N (2019) An ontology-driven personalized food recommendation in IoT-based healthcare system. *J Supercomputing* 75(6):3184–3216
18. Yang Y, Zheng X, Guo W, Liu X, Chang V (2019) Privacy-preserving smart IoT-based healthcare big data storage and self-adaptive access control system. *Inf Sci*:567–592
19. Ansari S, Aslam T, Poncela J, Otero P, Ansari A (2020) Internet of Things-based healthcare applications. In: *IoT architectures, models, and platforms for smart city applications*. IGI Global, pp 1–28
20. Falco M, Núñez I, Tanzi F (2019) Improving the fleet monitoring management, through a software platform with IoT. In: *International conference on Internet of Things and intelligence system (IoT&IS)*. IEEE, pp 238–243
21. Hameed S, Khan FI, Hameed B (2019) Understanding security requirements and challenges in Internet of Things (IoT): a review. *J Comput Netw Commun*

Wideband Sub-6 GHz Micro-strip Antenna: Design and Fabrication



Pankaj Jha, Shailendra Singh, and Ram Lal Yadava

Abstract In this paper, wideband micro-strip antenna has been presented for sub-6 GHz applications. The proposed antenna is designed using partial ground architecture. This antenna is designed with a $40 \times 30 \times 1.6$ mm dimensions and fabricated on the Fr-4 substrate. The proposed antenna maintains the return loss less than -10 dB from 3 GHz to 5.64 GHz. The gain of proposed antenna is changing from 1.73 to 3.22 dB, and radiation efficiency is achieving its maximum value of 90%.

Keywords Sub-6 GHz · Partial ground · Micro-strip antenna · Gain · Efficiency

1 Introduction

The high-speed wireless data service is one of the most important requirements of sub-6 GHz communication system for enhancing data transformation. We know that the frequency band between 3 and 5 GHz is allotted for 5G communication system and accordingly countries are using in-between spectrum such as 3.4 ~ 3.8 GHz in Europe, 3.1 ~ 3.55 GHz and 3.7 ~ 4.2 GHz in USA, and 3.3 ~ 3.6 GHz and 4.8 ~ 4.99 GHz in China [1]. Applications of micro-strip or patch antenna are increasing day by day and becoming more useful because it can be printed directly. That is why it is becoming more and more useful for mobile manufacturing industries. It is

P. Jha (✉)

Department of Electronics and Communication Engineering, IIMT College of Engineering,
Greater Noida, India
e-mail: pankaj.maahi@gmail.com

S. Singh · R. L. Yadava
Shiv Nadar University, Greater Noida, India

Galgotias College of Engineering and Technology, Greater Noida, India

S. Singh
e-mail: ss553@snu.edu.in

R. L. Yadava
e-mail: rlyadava.vps@gmail.com

cost effective and having low profile also. Due to miniaturization, it is being used in many applications like that of WLAN [2, 3], Wi-Fi [4], and Bluetooth [5]. Though patch antenna suffers with less gain and limited power handling, researchers are trying to overcome these issues with proposals in designing, for example, an array configuration in which homogeneous antennas are placed and oriented in same phase. With the help of this arrangement, we can get better directivity and gain. Similarly, we can find impedance control with the help of inset-fed micro-strip antenna [6].

2 Antenna Design

Initially, the simple patch was designed using Fr-4 substrate with dimension of ($13 \times 17 \times 1.6$ mm). Then, a slot was cut in the opposite of modified feed line and simulation was done applying parametric shift in x as well as y direction; again, another symmetrical cut was made in other side and by moving both slot positions in Y direction simulation was done but still the desired band of frequency was not obtained. Further one more slot was created with different dimensions, and results were obtained by shifting its parameters in x and y directions. After simulation of different designs, the proposed design provides the desire results. The substrate dimensions are taken ($30 \times 40 \times 1.6$ mm), and patch dimensions are taken ($17 \times 19 \times 1.6$ mm). There are 3 slots in the patch in which the above 2 slots are symmetrical having dimensions of (4×3 mm) at the distance of 1 mm from Y max position. The 3rd slot which is above feed line is having dimensions of (6.5×2 mm). The dimension of feed line is taken (10×3 mm). Ground is taken up to 10 mm from Y min of substrate. The proposed antenna is given in Fig. 1.

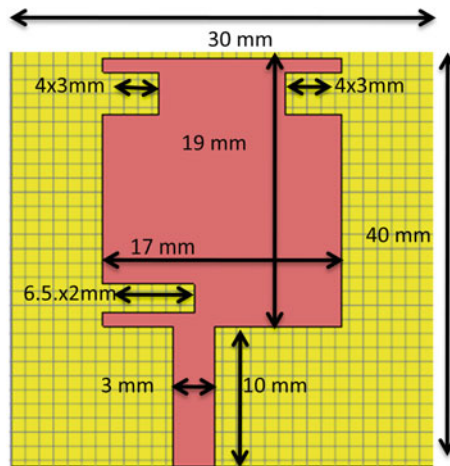


Fig. 1 Designed patch antenna with all dimensions

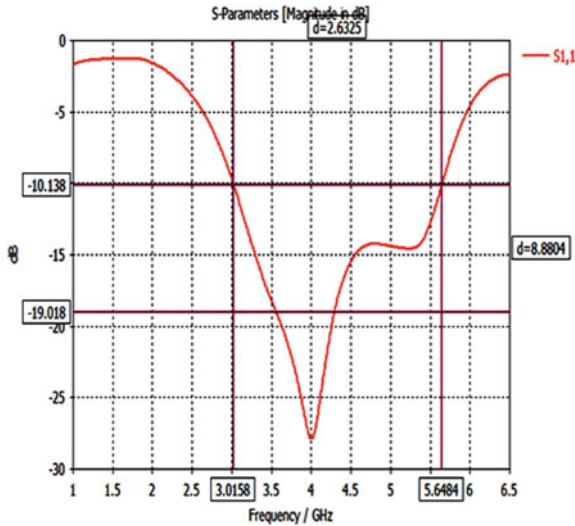


Fig. 2 Plot of return loss (S_{11})

3 Simulation Results

The simulation is done on CST STUDIO SUITE 2018. The different results are shown here.

3.1 Return Loss (S_{11})

The simulation result of return loss (S_{11}) shows that it maintains -10.00 dB for 3.00 – 5.64 GHz complete frequency band and at 4 GHz frequency it is -26.5 dB. The plot for S_{11} is given in Fig. 2.

3.2 Gain

The value of gain is quite low due to partial ground architecture. There are different suggestions by which we can increase gain of path antenna. The simulated value of gain is varying between 1.73 and 3.22 dB for selected band of frequency which is comparable with references [8, 9]. The simulation result of gain and realized gain are shown in Fig. 3.

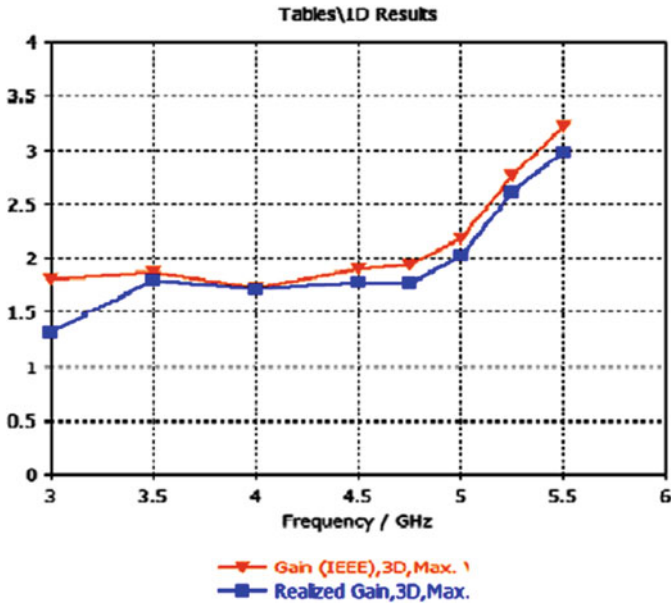


Fig. 3 Plot of gain and realized gain

3.3 Efficiency

The simulation results show that efficiency is less at lower frequency band but reaches up to 90% at 4.5 GHz. The plot of radiation efficiency and total efficiency is shown in Fig. 4.

3.4 Radiation Pattern

Here, the author shows two radiation patterns, one co-polar and one cross-polar radiation pattern at 4 GHz frequency. With these patterns, we can say that antenna is linearly polarized. Figure 5 shows the radiation pattern.

4 Result Comparison Table

The author compared the simulation result with reference [6, 7] and [8] which are given in tabular form (Table 1).

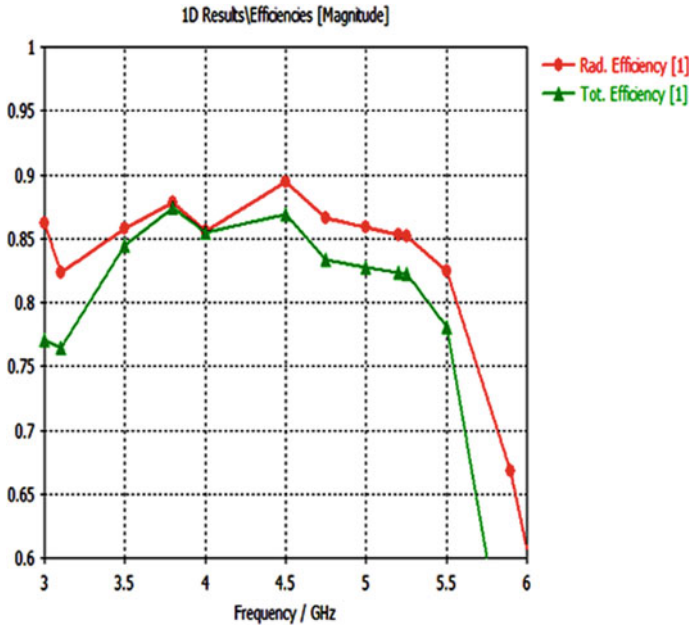


Fig. 4 Plot of radiation efficiency and total efficiency

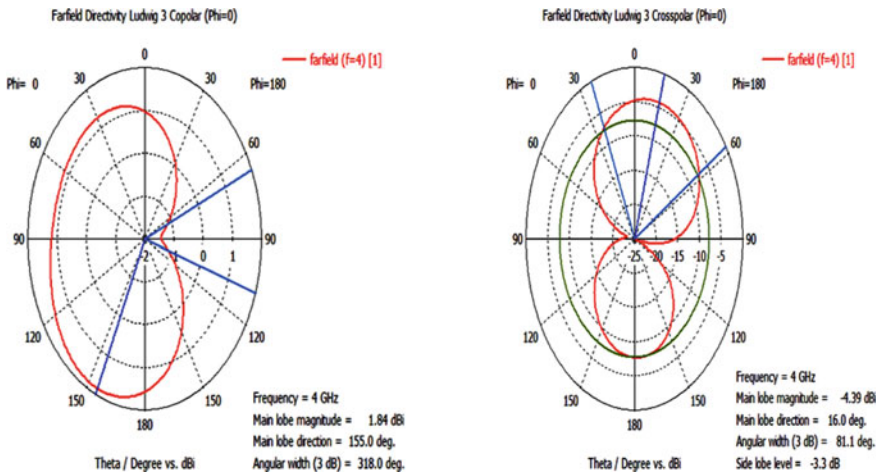


Fig. 5 Radiation pattern

Table 1 Result comparison with references

Ref.	Patch size (mm)	BW (GHz)	Gain	Efficiency
[6]	$17.30 \times 10.4 \times 1.6$	5–5.8	5.6 dBi	NA
[7]	$50 \times 19.75 \times 0.8$	2.5–4.8	1.8–2.9 dB	60–90
[8]	$47 \times 19 \times 0.8$	3.2–5.2	2.1–4.1 dBi	NA
This work	$40 \times 30 \times 1.6$	3–5.64	1.7–3.2 dB	74–90

From the above table, the following points can be summarized as a comparison.

- The size of proposed antenna is between sizes used in Refs. [6–8].
- Bandwidth is wider than others and covering full sub-6 GHz range of 5G.
- Gain and efficiency are better than that antenna reported in Ref. [7].
- The S_{11} is below -10 dB for entire range 3–5.6 GHz, and it achieves value of -26.5 dB at resonating frequency (at 4 GHz).
- The simulated co-polar/cross-polar plots have main lobe magnitude more than 20 dB for all frequencies.

5 Fabricated Antenna and Results

The proposed antenna fabricated on Fr-4 substrate. After fabrication, results were obtained. S_{11} maintains its value below -10 dB for selected range of frequency. The simulation result and fabrication results are also compared. The antenna views and results are given in Figs. 6, 7.

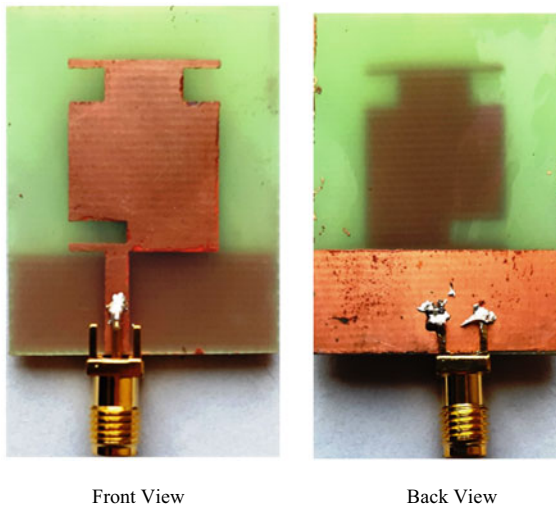
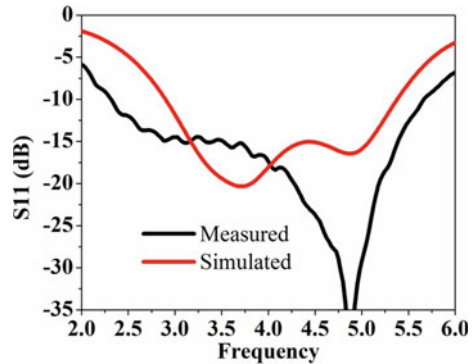
**Fig. 6** Front view and back view of fabricated antenna

Fig. 7 S_{11} comparison graph between simulated and fabricated antennas



6 Conclusion

This paper has introduced a design and fabrication of a micro-strip antenna for sub-6 GHz applications. The proposed antenna maintains value of S_{11} below -10 dB for entire range 3–5.6 GHz, and it achieves value of -26.5 dB at resonating frequency (at 4 GHz). The maximum gain is achieved up to 3.2 dB. The efficiency is very good at higher range of frequency in selected band. The radiation pattern shows that it is a linearly polarized antenna. The proposed antenna is suitable for WiMAX, Wi-Fi, and WLAN communication system.

References

1. An W et al (2018) Low-profile and wideband microstrip antenna with stable gain for 5G wireless applications. *IEEE Antennas Wirel Propag Lett* 17
2. Ghosh CK, Parui SK (2010) Design, analysis and optimization of a slotted microstrip patch antenna array at frequency 5.25 GHz for WLNA-SDMA system. *Int J Electr Eng Inf* 2
3. Mutiara AB, Refianti R, Rachmansyah (2011) Design of microstrip antenna for wireless communication at 2.4 GHz. *J Theor Appl Inf Technol* 33:184–192
4. Tecpoyotl-Torres M, Vera-Dimas JG, Vargas-Chable P, Damián-Morales JA, Torres-Cisneros M, Sánchez-Mondragón J (2009) Antenna prototypes for indoor and outdoor wi-fi communication. Conference of university of Guanajuato IEEE students chapter, 2009, pp 37–41
5. Majumder A (2013) Design of an H-shaped microstrip patch antenna for bluetooth applications. *Int J Inno Appl Stud* 3:987–994
6. Balti E, Johnson BK (2019) Sub-6 GHz microstrip antenna: design and radiation modeling. *IEEE Trans Antennas Propag*
7. Sekeljc N, Yao Z, Hsu H-H (2019) 5G broadband antenna for sub-6 GHz wireless applications. In: IEEE international symposium on antennas and propagation and USNC-URSI radio science meeting
8. Tang X, Jiao Y, Li H, Zong W (2019) Ultra-wideband patch antenna for sub-6 GHz 5G communications. In: International workshop on electromagnetics: applications and student innovation competition
9. Balanis CA (2005) *Antenna theory: analysis and design*. Wiley-Interscience

Performance Analysis of Deep Transfer Learning for Manifestation of COVID-19 Using Chest X-ray



Manish Arya, Amit Sehgal, and Rajeev Agrawal

Abstract Lungs can be affected by various bacterial and viral infections other than novel coronavirus, popular as COVID-19. Any machine learning technique should be capable to differentiate among these infections and classify an image to generate inference matching with actual cause of disease. In this paper, we have analyzed the performance of VGG19 for diagnosis of COVID-19 using X-ray images of lungs infected by bacterial and viral pneumonia. The visual clarity of X-ray images is very low compared to CT scan. However, the accuracy obtained by supports our claim of using VGG19 as a low coast and easily accessible automated alternate to CT scan based diagnosis. Datasets having images of 3-class (including normal, viral pneumonia and COVID-19) and 4-class (including normal, bacterial, viral pneumonia and COVID-19) categories were used to analyze the performance of VGG19 Deep Transfer Learning Model for accurate diagnosis of COVID-19. Sensitivity and accuracy of VGG19 were compared with AlexNet and ResNet19 models. VGG19 produced an accuracy of 98.2% with 3-class dataset and 94.4% with 4-class dataset.

Keywords COVID-19 · Chest X-ray · Transfer learning · VGG19

M. Arya
VaaaN Infra Pvt Ltd, Faridabad, India
e-mail: manisharya07@gmail.com

R. Agrawal
Department of Electronics and Communication Engineering, G. L. Bajaj Institute of Technology and Management, Greater Noida, India
e-mail: rajkecd@gmail.com

A. Sehgal (✉)
School of Engineering and Technology, Sharda University, Greater Noida, India
e-mail: amitsehgal26@gmail.com

1 Introduction

End of the calendar year 2019 opened the doors for the last year of this decade. But that was not the only special thing about December 2019. It will always be remembered for the outbreak of the pandemic caused by coronavirus disease 2019 or COVID-19 which has already become the biggest of twenty-first century by affecting more than 200 countries and territories till mid of April [1]. More than 1,880,000 confirmed cases of infection by COVID-19 have been reported across the world. The agent causing this disease with human-to-human transmission has been reported to be severe acute respiratory syndrome coronavirus (SARS-CoV-2) [2]. Similar to many other viruses affecting respiratory system of the humans, COVID-19 also spreads through the droplets released during cough or sneezing which can travel in air to a few meters [3]. The symptoms of infection by COVID-19 are similar to a seasonal flu and generally mild in most of the cases till several days [4]. Several patients recover after suffering from the mild to moderately severe symptoms which do not affect the respiratory system to a level which can be fatal. However, in the cases where the infection reaches deep into the lungs, the symptoms of acute pneumonia become visible and patient needs to be kept under intensive care with support of ventilator. This situation is more critical for people of higher age groups such as above 60 since the lungs have much lower reserve capacity [5] compared to those in the age group of 20–50, thus causing more number of deaths in senior age groups.

There have been no standard diagnosis techniques, and the initial diagnosis depends upon the nucleic acid testing. However, in several cases, the initial nucleic acid test was negative whereas the symptoms including significant changes in characteristics of lungs and breathing disorders were observed. After conducting multiple tests on such patients, positive result was reported [6]. CT scans and X-ray images of the chest area of the COVID-19 patients are being analyzed for radiologic verification of the presence of coronavirus in the lungs [7–10]. In CT scan of a human chest, normal lungs appear black in color. When an infection of any form causes inflammation of the alveoli, it is pneumonia. Such infection, at an early stage, can be spotted in the form of white sections inside the black portion of the lungs in CT scan. These white sections represent bacterial infection, when appeared as a blotch in one section of a lung. Pneumonia caused by viral infection can be diagnosed by the presence of hazy white patches which are called as “ground glass opacities” (GGO) [11]. In case of COVID-19 patients, these hazy patches have been observed to appear in the form of clusters of white area along the outer edge of both the lungs. This is perhaps due to the clogged air sacs, and thus the completely black portion of the air-filled lungs turns white in the portions which are not capable of storing air due to the infection. Identifying between the cases of COVID-19 and other forms of viral and bacterial infection through CT scan requires in-person analysis of the scan by a clinical expert. Figure 1a–d shows CT scans of human chest for 4 different cases, i.e., normal, fungal pneumonia, bacterial pneumonia and COVID-19-infected lungs, respectively. Figure 2a, b shows chest X-ray images from the 3-class dataset having images of normal pneumonia and COVID-19-infected lungs and

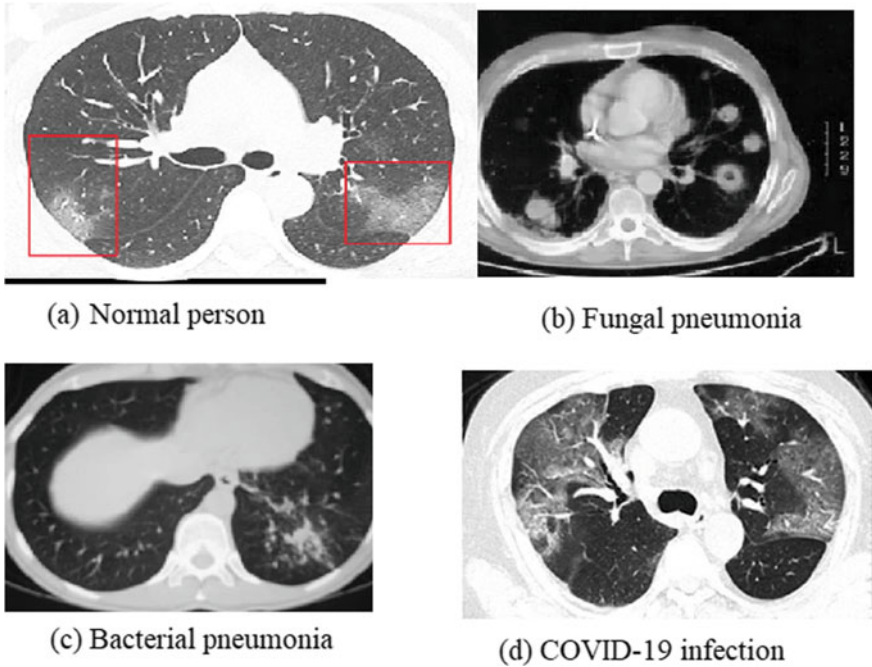


Fig. 1 CT scan of human chest

4-class dataset having images of normal, bacterial, viral pneumonia and COVID-19-infected lungs. Compared to CT scan, the difficulty in extracting visually verifiable details in X-ray images of COVID-19 patients is a major challenge in its adoption for diagnosis. Further, compared to CT scan, X-ray images have much wider diversity in terms of ambient conditions and patient attire in which these images are taken. This further reduces the suitability of X-ray as a radiography technique for diagnosis where the symptoms and its effects are similar to other types of infections. However, the cost of taking CT scan is much higher compared to X-ray. The facility for CT scan is also limited to medium to big hospitals and rarely found in small healthcare centers of rural areas or small towns, takes much longer time for the scanning process and requires much higher level of clinical expertise for diagnosis. These advantages in terms of low cost, high accessibility, ease of use and less time taking make X-ray a more popular radiography technique for diagnosis subject to the condition that accuracy of diagnosis is maintained.

Any autonomous system which can provide initial diagnostic inference will help to identify cases with higher probability of being infected by COVID-19 and thus sent to the experts for further analysis and treatment. Conventional rule-based diagnosis, when integrated with artificial intelligence schemes such as machine learning or deep neural learning, can be used not only for diagnosis but also for survivability model and treatment plan.

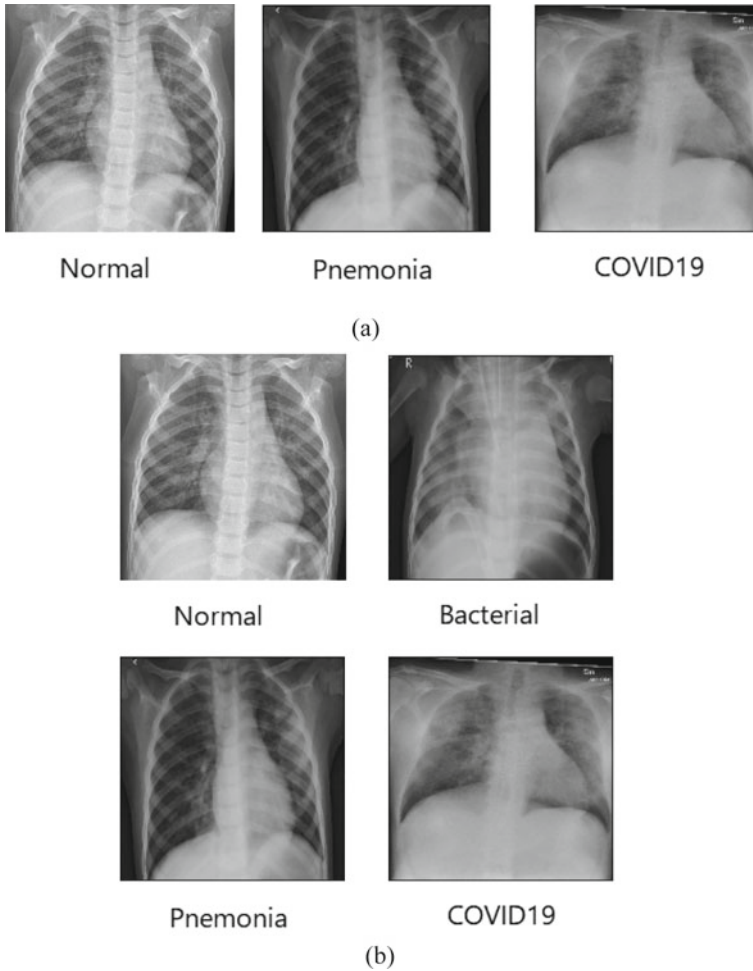


Fig. 2 a Chest X-ray forms 3-class dataset and b chest X-ray form 4-class dataset

2 Methodology

Similar to various other clinical domains, researchers have begun to explore the artificial intelligence (AI)-based techniques in CT scans for COVID-19 diagnosis [12, 13]. In a similar effort, Wang et al. tested inception convolution neural network (CNN) with transfer learning for analysis of CT scans of COVID-19 patients [14]. The internal validation accuracy of 79.3% was recorded. With this objective, deep learning approach has been tested on chest X-ray images [15]. On a test set of 78 images, internal validation accuracy of 93.8% was achieved. More such attempts have been made to accurately diagnose COVID-19 from X-ray images [16, 17]. The

major contribution of this paper is to analyze various CNN models to propose the best suited one for X-ray-based diagnosis of COVID-19.

CNN is a widely used base model for neural networks and the most fundamental operation to deploy machine learning. It is based on the principle of feature extraction from an image. Similar to a human brain, it processes input data in pictorial form and attempts to identify specific features and classify the objects into various categories. Visual Geometry Group (VGG), at Oxford, developed an improved AlexNet which was based on the traditional CNN [18, 19]. VGG provided better accuracy by using deep convolutional neural layers. Various variants of VGG such as VGG11, VGG 16 and VGG 19 have been developed. In this paper, we used VGG19 as a deep transfer learning model for analysis of X-ray images and results are compared with AlexNet and ResNet18. The basic layered architecture is given in Fig. 3. This model consists of 16 layers including 16 convolutional layers and 3 fully connected layers and 19.6 billion FLOPs.

Deep CNN has been used in various applications which require feature extraction and image classification such as computer vision and medical imaging-based diagnosis [20, 21]. Though deep CNN models are known to give results with high level of accuracy, a well-curated training dataset is required to achieve similar performance in cases with high visual heterogeneity. X-ray images of human chest come under such category of images. Another challenge faced while using X-ray images compared to CT scan is the presence of pulmonary nodules is hard to be verified visually compared to CT scan. This is a crucial diagnosis parameter for COVID-19. Thus, a CNN model with more layers is required to detect such features even in the images which are poor in quality or taken in nonstandard conditions.

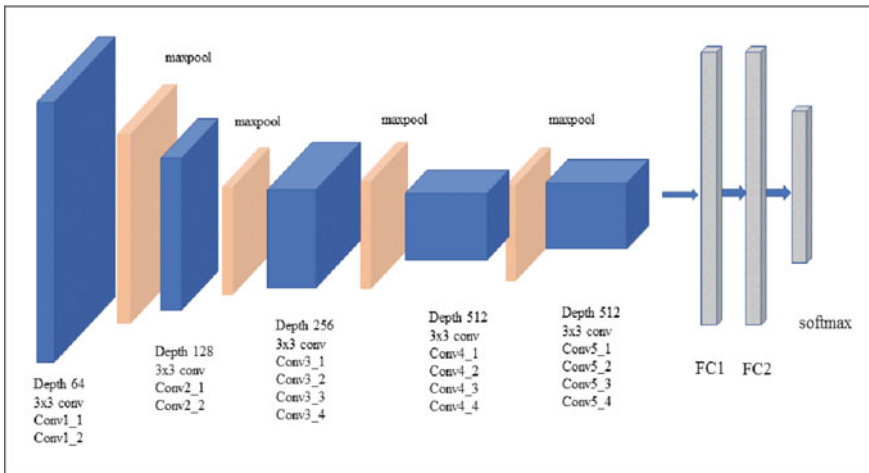
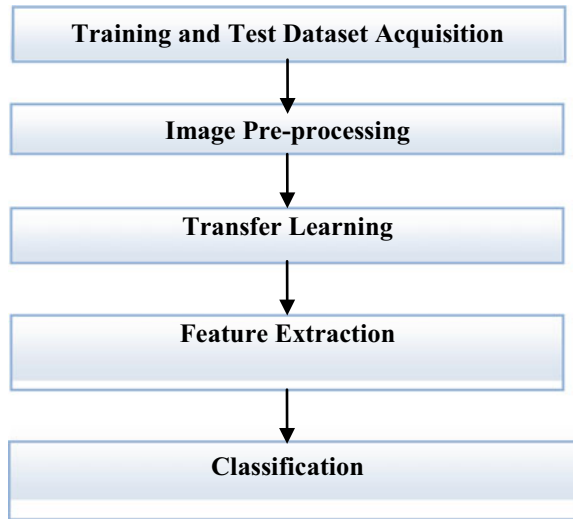


Fig. 3 Layered architecture of VGG19

Fig. 4 Methodology of image processing through CNN



The methodology followed in this research work is a five-step process as shown in Fig. 4. These steps are: image dataset acquisition, dataset preprocessing, transfer learning, feature extraction and classification.

Training and Test Dataset Acquisition: Application of deep CNN model requires two sets of image data—training and validation dataset. The CNN models to be used for feature extraction need to be pre-trained before they can be used on the real dataset to generate clinical inferences. Sample data with known characteristics is used as training dataset for this purpose. To verify that the models have been trained as needed, a comprehensive validation is required on another set of sample images. Such collection of image data is the validation dataset. Various open-source X-ray image datasets are available which can be used as training and validation dataset. Kaggle and github datasets were used for these purposes in this paper. Keywords such as COVID-19, novel corona and coronavirus were used to select the images for positive and negative dataset.

Image Preprocessing: A two-step preprocessing was followed on the dataset. In the first step, the full-resolution DICOM images were converted to 8-bit grayscale JPEG images using dcmj2pnm image transformation tool. The extreme values were truncated by using default min–max procedure of LUT transformation. In the second step of preprocessing, the images were downsized using a square aspect ratio and resolution of $224 \times 224 \times 3$.

Transfer Learning: Conventional machine learning algorithms were developed to be trained for a specific application and then implemented for the same on real-time dataset. However, in recent times, the concept of transfer learning has overcome this isolated learning paradigm [22]. In this modified approach, the learning acquired by a training model for one application can be utilized for another related application.

This has led to the evolution of “artificial general intelligence.” In this paper, pre-trained CNN models have been used through transfer learning approach since the dataset of X-ray images for COVID-19 cases is quite limited and also, training of fresh models is a long time-consuming process. The weights of the model to be used are learnable from the knowledge stored in weights of pre-trained models [23–27].

Feature Extraction: Deep learning CNN models are based on layered architecture in which different layers learn to extract different features from the image. In conventional machine learning, all the layers of a model are connected to the last fully connected layer which provides the final desired output. However, in case of transfer learning, the final feature extraction layer is not present in pre-trained network, thus making it flexible for multiple applications based on the final layer of the model to which the learning is transferred. The transfer learning architecture for feature extraction is shown in Fig. 5.

Classifier: Diagnosis of COVID-19 through X-ray images is a case of multiclass classification. After the desired features are extracted by transferring learning from pre-trained models to the target models, the classifier is used to validate input data for belonging to a specific class for which the image is being analyzed. In this paper, classifier is used to annotate the image for 3-class and 4-class test cases.

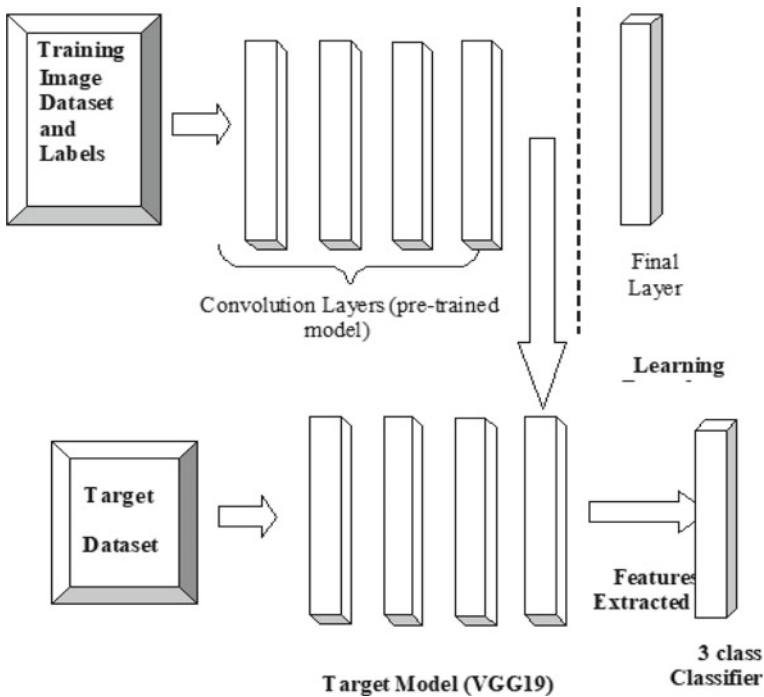


Fig. 5 Transfer learning architecture for feature extraction and classification

3 Results and Discussion

In this paper, the prime objective of implementing transfer learning model for analysis of chest X-ray images is to detect with high accuracy, the infection in lungs caused by novel corona virus. This would be helpful in cases where no visual symptoms of COVID-19 are present and the person needs to be tested as part of crowd tested in the infected region or the cases where symptoms are visual but the rapid pathological test is either not available or giving negative result. For this purpose, the models considered for analysis were processed for transfer of learning stored in their weights. Training, validation and testing were performed using Intel(R) Core(TM) i7-7700, 3.6 GHz processor with 32 GB RAM and Nvidia Quadro P2000 GPU. The Kaggle COVID-19 radiography dataset having a total of 2915 images of 3-class (see Fig. 6a) and github COVID-Net dataset having 4475 images of 4-class (see Fig. 6b) was used in a 80:20 proportion for training and testing. For 3-class, total training time was 483 min for 3-class and 642 min for 4-class. The inference time was 0.03 s in both cases.

The confusion matrix obtained for VGG19 is given in Fig. 6a for 3-class and Fig. 6b for 4-class datasets. In Figs. 7a and 8a, the diagonal cell confusion matrix shows the total number of images which are correctly classified for the 3-class, i.e., normal, viral pneumonia and COVID-19, and 4-class, i.e., normal, bacterial, viral pneumonia and COVID-19. The corresponding percentage of correct classification is given in Figs. 7b and 8b.

The accuracy for correct classification of COVID-19 cases is 98.2% for 3-class and 94.4% for 4-class. The loss and accuracy percentage of training and testing stages for 3-class and 4-class datasets is shown in Figs. 9 and 10, respectively.

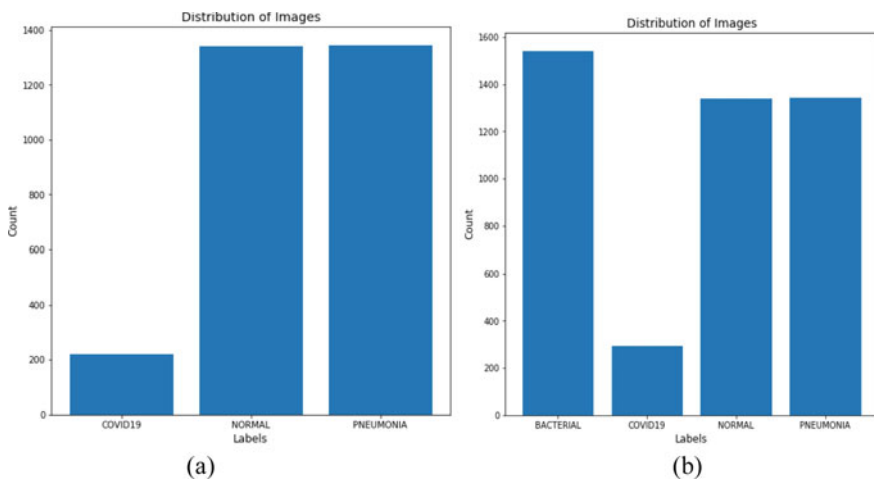
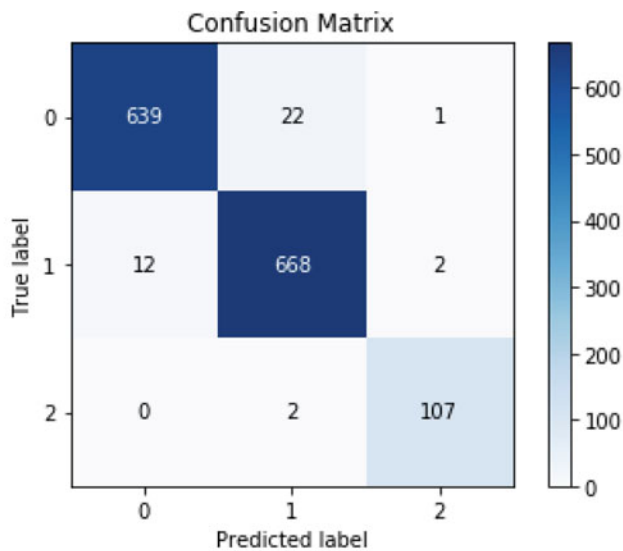
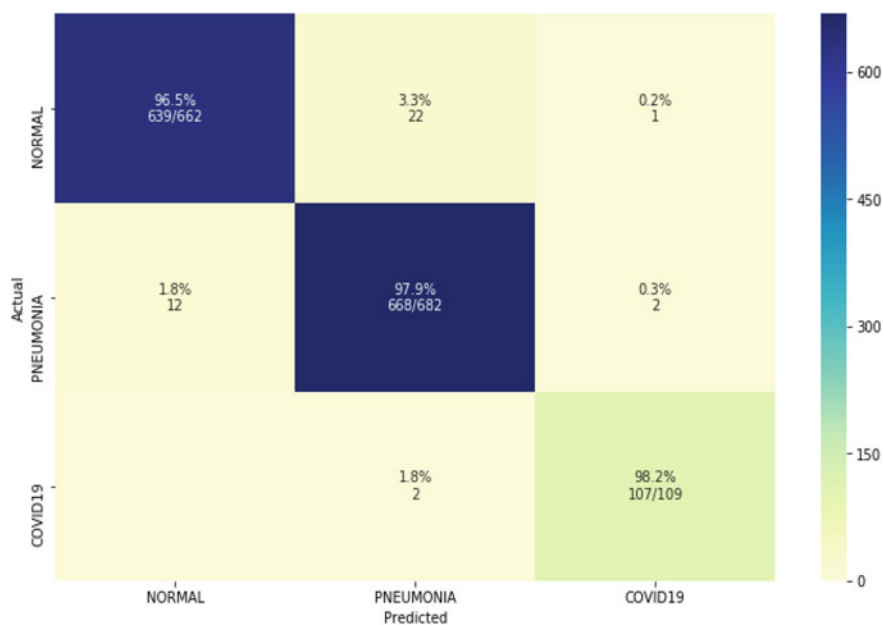


Fig. 6 Dataset used for training and testing of deep transfer learning models: **a** 3-class and **b** 4-class

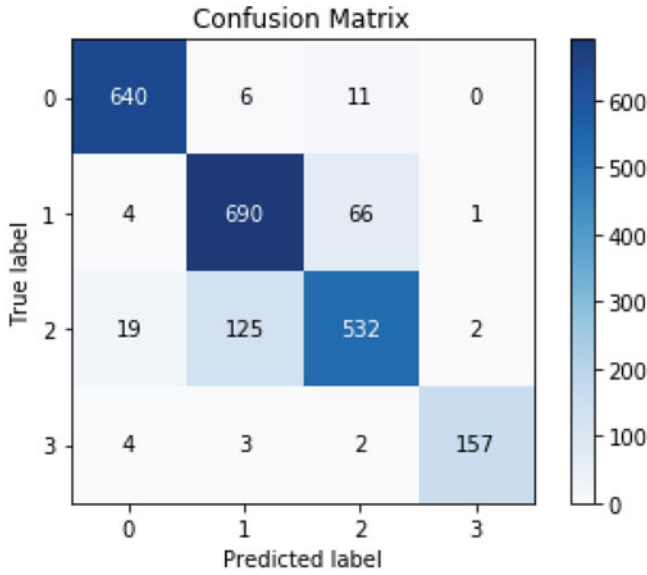


(a)

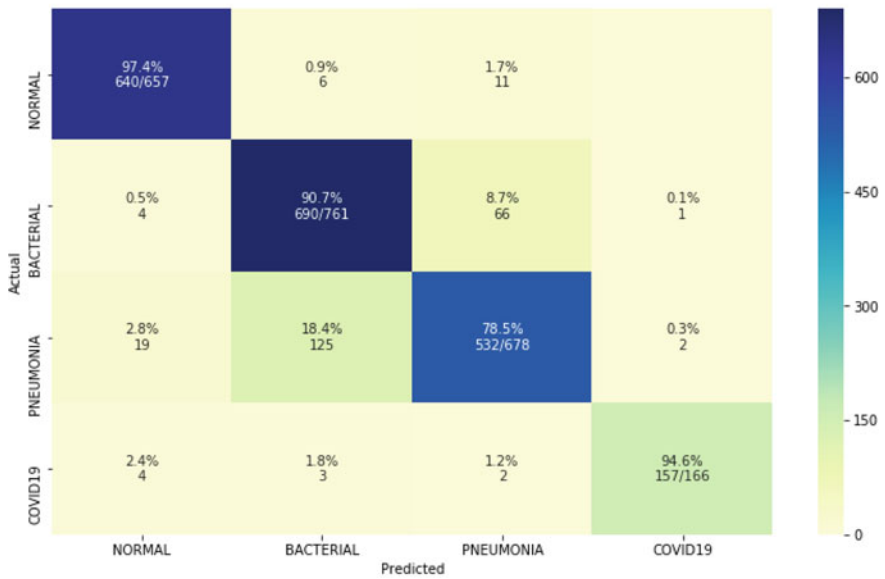


(b)

Fig. 7 Confusion matrix for VGG19: **a** total count and **b** count with percent accuracy for correctly classified images in 3-class dataset



(a)



(b)

Fig. 8 Confusion matrix for VGG19: **a** total count and **b** count with percent accuracy for correctly classified images in 4-class dataset

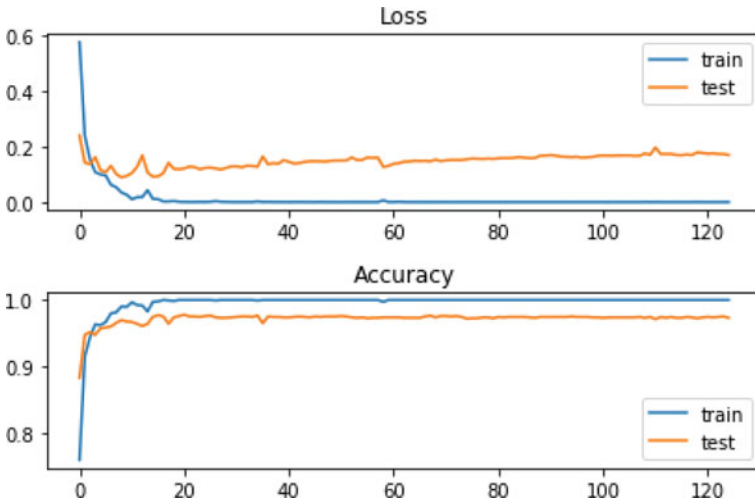


Fig. 9 Comparison of training and testing accuracy of VGG19 on 3-class dataset

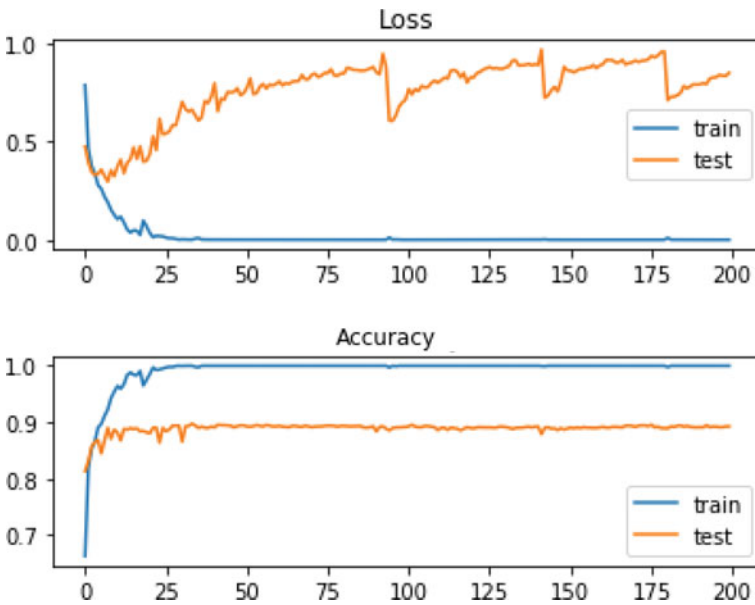


Fig. 10 Comparison of training and testing accuracy of VGG19 on 4-class dataset

Table 1 Comparison of accuracy and sensitivity of the models on the test dataset

Model	Sensitivity (%)		Accuracy (%)	
	3-class	4-class	3-class	4-class
AlexNet	93.8	83.4	95.4	86.4
ResNet18	95.6	92.3	97	88.6
VGG19	96.2	94.6	98.2	94.4

Table 1 presents a comparison of three models—AlexNet, ResNet18 and VGG19 in terms of accuracy and sensitivity. It can be clearly seen that for 3-class classification, sensitivity of ResNet18 and VGG19 is almost similar whereas VGG19 outperforms the other two models in terms of test accuracy. For 4-class classification, the performance of all three models drops compared to 3-class. VGG19 outperforms other two models in terms of both sensitivity and accuracy.

4 Conclusion

Background

- COVID-19, in its most widespread form, affects the lungs by clogging which limits their air flow capacity.
- CT scan is a more preferred radiography technique to detect COVID-19 manifestation.
- Its limited availability is demanding for other low-cost and readily available methods such as ultrasound and X-ray.
- Machine learning models such as AlexNet, ResNet18 and Inception V3 have been tested with CT scan and X-ray images to accurately detect the COVID-19 cases among various other types of infections.
- Models have been tested on 2- and 3-class datasets.

Contribution of the paper

- This paper presents performance analysis of VGG19 architecture as an accurate deep transfer learning model to analyze X-ray images for diagnosis of COVID-19.
- To test the model under challenging conditions of visual clarity in X-ray images, 4-class dataset was used which was a mix of normal, viral pneumonia and bacterial infection along with COVID-19 cases.
- Based on these results, it can be concluded that VGG19 can be used an accurate diagnosis system for pandemics such as COVID-19.
- This will serve as an alternate to the cities or countries where rapid pathology test is either not available or available in limited number compared to what is required for testing a large population.

Datasets having images of 3-class (including normal, viral pneumonia and COVID-19) and 4-class (including normal, bacterial, viral pneumonia and COVID-19) categories were used to analyze the performance of VGG19 deep transfer learning model for accurate diagnosis of COVID-19. Open-source datasets from Kaggle having 2915 images of 3-class images and from github having 4475 images of 4-class were used in a 80:20 ratio for training and testing dataset. For 3-class, total training time was 483 min for 3-class and 642 min for 4-class. The inference time was 0.03 s in both cases. Confusion matrix for both 3-class and 4-class datasets was obtained. Sensitivity and accuracy of VGG19 were compared with AlexNet and ResNet19 models. VGG19 produced an accuracy of 98.2% with 3-class dataset and 90.4% with 4-class dataset. For AlexNet and ResNet18, accuracy was reported to be 95.4% and 97% in case of 3-class dataset and 86.4% and 88.6% for 4-class dataset, respectively. Sensitivity for the three models (VGG19, ResNet18 and AlexNet) was (96.2%, 95.6% and 93.8%) for 3-class dataset and (94.6%, 92.3% and 83.4%) for 4-class dataset.

References

1. World Health Organization (2020) Coronavirus disease (COVID-19) situation reports—85, published 14 April 2020. https://www.who.int/docs/default-source/coronaviruse/situation-reports/20200414-sitrep-85-vid-19.pdf?sfvrsn=7b8629bb_2
2. Zhu N, Zhang D, Wang W et al (2020) A novel coronavirus from patients with pneumonia in China. *N Engl J Med* 382:727–733. <https://doi.org/10.1056/nejmoa2001017>
3. <https://www.wvtf.org/post/covid-19-travels-air-study-says>
4. Paules CI, Marston HD, Fauci AS (2020) Coronavirus infections—more than just the common cold. *JAMA* 323(8):707–708. <https://doi.org/10.1001/jama.2020.0757>
5. Feher J (2017) Lung volumes and airway resistance. In: Feher J (ed) *Quantitative human physiology*, Second edition. Academic Press, pp 633–641
6. Zhifeng J, Feng A, Li T (2020) Consistency analysis of COVID-19 nucleic acid tests and the changes of lung CT. *J Clin Virol* 127:104359
7. Ansari MA, Mehrotra R, Agrawal R (2020) Detection and classification of brain tumor in MRI images using wavelet transform and support vector machine. *J Interdisc Math*. <https://doi.org/10.1080/09720502.2020.1723921>
8. Zhang, X, Yao L, Wang X, Monaghan J, McAlpine D (2019) A survey on deep learning based brain computer interface: recent advances and new frontiers. *arXiv* (2019). [arXiv:1905.04149](https://arxiv.org/abs/1905.04149)
9. Litjens G, Kooi T, Bejnordi BE, Setio AAA, Ciompi F, Ghafoorian M, van der Laak JAWM, Ginneken B, Sánchez CI (2017) A survey on deep learning in medical image analysis. *Med Image Anal* 42:60–88
10. Sze-To A, Wang Z (2019) tCheXNet: Detecting pneumothorax on chest X-ray images using deep transfer learning. In: Karray F, Campilho A, Yu A (eds) *Image analysis and recognition, ICIAR 2019. Lecture notes in computer science*, vol 11663. Springer, Cham. https://doi.org/10.1007/978-3-030-27272-2_28
11. Ker J, Wang L, Rao J, Lim T (2018) Deep learning applications in medical image analysis. *IEEE Acc* 6:9375–9389. <https://doi.org/10.1109/access.2017.2788044>
12. Zi Yue Zu et al (2020) Coronavirus disease (COVID-19): a perspective from China. *Radiology* Feb 21:200490. <https://doi.org/10.1148/radiol.2020200490>
13. Xu X et al (2020) Deep learning system to screen coronavirus disease 2019 pneumonia, pp 1–29. *arXiv preprint* [arXiv:2002.09334](https://arxiv.org/abs/2002.09334)

14. Wang S et al (2020) A deep learning algorithm using CT images to screen for corona virus disease (COVID-19). Cold Spring Harbor Laboratory Press, medRxiv:2020.02.14.20023028
15. Joaquin AS Using deep learning to detect pneumonia caused by NCOV-19 from X-ray images developing a preliminary diagnosis model that can potentially fight the pandemic. <https://towardsdatascience.com/using-deep-learning-to-detect-ncov-19-from-x-ray-images-1a89701d1acd>
16. Narin A, Kaya C, Pamuk Z (2020) Automatic detection of coronavirus disease (COVID-19) using X-ray images and deep convolutional neural networks. [arXiv:2003.10849](https://arxiv.org/abs/2003.10849)
17. Oh Y et al (2020) Deep learning COVID-19 features on CXR using limited training data sets. [arXiv:2004.05758](https://arxiv.org/abs/2004.05758)
18. Deng J, Dong W, Socher R, Li LJ (2009) ImageNet: a large-scale hierarchical image database. In: 2009 IEEE conference on computer vision and pattern recognition. Miami, FL, pp 248–255
19. Muhammad N, Nasir A, Ibrahim Z, Sabri N (2018) Evaluation of CNN, Alexnet and GoogleNet for fruit recognition. Indonesian J Electr Eng Comput Sci 12(2):468–475
20. Simonyan K, Zisserman A (2015) Very deep convolutional networks for large-scale image recognition. CoRR, [arXiv:1409.1556](https://arxiv.org/abs/1409.1556)
21. LeCun Y, Bengio Y, Hinton G (2015) Deep learning. Nature 521:436–444. <https://doi.org/10.1038/nature14539>, PMID: 26017442
22. Pan SJ, Yang Q (2010) A survey on transfer learning. IEEE Trans Knowl Data Eng 22(10):1345–1359
23. Yosinski J et al (2014) How transferable are features in deep neural networks?. In: Advances in neural information processing systems 27, Proceedings of the neural information processing systems 2014, Neural Information Processing Systems Foundation, Inc. (NIPS), Montreal, QC, Canada, 8–13 Dec 2014, pp 3320–3328
24. Dai W et al (eds) (2008) Translated learning: transfer learning across different feature spaces. In: Advances in neural information processing systems 21, Proceedings of the neural information processing systems 2008, Neural Information Processing Systems Foundation, Inc. (NIPS), Vancouver, BC, Canada, 8–10 Dec 2008, pp 353–360
25. Raghu M, Zhang C, Kleinberg JM, Bengio S (2019) Transfusion: understanding transfer learning with applications to medical imaging. [arXiv \(2019\) arXiv:1902.07208](https://arxiv.org/abs/1902.07208)
26. Ravishankar H et al (2016) Understanding the mechanisms of deep transfer learning for medical images. In: Carneiro G (ed) Deep learning and data labeling for medical applications, DLMIA 2016, LABELS 2016, vol 10008. Springer, Cham, Switzerland
27. Yadav P, Agrawal R, Kashish K (2018) Heterogeneous network access for seamless data transmission in remote healthcare. Int J Grid Distrib Comput 11:69–86

Design of Single-Fed Dual-Polarized Planar Antenna for Dual-Band Automotive Applications



Niraj Agrawal, A. K. Gautam, Rajesh Mishra, and S. D. Choudhary

Abstract This proposed work revealed a novel structure of asymmetric v-shaped slots patch antenna fed with single coax-fed for generating dual bands, i.e. GPS L2 (1.227 GHz) and with SDARS (2.320–2.345 GHz) bands with right hand circular polarization and left hand circular polarization, respectively. Dual-band process and dual-polarization radiation are achieved by cut of four asymmetric v-shaped slots on the radiator. The entire volume of the proposed structure is only $61.67 \times 61.67 \times 1.6 \text{ mm}^3$, interpreting it gorgeous for the automotive systems market. A prototype of the proposed model is printed, and its simulated performance was validated with measurement. Measured data illustrated that the designed antenna radiates RHCP and LHCP wave independently.

Keywords Axial ratio (AR) · GPS · SDARS · Dual-polarization · Automotive vehicle

N. Agrawal (✉) · R. Mishra

Department of Electronics and Communication Engineering,
School of ICT, Gautam Buddha University, Greater Noida, India
e-mail: nirajagrawalg@gmail.com

R. Mishra

e-mail: raj25mis@gmail.com

A. K. Gautam

Department of Electronics and Communication Engineering,
GBPIT Uttarakhand, Pauri, Uttarakhand, India
e-mail: gautam1575@yahoo.co.in

S. D. Choudhary

Department of Electronics and Communication Engineering,
NIET, Greater Noida, India
e-mail: suryadeo.bit@gmail.com

© Springer Nature Singapore Pte Ltd. 2021

R. Agrawal et al. (eds.), *Advances in Smart Communication and Imaging Systems*,
Lecture Notes in Electrical Engineering 721,
https://doi.org/10.1007/978-981-15-9938-5_14

1 Introduction

Recent years vehicular-orientated navigation and telecommunication facilities are getting prevalent, and advance automotive systems are being furnished with several on sheet electronics systems, as the global positioning system (GPS) and digitally satellite audio services (SDARS). These facilities are normally integrated together on the same antenna. Consequently, less complex, low cost and low profile antennas are developed, which is necessity for vehicular systems. GPS working in L2-band (1.2276 GHz) with RHCP radiation and SDARS working in S-band (2.320–2.345 GHz) with LHCP radiation required different specifications to be attained and therefore need separate radiator specially for automotive use.

A number of reported work have been presented in the references that proposed design achieved dual band with different circular polarization [1–3, 5–8]. The aim of this work was to present a two layer antenna structure incorporated circular radiators with single feed for simultaneous dual sense CP radiation at two different bands [2]. In [6], presented a dual band antenna fed by CPW-feed with spiral slots incorporated ground plane for achieved dual bands with different circular polarization. [5] proposed a model for dual-polarized at SDARS (2.320–2.345) band with integrated low-noise amplifiers (LNAs). Integrated ceramic patch and square-ring microstrip antenna were projected in [8] for achieved GPS L1 and SDARD bands, respectively. The concentric arrangement of slot-loaded square patch and modified annular ring patch operated at GPS L1 and SDARS bands with RHCP and LHCP radiation, respectively, in [3]. In [7], an omnidirectional circular polarization at GPS band was realized by eight shorted metal pins with eight open slots incorporated with top and bottom patch, while a omnidirectional linear polarization radiation was formed by central part of top patch antenna. In [1], a radiator with four asymmetric hat-shaped slots is used to obtain triple bands with triple polarization. In [9], a pyramidal ground structure was used to enhance the beam-width of circular polarized wave.

In this proposed work, design of a single-fed dual-polarized planar antenna with compact size $61.67 \times 61.67 \times 1.6 \text{ mm}^3$ for GPS L2 and SDARS automotive applications. The antenna with four v-shaped slots contributes to RHCP and LHCP radiation waves and miniaturization of the size of designed antenna.

2 Antenna Design

Figure 1 depicts the entire design with detailed configurations of the dual-polarized CP antenna. The v-shaped slots patch with single fed is printed on FR-04 sheet, thickness of sheet $h = 1.6 \text{ mm}$ and relative permittivity of $\epsilon_r = 4.40$. The designed antenna comprises single coaxial feed of 50Ω impedance is connected at diagonal position to the patch. The RHCP and LHCP radiated waves are essential at GPS L2 and SDARS bands, respectively. The CP can be achieved by generating two orthogonal degenerated modes [4]. The presented design with four v-shaped slots is

Table 1 Optimized dimension shown in Fig. 1b

Parameters	Unit (mm)
W_g	61.67
W_1	6.50
W_2	5.80
W_{c1}	2.50
W_{c2}	2.70
S_1	4.0
L_p	50
L_1	6.50
L_2	5.80
L_{c1}	10
L_{c2}	9.50
X_f	15.80

introduced on the patch to generate two 90° phase difference degenerate modes. At the inception, the conventional coaxial-fed diagonal antenna shown in Fig. 2a that resonant 2.01 GHz in Fig. 3a is analysed to achieve CP but fails to obtain (see Fig. 3b). Then in further process, radiator is employed with two horizontal v-shaped slots as shown antenna 2 to obtain dual-band operation and circular polarization at the desired bands. Nevertheless, as shown in Fig. 3a, two tune frequencies at around 1.34, 2.29 GHz bands are obtained but fail to excite CP radiation as displayed in Fig. 3b. Further, introducing two vertical v-shaped slits in the patch is shown in antenna 3 to obtain dual-band operation and circular polarization at the desired bands. Nevertheless, as shown in Fig. 3a, two tune frequencies at around 1.345, 2.37 GHz bands are obtained but fail to excite CP radiation as revealed in Fig. 3b. Finally, after incorporated four v-shaped slits in antenna 4 to achieve good quality RHCP radiation 1.2276 GHz and LHCP radiation 2.3325 GHz as shown in Fig. 3a, b.

2.1 CP Radiation

Sense of circular polarization can be described with distributed magnetic surface currents on the proposed antenna at different time phase. Figure 4 reveals the magnetic surface currents at the different time phases at $t = 0^\circ$, $t = 90^\circ$, $t = 180^\circ$ and $t = 270^\circ$ for 1.2276 and 2.3325 GHz bands. The currents rotate counter-clockwise direction as shown in Fig. 4a to yield a RHCP radiation at 1.2276 GHz; meanwhile, the surface currents 2.3325 GHz illustrated in Fig. 4b rotate in clockwise direction to excite LHCP radiation.

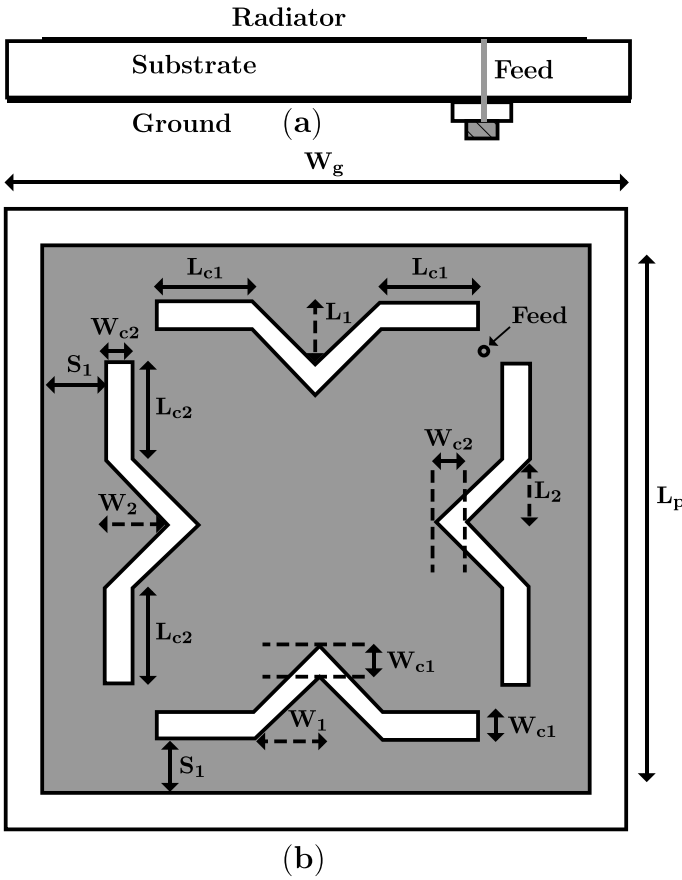


Fig. 1 Configuration of the designed structure. **a** Side vision. **b** Front vision

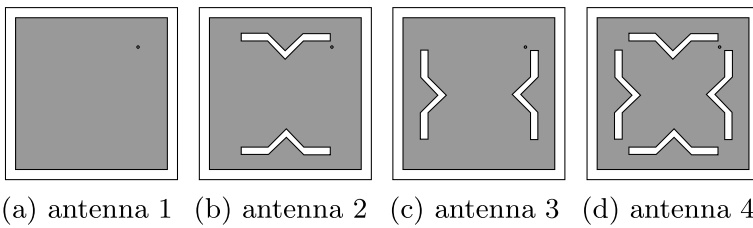


Fig. 2 Evolution process

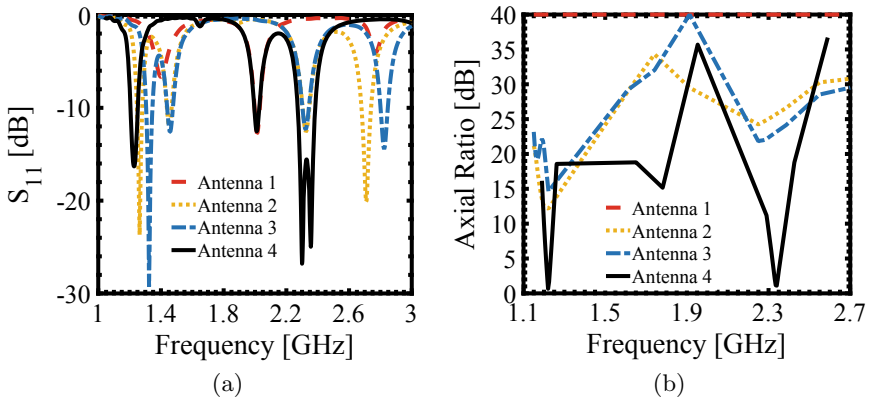


Fig. 3 Exploded process of the designed antenna a S_{11} and b axial ratio

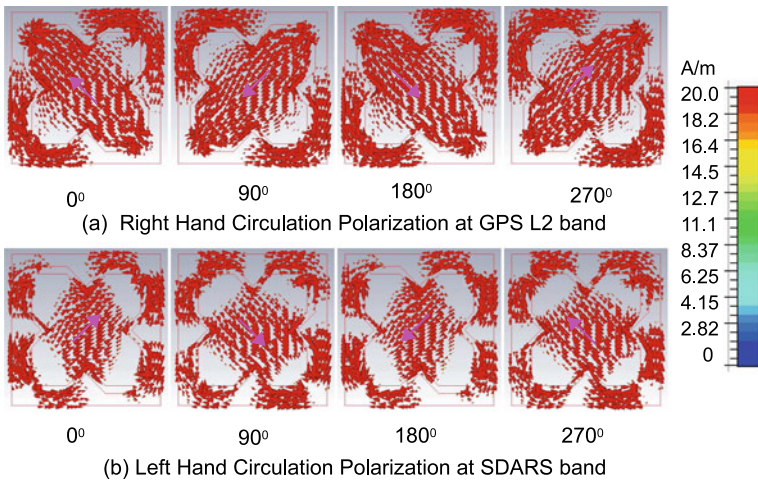
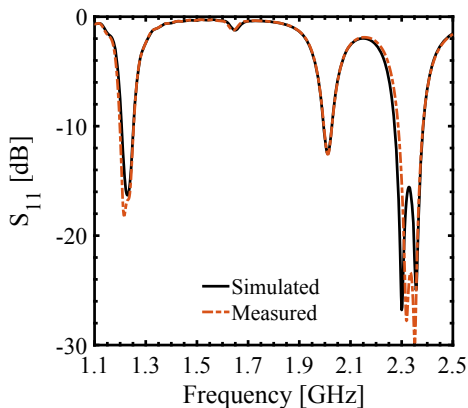


Fig. 4 Distributed surface currents at GPS L2 (1227.6 MHz) and SDARS (2332.5 MHz) bands for the presented antenna at 0° , 90° , 180° and 270°

3 Experimental Outcomes

After completed the simulation with the simulation package CST microwave studio. The prototype is fabricated in the antenna laboratory at G.B.P.I.T, Pauri. Figure 5 describes the measured and simulated S_{11} of GPS L2 with SDARS band. From Fig. 5, it is demonstrated that measure S_{11} is in acceptable agreement with simulated S_{11} . The slight discrepancies between return losses maybe due to the dielectric losses. The measured values exhibited that the impedance bandwidths are 47 MHz (1.205–1.252 GHz) for the lower GPS L2 band and 101 MHz (2.272–2.373 GHz) for the upper SDARS band.

Fig. 5 Comparison between Simulated and measured S_{11} of the designed antenna



The simulated radiation pattern graph at 1.2276 and 2.3325 GHz frequencies is to estimate the far field radiation performance of the fabricated antenna. Figure 6 illustrates the comparison of the simulated radiation patterns at GPS L2 (1.2276 GHz) and SDARS (2.3325 GHz) bands. From Fig. 6, it depicts that the simulated bore-sight gain was 3.94 and 6.48 dBic for GPS L2 and SDARS bands, respectively. It is also evident that the polar value of radiation pattern is about symmetry at both ($\phi = 0^\circ$) and ($\phi = 90^\circ$) principle planes. Further, co-polar radiation (RHCP) and cross-polar radiation (LHCP) pattern in both xz and yz principal planes for GPS L2; meanwhile co-polar radiation (LHCP) and cross-polar radiation (RHCP) pattern in both xz and yz principal planes for SDARS band, respectively, $>$ by 25 dB. Thus, outstanding cross-polarization discrimination is obtained in the bore-sight direction.

The axial ratio beam-width presented by the proposed structure is shown in Fig. 7. The minimum axial ratio values for lower (GPS L2) and upper (SDARS) bands in bore-sight ($\theta = 0^\circ$) direction are 0.65 and 1.17 dB, respectively. Furthermore, the 3-dB beam-width characteristic of GPS L2 (lower) and SDARS (upper) bands for the designed antenna is 121° and 152° , respectively, which shows wider beam-width at both bands is appropriate for many automotive applications.

The simulated and experimental axial ratio bandwidth characteristic in broad sight direction is plotted in Fig. 8. The antennas offer simulated and measured 15 MHz (1.214–1.229 GHz) axial ratio band width at GPS L2 and 25 MHz (2.320–2.345 GHz) axial ratio band width at SDARS band. The simulated and experimental 3-dB band width at both bands lies within $S_{11} < -10$ dB impedance bandwidths.

4 Conclusion

The proposed design of asymmetric v-shaped slots patch antenna fed with single coax-fed for generating dual bands, i.e. GPS L2 (1.227 GHz) and with SDARS (2.320–2.345 GHz) bands was effectively fabricated and experimental authenticated.

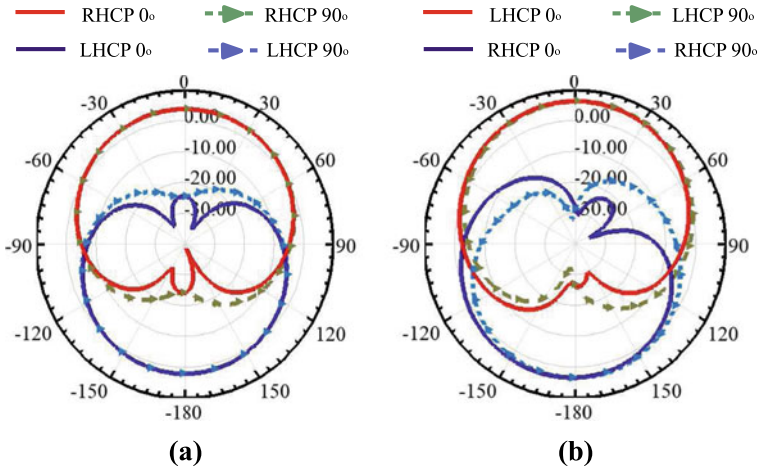


Fig. 6 Comparison between simulated radiation patterns at different plane **a** 1.2276 GHz and **b** 2.3325 GHz

Fig. 7 Simulated axial ratio beam-width versus θ

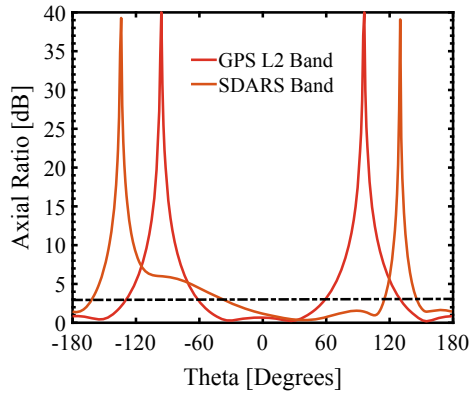
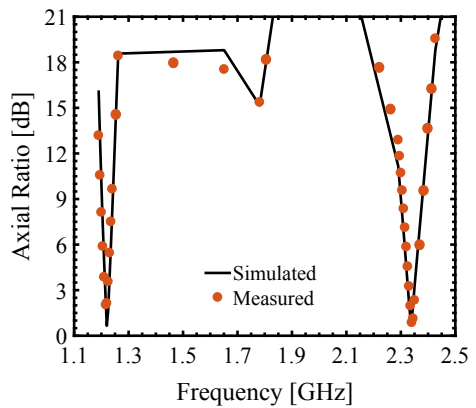


Fig. 8 Comparison between measured and simulated axial ratio band width



Dual impedance bandwidth and suitable polarization are achieved by cutting of v-shaped slots on the radiator. The experimental values exhibited that the printed antenna will be proficiently worked in two distinct bands, i.e. 47 MHz (1.205–1.252 GHz) and 101 MHz (2.272–2.373 GHz). moreover, the design will fulfil all requirements for navigation and digital audio services.

References

1. Agrawal N, Gautam AK, Rambabu K (2019) Design and packaging of multi-polarized triple-band antenna for automotive applications. *Int J Electron Commun AEU* 113
2. Bao X, Ammann M (2008) Dual-frequency dual circularly-polarised patch antenna with wide beamwidth. *Electron Lett* 21:1233–1234
3. Bilgic MM, Yegin K (2015) Modified annular ring antenna for GPS and SDARS automotive applications. *IEEE Antenna Wireless Propag Lett* 15:1442–1445
4. Gautam AK, Farhan M, Agrawal N, Rambabu K (2019) Design and packaging of a compact circularly polarised planar antenna for 2.45-GHz RFID mobile readers. *IET Microwaves, Antennas and Propagation* 13(13):2303–2309
5. Hong YP, Kim JM, Jeong SC, Kim DH, Choi MH, Lee Y, Yook JG (2006) S-band dual-path dual-polarized antenna system for satellite digital audio radio service (SDARS) application. *IEEE Trans Microwave Theo Tech* 54(4):1569–1575
6. Lin SY, Hunag KC (2009) Dual-band dual-sense circularly-polarized CPW-fed slot antenna with two spiral slots loaded. *IEEE Trans Antennas Propag* 6:1829–1833
7. Liu Y, Li X, Yang L, Liu Y (2017) A dual-polarized dual-band antenna with omni-directional radiation patterns. *IEEE Trans Antennas Propag* 65(8):4259–4262
8. Mariottini F, Albani M, Toniolo E, Amatori D, Maci S (2010) Design of a compact GPS and SDARS integrated antenna for automotive applications. *IEEE Antenna Wireless Propag Lett* 9:405–408
9. Su CW, Hunag SK, Lee CH (2007) CP microstrip antenna with wide beamwidth for GPS band application. *Electron Lett* 43(20):1062–1063

SCSZB: Sensor Congregate Stable Zonal-Based Routing Protocol Designed for Optimal WSN



Anshu Kumar Dwivedi, A. K. Sharma, Manju, Samayveer Singh,
and P. S. Mehra

Abstract WSN contains the sensor nodes, which can sense, collect and compute data from surrounding, providing economical solutions to an extensive variety of authentic real-life problems. It contains many small and energy-restricted sensor nodes (SNs) that help in accomplishing a sensing task. Numerous algorithms and protocols for CH selection and cluster formation have been proposed for energy-efficient WSNs, but most of them do not have the balance of energy dissipation among the SNs due to which the SNs start dying and the network lifespan is over. To enlarge the life span of the network, a sensor congregate stable zonal-based (SCSZB) routing protocol is proposed for heterogeneous WSNs, where the network is separated into five zones each zone has different types of nodes which have different characteristics. Ordinary nodes are placed in zone 1, advanced node in zone 2 and zone 3 and super advance node is placed in zone 4 and zone 5. The proposed SCSZB upturns the stability period and network lifespan of WSNs.

Keywords Clustering · Lifetime · Energy efficient · WSN · Cluster head · Zonal

A. Kumar Dwivedi (✉) · A. K. Sharma
Department of Computer Science and Engineering, M M M University of Technology,
Gorakhpur, India
e-mail: anshucse.dwivedi@gmail.com

A. K. Sharma
e-mail: akscse@rediffmail.com

Manju · P. S. Mehra
Department of Computer Science and Engineering, Jaypee Institute of Information Technology,
Noida, India
e-mail: manju.nunia@gmail.com

P. S. Mehra
e-mail: pawansinghmehra@gmail.com

S. Singh
Department of Computer Science and Engineering, Dr B R Ambedkar National Institute
Technology, Jalandhar, India
e-mail: samayveersingh@gmail.com

1 Introduction

WSNs have many SNs that are very inexpensive, low powered and multifunctional [1, 2]. SNs also have limited storage capacity, transmission range and energy resources [3]. Multi-hop routing is required to maintain the routes in the network so as to make the network more reliable [4, 5]. The SN senses the data and sends it to the base station (BS) followed by wireless communication between the BS and the SN with the help of radio frequency or laser approach [6, 7]. Some routing techniques are required for the transmission of data between the SN and sink. Due to various complexities in current routing algorithms, such as network lifetime, response time, security, power challenge and ease of deployment, we need to optimize such algorithms for maximizing the lifetime of WSN [8]. Various parameters affecting the energy of WSNs are transmission range, routing algorithm, the density of nodes, topology and in-network processing [9, 10]. Routing protocols are hierarchical protocols, data-centric protocols and location-based protocols [11] that are used separately in WSNs. Data-centric protocols typically include location-based protocols such as LEASE [12] SPIN [13], CADR [14], LEACH [15], PEGASIS [16], TEEN [17], AAP [18] SE-LEACH [19], etc. Hierarchical and location-based protocols can be widely used in geographic areas requiring dense sensor distribution [20, 21].

In this paper, an efficient SCSZB routing technique is proposed for WSN so as to improve the stability period and enhance the network life span of WSNs. The proposed method divided the deployed networks into five zones each zone that have different type of node having different characteristics as follows—ordinary nodes are placed in zone 1, advanced node in zone 2 and zone 3 and super advance node is placed in zone 4 and zone 5. Further, the simulation results show that SCSZB has noteworthy enhancement over SEP and Z-SEP.

This research article split into subsequent sections: Sect. 2 and 3 describes various similar works done on the problem identified and discuss network and energy model of the proposed work. Section 4 will examine the results of the proposed model. Section 5 describes the conclusion and future work.

2 Related Work

We have discussed numerous traditional protocols related to the proposed method. A well-known LEACH protocol [15] is proposed to reduce power consumption. LEACH works on a data aggregation process in which the original data is combined with smaller size data. The algorithm in LEACH is an arbitrary rotation of CHs and subsequent clusters for application-specific processing of data. This operation is mainly split into two rounds—(a) setup phase and (b) steady-state phase. However, LEACH cannot be considered suitable for heterogeneous environments. Stable election protocol is a heterogeneous [22] aware protocol that increases the stability period of the network before the death of the first node. It works on the remaining energy of

each node to become a CH. It consists of common and advanced nodes from which advanced nodes have a higher tendency to become CHs. The drawback of SEP is that an efficient node does not assure deployment. Design of Energy-Efficient Clustering Protocol (DEEC) [23] demonstrates multilevel heterogeneity. To select CHs in the network, it uses the initial and residual energy levels of nodes. DEEC evaluates the lifetime value of the network based on number of rounds of communication have been made by the SN. The Zonal-Stable Election Protocol (Z-SEP) [24] is an extension of the SEP protocol. Basically, it is a well-known hybrid phenomenon in which data is transmitted to the BS by CHs. Here, zones are categorized as 0, 1 and 2 head zones, wherein zone 0 having ordinary nodes, zones 1 and 2 consist of advanced nodes. In such deployment, the energy of the advance node is more as compare to ordinary node. However, Z-SEP is not considered a suitable protocol as it is not scalable. Another protocol for CH selection is Energy-Aware Routing Protocol (EAP) [25]. It works on the heterogeneous energy of the node. EAP protocol maintains the table of residual energy of each SN and also maintains the table of the single-hop node which is generally called a neighbor node. In this proposed protocol, the CH collects the sensed data from the sensor node and sends to the BS because it has more energy than all existing sensor node.

3 Presumed Network Model

Here, we consider the following network assumptions for the proposed protocol:

- Network is heterogeneous and static.
- Each SN is assigned a unique id and the BS is cognizant of the locations of each node in advance.
- A BS is positioned in the central part of the area where every node forwards the obtained data.
- A node is died when it is not able to forward the gathered information to BS.

3.1 Presumed Energy Model

We presume that the maximum portion of the energy is invested during a correspondence while organizing sensors in the network. Figure 1 shows the energy scattering model where receiving/sending data as a sensor.

Total energy consumed by SN in order to send m -bit data to base station and distance d is given by as follows:

$$E_{Tx}(m, d) = \begin{cases} mE_{elec} + m\epsilon_{fs}d^2, & d < d_o \\ mE_{elec} + m\epsilon_{mp}d^4, & d \geq d_o \end{cases} \quad (1)$$

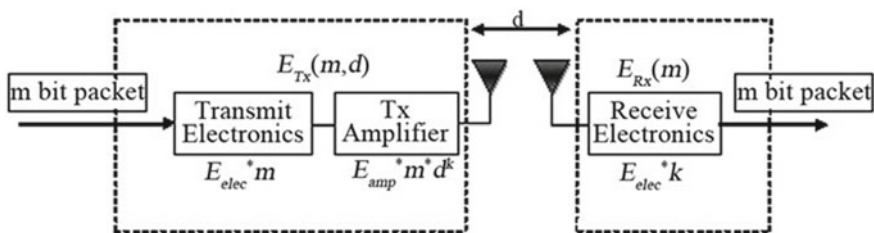


Fig. 1 Radio energy dissipation model

where $d_0 = \sqrt{\frac{\epsilon_{fs}}{\epsilon_{mp}}}$, d is the transmission distance.

Then, the requirement of energy for receiving m -bit message as follows

$$E_{Rx}(m) = E_{Rx-elec}(m) = m \cdot E_{elec} \quad (2)$$

4 Proposed Work: SCSZB

In this section, SCSZB routing protocol is proposed, which is a modified version of the Z-SEP [24]. This protocol plays a very important role to maximize the life span of the network compared to SEP and Z-SEP. Each zone of SCSZB protocol has a CH to communicate directly to the BS.

Network Architecture

In majority of routing protocols, nodes in the field are deployed arbitrarily and thus the energy use of the node is not efficient [26]. The given field as shown in Fig. 2 is spread over mainly five zones: one zone for ordinary nodes, two for advanced nodes and the remaining two for supernodes, based on the coordinate of the network field Y .

- Ordinary nodes are positioned arbitrarily in the area between $40 < Y \leq 60$.
- Advanced nodes are those which are positioned arbitrarily between $20 < Y \leq 40$ and $60 < Y \leq 80$.
- Finally, supernodes take place arbitrarily in the area between $0 < Y \leq 20$ and $80 < Y \leq 100$.

Such deployment is done in the field because the energy level of the ordinary node is less while the energy level of the supernode is high. The energy level of the advanced node is higher than the ordinary node and lower than the supernode. Therefore, the advanced node is deployed among the ordinary node and the supernode. If the nodes which are found in the corner of the network have more energy, only then they can communicate to the BS for a long time. Supernode always deploy near to the BS. Thus, by creating this type of network field architecture, the lifetime of the field

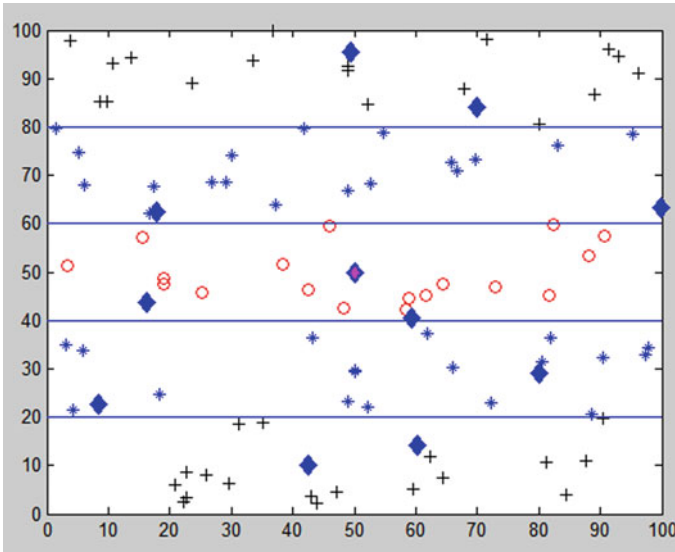


Fig. 2 Network architecture

increases, creating a more generalized and energy-efficient system. This protocol helped in the judicious use of energy in the super and advanced nodes, which steered the long-term stability field according to the higher values of additional energy.

4.1 CH Formation

CH formation is an important phase of the proposed protocol. Network area is mainly partitioned into five equal zones from zone 1 to zone 5. CH is elected in every zone on the basis of certain input parameter which includes, distance to sink and the residual energy of a node. Once the CHs selected, the cluster formation phase comes into existence. Non-cluster head (NON-CH) nodes are required to take the preference of joining the CH. NON-CH nodes have metrics such as distance around CH, its residual energy and average distance from CH to member node. All this important metrics, it will explore their opportunity. After the calculation of the chance of each CH node, the NON-CH node will pick a CH node with the most noteworthy possibility and send a packet (JOIN_CL). The CH node will acknowledge them and send an affirmation (ACK_ACCEPT_JOIN) to the requesting node with a TDMA plan. As such, every node of the networks is grouped. After each round of communication, the role of CHs changes. The proposed SCSZB is explained through flowchart in Fig. 3. Proper time scheduling is done for nodes in which they can communicate to CHs after performing aggregation. For this reason, CHs are expending more power than rest of the nodes. CHs are those nodes that send data to the central BS. Direct transmission from SN

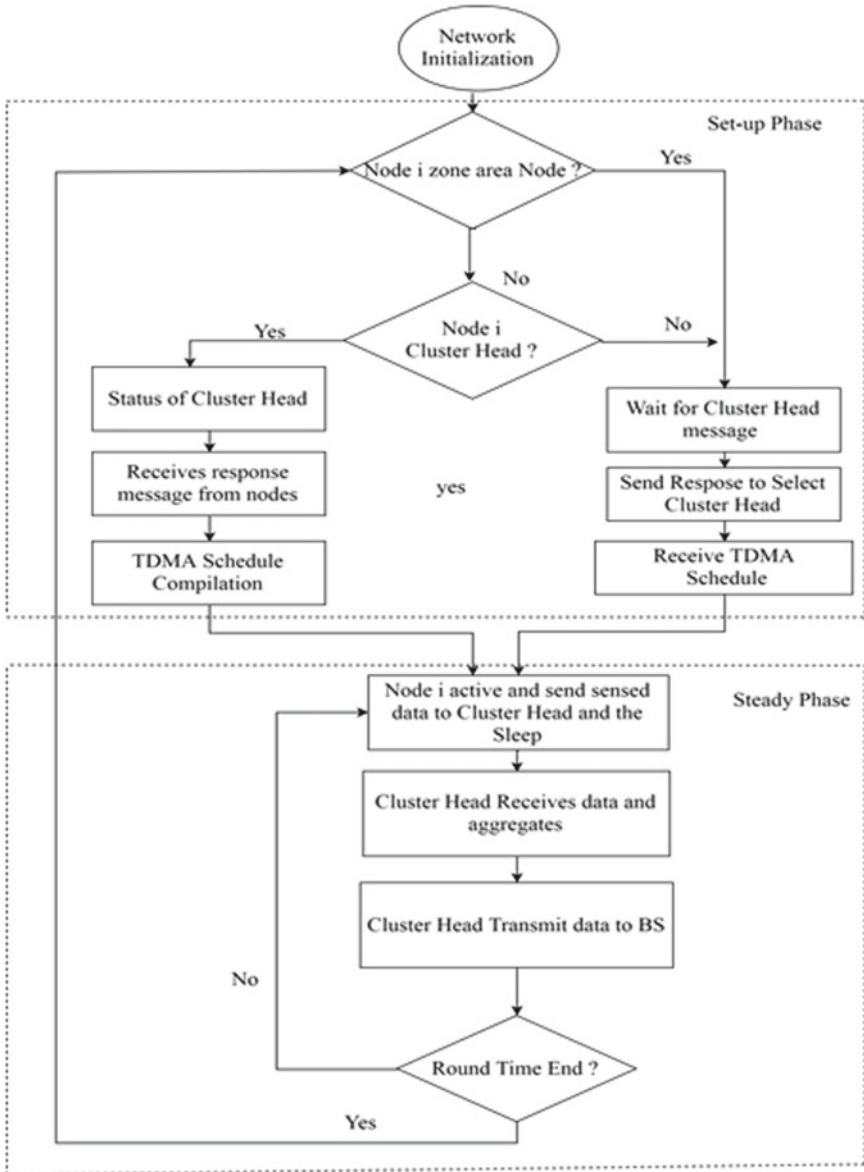


Fig. 3 Flowchart of SCSZB routing protocol

is avoided because when direct transmission occurs, SNs will die more quickly and which in turn reduces the network life span. The existence of both advanced and supernodes help to increase stability. Consequently, the suggested protocol is much able to maintain its period of stability in the presence of heterogeneous parameters.

5 Results and Simulation

An area $100\text{ m} \times 100\text{ m}$ is taken to simulate the proposed protocol. Energy-wise 100 nodes are deployed in specific areas. In the center of the field, BS is placed. Like the SEP protocol, the proposed protocol also uses a first-order radio model. MATLAB is used to implement the simulation for the proposed protocol. As discussed that 40% nodes are advanced, 40% nodes are super while remaining 20% nodes are normal, the nodes are randomly scattered across the region within their particular field dimensions. The simulation parameters are specified in Table 1.

We have used four performance metrics which are as follows.

- **Stability period and half node death:** Stability [27] is first node death and half node death means only 50% nodes are alive.
- **Node death rate:** The energy level of SN dissipate after a specific number of round, after some time, the node may die due to lack of energy and death rate basically provides the number of nodes which are still alive at any given moment.
- **Data packet transferred:** It basically shows the count of packets the sensors send to the BS in specific periods of time. This unit is important for analyzing data gathering of networks.
- **Network lifetime:** Network lifetime basically defines the total time of a network until last node dies in the network.

Table 1 Simulation metrics

Metric	Value
Network area	100×100
Energy (E_o) as initial energy	0.5 J
Advanced node's energy	$E_o(1+\alpha)$
Supernode's energy	$E_o(1+\beta)$
Energy used in data aggregation (E_{DA})	5 nJ/bit/signal
Energy (E_{elec}) for sending and receiving	5 nJ/bit
Short distance amplification energy (E_{fs})	10 pj/bit/m^2
Long distance amplification energy (E_{mp})	0.013 pj/bit/m^4

5.1 Stability Period and Half Node Dead

The death of half the nodes of any network is calculated by the death of 50% of the nodes from the beginning of the network. The input parameter is important because the network make use of around 85% of starting energy at the time when almost 50% nodes' death occurs. When half of the nodes of the field die, the appearance of the field is as follows (Table 2).

Now, the results of the addressed method is compared with previously described method, i.e., Z-SEP and SEP. Supernodes are introduced into the Z-SEP and SEP protocols with a similar setting, built into our protocol, which examines the performance of all protocols in the existence of supernodes to improve heterogeneous characteristics.

The main objective behind conducting the simulation is to investigate the period of stability of the SEP, Z-SEP and the proposed protocol to show the comparison and to prove the result better.

Table 2 Stability and half node death

Protocol	Stable period (rounds)	Half node dead (rounds)
SEP	1085	1486
Z-SEP	1535	2023
Proposed	1766	4424

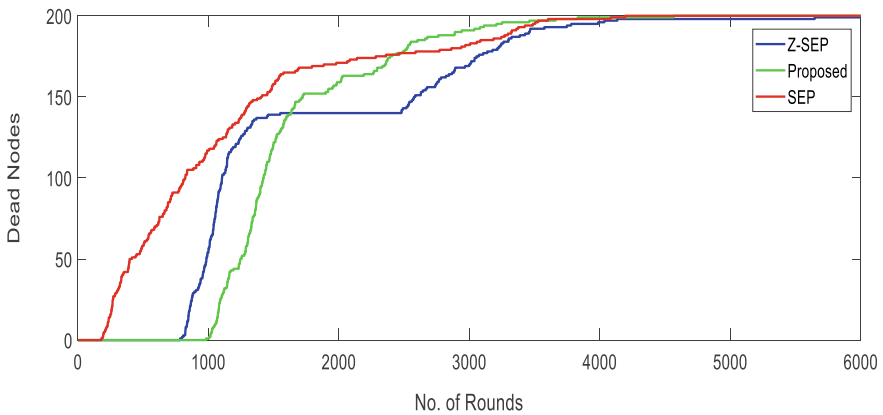


Fig. 4 Node death rate

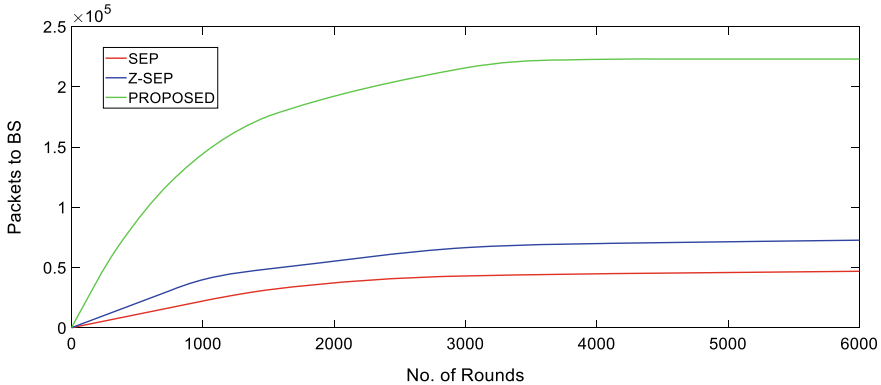


Fig. 5 Data received at BS

5.2 Node Death Rate

Figure 4 depicts node-by-node for SEP, Z-SEP and the proposed protocol SCSZB, an region of $100\text{ m} \times 100\text{ m}$ with 100 nodes taken for the network. The node mortality of SCSZB is lower than SEP and Z-SEP. The SCZB protocol consumes less energy than SEZ, Z-SEP.

5.3 Data Received at BS

Figure 5 showed all the information about the SNs and their sensory data to the data unit received at the BS in this metric. Unnecessary data not received on BS. Figure depicted maximum data obtained in BS only due to SCSZB protocol compared to SEP and Z-SEP.

5.4 Network Energy Level

Figure 6 shows the maximum network life span of the SCSZB protocol compared to SCZ and Z-SEP and the final node death of SCSZB protocol is much higher than that of SEP and Z-SEP which is closer to node BS, and it consumes less energy for communication. SCSZB outperforms SEP and Z-SEP and extends network lifetime.

According to the simulation consequence, the proposed protocol proves to be more energy-efficient in terms of SCSZB node mortality than the protocols such as SEP, Z-SEP, much longer than the lifetime network. Therefore, the simulation results suggest that the proposed protocol and its working method are superior to the old protocol.

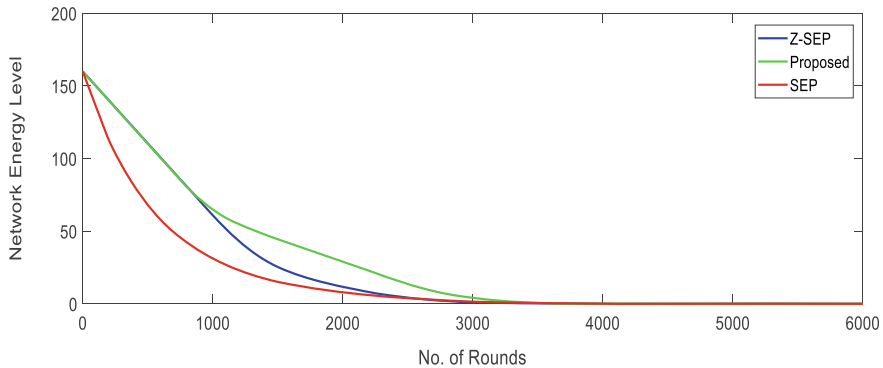


Fig. 6 Network energy level

6 Conclusion and Future Work

In this paper, a protocol with heterogeneous environment (SCSZB) is proposed: Three-level heterogeneity consisting of five regions. One zone has common nodes, two zones have advanced nodes and the remaining two have supernodes. In the proposed network, BS is located at the center of the sensing region. Subsequently, the area is virtually divided into two equal parts. This type of division results in the creation of five zones separated by zone 1, zone 2, up to zone 5. Subsequently, the clusters heads are selected for each five zones. These CHs will be used for data transmission purposes. The results showed that according to the energy of the nodes, the change in their deployment increased the period of stability. Therefore, the proposed protocol can be considered a better solution to provide more energy-efficient results. Therefore, the proposed protocol is more efficient than other protocols (SEP and Z-SEP) and provides better results. In the future direction, the SCSZB protocol will be used to inform the availability and scarcity of water in agriculture.

References

1. Pottie GJ, Kaiser WJ (2000) Wireless integrated network sensors. *Commun ACM* 43(5):51–58
2. Abbasi AA, Younis M (2007) A survey on clustering algorithms for wireless sensor networks. *Comput Commun* 30(14–15):2826–2841
3. Akyildiz IF, Su W, Sankarasubramaniam Y, Cayirci E (2002) Wireless sensor networks: a survey. *Comput Netw* 38(4):393–422
4. Kumar A, Mehra PS, Gupta G, Sharma M (2013) Enhanced block playfair cipher
5. Mehra PS, Doja MN, Alam B (2019) Codeword authenticated key exchange (CAKE) light weight secure routing protocol for WSN. *Int J Commun Syst* 32(3):e3879
6. Akkaya K, Younis M (2005) A survey on routing protocols for wireless sensor networks. *Ad Hoc Netw* 3(3):325–349
7. Kumar A, Mehra PS, Gupta G, Jamshed A (2012) Modified block playfair cipher using random shift key generation. *Int J Comput Appl* 58(5):975–8887

8. Manju, Chand S, Kumar B (2018) Genetic algorithm-based meta-heuristic for target coverage problem. *IET Wirel Sens Syst* 8(4):170–175
9. Manju, Chand S, Kumar B (2017) Selective α -coverage based Heuristic in wireless sensor networks. *Wirel Pers Commun* 97(1):1623–1636
10. Mehra PS, Doja MN, Alam B (2019) Enhanced clustering algorithm based on fuzzy logic (E-CAFL) for WSN. *Scalable Comput Pract Exp* 20(1):41–54
11. Al-Karaki JN, Kamal AE (2004) Routing techniques in wireless sensor networks: a survey. *IEEE Wirel Commun* 11(6):6–27
12. Mehra PS, Doja MN, Alam B (2015) Low energy adaptive stable energy efficient (LEASE) protocol for wireless sensor network. In: 2015 1st international conference on futuristic trends in computational analysis and knowledge management, ABLAZE 2015, pp 484–488
13. Perrig A, Szewczyk R, Tygar JD, Wen V, Culler DE (2002) SPINS: security protocols for sensor networks. *Wirel Netw* 8(5):521–534
14. Li C-T, Weng C-Y, Lee C-C, Lee C-W, Chiu P-N, Wu C-Y (2013) Security flaws of a password authentication scheme for hierarchical WSNs. *J Adv Comput Netw* 1(2):121–124
15. Heinzelman WR, Chandrakasan A, Balakrishnan H (2000) Energy-efficient communication protocol for wireless microsensor networks. In: Proceedings of the 33rd annual Hawaii international conference on system sciences. IEEE Computer Society, p 10
16. Lindsey S, Raghavendra CS (2002) PEGASIS: Power-efficient gathering in sensor information systems. In: Proceedings, IEEE Aerospace Conference, pp 3-1125–3-1130. IEEE
17. Manjeshwar A, Agrawal DP (2001) TEEN: a routing protocol for enhanced efficiency in wireless sensor networks. In: Proceedings of the 15th international parallel and distributed processing symposium
18. Gergely Ács GG, Buttyán L (2007) A taxonomy of routing protocols for wireless sensor networks
19. Mehra PS, Doja M, Alam B (2019) Stability enhancement in LEACH (SE-LEACH) for homogeneous WSN. *EAI Endorsed Trans Scalable Inf Syst* 6(20):156592
20. Yadav P, Agrawal R, Kashish K (2018) Protocols performance investigation using Ad Hoc WLAN for healthcare applications. *Pertanika J Sci Technol* 26:1333–1354
21. Yadav P, Agrawal R, Kashish K (2018) Performance Evaluation of ad hoc Wireless Local Area Network in Telemedicine Applications. *Procedia Comput Sci* 125:267–274
22. Smaragdakis G, Matta I, Bestavros A (2004) SEP: a stable election protocol for clustered heterogeneous wireless sensor networks. In: Second international workshop on sensor and actor network protocols and applications (SANPA 2004)
23. Jia D, Zhu H, Zou S, Hu P (2016) Dynamic cluster head selection method for wireless sensor network. *IEEE Sens J* 16(8)
24. Faisal S, Javaid N, Javaid A, Khan MA, Bouk SH, Khan ZA (2013) Z-SEP: zonal-stable election protocol for wireless sensor networks. *J Basic Appl Sci Res*
25. Liu M, Cao J, Chen G, Wang X (2009) An energy-aware routing protocol in wireless sensor networks. *Sensors* 9(1):445–462
26. Mehra PS, Doja MN, Alam B (2018) Stable period enhancement for zonal (SPEZ)-based clustering in heterogeneous WSN. In: Smart Innovation, Systems and Technologies. Springer, Deutschland GmbH, pp 887–896
27. Mehra PS, Doja MN, Alam B (2018) Stable period extension for heterogeneous model in wireless sensor network. In: Advances in Intelligent Systems and Computing. Springer, Singapore, pp 479–487

Web Object Ranking for Location-Based Web Object Search



**K. N. Anjan Kumar, T. Satish Kumar, R. Krishna Prasad,
and S. G. Ravi Kumar**

Abstract The Web search engines have been instrumental in providing information from all over the globe to the user. The advent of the Web search engines has resulted in obtaining the relevant information at the user's location. The central theme of all Web search engines is to provide the relevant information expected by the user. To address this issue, many sophisticated ranking functions have been developed, which rank the documents based on their relevance to the user's query. The ranking component is one of the most important components for designing Web object search engines. This component helps in contributing toward the activeness of Web object search engine w.r.t. user relevance. Designing of active result ranking functions, which also considers the geographical proximity of the queries, is extremely important to provide user relevant results.

Keywords Web search engine · Page rank · Web object · Scoring function · Ranking function

K. N. Anjan Kumar (✉) · S. G. Ravi Kumar
Department of Computer Science and Engineering, RNS Institute of Technology, Bangalore, India
e-mail: anjankn05@gmail.com

S. G. Ravi Kumar
e-mail: sgravikumar@gmail.com

T. Satish Kumar
Department of Computer Science and Engineering, BMS Institute of Technology and Management, Bangalore, India
e-mail: satish.savy@gmail.com

R. Krishna Prasad
Department of Computer Science and Engineering, Global Academy of Technology, Bangalore, India
e-mail: k.p23020@gmail.com

1 Introduction

The Web search engines [1] have been instrumental in providing information from all over the globe to the user. The central theme of all Web search engines is to provide the relevant information expected by the user. To address this issue, many sophisticated ranking functions have been developed, which rank the documents based on their relevance to the user's query.

1.1 Vector-Based Ranking Functions

Vector-based document models utilize these ranking functions. The documents are represented as vector of term weights as shown in Eq. 1. Here, d_j is the given document, the weight $w_{ij} > 0$, if the term i is found inside document d_j and t is the total number of terms that are indexed for the whole document collection.

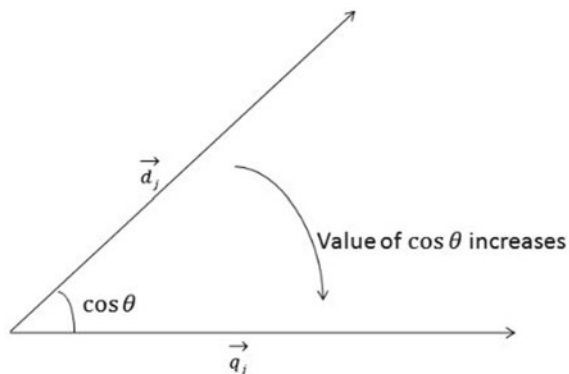
$$\vec{d}_j = [w_{1j}, w_{2j}, \dots, w_{tj}] \quad (1)$$

The user query is also modeled as a vector. The similarity between the query vector and document vector is calculated by using similarity functions such as cosine similarity as shown in Eq. 2. The cosine similarity function calculates the cosine of the angle between the vectors, \vec{d}_j and \vec{q} as shown in Fig. 1. If the document is highly relevant to the query, then cosine value decreases.

$$\cos(\vec{d}_j, \vec{q}) = \frac{\sum_{i=1}^t w_{ij} \times w_{iq}}{\sqrt{\sum_{i=1}^t w_{ij}^2} \times \sqrt{\sum_{i=1}^t w_{iq}^2}} \quad (2)$$

One of the popular mechanisms to calculate term weight is $tf - idf$ mechanism. The term frequency (tf) is the frequency of a term in the given document. The

Fig. 1 Cosine similarity function



normalized term frequency of term i inside document j is shown in Eq. 3. Here, f_{ij} is the frequency of the term inside document j , and $\max(f_{ij})$ is the maximum frequency of all the terms present inside document d_j .

$$tf_{ij} = \frac{f_{ij}}{\max(f_{ij})} \quad (3)$$

The inverse document frequency (*idf*) penalizes those terms which have more appearance in the document collection. The reason being that, such terms have low distinguishing power. Equation 4 illustrates this concept. Here, idf_i is the inverse document frequency of term i , n_i is the total number of documents which contain term i , and N is the number of documents present inside the document collection.

$$Idf_i = \log \frac{N}{n_i} \quad (4)$$

One of the major problems in $tf - idf$ ranking functions is indexed terms are assumed to be mutually independent, thus, it does not cater to the semantic relationship between query and the document. Another vector model ranking function called as the *Nutch* ranking function has been proposed [2]. Equations 5 illustrate this ranking function. Here, query Norm(d) is a score which Norm($t.field \in \vec{d}$) are the normalization factors, coord(\vec{q}, \vec{d}) is based on the number of query terms present inside \vec{d} , $t.boost(t.field \in \vec{d})$ assigns higher scores those terms which appear in certain sections of the document, and this ranking function provides facility to perform partial search on users query.

$$\begin{aligned} \text{score}(\vec{q}, \vec{d}) &= \text{queryNorm}(\vec{d}) \times \text{coord}(\vec{q}, \vec{d}) \times \sum_{t \in \vec{q}} tf(t \in \vec{d}) \\ &\times idf(t) \times t.boost(t.field \in \vec{d}) \times \text{Norm}(t.field \in \vec{d}) \end{aligned} \quad (5)$$

1.2 Boolean Model Scoring Function

The scoring function for the Boolean model addresses both **AND** semantics and **OR** semantics for the user query. The scoring function developed for the **OR** semantics is shown in Eq. 6, and the scoring function for the **AND** semantics is shown in Eq. 7. The query is assumed to have two terms t_1 and t_2 . The weights w_1 and w_2 are calculated by using Eqs. 8 and 9. Here, tf_1d and tf_2d are the frequency of the terms t_1 and t_2 inside document d . The parameters idf_1 and idf_2 are the inverse document frequency of the terms t_1 and t_2 .

$$\text{score}(q_{\text{or}}, d) = \sqrt{\frac{w_1^2 + w_2^2}{2}} \quad (6)$$

$$\text{score}(q_{\text{or}}, d) = 1 - \sqrt{\frac{(1 - w_1)^2 + (1 - w_2)^2}{2}} \quad (7)$$

$$w_1 = tf_1d \times idf_1 \quad (8)$$

$$w_2 = tf_2d \times idf_2 \quad (9)$$

1.3 Probabilistic Ranking Function

In this model [3], the degree of similarity between document and query is quantified through conditional probability as shown in Eq. 10. Here, R is an indicator random variable which takes the value 1, if the document d is relevant to the query \vec{q} , otherwise, R takes the value 0. If the probability of the event $R = 1$, is greater than the event $R = 0$, then the document \vec{d} is considered relevant to the query \vec{q} , otherwise, the document \vec{d} is considered irrelevant to the query \vec{q} .

$$P(R = 1|\vec{d}, \vec{q}) > P(R = 0|\vec{d}, \vec{q}) \quad (10)$$

The ranking function is designed by using a metric called as *odds of relevance*, which is shown in Eq. 11.

$$\text{score}(\vec{d}|\vec{q}) = \frac{P(R = 1|\vec{d}, \vec{q})}{P(R = 0|\vec{d}, \vec{q})} \quad (11)$$

By using naive Bayesian assumption, Eq. 11 can be rewritten as shown in Eq. 12.

$$\text{score}(\vec{d}|\vec{q}) = \left[\frac{P(R = 1|\vec{q})}{P(R = 0|\vec{q})} \right] \times \left[\frac{P(\vec{d}|R = 1, \vec{q})}{P(\vec{d}|R = 0, \vec{q})} \right] \quad (12)$$

By using the index term for the document repository, the Eq. 12 can be rewritten as shown in Eq. 13. Here, x_t is a term indexed in the inverted file created for the document repository. Every term are assumed to be independent of the other.

$$\text{score}(\vec{d}|\vec{q}) \approx \prod_{t=1}^M \frac{P(x_t|R = 1, \vec{q})}{P(x_t|R = 0, \vec{q})} \quad (13)$$

By using $p_t = P(x_t|R = 1, \vec{q})$ and $u_t = P(x_t|R = 0, \vec{q})$. The Eq. 13 can be rewritten as shown in Eq. 14. Here, $x_t = 1$, if the term t is present in the document \vec{d} . Otherwise, $x_t = 0$.

$$\text{score}(\vec{d}|\vec{q}) \approx \prod_{t:x_t=1}^M \frac{p_t}{u_t} \times \prod_{t:x_t=0}^M \frac{1-p_t}{1-u_t} \quad (14)$$

In practice, if no relevance information is available, then the approximations $p_t = 0.5$ and $u_t = \frac{n_t}{N}$ are used. Here, n_t is the number of documents inside document repository which contain term t , and N is the total number of documents present inside document repository. The *Okapi* ranking function [2] improves upon Eq. 14. Its structure is shown in Eq. 15.

$$\text{score}(\vec{d}|\vec{q}) \approx \sum_{t \in q} \log \frac{N}{n_t} \times \frac{(k_1 + 1)tf_{td}}{k_1 + tf_{td}} \quad (15)$$

The soft normalization of Okapi ranking function is shown in Eq. 16. Here, L_d is the document length, L_{ave} is the average length of all documents in the repository, and b is a tunable constant.

$$\text{score}(\vec{d}|\vec{q}) = \sum_{t \in q} \log \frac{N}{n_t} \times \frac{(k_1 + 1)tf_{td}}{k_1 \left((1 - b) + b \times \frac{L_d}{L_{ave}} \right) + tf_{td}} \quad (16)$$

1.4 Latent Dirichlet Allocation Ranking Function

The latent Dirichlet allocation (LDA) model has the following features:

1. It utilizes a probabilistic scoring function.
2. It utilizes both observed variable and unobserved variables.
3. The words in a document are considered as observed variables.
4. These words are assumed to be generated from topics, which are considered as unobserved variables.

2 Related Work

In [1], novel Web object ranking functions were proposed. Figure 3 exhibits the model utilized to design Web object ranking functions. The key features of this model are:

1. Information from different Web sources are extracted and integrated [4]. Some of the information that is extracted may not be consistent, because some of the

data sources might have poor quality information, and considerable extraction errors might occur.

2. The two stages in extraction process are: record extraction and attribute extraction. In [5], the first stage, relevant records are extracted from different data sources, and in [6] the second stage, different portions of the record are labeled by using attribute information. In most of the cases, both these stages might not be accurate. Wrong records or partial information about the data records might be extracted, and wrong labeling of attributes might occur. By using test dataset, accuracy values can be set for extraction process. Here, α_k indicates the record detection accuracy, and γ_k indicates the attribute extraction accuracy of record k . The two stages in extraction process are: record extraction and attribute extraction. In [5], the first stage, relevant records are extracted from different data sources, and in [6] the second stage, different portions of the record are labeled by using attribute information. In most of the cases, both these stages might not be accurate. Wrong records or partial information about the data records might be extracted, and wrong labeling of attributes might occur. By using test dataset, accuracy values can be set for extraction process. Here, α_k indicates the record detection accuracy, and γ_k indicates the attribute extraction accuracy of record k .
3. There are two-level descriptions for a Web object [7]. In the first description level, a Web object is seen as a set of data records, in which the attributes are not having a separate identity. But, in the second description level, the attributes are provided with distinguishing identities [8–12]. The Web object is seen as collection of data records and attributes [13, 14].
4. Every attribute will have certain importance in calculating the relevance of the Web object w.r.t user's query. The value β_j indicates this importance of attribute j . The mechanism of assigning different weights for different parameters is quite common in IR literature.

The scoring functions [4, 15, 16] are based on language models which estimate the relevance between a query and a document. The ranking functions are based on conditional probability as shown in Eq. 17. Here, Q is the query, and D is the document.

$$P(D|Q) \propto P(Q|D) \times P(D) \quad (17)$$

By using term independent assumption, Eq. 17 can be rewritten as Eq. 18. Here, w_i is the i th query term of the query Q , $|Q|$ is the length of the query, and $P(w_i|D)$ is the probability of w_i being generated from document D .

$$P(Q|D) = \prod_{i=1}^{|Q|} P(w_i|D) \quad (18)$$

Maximum likelihood estimation technique is commonly utilized to calculate the conditional probability $P(w|D)$. The language models utilize smoothing techniques to overcome data sparseness problem. The term probabilities are adjusted through

this smoothing technique. The Dirichlet prior smoothing technique is extensively used in the IR world. By using this Dirichlet smoothing technique, the conditional probability $P(w|D)$ is generated through Eq. 19. Here, $|D|$ is the document length, $tf(w, D)$ indicates the term frequency of w inside document D , $|C|$ is the total number of terms present in the document collection, and $tf(w, C)$ is the term frequency of w inside the document collection. The value of parameter λ is shown in Eq. 20.

$$P(w|D) = \lambda \times \frac{tf(w, D)}{|D|} + (1 - \lambda) \times \frac{tf(w, C)}{|C|} \quad (19)$$

$$\lambda = \frac{|D|}{|D| + \mu} \quad (20)$$

3 Problem Statement

Consider the Web object O , which is made up of K records indicated by— R_1, R_2, \dots, R_K , and each data record $R_k (1 \leq k \leq K)$ is made up of M attributes indicated by $O_{1k}, O_{2k}, \dots, O_{Mk}$. Let, Q be the query, which is generated to perform location-based Web object search, and Web object O is part of the result set for Q . Let, l_O , be the location label of O , and l_Q be the requested location of the query Q . Here, $l_O = l_Q$. The query Q_t is created from Q by removing the location term l_Q . The aim of the work is to design ranking functions to assign score to Web object O w.r.t. query Q , so that, a ranked list of Web object result set can be obtained.

4 Proposed Algorithmic Approach

4.1 Ranking Function for Data Records

The record level representation for Web objects is utilized to design data record ranking function. This representation is similar to unstructured data format. The attributes inside the data record are not differentiated. This representation overcomes the problem of attribute value extraction error, because it ignores the attribute existence, and only the record extraction errors will be considered. But, ignoring attribute existence can lead to poor effectiveness in the ranking function, because some of the attributes might not be relevant to the query term w .

The ranking function to rank the data records is represented in Eq. 25. Here, w represents the query term $\in Q_t$, $weight(w, R_k)$ as shown in Eq. 21, represents the weight of w w.r.t the data record R_k , the value of the parameter ntf is represented in Eq. 22, tf indicates the term frequency of w in R_k , the term ndl is represented in Eq. 23, dl represents the length of R_k , $avgdl$ represents average length of all data

records in the object repository, s represents a tunable constant, the term Idf^s is represented in Eq. 24, N^s indicates the number of Web objects present in the object repository, df^s indicates the frequency of query term w in all the Web objects, $\alpha(R_k)$ is the data extraction accuracy of that data source, which was used to extract record R_k , $f(l_o, R_k)$ indicates the frequency of location label l_o inside R_k , $\text{weight}(w, Q)$ indicates the weight of w in Q , and this weight is equal to the frequency of w in Q .

$$\text{weight}(w, R_k) = \frac{ntf \times idf^s \times (1 + f(l_o, R_k))}{ndl} \quad (21)$$

$$ntf = 1 + \log(tf) \quad (22)$$

$$ndl = \left(\frac{s \times dl}{\text{avgdl}} \right) (1 + \log(\text{avgdl})) \quad (23)$$

$$Idf^s = 1 + \log\left(\frac{N^s}{df^s + 1} \right) \quad (24)$$

$$\text{score}(Q, R_k) = \alpha(R_k) \sum_{w \in Q_i} \text{weight}(w, Q) \times \text{weight}(w, R_k) \quad (25)$$

4.2 Ranking Function for Attribute Values

The attribute value representation model identifies different attributes for each data record that belongs to the specified Web object. This model can be considered as a fine-grained representation model. Identifying different attributes in the data record helps in identifying the influential attributes, which contribute to the effectiveness of the search result. But, the effectiveness of attribute value ranking function depends on the accuracy of data record segmentation process for extracting attribute values. This accuracy parameter is essential in designing the ranking function.

The Eq. 28 represents the attribute value ranking function. Here, $\gamma(O_{jk})$ indicates the attribute value extraction accuracy for attribute value O_{jk} w.r.t the data source from which the record R_k and O_{jk} are extracted, the term $\cos(w, O_{jk})$ is represented in Eq. 26, the term $f(l_o, O_{jk})$ indicates the frequency of label l_o in O_{jk} , the term $\text{weight}(s)$ is represented in Eq. 27, f_w indicates the frequency of the query term w in O_{jk} , N^a indicates the number of Web objects which contain the same attribute label of O_{jk} , and f_s is the frequency of term s in all the Web objects in the repository.

$$\cos(w, O_{jk}) = \frac{\text{weight}(w) \times (1 + f(l_o, O_{jk})) \times f_w}{\sqrt{\sum \text{weight}(s)^2}} \quad (26)$$

$$\text{weight}(s) = 1 + \log\left(\frac{N^a}{f_s}\right) \quad (27)$$

$$\text{score}(Q, O_{jk}) = \left(\frac{\alpha_k + \gamma(O_{jk})}{2}\right) \sum_w \cos(w, O_{jk}) \quad (28)$$

The final ranking function for assigning score to the Web object O is designed by combining both scoring functions for attribute value and record model representations. This mechanism aids in obtaining the merits of both representation models. This ranking function is represented in Eq. 29. Here, $\beta(O_{jk})$ indicates the importance of attribute value O_{jk} for the Web object O .

$$\text{score}(Q, O) = \sum_{k=1}^k \sum_{j=1}^M (\text{score}(Q, R_k) + \beta(O_{jk})\text{score}(Q, O_{jk})) \quad (29)$$

5 Results and Discussion

The empirical analysis is performed separately on three Web object repositories—Wikipedia, DBLP and IMDB. A prototype and customized Web object search engine which utilizes the three created Web object repositories are subjected to empirical evaluation; wherein, two versions of the Web object search engine is created. The first version utilizes the proposed ranking component, and the second version is devoid of any ranking components.

The empirical results w.r.t. Wikipedia and DBLP repository is illustrated in Figs. 2, 3, 4, 5, 6, 7 and 8; correspondingly the values are tabulated in Tables 1, 2, 3, 4, 5, 6, 7 and 8. The two different experiments, totally execute 10 location-based Web object queries, and these queries are identified through numbers. The reciprocal rank obtained by new-rank and no-rank are analyzed. The queries were divided into two groups of 10 queries each. The queries of the first group had result set size which was

Fig. 2 Reciprocal rank (|result set| < 10) (Wiki)

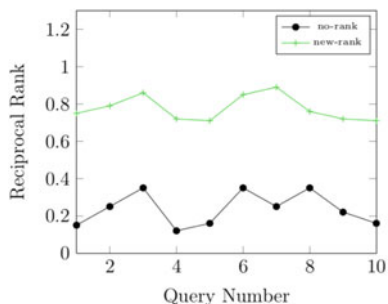


Fig. 3 Reciprocal rank
(result setl < 30)

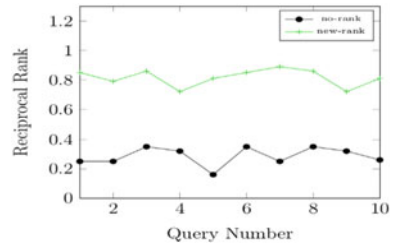


Fig. 4 Execution time
(result setl < 10) (Wiki)

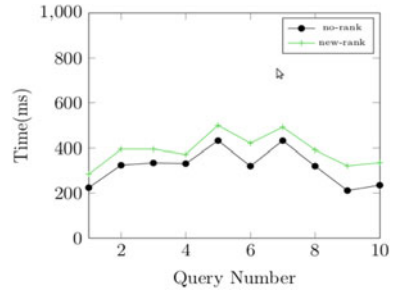


Fig. 5 Execution time
(result setl < 30)

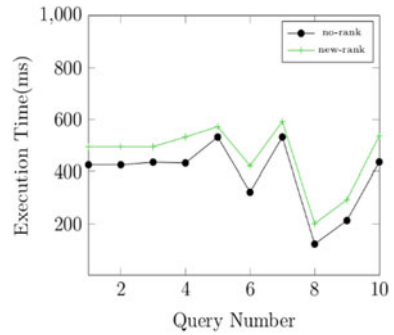


Fig. 6 Reciprocal rank
(result setl < 10) (DBLP)

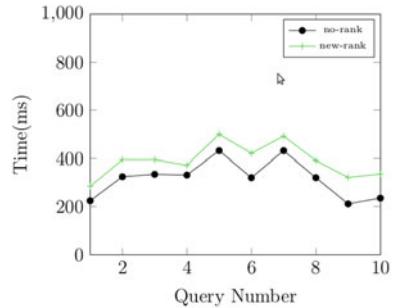


Fig. 7 Reciprocal rank
(result setl < 30)

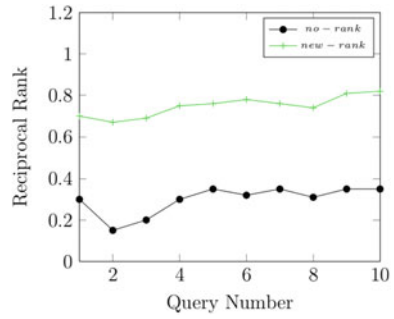


Fig. 8 Execution time
(result setl < 10) (DBLP)

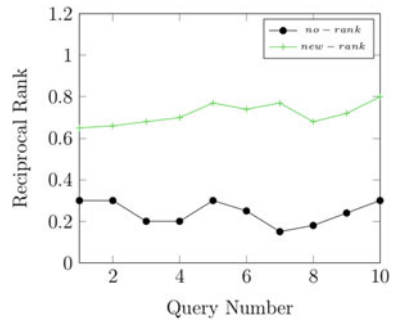


Table 1 Reciprocal rank
(result setl < 10) (Wiki)

Query number	Reciprocal rank (new-rank)	Reciprocal rank (no-rank)
1	0.75	0.1
2	0.78	0.2
3	0.8	0.3
4	0.75	0.1
5	0.73	0.2
6	0.8	0.25
7	0.85	0.25
8	0.77	0.3
9	0.75	0.2
10	0.74	0.2

within 10 Web objects. Similarly, the second group queries had result set size which was within 30. New-rank utilizes ranking component, and it consumes extra time compared to no-rank. But, this extra execution cost is just within 20% of the no-rank execution cost. This efficiency of new-rank is largely due to the design mechanism implemented for computing the ranking function.

Table 2 Reciprocal rank
(lresult setl < 30) (Wiki)

Query number	Reciprocal rank (new-rank)	Reciprocal rank (no-rank)
1	0.8	0.25
2	0.75	0.25
3	0.8	0.25
4	0.7	0.23
5	0.75	0.15
6	0.8	0.3
7	0.83	0.25
8	0.81	0.3
9	0.75	0.3
10	0.78	0.25

Table 3 Execution time
(lresult setl < 10) (Wiki)

Query number	Execution time (ms) (new-rank)	Execution time (ms) (no-rank)
1	270	220
2	390	300
3	370	320
4	350	330
5	500	400
6	420	320
7	420	380
8	370	300
9	310	220
10	330	240

Table 4 Execution time
(lresult setl < 30) (Wiki)

Query number	Execution time (ms) (new-rank)	Execution time (ms) (no-rank)
1	470	410
2	475	405
3	479	415
4	530	410
5	550	520
6	420	350
7	520	480
8	200	150
9	250	200
10	500	420

Table 5 Reciprocal rank (result set < 10) (DBLP)

Query number	Reciprocal rank (new-rank)	Reciprocal rank (no-rank)
1	0.71	0.2
2	0.67	0.15
3	0.81	0.34
4	0.80	0.3
5	0.69	0.2
6	0.75	0.3
7	0.70	0.25
8	0.78	0.23
9	0.76	0.2
10	0.72	0.15

Table 6 Reciprocal rank (result set < 30) (DBLP)

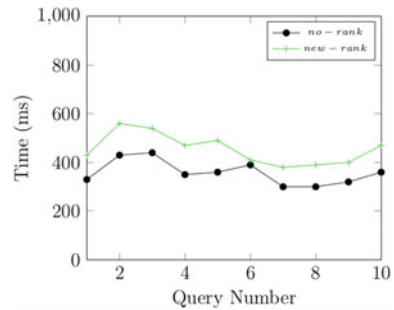
Query number	Reciprocal rank (new-rank)	Reciprocal rank (no-rank)
1	0.7	0.3
2	0.67	0.15
3	0.69	0.2
4	0.75	0.3
5	0.76	0.35
6	0.78	0.32
7	0.76	0.35
8	0.74	0.31
9	0.81	0.35
10	0.82	0.35

Table 7 Execution time (result set < 10) (DBLP)

Query number	Reciprocal rank (new-rank)	Reciprocal rank (no-rank)
1	350	240
2	340	260
3	390	300
4	450	300
5	430	340
6	330	310
7	350	320
8	470	290
9	360	270
10	390	280

Table 8 Execution time (result set < 30) (DBLP)

Query number	Execution time (ms) (new-rank)	Execution time (ms) (no-rank)
1	430	330
2	560	430
3	540	440
4	470	350
5	490	360
6	410	390
7	380	300
8	390	300
9	400	320
10	470	360

Fig. 9 Execution time (result set < 30)

6 Conclusion

IR ranking functions was presented, existing ranking functions presented in the literature for Web object ranking were described, for the first time—ranking functions to rank the result set of location-based Web object query was presented, empirical results for the proposed ranking framework were demonstrated on real-world datasets, and empirical results establish the necessity of the proposed ranking framework—by providing appreciable user relevant results.

References

1. Carpineto C, Romano G, Giannini V (2002) Improving retrieval feedback with multiple term-ranking function combination. *ACM Trans Inf Syst (TOIS)* 20(3):259–290
2. Callan P (2000) Distributed Information retrieval. In: Bruce Croft W (ed) *Advances in information retrieval. Recent research from the center for intelligent information retrieval*. Kluwer Academic Publisher, pp 127–150

3. Anjan Kumar KN, Chitra S, Satish Kumar T (2019) Probabilistic classification techniques to perform geographical labeling of web objects. *Cluster Comput* 22(1):277–285
4. He B, Ounis I (2009) Finding good feedback documents. In: *Proceedings of the 18th ACM conference on information and knowledge management*. ACM
5. Natsev AP et al (2007) Semantic concept-based query expansion and re-ranking for multimedia retrieval. In: *Proceedings of the 15th ACM international conference on Multimedia*. ACM
6. Davis CA, Fonseca FT (2007) Assessing the certainty of locations produced by an address geocoding system. *Geoinformatica* 11(1):103–129
7. Dalton J, Blanco R, Mika P (2011) Coreference aware web object retrieval. In: *Proceedings of the 20th ACM international conference on Information and knowledge management*. ACM
8. Chen L et al (2006) Ranking web objects from multiple communities. In: *Proceedings of the 15th ACM international conference on information and knowledge management*. ACM
9. Efthimiadis EN (1993) A user-centred evaluation of ranking algorithms for interactive query expansion. In: *Proceedings of the 16th annual international ACM SIGIR conference on research and development in information retrieval*. ACM
10. Buyukokkten O et al (1999) Exploiting geographical location information of web pages
11. Sengar V et al (2007) Robust location search from text queries. In: *Proceedings of the 15th annual ACM international symposium on advances in geographic information systems*. ACM
12. Wu D, Cong G, Jensen CS (2012) A framework for efficient spatial web object retrieval. *VLDB J* 21(6):797–822
13. Cao G et al (2007) Extending query translation to cross-language query expansion with markov chain models. In: *Proceedings of the sixteenth ACM conference on conference on information and knowledge management*. ACM
14. Broder A et al (2009) Online expansion of rare queries for sponsored search. In: *Proceedings of the 18th international conference on World wide web*. ACM
15. Fetahu B, Gadiraju U, Dietze S (2015) Improving entity retrieval on structured data. In: *International semantic web conference*. Springer, Cham
16. Wu D, Cong G, Jensen CS (2012) A framework for efficient spatial web object retrieval. *VLDB J* 21(6):797–822

OCHEP: An Optimized Cluster Head Election Protocol for Heterogeneous WSNs



Samayveer Singh, Piyush Yadav, Aruna Malik, and Rajeev Agrawal

Abstract In wireless sensor networks (WSNs), the nodes have the constraint of energy. The sensor nodes have consumed energy in sensing, transmission, receiving, etc. If the energy of a sensor node exhausted completely, then there is no use of sensor nodes because nodes are not replaceable. Thus, there is a dire need to increase the lifespan of the networks so that sensors can work for a longer time in the networks. In this paper, we recommend an enhanced cluster head determination routing protocol for heterogeneous WSNs. The heterogeneous WSNs are consist of three levels of heterogeneity which helps in extending the network lifetime. In the enhancement of the proposed method, a threshold-based formula is deliberated for choosing the cluster head nodes (CH). This threshold formula considered three criteria namely node distance from the sink, outstanding energy of sensors, and total energy of the networks which decreases energy consumption. This proposed scheme can provide efficient and effective communication outside the cluster and within the cluster by considering communication cost matrices. The number of alive and dead, the sum of energy consumption, and the number of messages transferred to the control node matrices are considered to examine the enactment of the proposed scheme by using the MATLAB. After a comprehensive analysis, it has been evident that the projected scheme accomplishes superior to that of the existing methods.

S. Singh (✉) · A. Malik

Department of Computer Science and Engineering, Dr B R Ambedkar National Institute of Technology, Jalandhar, Punjab, India
e-mail: samayveersingh@gmail.com

A. Malik

e-mail: arunacrke@gmail.com

P. Yadav · R. Agrawal

Department of Electronics and Communication Engineering, G L Bajaj Institute of Technology and Management, Greater Noida, U.P., India
e-mail: piyushyadav1985@gmail.com

R. Agrawal

e-mail: rajkecd@gmail.com

© Springer Nature Singapore Pte Ltd. 2021

R. Agrawal et al. (eds.), *Advances in Smart Communication and Imaging Systems*,
Lecture Notes in Electrical Engineering 721,
https://doi.org/10.1007/978-981-15-9938-5_17

Keywords Network lifespan · Heterogeneous WSNs · Optimum clustering · Network energy efficiency

1 Introduction

Nowadays, communications are the most important part of today's digital world for sharing data or information among the communicating parties. It is not concerned as the actual creating of the information as well as the resulting task performed on the information at the time receiving data. Generally, the human gets instant information through some processing devices which can collect information and process it and then send that information to the other processing devices. In that way, humans can get information in a comprehensible manner and take instant decisions, accordingly. Nowadays, wireless sensor networks (WSNs) are one of the furthestmost prevalent systems with their advances in electronic technology [1]. One of the most important challenging fields in networking is WSNs. It is designed for the remote and harsh areas in our surroundings. The WSN can be expressed as an autonomous network of distinct devices that can communicate the actual information collected from a targeted area through wireless links. A WSN is a structure of dedicated transducers or sensor nodes with a well-controlled communication infrastructure for monitoring and collecting parameters from diverse locations where the sensors have been deployed. Normally, monitored parameters are environment temperature, level of humidity, sound intensity, pressure, illumination intensity, wind flow speed and direction, power-line drop in voltage, vibration intensity, pollutant levels, patient body functions, etc. [2]. A WSN composed of multiple detection stations can be interpreted as sensor nodes, each of sensor nodes is lightweight, small in size, and portable. Every sensor node is consisting of transducer, active or passive power source, transceiver, and microcomputer. The transducer senses the variations in a physical quantity from surroundings where they positioned and translate into electrical signs. The power source for each node can be regular supply or battery-based. The important function of the transceiver is to receive the commands from a base station or central computer and transmit the data to that location. The duty of the microcomputer just processes and stores the sensor output for analyzing. Generally, there are lot of applications, where we can deploy WSNs such as water quality monitoring, building health structure monitoring, surveillance of various types of buildings, gas leakage in the various gas and chemical plants, productivity, humidity, water requirement, fertilizer monitoring in the agriculture monitoring, health monitoring in medical application, wild animal monitoring the parks, fire detection in the multistory building, green park watering system, and so on [3].

There are two broad categories of the WSNs such as homogeneous and heterogeneous. In the first one, all the deployed nodes have the same power capabilities, whereas nodes have different capabilities in case of heterogeneous networks as energy, link capacity, memory, processing power, etc. Thus, based on the above discussion, we can categorize the heterogeneity into multiple categories namely

energy, link, and computational heterogeneity. In case of energy heterogeneity, heterogeneous networks consist of multiple types of batteries means they have different-different Volts or Jules batteries. Link heterogeneity means sensor nodes have different capabilities of link for transferring data over the deployed networks like some of the networks have 10 Mbps and some of the links 50 Mbps bandwidth for transferring information. In the computational heterogeneity, sensor nodes have multiple types of microprocessor, memories, etc. Based on the above discussion, we can conclude that the nodes in the sensor networks have many restrictions like energy limitation, cost of the nodes, speed, processing power, etc. Thus, there is a dire need to develop energy effective and efficient algorithm which can overcome the above-discussed problems of the networks for various applications. Perhaps, clustering plays a very effective role for improving the performance of the wireless sensor networks by effective utilization of the heterogeneous resources like energy limitation, cost of the nodes, speed, processing power, etc. In this paper, we proposed an optimized cluster head election protocol for heterogeneous WSNs. A threshold-based formula is considered for effective selection of the proposed method. This threshold-based formula considered three criteria namely distance between the nodes and the sink, nodes remaining energy, and the sum of the energy of the networks. These three parameters help in diminishing the energy depletion within the clusters and outside the clusters also. The number of alive and dead is showing the sustainability and the lifetime of the proposed method in terms of first, half, and last node dead, the sum of energy consumption as the remaining energy, and the number of messages transferred to the control node as showing the throughput of the proposed method matrices are considered to investigate the enactment of the projected scheme.

The association of the paper is defined as follows: in the 2nd section the literature review of the existing clustering-based is discussed and the 3rd section discusses the various assumption for deploying networks, radio, and energy models. The 4th section discusses the proposed method including the threshold-based formula which helps in increasing the sustainability of the proposed method. The 5th section discusses the results of the simulation of the proposed and the existing methods and paper is concluded in the 6th section.

2 Literature Review

The wireless sensor networks (WSNs) are consumed more energy in the transmission and reception of information instead of sensing, computing, ideal, and others states. There are many other limitations of the WSNs such as low size, low battery power, no recharging facility, and non-replaceability of the nodes. Thus, there is a terrible need to develop energy effective and efficient algorithm which can overcome the above-discussed problems of the networks for various applications. In the literature, there are various clustering-based algorithms which try to balance the load among the clusters. The first clustering protocols are low energy adaptive clustering hierarchy (LEACH) protocol which tries to equilibrium the consignment among the clusters [3].

The working of LEACH divided into two phases namely setup and steady phase. In the setup phase, nodes are deployed and possible cluster heads are selected for further processing, whereas the data collection is considered in the steady phase. LEACH is further improved in the form of power-efficient gathering in sensor information systems (PEGASIS) protocol [4]. It designed chains in the networks for collecting the data and data collection always started from the farthest nodes to the near node from the base station and it created multiple chains in this process. The main disadvantage of this method is that these are fit only small networks not for large networks. These protocols are defined for the homogeneous networks but after a time some of the heterogeneous protocols are discussed.

The first heterogeneous protocol is stable election protocol (SEP) which is discussed for the two-level and multilevel heterogeneity. The hetSEP [5] is the extension of the SEP protocol by integrating the 2 and 3 levels of heterogeneity. It uses the probability formula for nominating the cluster heads. It increases the network overheads if the packet transmission is too long. After that, distributed energy-efficient clustering (DEEC) protocol is discussed by considering the 2 and 3 levels of heterogeneity [6]. It also uses a probability formula for electing the cluster heads by considering the residual and average energy. In DEEC, the energy of the networks is not used efficiently. In paper [7], the selection of the clusters is based on the outstanding energy of the nodes and the networks. It only considered the three-level of heterogeneity of the nodes in the deployed networks. These methods require the extra energy in the process of reclustering at the time of next rounds. To improving the further performance of the methods, Maheshwari et al. discussed a two-level of grouping for collecting the data by considering the node degree [8]. It method increases the load of the sink and somehow creates the problem of the hotspot in the deployed networks. The methods discussed in papers [9–11] are considered heterogeneity of the multiple levels. These papers are not considered the data aggregation process and chaining approach for efficient collection of data. In paper [12], a fuzzy-based clustering approach is discussed for prolonging the lifetime of networks. It considered the many parameters for the distance between the nodes and sink, residual energy of the clusters for cluster heads election. However, it agonizes the load balancing during the collection of the data. It is also not considered the data combination procedure.

In paper [13], the authors discuss the hybrid routing technique based on the zone of the deployed fields. The clustering process is adopted by it is similar as defined in the LEACH protocol. This approach is not involving normal nodes in the clustering process. This method is further extended by the [14] by considering hybrid clustering concept and multi-hop data collection process. It does not use all the methods in the clustering process but only a few nodes have been used in the clustering process. This method grieves the consignment balancing the difficulty of the system. The paper [15] is also discussed for the heterogeneous protocols for prolonging the network lifetime. It considers the probability function for cluster heads election. It defines the two and multilevel heterogeneity in the deployed networks. The paper [16] discusses a routing-based technique which collects data on the bases of the chains. There are two phases of the process. In the first phases, nodes direct their data to the cluster heads, whereas, in the second phase, clusters heads send their data to the sinks as

they received data from the respective clusters by performing data aggregation. Wang et al. discuss a cluster routing protocol which elects the cluster head efficiently [17]. It also improved the node processing and inter-cluster routing problem. This method partially suffers from an effective cluster and data aggregation. Chen et al. discuss a chain-based hierarchical routing protocol in WSNs [18]. It divided monitoring areas into slighter fields to create restraints. It reduces excessive routes and also recovers energy. This method created many small chains in the networks. Linping et al. discuss an improved algorithm of PEGASIS protocol which is based on double cluster heads in WSN [19]. It usages low-level clusters header for upgraded load balancing. This protocol useful for large networks and executes better than the PEGASIS algorithm. The preliminary installations of this method create high overhead. Nadeem et al. discuss a gateway-based energy-efficient routing method for WSNs called M-GEAR by dividing the area into four different logical regions [20]. Saranraj et al. discussed the energy-efficient cluster head selection method for called OEECHS. The election of cluster heads (CHs) is based on consumed battery and distance [21]. This method undergoes from the load balancing difficult between the nodes. Piyush et al. discuss the importance of protocols in healthcare applications in [22]. In the subsequent section, we considered the network conventions, the proposed energy model and energy overindulgence model which will assist in competent clustering.

3 Network Model, Energy Model, and Radio Dissipation Model

In this division, the fundamental assumptions of the proposed system model are given as all the sensors have an ID and fixed location because the nodes are immobile. The sensors can be heterogeneous and its preliminary energies depend upon the level of heterogeneity. Sensors have symmetric in terms of resource capabilities like connections, capacities, computational, and memory powers. The sink is positioned in the inside of the defined territory. Here, we deliberate a three-tier heterogeneity model consists of N nodes. The energies of level-1, -2, and -3 nodes are denoted as e_1 , e_2 , and e_3 , respectively, by seeing the ailment $e_1 < e_2 < e_3$ and their numbers are denoted as N_1 , N_2 , N_3 , respectively, by considering the condition $N_1 > N_2 > N_3$. The system energy is given as follows:

$$e_{\text{Total}} = \zeta \times N \times e_1 + \zeta^2 \times N \times e_2 + (1 - \zeta - \zeta^2) \times N \times e_3 \quad (1)$$

e_{Total} can define level-1, -2, and -3 heterogeneity using the value of ζ which is a parameter of the model. The level-1 nodes are minimum in number, i.e., $\zeta \times N$ and having a minimum amount of energy denoted as e_1 where the range of model parameter ζ is $0 \leq \zeta \leq 1$. The level-2 nodes are less in number from level-1 nodes, i.e., $\zeta^2 \times N$ and having more energy from level-1 nodes designated as e_2 . The level-3 nodes are less in number from level-1 and level-2 nodes, i.e., $(N - (\zeta \times N + \zeta^2 \times N))$ and having

more energy from level-1 and level-2 nodes designated as e_3 that means they have a maximum amount of energy.

Level-1 heterogeneity: For $\zeta = 0$, Eq. (1) defines the network has consisted only of one type of nodes. Thus, the entire system energy is given below

$$e_{\text{Total}} = N * e_3 \quad (2)$$

where e_3 is the preliminary energy of the nodes. It is indicating the level-3 nodes instead of level-1 nodes. We impose a condition for converting the energy of level-3 nodes into level-1 nodes. It can be attained by using the given representation:

$$\zeta = \frac{e_3 - e_1}{\beta * f(e_2, e_3)} \quad (3)$$

where f and β are the functions of e_2 and e_3 , and positive integer where $\beta > 1$. The function f can have either $(e_3 + e_2)$ or $(e_3 - e_2)$.

Level-2 heterogeneity: For $1 - \zeta - \zeta^2 = 0$, find the value of ζ which defines two different types of sensors namely level-1 and -2 nodes. The relation $1 - \zeta - \zeta^2 = 0$ is not selected arbitrarily which is diminished by the third term of the Eq. (1). The relation $1 - \zeta - \zeta^2 = 0$ gives two solutions, i.e., $(\sqrt{5} - 1)/2$ and $(\sqrt{5} + 1)/2 > 1$.

where $(\sqrt{5} + 1)/2 > 1$ is not true by the bound value of the $0 \leq \zeta \leq 1$. Thus, the valid $(\sqrt{5} - 1)/2$ is the correct solution. This solution defines two types of sensor nodes with their preliminary energies e_1 and e_2 .

Level-3 heterogeneity: We have considered the upper and lower bound value of ζ is $0 \leq \zeta \leq 1$, but in level-2 heterogeneity, we have fixed the range value of the upper bound is $(\sqrt{5} - 1)/2$ denoted by ζ_{ub} . Consider the lower bound of ζ be ζ_{lb} , i.e., which needs to be determined. The range of ζ is $\zeta_{\text{lb}} < \zeta < \zeta_{\text{ub}}$ for three-level heterogeneity and consider function value f as $(e_3 - e_2)$ and ζ from Eq. (3). Thus, the lower bound as

$$\zeta_{\text{lb}} < \zeta < \zeta_{\text{ub}}$$

Put the values of ζ and ζ_{ub} in the above equation and calculate the value of the ζ_{lb} as follows:

$$\zeta_L < \frac{e_3 - e_1}{\beta * (e_3 - e_2)} < ((\sqrt{5}) - 1)/2 \quad (4)$$

Let $e_2 = \alpha_1 + e_1$ and $e_3 = \alpha_2 + e_2$ and using Eq. (4), we get the following relation.

$$\begin{aligned} \zeta_{lb} &< \frac{\alpha_2 + \alpha_1}{\beta * \alpha_2} \\ \frac{\alpha_2}{\alpha_1} &< \frac{1}{\beta * \zeta_{lb} - 1} \\ -\frac{\alpha_2}{\alpha_1} &\geq \frac{1}{1 - \beta * \zeta_{lb}} \end{aligned} \tag{5}$$

Subsequently, L.H.S. of Eq. (5) is negative, thus, just put $-\frac{\alpha_2}{\alpha_1} = 0$. We have the following relation:

$$\begin{aligned} 1 - \beta * \zeta_{lb} &< 0 \\ \frac{1}{\beta} &< \zeta_{lb} \end{aligned} \tag{6}$$

Equation (4) can be as

$$(e_3 - e_1) \leq \frac{\beta * (\sqrt{5}) - 1}{2} * (e_3 - e_2) \tag{7}$$

This inequality may be written as

$$\beta * (\sqrt{5}) - 1 * e_2 - 2 * e_1 \leq (\beta * (\sqrt{5}) - 1) - 2 * e_3 \tag{8}$$

The level-1, -2, and -3 nodes energy are given as e_1 , $e_2 = e_1 * (1 + \omega)$, and $e_3 = e_1 * (1 + \eta)$, respectively. And the value of coefficients ω , and η are 0.06 and 0.11, respectively. Thus, the above-mentioned procedure defines the three-level heterogeneity model in WSNs.

Now, we deliberate a debauchery energy radio model to compute the energy consumption in the conveying and reception by the nodes during sensing, transmission, and computational procedure. The energy collapse for conveying the L -bit message over the distance d is quantified as follows [3]:

$$E_{TXS} = L * \epsilon_{elec} + L * \epsilon_{fs} * d^2 \text{ if } d \leq d_0 \tag{9}$$

$$E_{TXL} = L * \epsilon_{elec} + L * \epsilon_{mp} * d^4 \text{ if } d > d_0 \tag{10}$$

where ϵ_{elec} , ϵ_{fs} and ϵ_{mp} are the vitality/energy decadent and d_0 is threshold distance is given below:

$$d_0 = \sqrt{\frac{\epsilon_{fs}}{\epsilon_{mp}}} \tag{11}$$

The energies expended in receiving (E_{Rx}) and in sensing (E_{Sx}) are specified in (12) and (13) as follows:

$$E_{Rx} = L * \epsilon_{elec} \quad (12)$$

$$E_{Sx} = L * \epsilon_{elec} \quad (13)$$

In the next fragment, we deliberate the procedure for optimizing the electing the CHs which helps in load balancing.

4 Optimized Cluster Head Election Routing Protocol

In this paper, we have optimized the suggested method using a clustering algorithmic procedure for three-level heterogeneity. This methodology elects suitable CHs based on the three measures namely the distance of the node from the BS, the nodes remaining energy, and total network energy. The selection of the cluster heads method is used as a dynamic clustering procedure. The aim of this method is to elect cluster heads that consume less energy in inter and intracluster communication. The complete process of the proposed method is divided into rounds and CHs are designated for each round. Initially, a defined percentage is used to electing the cluster heads and then a number of CHs are added conferring to the coverage of the number of deployed sensor nodes. It employs a condition of the vicinity of cluster heads. A cluster head may not possible in the vicinity of other selected cluster heads in this scenario. The choice of selecting the cluster heads depends on the threshold value of the level of the heterogeneity. The value of the threshold is associated with an arbitrary number which is created between 0 and $e_{average-nch}/e_{i-init}$. If the value of the threshold is greater than the created number between 0 and $e_{average-nch}/e_{i-init}$, then the sensor node of a particular level of heterogeneity converts the current node into the cluster head for the contemporary round. The proposed method threshold formula is given as follows:

$$e_i = \frac{e_{i-curr}}{e_{i-init}} \quad (14)$$

$$e_t = \left(\frac{e_{i-res}}{e_{i-max}} + r \operatorname{div} \frac{1}{p_i} \right) \times (1 - e_{i-res}) \quad (15)$$

$$T(n) = \begin{cases} \frac{p_i}{N-p_i \left[r \operatorname{mod} \left(\frac{N}{p_i} \right) \right]} \times e_i \times e_i \times \text{if } n \in G & \\ 0 & \text{otherwise} \end{cases} \quad (16)$$

where $e_{i\text{-curr}}$, $e_{i\text{-init}}$, $e_{i\text{-max}}$ and $e_{i\text{-res}}$ are the current vitality of the networks, preliminary vitality of the nodes, node maximum preliminary energy, and residual energy. The N and r are the numbers of sensor nodes and rounds. The e_i and e_t are the constant values which are defined in Eqs. (14) and (15). In the proposed method, a dynamic range is considered for the comparison with the threshold value for choosing the final cluster heads which are given as follows in Eq. (2).

$$\left[0, e_{\text{average-nch}}/e_{i\text{-init}}\right] \quad (17)$$

where $e_{\text{average-nch}}$ and $e_{i\text{-init}}$ are the node's average energy which is not CHs in the current round and preliminary energy of the nodes, respectively.

The whole energy of the defined network which is consist of three types of nodes, i.e., level-1, -2, and -3 are represented by e_T is given as below:

$$\zeta \times N \times e_1 + \zeta^2 \times N \times e_2 + (1 - \zeta - \zeta^2) \times N \times e_3 \quad (18)$$

$$N \times (\zeta \times e_1 + \zeta^2 \times e_2 + (1 - \zeta - \zeta^2) \times e_3) \quad (19)$$

$$e_1 \times N \times (\zeta + \zeta^2 \times e_2/e_1 + (1 - \zeta - \zeta^2) \times e_3/e_1) \quad (20)$$

Now, we will discuss the clustering process of the proposed method which contains three types of nodes. The e_1 is the preliminary energy of the level-1 nodes. If all the nodes having preliminary energy e_1 , then the total energy of the networks is $e_1 \times N$. Therefore, there is an increment factor of the energy according to Eq. (20) as $(\zeta + \zeta^2 \times e_2/e_1 + (1 - \zeta - \zeta^2) \times e_3/e_1)$. Means, heterogeneous nodes have $(\zeta + \zeta^2 \times e_2/e_1 + (1 - \zeta - \zeta^2) \times e_3/e_1)$ times more energy than the homogeneous nodes.

Generally, every sensor node become CH in case of homogeneous networks after $1/p_i$ rounds. Thus, the average cluster heads for homogeneous networks in a particular round will be $N \times 1/p_i$. But in the case of heterogeneous networks, every sensor node becomes CH after $1/p_i \times (\zeta + \zeta^2 \times e_2/e_1 + (1 - \zeta - \zeta^2) \times e_3/e_1)$ rounds. Thus, the average cluster heads for heterogeneous networks in a particular round will be $N \times 1/p_i \times (\zeta + \zeta^2 \times e_2/e_1 + (1 - \zeta - \zeta^2) \times e_3/e_1)$. The threshold values of level-1, -2 and -3 are fixed according to the preliminary energies of the respective levels. Thus, each sensor of level-1 become a CH once in every $1/p_{\text{opt}}$ rounds and level-2 and -3 sensor nodes turn into a CH $(1 + \alpha)$ and $(1 + \beta)$ times more than that of the level-1 sensors in every $(\zeta + \zeta^2 \times e_2/e_1 + (1 - \zeta - \zeta^2) \times e_3/e_1)/p_i$ rounds, respectively. Thus, the heterogeneity is despoiled the set constraints which is $N \times 1/p_i$. The $E_0/(\zeta \times e_1 + \zeta^2 \times e_2 + (1 - \zeta - \zeta^2) \times e_3)$ is the weight of a node in the defined networks. In the proposed method, the weighted probabilities of the level-1, -2, and -3 nodes which are denoted by $p_{\text{level-1}}$, $p_{\text{level-2}}$, and $p_{\text{level-3}}$, respectively, and defined as follows:

$$p_{\text{level-1}} = \frac{p_i \times E_1}{(\zeta \times e_1 + \zeta^2 \times e_2 + (1 - \zeta - \zeta^2) \times e_3)} \quad (21)$$

It can be as follows:

$$p_{\text{level-1}} = \frac{p_i}{(\zeta + \zeta^2 \times e_2/e_1 + (1 - \zeta - \zeta^2) \times e_3/e_1)} \quad (22)$$

$$p_{\text{level-2}} = \frac{p_i \times E_1}{(\zeta \times e_1 + \zeta^2 \times e_2 + (1 - \zeta - \zeta^2) \times e_3)} \quad (23)$$

It can be as follows:

$$p_{\text{level-2}} = \frac{p_i}{(\zeta + \zeta^2 \times e_2/e_1 + (1 - \zeta - \zeta^2) \times e_3/e_1)} \quad (24)$$

$$p_{\text{level-3}} = \frac{p_i \times E_1}{(\zeta \times e_1 + \zeta^2 \times e_2 + (1 - \zeta - \zeta^2) \times e_3)} \quad (25)$$

It can be as follows:

$$p_{\text{level-3}} = \frac{p_i}{(\zeta + \zeta^2 \times e_2/e_1 + (1 - \zeta - \zeta^2) \times e_3/e_1)} \quad (26)$$

The $p_{\text{level-1}}$, $p_{\text{level-2}}$, and $p_{\text{level-3}}$ are the optimum weighted probabilities for the level-1, -2, and -3 nodes. Thus, the threshold value of the level-1 is given as follows:

$$T(n_{\text{level-1}}) = \begin{cases} \frac{p_{\text{level-1}}}{N - p_{\text{level-1}}} \left[r \bmod \left(\frac{N}{p_{\text{level-1}}} \right) \right] \times e_i \times e_t & \text{if } n_{\text{level-1}} \in G' \\ 0 & \text{otherwise} \end{cases} \quad (27)$$

$$T(n_{\text{level-2}}) = \begin{cases} \frac{p_{\text{level-2}}}{N - p_{\text{level-2}}} \left[r \bmod \left(\frac{N}{p_{\text{level-2}}} \right) \right] \times e_i \times e_t & \text{if } n_{\text{level-2}} \in G'' \\ 0 & \text{otherwise} \end{cases} \quad (28)$$

$$T(n_{\text{level-3}}) = \begin{cases} \frac{p_{\text{level-3}}}{N - p_{\text{level-3}}} \left[r \bmod \left(\frac{N}{p_{\text{level-3}}} \right) \right] \times e_i \times e_t & \text{if } n_{\text{level-3}} \in G''' \\ 0 & \text{otherwise} \end{cases} \quad (29)$$

where G' , G'' , and G''' are the conventional of level-1, -2 and -3 nodes which have not become CHs within last $\frac{1}{p_{\text{level-1}}}$, $\frac{1}{p_{\text{level-2}}}$, and $\frac{1}{p_{\text{level-3}}}$ rounds, respectively. The $T(n_{\text{level-1}})$, $T(n_{\text{level-2}})$, and $T(n_{\text{level-3}})$ are the threshold applied to type-1, -2, and -3 nodes, respectively. Thus, deployed sensor nodes converted into dynamic clusters by using their probabilities and thresholds which helps in lifespan prolonging.

5 Simulation Results and Discussion

We comprehensive deliberate the consequences of the projected method and the OEECHS [21], M-GEAR [20], and LEACH [3] existing methods in this section. The number of active and dead showing the sustainability and the lifetime of the proposed method in terms of first, half, and last node dead, the sum of energy depletion as the remaining energy, and number of message transferred to the control node as presenting the throughput of the proposed method matrices are considered to examine the concert of the projected scheme and existing schemes. The proposed network is considered 100 numbers of sensor nodes, sink at the center of the area, preliminary energy of the normal 0.5 Jules, and results are simulated using MATLAB. The proposed network is considered three levels of heterogeneity by using three types of nodes namely normal, advanced, and super as are 50, 30, and 20 in numbers, respectively, and their energies are 0.5 J, 1.0 J, and 1.75 J, respectively. The power consumption is 50 nJ/bits in running the circuit, 10 pJ/bits/m² to transmit the signal in the shorter distance, 0.0013 pJ/bits/m⁴ to transmit signal in the longer distance. The energy consumption model also considered the packet length is 4000 bits, cluster range is 25 m, and the threshold distance is 75 m. We have commonly used 25 simulations and taken an average of all the simulations for calculating the final simulation results.

Figure 1 shows the imitation of the consequences of the projected method and the OEECHS [21], M-GEAR [20], and LEACH [3] existing methods in relationships of

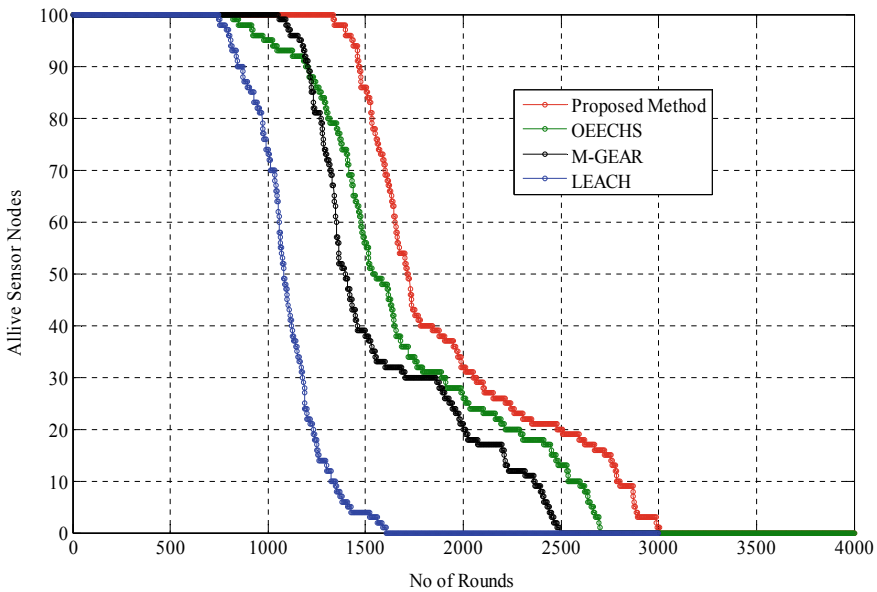


Fig. 1 Analysis of LEACH [3], M-GEAR [20], OEECHS [21], and the proposed model alive nodes

the number of alive nodes with reference of the number of rounds. The projected technique covers 3009 number of rounds before going to die every node in the deployed networks, whereas the OEECHS [21], M-GEAR [20], and LEACH [3] existing methods cover 2701, 2489, 1611, number of rounds, respectively. The network lifetime increment in M-GEAR [20], OEECHS [21], and the proposed method is 54.50%, 67.66%, and 86.77%, respectively, in comparison with the LEACH [3] protocol. Thus, it is evident from the results that the projected technique gives better results in respect to the existing techniques because the selection of CHs is efficiently due to the selected parameters. Furthermore, it decreases the communication cost in the data collection process and increases the lifetime of the networks. The proposed threshold-based formula helps in extended the lifetime by using different energy factors. The sustainability period of the M-GEAR [20], OEECHS [21], and the proposed technique is 10.51%, 42.85%, and 80.18%, respectively, which is calculated by considering the first node dead information concerning LEACH [3]. Figure 2 demonstrates the number of dead nodes vs rounds for LEACH [3], M-GEAR [20], OEECHS [21], and the proposed method. Moreover, the half node dead (HND) of the M-GEAR [20], OEECHS [21], and the proposed method outperforms by 29.17%, 42.28%, and 59.37%, as a comparison with LEACH [3], significantly, respectively.

Figure 3 shows the imitation consequences of the total energy dissipation regarding number of rounds for three-level of heterogeneity. The preliminary total energy of the three levels of heterogeneity network is 50 J. The projected method

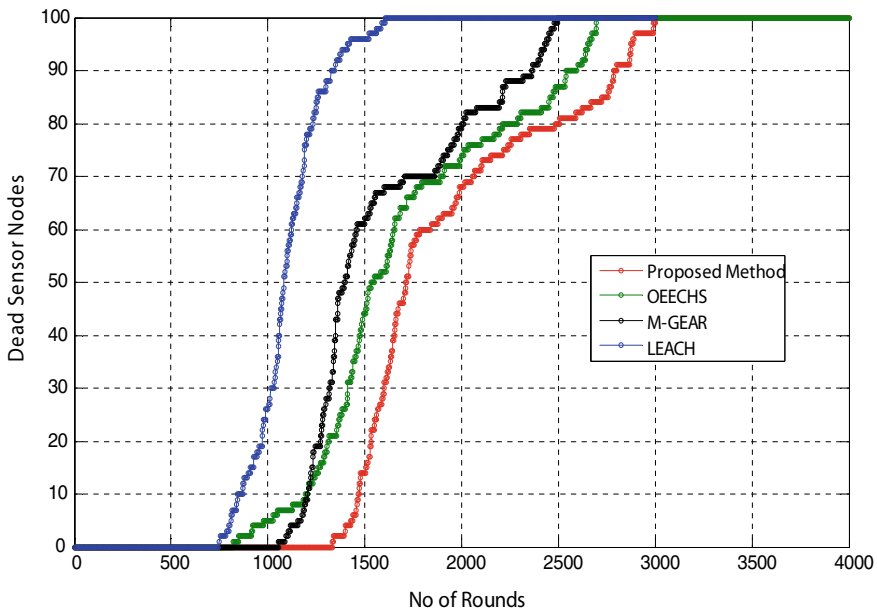


Fig. 2 Analysis of LEACH [3], M-GEAR [20], OEECHS [21], and the proposed a model for dead sensor nodes

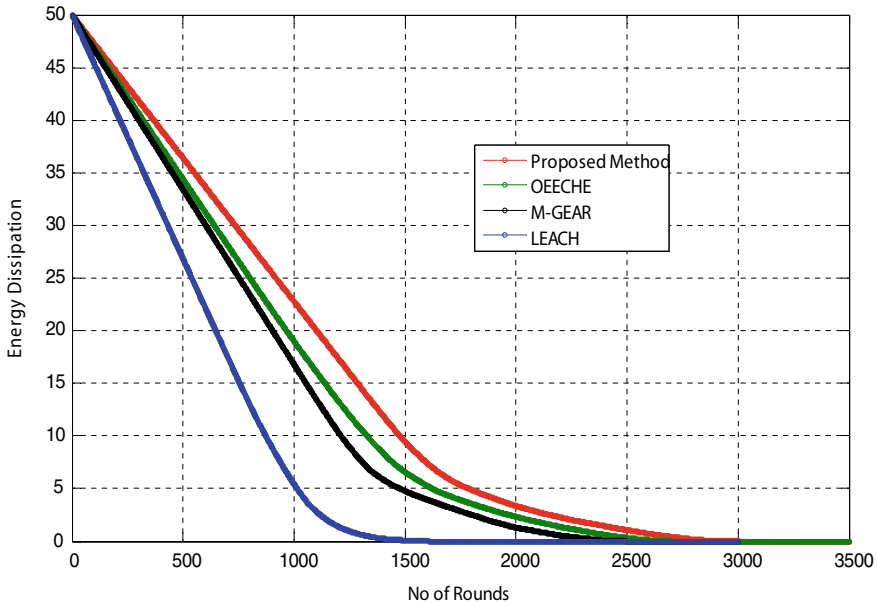


Fig. 3 Analysis of LEACH [3], M-GEAR [20], OEECHS [21], and proposed a model for energy consumption

is performing well than that of the LEACH [3], M-GEAR [20], and OEECHS [21] existing methods because the proposed method sensing data for a longer period and conserves very less energy during the data collection from the CHs and cluster members. It is also decreasing the cost of communication in a very effective manner. The simulation results of the number of packets sent to the BS concerning the number of rounds are shown in Fig. 4 for LEACH [3], M-GEAR [20], and OEECHS [21] existing methods and the proposed method using three-level of heterogeneity. The proposed method, OEECHS [21], M-GEAR [20], and LEACH [3], are sending 1.18×10^{-4} , 1.00×10^{-4} , and 0.97×10^{-4} , and 0.28×10^{-4} , the number of packets to the sink, respectively.

It is evident from the consequences that the projected method can transmit packets to the sink as a comparison to the LEACH [3], M-GEAR [20], and OEECHS [21] existing methods. The more number of packets sent by the proposed method because of the alive time of the deployed nodes are more concerning other methods like LEACH [3], M-GEAR [20], and OEECHS [21].

Figure 5 shows the proportional analysis in terms of last node dead (LND), half node dead (HND), and first node dead (FND) of the lifespan of the network for LEACH [3], M-GEAR [20], OEECHS [21], and the proposed method. It is evident from Table 1, the maintainable epoch (also called the first node dead (FND) timing) of the M-GEAR [20], OEECHS [21], and the proposed method outstrips by 10.51%, 42.85%, and 80.18%, as a comparison with LEACH [3] significantly, respectively.

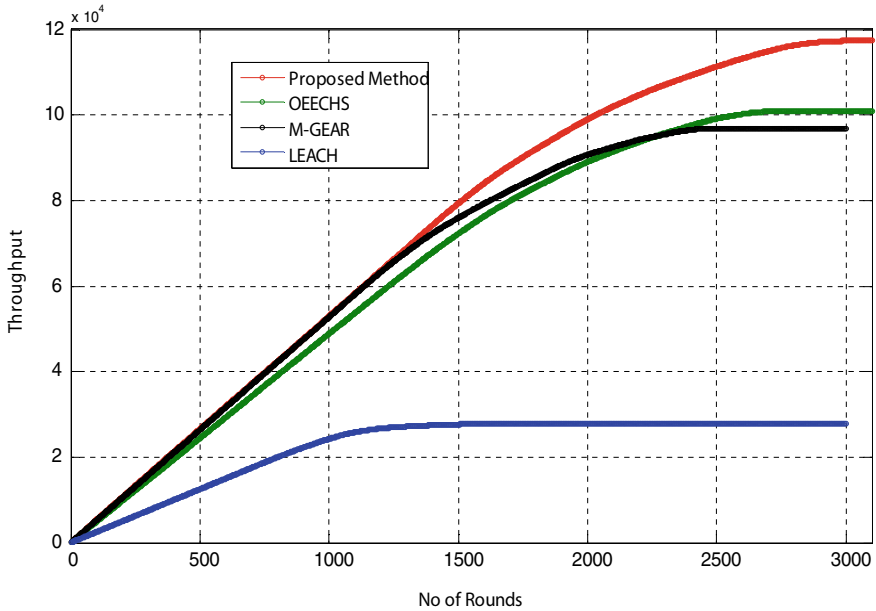


Fig. 4 Analysis of LEACH [3], M-GEAR [20], OEECHS [21], and the proposed model for throughput

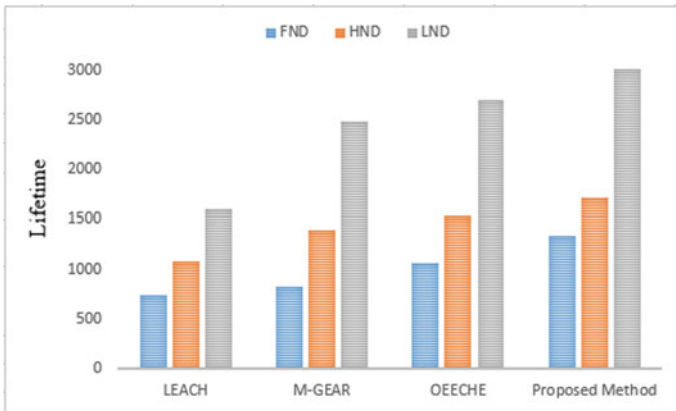


Fig. 5 Analysis in terms LND, HND, and FND of the network lifespan for LEACH [3], M-GEAR [20], OEECHS [21], and the proposed method

Moreover, the half node dead (HND) of the M-GEAR [20], OEECHS [21], and the proposed method outperform by 29.17%, 42.28%, and 59.37%, as a comparison with LEACH [3] significantly, respectively.

Table 1 Comparative analysis for LEACH [3], M-GEAR [20], OEECHS [21], and the proposed method

Protocols	Network lifetime			Energy consumption	Throughput	% increment in network lifetime
	FND	HND	LND			
LEACH	742	1083	1611	50 J	0.28×10^{-4}	–
M-GEAR	820	1399	2489	50 J	0.97×10^{-4}	54.50%
OEECHS	1060	1541	2701	50 J	1.00×10^{-4}	67.66%
Proposed method	1337	1726	3009	50 J	1.18×10^{-4}	86.77%

Furthermore, the last node dead (LND) of the M-GEAR [20], OEECHS [21], and the proposed method outperform by 54.50%, 67.66%, and 86.77%, as a comparison with LEACH [3] significantly, respectively. The throughput for the proposed method, OEECHS [21], M-GEAR [20], and LEACH [3] is 1.18×10^{-4} , 1.00×10^{-4} , 0.97×10^{-4} , and 0.28×10^{-4} , respectively. This method transmits an additional quantity of packets to the BS as compared to the existing ones. The lifespan prolonging of the M-GEAR [20], OEECHS [21], and the proposed method is 54.50%, 67.66%, and 86.77% as compared with the LEACH [3], deprived of addition energy of the network, i.e., 50 J, respectively.

6 Conclusion

In this paper, an effective and optimized cluster head election routing protocol for HWSNs is proposed. It has considered for heterogeneous networks and compared with the existing OEECHS [21], M-GEAR [21], and LEACH [3] methods. The developed method conveys a threshold-based dynamic clustering technique which helps in increasing sustainable of the system accomplishment since the choice of nodes in the process of CH election is efficient which has higher residual energy, node distance from the base station, and total network energy. The simulation results of the proposed method demonstration lifetime are increased by 86.77% for 50 J network energy as compared with LEACH [3], respectively. The throughput for the proposed method, OEECHS [21], M-GEAR [20], and LEACH [3] methods is 1.18×10^{-4} , 1.00×10^{-4} , 0.97×10^{-4} , and 0.28×10^{-4} , respectively. This method achieves better results than that of the OEECHS [21], M-GEAR [20], and LEACH [3] methods.

References

1. Singh S, Chand S, Kumar B (2013) Performance investigation of heterogeneous algorithms in WSNs. In: 3rd IEEE International Advance Computing Conference (IACC), pp 1051–1054
2. Singh Y, Singh S, Kumar R (2012) A distributed energy-efficient target tracking protocol for three level Heterogeneous sensor networks. *Int J Comput Appl* 51:31–36
3. Heinzelman WR, Chandrakasan AP, Balakrishnan H (2002) An application-specific protocol architecture for wireless microsensor networks. *IEEE Trans Wirel Commun* 1:660–670
4. Lindsey S, Raghavendra CS, Sivalingam KM (2002) Data gathering algorithms in sensor networks using energy metrics. *Trans Parallel Distrib Sys* 13:924–935
5. Singh S, Malik A (2017) hetSEP: Heterogeneous SEP protocol for increasing lifetime in WSNs. *J Inf Optim Sci* 38:721–743
6. Qing L, Zhu Q, Wang M (2016) Design of a distributed energy-efficient clustering algorithm for heterogeneous wireless sensor networks. *Comput Comms* 29:2230–2237
7. Singh S, Malik A, Kumar R (2017) Energy efficient heterogeneous DEEC protocol for enhancing lifetime in WSNs. *Eng Sci Technol Int J* 20:345–353
8. Maheswari DU, Sudha S (2018) Node degree Based energy efficient two-level clustering for wireless sensor networks. *Wirel Pers Commun* 104:1209–1225
9. Chand S, Singh S, Kumar B (2014) Heterogeneous HEED protocol for wireless sensor networks. *Wirel Pers Commun* 77:2117–2139
10. Singh S, Chand S, Kumar B (2016) Energy efficient clustering protocol using fuzzy logic for heterogeneous WSNs. *Wirel Pers Commun* 86:451–475
11. Singh S, Chand S, Kumar B (2017) Multilevel heterogeneous network model for wireless sensor networks. *Telecommun Syst* 64:259–277
12. Singh S, Chand S, Kumar B (2014) An energy efficient clustering protocol with fuzzy logic for WSNs. In: 5th international conference-confluence the next generation information technology summit, pp 427–431
13. Faisal S, Javaid N, Javaid A, Khan MA, Bouk SH, Khan ZA (2013) Z-SEP: zonal-stable election protocol for wireless sensor networks. *J Basic Appl Sci Res* 3(5):132–139
14. Khan FA, Khan M, Asif M, Khalid A, Haq IU (2019) Hybrid and multi-hop advanced zonal-stable election protocol for wireless sensor networks. *IEEE Access* 7:25334–25346
15. Smaragdakis G, Matta I, Bestavros A (2004) SEP: a stable election protocol for clustered heterogeneous wireless sensor networks. Technical Report BUCS-TR-2004-022, Boston University Computer Science Department, pp 1–11
16. Tang F, You I, Guo S, Guo M, Ma Y (2012) A chain-cluster based routing algorithm for wireless sensor networks. *J Intell Manuf* 23:1305–1313
17. Wang Z, Zhang M, Gao X et al (2019) A clustering WSN routing protocol based on node energy and multipath. *Cluster Comput* 22:5811–5823
18. Chen KH, Huang JM, Hsiao CC (2009) CHIRON: an energyefficient chain-based hierarchical routing protocol in wireless sensor networks. In: Proceeding of IEEE symposium on wireless telecommunications, pp 1–5
19. Linping W, Wu B, Zhen C, Zufeng W (2010) Improved algorithm of PEGASIS protocol introducing double cluster heads in wireless sensor network. In: IEEE international conference on computer, mechatronics, control and electronic engineering, pp 148–151
20. Nadeem Q, Rasheed MB, Javaid N, Khan ZA, Maqsood Y, Din A (2013) M-GEAR: Gateway-based energy-aware multi-hop routing protocol for WSNs. In: 2013 eighth international conference on Broadband and Wireless Computing, Communication and Applications (BWCCA), pp 164–169. <https://doi.org/10.1109/bwcca.2013.35>
21. Saranraj G, Selvamani K, Kanagachidambaresan GR (2019) Optimal energy-efficient cluster head selection (OEECHS) for wireless sensor network. *J Inst Eng India Ser B* 100(4):349–356
22. Yadav P, Agrawal R, Kashish K (2018) Protocols performance investigation using Ad Hoc WLAN for healthcare applications. *Pertanika J Sci Technol* 26:1333–1354

Internet of Things: Architecture, Applications and Future Aspects



Anu Priya, Amrita Rai, and R. P. Singh

Abstract This paper describes Internet of things (IoT)—What it is, the way it works, its applications and the way much it is steady. Almost all gadgets primarily based on emerging technologies are equipped with diverse types of sensors and controllers and have embedded intelligence. Because of all this, they are turned into “smart gadgets”, and they can be controlled from everywhere internationally with much less consumption of strength and energy. Connections between various devices through net are a new paradigm and discover lot of scope for researchers and industries. In this paper, it is far discussed how IoT generation has emerged as most trending era in today’s generation and feature turn out to be base for the destiny evolution in technologies.

Keywords Sensors · Connectivity · Network · Low power consumption · Smart gadgets

1 Introduction

The Internet of things is the network of embedded generation which can experience or talk or engage with internal or external environment and transfer the respective states with the assist of powerful Wi-Fi protocols. This technology may be made through sensors, less expensive processors and additionally with low power intake gadgets. Due to assist of IoT systems, we will have ability to acquire deeper automation,

A. Priya (✉)

Software Engineer, HCL Technologies, Noida, India
e-mail: anu.priya806@gmail.com

A. Rai

Department of Electronics and Communication Engineering, G L Bajaj Institute of Technology and Management Greater Noida, Noida, India
e-mail: amritaskrai@gmail.com

R. P. Singh

Haramaya Institute of Technology, Diredawa, Ethiopia
e-mail: rps.bslogics@gmail.com

© Springer Nature Singapore Pte Ltd. 2021

R. Agrawal et al. (eds.), *Advances in Smart Communication and Imaging Systems*,
Lecture Notes in Electrical Engineering 721,
https://doi.org/10.1007/978-981-15-9938-5_18

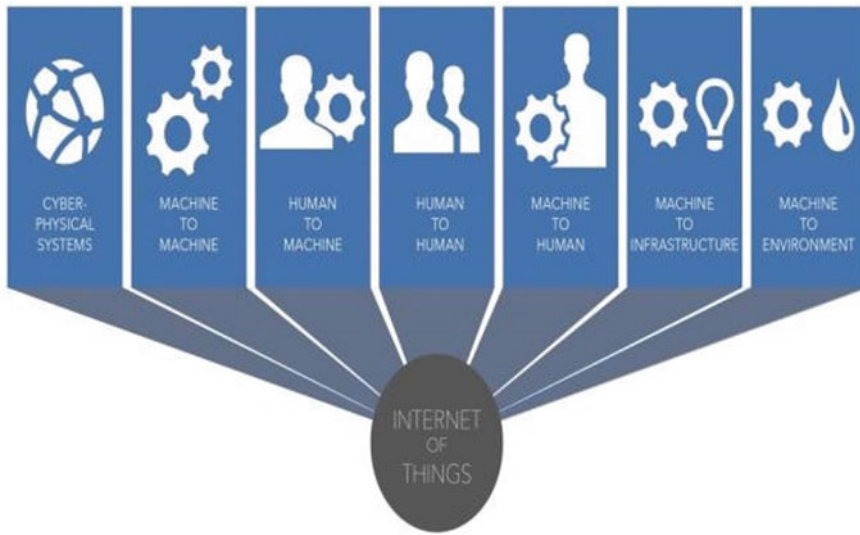


Fig. 1 Internet of things environment

analysis and integration inside a machine. This facilitates in accuracy and low intake of time. IoT utilizes present and emerging technology for sensing networking and robotics.

IoT explores increased innovation in software, falling hardware charges and present day attitudes toward technology. This generation is bringing major modifications daily to each day paintings and making life much less complicated in phrases of shipping of products, goods and services and the social, economic and political impact of those adjustments. In fact IoT is a semantically way of a worldwide network interconnected objects, which is uniquely addressable and based on standard communication protocols. This states a huge number of probable heterogeneous gadgets involved inside the system.

Figure 1 describes the fundamental IoT surroundings, how its miles connected to approx. all the things within the world.

1.1 Architecture

Architecture for implementation of IoT includes several layers: from the field data acquisition layer at the lowest to the application layer at the top. This layered structure is designed to satisfy the necessities of diverse industries, enterprises, societies, institutes, governments etc. Figure 2 offers a conventional layered architecture for IoT. Following are the diverse layers which are discussed briefly down below: [1, 2]

Network – supported services

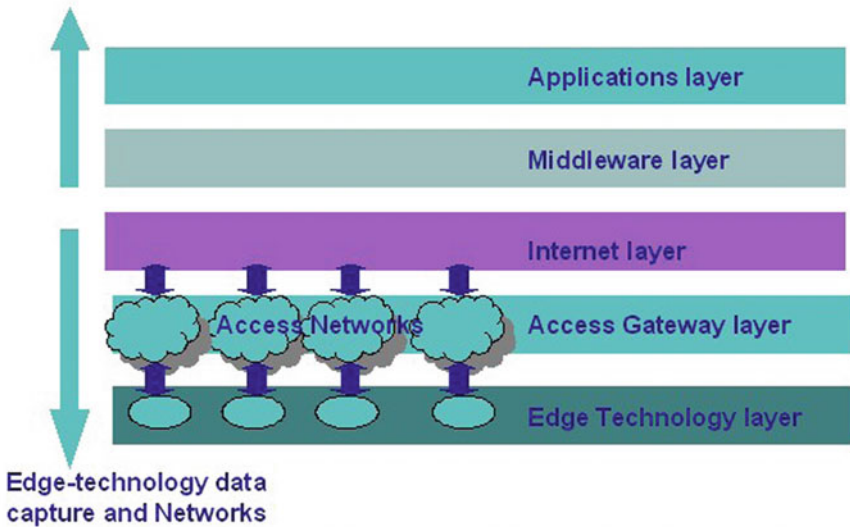


Fig. 2 Layered architecture of Internet of Things

1. Edge layer: This layer includes sensor networks, embedded systems, RFID tags and readers or other tender sensors in one of a kind forms. These devices collect record and deployed inside the field.
2. Access gateway layer: This is first layer where data handling is done. It takes care of message routing, publishing and subscribing and performs cross platform communication, if required.
3. Middleware layer: This layer operates in bidirectional mode. It presents interface among the hardware layer at the bottom and application layer at the top. It manages critical capabilities, for example, device management and statistics management, information filtering, data aggregation, semantic evaluation, access control, information discovery.
4. Application Layer: This layer at the top of the stack which is accountable for transport of numerous applications on the user end in IoT. These programs can range from users need to want that how they want to implement IoT to their devices.

2 Working

A complete IoT system works with the assist of four wonderful components: sensors/devices, connectivity, data processing and a user interface. Below is the short explanation of every component.

2.1 Sensors/Devices

At first, sensors or devices collect the required data from the environment. This can be temperature studying, stress reading or full video feed. We constantly say “sensors/devices” because more than one sensors may be placed all together and can be the part of a device that does extra than just experience things. However, whether it is a standalone sensor or a full device, within the first step of IoT, it is all about collecting information from environment via something like sensors and IoT devices. It is also a wireless sensor network that can feed data at desired.

2.2 Connectivity

Next step is sending the accrued statistics to the cloud. For which right connectivity is needed between two communicating ends or nodes. There are numerous methods of connectivity: cellular, satellite, Wi-Fi, low power WAN (LPWAN) or connecting directly through the Internet via Ethernet. For setting up this sort of connectivity, distinctive sort of wireless protocols may be considered, like ZigBee, RFID, Bluetooth and 6LoWPAN, RPL, CoAP, AMQP and MQTT [3].

For connectivity, in particular two protocols are used for transmission: transmission control protocol (TCP) and user datagram protocol (UDP). TCP’s flow control mechanism is used particularly for stresses out connections at the same time as UDP is used in particular for wireless connections. UDP supports multicast as well as have decreased overhead; however, TCP does not have multicast support. Each option has trade-offs between power intake, range and bandwidth. It is all about deciding on the nice connectivity primarily based on the person’s need to accomplish the task: getting information to the cloud.

2.3 Data Processing

When data receives to the cloud, subsequent step is doing a little type of processing on it. This step could be simple, including checking that the strain or temperature studying is within a required variety. Or it could be very complex, such as using computer vision on video to identify gadgets.

2.4 User Interface

Now, the information is made useful through data processing for the end user, and this data can be sent to the user through email, text, notification, etc. Also, user

possibly interfaces to proactively test on the machine. For example, a user might want to test the video feeds in their residence via a smartphone application or a Web browser. However, depending on IoT application, it is now not continually a one-manner avenue like most effective to send data to the user. But also the user may be able to carry out an action and affect the system.

3 Application

The potentialities offered by way of the IoT make it possible to develop several programs based on it, of which just a few applications are currently deployed. Some of the implemented applications are labeled on the premise of various regions and briefly mentioned [1–11].

3.1 Engineering, Industry and Infrastructure

In these areas, programs of IoT strongly include monitoring diverse procedures on the basis of production, marketing, service shipping and protection. IoT additionally affords transparency in the techniques and creates extra visibility for improvement opportunities. IoT is likewise very useful in assembly of the client needs, controls the actions wanted for nonconforming product, malfunctions in equipment, issues in connecting networks and more.

Exact monitoring and controlling operations of rural infrastructures like bridges, railway track is also required IOT networking. IoT infrastructure affords monitoring of any events or adjustments in the system and reduces threat and increases safety. It also can provide regular repair and maintenance activities. These all functions carried out with the help of IoT infrastructure have more transparency, reliability and low cost of operation.

3.2 Health and Medicine

IoT pushes us in the direction of our imagined destiny of drugs which exploits extraordinary integrated community of sophisticated clinical gadgets. Today, IoT has rising response in clinical studies, scientific gadgets, health and care. The combination of all the elements affords extra reliability, accuracy, discount in reaction time and expenses.

With all these blessings, IoT has also given remarkable facility to medical field with the aid of attaching smart labels to drugs. Due to this, all of the information of that drug may be accessed without difficulty and assist in tracking and monitoring their repute with sensors. A smart medicine cabinet can also be designed with the

assist of IoT structure which can read statistics transmitted by using the drug labels and patients may be reminded at a appropriate periods to take their drug treatments and affected person compliance may be monitored.

3.3 Agriculture

IoT can play a crucial position in agriculture field. It can make feasible actual time detection of animals in the course of the outbreak of contagious disease. IoT can also help in weather monitoring that may give the amazing assist to farmers for their farming making plans. It can also screen the procedure of farming via monitoring soil, plants, surroundings greater and replace it to officers for farming analysis, in order that the farming development measures can be planned accordingly.

Also, IoT infrastructure may be built for the farmers, in order that they will be able to deliver the crops without delay to the purchasers. It might be very much useful in decreasing costs and frauds and make the infrastructure more transparent and simple.

3.4 Government and Safety

IoT applied to government and safety lets in progressed and transparent law enforcement, defense, planning a city, financial control and lots of greater. The technology can fill the gaps and assist within the governing social as well as financial environment [11].

3.5 Smart Retail

In today's era, retailers as well as consumers have started out to adopt IoT solutions to enhance keep operations, growing purchases, reducing theft and improving consumer's shopping enjoy through making it less complicated for them to shop for extra objects while saving money [2].

3.6 Extreme Weather and Pollution

Currently, tracking of air and water safety primarily uses manual labors in conjunction with develop and automated devices and lab processing. Using IoT technology, human labor also can be decreased and allows common sampling and checking out on-site. This permits us to save you enormous contamination and associated disasters. IoT can offer powerful, superior and deep monitoring functions within the

structures consisting of radar and satellites that could forecast the required excessive information of the weather which could save loss of lifestyle and property [1, 6].

4 IoT—Advantages and Disadvantages

IoT has many blessings move every location of way of life and business. Here are some of the advantages:

- IoT encourages the status quo of communication among devices, commonly referred to as machine-to-machine (M2M) communication. It offers less difficult connections with greater first class and less value [4, 9].
- IoT promotes automation by offering wireless infrastructure in order that machines can be capable of speak every different and capable of providing necessary records faster and on time without any human interference [3].
- Through IoT infrastructure, more records may be amassed from the outer surroundings at very low cost and less supplies on the way to be very much beneficial for studies and development purposes.
- IoT infrastructure provides a solid platform for tracking function. By which analyzing the simulation for any surroundings can end up much less difficult and accurate.
- Adopting IoT can also store money and time and also makes excellent of life.

Here are some disadvantages of IoT:

- **Compatibility:** Currently, there is no international standard of compatibility for tagging and monitoring equipment.
- **Complexity:** IoT infrastructure can also increase the complexity by adding greater complex protocols for the relationship of the gadgets.
- **Privacy/Security:** This parameter is the most important and major downside of IoT. Till date, there is no stable, and reliable IoT infrastructure has been made which could deliver privations and security guaranteed. IoT data/ statistics may be hacked effortlessly if no required and strong security features taken [1, 5–8]
- **Lesser Employment:** As IoT ends in automation, the unskilled people may come to be dropping their jobs. Technology takes manage of existence like if enviorment increasingly more automation could be adopted, an increasing number of dependency on it will increase.

5 Conclusion and Future Aspects

In today’s generation, we are able to see the surroundings have end up a kingdom of the art technologies. How IoT has received the rising technologies and making more automated. It is deploying on a big scale at the surroundings. It is likewise wished

to indicate paintings inside the governance of IoT and make some standardized approach for it.

There are many destiny elements in IoT as that is most rising generation now and also in future. Some of future aspects are mentioned below:

1. Cities will end up “smart”.
2. Wireless exchange may be more steady and smarter.
3. G network will give greater fuel to IoT growth.
4. Security and privacy will have more worries and standardized parameters.
5. More encryption stage will drive law and regulatory activities.
6. Artificial intelligence will evolve more with the help of IoT infrastructure and emerge as a bigger thing.

References

1. Atzori L, Gubbi J, Buyya R, Marusic S, Palaniswami M (2013) Internet of Things (IoT): A vision, architectural elements, and future direction. *Future Gener Comput Syst*
2. Gruen TW, Corsten DS, Bharadwaj S (2002) Retail out of stocks. Technical Report
3. Kushalnagar N, Montenegro G, Schumacher C (2009) IPv6 over Lo-Power Wireless Personal Area Networks (6LoWPANs): overview, assumptions, problem statement, and goals. IETF RFC 4919
4. Lee J, Bagheri B, Kao H-A (2015) Cyber-physical systems architecture for Industry 4.0-based manufacturing systems
5. Narayanan A (2014) Impact of Internet of Things on the retail industry. PCQuest. Cyber Media Ltd
6. Al-Ali R, Zualkernan I, Aloul F (2010) A mobile GPRS-sensors array for air pollution monitoring. *IEEE Sens J* 10(10):1666–1671
7. Ersue M, Romascanu D, Schoenwaelder J, Sehgal A (2014) Management of networks with constrained devices: use cases. IETF Internet Draft
8. Vermesan O, Friess P (2011) Internet of Things—global technological and societal trends. The River Publishers series in communications
9. Santucci G (2009) Internet of the future and internet of things: what is at stake and how are we getting prepared for them? In: eMatch’99—Future Internet Workshop
10. Kelesidis T, Kelesidis I, Rafailidis P, Falagas M (2007) Counterfeit or substandard antimicrobial drugs: a review of the scientific evidence. *J Antimicrob Chemother* 214–236
11. Hardgrave BC, Waller M, Miller R (2006) RFID’s impact on out of stocks: a sales velocity analysis. Research Report from the University of Arkansas

Demand Response-Based Congestion Management Considering Wind Energy Source in Competitive Power Market



Anjali Agrawal, Seema N. Pandey, and Laxmi Srivastava

Abstract Transmission line congestion has become a crucial issue due to competitive market environment and profit maximization tendency of market players. This congestion may lead to the cascading outages which forces the system to collapse. This paper presents demand response-based congestion management method considering wind power generation. Artificial intelligent technique-based genetic algorithm is used for optimal placement of wind power generator at load buses for reducing overloading of transmission lines. Demand response (DR) program provides opportunity to the end user consumer for involving in congestion management and reduces the network congestion. Addition of DR program optimizes the transmission line power flows more efficiently and decreases the system operation cost effectively. A comparative analysis is presented with GA-based wind power generator and DR program for congestion management. The proposed methodology is tested on IEEE30 bus system.

Keywords Congestion management (CM) · Wind power generation · Demand response (DR) · Genetic algorithm (GA)

A. Agrawal (✉) · L. Srivastava
Department of Electrical Engineering, Madhav Institute of Technology and Science, Gwalior, MP,
India
e-mail: anjali Gupta@gmail.com

L. Srivastava
e-mail: srivastaval@hotmail.com

S. N. Pandey
Department of Electrical Engineering, Dr. Bhim Rao Ambedkar Polytechnic College, Gwalior,
MP, India
e-mail: se_np@rediffmail.com

1 Introduction

After deregulation, power system has become a power market and all entities like Gencos, Transcos, Discos and aggregators are market players [1]. To meet the level of demand, DGs and renewable energy sources are also included in deregulated power market. Now electricity is traded like a commodity. Market players make forward and future contracts among selves in electricity market [2]. In this competitive environment of deregulated market, physical capacity of transmission network creates barrier to accommodate all transactions requested by market participants. For secure and smooth operation of power market system operator interfere with scheduled or contracted transactions to avoid the overloading of transmission system. A number of CM methods are developed and are being currently used around the world [3, 4]. CM methods can be divided in two categories market-based and nonmarket-based methods. Methods like first come first serve, prorated rationing curtailment and FACTS devices [5–7] are based on physical availability of transmission path known as nonmarket-based methods can reduce congestion in a limited manner. Because in competitive environment of power market congestion is not only a simple problem of physical path but also a market management issue. For making CM methods, more effective generation side approaches were involved in strategic bidding [8], LMP [9] and price area [10] CM. Under new era of rapidly increasing demand and presence of renewable energy sources has made the problem of congestion more complex and only generation side approaches are not sufficient to overcome. In congested network by supplying the electric energy at the bottleneck location, DGs can reduce the congestion of transmission system [11, 12]. Under new era of rapidly increasing demand implementation of solar and wind energy sources can fulfil the energy requirement but these sources are not available all the times [13]. As well as at the peak hours these energy sources may create penetration of electric energy and may lead to unexpected overloading of transmission grid. Reduction or shifting of demand from peak hours to off peak hours can reduce the chances of congestion without any panic situation. Therefore, motivational involvement of end user consumers can eliminate the congestion problem more efficiently and effectively.

1.1 Demand Response-Based Congestion Management

Due to the lack of information consumers were not motivated to shift or reduce their demands at the peak hours. This can lead to higher energy prices and more congested network [14]. System operator having information about the transmission network and REPs provide the bridge of proper information gap between system operator and with end user consumers. Because REP having direct contacts with end use consumers [15]. Loads with elastic demands provide more effective and efficient market solutions for secure system operation and CM [16]. Some challenges for the implementation of DR and potential solutions for congestion management are

addressed [17]. Involvement of customer response results in smaller price spikes and can lead to lower LMPs [18]. A pool-based DR exchange was proposed [19] in which DR exchange operator collects the bid from buyers and sellers and clears the market for economic benefit for all players under network security consideration. When price-based load reduction method fails at the time of peak hours transfer agent can handle the problem by maintaining the house hold load under a prescribed limit [20]. DRs manage energy consumption from load side directly. Therefore, can mitigate congestion without any fuel cost and finally reduce the system operation cost.

1.2 Wind Power Generation

Wind energy is under the category of renewable energy. The running cost of wind generator is not so much high as well as it eliminates the variations in energy price. Wind generators do not create any pollution for the environment. This attractive property of wind generator has made it more common and fastest growing energy source in worldwide. The electric energy generated by wind turbine can be shown by the following equation

$$P_{\text{wind}} = \frac{1}{2} \rho_{\text{wind}} A \gamma V_{\text{wind}}^3. \quad (1)$$

where ' ρ_{wind} ' is the air density factor, ' A ' is the swept area of wind turbine, γ overall efficiency of wind power plant and V_{wind}^3 is the wind speed for the given height. Wind speed is not fixed and its electrical power output is variable all the times. The speed forecasted data can and cost of electric power generated by wind turbine 3.75 s/MW for 1 h are taken from [21].

2 Problem Formulation

The main object of the proposed method is to eliminate the congestion of transmission system with DR and wind integration. For optimal placement of wind power generator AI-based technique GA is implemented. Objective function having following three sections. First part is minimization of generation cost of thermal power generators, second part is incentive given to end user consumers for adjusting their loads and third one is the cost of wind power generators.

$$\min \left(\sum_{G_i=1}^n a_{G_i} (P_{G_i})^2 + b_{G_i} (P_{G_i}) + c_{G_i} + \sum_{m=1}^{N_{\text{DR}}} INC^m + C_{\text{cost}}^{\text{wind}}(P_{\text{wind}}) \right). \quad (2)$$

2.1 Minimum Generation Cost

Cost of thermal generators can be represented by the following equation. Where abc are the generator coefficients, n is the number of generators and P_{G_i} is the power generated by the respective generators.

$$C_{G_i}(P_{G_i}) = a_{G_i}(P_{G_i})^2 + b_{G_i}(P_{G_i}) + c_{G_i}. \quad (3)$$

2.2 Minimum DR cost

End user consumers reduce energy consumption under the DR in two cases. First when electric energy prices are changing at the consumer level, second satisfactory incentives are provided to consumers. In both cases costumer want to get maximum profit for adjusting or reducing their demands. For CM set of loads are selected for implementing DR on the basis of transmission network configuration. Penalty and incentive-based elastic load model is proposed for CM. The demand adjustment at m -th response bus can be shown by the following equation.

$$\Delta D^m = D^{0m} - D^m. \quad (4)$$

The total incentives given to the consumers at m -th response bus can be shown by Eq. (5). Incentive coefficient is considered from 0.1 to 10 times of electricity prices.

$$INC^m = INC[D^{0m} - D^m]. \quad (5)$$

Once consumers are participating in DR, they have to reduce their load at the required minimum demand, if they do not response they have to pay a penalty for that. Penalty function can be shown in Eq. (6).

$$PEN^m = PEN[LR^m - \Delta D^m]. \quad (6)$$

Minimum load reduction requested by the system operator is shown by LR. Linear responsive load modal is proposed in this paper is shown in Eq. (7).

$$D^m = D^{0m} \left[1 + \epsilon \frac{\sigma - \sigma^0 + INC - PEN}{\sigma^0} \right]. \quad (7)$$

where ϵ is the load elasticity σ and, σ^0 are the electricity prices after and before.

2.3 Equality constraints

The system network having equality constraints in terms of active and reactive power available at all nodes. Sum of active and reactive power at each will be zero, respectively. Power balance equations at each node:

$$P_i - P_{G_i} + P_{D_i} + P_{DG} = 0, \quad i = 1, 2 \dots N_i. \quad (8)$$

$$Q_i - Q_{G_i} + Q_{D_i} = 0, \quad i = 1, 2 \dots N_i. \quad (9)$$

2.4 Inequality constraints

Generator, transmission line constraints and wind power generation limit

$$V_i^{\text{Min}} \leq V_i \leq V_i^{\text{Max}}, \quad i = 1, 2 \dots N_i. \quad (10)$$

$$P_{G_i}^{\text{Min}} \leq P_{G_i} \leq P_{G_i}^{\text{Max}}. \quad (11)$$

$$Q_{G_i}^{\text{Min}} \leq Q_{G_i} \leq Q_{G_i}^{\text{Max}}. \quad (12)$$

$$T_{k_i} \leq T_{k_i}^{\text{Max}}, \quad k = 1, 2 \dots T_L. \quad (13)$$

$$0 \leq P_{\text{wind}} \leq P_{\text{wind}}^{\text{max}}. \quad (14)$$

Incentive limits for DR Program:

$$\text{INC}_{\text{min}}^m \leq \text{INC}^m \leq \text{INC}_{\text{max}}^m. \quad (15)$$

3 Genetic Algorithm (GA)

GA is a basic algorithm under all nature inspired artificial intelligence-based heuristic algorithm for optimization. It was developed by Prof. John Holland in 1960 [22]. GA is a robust and effective tool for optimization of nonlinear issues. GA was proposed as optimization technique for optimal power flow solution in case of contingency [23] and multimode electricity market [24]. For making the network congestion cost-free genetic algorithm provides the optimal location and size of wind power generators

as well as load after DR. The generation and DR cost and transmission congestion cost are taken as the fitness function. Generator active power outputs and voltages are modelled as control variables. Line limits along line flows, active and reactive power generation, voltage magnitude and DR limits are constraints. GA operates according to the following steps.

1. Define fitness function: Fitness function is the energy cost of the entire generators, DR cost and transmission congestion cost also with satisfying all the equality and inequality constraints.
2. Create initial random population (200).
3. Find the fitness function value for each solution.
4. Completion and repetition of further operations Selection, crossover and mutation to generate the required off-springs.
5. On the basis of new off-springs, fitness function is calculated.

4 Result and Analysis

In this section, economic effect of DR program and optimal placement of wind power generator for congestion management is discussed. For finding optimum size and location of wind power generator, GA is used as optimization technique and the proposed technique is tested on IEEE-30 [14] bus system in MATLAB software environment. For congestion management, only 7 loads located at bus Nos. 7, 8, 12, 17, 19, 21 and 30 take part in DR program based on generation shift factors. Generator cost function can be represented by (3). When transmission line rating is considered 35 MVA for base case optimal power flow system operation cost is 575.15149 Rs. and no transmission line is overloaded. When transmission line rating is considered 32 MVA line no. 10 and 29 having power flows 32.4624 MW and 32 MW means both lines are overloaded. To reduce the overloading of transmission lines, wind power generator and DR program are implemented in different following cases with line rating 32 MVA.

Simulation results of four cases are shown in tables. Table 1 shows the generator dispatch with power losses. Table 2 shows the system operation cost, congestion cost and demand response cost. Table 3 shows the demands in all cases. MVA power flows for all cases are shown in Fig. 1.

4.1 Base Case Optimal Power Flow

Bus system is simulated with line rating 32 MVA without any wind power generator and DR program.

Table 1 Generator dispatch, wind power generation and power losses

Gen Dispatch/ Power Losses (MW)	Base Case	GA-based Wind Power Gen. without DR	Only DR	GA-based Wind Power Gen. with DR
PG1	33.0359	40.9506	42.0773	40.3793
PG2	45.4571	54.743	56.0579	54.0749
PG3	25.5697	22.1080	22.5039	21.8363
PG4	40	25.8774	28.5283	26.0389
PG5	29.9909	14.6972	15.5576	14.1232
PG6	17.625	14.7017	15.7201	14.2978
PG (Wind)	00	18.3529	00	9.4391
Power losses	2.4786	2.5909	2.31	2.1712

Table 2 Generation cost, Wind power generation cost, Congestion cost, DR cost and Total system Operation cost

Cost in Rs	Base Case	GA-based Wind Power Gen. without DR	Only DR	GA-based Wind Power Gen. with DR
Gen. Cost	575.1543	505.0269	532.2818	496.4502
Pwind Gen. Cost	00	61.8493	00	35.3965
Congestion Cost	57.57	6.9738	00	00
DR cost	00	00	3.318	3.3108
Total System Operation Cost	632.7243	573.85	535.6998	535.1575

Table 3 Loads at responsive load buses after DR program

Loads after DR (MW)	Base case	GA-based Wind Power Gen. without DR	Only DR	GA-based Wind Power Gen. with DR
PD7	22.8	22.8	20.5204	20.5247
PD8	30	30	27.0011	27.0065
PD12	11.2	11.2	10.0806	10.0821
PD17	9	9	8.1021	8.1014
PD19	9.5	9.5	8.553	8.5558
PD21	17.5	17.5	15.7504	15.7526
PD30	10.6	10.6	9.5424	9.5410

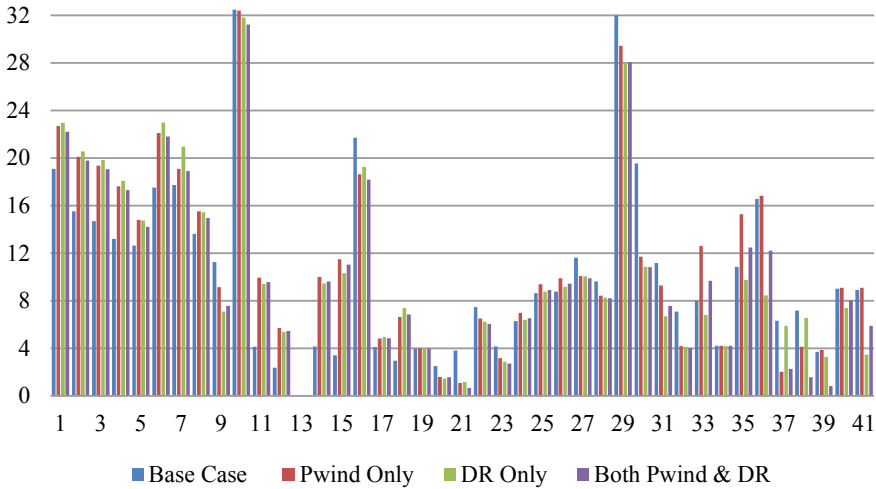


Fig. 1 MVA Power on Transmission Lines, X-axis is the Transmission Line Numbers and Y-axis is the MVA power flows on transmission lines

4.2 GA-Based Optimal Sizing and Siting of Wind Power Generator Without DR

For congestion management bus system is simulated with GA to that results optimum location 8 and size of wind generator 18.3529 MW now the MVA flows on line no 10 and 29 are 32.3967 and 29.4207 MW means power flows on both lines are not under limit. Reduction of congestion cost reduces the system operation cost. But still more improvement is required MVA power flows on transmission line no. 10.

4.3 Only DR Program is Implemented

Now only DR program is implemented without any wind power generator. After DR implementation power flows on line no 10 and 29 are 31.8109 and 28.0527 MVA respectively. Responsive demands are shown in Table 3. It is clear from the table now the system cost and losses have also reduced and power flows at transmission line no 10 has improved than the previous two cases.

4.4 GA-Based Optimal Sizing and Siting of Wind Power Generator with DR

In this case with same line rating DR and wind power generator both are simulated simultaneously with GA. Location of wind power generator is bus no 20 with 9.4391 MW. and new demands after simulations are shown in Table 3. Now power flows on line no. 10 and 29 are 31.2257 and 28.0422 MVA which is lowest in all four cases. It is clear from the table that system operation cost is minimum in this case due to the reduction of congestion cost and system power losses. Hence, the proposed demand response-based CM method has given the best results. Optimal placement of wind power generator alone can reduce the overloading of transmission lines up to some extent but transmission line is not congestion-free. Implementation of DR has made the transmission system totally congestion free with reduced energy cost and power losses.

5 Conclusion

In competitive environment of power market congestion has become a market management issue. Only technical aspects are insufficient to overcome the problem of congestion. To eliminate the congestion from transmission line effectively, market-based strategy has to be implemented. In the proposed method, DR program is efficient to mitigate the congestion with reduced cost and reduced power losses on IEEE 30 bus system. The comparison of GA-based optimal placement of wind power generators without and with DR clears that the DR program can diminish congestion of transmission system very effectively and economically with reduced system losses. Under incentive-based DR for CM, end user consumers can take part and reduce their demands in peak hours that are the main cause of congestion. DR program is the economic and efficient financial tool for CM in deregulated power market.

References

1. Raikar SB, Jagtap KM (2018) Role of deregulation in power sector and its status in India. National Power Engineering Conference (NPEC) (2018) 1–6
2. Lai LL (2001) Power system restructuring and deregulation trading, performance and information technology. John Wiley & Sons, Chichester, UK
3. Agrawal A, Pandey SN, Srivastava L (2020) A review and study on market based congestion management techniques in restructured power market. In: Proceedings 27–28 Feb., 2020, International Conference on Advances in Systems, Control & Computing (AISCC-2020) Sponsored by Springer Under TEQIP-III, MNIT Jaipur
4. Pillay A, Karthikeyan SP, Kothari DP (2015) Congestion management in power system—a review. *Int J Electric Power Energy Syst* 70:83–90

5. Reddy SS (2017) Multi-objective based generation rescheduling and load shedding. *IEEE Trans Power Syst* 32:852–863
6. Kirthika N, Balamurugan S (2016) A new dynamic control strategy for power transmission congestion using series compensation. *Int J Electric Power Energy Syst* 77:271–279
7. Khan MT, Siddiqui AS (2017) Congestion management in deregulated power system using FACTS device. *Int J Syst Assurance Eng Manage* 8:1–7
8. Jain R, Siddiqui AS, Jamil M (2017) A strategy for FTR bidding in deregulated electricity market. *Int J Syst Assurance Eng Manage* 8:78–89
9. Wang Q, Zhang G, McCalley JD, Zheng T, Litvinov E (2014) Risk based locational marginal price and congestion management. *IEEE Trans Sustain Energy* 29:2518–2528
10. Jain AK, Srivastava SC, Singh SN, Srivastava L (2015) Bacteria foraging optimization based bidding strategy under transmission congestion. *IEEE Trans Power Syst* 9:141–151
11. Gill HA, Joos G (2008) Models for quantifying the economic benefits of distributed generations. *IEEE Trans Power Syst* 23:327–335
12. Agrawal A, Pandey SN, Srivastava L (2020) Genetic algorithm based sizing & siting of DG for congestion management in competitive power market. In: Proceedings 27–28 Feb., 2020, International Conference on Advances in Systems, Control & Computing (AISCC-2020) Sponsored by Springer Under TEQIP-III, MNIT Jaipur
13. Murphy C, Soroudi A, Keane A (2016) Information gap decision theory-based congestion and voltage management in the presence of uncertain wind power. *IEEE Trans Sustain Energy* 7:841–849
14. Kohan FZ, Razmi H, Daogou-Mojarrad H (2018) Multi-objective transmission congestion management considering demand response programs and generation rescheduling. *Appl Soft Comput* 70:169–188
15. Babar M, Haque NMM, Nguyen PH, Cul V, Kamphuis IG, Slootweg JG, Bongaerts M (2017) Learning technique for real-time congestion management in an active distribution networks. In: 2017 IEEE Manchester Power Tech, Manchester (2017) 1–6
16. Shayesteh E, Moghaddam MP, Taherynejhad S, Sheikh EL, Eslami MK (2008) Congestion management using demand response programs in power market. In: IEEE Power and Energy Society General Meeting—Conversion and Delivery of Electrical Energy in the 21st Century, Pittsburgh, PA (2008) 1–8
17. Rahimi F, Ipakchi A (2010) Demand response as a market resource under the Smart Grid paradigm. *IEEE Trans Smart Grid* 1:82–88
18. Aazami R, Aflaki K, Haghifam MR (2011) A demand response based solution for LMP management in power markets. *Int J Electrical Power Energy Syst* 33:1125–1132
19. Nguyen DT, Negnevitsky M, Groot M (2011) Pool-based demand response exchange concept and modeling. *IEEE Trans Power Syst* 26:677–685
20. Haque ANMM, Nijhuis, Nguyen MG, Ye PH, Bliet FW, Slootweg JG (2019) Integrating direct and indirect load control for congestion management in LV networks. *IEEE Trans Smart Grid* 10:741–751
21. Tiwari PK, Mishra MK, Dawn S (2019) A two step approach for improvement of economic profit and emission with congestion management in hybrid competitive market. *Int J Electric Power Energy Syst* 110:548–564
22. Hooland J (1975) Adaptation in natural and artificial systems. University of Michigan Press, An Arbor, MI, USA
23. Lai LL, Ma JT, Yokoyama R, Zhao M (1997) Improved genetic algorithm for optimal power flow under both normal and contingent operation states. *Int J Electric Power Energy Syst* 19:287–292
24. Numnonda T, Annakkage UD (1999) Optimal power dispatch in multinode electricity market using genetic algorithm. *Electric Power Syst Res* 49:211–220 (1999)

Power Transfer Loadability Enhancement of Congested Transmission Network Using DG



Divya Asija and Pallavi Choudekar

Abstract Transmission network congestion is one of the prevailing issues which impacts the power transfer capability of transmission lines resulting in further impact on the power market transactions. One of the easiest methods of exterminating this issue is to expand the transmission network by linking new transmission lines with the existing transmission network. But it has been restricted due to several environmental, financial, and hazardous effects on human beings. The utilization of distributed generators (DGs) has been considered as the most viable option for enhancing the power transfer capability of the transmission network. They are directly linked at the load end serving as negative load to decrement the overall load demand. DG will improve the overall system performance by decreasing the network losses as well as increasing the system loadability limits. This paper shows the enhanced system performance with DG, considering social welfare (wt_1) and network security (wt_2) as two significant weighting factors with CPF and OPF techniques. Proposed techniques have been implemented on IEEE 14 bus system to validate their effectiveness.

Keywords MATLAB/simulink · CPF · OPF · DG · ALC · TTL · TML

1 Introduction

Small electricity has become one of the important commodities of our day-to-day life. Though this utility meets various challenges like over usage of transmission capacity, transmission losses, and poor quality in power supply because of increasing power demand, this problem is taken into account as a serious problem due to large size of dynamically changing network and its different behaviors with inter connected equipment. Interconnections need to deliver the energy from various generating

D. Asija (✉) · P. Choudekar
Department of Electrical and Electronics Engineering, Amity University, Noida, India
e-mail: dasija@amity.edu

P. Choudekar
e-mail: pachoudekar@amity.edu

plants into different load hubs in order to minimize the fuel cost and the power generation capacity. During power transmission, some of the energy is dissipated. A perfect power transmission lines should transfer energy without any loss, balance the load, and reduce the fuel cost. In order to solve the above-mentioned problems, OPF method is selected as the optimum solution in electricity network. One of the static, single or multi-objective, and nonlinear optimization problems in electrical power system is OPF. Since the power industries are growing in highly competitive environment, OPF is considered as a tool to exchange the power in most effective manner. The main objectives of the OPF problem are used to deliver power at less cost with voltage profile maintenance, reducing the losses and increasing the power support.

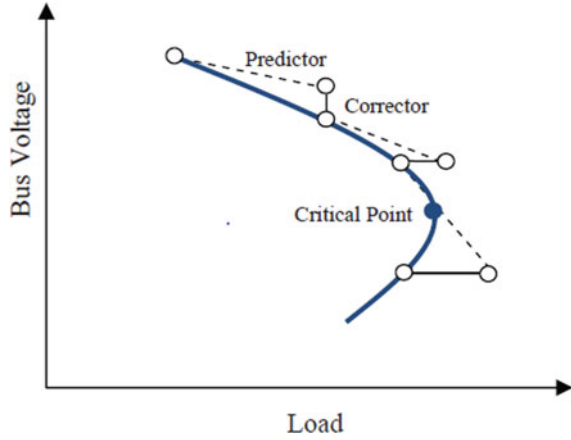
OPF technique has been implemented. OPF routine has delivered price-based nodal parameters such as LMP and NCP at each node. These parameters are computed with two weighting factors w_{t2} for network security and w_{t1} for social welfare. Optimum weightage will provide the efficient system. The node which is having higher LMP and NCP values is considered as best position for locating DG. After installation of DG in to the network, parameters such as power losses, maximum line loading, maximum load point value, and other power values at load and generator buses are computed and compared. Improved parameters value will indicate the benefit of installing DG at appropriate location. Further, in this chapter, available loading capability (ALC) and the total maximum loadability (TML) have been computed for $w_{t1} = 1$ to 9 without and with DG at optimum location. Results obtained would lead to conclusion that DG enriches the system with both the total maximum loadability and available loading capability.

2 Continuation Power Flow Technique

Continuation power flow (CPF) is a method used for voltage stability analysis. It overpowers the convergence problem which usually exists in conventional power flow at working conditions which is near the voltage stability limit. Convergence problem gives rise to singular Jacobian matrix at stability limit. In order to find the precise estimation of critical point located on the load curve of the power system, CPF techniques are predominantly utilized. It makes use of the predictor–corrector method for tracing the power flow solution curves using local parameterized continuation method.

Approximation of critical point by predictor–corrector step is presented in Fig. 1 shows the critical point approximated by predictor–corrector method [1]. Maximum loading point determination is a very crucial aspect for analyzing voltage stability parameter and is one of the main concerns for power engineers. Conventional load flow analysis method is not an appropriate method as it does not provide the crisp or exact data [2]. Moreover, it is found that the outcome from conventional power flow solution method provides a Jacobian matrix which becomes singular near the voltage collapse point [3]. Thus, we rarely utilize this method to avoid such condition.

Fig. 1 Critical point approximation by prediction–correction step technique



CPF method is mainly exploited to provide an effective solution. It avoids the singularity problem relating to the Jacobian matrix, thereby reinventing the power flow equation and dispersing a locally parameterized continuation technique. In a load scenario, CPF method provides the successive load flow solution and considered to be the most sustainable method providing the appropriate solution.

In the proposed system, CPF method is utilized to find the critical bus which is having high voltage instability. Critical bus location has been realized as the location for placement of DG. CPF technique is basically quasi-static voltage stability analysis.

Load parameter is defined by following equations [4–6]:

$$0 \leq \psi \leq \psi_{\text{critical}} \tag{1}$$

where $\Psi = 0$ belongs to the base load.

$\Psi = \Psi_{\text{critical}}$ belongs to the critical load.

After this point, system is approaching to voltage instability condition. The system equations after critical point have been shown via Eqs. 2 and 3.

$$P_{Gmo}(1 + \lambda k_{Gm}) - P_{Lmo} - \psi(k_{Lm} S_{\Delta\text{base}} \cos \theta_m) - P_{Tm} = 0 \tag{2}$$

$$Q_{Gmo}(1 + \lambda k_{Gm}) - Q_{Lmo} - \psi(k_{Lm} S_{\Delta\text{base}} \sin \theta_m) - Q_{Tm} = 0 \tag{3}$$

where P_{Lmo} , Q_{Lmo} are active and reactive loads at bus m .

k_{Lm} represents the multiplier which denotes the rate of change of load m as ψ changes.

θ_m represents the load power angle at bus m .

$S_{\Delta\text{base}}$ is the apparent power for the base case.

P_{Gmo} represents the active power generation at bus m for the base case.

k_{Gm} is the rate of change of generation with variation in ψ .

P_{Tm}, Q_{Tm} represents the injected active and reactive power at bus m .

After application of reformulated power flow equations, the Eqs. 1–3 are written in compact form as

$$f(\delta, v, \psi) = 0 \tag{4}$$

where δ is the generator angle,

v is voltage at bus.

Ψ represents the loading parameter.

CPF method is based on predictor–corrector stage technique to attain solution of reformulated power flow equations. For prediction stage, tangent vector is obtained by solving power flow equations to obtain the solution as follows:

$$\begin{bmatrix} f_\delta & f_v & f_\psi \end{bmatrix} \begin{bmatrix} d_\delta \\ d_v \\ d_\psi \end{bmatrix} = 0 \tag{5}$$

Parameterization expansion is one of the viable techniques for correcting slope of the curve. It discovers the precise solution while tracing the curve or path of the voltage curve. The weak buses has been initiated by the tangent vector demonstrating together the direction of the solution path and voltage sensitivity analysis with the help of tangent vector. A weak bus has been defined as the bus indebted with a large ratio of differential voltage variation with respect to differential variation in load. This ratio is adaptable by exploiting the tangent vector.

Therefore, the tangent vector (TANV) at bus n becomes

$$TANV_n = \left[\frac{dV_n}{dP_{total}} \right] = \left[\frac{dV_n}{Cd\psi} \right] = \max \left[\left| \frac{dV_1}{Cd\psi} \right| \left| \frac{dV_2}{Cd\psi} \right| \left| \frac{dV_3}{Cd\psi} \right| \left| \frac{dV_j}{Cd\psi} \right| \right]$$

The DG location estimation using CPF method has been illustrated in the flowchart shown in Fig. 2.

3 Optimal Power Flow Technique

In restructured markets, the problem of congestion is one of the prevailing issues. This occurs in the system due to the consideration of electricity as a commodity which can be exchanged in the electricity market [3, 7, 8]. Consumers have multiple options to buy the electricity from multiple sellers each having its own price fixed for bidding. So in this condition, the customer will buy from the seller having least cost. All transactions will now carry over a single transmission route. This will create congestion problem due to multiple transactions over a single route. Thus, CM is an

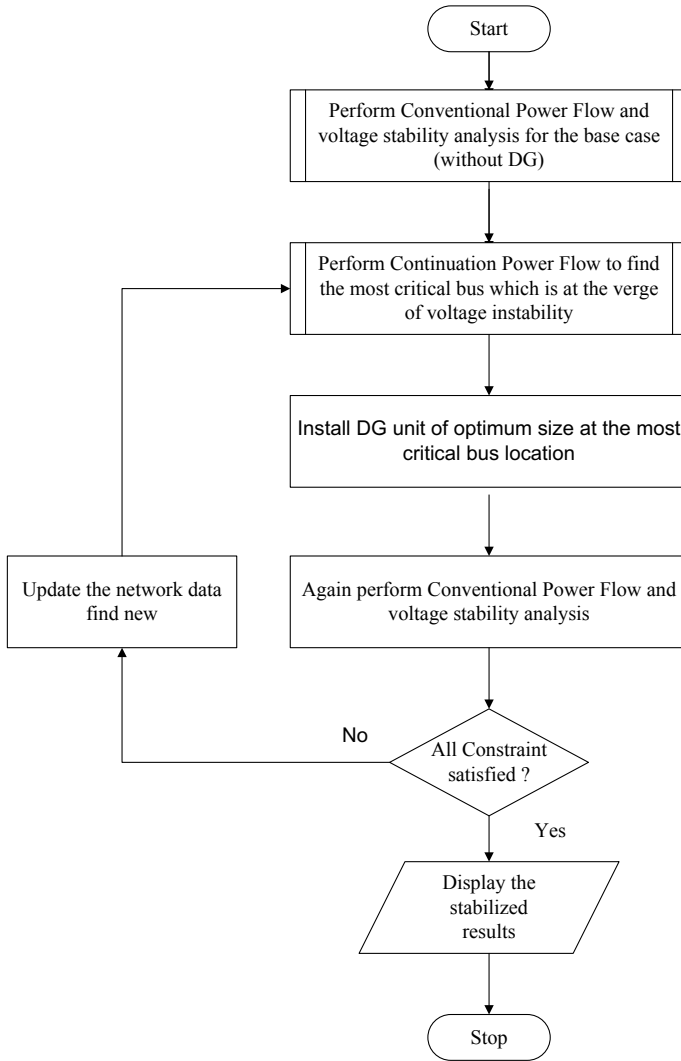


Fig. 2 Flowchart for estimating DG location with CPF method

essential action taken to relieve the network from unwanted electrical transactions, thereby enhancing the system security and reliability.

OPF technique provides the transfer of power in the optimum manner considering system operational and security constraints [9–13]. It is a mathematical tool which mainly combines the power flow equations along with economic dispatch routine with respect to numerous equality and inequality constraints.

3.1 Formulation of OPF Problem

Objective function is shown in Eq. 6. Modeling of OPF with and without DG has been shown from Eqs. 6–9.

$$\text{Min. } F = -wt_1 \left[\sum_{i=1}^n (C_{di} P_{di} - C_{si} P_{si}) \right] - wt_2 \lambda_c \quad (6)$$

wt_1 is weighting factor used for social welfare and wt_2 weighting factor for network security:

$$\left. \begin{aligned} 0 < wt_1 < 1, \\ 0 < wt_2 < 1 \\ wt_1 = 1 - wt_2 \end{aligned} \right\} \quad (7)$$

Consumers benefit function:

$$C_{di} P_{di} = x_{di} + y_{di} P_{di} - z_{di} (P_{di}^2) \quad (8)$$

Supplier offer function:

$$C_{si} P_{si} = x_{si} + y_{si} P_{si} + z_{si} (P_{si}^2) \quad (9)$$

Power flow equation:

Subject to

$$f(P_S, P_D, Q_G, \theta, V) = 0 \quad (10)$$

Power flow equation for maximum load:

Subject to

$$f(P_S, P_d, Q_{gc}, \theta_c, V_c, \lambda_c) = 0 \quad (11)$$

Loading range:

$$\lambda_{cmin} < \lambda_c < \lambda_{cmax} \quad (12)$$

Generator supply bid:

$$0 \leq P_S \leq P_{Smax} \quad (13)$$

Consumer demand bid:

$$0 \leq P_D \leq P_{D\max} \quad (14)$$

Thermal limits:

$$\left. \begin{aligned} I_{ab}(\theta, V) &\leq I_{ab\max} \\ I_{ba}(\theta, V) &\leq I_{ba\max} \\ I_{ab}(\theta_c, V_c) &\leq I_{ab\max} \\ I_{ba}(\theta_c, V_c) &\leq I_{ba\max} \end{aligned} \right\} \quad (15)$$

Generator Q limits:

$$\left. \begin{aligned} Q_{g\min} &\leq Q_g \leq Q_{g\max} \\ Q_{g\min} &\leq Q_{gc} \leq Q_{g\max} \end{aligned} \right\} \quad (16)$$

Voltage security limits:

$$\left. \begin{aligned} V_{\text{lower}} &\leq V \leq V_{\text{higher}} \\ V_{\text{lower}} &\leq V_c \leq V_{\text{higher}} \end{aligned} \right\} \quad (17)$$

The objective function with DG is shown by Eq. 18:

$$\text{Min. } F = -wt_1 \left[\sum_{i=1}^n (C_{di} P_{di} - C_{si} P_{si} - C_{dgi} P_{dgi}) \right] - wt_2 \lambda_c \quad (18)$$

Offer function of DG is given as

$$C_{dgi} P_{dgi} = x_{dgi} + y_{dgi} P_{dgi} + z_{dgi} (P_{dgi}^2) \quad (19)$$

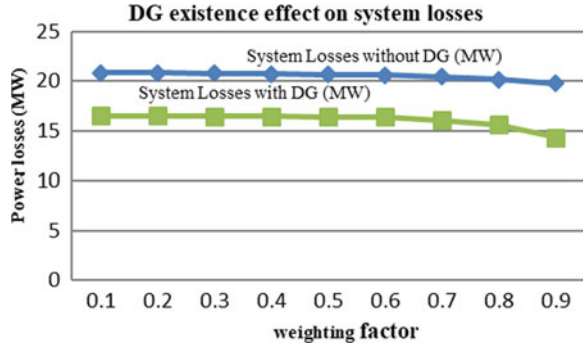
where.

C_s is the cost of supply (\$/MWh), C_d is the cost for demand (\$/MWh), C_{dgi} is the cost for supply of DG (\$/MWh), P_{si} is output power of generating unit i (MW), P_{di} is the power demand (MW), P_{dgi} is generated power of DG (MW), Q_g is the reactive power unit i (MVar), λ_c is the critical loading parameter, I is the total generating units, J is the total consumer units, N is the total transmission lines, μ_i is 1 for online unit i .

4 Results and Discussion

OPF and CPF routines are implemented on IEEE 14 bus standard system and modified system with inclusion of DG. System parameters have shown to have the improved values in the modified system [14–16]. As for consideration, the decrement in system

Fig. 3 System losses



losses after installation of DG has been shown via Fig. 3. Percentage decrement varies in range from 20 to 27% with different values of weighting factor w_{t1} . This linear increment shows the stability of the system with high weightage level.

4.1 Total Maximum Loadability and Available Loading Capability

In the voltage stability constrained OPF-based approach, the critical loadability λ_c can be expressed in terms of degree of system congestion. The loadability is maximized to the highest level for receiving the influence of the voltage stability limit. Therefore, the ALC and the TML can be defined, respectively, as

$$ALC = \lambda_c \sum P_{Li} = \lambda_c TTL \tag{20}$$

$$TML = (1 + \lambda_c) \sum P_{Li} \tag{21}$$

where λ_c is critical loading parameter, P_{Li} is load power for bus I , TTL is total transaction level.

The different values of TML and ALC with different weighting factors for base system have been shown in Fig. 4, while Fig. 5 shows the different values of TML and ALC with different weighting factors for proposed system. Total maximum loading obtained without DG is 66.311 MW, and available loading capability is 39.624 MW at $w_{t1} = 0.1$. While after sitting of DG, TTL has been alleviated to 110.276 MW, and ALC has been alleviated to 141.352 MW. Thus, DG enriches the system with both the total maximum loadability and available loading capability [17, 18].

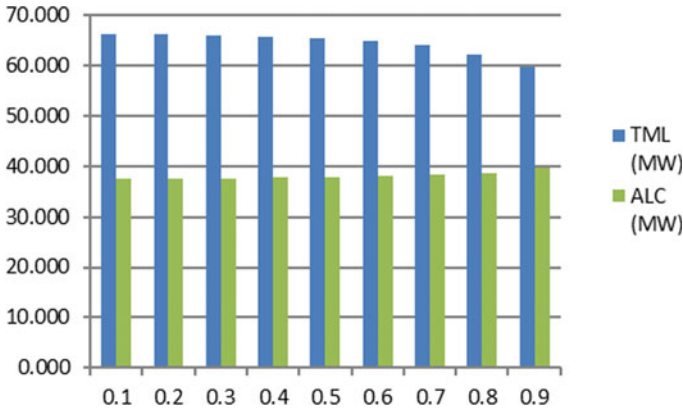


Fig. 4 TML and ALC for different weighting factors without DG

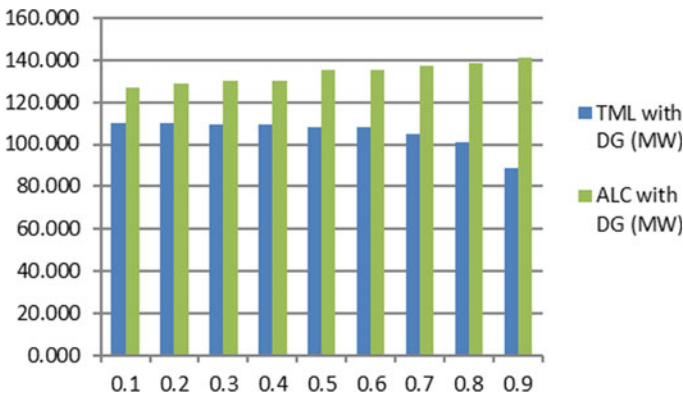


Fig. 5 TML and ALC for different weighting factors with DG

5 Conclusion

In this work, power transfer capability of the transmission network has been increased by the utilization of DGs. Since they are directly linked at the load end, serving as negative load, so they fulfill the load requirement at the place of commencement. Moreover, DGs also reduce the transmission losses which cultivate while transferring the power from one node to another. The system loadability limits are also augmented. In consequence, we can conclude that system losses, total maximum loadability and available loading capability would increase after installing of DG at optimum location. This work is of significant practical importance due to the enhanced system performance with DG, considering social welfare (wt1) and network security (wt2) as two significant weighting factors with CPF and OPF techniques.

References

1. Bavithra K, Raja SC, Venkatesh P (2016) Optimal setting of FACTS devices using particle swarm optimization for ATC enhancement in deregulated power system. *IFAC-PapersOnLine*
2. Mishra A, V. N. K. G (2016) Congestion management of deregulated power systems by optimal setting of interline power flow controller using gravitational search algorithm. *J Electr Syst Inf Technol*
3. Nayanatara C, Baskaran J, Kothari DP (2016) Hybrid optimization implemented for distributed generation parameters in a power system network. *Int J Electrical Power Energy Syst* 78:690–699
4. Saravanan M, Slochanal SMR, Venkatesh P, Abraham JPS (2007) Application of particle swarm optimization technique for optimal location of FACTS devices considering cost of installation and system loadability. *Electric Power Syst Res*, 276–283, March 2007
5. Bhattacharya B, Kumar S (2016) Loadability enhancement with FACTS devices using gravitational search algorithm. *Electrical Power Energy Syst* 78:470–479
6. Kashyap M, Kansal S (2018) Hybrid approach for congestion management using optimal placement of distributed generator. *Int J Ambient Energy* 39(2):132–142
7. Akorde MF, Nizam H, Aris I, Abkadir MZA (2010) A review of strategies for optimal placement of distributed generation in power distribution systems. *Res J Appl Sci* 5(2):137–45
8. Gautam D, Mithulananthan N (2007) Locating distributed generator in the LMP-based electricity market for social welfare maximization. *Electric Power Components Syst* 35:489–503
9. Kang CQ, Chen QX, Lin WM, Hong YR, Xia Q, Chen ZX, Wu Y, Xin JB (2013) Zonal marginal pricing approach based on sequential network partition and congestion contribution identification. *Int J Electr Power Energy Syst*
10. Sarwar M, Siddiqui AS (2016) An approach to locational marginal price based zonal congestion management in de-regulated electricity market. *Front Energy* 10(2):240–248
11. Afkousi-Paqaleh M, Noory AR, Abbaspour A, Rashidinejad M (2010) Transmission congestion management using distributed generation considering load uncertainty. In: *Asia-Pacific Power and Energy Engineering Conference, APPEEC*
12. Sood YR, Singh R (2010) Optimal model of congestion management in deregulated environment of power sector with promotion of renewable energy sources. *Renew Energy*
13. Khanabadi M, Doostizadeh M, Esmailian A, Mohseninezhad M (2011) Transmission congestion management through optimal distributed generation's sizing and placement. In: *2011 10th International Conference on Environment and Electrical Engineering, IEEEIC. EU 2011—Conference Proceedings*
14. Singh K, Parida SK (2013) Congestion management with distributed generation and its impact on electricity market. *Int J Electr Power Energy Syst*
15. Jeerapong P, Ongsakul W (2007) Optimal placement of multi-type FACTS devices for total transfer capability enhancement using hybrid evolutionary algorithm. *Electric Power Components Syst* 35:981–1005
16. Choudekar P, Asija D (2017) Prediction of voltage collapse in power system using voltage stability indices. In: *Proceeding of international conference on intelligent communication, control and devices*, pp 51–58
17. Christie RD, Wollenberg BF, Wangenstein (2000) Transmission management in the deregulated environment. *Proc IEEE* 88(2):170–195
18. Dulau LI, Abrudean M, Bica D (2016) Optimal location of a distributed generator for power losses improvement. *Proc Technol* 22:734–739

Performance Analysis of Free Space Optical Communication System Over Double Generalized Gamma Distribution with Polarization Shift Keying Modulation



Tanmay Singh, Sandhya, Rupali Srivastava, Sunil Yadav, M. Lakshmanan, Saurabh Katiyar, and Piyush Jain

Abstract Free space optical (FSO) communication system is a technology in the field of wireless communication which provides unlicensed transmission of data, bandwidth scalability and high data rate for shorter range. Atmospheric turbulence in link-area is major factor of determining performance of the system. Here, double generalized gamma (GG) distribution is used to model the irradiance fluctuations covering all atmospheric turbulent conditions. We analyse performance of the system with polarization shift keying (PolSK) modulation scheme under moderate and strong atmospheric turbulent conditions with plane and spherical wave. Further, we compare results of PolSK modulation with on-off keying (OOK) modulation. From the simulation results, it is seen that system with PolSK modulation gives 51% and 37% improvement over OOK modulation scheme under moderate and strong turbulent conditions, respectively, for plane wave and shows 53% and 48% improvement over OOK modulation scheme under moderate and strong turbulent conditions, respectively, for spherical wave.

Keywords BER · FSO · Double GG distribution · PolSK modulation

T. Singh (✉) · Sandhya · R. Srivastava · S. Yadav · M. Lakshmanan · S. Katiyar · P. Jain
Department of Electronics and Communication Engineering, Galgotias College of Engineering
and Technology, Greater Noida, India
e-mail: tanmaysinghofficial01@gmail.com

R. Srivastava
e-mail: srivastavarupali94@gmail.com

S. Yadav
e-mail: sunilyadav4640@gmail.com

M. Lakshmanan
e-mail: tmlakshmanan@gmail.com

S. Katiyar
e-mail: saurabh0277@gmail.com

P. Jain
e-mail: piyushjain181@gmail.com

1 Introduction

Free space optical (FSO) communication system transfers video, voice and data in the form of optical signals through air as the medium for transmission. In FSO, free space acts as channel between transmitter and receiver thereby no need of optical fibre cable. FSO offers various benefits over radio frequency (RF) links due to high security features, wide permit free bandwidth, quick organization, bandwidth scalability and lesser cost. It is preferred over broadband communication as it provides higher data transfer rate and protected system due to LOS operation. It provides insusceptibility to radio frequency interferences. The significant limiting element is the presence of fog and haze, rain, physical obstruction, assimilation, scattering and atmospheric turbulence which impacts the transmission of signal in the system [1, 2]. The performance of the communication system firmly relies on atmospheric conditions in zone where the connection is set up. There are various factors that impact the circulation of laser beam transmitted in free space, thereby decreasing the overall efficiency of FSO link. Atmospheric turbulence is one of the deciding factors among them. Depending on the weather conditions, turbulence is characterized as weak, moderate or strong [4, 5].

Various channel distributions are proposed to understand the effect of atmospheric turbulence in FSO communication system. Some of them are log normal distribution which works well under weak atmospheric turbulence condition, Gamma-Gamma (GG), I-K and Malaga distribution that works well under weak to strong atmospheric turbulence condition, negative exponential and K distribution that perform better under strong turbulence condition [5, 6].

Negative exponential distribution is used for long distance communication and strong turbulence conditions only [5]. Log normal distribution is a simple distribution with minimum calculation and good diversity gain by averaging the aperture of the antenna. This distribution performs well up to the propagation distance of 100 m [1]. Malaga distribution helps in perceiving the complete analysis of different parameters to obtain the diversity due to the effect of the turbulence in the system. This distribution performs under weak, moderate and strong turbulence condition [7]. Gamma distribution performs better under all the turbulence, and it is used to model the independent gamma random variables [8].

In this paper, we model the irradiance fluctuations using double generalized gamma (GG) distribution. It is the product of irradiance fluctuations in small-scale and large-scale eddies [3]. This is a type of generalized gamma distribution which takes the fluctuations by received irradiance is thought to be the mixing of small-scale by large-scale irradiance fluctuations. This distribution describes fluctuation of irradiance over atmospheric channel under the wide range of turbulent conditions accurately. Double GG distribution fits for all turbulence conditions [1, 7].

Modulation techniques are required for high information transmission rate and lesser bit error rate (BER). On-off keying (OOK) technique is mostly used modulation scheme due to simple execution with minimal cost, whereas amplitude distortion is the limitation of OOK modulation technique. Other modulation schemes like binary

phase shift keying (BPSK) and differential phase shift keying (DPSK) schemes have a downside because of complexity in the structure of receiver [3].

Polarization shift keying (PolSK) scheme is the recent modulation technique applied in FSO communication system [10]. In this paper, we use PolSK due to its limited spectrum and substandard BER performance. In this modulation technique, it is not necessary for the transmitter to coordinate polarization alignments with the receiver. Further, the intensity of light beam is more uniform while travelling through atmospheric turbulence. It provides better immune to atmospheric scintillation, better error rate performance and faster data transmission. Also, it decreases the sensitivity to phase noise of laser. Hence, PolSK modulation technique is a better choice to be used in FSO communication system [2, 10].

The arrangement of this paper can be described in the following way. Section 2 presents system model and channel model used in the research. Section 3 describes results of BER for the system with PolSK modulation used in the research are analysed and compared with OOK modulation. Lastly, the conclusion of this work is described in the Sect. 4.

2 System Model

In this work, FSO communication system is analysed for case of single input single output (SISO). The signal is modulated with PolSK modulation technique and is transmitted through additive white Gaussian noise (AWGN) channel. The optical signal received by the photo detector s is given as [8],

$$s = hRx + n \tag{1}$$

where x represents transmitted optical signal, h represents channel state, R represents the responsivity of photo detector, and n represents different noises generated in the channel.

We assume that irradiance of the received optical signal I is modelled using double GG distribution. Double GG distribution is represented in the form of probability density function (PDF) and expressed in the series form as [9]

$$f_I(I) = \sum_{l=0}^{\infty} a_l(m_1\Upsilon_1, m_2\Upsilon_2) I^{(m_1\Upsilon_1+l\Upsilon_1-1)} + a_l(m_2\Upsilon_2, m_1\Upsilon_1) I^{(m_2\Upsilon_2+l\Upsilon_2-1)} \tag{2}$$

where

$$a_l(m_1\Upsilon_1, m_2\Upsilon_2) = \frac{\Upsilon_1(-1)^l}{\Gamma(m_1)\Gamma(m_2)(l)!} \left(\Gamma\left(m_2 - [m_1 + l] \frac{\Upsilon_1}{\Upsilon_2}\right) \right) \left[\left(\frac{m_2}{\Omega_2}\right)^{\frac{\Upsilon_1}{\Upsilon_2}} \left(\frac{m_1}{\Omega_1}\right) \right]^{(m_1+l)} \tag{3}$$

$$a_l(m_2\Upsilon_2, m_1\Upsilon_1) = \frac{\Upsilon_2(-1)^l}{\Gamma(m_1)\Gamma(m_2)(l)!} \left(\Gamma\left(m_1 - [m_2 + l] \frac{\Upsilon_2}{\Upsilon_1}\right) \right) \left[\left(\frac{m_1}{\Omega_1}\right)^{\frac{\Upsilon_2}{\Upsilon_1}} \left(\frac{m_2}{\Omega_2}\right) \right]^{(m_2+l)} \tag{4}$$

$\Upsilon_i > 0, m_i > 0.5$ and $\Omega_i, i = 1, 2$ represent the parameters of the generalized gamma distribution.

Υ_1 and Υ_2 represent the distribution parameters, m_1 and m_2 represent the shaping parameters, Ω_1 and Ω_2 represent the average power of the distribution parameters.

The conditional BER for PolSK modulation is given as [10]

$$P_c = \frac{1}{2} \operatorname{erfc} \left(\sqrt{\frac{R^2 h P}{2\sigma^2}} \right) \tag{5}$$

where R represents photo detector responsivity, P represents local oscillator power and σ^2 represents variance of channel noise.

The received instantaneous electrical signal to noise ratio (SNR) γ using PolSK modulation technique is denoted by [7]

$$\gamma = \frac{R^2 h P}{\sigma^2} \tag{6}$$

From [5],

$$\gamma = \frac{(\eta I)^2}{N_0} \tag{7}$$

where N_0 denotes double-sided power spectral density(PSD) of the white Gaussian noise and η represents effective photo-current conversion ratio of the receiver.

Using (5), (6) and (7), we get

$$P_c = \frac{1}{2} \operatorname{erfc} \left(\sqrt{\frac{\mu}{2}} I \right) \tag{8}$$

where μ represents average electrical SNR and is given as $\mu = \frac{(\eta I)^2}{N_0}$.

The unconditional BER [10] is given as

$$P_e = \int_0^\infty P_c f_I(I) dI \tag{9}$$

Using (2), (8) in (9), we obtain

$$P_e = \frac{1}{2} \int_0^\infty \operatorname{erfc}\left(\sqrt{\frac{\mu}{2}} I\right) \times \left(\sum_{l=0}^\infty a_l(m_1 \Upsilon_1, m_2 \Upsilon_2) I^{(m_1 \Upsilon_1 + l \Upsilon_1 - 1)} + a_l(m_2 \Upsilon_2, m_1 \Upsilon_1) I^{(m_2 \Upsilon_2 + l \Upsilon_2 - 1)} \right) dI \tag{10}$$

$$P_e = \frac{1}{2} \sum_{l=0}^\infty a_l(m_1 \Upsilon_1, m_2 \Upsilon_2) \int_0^\infty I^{(m_1 \Upsilon_1 + l \Upsilon_1 - 1)} \operatorname{erfc}\left(\sqrt{\frac{\mu}{2}} I\right) dI + \frac{1}{2} \sum_{l=0}^\infty a_l(m_2 \Upsilon_2, m_1 \Upsilon_1) \int_0^\infty I^{(m_2 \Upsilon_2 + l \Upsilon_2 - 1)} \operatorname{erfc}\left(\sqrt{\frac{\mu}{2}} I\right) dI \tag{11}$$

From [11]

$$\int_0^\infty x^{\alpha-1} \operatorname{erfc}(Cx) dx = \frac{1}{\alpha C^\alpha \sqrt{\pi}} \Gamma\left(\frac{\alpha+1}{2}\right) \tag{12}$$

Using (11) and (12), we obtain the final expression for unconditional BER as,

$$P_e = \frac{1}{2} \sum_{l=0}^\infty a_l(m_1 \Upsilon_1, m_2 \Upsilon_2) \Delta_1 + a_l(m_2 \Upsilon_2, m_1 \Upsilon_1) \Delta_2 \tag{13}$$

where

$$\Delta_1 = \frac{1}{2} \left(\frac{1}{(m_1 \Upsilon_1 + l \Upsilon_1) \left(\sqrt{\frac{\mu}{2}}\right)^{(m_1 \Upsilon_1 + l \Upsilon_1)} (\sqrt{\pi})} \right) \times \left(\Gamma\left(\frac{m_1 \Upsilon_1 + l \Upsilon_1 + 1}{2}\right) \right) \tag{14}$$

$$\Delta_2 = \frac{1}{2} \left(\frac{1}{(m_2 \Upsilon_2 + l \Upsilon_2) \left(\sqrt{\frac{\mu}{2}}\right)^{(m_2 \Upsilon_2 + l \Upsilon_2)} (\sqrt{\pi})} \right) \times \left(\Gamma\left(\frac{m_2 \Upsilon_2 + l \Upsilon_2 + 1}{2}\right) \right) \tag{15}$$

3 Simulation Result and Discussion

We use MATLAB to evaluate bit error rate (BER) of the free space optical system with PolSK modulation over double GG distribution. It is required to truncate (13) into finite series for numerical calculation. So, the maximum limit of l in (13) is required to be finite value. We consider the maximum limit of l as 20, 50, 100, and the result is found to be almost equal. Here, we present the result for the values of l varying from 0 to 20.

Figure 1 illustrates average BER of double GG distribution using PolSK modulation and comparison with OOK modulation for $\sigma_{rytov}^2 = 2$ and $\frac{I_0}{R_o} = 0.5$. We use the parameters of plane wave and moderate atmospheric turbulence condition which are, $m_1 = 0.55, m_2 = 2.35, \Upsilon_1 = 2.169, \Upsilon_2 = 0.8530, \Omega_1 = 1.5$ and $\Omega_2 = 0.9671$ [12]. It is found that at average electrical SNR of 60 dB, BER is 0.0003001 and 0.0001989 for double GG distribution using OOK and PolSK modulation techniques, respectively.

Figure 2 illustrates average BER of double GG distribution using PolSK modulation and comparison with OOK modulation for $\sigma_{rytov}^2 = 25$ and $\frac{I_0}{R_o} = 1$. We use the parameters of plane wave and strong atmospheric turbulence condition which are, $m_1 = 0.5, m_2 = 1.8, \Upsilon_1 = 1.8621, \Upsilon_2 = 0.7638, \Omega_1 = 1.5074$ and $\Omega_2 = 0.9280$ [12]. It is found that at average electrical SNR of 60 dB, BER is 0.001997 and 0.001459 for double GG distribution using OOK and PolSK modulation techniques, respectively.

Figure 3 illustrates average BER of double GG distribution using PolSK modulation and comparison with OOK modulation for $\sigma_{rytov}^2 = 2$ and $\frac{I_0}{R_o} = 0$. We use

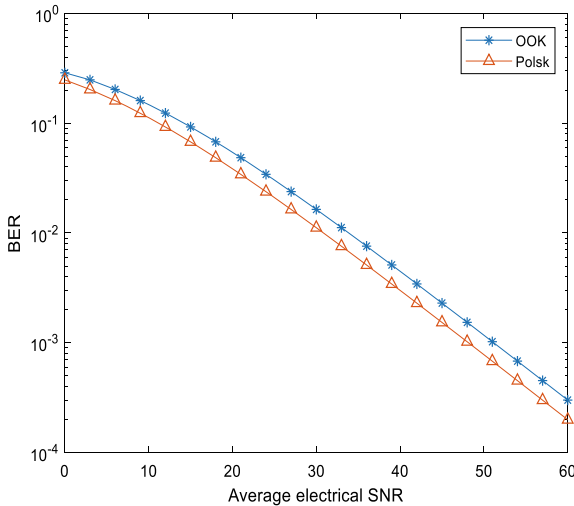


Fig. 1 Average BER of double GG for plane wave and moderate turbulence with $\sigma_{rytov}^2 = 2$ and $\frac{I_0}{R_o} = 0.5$

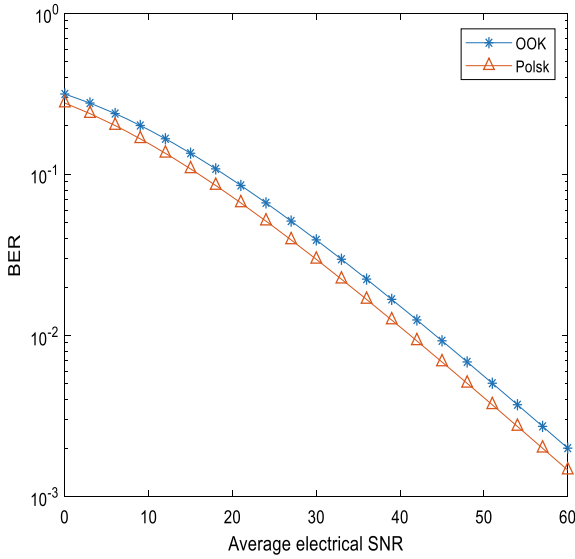


Fig. 2 Average BER of double GG for plane wave and strong turbulence with $\sigma_{rytov}^2 = 25$ and $\frac{I_0}{R_o} = 1$.

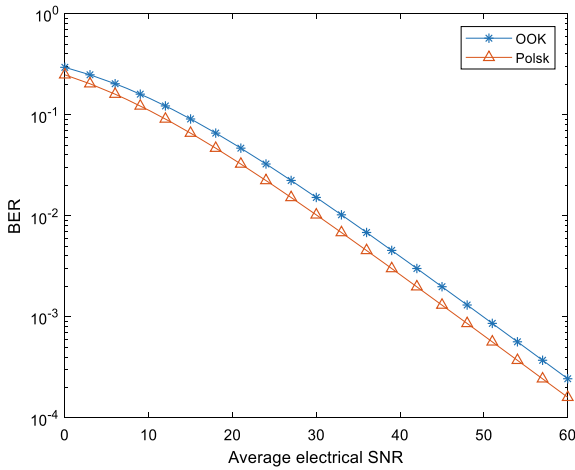


Fig. 3 Average BER of double GG for spherical wave and moderate turbulence with $\sigma_{rytov}^2 = 2$ and $\frac{I_0}{R_o} = 0$.

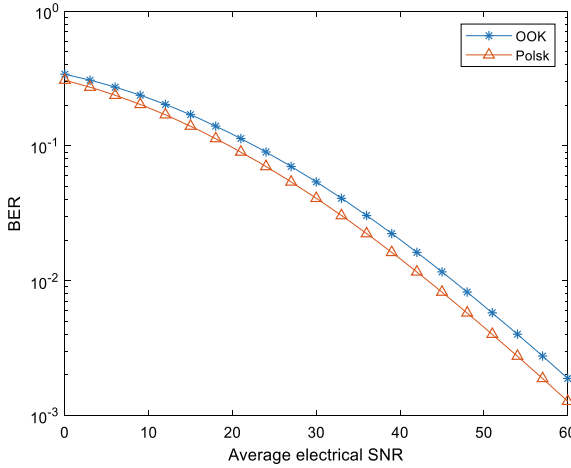


Fig. 4 Average BER of double GG for spherical wave and strong turbulence with $\sigma_{rytov}^2 = 5$ and $\frac{I_0}{R_o} = 1$

the parameters of spherical wave and moderate atmospheric turbulence condition which are $m_1 = 2.65$, $m_2 = 0.85$, $\Upsilon_1 = 0.9135$, $\Upsilon_2 = 1.4385$, $\Omega_1 = 0.9836$ and $\Omega_2 = 1.175$ [12]. It is found that at average electrical SNR of 60 dB, BER is 0.0002437 and 0.0001597 for double GG distribution using OOK and PolSK modulation techniques, respectively.

Figure 4 illustrates average BER of double GG distribution using PolSK modulation and comparison with OOK modulation for $\sigma_{rytov}^2 = 5$ and $\frac{I_0}{R_o} = 1$. We use the parameters of spherical wave and strong atmospheric turbulence condition which are, $m_1 = 3.2$, $m_2 = 2.8$, $\Upsilon_1 = 0.4205$, $\Upsilon_2 = 0.6643$, $\Omega_1 = 0.8336$ and $\Omega_2 = 0.9224$ [12]. It is found that at an average electrical SNR of 60 dB, BER is 0.00188 and 0.001271 for double GG distribution using OOK and PolSK modulation techniques, respectively.

Double GG distribution is the generalized distribution model, and it performs under wide range of atmospheric turbulent conditions, i.e. from weak to strong. From the simulation results, BER of double GG with PolSK modulation technique for plane and spherical wave under moderate and strong turbulent condition performs better than OOK modulation. This is because PolSK has limited spectrum and substandard BER performance. PolSK provides better immune to atmospheric scintillation, better error rate performance and faster data transmission as compared to OOK modulation technique.

4 Conclusion

In this paper, BER performance of FSO communication system was analysed with PolSK modulation technique over double GG distribution for average electrical SNR between 0 to 60 dB. Then, the results were compared with OOK modulation technique. Here, we analysed the performance of the system with polarization shift keying (PolSK) modulation scheme under moderate and strong atmospheric turbulent conditions with plane and spherical wave. Further, we compared the results of PolSK modulation with on-off keying (OOK) modulation. From the results, it was found that the system with PolSK modulation had 51% and 37% improvement over OOK modulation under moderate and strong atmospheric turbulent conditions, respectively, for plane wave and offered 53% and 48% improvement over OOK modulation under moderate and strong atmospheric turbulent conditions, respectively, for spherical wave as PolSK experienced less amplitude distortion and more stability due to the polarization states compared to OOK modulation technique. Thus, PolSK modulation technique performed better in double GG distribution modelled free space optical communication system.

References

1. Anbarasi K, Hemanth C, Sangeetha RG (2017) A review on channel models in free space optical communication systems. *Opt Laser Technol* 97:161–171
2. Jeyaseelan J, Kumar DS, Caroline BE (2018) PolSK and ASK modulation techniques based BER analysis of WDM-FSO system for under turbulence conditions. *Wireless Pers Commun* 103(4):3221–3237
3. Tiwari P, Kumar N, Singh P, Srivastava C, Lakshmanan M, Jain P, Katiyar S (2019) Modeling and analysis of hybrid SIM with L-PPM and MSK over double generalized gamma distribution in free space optical communication system. In: 2019 International Conference on Vision Towards Emerging Trends in Communication and Networking (ViTECoN) IEEE, pp 1–4
4. Jain P, Jayanthi N, Lakshmanan M, Saxena A, Jain A (2019) Outage probability and average capacity analysis over α - μ distribution in free space optical communication system. In: 2019 International Conference on Vision Towards Emerging Trends in Communication and Networking (ViTECoN). IEEE, pp 1–4
5. Nistazakis HE, Assimakopoulos VD, Tombras GS (2011) Performance estimation of free space optical links over negative exponential atmospheric turbulence channels. *OPTIC-Int J Light Electron Optics* 122(24):2191–2194
6. Majumdar AK (2005) Free-space laser communication performance in the atmospheric channels. *J Optical Fiber Commun Rep* 2(4):345–396
7. Prabu K, Gupta S, Jaiswal S (2018) Impact of pointing errors and turbulence effects over generalized turbulence channel model. *Photonic Netw Commun* 36(1):96–105
8. Kaur P, Jain VK, Kar S (2014) Effect of atmospheric conditions and aperture averaging on capacity of free space optical links. *Opt Quant Electron* 46(9):1139–1148
9. Yi X, Yao M, Wang X (2017) MIMO FSO communication using subcarrier intensity modulation over double generalized gamma fading. *Optics Commun* 382:64–72
10. Prabu K, Cheepalli S, Kumar DS (2014) Analysis of PolSK based FSO system using wavelength and time diversity over strong atmospheric turbulence with pointing errors. *Optics Commun* 324:318–323

11. Prudnikov AP, Brychkov IA, Marichev OI (1992) Integrals and series, vol. 2, pdf
12. Kashani MA, Uysal M, Kavehrad M (2015) A novel statistical channel model for turbulence-induced fading in free-space optical systems. *J Lightwave Technol* 33(11):2303–2312

Binary Differential Evolution-Based Feature Selection for Hand Gesture Classification



Anamika, Rinki Gupta, and Ghanapriya Singh

Abstract In any classification problem involving a large feature set, the feature selection step is essential for not only reducing the computational complexity of the classifier by removing the redundant features, but also possibly improving the classification accuracy by utilizing the most relevant features. The utility of evolutionary algorithms such as differential evolution and genetic algorithm in feature selection has been shown in literature. However, unlike other evolutionary algorithms, including genetic algorithm, the use of differential evolution algorithm on a binary representation of the variables to be optimized is not straight forward, since the standard differential evolution needs to be modified. In this paper, a correlation-based feature subset selection strategy is formulated using a modified mutation operator given in literature for solving binary space optimization using differential evolution. The proposed feature subset selection strategy is applied to hand-activity classification using data collected from multiple surface electromyogram (sEMG) and motion sensors. The effect of tuning the crossover rate in the proposed algorithm on the feature selection process is studied. For the considered feature set, the proposed algorithm performs better as compared to genetic algorithm and other conventional approaches such as rank-based strategy ReliefF and the best first approach. The performance of the feature selection algorithms is compared in terms of the dimension of the selected feature subsets as well as the accuracies with which the hand activities are classified.

Anamika · R. Gupta (✉)

Electronics and Communication Engineering Department, Amity University Uttar Pradesh,
Noida, UP, India

e-mail: rgupta3@amity.edu

Anamika

e-mail: anamikasmailbox@gmail.com

G. Singh

Department of Electronics Engineering, National Institute of Technology Uttarakhand, Srinagar,
HP, India

e-mail: ghanapriya@nituk.ac.in

© Springer Nature Singapore Pte Ltd. 2021

R. Agrawal et al. (eds.), *Advances in Smart Communication and Imaging Systems*,

Lecture Notes in Electrical Engineering 721,

https://doi.org/10.1007/978-981-15-9938-5_22

Keywords Feature selection · Binary differential evolution · Electromyogram · Accelerometer · Hand-activity classification

1 Introduction

Hand-activity classification using non-invasive, wearable sensors finds utility in wide range of applications such as in developing assistive devices, prosthetic limb controls, health monitoring, sport sciences and rehabilitation studies [1, 2]. In literature, the combined use of surface electromyography (sEMG) and accelerometers has been shown to be useful in capturing the motion of human hand [3]. Surface electromyography records the electric potential developed in the muscles when it is utilized in performing an activity. Whereas the signal recorded from accelerometer is indicative of the tilt angle of the point, where it is placed on the hand with respect to the earth. Directly using the signals acquired from multiple sensors for classification is impractical, since it will require huge memory storage and large computation time. Moreover, such signals have uncertainty in parameters that define their generation and their representation in exact mathematical function is not feasible. Hence, the signals are represented using statistical measures such as mean absolute value, standard deviation, auto-regressive (AR) coefficients and mean frequency [4, 5].

A primary challenge in multi-class classification problems is to determine a subset of most relevant features that would perform equally well as that of the original feature set in terms of achievable classification accuracies. These techniques can broadly be classified into two classes, namely the wrapper method and the filter method. In the wrapper method, the search for the best feature subset is performed using a heuristic search method that involves the classifier itself in the algorithm [6–8]. This method is more effective in providing high classification accuracies as compared to the filter method, however, the computation time and memory requirement is significantly higher. The filter method selects the feature subset independent of a classifier. Here, the *worth* of the feature subset is evaluated using parameters like correlation between features and that between features and the target class. Filter method is a faster approach and can be used with any classifier.

In this work, we propose a filter-based feature selection approach to select a subset of features extracted from multiple sEMG and accelerometer signals for hand-activity classification. The proposed correlation-based binary differential evolution (CBDE) for feature selection is experimentally tuned to improve speed of convergence, while keeping the number of selected features to a minimum. The remaining paper is arranged as follows. Section 2 comprises brief description of the classification problem in general and the algorithms available in literature for feature selection. Section 3 describes the formulation of the proposed CBDE algorithm for feature selection. Section 4 contains experimental results with actual sEMG and accelerometer signals for classification of hand activities. Effect of tuning the crossover rate (CR) on CBDE and the performance of the CBDE algorithm and other conventional

feature selection techniques are presented. Section 5 contains conclusions drawn from the proposed work.

2 Related Work

2.1 Basic Steps in Signal Classification

The basic steps involved in a classification problem include pre-processing of signals, extraction of multiple features, feature selection for dimensionality reduction and classification using a suitable classifier. Pre-processing involves removal of baseline in data and segmentation of data, i.e., identification of start points and end points of activity from the rest period, which has already been done in the database. In feature extraction, the sEMG and motion sensors signals are converted into some form of numerical features or statistical measure that can be fed to the classifier. The features that are used for sEMG in the experiment are given in Table 1, where N is the total number of samples in the signal considered. Mean value is given by $\bar{x} = (1/N) \sum_{i=1}^N x_i$. The threshold μ in evaluation of zero-crossing parameter is taken as two times the standard deviation of the sEMG signal recorded during rest period, when no activity is being performed. In Table 1, parameter P_j is the power spectrum of sEMG at

Table 1 Features extracted for each channel for sEMG and accelerometer

Feature	Definition (per channel)
Mean absolute value	$MAV = \frac{1}{N} \sum_{i=1}^N x_i $
Standard deviation	$STD = \left(\frac{1}{N} \sum_{i=1}^N (x_i - \bar{x})^2 \right)^{\frac{1}{2}}$
Root mean square	$RMS = \sqrt{\frac{1}{N} \sum_{i=1}^N x_i^2}$
Zero crossing	$ZC = \sum_{i=1}^{N-1} [\text{sgn}(x_i \times x_{i+1}) \cap x_i - x_{i+1}] \geq \mu$
Mean frequency	$MNF = \frac{\sum_{j=1}^M f_j P_j}{\sum_{j=1}^M P_j}$
Median frequency	$MDF = \sum_{j=1}^{MDF} P_j = \sum_{j=MDF}^M P_j = \frac{1}{2} \sum_{j=1}^M P_j$
AR coefficient	$x_i = \sum_{m=1}^M a_m x_{i-m} + w_i$

frequency $f_j, j = 1, 2 \dots N; a_m, m = 1, 2 \dots M$, are the AR model coefficients for order M and w_i is the prediction error.

Mean absolute value and standard deviation have also been extracted from accelerometer signals [4]. These features are calculated for each channel. Now, feature selection techniques are used to select features that have good relevance and performance. The feature selection techniques considered in this paper are discussed in the following section. The feature set is then used for learning a classifier to enable it to predict the target class from given a set of test features. In literature, many classifiers are used and support vector machine (SVM) has been reported to perform better [1]. Hence, in this work, SVM has been used for classification of hand activities.

2.2 Conventional Feature Selection Techniques

ReliefF is a ranking algorithm that allots weight to each of the feature based on their relevance to the class [6]. Weights are given in range of $[-1, 1]$ in a way that large positive value corresponds to the more significant features. Although the computation is fast, but redundant features cannot be determined. Best first strategy (BFS) is a heuristic search strategy that selects the most favorable feature and then expands the set of selected features by adding one feature at a time in accordance with the fitness function [6]. Search of BFS is often limited to fixed number of subset expansion, say N , since the exploration of the entire feature set would require considerable amount of time.

Evolutionary algorithms (EA) have gained attention in recent years because of their effective global search on optimization problems. One of the popular EA is genetic algorithm (GA) that imitates the process of natural selection to find the fittest outcome for optimization problems [7]. Crossover and mutation are carried out on randomly selected parents from one generation to generate evolved children for the next generation. The performance of GA highly depends upon initialization that is the initial population and number of features given as input. Another EA is the differential evolution (DE) algorithm (DE/RAND/1/BIN) which was developed by Storn and Price [8] for optimization problems. Here, RAND, 1 and BIN indicate random population initialization, number of differences taken and crossover due to independent binomial experiments, respectively. These population-based search techniques provide the means for extracting the best possible performance features of a system by using an objective function to evaluate the fitness of individuals in a generation. While in GA, the objective function is designed to be minimized, in DE, the optimization is designed such that the objective function is to be maximized. Limits may be defined for each variable as.

$$X_j^L \leq X_{j,i,1} \leq X_j^U, \quad (1)$$

where $i = 1, \dots, N_p$ and $j = 1, \dots, D$. The first generation is randomly initialized with population of size N_p and dimension D with parameter values assigned

uniformly between the limits defined in (1). In GA, each individual is known as a chromosome. Many developments have been done for the representation of individuals, such as binary, integer or real-valued representations [7]. In DE, basic representation of individual is in real values and use of DE with binary representation of individuals is an active area of research. For both GA and DE, the calculation of the objective function is carried out for each individual; however, the mutation and crossover criteria are different.

The selection of parent chromosome in GA that will reproduce depends upon the objective function; higher the function higher will be the chances of selection. In this work, it has been determined experimentally that proportional scaling function and stochastic uniform selection function perform better as compared to other possible techniques. Then, crossover is performed on more than one parent chromosome in which a segment is exchanged to form new individual called as off-spring. To increase the search space mutation, random flipping is performed. If the off-spring has fitter objective function, then it will replace the chromosome with lower fitness value. The process repeats till the stopping criterion is satisfied, which may be the maximum number of iteration that may be carried out to search the best individual or using a stalling criterion. Here, when the improvements in the objective function are within the tolerance limits of 1×10^{-6} or 1×10^{-10} for at least 50 iterations then the algorithm stalls.

In DE, each individual, named as the target vector $X_{j,i,G}$ in (3), is selected sequentially once per iteration, and three more distinct vectors, $X_{r1,G}$, $X_{r2,G}$ and $X_{r3,G}$ are randomly selected to perform mutation using.

$$V_{i,G+1} = X_{r1,G} + F(X_{r2,G} - X_{r3,G}) \quad (2)$$

where the mutation factor $F \in [0.5, 2]$ and $V_{i,G+1}$ is the mutant vector. The recombination process in DE includes the selection between previous generation and new generation. Depending on the crossover rate (CR) probability, elements are selected from the target vector $X_{j,i,G}$ or the mutant vector $V_{i,G+1}$ to form a trial vector $U_{i,G+1}$, giving

$$U_{j,i,G+1} = \begin{cases} V_{j,i,G+1} & \text{if } \text{rand}_{j,i} \leq \text{CR} \text{ or } j = I_{\text{rand}} \\ X_{j,i,G} & \text{if } \text{rand}_{j,i} > \text{CR} \text{ and } j \neq I_{\text{rand}} \end{cases} \quad (3)$$

Just like in GA, comparison is carried out between the function of target and trial vector. The fitter individual is included in the next generation. The algorithm is executed till some stopping criterion is reached.

Binary DE is recent variant of aforementioned basic DE. Binary representation is required in problems where the solution contains either 'yes' or 'no'. In the considered problem, either feature is 'selected' or 'not selected'. Selected features are represented by value 1 and a 0 value indicates that the feature is removed from selected feature subset. The use of binary representation obviates the need to ensure that there

is no repetition of features in the selected subset, which is otherwise required if real-valued representation is used in DE for feature selection [9]. The proposed CBDE comprises of binary DE with a correlation-based objective function. The details of CBDE are given in the next section.

3 Proposed Feature Selection Algorithm

3.1 Correlation-Based Selection of Features

The intension of selecting only a subset of feature for classification instead of the whole dataset is that many features are redundant. These features do not contribute much toward classification and thus can be removed without causing loss of information. Proposed algorithm evaluates correlation of each feature with the class as well as the inter-correlation among features. Search of the optimization process depends upon the objective function which calculates the *worth* of the feature subset. The objective function $f(S)$ [6] used in the algorithm for a subset S containing k number of features is given as

$$f(S) = \frac{k * r_{cf}}{\sqrt{k + k(k - 1)r_{ff}}}. \quad (4)$$

In (4), the average correlation between feature and class is given by r_{cf} , whereas that between two features is given by r_{ff} . Thus, r_{cf} is a measure of the relevance of the features and r_{ff} is a measure of the redundancy among the features. The feature dataset must be quantized before calculating the correlation. Here, symmetrical uncertainty (SU) [10] has been considered to evaluate the correlations. Symmetrical uncertainty is a normalized variant of the mutual information, defined as

$$SU = 2 * \frac{H(M) - H(M|N)}{H(M) + H(N)}, \quad (5)$$

where $H(M)$ and $H(N)$ are the entropy of random variables M and N , while $H(M|N)$ is the entropy of M when N is given. Information gain gives a biased value for features having higher values, whereas SU makes the effect of all features comparable. The correlation matrix containing correlation of each feature with every other feature is given as input to the CBDE algorithm.

3.2 Binary Differential Evolution

The significant difference between CBDE and DE is in the binary mutation criteria required in CBDE. The binary mutation operator is defined in terms of certain probability pf that is predefined to a value 0.25 [11], giving

$$V_{G+1} = \begin{cases} 1 - X_1 & \text{if } X_2 \neq X_3 \wedge \text{rand} < pf \\ X_1 & \text{otherwise} \end{cases} \quad (6)$$

A pseudo-code for proposed CBDE used in the program is given as follows.

```

begin
  randomly generate initial population in binary
  format
  calculate fitness of individuals in population using
  (4, 5)
  while not(stopping criteria is met) do
    for i=1 to number of individual
      Choose target vector
      Randomly choose 3 parent vectors:  $X_{1,G}$ ,  $X_{2,G}$ 
      and  $X_{3,G}$ 
      if  $X_{2,G}(n) \neq X_{3,G}(n)$  and  $\text{rand} \leq pf$ ,
         $V_{j,k,G+1}(n) = 1 - X_{1,G}$ 
      else
         $V_{j,k,G+1}(n) = X_{1,G}$ 
      end
      if  $V_{j,k,G+1}(n)$  have probability  $\geq CR$  then
         $U_{j,k,G+1}(n) = V_{j,k,G+1}(n)$ 
      end
      if U has better fitness than  $X_1$  then
        replace  $X_{1,G+1}$  by  $U_{j,k,G+1}$ 
        replace fitness of  $X_{1,G+1}$  by fitness of  $U_{j,k,G+1}$ 
      end
    end
  end
end.

```

4 Results

In this experiment, actual sEMG and accelerometer data available in the open-source Ninapro database have been utilized [3]. The features extracted from the sEMG and accelerometer signals that were used for classification are summarized in Table 1. Six wrist activities performed by six healthy subjects have been considered. The activities include wrist activities, such as supination, pronation, radial deviation ulnar deviation, extension, and flexion. The data is recorded from the forearm of the subjects, using 10 surface electrodes placed on it. Eight electrodes were placed at the periphery of radio-humeral joint with equal spacing and two were placed on major

activity spots of forearm. The data from sensors were transferred to the computer for further processing. Features were extracted according to Sect. 2.2 above from the pre-processed data.

In CBDE, the population size is selected as 50 individuals, which is a typical value for EA. In EA, it is favorable to have maximally distinct individuals in the initial population to broaden the search space. In CBDE, the initial set of individuals is generated randomly to contain 2 to 100 features. The number of ones in the individuals, which denotes subset size in this work, changes with the search for fittest subset. Moreover, the effect of CR parameter tuning on convergence and number of feature selected are shown in Figs. 1 and 2, respectively. Here, the tolerance value of 1×10^{-6} for 50 consecutive iterations was taken as the stalling criteria.

In Fig. 1, the optimum value objective function is plotted for different values of CR for the best individual in every iteration of the algorithm. When CR is lower than 0.4, as shown for CR = 0.1 in solid black line in Fig. 1, the rate of convergence is slow and the algorithm executes for more iterations to search for the best individual. Whereas when a high value of CR is considered, say 0.9, depicted in dotted lines in Fig. 1, the CBDE algorithm converges faster, however, the best objective function is lower than those obtained with other CR values. When convergence rate is considered, the

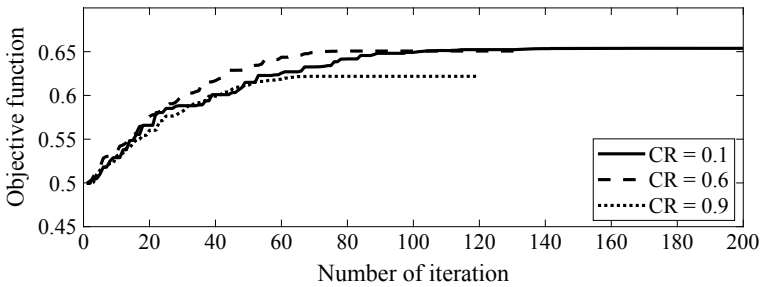


Fig. 1 Objective function of CBDE for CR values of 0.1 (solid line), 0.6 (dashed line), 0.9 (dotted line)

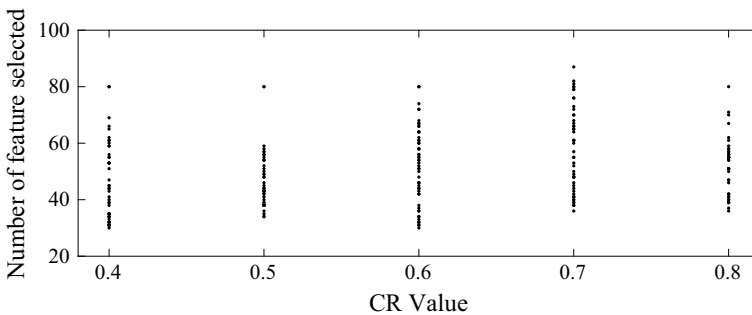


Fig. 2 Number of features selected for CR values between 0.4 and 0.8

optimal range of CR is determined to be between 0.4 and 0.7. The best objective functions for CR = 0.6 are plotted in dashed line as shown in Fig. 1. Figure 2 depicts the number of features selected in different iterations of the CBDE algorithm for different CR values. The minimum number of features is obtained as 31 for CR values 0.4 and 0.6. Other CR values result in a higher dimension of the best feature subset.

The classification accuracy using SVM taking the complete feature set of 170 features is 96.29%, whereas that for subsets selected using CBDE are 96.29% for CR = 0.4 and 98.15% for CR = 0.6. Thus, at CR = 0.6, the selected subset is obtained at fastest rate with least size and classification accuracy higher than that obtained using the entire feature set. Even when the tolerance value of the stalling criterion in the CBDE algorithm was increased to 1×10^{-4} , the same feature set was selected and the algorithm performed equally well. The performance of CBDE is compared with that of GA and other conventional algorithms.

The binary DE is based on maximization of fitness function while GA will try to minimize fitness function, thus, the tolerance function of the two are different. The convergence of objective function of GA is shown in Fig. 3. Table 2 contains the performance of GA, CBDE, ReliefF and best first approach for selecting best feature sets for classifying the considered six wrist activities.

When the tolerance (stated as *tol fun* in Table 2) of 1×10^{-6} was considered, the numbers of features selected by GA are 57 with the classification accuracy of

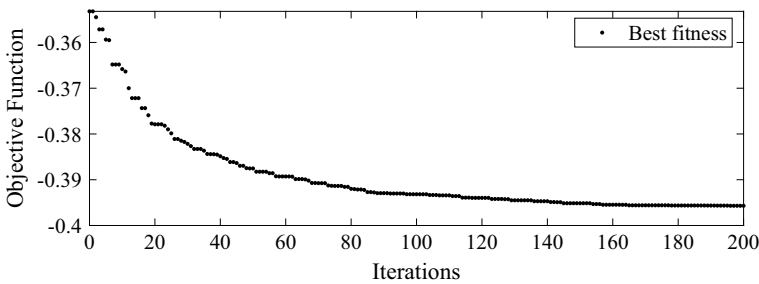


Fig. 3 Best fitness of objective function of genetic algorithm

Table 2 Number of features selected in a subset and their accuracies for BDE, GA, ReliefF and best first search strategies

Search strategy	Number of features selected	Accuracy (%)
GA (tol fun = 1×10^{-6})	57	96.29
GA (tol fun = 1×10^{-10})	44	96.29
CBDE (tol fun = 1×10^{-4})	31	98.15
CBDE (tol fun = 1×10^{-6})	31	98.15
ReliefF	31	96.29
Best first	31	96.29

96.2963%. Even for a considerably lower tolerance of 1×10^{-10} , the number of features selected is only reduced to 44, however, the classification accuracy remains same. For the ranking algorithms, the selection of final feature set was chosen according to the number of the feature in final subset of CBDE. According to the ranking algorithm ReliefF, the best 31 features resulted in the classification accuracy of 96.29%. Best first approach also provided the same classification accuracy for the feature set containing 31 features.

Additionally, it is observed from the subset selected by CBDE that classification of activities show improvement in performance when more number of accelerometer features are selected than EMG features [12]. The algorithms CBDE, ReliefF and best first selected 19, 18 and 22 accelerometer features and 12, 13 and 9 sEMG features, respectively. No such selection pattern was observed in GA.

5 Conclusion

Real-world applications of hand-activity recognition including human-machine interface, prosthetic control and rehabilitation sciences require the collection of data from multiple sensors, such as electromyogram (EMG) and motion sensors. For classification of the activities, a suitable set of features is extracted from the data. Any redundancy, noise or presence of artifacts in data could reduce its classification accuracy. Hence, for high dimensional feature sets, the redundant features must be removed to reduce the computation process, while the relevant features are retained to avoid deteriorating the performance of the classifier in terms of classification accuracy. This paper presents a correlation-based feature subset selection strategy using the binary differential evolution (CBDE) algorithm. From experiments, it is found that the CR value can neither be very low nor very high for an ideal performance. For the considered feature set containing the most prominently used features for EMG and accelerometer data, classification accuracy for the feature subset selected using the proposed CBDE algorithm is higher as compared to that obtained using feature subsets selected using GA, ReliefF and best first, and even when the entire feature set is used for classification.

Acknowledgements The authors would like to recognize the funding support provided by the Science & Engineering Research Board, a statutory body of the Department of Science & Technology (DST), Government of India, SERB file number ECR/2016/000637.

References

1. Kuzborskij I, Gijsberts A, Caputo B (2012) On the challenge of classifying 52 hand movements from surface electromyography. In: 34th Annual Int Conference of the IEEE Engineering in Medicine and Biology Society, pp 4931–4937

2. Porciuncula F, Roto AV, Kumar D, Davis I, Roy S, Walsh CJ, Awad LN (2018) Wearable movement sensors for rehabilitation: a focused review of technological and clinical advances. *PM&R* 10(9):S220–S232
3. Gupta R (2019) A quantitative performance assessment of surface EMG and accelerometer in sign language recognition. In: 2019 9th Annual Information Technology, Electromechanical Engineering and Microelectronics Conference (IEMECON), pp 242–246
4. Phinyomark A, Phukpattaranont P, Limsakul C (2012) Feature reduction and selection for EMG signal classification. *Expert Syst Appl* 39(8):7420–7431
5. Gupta R, Kulshreshtha A (2016) Analysis of dual-channel surface electromyogram using second-order and higher-order spectral features. In: 2nd IEEE International Conference on Communication Control and Intelligent Systems (CCIS), pp 49–53
6. Hall MA (2000) Correlation-based feature selection of discrete and numeric class machine learning. In: *Proceeding of the seventeenth international conference on machine learning*, pp 359–366
7. Frohlich H, Chapelle O, Scholkopf B (2003) Feature selection for support vector machines by means of genetic algorithm. In: 15th IEEE international conference on Tools with artificial intelligence, proceedings
8. Storn R, Price K (1997) Differential evolution—a simple and efficient heuristic for global optimization over continuous spaces. *J Global Optim* 11(4):341–359
9. Ani AA, Alsukker A, Khushaba RN (2013) Feature subset selection using differential evolution and a wheel based search strategy. *Swarm Evol Comput* 9:15–26
10. Sosa-Cabrera G, García-Torres M, Gómez-Guerrero S, Schaerer CE, Divina F (2019) A multivariate approach to the symmetrical uncertainty measure: application to feature selection problem. *Inf Sci* 494:1–20
11. Deng C, Liang C (2010) Binary differential evolution algorithm with new mutation operator. In: *IEEE international conference on intelligent computing and intelligent systems*, vol 1
12. Zhang X, Chen X, Li Y, Lantz V, Wang K, Yang J (2011) A framework for hand gesture recognition based on accelerometer and EMG sensors. *IEEE Trans Syst Man Cybern B Cybern Part A: Syst Humans* 41(6):1064–1076

LoRa-Based Wireless Automation and Monitoring System



Mayank Tiwari, Kumar Abhishek Ranjan, Amit Sehgal, Akash Kumar,
and Saurabh Srivastava

Abstract IoT is the basic need of the present scenario. There exist several methods in network architecture to implement IoT. With growing technology, low power wide area network (LPWAN) is the latest technology in the IoT field. LoRaWAN is one of the open protocols for LPWAN which gives the better performance in urban areas in the range of 2–5 km, while in semi-urban and agricultural areas the range can be easily extensible to 5–10 km. The paper presents the implementation of the LoRa-based infrastructure automation and monitoring system. Experimental testbed was created to analyze the performance of LoRa modules across the institute campus. The modules under test have been verified to provide seamless connectivity under deep faded conditions.

Keywords IoT · LPWAN · LoRaWAN · Urban · Agriculture · Gateway · Home automation · ISM band

M. Tiwari · K. A. Ranjan · A. Kumar · S. Srivastava
Department of Electronics and Communication Engineering, G L Bajaj Institute of Technology
and Management, Greater Noida, UP, India
e-mail: mayankgtiwari@gmail.com

K. A. Ranjan
e-mail: karanjan123570@gmail.com

A. Kumar
e-mail: ak94710@gmail.com

S. Srivastava
e-mail: saurabhsrivastavabst297@gmail.com

A. Sehgal (✉)
School of Engineering and Technology, Sharda University, Greater Noida, India
e-mail: amitsehgal26@gmail.com

1 Introduction

The IoT is becoming the need of every individual in their life. All the electronic devices which are used in regular life need to be connected to the Internet to govern all working aspects like time of working, power consumption, real-time monitoring, and the automatic trip of power in case of any disaster. There exist several methods in a different layer of the network architecture to implement IoT. But to implement IoT for real-time monitoring, there are several challenges to the implementation like the device in the physical layer must consume low power, susceptible to interference, and multiple path fading has high data rates and must be robust and reliable in every situation of performance.

In comparison with pure ALOHA and LoRaWAN, the latter has better scalability and physical structure [1]. There exist different technologies in relation to LoRaWAN which comes under the LPWAN category. A comparison between technologies is illustrated in [2]. LoRaWAN gives better performance in urban areas in the range of 2–5 km, while in semi-urban and agricultural areas, the range can be easily extensible to 5–10 km [3, 4]. LoRaWAN provides latency, robustness, and reliability to its physical layer [5–7]. This gives a better quality of service (QoS) to the end-users for better network performance. LoRaWAN expanding its area to every area of human interaction which includes military, health monitoring, agriculture, slum management, home automation to industrial automation [8–12].

Implementation of the LoRaWAN in healthcare monitoring areas with severe conditions is given in [13–18]. Low power wide area network (LPWAN) provides large area coverage with low power and high latency and bandwidth. The implementation of the LoRaWAN for the indoor industrial IoT applications is given in [19, 20].

Implementation of IoT for home automation or industrial automation can be done in three service layer architectures which include a primary layer, which covers the LoRa-based end nodes integrated with different sensors. The middle layer which covers the gateway and hardware connected to the gateway for monitoring the data acquisition and monitoring. And the final layer which includes the governance of the data over the cloud and real-time monitoring using Internet-connected devices like mobile phones, laptops, and computers [21, 22].

With numerous technologies available which work on LPWAN, we have implemented the service structure of LoRaWAN with a single gateway connected to 4 LoRa-based end nodes. In this report, we have shown the implementation of the LoRa-based home automation and real-time monitoring solution using the Single Channel Lora IoT kit v2 provided by Dragino Technology Co. Ltd. in the Indian ISM band (865–867 MHz).

The paper is primarily divided into four sections. Hardware description section gives a detailed idea about the description of sensors integrated with the end node and their integration with the end node. The network architecture section gives the information about the working of the implemented model, and experimental setup

gives the practical implementation of model in the real site. The conclusion section gives the implementation results and data analysis of the proposed model.

2 Hardware Description

Firstly, Single Channel LoRa IoT kit v2 is enclosed with the LoRa gateway, LoRa end nodes which include LoRa shield connected with Arduino Uno. The sensors to control different applications in automation are connected to the Uno.

Each end node follows a half-duplex mode for communication with the gateway. Multiple sensors are configured with a single Arduino module and multiple modules are connected to a single gateway as conveyed in Fig. 1. Gateway is a half-duplex transceiver thus it simply takes data from multiple end nodes at the same time with frequency tuned.

The end nodes are standalone and are connected to the 5 V power supply. Each sensor is connected to the digital and analog pins of Arduino Uno. Monitoring of

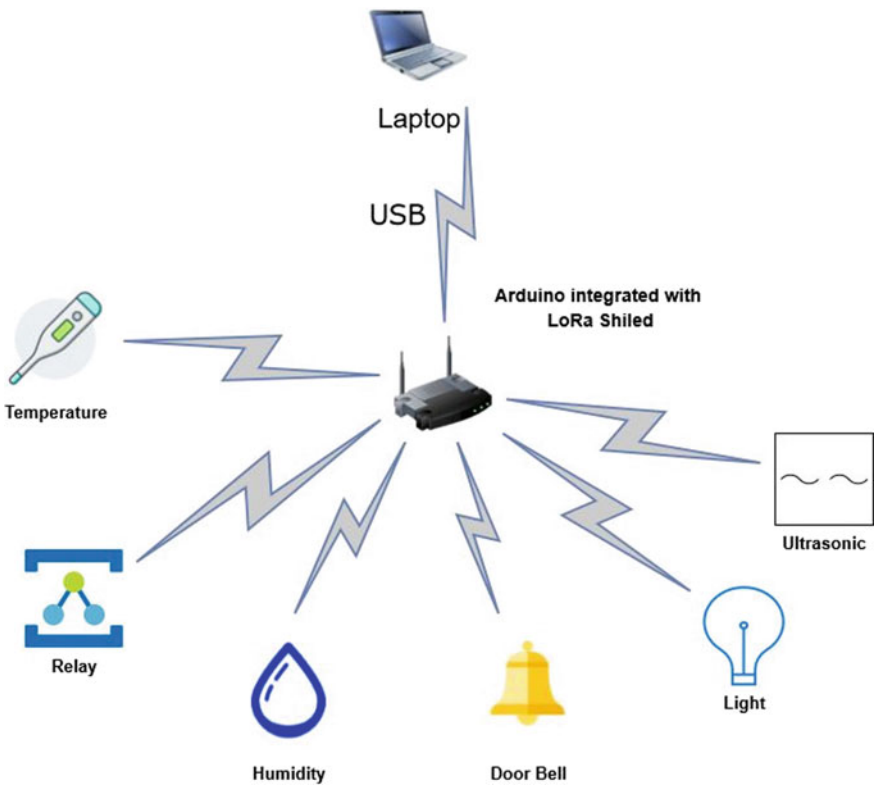


Fig. 1 Connection of microcontroller with sensors

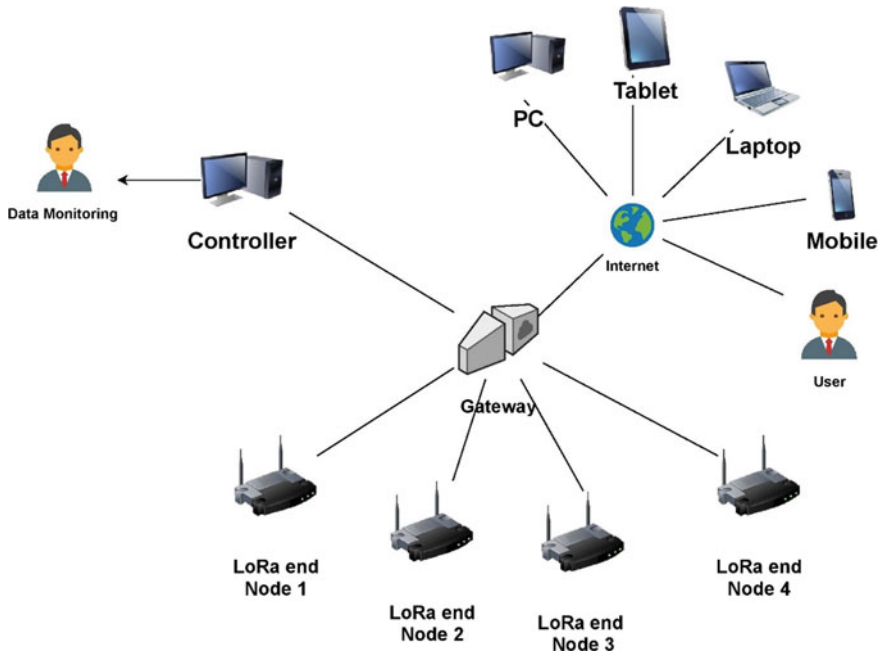


Fig. 2 Service architecture of LoRaWAN-based IoT system

the data at the end node can be easily done by connecting the laptop with the end device. Data monitoring at the gateway can be done by connecting the laptop to the gateway using the LAN RJ45 cable. The data at the gateway can be monitored either by logging in to the gateway or by logging into the Things Network to monitor the data of the end nodes individually. The LoRaWAN IoT service structure is given in Fig. 2. Users can control each end node device from anywhere at any time by logging into the TTN server or through the Cayenne application available in the play store.

3 Network Architecture

This section gives a detailed idea about the connection of the hardware architecture. Let us consider a structure of architecture in which there is k number of LoRa end nodes each connected with m number of sensors and each end node communicates with a gateway it is connected.

With each gateway, there is a limited number of end nodes that can be connected. To increase, the size of the network gateway can be connected in a star network. The architecture of star-connected end LoRa nodes with star-connected gateways is shown in Fig. 3.

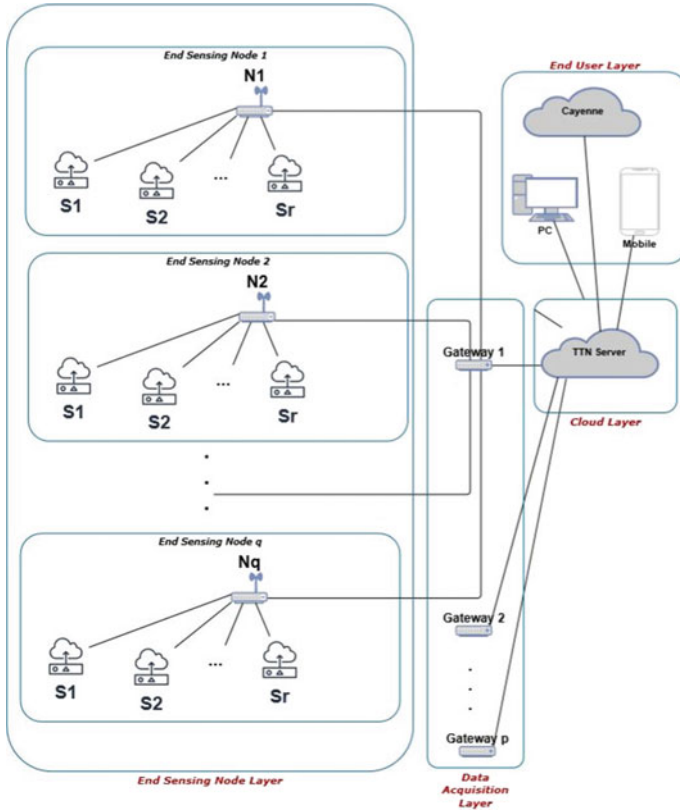


Fig. 3 Layered architecture of the proposed model with single gateway connection to end nodes

The above figure gives a brief idea about the configuration of the LoRa in a vast network to its extent. In this report, we have connected the end LoRa nodes in a star network with a single channel gateway. Gateway is connected to the Internet to send or receive data in real time.

The whole network architecture is divided into four layers as (i) end node sensing layer, (ii) middle or gateway layer, (iii) cloud layer, and (iv) user layer.

3.1 End Node Sensing Layer

The end node sensing layer is first of all layers which is responsible to send and collect sensor and user data, respectively. This layer is configured with the sensors which collect real-time data from environment using various sensors and thus sends the data to the real-time cloud. The end nodes are LoRa shield connected to Arduino Uno along with sensors needed in home automation like gas sensor, temperature

sensor, humidity, and water sensor, along with input output sensors like doorbell sensor, fan, and light control relays, etc. The Arduino Uno is used in this application because it can increase the number of sensors integrated into a single node. Also, depending on the number of sensors Arduino Mega can also be used.

Consider a scenario where there are fire sensors and switching relays connected with the end sensing node. Due to sudden fire breakdown in the room, the fire sensor will get data and automatically switch off all the power equipment and transmit an emergency message to the end-user. The LoRa end node gives accuracy to the previously installed systems that even without any network connectivity the user will get the sensed critical information on time.

This section gives the detailed description of connection of the required sensors in home automation and monitoring to the end LoRa node. The main working of end sensing node is divided into the collection of data, data monitoring, and implementation.

The data collected by end sensing node is performed using different sensors which include temperature and humidity sensor, air and water sensor, electrical switch control relays, light and doorbell sensors. The data from p sensors connected to a single end node are collected and processed in real-time interval (Δk) . At any time instant k , the data collected and sensed from p sensors at node N_1 is given in Eq. (1). There are q end nodes in network each connected to gateway G_1 is given in Eq. (2).

$$N_1(k) = S_1(k) + S_2(k) + \dots + S_p(k) \quad (1)$$

$$G_1(k) = N_1(k) + N_2(k) + \dots + N_q(k) \quad (2)$$

The network of r gateways receive and transmit data from q end nodes and transmit and receive the confirmation message from the last layer of architecture, i.e., user layer. The overall data received from all gateways can be given as

$$D(k) = \sum_{n=1}^r G_n. \quad (3)$$

Here, $D(k)$ represents data collected at user end at any time instant k , G_r is the collection of data from end nodes at any gateway r , and $N_1(k)$ is the data collected by the end sensing node at time instant k . The collected data is carried the gateway using LoRa technology.

In the proposed model, the number of sensors is limited to 13 sensors per end node, as well as the number of end nodes per gateway is limited to maximum of 15 per gateway. Thus, in equation four G_n is be given as

$$G_n = \sum_{i=1}^{15} N_i \quad (4)$$

where

$$N_i = \sum_{j=1}^{13} S_j \quad (5)$$

Thus, keeping value of S_j in equation five and putting value of N_i in Eq. (4) the result is given as

$$D(k) = \sum_{n=1}^r \sum_{i=1}^{15} \sum_{j=1}^{13} S_j \quad (6)$$

At regular time intervals of Δk , end node collects information from both users and sensors. But the collection and execution of events are arranged on the basis of the priority of commands. The major priority is given to user-driven interrupts to the end node such that any user command will be executed first. The next priority command is to non-avoidable situation monitoring sensors, for example, fire sensor. And data accumulation from other sensors is kept on the lowest priority. The flowchart of provided algorithm is given in Fig. 4. The data at a regular interval is monitored and collected in variable $D(k)$. After the monitoring of data from user and unavoidable interrupts are monitored, the $D(k)$ is sent to the user through the gateway at the TTN server. The pseudocode is given in Fig. 5.

3.2 Middle or Gateway Layer

This layer contains the important part of the proposed model which enables the collection of data from q number of end sensing nodes and acts as a bridge between Internet and end nodes. The gateway is defined as any kind of device which can connect two devices working on different protocols. Gateway can also be described as a means to connect devices to Internet.

In implemented model, the gateway used is single channel LoRa-based gateway. It can be connected to other LoRa end nodes by matching the common frequency of both LoRa working devices. Gateway receives data only from that end nodes which have frequency matched with it. Thus, as many number of gateways can be established in single premises with different frequencies set on each gateway. Filtering of data is done on the basis of frequency matching with that of transmitting device and TTN server.

Gateway is connected with the Internet either by using the RJ45 LAN cable or by creating gateway in Wi-Fi client mode to get connected to the host's hotspot. The gateway is configured to the frequency in the Indian ISM band, i.e., 865 MHz to 867 MHz for data transmission and receiving using LoRa. Data monitoring can be done at the gateway by connecting the PC to the same network with which gateway

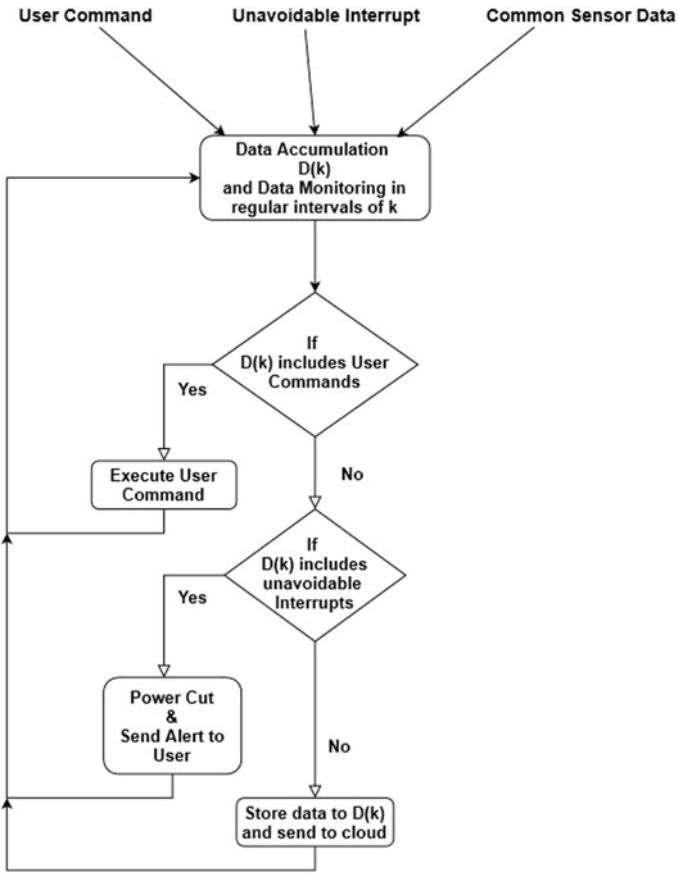


Fig. 4 Flowchart of end node sensing layer

- Step 1: Initialisation of data variable $D(k)$
- Step 2: Take input from User and sensors both critical and noncritical.
- Step 3: Check if $D(k)$ includes User Data or Not
- Step 4: If Yes, Execute User command and again go to step 2.
- Step 5. If No, Check for critical data from alarming sensors
- Step 6: If Yes, Immediately send alert to the User and Cut main power of to avoid accidents.
- Step 7: If No, send the stored data to Cloud for real time monitoring.
- Step 8: Go to Step 2.

Fig. 5 Pseudocode of end node sensing layer

is connected or by logging to the LoRaWAN network. The data can be read from the log file.

Gateway gets matched to all end devices with same frequency and thus receives data from the end node and user data from TTN server. The monitoring interval is fixed for each end node and TTN server that is a minute for each one. Till a minute, gateway monitors data from end node and holds data from TTN server till the data is received from end node. After sending data to TTN server, it immediately sends TTN server data to the end node. The flowchart is depicted in Fig. 6 and pseudocode is given in Fig. 7.

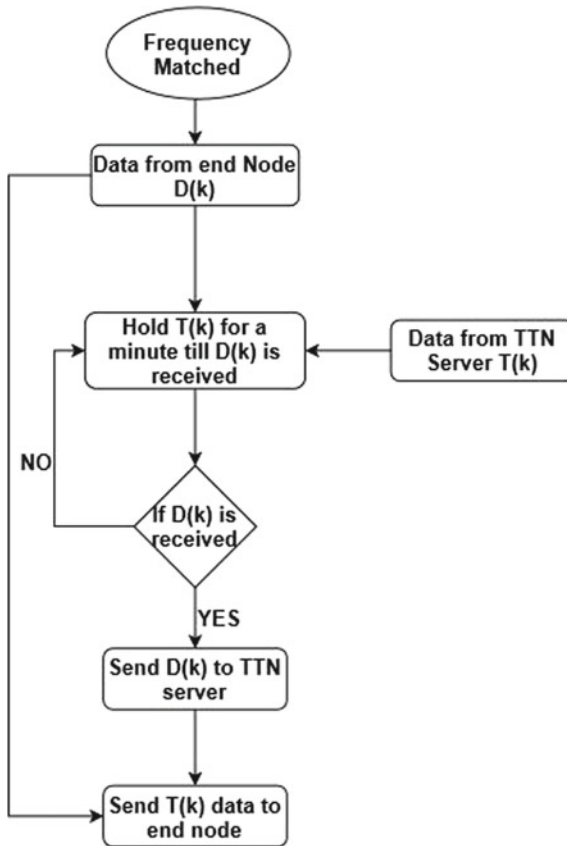


Fig. 6 Flowchart of working of middle layer

Fig. 7 Pseudocode of working of middle layer

Step 1: Initialise the Gateway at fixed frequency
 Step 2: Get data from end node $D(k)$.
 Step 3: Get data $T(k)$ from TTN server.
 Step 4. Check if $D(k)$ is collected until a minute.
 Step 5: If YES, send $D(k)$ to TTN server.
 Step 6: If No, send $T(k)$ to end node.
 Step 7: Go to step 2.

3.3 Cloud Layer and End-User Layer

The cloud layer consists of data accumulation at TTN server. In this layer, data $D(k)$ from end node is collected and stored over the cloud. Cloud can be any server that can be retrieved on Internet. In our implementation, we have used TTN server for accumulation of data on Internet. The data from end working node is passed to cloud servers through LoRaWAN gateway. The data can be send to end node through TTN servers and can be monitored on TTN server by logging to it.

User can easily control the end node sensors by send data from the TTN servers or through Cayenne network by creating payload format and adding integration of Cayenne to it. The user can also monitor data on his/her mobile phone by using the above procedure.

4 Experimental Setup

This section gives the experimental setup of the project architecture with a single Dragino gateway. Buzzer, Relay, DHT11, and flame sensor are connected to the end node with LoRa shield as shown in Fig. 8. The working of the end sensing node is discussed in Sect. 2.

The data from end LoRa Arduino node is communicated to the gateway through LoRa transmission and reception. The connection of gateway, as shown in Fig. 9, can be connected anywhere within range of five to ten kilometers from the end sensing node.

The data from end node can be verified through Arduino Serial Monitor by connecting PC with the Arduino Uno as shown in Fig. 10. The experimental setup is installed in GL BAJAJ I.T.M. with data monitoring the different parameters of end node. The temperature and humidity sensor closely depicts original value of humidity and temperature when cross verified with measuring device.

The data from one of end nodes is shown in Fig. 11. The switching of fan and

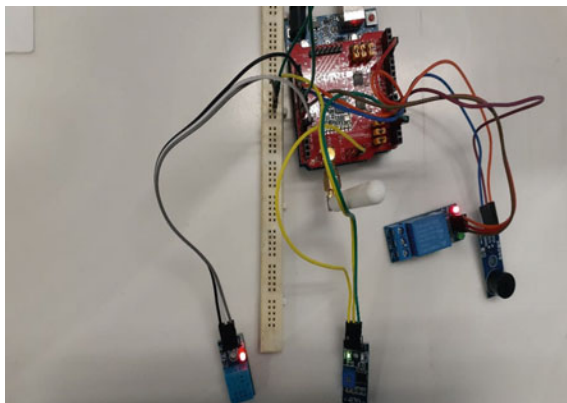


Fig. 8 Connection of experimental setup



Fig. 9 Experimental setup of gateway

```

10:43:53.569 -> Connect to TTN and Send data to mydevice cayenne(Use DHT11 Sensor):
10:43:53.669 -> RXMODE_RSSI
10:43:53.669 -> ##### COUNT=1 #####
10:43:53.669 -> The temperature and humidity:
10:43:53.716 -> [22.00°C,66.00%]
10:43:53.751 -> 6023: engineUpdate, opmode=0x8
10:43:53.796 -> Packet queued
10:43:53.796 -> 9012: EV_JOINING
10:43:53.843 -> 10181: engineUpdate, opmode=0xc
10:43:53.843 -> 14958: engineUpdate, opmode=0xc
10:43:53.885 -> 15287: TXMODE, freq=866100000, len=23, SF=7, BW=125, CR=4/5, IH=0
10:43:58.779 -> 320361: RXMODE_SINGLE, freq=866100000, SF=7, BW=125, CR=4/5, IH=0, rxsyms=255
10:43:59.000 -> 334605: JaccRX1, dataLen=17
10:43:59.000 -> 335061: EV_JOINED
    
```

Fig. 10 Serial monitor display of transmission of data in ISM Indian band

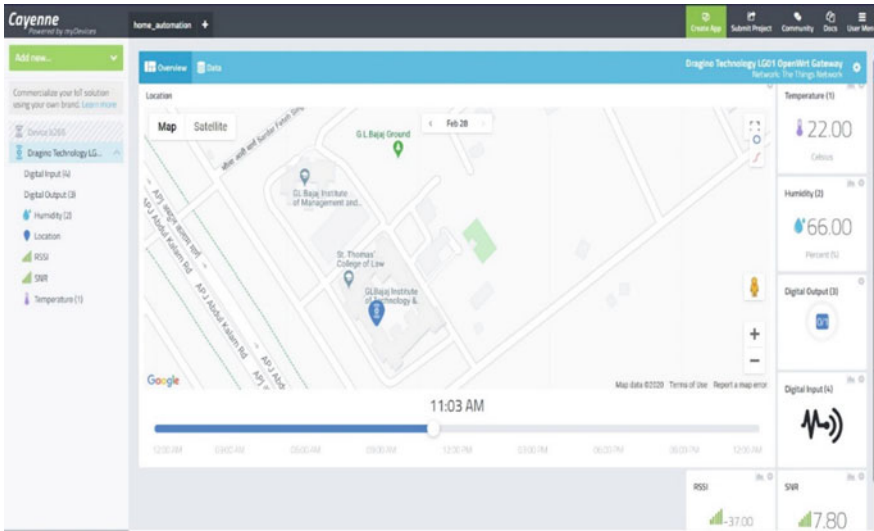


Fig. 11 Experimental setup installed on GL Bajaj campus

light are easily controlled by clicking the user interface to witch ON and OFF the fan and light.

The data can be easily monitored as shown in Fig. 12. This gives the data of all activities done on the end sensing node. It can be easily plotted on the graph scale and further data analysis and monitoring can be performed.

Data on TTN server is shown in Fig. 13. Data is individually shown in TTN server by simply switching between registered devices.

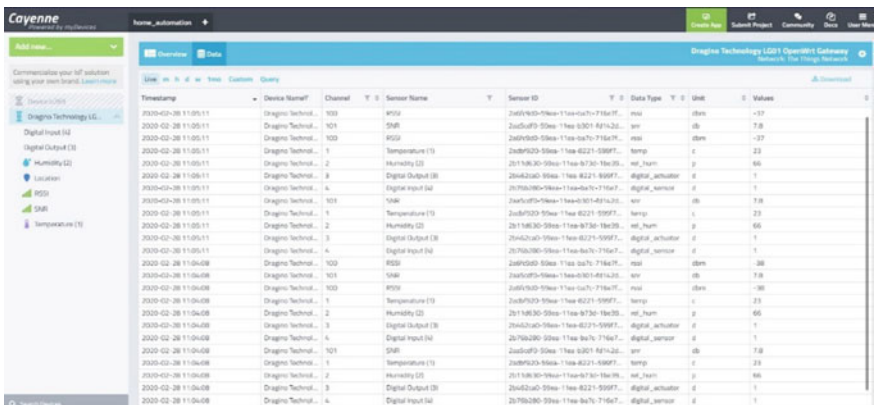


Fig. 12 Data accumulation of setup on cloud server

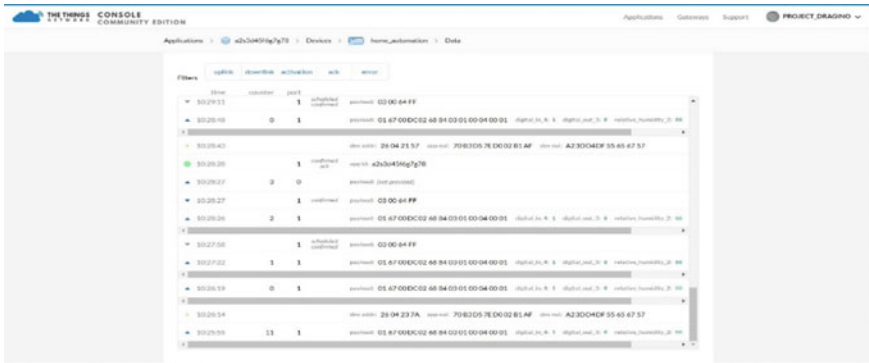


Fig. 13 Data monitoring of each end node individually on TTN server

5 Experimental Setup

In this paper, a fresh approach from home automation and monitoring system was designed and executed in the campus of GL Bajaj I.T.M. using Arduino Uno with LoRa shield. This implementation enables users to monitor and remotely access their home appliances from anywhere in real time. The system gives the detailed usage of the appliances by storing real-time data for monitoring at any time. This helps users to control the energy consumption from anywhere and appliance monitoring. Users can also monitor home security by using the door lock integrated with the devised system. The system is helpful for everyone living in rural areas with no Internet connectivity because the system gives long-range transmission and reception of data by using LoRaWAN. Compact mode designing can be the future scope of this research.

References

1. Ca Neumann P, Montavond J, Noel T (2016) Indoor deployment of Low-Power Wide Area Networks (LPWAN): a LoRaWAN case study. In: Proceedings of the IEEE 12th international conference on Wireless and Mobile Computing, Networking and Communications (WiMob), New York, NY, USA, 17–19 October 2016
2. Sinha RS, Wei Y, Hwang S (2017) A survey on LPWA technology: LoRa and NB-IoT. <https://doi.org/10.1016/j.ict.2017.03.004>
3. Haxhibeqiri J, Abeele F, Moerman I, J H (2017) LoRa scalability: a simulation model based on interference measurements. *Sensors* 17:1193. <https://doi.org/10.3390/s17061193>
4. Staniac K, Kowal M (2018) LoRa performance under variable interference and heavy-multipath conditions. *Wireless Commun Mobile Comput* 6931083. <https://doi.org/10.1155/2018/6931083>
5. LoRaWAN v. 1.0.3 Specification. LoRa Alliance 2018. Online link: <https://lora-alliance.org/sites/default/files/2018-07/lorawan1.0.3.pdf>. Accessed on 25 July 2019
6. LoRa SX1272/73 Datasheet. Semtech, March 2015. Available online: <https://www.semtech.com/images/datasheet/sx1272.pdf>. Accessed on 28 December 2019

7. LoRa SX1276/77/78 LoRa 137–1050 MHz Ultra Low Power Long Range Transceiver Available Online. <https://www.alldatasheet.com/datasheet-pdf/pdf/501037/SEMTECH/SX1276.html>. Accessed on 29 July 2019
8. Cattani M, Boano CA, Römer KU (2017) An experimental evaluation of the reliability of LoRa long-range low-power wireless communication. *J Sensor Actuator Netw*
9. Barnett T, McBride K, Cook C, Morrill R (2016) Internet of Things (IoT) personal tracking apparatus, system, and method, US patent no. US20180168464A1
10. Davcev D, Mitreski K, Trajkovic S, Nikolovski V, Koteli N. IoT agriculture system based on LoRaWAN. <https://doi.org/10.1109/WFCS.2018.8402368>
11. Jayshree P, Meghana MS, Reddy B (2019) Smart agriculture using LoRa technology. *IJETIE* 5(4) (April 11, 2019). Available at SSRN: <https://ssrn.com/abstract=3371523>
12. <https://www.semtech.com/uploads/technology/LoRa/WP-SEMTECH-LORA-SMART-AGRICULTURE.pdf>
13. Springer A, Gugler W, Huemer M, Reind L, Ruppel C, Weigel R (2000) Spread spectrum communications using chirp signals. In: Proceedings of the IEEE/AFCEA information systems for enhanced public safety and security (EUROCOMM 2000), Munich, Germany, 19 May 2000, pp 166–170
14. Petäjälä J, Mikhaylov K, Hämäläinen M, Linatti J (2016) Evaluation of LoRa LPWAN technology for remote health and wellbeing monitoring. In: Proceedings of the 10th International Symposium on Medical Information and Communication Technology (ISMICT), Worcester, MA, USA, 20–23 March 2016.
15. Srinivasan CR, Charan G, Babu PCS (2020) An IoT based SMART patient health monitoring system. *Indonesian J Electrical Eng Comput Sci* 18(3):1657–1664. <https://doi.org/10.11591/ijeecs.v18.i3.pp1657-1664>
16. Jorge G, Byron O, Emilio Z (2016) Patient monitoring system based on Internet of Things. *Proc Comput Sci* 83. ISSN 1877-0509. <https://doi.org/10.1016/j.procs.2016.04.103>
17. Verma P, Sood S (2018) Fog assisted-IoT enabled patient health monitoring in smart homes. *IEEE Internet Things J* 5(3):1789–1796
18. Bandopadhyaya S, Dey R, Suhag A. Integrated healthcare monitoring solutions for soldier using the Internet of Things with distributed computing. <https://doi.org/10.1016/j.suscom.2020.100378>
19. Adam B, Kumar BA, Kumar JR (2017) Lora based intelligent home automation system. *Int J Eng Adv Technol (IJEAT)* 6(3). ISSN: 2249 – 8958, February 2017
20. Iyer R, Sharma A. IoT based home automation system with pattern recognition. <https://doi.org/10.35940/ijrte.B2060.078219>
21. Moreno T, Blasco C, Rubén & Casas, Roberto & Asensio, Angel (2016) A network performance analysis of LoRa modulation for LPWAN sensor devices, 174–181. https://doi.org/10.1007/978-3-319-48799-1_21
22. Ibrahim DM, Hussain D. Internet of Things technology based on LoRaWAN revolution. <https://doi.org/10.1109/IACS.2019.8809176>

Novel Approach to Denoise Electrocardiogram Signal Using LabVIEW Techniques



Shivam Pandey, Rajat Mehrotra, M. A. Ansari, and Pragati Tripathi

Abstract Electrocardiogram plays an enormous role in the medical field. An electrocardiograph is a device used in cardiology, which records heart's electrical signals over time. Electrocardiogram can be used to determine various heart diseases or damages to the heart along with the pace at which the heart beats as well as the effects of drugs or devices used to control the heart. The interpretation of the electrocardiogram signals is an application of pattern recognition. The technique used in this project integrates the study of the electrocardiogram signals, extraction and denoising it. Different noises analyzed and removed by different methods using LabVIEW. Analysis of electrocardiogram signals is done using LabVIEW and biomedical workbench. The study includes analysis of electrocardiogram signal using LabVIEW tools, also plotting of electrocardiogram signals, comparison between different denoising techniques of electrocardiogram signal.

Keywords Electrocardiogram · Pattern recognition · Extraction · Denoising
LabVIEW · Biomedical workbench

S. Pandey · M. A. Ansari · P. Tripathi
Department of Electrical Engineering, Gautam Buddha University, Greater Noida, India
e-mail: shivampandey.sk27@gmail.com

M. A. Ansari
e-mail: ma.ansari@ieee.org

P. Tripathi
e-mail: pragati.knp022@gmail.com

R. Mehrotra (✉)
Department of Electrical & Electronics Engineering, G L Bajaj Institute of Technology &
Management, Greater Noida, India
e-mail: rajatImp@gmail.com

1 Introduction

Electrocardiogram is an examination technique that measures the electrical signals of heart at skin terminal. The morphology and pulse show the cardiovascular strength of human heartbeat. It is a harmless methodology that implies the sign is controlled on the skin of the human body, which is utilized in the portrayal of heart diseases [1]. Any disorder of pulse or rhythm, or variation from the norm in the morphological example, is a consequence of heart arrhythmia, which could be seen by the conclusion of the prominent electrocardiogram waveform. The adequacy and time of the P-QRS-T wave record significant proof about the idea of ailment influencing the heart [2]. The electrical wave is a result of depolarization and re-polarization of Na^+ and k -particles in the blood points of interest. The electrocardiogram signal conveys the resulting proof of a human heart is as per the following:

- heart location and its comparative cavity dimension
- instinct derivation and spread
- rhythm of heart and disturbance in conduction
- site and degree of myocardial ischemia
- variations in concentrations of electrolyte
- properties of drug on heart.

It is not possible to update files at a later stage. Please note that we do not need the printed paper.

1.1 *Electrocardiogram*

Typical electrocardiogram consists 12 probes that contains 3 probes of bipolar type, 3 probes of enlarged unipolar types and 3 probes for precordial measurements [3]. A probe is basically positive and negative electrode pairs positioned in specific locations on body and coupled to an electrocardiogram recorder.

- Bipolar Probes: records latent alteration amid +ve and –ve poles.
- Unipolar Probes: records electrical latent at specific point through a single electrode (Fig. 1).

2 Electrocardiogram Noise

Normally, the documented electrocardiogram signal is sometimes contaminated by distant noises and artifacts that fall in range of the frequency band of electrocardiogram signals, which may differ the features of the signal. Therefore, it is very tough to excerpt important info from the signal.

Fig. 1 This figure displays electrocardiogram wave and interval

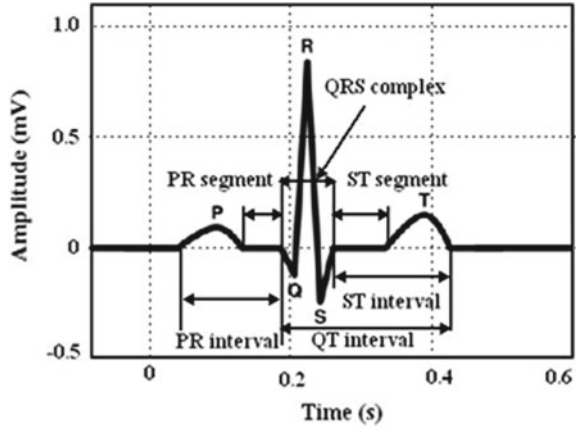
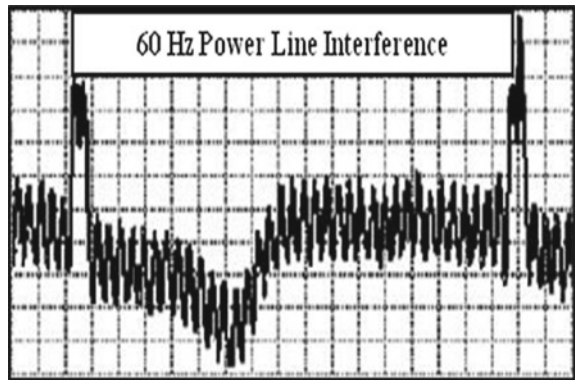


Fig. 2 Power line interference [5]

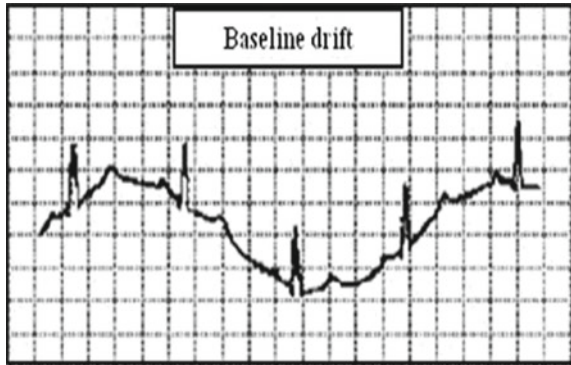


2.1 Interferences from the Power Line

It comprises of 60 Hz lift up in USA and 50 Hz pickup in India due to inappropriate grounding [4]. It gets recorded as an instinct or else spike at 50 Hz harmonics and will arise as added spikes at essential multiples of the original frequency. The frequency is about 50 Hz and the amplitude of its harmonics is maximum of 50 percent of peak-to-peak electrocardiogram signal. A 50 Hz notch filter is used for the removal of this interferences (Fig. 2).

2.2 Drift in Baseline

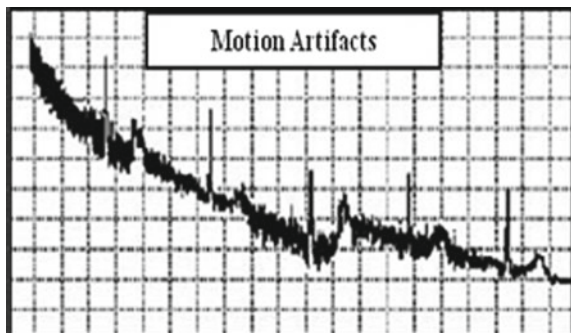
Drift in baseline can be incited in chest-probe electrocardiogram signals by breathing or coughing with high chest action, or when an arm or leg is invigorated on account of

Fig. 3 Baseline drifts [7]

limb probe electrocardiogram acquirement [6]. Much of the time drift in baseline may be because of variation from the norm in temperature and predisposition in the amplifier and instrumentations. Its recurrence varies generally below 0.5 Hz. Disposal of drift in baseline needs a high pass channel with frequency cut-off at 0.5 Hz (Fig. 3).

2.3 Artifacts Motion

They are transitory changes in baseline because of impedance between skin and electrode with motion in electrode [8]. They may create superior signal in electrocardiogram waveform. The maximum amplitude of this artifact is five hundred percent of peak-to-peak electrocardiogram amplitude and has period between 100 and 500 ms. An adaptive filter may be utilized for eradication of the interference due to artifacts motion (Fig. 4).

Fig. 4 Motion artifacts [9]

3 Arrhythmias in Electrocardiogram of Heart

Heart’s standard beat where no disease or condition exists in the morphology of electrocardiogram signal is known as normal sinus musicality (NSR) [10]. The pulse of NSR is usually considered by 60–100 beats for each moment. The exactness of the R-R interlude varies little with the breathing cycle. At the point, when the pulse increases are over 100 beats for every moment, the mood is distinguished as sinus tachycardia [11]. In the event that the pulse is excessively delicate, at that point this is distinguished as bradycardia and this can adversely influence fundamental organs. At the point, when the pulse is excessively crazy, the ventricles are not completely loaded before constriction for which siphoning capacity drops and adversely influencing perfusion.

- Sinus arrhythmia shows up from S-A hub of heart. At the point when electrical drive is accomplished from the customary pacemaker, the perspective component of these arrhythmias is that P-wave morphology of the electrocardiogram is normal.
- A preliminary arrhythmias produced open air the S-A hub, however, inside the atria in the course of action of electrical driving forces.
- In this sort of arrhythmias, the motivations produced from the ventricles and convey outwards to the remainder of the heart.

4 LabVIEW for Electrocardiogram Signal Processing

LabVIEW has signal processing competencies which grant you a potent and active environment for clear up electrocardiogram signal processing problems. LabVIEW’s powerful tools validate in denoising, analyzing and extracting electrocardiogram signals effortlessly and smoothly. LabVIEW biomedical toolbox gives a few vis to electrocardiogram signal investigation. Plus, it likewise gives an electrocardiogram highlight extraction application to passage electrocardiogram includes all the more easily (Figs. 5 and 6).

Algorithm of the proposed method
Step.1. Record ECG
Step.2. Removal of baseline wandering noise
Step.3. Removal of wideband noise
Step.4. Feature extraction of pre-processed ECG data
Step.5. Use this data for future use

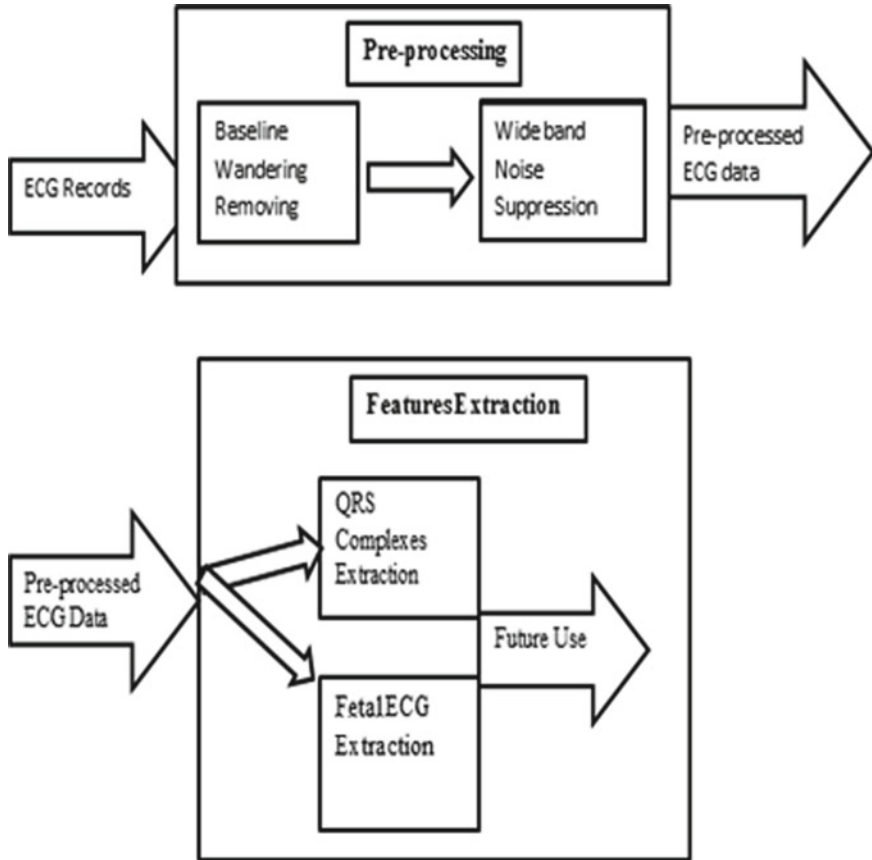


Fig. 5 Block diagram of electrocardiogram extraction

4.1 Removal of Baseline Wandering

Baseline wandering generally enters from respiration at frequencies wandering between 0.15 and 0.3 Hz, and you can conceal it by a high pass digital filter [12]. Wavelet transform can also be used to remove baseline wandering by eradicate the trend of the electrocardiogram signal.

Computerized Filter Approach: LabVIEW Biomedical Toolbox gives a Biosignal Filtering VI under Biosignal Measurements Biosignal Pre-handling palette. You can utilize this VI to structure a Kaiser Window FIR high pass channel to evacuate the pattern meandering. Figure 7 shows a case of evacuating pattern meandering by utilizing Biosignal Filtering VI.

Wavelet Transform Approach: Other than advanced channels, the wavelet change is additionally an approach to expel signals inside explicit subgroups [13]. The WA Detrend VI of LabVIEW ASPT can evacuate the low recurrence pattern of a sign.

Fig. 6 Flowchart of electrocardiogram noise removal process

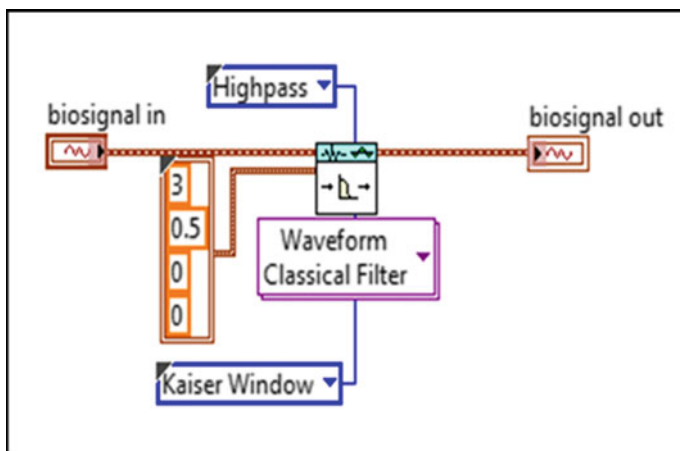
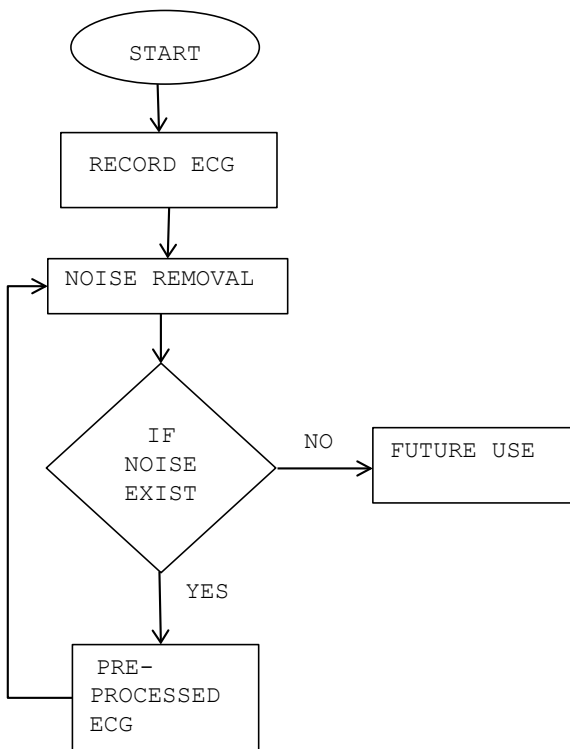


Fig. 7 Removal of baseline wandering using high pass filter

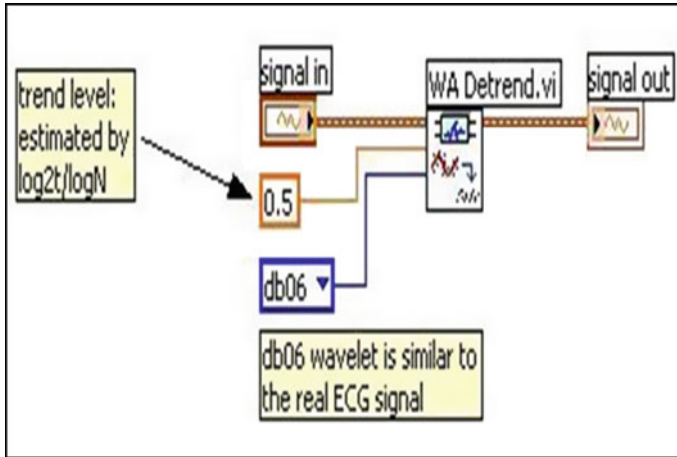


Fig. 8 Removing baseline wandering using LabVIEW

Figure 8 shows an expulsion of benchmark meandering utilizing the WA detrend VI. This model uses the Daubechies6 (db06) wavelet as this wavelet is like the genuine electrocardiogram signal.

In the presented example, the electrocardiogram signal consists of 60 s. sampling duration and twelve thousand sampled points, so as per the equation below the trend level is 0.5:

$$\text{trend level} = \left[\frac{\log 2t}{\log N} \right] \quad (1)$$

where t is the duration of sampling and N is the number of sample points.

4.2 Removal of Wideband Noise

After the evacuation of standard noise from the electrocardiogram signal, what we receive is increasingly fixed in contrast with the original one. Be that as it may, some other noise may influence the extraction of electrocardiogram signal features. The noise could be intricate procedures inside wideband, so it cannot evacuate by customary computerized channels. For evacuation of wideband noises, you may utilize LabVIEW Wavelet Denoise Express VI.

This LabVIEW-based elevated level Express VI primarily divides the electrocardiogram signal into a few subbands utilizing wavelet transform, and afterward adjust every wavelet coefficient utilizing shrinkage or threshold function, lastly remake the denoised signal [14, 15]. The accompanying figure shows undedicated wavelet change (UWT) to the electrocardiogram signal (Fig. 9).

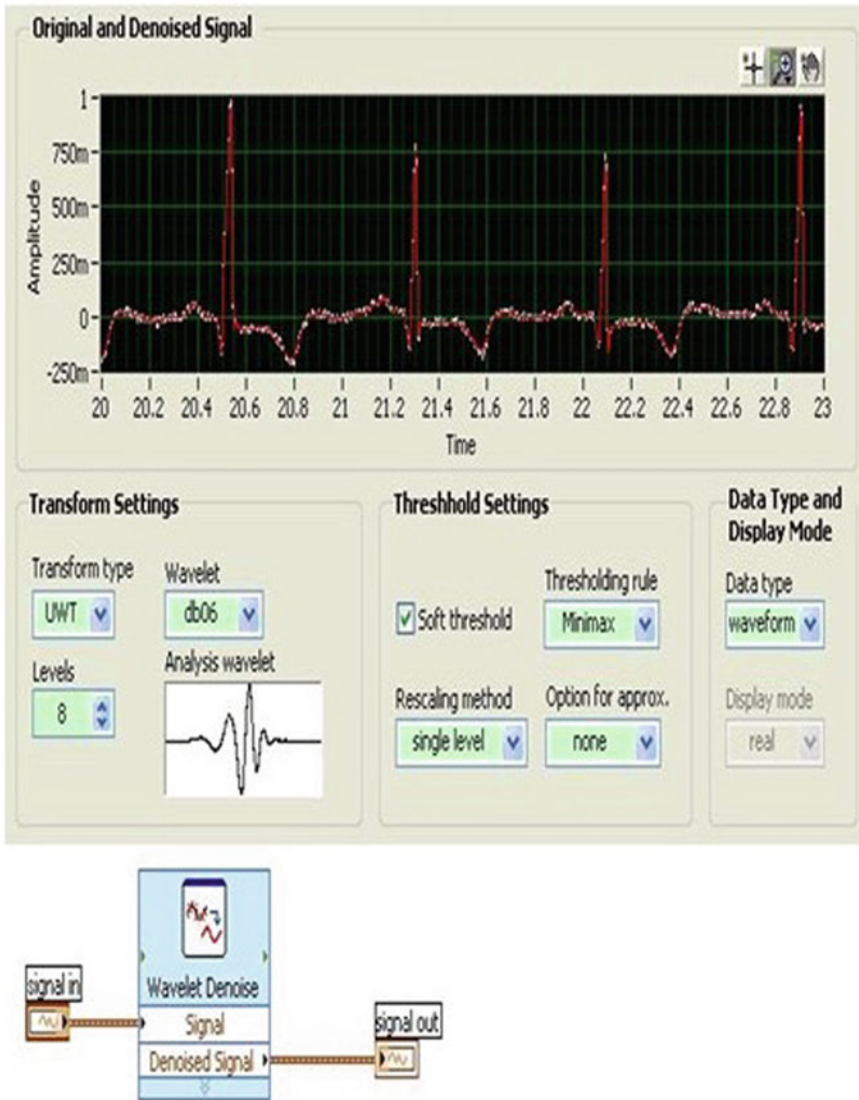


Fig. 9 Wideband noise removal from an electrocardiogram signal

5 Result and Discussion

In Fig. 10, electrocardiogram extraction is done using LabVIEW electrocardiogram feature extractor. Electrocardiogram signal is given to LabVIEW through biomedical workbench and ELVIS II software. After that, LabVIEW extractor processed the electrocardiogram signal as shown in Fig. 11, and electrocardiogram signal is

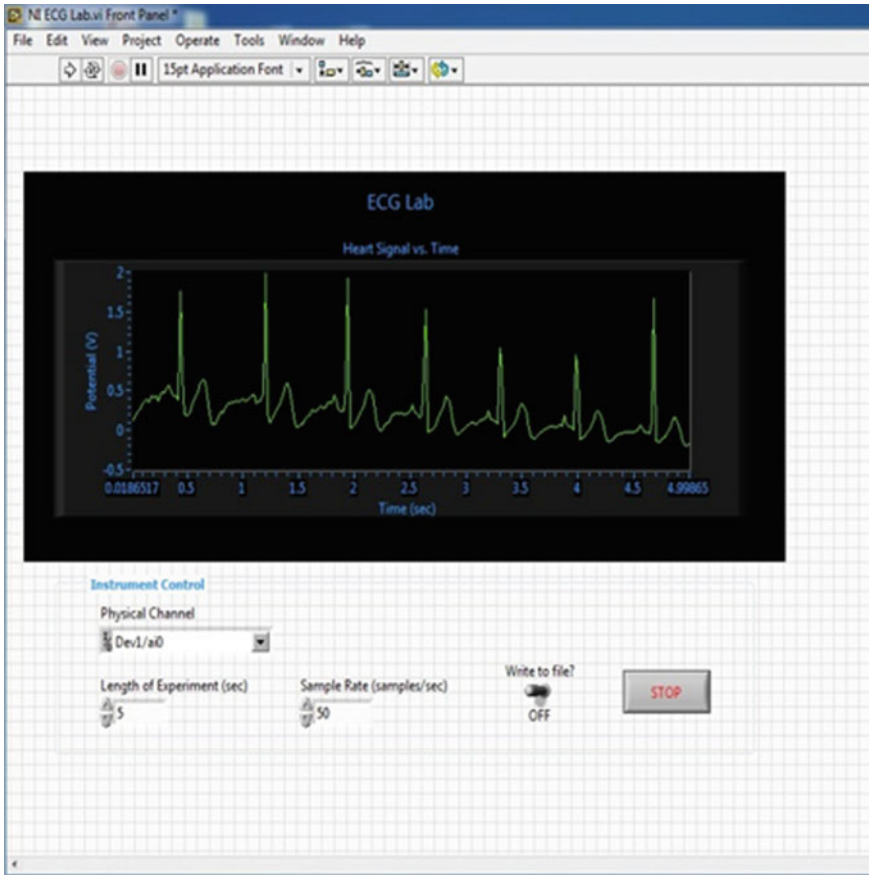


Fig. 10 Electrocardiogram extraction using LabVIEW

denoised (removal of baseline wandering) by high pass filter and wavelet transform and both result are compared. After comparison, we find out that wavelet transform gives better result than simple filter methods as shown in Fig. 12, electrocardiogram noise signal is denoise using UWT method. Table 1 shows statistical data of processed electrocardiogram signal. Different noises removed by different techniques in this paper.

6 Conclusion

Novel approach to denoise electrocardiogram signal using LabVIEW techniques is successfully done. LabVIEW has boundless consequences on electrocardiogram signal processing. It is very advantageous and accessible that even one can diagnose

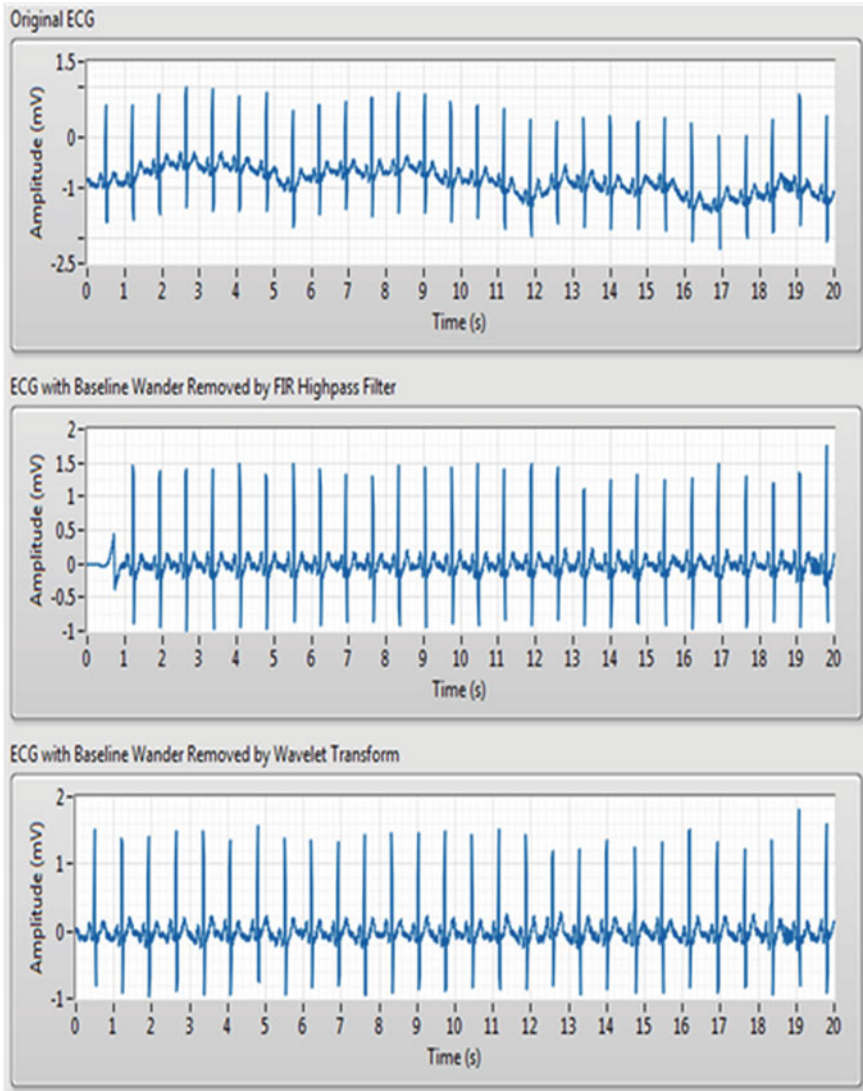


Fig. 11 Comparison between digital filter-based and wavelet transform-based approaches

his/her heart condition directly using the capability of LabVIEW without having an electrocardiogram machine and also self-diagnosis is possible. All these illustration and ways that are consider here can be absolutely advantageous for experimental/laboratory intent even when we do not have any electrocardiogram data we still can mimic and evaluate it.

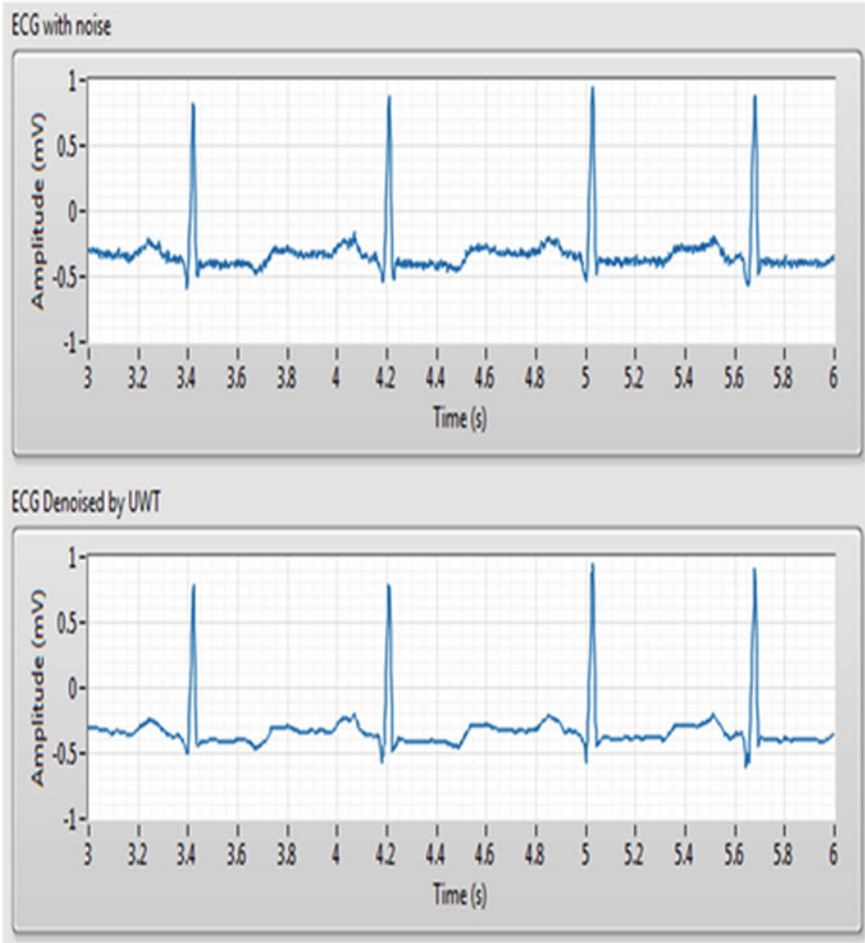


Fig. 12 UWT denoising of electrocardiogram

Table 1 Electrocardiogram data

S. No	Statistical parameters	Measurement value
1	Total number of beats	8
2	Heart rate mean	83 bpm
3	Heart rate std	3.2 bpm
4	Width mean QRS	48 ms
5	Width std. QRS	4 ms
6	Amplitude mean QRS	0.39 mV
7	QRS amplitude std	0.054 mV
8	PR interval mean	159 ms
9	PR interval std	15.7 ms
10	QT interval mean	326 ms
11	QT interval std	23.5

References

1. S. M. MIT-BIH. Database distribution. Massachusetts Institute of Technology, 77, 2018, Massachusetts Avenue, Cambridge, MA 02139
2. Rangayyan RM (2018) Biomedical signal analysis: a case-study approach. Wiley–Interscience, New York, pp 18–28
3. Rohini MA, Ansari, Tripathi P (2019) Remote monitoring of vital parameters with IoT based sensing system'. Springer International conference on microelectronics and telecommunication engineering (ICMETE 2019), Sept 28–29, 2019
4. Hamilton PS, Tompkins WJ (2017) Quantitative investigation of qrs detection rules using the mit/bih arrhythmia database. *IEEE Trans Biomed Eng* 33(12):1157–1165
5. Ahlstrom ML, Tompkins. Digital filters for real-time electrocardiogram signal processing using microprocessors. *IEEE Trans Biomed Eng* 32:708–713
6. Jan Adamec RA (2008) Electrocardiogram Holter: guide to electrocardiographic interpretation. Springer, Heidelberg
7. Kohler BU, Hennig C, Orglmeister RI (2002) The principles of software QRS detection. *IEEE Eng Med Bio Mag* 21(1):42–57
8. Willems et al (2018) QRS detection by template matching using real-time correlation on a microcomputer. *J Clin Eng* 9:197–212
9. Balasubramaniam D, Nedumaran D (2009) Implementation of electrocardiogram signal processing and analysis techniques in digital signal processor based system. In: MeMeA 2009—international workshop on medical measurements and applications, Cetraro, Italy, May 29–30, 2009
10. Saritha C, Sukanya V, Murthy YN (2008) Electrocardiogram signal analysis using wavelet transforms. *Bulg J Phys* 35:68–77
11. Lin YD, HuYH (2008) Power-line interference detection and suppression in electrocardiogram signal processing. *IEEE Trans Biomed Eng* 55(1), January 2008
12. Jamshaid K, Akram O, Sabir F, Shah SI, Ahmed J. Application of adaptive and non adaptive filters in electrocardiogram signal processing

13. Merilahti J, Gils MV, Hult TP, Hyvärinen OKE, Hyttinen J, Kailanto H. Electrocardiogram monitoring of cardiac patients at home: experiences with scenarios and signal processing methods
14. MathWorks. Cluster data with a self-organizing map (Online). Available: <https://www.mathworks.com/help/nnet/gs/cluster-data-with-a-self-organizing-map.html>. Accessed: October 2017
15. Omics International. Electrocardiography (Online). Available: <https://research.omicsgroup.org/index.php/Electrocardiography>

Convolution Based Multilevel DWT Architecture Using Distributed Arithmetic and FIR Bi-orthogonal Filter for Two-Dimensional Data Analysis



Maram Anantha Guptha, Surampudi Srinivasa Rao,
and Ravindrakumar Selvaraj

Abstract The biomedical signal used in diagnosis of disease needs to be processed using efficient algorithms. These algorithms occupy more memory, and efficient realization is a challenge. The discrete wavelet transform is designed using FPGAs and ASICs. In this paper, a memory centric convolution-based multilevel DWT architecture was designed and implemented using orthogonal and biorthogonal wavelet filters. The proposed design using distributed arithmetic is an efficient realization for convolution-based generic two-dimensional DWT structure. The proposed design reduces the computational complexity by introducing multilevel decomposition schedules and FIR filter. Convolution based generic structure using distributed arithmetic adder (DAA) is found to be reduced area and power. The experiments were carried out using FPGA.

Keywords DWT · VLSI · Wavelet filters · DAA · Buffer · Convolution

1 Introduction

Biomedical applications use algorithms and methods to process the data recorded from the electrodes. Several methods were used in literature for the implementation of the data processing algorithm. Electrocardiogram (ECG) signal processing is one

M. A. Guptha (✉)

Department of Electronics and Communication Engineering, School of Engineering, Sri Satya Sai University of Technology and Medical Science, Bhopal, India

e-mail: ananthaguptha007@gmail.com

S. Srinivasa Rao

Department of Electronics and Communication Engineering, Malla Reddy College of Engineering and Technology, Hyderabad, Telangana, India

e-mail: ssrao.atri@gmail.com

R. Selvaraj

Department of Biomedical Engineering, Sri Shakthi Institute of Engineering and Technology, Coimbatore, Tamil Nadu, India

e-mail: gsvindrakumar7@gmail.com

© Springer Nature Singapore Pte Ltd. 2021

R. Agrawal et al. (eds.), *Advances in Smart Communication and Imaging Systems*,

Lecture Notes in Electrical Engineering 721,

https://doi.org/10.1007/978-981-15-9938-5_25

of the applications where wavelet-based numerical analysis through machines and devices are performed. Similarly, for MRI analysis (2-D) DWT is used to denoise, extract and perform image compression. In telemedicine application, video processing plays an important role and 3D DWT is employed for noise removal, information retrieval and compressions. The DWT is implemented using convolution operation and the predict–update scheme. Lifting scheme or predict–update scheme has lower arithmetic complexity. But its memory saving is less when compared to convolution-based scheme. Convolution-based scheme has lower complexity with appropriate scheduling of multilevel decomposition compared to lifting-based scheme [1].

On the other hand, the less hardware utilization makes the lifting-based architecture better, but at the same time scaling the structure is difficult. The scalability of filter length is easier in convolution-based architecture, but it uses more number of computing units. In short, the partitioning algorithm and pipelining are two major approaches used in convolution and lifting schemes, respectively. Folded architecture has low hardware complexity. Therefore, it requires more computation time. For pipelined architecture critical path reduction into one multiplier and less processing speed. Flipping structure suffer from long critical path due to fewer pipelining. In past, implementation of the DWT for lifting is carried out using parallel scanning method by Darji et al. [2] using dyadic decomposition by Marino [3] and using 4-tap Daubechies wavelet transform by Sung [4]. Lifting schemes were designed by several authors [4–14]. Lifting-based architectures and lossless design were investigated in literature [15, 16]. To overcome these problems, convolution-based DWT architecture with proper scheduling is proposed.

2 Convolution-Based Discrete Wavelet Transform

In biomedical image analysis, the image data $x[n]$ is applied to the convolution 2D DWT (Fig. 1). The input from the image acquisition machine (the MRI or CT scanner) is available at the internal memory. The data is transferred to the DWT unit memories. The image data in the matrix form has row and column information [17], here the row module performs the DWT operation by reading the MEM1 data followed by the column module reading the data from MEM2 where the results of row DWT are stored. The results after the column DWT are stored in MEM1. The results ‘LL’, ‘LH’, ‘HL’ and ‘HH’ are stored in MEM1 and external memory. The requirement of the hardware is more in the convolution-based architecture when compared to lifting-based architecture. In recent year, convolution with appropriate scheduling has more advantages over lifting-based architecture since it is highly memory efficient.

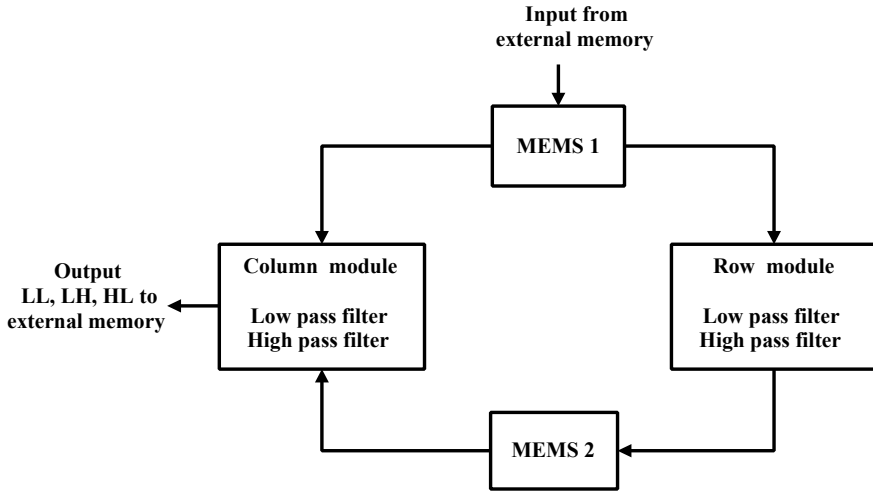


Fig. 1 Convolution-based architecture

3 Existing Methodology

The smaller number of hardware architecture and lower complexity makes the lifting-based scheme advantageous when compared to the convolution method. When appropriate scheduling is added to the convolution architecture, the complexity is reduced when compared to lifting-based scheme. The frame buffer can be eliminated by using pipeline structure. Existing system has convolution-based three-level 2-D DWT using Wallace-tree-based generic booth multiplier [18] shown in Fig. 2.

On investigating the existing convolution-based generic structure shown in Fig. 2, it is understood that the concurrency is followed in computation instead of feedbacks. The parallel structure in data access makes it faster even though more hardware is used. The filters are orthogonal and bi-orthogonal wavelets type. This reduces the memory requirement at each stage with suitable block size. By achieving maximum DWT levels, the HUE can be maximum provided suitable block size has to be selected at the first-level stage.

4 Proposed Methodology

Due to the stability concerns and less complexity in implementation, finite impulse response (FIR) filters are preferred for signal and image-processing applications. But the direct computation involves multiplier blocks which will increase the critical delay. In addition, the power consumption and area increases. The problems can be rectified using distributed architectures. Since image-processing and signal-processing applications require more computations, using a direct multiplier-based

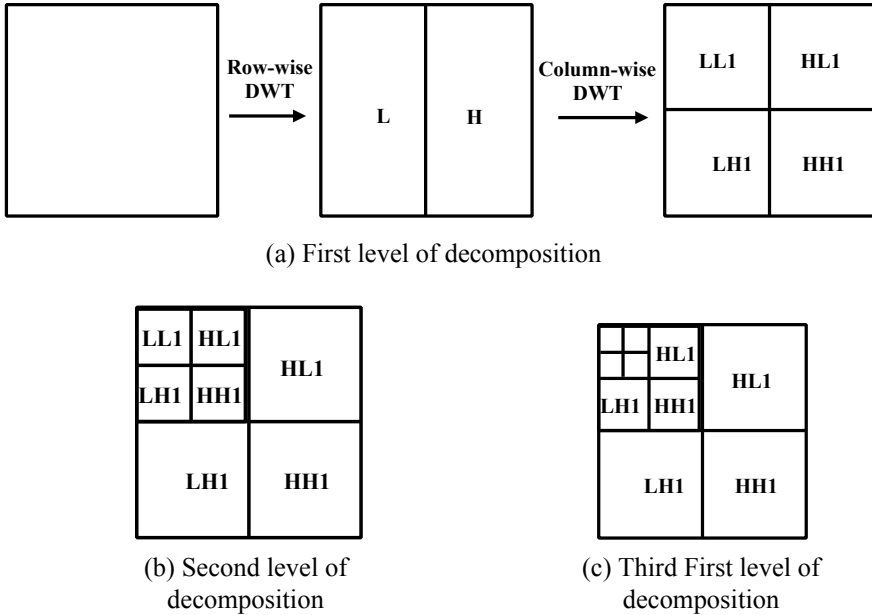


Fig. 2 Three-level decomposition of 2 D DWT

architecture like Wallace tree, booth, BK multiplier will increase the area and power. These existing multipliers will increase the area to perform the shift and add operation. Compressor-based multiplier will reduce the accuracy. Using the pipelining, the critical delay can be reduced. But additional registers are required for the same. The expression for FIR structure implemented in DWT architecture with input $x(k)$ is given by the form.

$$y[n] = \sum_{k=0}^{L-1} w[k]x[n - k] \tag{1}$$

where k is length, $h[k]$ is the filter coefficients. In proposed system, distributed arithmetic adder is used instead of shift and add. The pipelining combined with DAA increased the speed and resource utilization.

Distributed arithmetic adder uses look-up table (LUT)-type architecture [19]. Each computation blocks are named processing unit (PU). So to perform a three-level DWT process for image-processing application, the structure in Fig. 3 is suitable. It consists of processing element like adders, delay units and buffers. The low- and high-pass coefficients are computed in the blocks, and the results of one decomposition level are added in next adder trees for further process. The next adder tree performs the computation with the outputs of previous DAA. The bi-orthogonal filters are realized using the additional adder. The computational unit determines the PSNR

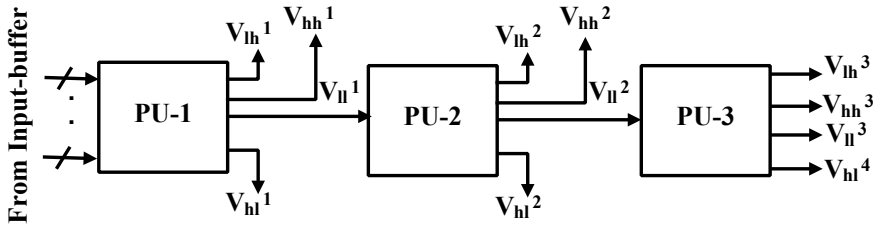


Fig. 3 Proposed structure for computation of three-level 2 D DWT

value of the output image. However, biomedical image processing has information about the disease, so proper analysis is required.

Figures 4 and 5 show the subcell architecture of orthogonal and bi-orthogonal filter with better hardware utilization efficiency. Overlapped input blocks are read from input buffer. PEs consist of subcells and delay unit. Figure 4 shows the proposed subcell structure for orthogonal filter, and Fig. 5 shows the proposed subcell structure FIR bi-orthogonal filter. Several blocks of adders and DAA were used. The decomposed filter details are obtained at intermediate stages and finally combined. The output is the low-pass filtered and high-pass filtered outputs. There are ‘k’ DAA stages to perform the ‘k’ filter lengths.

For orthogonal filter, the file size of input image is 8651 bytes and file size of compressed image is 3672 bytes. The PSNR value of orthogonal filter is 62.4991. For bi-orthogonal filter, the file size of input image is 8651 bytes and the file size of compressed image is 5143 bytes. The PSNR value bi-orthogonal filter is 52.5006. While comparing both filters, orthogonal has higher image quality than bi-orthogonal filter. This work is an investigation of the reconfigurable architecture using distributed

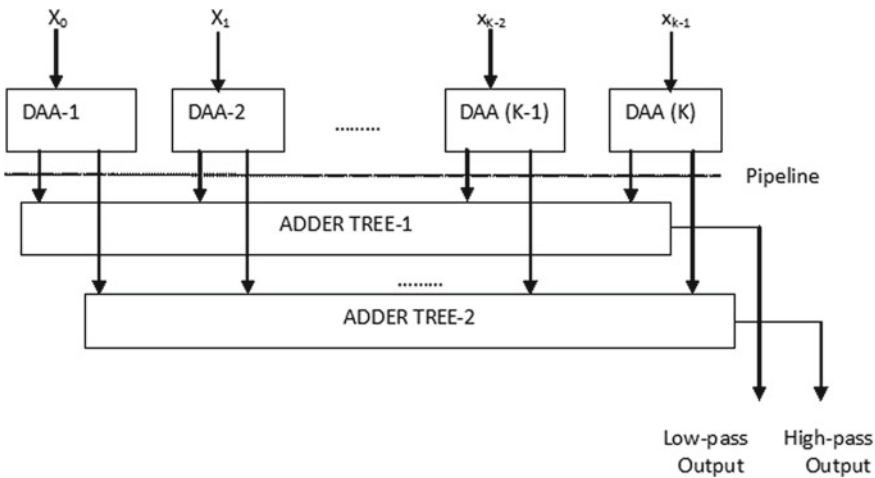


Fig. 4 Proposed subcell structure for orthogonal filter

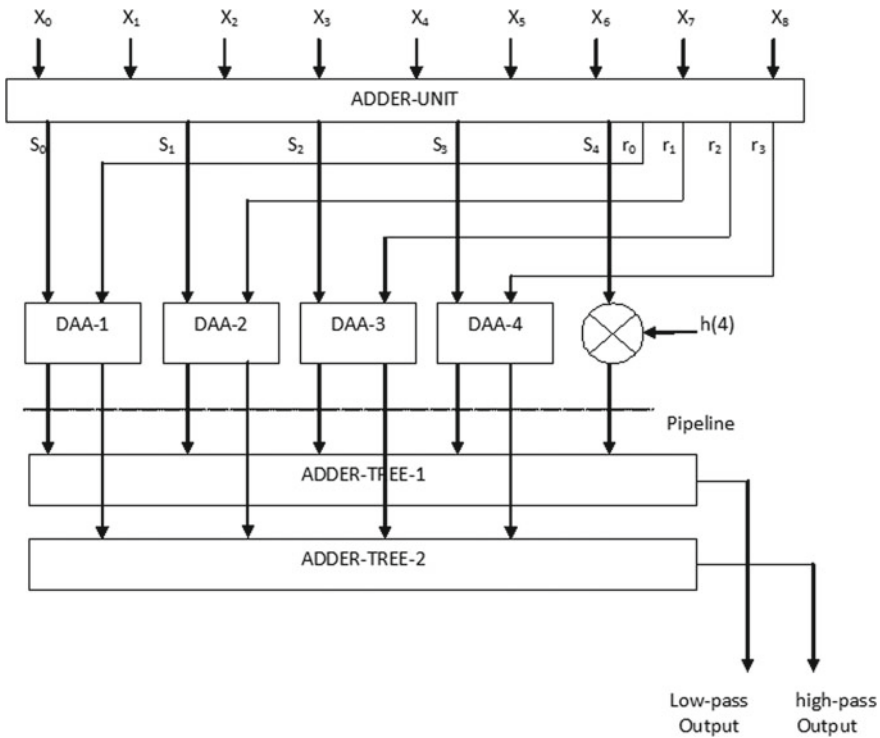


Fig. 5 Proposed subcell structure FIR bi-orthogonal filter

arithmetic for DWT. The work will be further enhanced using device based approach where the power and area can be reduced further. Eventhough reconfigurable architecture of the existing and proposed work is flexible in redesigning, when ASIC is concern, device level is better. So the investigation is a programmable approach which can be further improved through a device level implementation. The work is to be extended using FinFET-based approach to minimize the leakage current and power.

5 Result and Discussion

The implementation of the filter is done, and the results are presented in Figs. 6, 7, 8 and 9 for the input image in Fig. 8. Table 1 shows the power and gate count for the existing and proposed method. The gate count has reduced to a higher percentage when compared to the existing method.

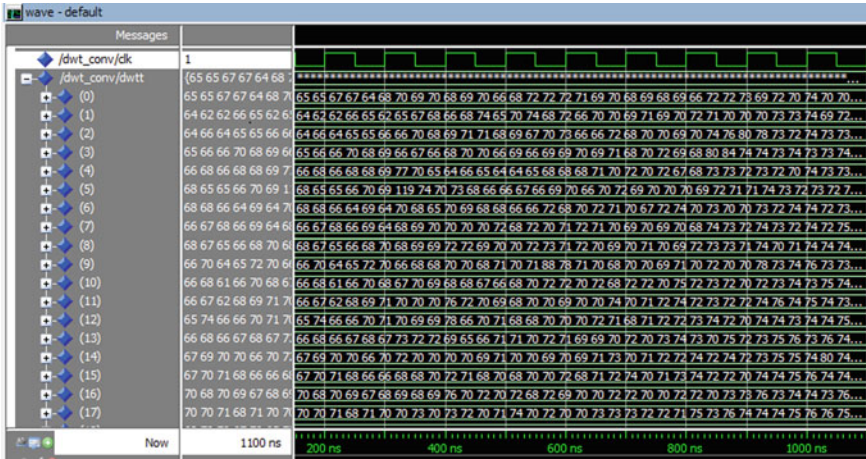


Fig. 6 Orthogonal filter

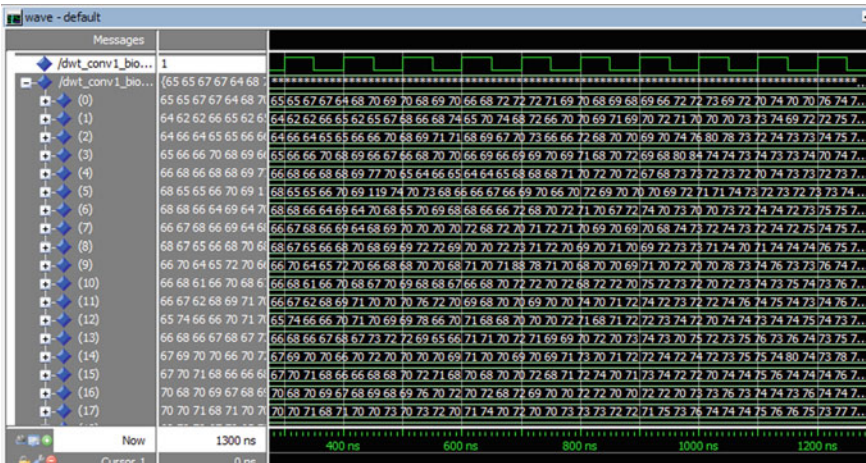


Fig. 7 FIR bi-orthogonal filter

6 Conclusion

For biomedical image processing application, the number of computation units is important. Especially the memory complexity should be low. Direct based convolution methods are easy to implement but occupies more area and power. In this paper, the power and area are improved by using the distributed arithmetic architecture to compute the three-level 2-D DWT. The implementation was done using both orthogonal and bi-orthogonal wavelet filters. In future, a multiplier less architecture will be



Fig. 8 Input image (512 × 512)



Fig. 9 Three-level 2D-DWT output image

Table 1 Comparison table

Methodology	Power (mW)	Gate count
Existing	128	12,038
Proposed	127	1416

proposed. Alternate devices will be used instead of a CMOS-based reconfigurable approach.

References

1. Vishwanath M (1994) The recursive pyramid algorithm for the discrete wavelet transform. *IEEE Trans Signal Proc* 42:673–676
2. Darji D, Bansal R, Merchant SN, Chandorkar AN (2011) High speed VLSI architecture for 2-D lifting discrete wavelet transform. In: Proceedings of the 2011 conference on design and architectures for signal and image processing (DASIP), Tampere, pp 1–6
3. Marino F (2000) Efficient high-speed/low-power pipelined architecture for the direct 2-D discrete wavelet transform. *IEEE Trans Circ Syst II: Analog Digital Sig Proc* 47:1476–1491
4. Sung T, Shieh Y, Yu C, Hsin H (2006) Low-power multiplierless 2-D DWT and IDWT architectures using 4-tap Daubechies Filters. In: Seventh international conference on parallel and distributed computing, applications and technologies (PDCAT'06), Taipei, pp 185–190
5. Xiong C, Zheng S, Tian J, Liu J, Xiong C (2004) The improved lifting scheme and novel reconfigurable VLSI architecture for the 5/3 and 9/7 wavelet filters. In: International conference on communications, circuits and systems (IEEE Cat. No.04EX914), Chengdu, pp 728–732
6. Kumar CA, Madhavi BK, Lalkishore K (2016) Pipeline and parallel processor architecture for fast computation of 3D-DWT using modified lifting scheme. In: International conference on wireless communications, signal processing and networking (WiSPNET), Chennai pp 2123–2128
7. Das B, Banerjee S (2005) Data-folded architecture for running 3D DWT using 4-tap Daubechies filters. *IEE Proceedings—circuits, Devices and Systems*, 152:17–24
8. Jain R, Panda PR (2007) memory architecture exploration for power-efficient 2D-discrete wavelet transform. In: 20th international conference on VLSI design held jointly with 6th international conference on embedded systems (VLSID'07), Bangalore, pp 813–818
9. Bhosale NV, Kanade SS (2017) 2D DWT lifting image compression scheme for error tolerant applications. In: 2017 International conference on intelligent sustainable systems (ICISS), Palladam, pp 205–210
10. Ravasi M, Tenze L, Mattavelli M (2002) A scalable and programmable architecture for 2-D DWT decoding. *IEEE Trans Circ Syst Video Technol* 12:671–677
11. Mohanty BK, Meher PK (2011) Memory efficient modular VLSI architecture for high throughput and low-latency implementation of multilevel lifting 2-D DWT. In: *IEEE Trans Signal Proc* 59:2072–2084
12. Ibraheem MS, Hachicha K, Ahmed SZ et al (2019) High-throughput parallel DWT hardware architecture implemented on an FPGA-based platform. *J Real-Time Image Proc* 16:2043–2057
13. Senthilkumar VM, Ravindrakumar S, Nithya D, Kousik NV (2019) A vedic mathematics based processor core for discrete wavelet transform using FinFET and CNTFET technology for biomedical signal processing. *Microprocess, Microsyst*
14. Maurizio M, Guido M, Massimo RR, Gianluca P (2015) Result-biased distributed-arithmetic-based filter architectures for approximately computing the DWT. *IEEE Trans Circ Syst* 62:2103–2113

15. Wei Z, Zhe J, Zhiyu G, Yanyan L (2012) An efficient VLSI architecture for lifting—based discrete wavelet transform. *IEEE Trans Circ Syst-II* 59:158–162
16. Hasan MM, Wahid KA (2018) Low-cost lifting architecture and lossless implementation of Daubechies-8 Wavelets. *IEEE Trans Circ Syst I: Regular Papers* 65:2515–2523
17. Huang C-T, Tseng P-C, Chen L-G (2005) Generic RAM-based architectures for 2-D discrete wavelet transform with line-based method. *IEEE Trans Circuits Syst Video Technol* 910–920
18. Mohanty BK, P Kumar Meher (2013) Memory-efficient high-speed convolution-based generic structure for multilevel 2-D DWT. *IEEE Trans Circ Syst Technol*
19. Zhou Y, Shi P (2011) Distributed arithmetic for FIR filter implementation on FPGA. In: *Proceeding IEEE on international conference in multimedia technology (ICMT)* pp 294–297

Closed-Form Expressions of BER and Capacity for Co-operative NOMA



Simran Sethi, Soumil Tripathi, Shreya Srivastava, Saurabh Katiyar, S. Pratap Singh, and M. Lakshmanan

Abstract One of the most propitious techniques for designing of 5G wireless networks is non-orthogonal multiple access. It surpasses over the prevalent orthogonal multiple access (OMA) scheme in terms of different parameters. Cooperative communication, on the other hand, is a natural continuation of the customary relaying systems. This infers that cooperative NOMA (C-NOMA) can be an efficient technique for spanning coverage areas of the networks. Also, various factors like path loss, shadowing and fading can be improved using C-NOMA in addition to providing communication reliability. Keeping above very facts in mind, this paper presents performance analysis of C-NOMA by presenting the analytical expressions for bit error rate (BER) and capacity. Also, both full-duplex (FD) and half-duplex (HD) methods are incorporated into the analysis. It is noteworthy to mention that analysis is carried out for D1 user, whereas that for D2 can be presented as an extension.

Keywords NOMA · Outage probability · Bit error rate · Capacity · Cooperative relaying

1 Introduction

NOMA has been recognized as the major propitious approach for the design of 5G wireless networks [1, 2]. It surpasses the traditional OMA system concerning all the important parameters like latency, throughput, spectral efficiency, and reliability as well [3]. NOMA operates under two essential methods: the power domain and the code domain. NOMA's underlying principle is to facilitate numerous users by dividing them into the transmitter's power domain multiplexing, where the signals are superposed by splitting them in the power domain. Successive interference cancellation (SIC) on the receiver side is utilized to separate the multiplexed user signal, thereby allowing numerous users to be served at the identical time, frequency and spreading codes but at distinct power levels [4, 5]. NOMA designates lower power

S. Sethi · S. Tripathi · S. Srivastava · S. Katiyar · S. Pratap Singh · M. Lakshmanan (✉)
Galgotias College of Engineering and Technology, Greater Noida, India
e-mail: lakshmanan.m@galgotiacollege.edu

© Springer Nature Singapore Pte Ltd. 2021
R. Agrawal et al. (eds.), *Advances in Smart Communication and Imaging Systems*,
Lecture Notes in Electrical Engineering 721,
https://doi.org/10.1007/978-981-15-9938-5_26

for users having prosperous channel state and allots higher power to those having poor channel state which assures user integrity. The use of NOMA affirms that user having poor channel realization is served, but also the user with enhanced channel realization can parallelly use the corresponding bandwidth resource as the weak user which ensures user fairness [6, 7].

To further strengthen the reliability of NOMA, this technique has been protracted to cooperative transmission schemes. In a cooperative NOMA network, the user and relays cooperate to solve channel fading and to boost the efficiency of the system [8]. Cooperative NOMA is an efficient approach for spanning the coverage area of the networks which helps in overcoming the channel deterioration which includes the factor like fading, shadowing and path loss as well as to increase communication authenticity. Cooperative NOMA is the usual continuation of the obsolete relaying scheme which takes the upper hand of the decreased weakening between a relay node and weak NOMA users. But, an additional slot cost for the system is added while using C-NOMA. Intending to overcome this problem, the effective solution is the employment of full-duplex (FD) relaying technology. In FD relaying, the transmission, as well as the reception, is simultaneously done in a similar frequency band and during the same time window. Due to its potential to enhance the spectral efficiency, FD relaying has captivated substantial attention by allowing concurrent downlink and uplink transmission in the same frequency band [9, 10].

Outage probability, BER, capacity analysis and system throughput are essential performance metrics of any communication system. However, as per our best knowledge, it can be noticed that BER and the capacity of the CRS-NOMA system under FD/HD have not been presented in the literature till date. So in this paper, analysis of BER and capacity is presented followed by proposing the analytical expressions for the given system.

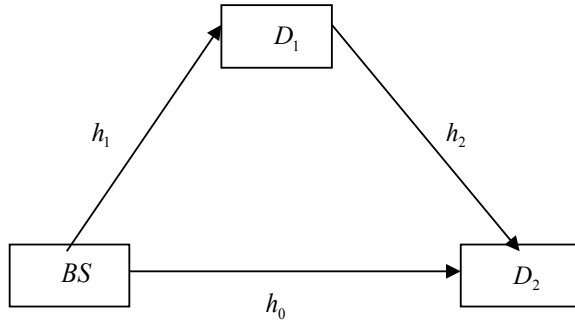
Further, the paper is structured as follows: Sect. 1 puts forward a summarized introduction of the topic under consideration. Section 2 outlines the model of the system under review. Section 3 proposes various analytical expressions of BER and capacity for NOMA in the context of a cooperative relay. Section 4 discusses the numerical analysis. Finally, the paper is finalized in Sect. 5.

2 System Model

Figure 1 depicts a cooperative relaying system which consists of base station (BS), two D_1 and D_2 users, both near user and remote user, respectively.

It is noticeable that under cooperative communication with the assistance of close user D_1 , the BS interacts with far user D_2 . D_1 uses decoding and forwarding (DF) method to transmit the information to D_2 . D_1 features one transmitting antenna and one receiving antenna to allow FD communication, whereas BS and D_2 are single-antenna devices. Further different fading channels are modeled as Rayleigh fading distribution with channel coefficients as h_1 , h_2 and h_0 for $BS \rightarrow D_1$, $D_1 \rightarrow D_2$ and

Fig. 1 Cooperative relaying system under NOMA



BS \rightarrow D_2 links, respectively. Noise is also modeled as additive white Gaussian noise having mean power as N_0 .

The cumulative distributive function (CDF) for the near user D_1 under FD NOMA can be as [11]

$$F_{\gamma}^{D_1,FD}(\gamma) = 1 - \frac{\Omega_1 a_1 \rho}{a_1 \Omega_1 \rho + \rho \gamma \Omega_{LI}} e^{-\frac{\gamma}{a_1 \rho \Omega_1}} \tag{1}$$

where $\rho = \frac{E_0}{N_0}$ is transmit signal-to-noise ratio, a_1 is the coefficient for power allocation and h_{LI} and Ω_{LI} channel coefficient and average power for feedback channel, respectively.

Without loss of generality CDF for the near user D_1 for half-duplex NOMA can be given as [12]

$$F_{\gamma}^{D_1,HD}(\gamma) = 1 - e^{-\frac{\gamma}{a_1 \rho \Omega_1}} \tag{2}$$

3 Closed-Form Expressions of BER and Capacity Under CRS-NOMA

According to [12], the average BER for a wide-ranging series of various varieties of binary modulation schemas is given by

$$P_e(\rho) = \frac{a^b}{2\Gamma(b)} \int_0^{\infty} \gamma^{b-1} e^{-a\gamma} F_{\gamma}(\gamma) d\gamma \tag{3}$$

where the specific modulation scheme is specified by the parameters a and b . Substituting the values as $b = 0.5$ and $a = 1$, the average BER of binary phase shift keying is obtained, $b = 1$ and $a = 1$ for differential phase shift keying, and the corresponding

values for obtaining BER for binary frequency shift keying are $a = 0.5$ and $b = 0.5$, respectively.

3.1 BER Under Full Duplex

BER of full-duplex NOMA for D_1 can be obtained by substituting Eq. (1) in Eq. (3)

$$P_e^{\text{FD}}(\rho) = \frac{a^b}{2\Gamma(b)} \int_0^\infty \gamma^{b-1} e^{-a\gamma} \left(1 - \frac{\Omega_1 a_1 \rho}{a_1 \Omega_1 \rho + \rho \gamma \Omega_{LI}} e^{-\frac{\gamma}{a_1 \rho \Omega_1}} \right) d\gamma \quad (4)$$

$$P_e^{\text{FD}}(\rho) = \frac{a}{2\Gamma(b)} \left(\int_0^\infty \gamma^{b-1} e^{-a\gamma} d\gamma - \int_0^\infty \frac{\Omega_1 a_1 \rho}{a_1 \Omega_1 \rho + \rho \gamma \Omega_{LI}} \gamma^{b-1} e^{-a\gamma} e^{-\frac{\gamma}{a_1 \rho \Omega_1}} d\gamma \right) \quad (5)$$

Using table of integral [12, p. 340,]

$$P_e^{\text{FD}}(\rho) = \frac{a^b}{2\Gamma(b)} \left((b-1)! a^{-b} - \frac{\Omega_1 a_1 \rho}{\rho \Omega_{LI}} \int_0^\infty \frac{\gamma}{\gamma + \frac{a_1 \Omega_1}{\Omega_{LI}}} e^{-\gamma \left(a + \frac{1}{a_1 \rho \Omega_1} \right)} d\gamma \right) \quad (6)$$

Using equation [12, p. 341]

$$P_e^{\text{FD}}(\rho) = \frac{a^b}{\Omega_{LI}} \left((b-1)! a^{-b} - \frac{\Omega_1 a_1}{\Omega_{LI}} \left((-1)^{b-2} \left(\frac{a_1 \Omega_1}{\Omega_{LI}} \right)^{b-1} e^{\frac{a_1 \Omega_1}{\Omega_{LI}} \left(a + \frac{1}{a_1 \rho \Omega_1} \right)} \right) \right. \\ \left. Ei \left(\frac{-a_1 \Omega_1}{\Omega_{LI}} \left(\frac{1}{\rho a_1 \Omega_1} + a \right) \right) + \sum_{k=1}^{b-1} (k-1)! \left(\frac{-a_1 \Omega_1}{\Omega_{LI}} \right)^{b-1-k} \left(\frac{1}{a_1 \rho \Omega_1} + a \right)^{-k} \right) \quad (7)$$

3.2 BER Under Half Duplex

BER of HD NOMA for D_1 can be obtained by substituting Eq. (2) in Eq. (3)

$$P_e^{\text{HD}}(\rho) = \frac{a^b}{2\Gamma(b)} \int_0^\infty \gamma^{b-1} e^{-a\gamma} \left(1 - e^{-\frac{\gamma}{a_1 \rho \Omega_1}} \right) d\gamma \quad (8)$$

Using table of integral [12, p. 340]

$$P_e^{\text{HD}}(\rho) = \frac{a^b}{2\Gamma(b)} \left((b-1)!a^{-b} - (b-1)! \left(a + \frac{1}{a_1\Omega_1\rho} \right)^{-b} \right) \tag{9}$$

3.3 Capacity for FD Under NOMA

$$C_{D_1}^{\text{FD}} = \frac{1}{\ln(2)} \int_0^\infty \frac{1 - F_\gamma(\gamma)}{1 + c\gamma} d\gamma \tag{10}$$

where $F_\gamma(\gamma) = 1 - \frac{a_1\Omega_1\rho}{a_1\Omega_1\rho + \rho\gamma\Omega_{LI}} e^{-\frac{\gamma}{a_1\Omega_1\rho}}$

Substituting the value of $F_\gamma(\gamma)$ in Eq. (10) and solving, we get

$$C_{D_1}^{\text{FD}} = \frac{1}{\ln(2)} \int_0^\infty \frac{\Omega_1 a_1 \rho}{(1 + c\gamma)(\Omega_1 a_1 \rho + \rho\gamma\Omega_{LI})} e^{-\frac{\gamma}{a_1\Omega_1\rho}} d\gamma \tag{11}$$

By partial fraction

$$C_{D_1}^{\text{FD}} = \frac{1}{\ln(2)} \left(\int_0^\infty \frac{A}{(a_1\Omega_1\rho + \rho\gamma\Omega_{LI})} + \frac{B}{1 + c\gamma} \right) e^{-\frac{\gamma}{a_1\Omega_1\rho}} d\gamma \tag{12}$$

where $A = \frac{\Omega_1 a_1 \rho \Omega_{LI}}{\Omega_{LI} - a_1 c \Omega_1}$ and $B = \frac{\Omega_1 a_1 c}{c a_1 \Omega_1 - \Omega_{LI}}$

From the values of A and B and using equation [12, pp. 341], we get

$$C_{D_1}^{\text{FD}} = \frac{1}{\ln(2)} \left(\frac{A}{\rho\Omega_{LI}} (-e)^{\frac{a_1\Omega_1}{\Omega_{LI} a_1 \rho \Omega_1}} Ei \left(\frac{-1}{\rho\Omega_{LI}} \right) + \frac{B}{c} (-e)^{\frac{1}{c\rho a_1 \Omega_1}} Ei \left(\frac{-1}{c\rho a_1 \Omega_1} \right) \right) \tag{13}$$

4 Numerical Analysis

The simulated results of the derived closed expression of BER and capacity is presented in this section.

Without the lack of generalization, we presume the distance between BS and D_2 is standardized to unity, $\Omega_{SD_1} = d^{-\alpha}$ and $\Omega_{D_1 D_2} = (1 - d)^{-\alpha}$, d is considered as the standardized distance between the base station and the near user, setting to be $d = 0.3$

and path loss exponent $\alpha = 2$. The coefficients of power allocation for CRS-NOMA are $a_1 = 0.2$ and 0.4 for full-duplex NOMA, $a_1 = 0.4$ and 0.5 for half-duplex NOMA and $a_2 = 0.8$, respectively.

Figure 1 represents the BER versus SNR for user D_1 for both FD and HD NOMA under DPSK modulation scheme. The presented closed form for HD and FD in Eqs. (7) and (9), respectively, is used to obtain different curves of DPSK modulation scheme (with $a = 1$ and $b = 1$). It is observed that the BER of HD NOMA is less than FD NOMA for any value of a_1 because of the existence of loop interference in FD NOMA. It is observed that on increasing the value of a_1 for HD NOMA, BER decreases. On increasing the value of a_1 for FD NOMA, BER decreases for fixed value of Ω_{LI} .

Figure 2 represents the BER versus SNR for user D_1 for both FD and HD NOMA under BFSK modulation scheme. The presented closed form for HD and FD in Eqs. (7) and (9), respectively, is used to obtain different curves of BFSK modulation scheme (with $a = 0.5$ and $b = 0.5$). It is observed that the BER of HD NOMA is less than FD NOMA for any value of a_1 . This is because loop interference prevails in full-duplex NOMA. It is also observed that on increasing the value of a_1 for HD NOMA, BER decreases. On increasing the value of a_1 for FD NOMA, BER decreases for fixed value of Ω_{LI} .

Figure 3 represents the BER versus SNR for user D_1 for both FD and HD NOMA under BPSK modulation scheme. The presented closed form for HD and FD in Eqs. (7) and (9), respectively, is used to obtain different curves of BPSK modulation scheme (with $a = 1$ and $b = 0.5$). It is observed that the BER of HD NOMA is less than FD NOMA for any value of a_1 . This is because loop interference prevails in full-duplex NOMA. It is also observed that on increasing the value of a_1 for HD NOMA, BER decreases. On increasing the value of a_1 for FD NOMA, BER decreases for fixed value of Ω_{LI} which satisfy the theoretical analysis.

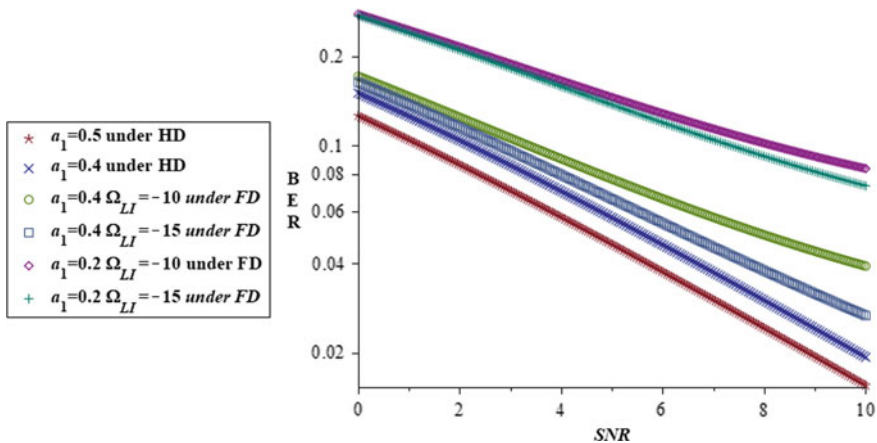


Fig. 2 BER of DPSK scheme under HD and FD NOMA

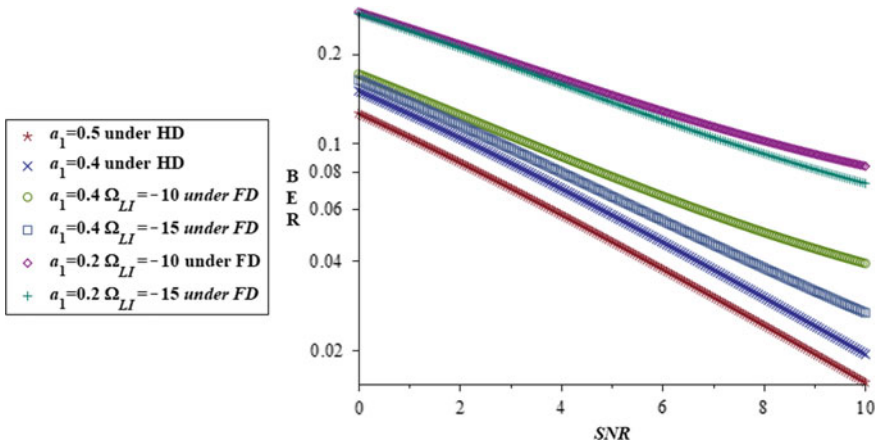


Fig. 3 BER of BFSK scheme under HD and FD NOMA

Figure 4 represents the capacity versus SNR for user D1 for FD NOMA. The presented closed form for FD in Eq. (13) is used to obtain different curves (with $a_1 = 0.2, 0.3, 0.4$ and $\Omega_{LI} = -10$ dB, -15 dB). It is observed that as the value of a_1 is increased for a fixed value of Ω_{LI} the capacity increases. It is also observed that for a fixed value of a_1 increasing Ω_{LI} , capacity decreases as shown in Fig. 5.

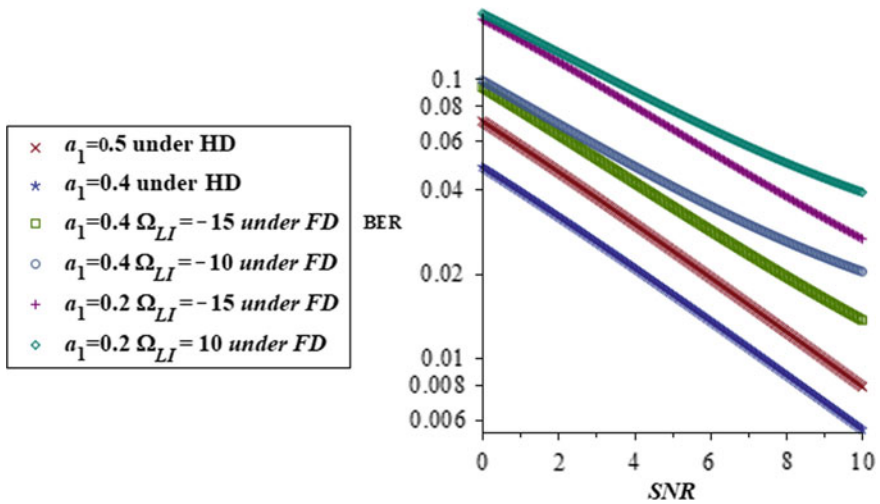


Fig. 4 BER of BPSK scheme under HD and FD NOMA

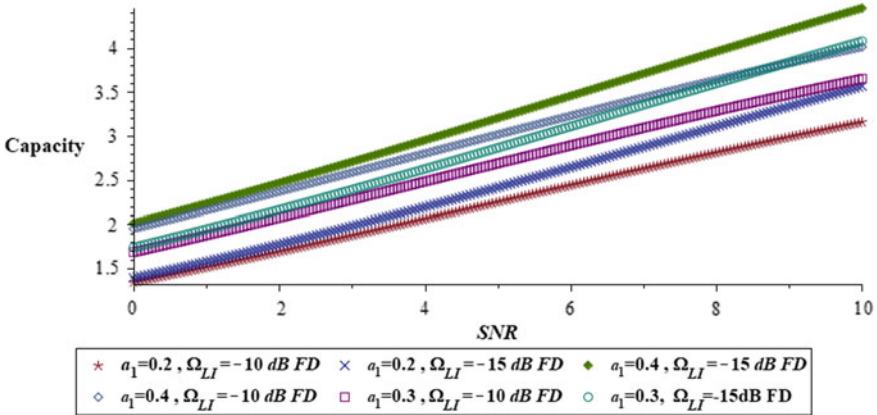


Fig. 5 Capacity for full-duplex NOMA

5 Conclusion

In this paper, FD NOMA and HD NOMA are analyzed in terms of BER and capacity. Three modulation schemes, namely BPSK, BFSK and DPSK, are analyzed for both FD and HD NOMA. However, for each of the cases power allocation coefficient (a_1) and average power of loop interference (Ω_{LI}) are taken as parameters. Irrespective of modulation schemes, it is observed that increase in a_1 decreases the BER and vice versa. It is also noticed that increase in Ω_{LI} increases the BER. Also, increase in a_1 improves the capacity, whereas increase in Ω_{LI} deteriorates the capacity. The obtained analysis has perfectly matched with theoretical background. Finally, it is noteworthy to mention that this paper presents analysis for D_1 user only while that for D_2 is left for future analysis.

References

1. Islam SR, Avazon N, Dobre OA, Kwak KS (2016) Power domain non orthogonal multiple access (NOMA) in 5G systems: potentials and challenges. *IEEE Commun Surv Tutor* 19(2):721–742
2. Islam SM, Zeng M, Dobre OA (2017) NOMA in 5G systems: “Exciting possibilities of enhancing spectral efficiency”. arXiv preprint arXiv: 1706.08215. (2017)
3. Saito Y, Kishiyama Y, Benjebbour A, Nakamura T, Li A, Higuchi K (2013) Non orthogonal multiple access (NOMA) for cellular future radio access. In: 2013 IEEE 77th vehicular technology conference (VTC Spring). IEEE, pp 1–5
4. Ding Z, Liu Y, Choi J, Sun Q, ElKashlan M, CHih-Lin I, Poor HV (2017) Application of non-orthogonal multiple access in LTE and 5G networks. *IEEE Commun Magaz* 55(2):185–191
5. Ding Z, Yang Z, Fan P, Poor HV (2014) On the performance of non-orthogonal multiple access in 5G systems with randomly deployed users. *IEEE Sign Process Lett* 21(12):1501–1505
6. Ding Z, Peng M, Poor HV (2015) Cooperative non-orthogonal multiple access (NOMA) in 5G systems. *IEEE Commun Lett* 19(8):1462–1465

7. Kim JB, Lee J, Kim D, Choi, Y (2017) System-level performance evaluation for non-orthogonal multiple access (NOMA) in co-ordinated direct and relay transmission. In: 2017 international conference on information and communication technology convergence (ICTC). IEEE, pp 1296–1298
8. Laneman JN, Tse DN, Wornell GW (2004) Cooperative diversity in wireless networks: efficient protocols and outage behavior. *IEEE Trans Inf Theo* 50(12):3062–3080
9. Kader MF, Shin SY, Leung VC (2018) Full-duplex non-orthogonal multiple access in cooperative relay sharing for 5G systems. *IEEE Trans Veh Technol (VTC)* 67(7):5831–5840
10. Yue X, Liu Y, Kang S, Nallanathan A, Ding Z (2017) Outage performance of full/half-duplex user relaying in NOMA systems. In: 2017 IEEE international conference on communications (ICC). IEEE, pp 1–6
11. Sharma N, Bansal A, Garg P (2016) Decode and forward relaying in mixed $\eta - \mu$ and gamma-gamma dual hop transmission system. *IET Commun* 10(14):1769–1776
12. Gradshteyn IS, Ryzhik IM (2014) Table of integrals, series, and products. Academic press

Real Time Physical Fitness Monitoring App: BeTough



Pushpa Choudhary, Akhilesh Kumar Choudhary, Arun Kumar Singh, and Ashish Tripathi

Abstract State of health is called physical fitness basically it is an ability to perform a specific task like sports, occupation, and daily activities. Physical fitness can be achieved by good nutrition, proper exercise, and proper rest. In this paper, an app is proposed for awareness of fitness known as “BeTough” is a fitness movement to encourage people to take a step ahead for their better health. BeTough is a platform where fitness data of a person is recorded and monitored. It also has a series of functions such as improving the scientific guidance, rationally formulating the fitness plan, strengthening the persistence of exercise, changing the single evaluation, and improving the consciousness of exercise. The Web app is simple and portable.

Keywords Chief executive officer (CEO) · Real-time fitness app (RTFA)

1 Introduction

Physical activity not only helps to improve physical function of the body, but it also helps in social and mental well-being. However, for several groups of people (such as older and adults), doing regular workout at gym or outdoor may be inconvenient or impossible. The most important reason is no body is having time for an extracurricular

P. Choudhary (✉) · A. K. Singh · A. Tripathi
Department of Information Technology, G. L. Bajaj Institute of Technology and Management,
Greater Noida, India
e-mail: pushpak2728@gmail.com

A. K. Singh
e-mail: arun.k.singh.iiit@gmail.com

A. Tripathi
e-mail: ashish.mnnit44@gmail.com

A. K. Choudhary
Bharat Sanchar Nigam Limited, Ghaziabad, India
e-mail: choudhary.akhilesh@gmail.com

physical exercise activity at their workplace or home due to that obesity problem has been increased. And obesity generates number of disease in human body.

There are number of applications related to health care is available on Internet. Till January 2015, 242.92 million people using mobile Internet in India. And till 2019, it reaches to 627 million. India is the second-largest country in the world where number of mobile Internet user is available after China [1].

In addition, due to fierce social competition and increased pressure on people's lives, most people often work overtime, staying up late, living irregularly, lacking exercise, and more and more people are paying attention to physical health problems. Nowadays, people do not have time for exercise due to their lifestyle, but the development of the network to cultivate sports. People can develop their own exercise habits. If anyone is not fully mobilized to actively participate in extracurricular sports activities at their workplace or home. Yes, it is difficult for some period of time but not impossible.

In this paper, an application has been introduced which is not only for college students or youth but it also includes people from any age group. People won't initialize themselves till they are not attracted or affected completely by it.

As a part of study report, Gympik [2] has developed a Fitness Health Index by taking five major parameter. Those are regularity, diet, health consciousness, stress levels, and gym membership. By doing survey they found that, responses from people of 1.06 million, mainly in the age group of 20–35 years, survey of Gympik study notice that 52% do not find time to do exercise, and 36% people join a fitness center by the motivation. In fact, 14% claim to be absolutely clueless about where to begin their fitness journey. Commenting on the research, Amaresh Ojha, Founder and CEO, Gympik, said, "In India, the top fitness players barely constitute 15% of the market share as compared to that of Japan and Singapore where 40% market share is covered by the top five players. There's massive scope for consolidation in the organized fitness sector in India."

Figure 1 shows the total data showing people involved in fitness activities and total revenue generated from this industry along with the market size. Figure 2 showing India's contribution along with the age groups involved in these fitness activities with their interest which is very less as compared to USA or any other country [3].

In this paper, an app is proposed for awareness of fitness known as "BeTough" is a fitness movement to encourage people to take a step ahead for their better health. It has been observed by many researches that if any task done by repeatedly, a habit can form after some days; after sometimes, it's becomes a part of your daily routine. BeTough app will provide a strong base for fitness and reduce the chances of picking up injuries, when you start the training hard.

College students are one of the most active thinking groups and the fastest acceptance of new things in society. Sports app have the functions of fitness teaching, data recording, user's actual movement track, sports video sharing, and sports fitness program learning. App also has communication and evaluation functions similar to forum functions, but also can make appointments with friends, everyone to exercise together to increase fun and enthusiasm, but there are also many drawbacks.

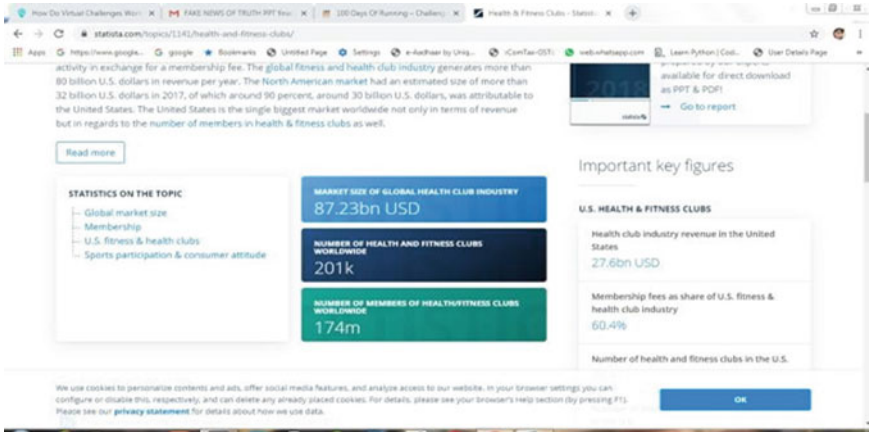


Fig. 1 States showing people involved in fitness activities worldwide

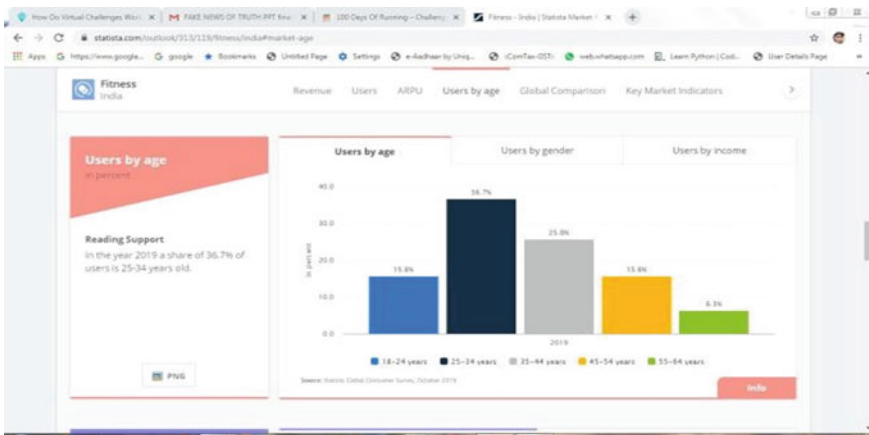


Fig. 2 India contribution in fitness with different age groups

There are few studies on the effect of sports health app on people’s physical exercise behavior and habit formation, and foreign studies on sports app mainly focus on the realization of fitness function and fitness technology path. Sports app also have the functions of formulating sports plans according to personal data and goals, and executing and implementing sports plans. As long as you have time and network, you can use your own fragmented time to exercise with sports app, break the traditional way of exercise, so that users can use lunch break time, break time can launch flexible and diverse ways of fitness.

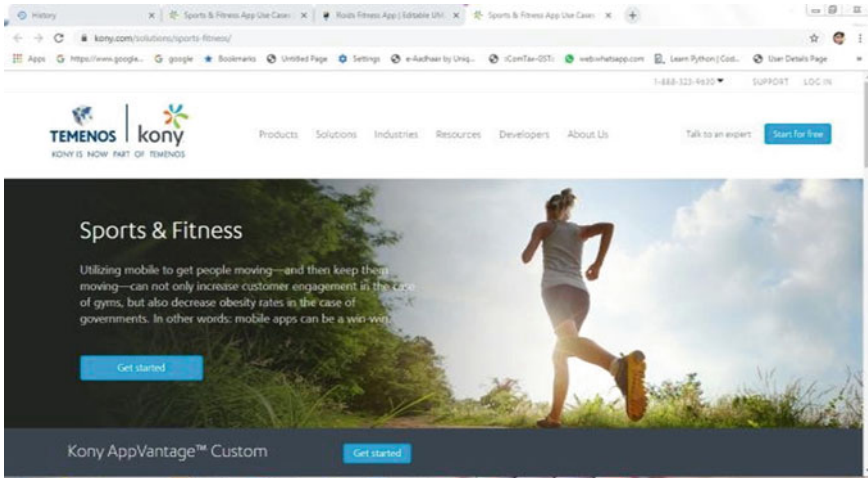


Fig. 3 Existing app Kony [4]

2 Relevant Work and Existing Systems

There are various application introduced in the market which are majorly focused on the health issues but very few application which is introducing challenges for various fitness and sports activities [5–10]. Other applications involving around taking data and providing measures to stay fit and providing record summary as well but encouragement is still an issue.

Following are list of fitness application:

1. myFitness Companion
2. mHealth
3. FitnessFreak
4. Kony [4]
5. 100 Days of Running
6. Truweight.

Figure 3 is a fitness-based application for records of the individual and consisting about health records, i.e., it is basically find out the entire existing project but only providing storing measures not for promoting and the challenges.

3 Proposed Work

The “BeTough” application is that which is giving an opportunity to all to indulge in the activity and record themselves. Also, it will help them to maintain a proper time table so that they can take care of their health. It will introduce various challenges

after their completion one can record themselves and find out the changes which will arrive after this. In all to avoid the casual approach taken by the people, this will help to motivate those to stay fit and healthy and people will participate more. Entering virtual challenges is the ultimate way of staying active, keeping fit, and earning awesome rewards.

Various steps are as follows:

- Enter a challenge online
- Show your BeTough skills
- Submit your evidence
- Get your rewards
- Enter another challenge and smash it
- Daily meal details
- Doctor consultancy about diet.

Each calendar month, running the challenges on verifying distances that one can sign up for once registered, people have the entire month to complete the task through various activities introduced like running, cycling, swimming, etc. And if the person successfully completed the task, then he/she will get prestigious rewards like vouchers, coupons, medals, etc.

Following are various challenges:

- Running
- Walking
- Swimming
- Cycling.

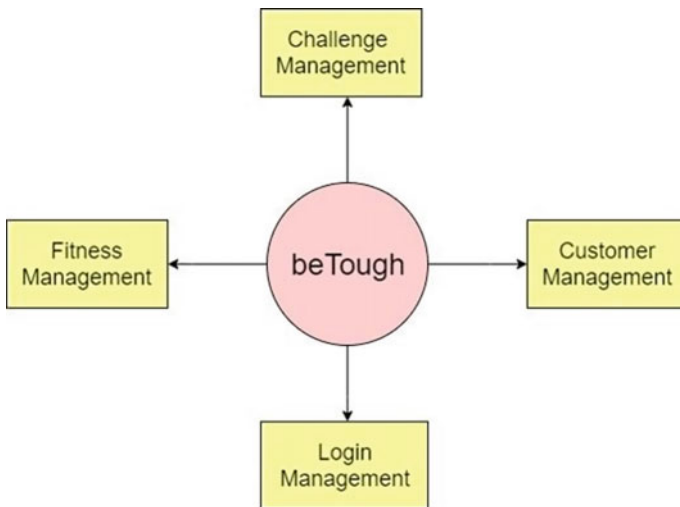


Fig. 4 Modules present in the proposed models

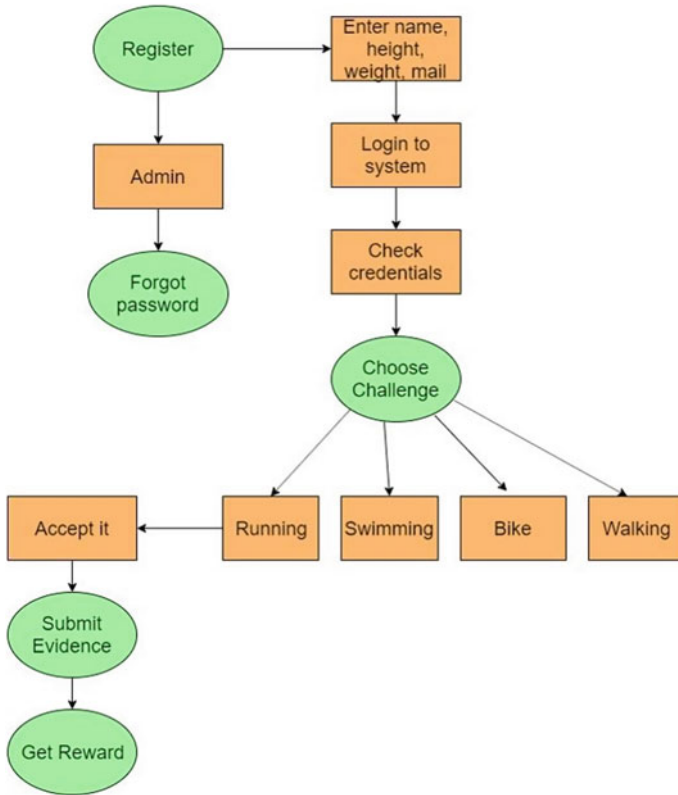


Fig. 5 Working process of the proposed model

Nowadays, focus either on their work or on technology and are not involved in any kind of physical activities and that’s why directly affecting their health. Mostly people get involve into those activities where they get some profits and they do ignore even if this is for their health.

Hence, in this paper, app is introduced as a solution to this problem called “BeTough” in which people fitness is the major concern and they will be rewarded with the exciting prizes for completing the task provided to them.

4 Experimental Result

See Figs. 6 and 7.

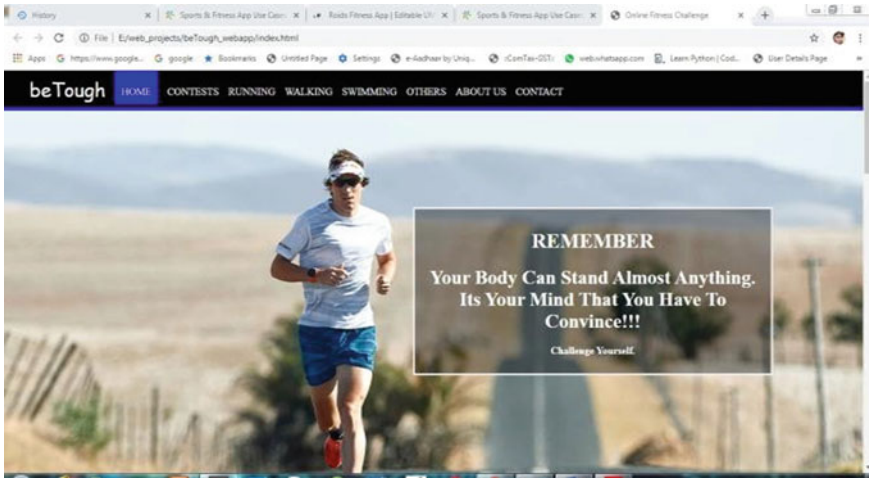


Fig. 6 BeTough home page

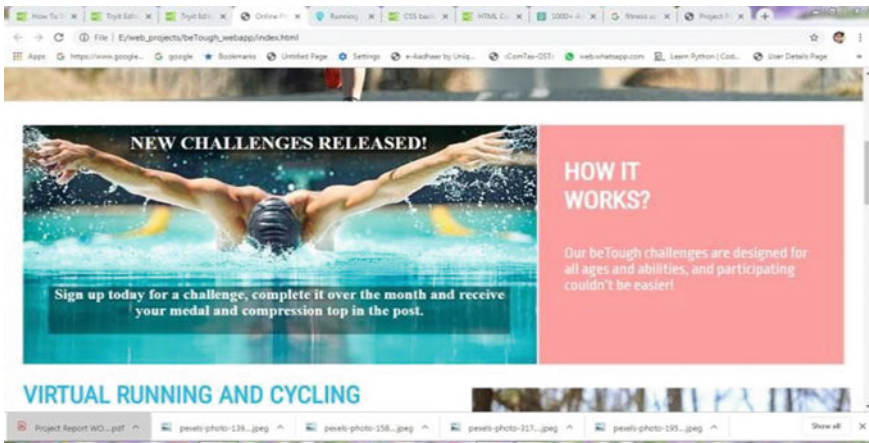


Fig. 7 BeTough challenge page

5 Conclusion and Future Scope

“BeTough” is a platform where fitness data of a person is recorded and monitored. It also has a series of functions such as improving the scientific guidance, rationally formulating the fitness plan, strengthening the persistence of exercise, changing the single evaluation, and improving the consciousness of exercise. The Web app is simple and portable. Although indulging themselves into various challenges will promote their physical fitness and also for a strong healthy youth, not only youth, young , old, any kind of age group can participate and take it ahead easily with a great

motive. Therefore, the exerciser should choose this type of application scientifically according to his actual situation and exercise needs, so that he can develop good exercise habits in continuous exercise. The results show that using these types of application reasonably and scientifically cannot only improve everyone physical fitness, but also develop good exercise habits.

In addition to the existing approach, “BeTough” will also use the functionality of artificial intelligence in the future to make the application more advances.

And if we see this to be in futuristic approach, then this application will be beneficial for our country as the data of fit and unfit people recorded can be used for data analysis. Through this, data of people can be taken, so that to know about the percentage ratio of fit to unfit, in other words, what is the actual population count which is fit as compared to other countries.

References

1. Gay V, Leijdekkers P (2015) Bringing health and fitness data together for connected health care: mobile apps as enablers of interoperability. *J Med Internet Res* 17(11):e260
2. Gowin M et al (2015) Health and fitness app use in college students: a qualitative study. *Am J Health Educ* 46(4):223–230
3. Higgins JP (2016) Smartphone applications for patients’ health and fitness. *Am J Med* 129(1):11–19
4. Chen K, Zdorova M, Nathan-Roberts D (2017) Implications of wearables, fitness tracking services, and quantified self on healthcare. In: *Proceedings of the human factors and ergonomics society annual meeting*, vol 61, no 1. SAGE Publications, Sage CA: Los Angeles, CA
5. Lupton D (2020) ‘Better understanding about what’s going on’: young Australians’ use of digital technologies for health and fitness. *Sport, Educ Soc* 25(1):1–13
6. Wei J et al (2020) Understanding and predicting the adoption of fitness mobile apps: evidence from China. *Health Commun* 1–12
7. Thomas B (2020) Fitness technology: virtual assistants, apps and apparatus in the cyberage. *Stud Ind Place Names* 40(3):7507–7519
8. Busch L et al (2020) The influence of fitness-app usage on psychological well-being and body awareness—a daily diary randomized trial. *J Sport Exerc Psychol* 42(3):249–260 (2020)
9. Kagkini A(2018) Development of an android fitness app
10. Saksono H et al (2020) Storywell: designing for family fitness app motivation by using social rewards and reflection. In: *Proceedings of the 2020 CHI conference on human factors in computing systems*

A Novel Scheme for Medical Image Compression Using Huffman and DCT Techniques



Ankit Kumar Chaudhary, Rajat Mehrotra, M. A. Ansari,
and Pragati Tripathi

Abstract Image compression is one of the data compression applications in which we convert the original data into a few bits. In image compression, we can simply preserve the data needed by removing unwanted data to be proficient to record or refer data in a functioning form. Hence, the image compression reduces the communication time and increases the communication speed. We mainly use lossy and lossless techniques to remove this type of problem. There is no data loss when we compress images with a lossless image compression technique while some of the unnecessary data losses in lossy image compression technique. By using these processes, we can reduce the data size, which we can save more data in less memory. Here, we have done the uses of Huffman and DCT techniques for image compression.

Keywords Image compression · Lossy and lossless techniques · Huffman and DCT coding

1 Introduction

Image compression is an application of data compression in which we convert the original image to some bits [1–3]. With the help of image compression, we compress the medical image to facilitate the transfer of this from one place to another [4]. In

A. K. Chaudhary (✉) · M. A. Ansari · P. Tripathi
Department of Electrical Engineering, Gautam Buddha University, Gr. Noida, India
e-mail: ankitkchy012@gmail.com

M. A. Ansari
e-mail: ma.ansari@ieee.org

P. Tripathi
e-mail: pragati.knp022@gmail.com

R. Mehrotra
Department of Electrical & Electronics Engineering, GL Bajaj Institute of Technology & Management, Gr. Noida, India
e-mail: rajatImp@gmail.com

image compression, we can reduce the dimensions of the original data to reduce the size of the original data. When we compress a medical image, our purpose is to make sure that none of the original image is the lost of the required data. Compression techniques are technically advanced to allow large files to be compressed easily. By quick improvement in a suitable way via impressive procedures, a huge scope of image data ought to store those images typically outcomes in the compressing images. There are some algorithms used to complete these. Types of compression in several actions such as lossless and lossy [5]. The image that needs to be compressed to a pixel range of grayscale ranges from 0 to 255. While compressing any data, it has to be kept in mind that any data required will not be lost in the body. Also, low bits are needed in saving data in digital media and sending. Compression to some range shows that there is a section of data whose size is required to decrease. Now, this JPEG format is absolute option for digital image. The Joint Photographic Expert Group (JPEG) which depends on discrete cosine transform (DCT) is a very extensively second choice formula for compression [6]. Image compression is one of the incredible familiar ways in image operation. In this way, we can have many basis ideas and play a significant role in the actual storage and transmission of images. In image compression, in the proposed model to reduce unnecessary data, we will use less sample to facilitate sending and saving of this. The main goal of reducing the number of bits per large base to compress images is to decrease the transmission time to display this image and broadcast the image and regenerate once again by Huffman encoding.

2 Image Compression

The main purpose of image compression is to compress data allowing it to be saved and transmitted [7]. This technic uses three initial stages in which first stage converts image to each other symbol. In second stage, we decrease pixel, and in third stage, we are coding it with the help of coefficient. This technique is better than analytical techniques because it has compression of data easily and well. Realization of compression of any data occurs by removing one or more redundancies:

1. Coding redundancy: We use that over there where we must use a small code word.
2. Inter-pixel redundancy: It gives the result of similarity between pixels of the image.
3. Psycho-visual redundancy: In it, some information is ignored by human visual system (i.e. Do not need useless information). For more operative coding in image compression, we use redundancy.

What is the need for compressing image?

- Suitable growth of memory size.

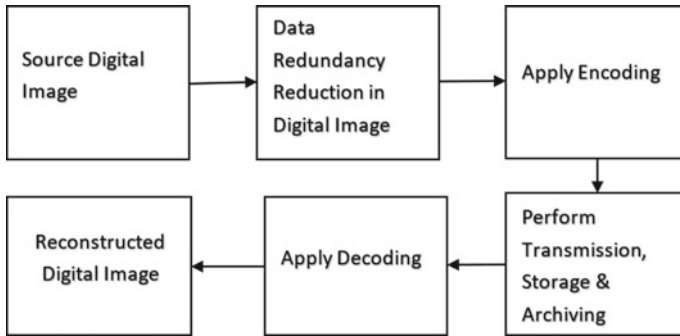


Fig. 1 Block diagram of proposed system

- Broadcasting time reduces so it makes it easier to send image through Internet and download from webpages.
- Telemedicine.
- Tele-radiology (Fig. 1).

3 Types of Image Compression

Image compression can be divided into two types like lossy image compression and lossless image compression. In lossy compression as the name itself suggests it leads to some information loss. In this technique, we do not get original data if again decompress after compressing original data because it has loss of some data during process [8]. So, this technique we use in compressing generally photographs. The best example of lossy compression technique is a JPEG. Whereas no data is lost in lossless compression technique when we compress any image using this technique, so when we again decompress data in this case, we get the original image again. We use this technique in compressing PNG and GIF file. GIF file over here is just 8-bit images. We use either of the two techniques according to our need.

3.1 Lossless Compression

There is no information loss during this when we compress an image by lossless image compression so when we decompress this compressed image again, we get the original data again. In this case when we compress binary data like image, video, audio, etc., then we must decompress it to get the original data. It is important to remember that there is some or no error between the original image and the compress image. It contains no any noise add in signal or compress image, so it is called cool process. This technique is also called entropy technique coding because it is also used

to remove or reduce redundancy. It is only used in medical image and application required. Which of the following we use some technique as lossless technique:

1. Huffman coding
2. Run-length coding
3. Arithmetic coding
4. Dictionary techniques
5. Bit Plane coding.

3.1.1 Huffman Coding

Huffman coding technique also known as greedy technique is used to compress the data and convert it into digital form. It contains all the character defined by a unique bit.

The Huffman code procedure needs the two explanations professed below:

1. First of it, we pick the characters of two smallest frequency.
2. Two characters that originate the smallest frequency may have an identical length.

In its first, we select the character of the two smallest frequencies, then by totaling them, we get a new character which we also called base element. In the left of this, base element writes the small character and writes the big character in right. Do this until all characters are finished. In this way, we get a tree. Top element of this tree is called root element. From this root element, we do numbering. Write the zero in its left and write the one in its right. For any character element that needs to go, we will follow the path from root element to that element. Then after, we write down all the numbers of path on it. Thus, we get the code of that character. A Huffman code has been created as the classification of the code tree [9]. This is the best proposed code which we use to compress the data. By it, we change the dimension of data. As a result, the average length of the code is decreased, and we are thus compressing the data. In order to reduce redundancy, we use Huffman algorithm [4] (Table 1).

Table 1 Algorithm of Huffman code

Step 1: Generate organized nodes created on the possibility
Step 2: Jump loop
Step 3: Discover & take away two lowest likelihood nodes
Step 4: Generate new node [$W[\text{Node}] = W[N1] + W[N2]$]
Step 5: Pull-out new node, posterior to arranged list.
Step 6: Recurrence the loop while waiting for only one preceding node is existing in the list

3.2 Lossy Compression

In lossy compression techniques, we remove the unnecessary data, so it reduces the data bits. The process of reducing the size of data file is usually called data compression before its send even through it is formally called source coding. Some data losses may be acceptable during this process [10]. Storage capacity should be increased by removing unnecessary data from the source data. Lossy image compression technique we use in digital camera in which we can increase storage capacity by reducing quality of image. Similarly, by removing unnecessary data in DVDs also, we use data by compressing. In the lossy audio compression, the techniques of psycho audibility have been used to remove the non-audible or less perceptible components of the signal [11].

Some benefits of the image compression technique are as follows:

1. Sending data requires less cost because the telephone network allows us to send fewer data saving time and money.
2. This not only reduces storage but also reduces execution time.
3. The possibility of getting an error at the time of transmission decreases as we already remove some data.
4. It is highly valued in terms of security (Figs. 2 and 3).

4 Mathematical Modeling of Huffman and DCT Technique

The entropy of the weighted sum of the Huffman technique

$$H(A) = \sum_{w_i > 0} w_i h(a_i) = \sum_{w_i > 0} w_i \log_2 \frac{1}{w_i} = - \sum_{w_i > 0} w_i \log_2 w_i \tag{1}$$

where $h(a_i) = \log_2 \frac{1}{w_i}$.

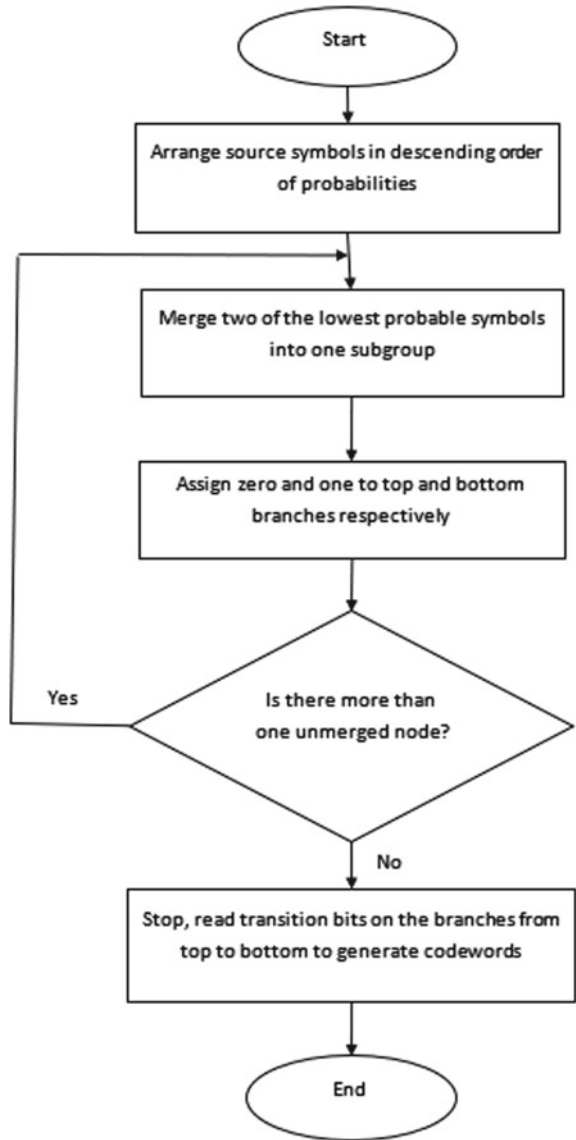
The DCT equation (Eq. 2) computes the i, j th input element of the DCT of an image.

$$D(i, j) = \frac{1}{\sqrt{2N}} C(i)C(j) \sum_{x=0}^{N-1} \sum_{y=0}^{N-1} p(x, y) \cos \left[\frac{(2x+1)in}{2N} \right] \cos \left[\frac{(2y+1)jn}{2N} \right] \tag{2}$$

$$C(u) = \begin{cases} \frac{1}{\sqrt{2}} & \text{if } u = 0 \\ 1 & \text{if } u > 0 \end{cases} \tag{3}$$

Here, $P(x, y)$ is the data element represented by the matrix p . N is the number of blocks on which we apply the DCT. By the equation, we obtain the value of pixels of a compressed image from the matrix of the original image. The original image we

Fig. 2 Flow chart of Huffman algorithm



have represented by the matrix of 8×8 blocks then applies DCT on it. The range of x and y is 0 to 7, while N is equal to 8. Thus, the value of $D(i, j)$ can be found out from Eq. (4).

$$D(i, j) = \frac{1}{4} C(i)C(j) \sum_{x=0}^7 \sum_{y=0}^7 p(x, y) \cos\left[\frac{(2x+1)i\pi}{16}\right] \cos\left[\frac{(2y+1)j\pi}{16}\right] \quad (4)$$

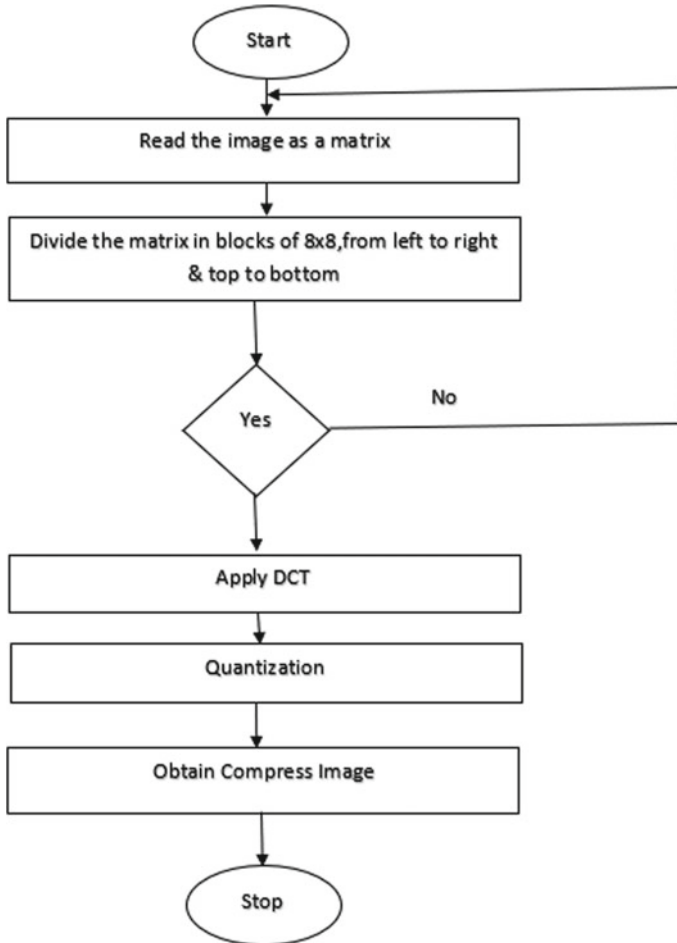


Fig. 3 Flow chart of DCT algorithm

$$T_{i,j} = \left\{ \begin{array}{ll} \frac{1}{\sqrt{N}} & \text{if } i = 0 \\ \sqrt{\frac{2}{N}} \cos \left[\frac{(2j+1)i\pi}{2N} \right] & \text{if } i < N \end{array} \right\} \quad (5)$$

5 JPEG: DCT-Based Image Coding Standard

JPEG can be compressed for that we firstly compressor it's the pixel. This data occurs in continuous time. It is easier to compress with the DCT method because it is very

Table 2 Algorithm of DCT code

Step 1: Deliver the image as a matrix.
Step 2: Divide the matrix in a wedge of 8x8.
Step 3: DCT is used for each pixel from left to right and top to bottom.
Step 4: All pixels are compressed with quantization.
Step 5: Compressed pixels of the image reduces the memory size.

fast. Its depth is 6 to 24 bits. Discrete cosine transform (DCT) is a secure array of data points in the relation of the sum of the variable cosine purposes at different incidences [4]. DCTs are significant for several executions in the ground of science and engineering, for a sample from lossy compression of audio, for example, MP3 and JPEG in which unimportant high-frequency basics can be discarded, partial differential equations are used to find out their arithmetical value. Replacing the sine function is to use the cosine, and this operation creates confusion: for compression, in which it was originated that the cosine purpose is so actual as labelled here, some roles would need an exact signal to be accurate, while the differential equation for the cosine function clarifies a precise variety of borderline conditions. JPEG image compression achieves non-essential bits of data in part complete rounding [5]. There is a related trade-off amid data loss and size reduction. Dissimilar information of different compression techniques has attained these spontaneous differences, utilizing composition files, videos, and images. So, lossy image compression technique is best for JPEG, but it is less good for the colourful image. DCT separates some part of the image based on the frequency of the image, with the lesser serious incidences being disregarded out through the quantization procedure and the extra critical rate of recurrence is being used to save the image throughout the fragmentation process [10] (Table 2).

6 Results and Discussion

Here, Huffman coding is been used in lossless technique where the compression of actual data is done with none of the information loss as shown in Figs. 4, 5, and 6 of the lossless image compression technique (Figs. 7, 8 and 9).

Table 3 illustrates that the compressed image has a smaller size as compared to the original image with no data loss where the DCT-based image coding technique is used in the lossy technique. The compressed image in the lossy technique is less in size than lossless, but it loss some information. In Table 4, compressed images are much lesser than the compressed image in Table 3.

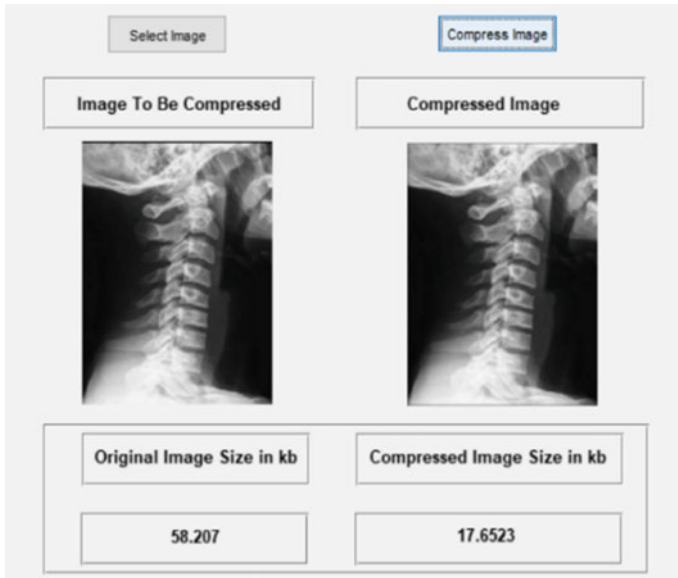


Fig. 4 Cervical spine by lossless technique

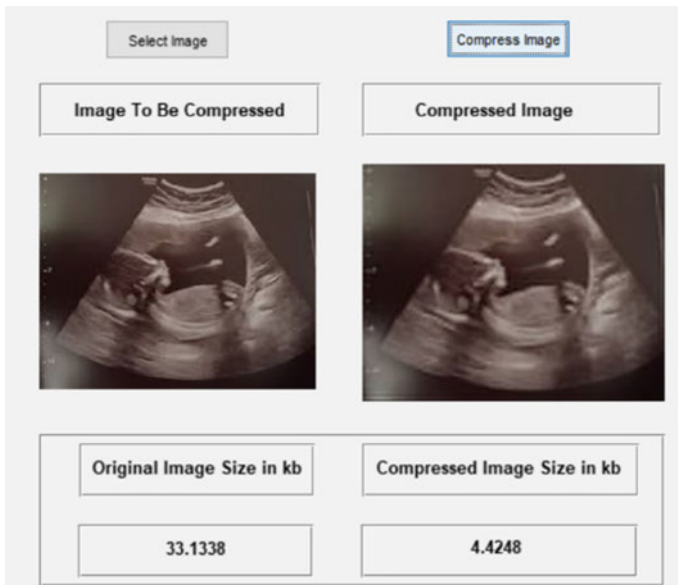


Fig. 5 Ultrasound by lossless technique

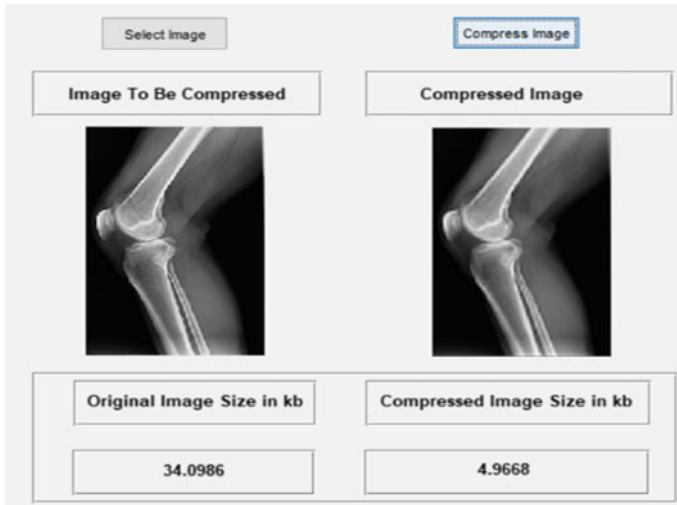


Fig. 6 Knee display by lossless technique

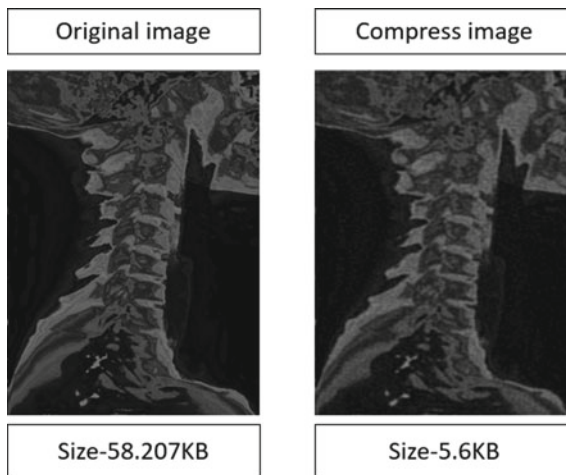


Fig. 7 Cervical spine by lossy technique

7 Conclusion

With Huffman coding here DCT image compression technique has been used to compress the image. Huffman technique has no information lost while compressing the image in the DCT technique has a loss of some information [5]. In a Huffman, compressed image can be obtained again in original form by using the decompression, while in the DCT, we cannot retrieve the original image again in the original

Fig. 8 Ultrasound by lossy technique

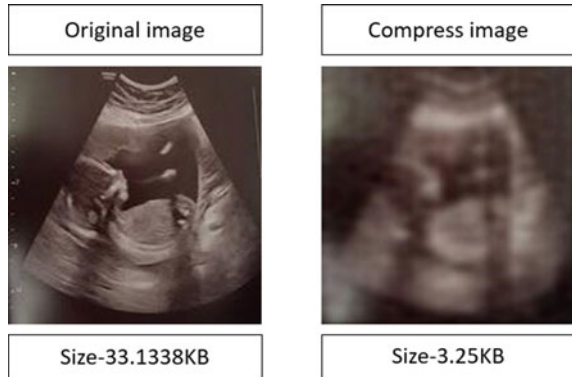


Fig. 9 Knee display by lossy technique

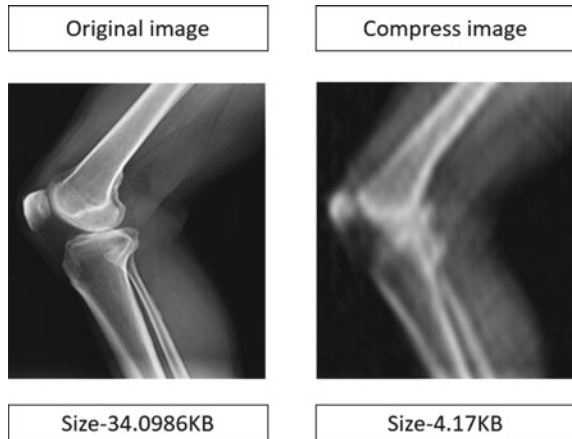


Table 3 Lossless technique

Image	Original size (KB)	Compressed size (KB)	Compression ratio
Cervical	58.207	17.6523	0.30
Ultrasound	33.1338	4.4248	0.133
Knee	34.0986	4.9668	0.145

Table 4 Lossy technique

Image	Original size (KB)	Compressed size (KB)	Compression ratio
Cervical	58.207	5.6	0.096
Ultrasound	33.1338	3.25	0.098
Knee	34.0986	4.17	0.12

Table 5 Comparison between lossy and lossless techniques

Parameters	Lossless technique	Lossy technique
Information	Have information without losses	Have information some losses
Size	Reduce data size	Reduce more data size compared to lossless
Transmission	Harder to transmit compressed file	Easy to transmit due to less bandwidth

form. This paper can be useful for people who are developing new software to compress the image. By using the above technique, we can reduce both memory size and communication time. The testing of these two techniques leads to the conclusion that a lossless technique is more useful for the medical field [12]. Lossy compression methods are second handed for advanced compression fractions, and lossless compression is second hand in the situation of the actual image and for the recreated image that requirements to be the same [9] (Table 5).

References

1. Luís FRL, Rodrigues NMM, da Silva Cruz LA, de Faria SMM Lossless compression of medical images using 3D predictors. *IEEE Trans. Med. Imaging* <https://doi.org/10.1109/TMI.2017.2714640>
2. Ansari MA (2015) A novel algorithm by context modeling of medical image compression with discrete wavelet. *Springer Book Series on industrial and applied mathematics: mathematical models, methods and applications* pp 197–228. ISBN 978981-287-9738
3. Ansari MA et al (2015) Analysis and evolution of proposed for advanced options of H. 263 and H. 264 video codec. *Int. J. Appl. Eng. Res.* 10(11):28711–28731
4. Singh M, Kumar S, Chouhan SS, Shrivastava M (2016) Various image compression techniques: lossy and lossless. *Int J Comput Appl* 142(6):0975–8887
5. Anamika M, Preeti M (2015) JPEG compressor using matlab. *Int J Adv Eng Res Technol (IJAERT)* 3(5):2348–8190
6. Eben Sophia P, Anitha J (2014) Implementation of region based medical image compression for telemedicine application. In: 2014 IEEE international conference on computational intelligence and computing research
7. Wu D, Tan DM, Baird M, DeCampo J, White C, Wu HR (2006) Perceptually lossless medical image coding. *IEEE Trans Med Imaging* 25(3)
8. Sadchenko OK, Plachinda O (2016) Fast lossy compression algorithm for medical images. In: 2016 international conference on electronics and information technology (EIT)
9. Masoodhu Banu NM, Sujatha S (2015) 3D medical image compression: a review. *Ind J Sci Technol* 8(12). <https://doi.org/10.17485/ijst/2015/v8i12/56231>
10. Parikh S, Ruiz D, Kalva H, Fernández-Escribano G, Adzic V (2017) High bit-depth medical image compression with HEVC. *IEEE J Biomed Health Inform* <https://doi.org/10.1109/JBHI.2017.2660482>
11. Bhavani S, Thanushkodi KG (2013) Comparison of fractal coding methods for medical image compression. *IET Image Proc* 7(7):686–693
12. Firoozbakht M, Dehmeshki J, Martini M, Ebrahimdoost Y, Amin H, Dehkordi M, Youannic A, Qanadli SD (2010) Compression of digital medical images based on multiple regions of interest. In: 2010 fourth international conference on digital society

Review on Next Step Home Automation Using Wi-Fi Module



Himanshu Kumar Patel, Vishvapriya Gaur, Shivam Kumar,
Ayush Kumar Singh, and Sudhanshu Mittal

Abstract Home automation system is that which turns the system to some extent and makes automated. As the consumption of energy is today's priority with the increase in population. So the necessity of consumption is taken into consideration. As it is clear from the name "home automation" which makes the system fully automated and provides comfort, quality of life and it is also used for security purposes and provides an ease to old and disabled people which reduces the human effort. ESP8266 Wi-Fi module and Arduino NodeMCU as a microcontroller and Google firebase server and graphical user interface (GUI) is used which involve all devices needed to display in the android screen.

Keywords Home automation system · Electrical and electronics devices · ESP8266 Wi-Fi module · Arduino NodeMCU

1 Introduction

In today's era, information technology (IT) plays a great role in modernization in India. As the population increases, the demand and the necessity of the people also increasing day-by-day. So, it becomes necessary to maintain it at an appropriate level.

H. K. Patel · V. Gaur · S. Kumar · A. K. Singh · S. Mittal (✉)
Department of Electrical Engineering, Galgotias College of Engineering and Technology, Greater Noida, India
e-mail: Sudhanshu.mittal@galgotiacollege.edu

H. K. Patel
e-mail: himanshupatel123456789@gmail.com

V. Gaur
e-mail: vishvapriyaofficial@gmail.com

S. Kumar
e-mail: shivam08081997@gmail.com

A. K. Singh
e-mail: ayushjee105@gmail.com

Information technology (IT) takes India towards the next step which makes the life of the people completely automated. As everything becoming automated, it comes forward as an advantage as well as disadvantage. It reduces the effort of humans, changes the way of living and provides all the comfort to the people and makes the life of the humans easy. As it changes the human life and also comes forward as an advantage for the consumption of energy and reduces the time of people, it plays a vast role in security purposes and reduces the amount of labour work in industries as well. Arduino Board, ESP8266 Wi-Fi module, Arduino NodeMCU (microcontroller), electromagnetic relay, sensors, transformer (step-down), etc., is used for the next step home automation as shown in Fig. 3.

The basic idea of home automation is to employ sensors and control systems to monitor a dwelling and adjust the various mechanisms that provide heat, ventilation, lighting and other devices [1]. For the economical perspective, it increases the lifelong of the appliances and reduces the maintenance expenses [2, 3].

To operate (ON/OFF) this system by using a mobile phone, in which the mobile application is installed and Internet protocol (IP) has been set up and connected to the Wi-Fi module as shown in Fig. 3a and few of them based on a personal computer approach [4]. It can also be operated by using GSM, Zig-Bee, Bluetooth, etc., for remote control of household devices [5, 6].

2 Methodology

Home automation system makes your home advance and more comfortable with the help of the controllable and electronic devices [7] and also makes your home more customized, efficient and secure. In this model, mainly four parts that are NodeMCU ESP8266 Wi-Fi module, electromagnet relay drivers, android application and step-down transformer. Look forward to the working, firstly, power supply is provided to the step-down transformer as shown in transformer circuit Fig. 3c, which steps down the input voltage of the supply and given the power to the NodeMCU ESP8266 Wi-Fi module with Vin pin. The electromagnet relay as shown in Fig. 3b is also connected with a 12 V SMPS supply adopter that provides the information to the microcontroller and this microcontroller reads the information and sends it to the relay drivers which work as a “switch” that switches is used to connect the home appliances which is connected separately [8]. In the NodeMCU ESP8266 Wi-Fi module, programming has been done according to the working module and fixes the application by inserting Wi-Fi password of the particular devices accordingly to perform some mathematical and logical operation to control the relay drivers [9].

From Figs. 1 and 2, the system is controlled by using an android smartphone and ESP8266 Wi-Fi module which is directly connected to the four-channel electromagnetic relays are connected to the four devices particularly. Assume one device (FAN) is connected to the one relay, another device (LED) is connected to the second relay, third device (BUZZER) is connected to the third relay and similarly fourth device

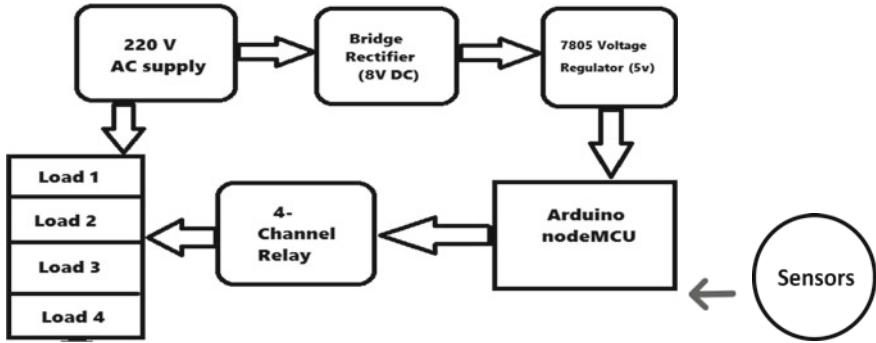


Fig. 1 Block diagram of home automation system

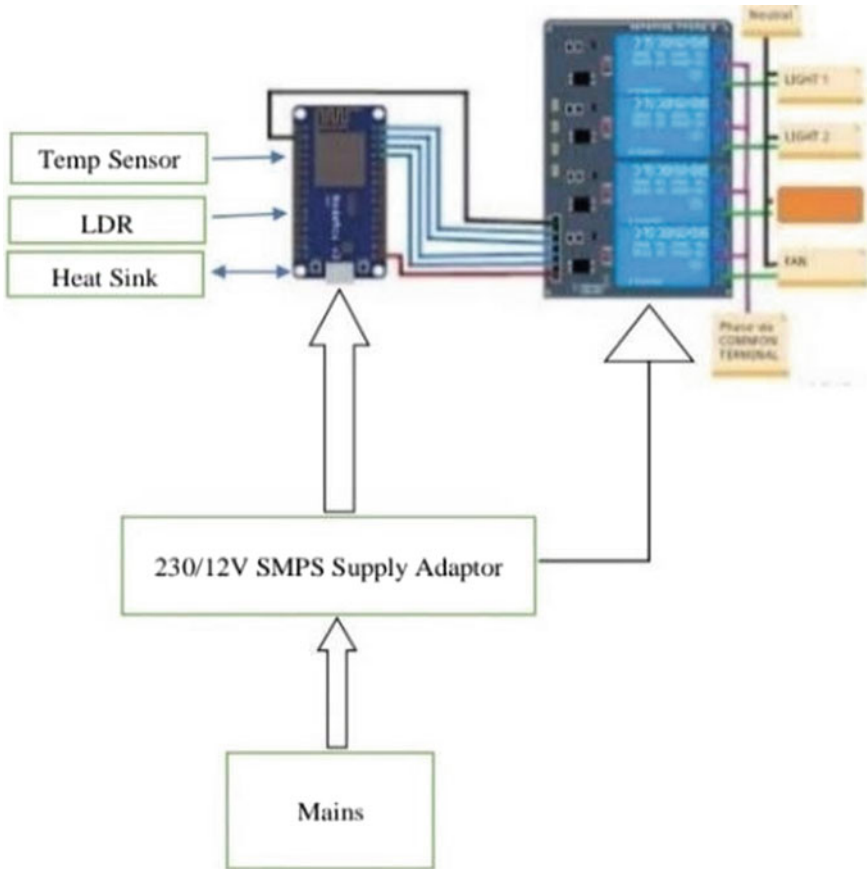


Fig. 2 Circuit diagram of home automation

may be (BULB) with the fourth relay and 230 V AC supply is applied from step-down transformer.

All the devices are connected to the common network (Internet) like NodeMCU, smartphone and router are used to create a common network and Arduino NodeMCU is used to maintain the Web server, which collects data and analyses it simultaneously [10]. In this, input-output pin are of Arduino NodeMCU are connected to the relay and mainly the work of relay switch is used to connect the home appliances which is connected separately.

3 Advantages

1. It makes whole system fully automated.
2. It provides human comfort, especially to the physically disabled people.
3. It can be operate with Wi-Fi module at a suitable range.
4. Home automation provides time consumption.

4 Applications

1. Home automation can be useful in indoor and outdoor lighting system.
2. Home automations can be useful in security systems.
3. Home automation can be used in commercial and industrial purposes.

5 Project Model

In this model, Fig. 3 shows overall circuit model of home automation and also main components of this model is ESP8266 Wi-Fi module circuit, 4-channel electromagnet relay circuit and transformer circuit which are shown in Fig. 3a–c, respectively.

6 Components Required

In this proposed model, various components with different ratings are used which are describe below.

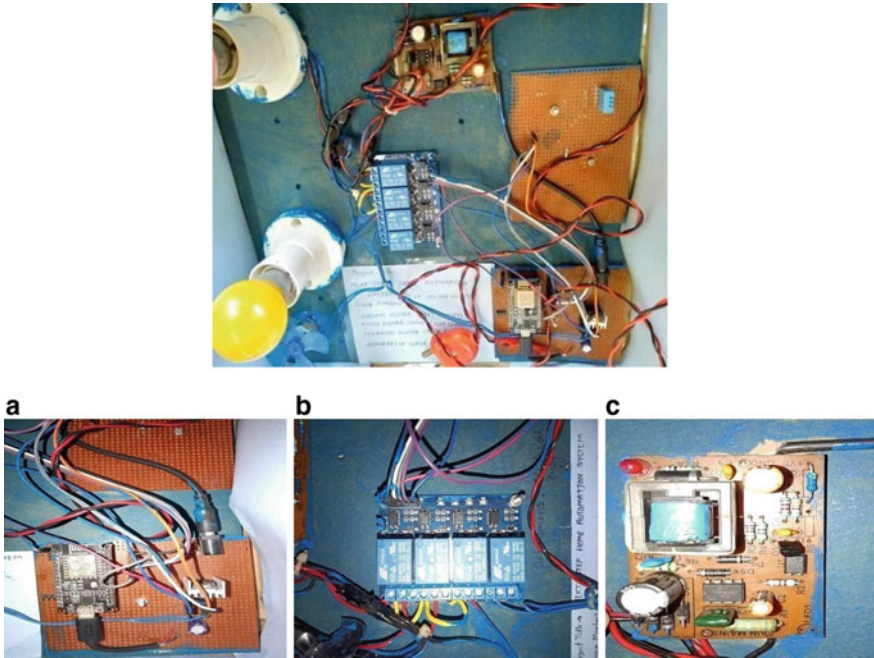


Fig. 3 Model of home automation with components, **a** Wi-Fi module circuit, **b** electromechanical four-set relay circuit, **c** transformer circuit

7 Result

Interaction of mobile application and ESP8266 Wi-Fi module, system data is monitored, and Fig. 4 shows the mobile application page. This allows the user to interact and control the equipment. By entering the assigned IP address in the application, this web page will appear and motion state in the house. From the application, the status of the appliances it is either ON or OFF. Ratings of the components are shown in above Table 1.

8 Conclusions

The home automation using ESP 8266 Wi-Fi module gives the desired output and proven effective in controlling the equipment remotely using Wi-Fi or Internet. The system not only actuates the equipment but also records the data by using the sensors. The data is in the form of temperature, light and motion sensor. It switches OFF the light when there is dark or no one in the room. It helps to consume the electricity and uses of the electrical equipment's efficiently.

Fig. 4 Mobile application page



Table 1 Components required

S. No.	Components required	Rating
1	SMPS supply adaptor	12 V
2	Microcontroller	NodeMCU ESP8266
3	7805 voltage regulator	5 V
4	Relay (electromagnetic)	SRD 05 V DC
5	DC fan	5 V
6	Heat sink	1.0 A
7	Transistor	KA431AZ
8	LDR	10 kΩ
9	Heat sensor	DC 3.5–5 V
10	Resisters	R1 = 2.4 kΩ, R2 = 2.6 5 kΩ, R3 = 9 kΩ, R4 = 54 kΩ, R5 = 10 kΩ, R6 = 1.4 Ω
11	Capacitors	C = 10 μF (63 V) C = 6 μF (400 V) C =1.4 nF (16 V)
12	Paper capacitor	0.047 μF (100 V)
13	Step-down transformer	230/12 V (AC)

9 Future Work

There are various ad-ons with the project which can be implemented in the future. By increasing the number of sensors you can record data of camera which records malicious activities of people who want to enter the house without your permission. Here, four devices are used to the system, but for the future implementation, the

number of devices can be increased with the help of Google API, and the performance of the system can be improved. It can be expanded with a Google Voice interactive system facility.

In further implementation, various things can be implemented, i.e. remote access or android access facility can be eliminated and makes the whole system fully automated by using various sensors. Discuss this case as an example, assume in the class strength of 40 students (having 8 rows and 5 columns), in the class two fans are situated at the front and two at the backend side of the class and two tube lights are installed at the middle of the class. If only few students (20) present in the class and sit in the front row, so only front side fan switch ON and tube light, which is placed in the middle.

Switching operation can be performed accordingly with the help of sensors which senses the presence of the human being (body heat) and gets switched OFF when no one in the class. Electricity consumption, time consumption, less human effort, etc., are some of the advantages which came across by implementing the home automation using IoT.

References

1. weblink: <http://depts.washington.edu/dmGftp/publication/html/smarthouse98-mdg.html>
2. Kumar P, Martini C, Morawska L, Norford L, Choudhary R, Bell M, Leach M (2016) Indoor air quality and energy management through real-time sensing in commercial buildings. 111:145–153 (2016)
3. Ghazvini MAF, Soares J, Abrishambaf O, Castro R, Vale Z (2017) Demand response implementation in smart households. *Energ Build* 143:129–148
4. Shuang-Hua Y (2014) Zig-bee smart home automation systems-wireless sensors networks: principles, design and applications. Springer-Verlag, London
5. Hishama AAB, Ishaka MHI, Teika CK, Mohameda Z, Idrisb NH (2014) Bluetooth based home automation system using an android phone. *J Teknol (Sci Eng)* 70(3):57– 61 (2014)
6. Bharanialankar SR, Babu CSM (2014) Intelligent home appliance status intimation control and system using GSM. *Int J Adv Res Comput Sci Soft Eng* 4(4):554–556
7. Sirsath NS, Dhole PS, Mohire NP, Naik SC, Ratnaparkhi NS Home Automation using cloud network and mobile devices. Department of Computer Engineering, University of Pune, 44, Vidyanaigari, Parvati, Pune, 411009, India
8. Hamed B (2012) Design and implementation of smart house control using labVIEW. *Int J Soft Comput Eng (IJSCE)*, 1(6). ISSN: 2231–2307
9. Thaker T (2016) ESP8266 based implementation of wireless sensor network with Linux based web-server. Symposium on colossal data analysis and networking (CDAN), Indore (2016)
10. Piyare R, Lee SR (2014) Smart home-control and monitoring system using smart phone. In: *The 1st international conference on convergence and its application*, vol 84 (2014)

Literature Review: Predicting Faults in Object-Oriented Software



Ankush Joon, Rajesh Kumar Tyagi, and Krishan Chillar

Abstract Software fault prediction has become quite famous in the software engineering. If software faults are predicted earlier, it leads to good quality of software, and it reduces the resources and time required for testing, which ultimately leads to saving a considerable cost and effort that are used for testing purpose. In this literature study, we studied the major works done so far in the software defect prediction paradigm to find out the various benefit of predicting faults at initial phases of software product development. This paper aims to find answers to questions such as what are the merits and limitations of models developed so far, what are the possible areas of software fault prediction paradigm that are still open for research, what are the best suitable metrics used for predicting errors, and many more. From the literature survey, we analyzed that research conducted for predicting errors in object-oriented software so far was conducted on a small scale and using the limited metric suite. None of the studies gave a generalized model that could perform well for most of the datasets. They do not handle well the problem of imbalanced class distribution and noisy data. Many prediction models have already been developed so far, but most of them focus only on classification problem that is detecting faulty/not faulty classes.

Keywords Software fault prediction · Machine learning · Performance evaluation parameters · Software metrics

A. Joon (✉) · R. K. Tyagi · K. Chillar
Amity University, Gurgaon, Haryana, India
e-mail: ankushjoon77@gmail.com

R. K. Tyagi
e-mail: tyagirajesh2610@gmail.com

K. Chillar
e-mail: krishanchhillar@gmail.com

1 Introduction

A software defect is the unexpected or unintended or incorrect functionality of a software system. When the faults in a software system are predicted before deploying the product, it is called software error prediction.

Finding early classes that are more prone to failure helps in saving many resources and leads to a better quality of software process as well as the product [1].

Another reason for the importance of software fault prediction is because it proved that 50–80% of the effort that is used for developing any software project is spent on testing by a software company [2].

The traditional testing methodologies, such as structural testing and glass box testing techniques, require the tester to be familiar with the internal functioning and technical details about the software for testing. Machine learning here becomes vital because it does not require the above-stated requirements and still helps in detecting and predicting the software faults effectively and efficiently.

The objective of this literature study is to get insights into the major machine learning models developed so far for predicting faults in the software, studying the most widely deployed datasets for making such predictions, and what are the different sources of these datasets. This review gives a brief of the papers studied in order to get various details about the process of predicting bugs in object-oriented software paradigms.

The rest of the review paper consists of the sections in the given order: Sect. 2 elaborates the review methodology we used. Section 3 presents the crux of the papers reviewed. Section 4, titled as results, gives the answers to the review questions. Finally, the summary of the findings of this literature review is presented in the form of a conclusion.

2 Review Methodology

The review methodology followed for reviewing major studies done so far for predicting errors in software products is shown in Fig. 1. The review methodology is broadly divided into three steps, the first being the initial state, after that data extraction and analysis is the second step, and then the third and final one is review writing step. These three steps further consist of several sub-steps.

The review methodology is designed by keeping in mind the review questions that form the basis for conducting this literature review. The review questions are as follows:

1. What is the benefit of predicting errors in software products?
2. What studies and research have already been conducted for predicting defects in software modules?
3. What are the different areas that are still open for research and improvement?

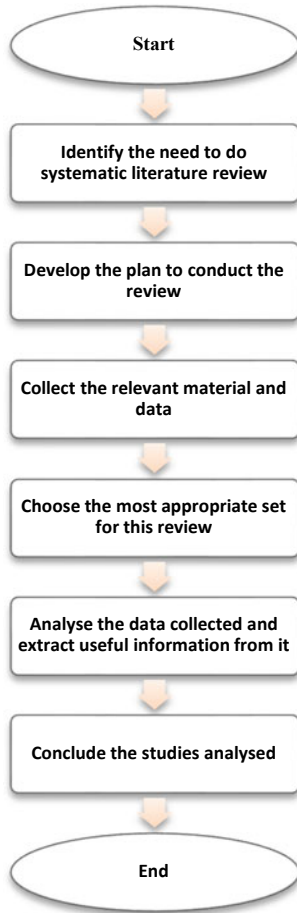


Fig. 1 Review steps

4. What are the different datasets available, and what are the sources of data collection?
5. What are the various software attributes that are most frequently used for predicting errors in software?
6. What are the different performance parameters for validating the models built in the software defect prediction paradigm?
7. What are some recent algorithms used for defect prediction in the software using the object-oriented paradigm?

The primary objective for conducting this literature survey is to know the reasons for which software fault prediction is important (RQ1).

3 The Crux of the Papers Reviewed

Aziz et al. [3] verified the effect of inheritance metrics on software error prediction and also indicated that higher the inheritance, the more is the introduction of faults. This paper uses the ANN model for predicting the defects in the 30 base datasets. They used five measures, i.e., accuracy, TNR, precision, f1 measures, and recall for validating their model.

Bibi et al. [1] used regression along with classification as defect prediction technique. It utilizes the advantages of both regression and classification techniques and overcomes the disadvantages offered by them. This model first discretizes the defect variable into several intervals and then applies a classification technique for predicting possible faultiness of classes and finally transforms the result into numerical output. The model provided excellent results in terms of regression error. For future work, they suggested using stacking and effective voting technique with machine learning models for enhancing their prediction capabilities for predicting defective classes in the software products.

Kang Yang et al. [4], in their work, used the Fourier learning model for predicting bugs in software systems. They predicted the defect by evaluating the value of function $f(x)$ from the value of any feature vector x . They converted the NASA datasets to a feature vector of 0/1 datasets for their experiment, and then, the dataset is decomposed into train and test sets. Then, they used the information gain algorithm for selecting important features. After applying feature selection, the defect prediction model was built using a Fourier coefficient and then estimating the value of defect function from Fourier coefficient values. Fourier coefficients were obtained using

$$f(z) = \langle f, X_z \rangle = 1/2^n \left[\sum_{z \in \{0,1\}^n} f(z) \cdot X_z(x) \right] \quad (1)$$

Function value using

$$h(x) = \sum_{z \in \{0,1\}^n} \hat{h}(z) \cdot X_z(x) \quad (2)$$

The model developed was evaluated in terms of AUC value, and they got an AUC value of 0.78 [4].

Wahono [5] From this paper, we found that predicting error software in early phases of development results in reducing cost, making testing more efficient by focusing more on fault-prone classes, and improve software quality. This paper analyzed the possible research fields in software prediction, i.e., estimation, association, classification, clustering, and data analysis. It concluded that classification is the primary area, with most of the studies being focused on it. This paper suggests that most commonly used methods for software fault prediction are KNN, Naïve Bayes, neural network, random forest, logistic regression, SVM, and decision trees, with 75% of the studies being focused on NB, NN, decision trees, and random forest classification models. This paper suggests that the major problems with existing

software defect prediction framework are: incomplete validation mechanism, less reliable research procedures, class imbalance problem in datasets, and mechanisms for dealing with noisy data are still an open issue.

According to Kamei and Shihab [6], the main future challenges in the area of software fault predictions are generalizing the models for all kinds of datasets. Predicting errors at initial phases of software development, addressing the new regions for software error prediction such as mobile applications are open for research. Along with predicting defects, looking for reasons why a particular defect occurred and how to fix that defect needs to be addressed.

Kaur and Kaur [7] this paper analyzed that various studies done for software error prediction were conducted on a small scale on very few datasets and using the limited metric suite. None of the studies gave a generalized model that could perform well for most of the datasets. The studies conducted are specific to some datasets and some metric suites.

Viet et al. [8] implemented transfer learning techniques for predicting bugs in software systems. It is a technique to train deep NN in problems where insufficient data is available. In the software defect prediction paradigm, the datasets available are very limited and suffer from the class imbalance problem. So, transfer learning can be useful for predicting faults of within and cross-project software systems. They used four datasets SUMTRAIN, MNMX, HOW16, and SUB INC from CodeChef submission, for their experiment. They did not use software metrics. Here, assembly instruction sequences were used for predicting bugs in the system. Deep learning technique known as multilayer convolution NN was implemented having four layers: embedding layer, then convolution layer, then pooling, and finally fully connected layer. The feature map of the input sequence, $X = \{X_1, X_2, \dots, X_n\}$ is given by

$$C_i = f(W.x_{[i:i+h-1]}+b) \quad (3)$$

where b represents bias value, and f is representative of the activation function. Then, they applied global max pooling to overcome the problem of overfitting, and then, the fully connected layers with Softmax activation give the output. For predicting faults, the fully connected layers are removed, and then, feature vectors for datasets are produced. Finally, SVM and KNN are used for predicting bugs.

Rizwan et al. [9] this literature review suggests that choosing the right and best model out of these numerous models is a difficult task. It depends on the performance measures. This paper suggests that G-mean and F-measure are most appropriate for verifying and validating the methods for predicting defects in software. But they are not suitable if there is a large probability of getting zero in one of the four parameters of the confusion matrix. In that case, precision is a good measure.

Borandađ et al. [10] developed a majority vote algorithm for selecting attributes (MVFS) so as to find out the best suitable features for detecting bugs in software modules, thereby improving the accuracy value of machine learning methodologies used for the error prediction. They considered six datasets, four NASA datasets, and Eclipse Equinox, and Eclipse JDT for their experiment. Machine learning methods Naive Bayes, KNN, and j48 are implemented as classification techniques. They

used a filtering-based feature selection algorithm, i.e., info gain, relief, symmetrical uncertainty, and correlation-based followed by majority vote ensemble scheme to select the most relevant metric suite. Their result showed that by using this technique, the performance of the methods used for detecting errors increases. This method is domain-specific and does not present a generalized model.

Rathore and Kumar [11] the study was performed on ten software projects of PROMISE repository. The result showed that the genetic programming algorithm is sensitive for small datasets. It works well only for large datasets with sufficient completeness. Also, in the genetic programming model, the need to optimize the control parameters becomes a problem when there is a large number of independent attributes.

Erturk and Sezer [12] defined a hybrid process for software error prediction that used a fuzzy inference system for initial prediction and ANN afterward. They implemented the proposed strategy as an eclipse environment plugin. They showed that the process of detecting errors in software could be converted to a tool that can run on its own. Software fault prediction is beneficial only if it can assess the probability of a module being risky at the initial stages of the development process. The study proposed a model for systematic predictions during the ongoing software development process.

Panda [13] this paper presented a hybrid software defect prediction technique that uses a radial basis function NN classifier combined with a distribution base balance-based feature selection method. They used datasets from NASA, PROMISE, and Softlab repositories for the experiment and analyzed the model performance on the basis of recall, F-measure, ROC-AUC, and precision. As future work, they proposed to apply this model to cross-platform projects with more performance measures to validate the model.

Wang et al. [14] proposed the SVM classification method for error detection in object-oriented software that is based on particle swarm optimization and relief method for feature selection. The limitation of this model is that it is not optimal with respect to time, and it cannot handle the prediction problem in software running process.

Kamei and Shihad [6] at present, software plays a crucial role in everyone's life, and their importance is increasing and so their complexity. It becomes more complicated to ensure good reliability and better quality of software products. Here, predicting software defects becomes important because it helps the tester to put primary efforts on the risky classes of software, thereby saving time, effort, and cost, which eventually leads to better reliability and good quality of the software. According to this review study, the most widely used techniques for software fault prediction are decision trees, LDA, Naïve Bayes, SVM, and random forest. They concluded that generalization of the models for software defect prediction that fits various types of software projects is still an open issue.

Rhmann et al. [15] used five techniques, i.e., three methods of machine learning (multilayer perceptron, random forest, and J48) and two hybrid search-based algorithms (fuzzy AdaBoost and LogitBoost) for detecting errors in software using software change metrics. They conducted the experiment on Android datasets collected

from the Git repository and used recall and precision for validating the methods used for predicting faults. They concluded that GFS-LogitBoost gives better performance as better precision, and more recall values are obtained [15].

Table 1 Literature review table

S. No.	Year	Authors	Methods used	Datasets used	Performance evaluation parameters used
1	2019	Aziz et al.	Artificial neural network	From tera-Promise and D’Ambros repositories	Accuracy, recall, precision, F1-measures, TNR
2	2016	Stamatia Bibi et al.	RvC Using IBk, JRip, PART, J48, SMO	Pekka dataset	Average mean absolute error, accuracy
3	2018	Kaur and Kaur	J48, IB1, random forest, bagging, logistic regression [7]	Java projects: Find bugs, PMD, EMMA, Dr Java, trove	Accuracy, precision, specificity, F-measure, J_coefficient, ROC curve
4	2016	Ezgi Erturk and Ebru Sezer	ANN and adaptive neuro- FIS	Ant, jEdit, Camel, Xalan, Log4j, Lucene [16]	ROC-AUC curve
5	2018	Borandag et al. [10]	Majority vote feature selection with J48, Naïve Bayes, KNN	NASA MDP datasets and eclipse equinox, eclipse JDT	Geometric Mean-I
6	2018	Mrutyunjaya Panda	Radial basis function NN with distribution base balance instance selection	From NASA, PROMISE, and Softlab repositories	Accuracy, F-measure, AUC, recall, precision, and balance
7	2019	Rhmann et al.	Random forest, multilayer perceptron, j48, fuzzy AdaBoost, LogitBoost	Android datasets from Git repository	Precision, recall
8	2019	Yanan Wang et al.	Particle swarm optimized SVM	KC1, Eclipse 2.0, Eclipse 3.0, ant 1.7	Accuracy, precision, recall, F-value
9	2015	Rathore and Kumar	Genetic programming	From PROMISE repository	Error rate, recall, completeness

The literature review Table 1 provides the methods deployed, the datasets used, and the performance evaluation parameters used by different studies.

4 Results

The result section presents answers to the review questions.

1. **Review Question 1:** Software error prediction helps in making the software reliability as well as quality better and in better utilization of resources such as time, effort, and cost.
 Predicting software faults helps the software tester to design the test plan in such a manner that faulty classes have higher priorities and thus help in efficient testing with much less effort required.
 As the software in an intangible product, so while dealing with new software, the development team faces software projects having inconsistencies, and that is not within time and budget. Software error prediction eliminates these problems by finding out essential data from previous similar kinds of projects and using it to make a prediction for future projects.
2. **Review Question 2:** major studies conducted for predicting software errors focus on classification problems (77.46%), estimation methods (14.08%), and merely 1.41% on association methods techniques.
 From the literature survey, it is found that the most widely used machine learning methods of software fault prediction are Naïve Bayes, SVM, neural networks, random forest, logistic regression, decision tree, and KNN. Among all, 75% of the studies used Naïve Bayes, decision trees, neural networks, and random forest only.
3. **Review Question 3:** Literature survey suggests that the existing software defect prediction frameworks have the following significant problems:
 - a. Processing of class imbalance problems in the dataset is required.
 - b. An adequate mechanism to deal with noisy data needs to be developed.
 - c. More systematic methods that are unbiased for comparing the performance of models are required.
 - d. A generalized model that performs well for all types of datasets like Android projects, public datasets, and open-source software projects is still an open research area.
 - e. Most of the studies concentrate on classification problems, i.e., classifying into faulty/non-faulty classes. Other issues such as the number of faults, severities of defects, possible causes of errors, and methods to fix the detected faults are not much explored.
 - f. A best metric suite for software fault prediction covering all possible parameters needs to be discovered.

4. **Review Question 4:** From the literature survey, it is concluded that mostly public datasets are used for detecting errors in software products. Very few studies used private datasets.

The most widely used sources for public datasets for classifying software modules into faulty/not faulty are tera-promise repository that contains NASA datasets and D'Ambros repository that contains datasets for Eclipse JDT core, Equinox, Lucene, Mylyn projects. Another possible dataset source is the Git repository.

5. **Review Question 5:** From the literature survey, we found that Chidamber and Kemerer (CK) are the most appropriate and most widely deployed object-oriented metrics for defect prediction in software products. CK metric suite consists of features such as WMC, NOC, DIT, RFC, CSO, and LCOM. Li's inheritance metrics are also important.

Static code metrics such as lines of code and complexity of software products are inefficient for highly iterative software products, and process metrics such as the lifetime of modules, the number of modifications, and code churn are more effective for industrial use.

From the literature survey, we found that out of all object-oriented matrices are most suitable for software fault prediction.

6. **Review Question 6:** Performance measures used for validating the methods used for predicting errors are accuracy, F1-measure, precision, recall, ROC-AUC curve, and true negative rate.

A study done by Rizwan et al. shows that F-measures and G-mean are the suitable performance validation parameters to check the software error prediction methods. But in some situations, precision is a better choice.

7. **Review Question 7:** Table 2 provides an analysis of some of the most recently used algorithms for detecting defects in the object-oriented software.

5 Conclusion

If software faults are predicted earlier, it leads to good quality of software, and it reduces the resources and time required for testing, which ultimately leads to saving a considerable cost and effort that are used for testing purpose.

From the literature survey, it is clear that software fault prediction is beneficial only if it can assess the probability of a module being risky at initial stages of the development process [12]. The studies conducted in the software error prediction paradigm mainly focus on classification problems (77.46%), estimation methods (14.08%), and merely 1.41% on association methods techniques. Among all studies, 75% of the studies used NB, decision trees, NN, and random forest only [21].

Performance parameters used for software error prediction are accuracy, F1-measures, ROC-AUC, TNR, recall, and precision. From the literature survey, we found that Chidamber and Kemerer (CK) are the best and most used metrics for predicting faults in software using object-oriented paradigm.

Table 2 Analysis of some recent algorithms used for predicting faults in object-oriented software

Year	Authors	Algorithm used	Algorithm description	Results
2019	Immaculate et al. [22]	Supervised machine learning	First preprocessing was done to convert imbalanced datasets to the balanced one. Then, the model is built using LR, DT, NB, and random forest algorithms. Finally, the model is evaluated using 10-fold cross-validation	The accuracy values obtained are LR (96%), DT (96%), NB (92%), and RF (97%)
2018	Kang Yang et al.	Fourier learning	The NASA dataset is converted to a feature vector of 0/1 dataset, and it is divided into train and test datasets. Then, the information gain algorithm is used for feature selection. Finally, the prediction model is built using the Fourier learning technique	The algorithm gave an AUC value of 0.78, and it provided a stable model for fault prediction

(continued)

Table 2 (continued)

Year	Authors	Algorithm used	Algorithm description	Results
2019	Viet et al.	Transfer learning with multilayer convolution NN [8]	<p>A deep learning technique, known as multilayer convolution NN, was used. The algorithm consists of below-listed steps: The assembly instruction sequence in the feature vector form is input to the convolution layer. It helps in learning the significant attributes</p> <p>Then, global max pooling is performed to overcome overfitting. Now, fully connected layers of network use Softmax activation function to give output</p> <p>Finally, SVM and KNN are used after CNN to predict bugs</p>	The proposed model provided good accuracy for all the datasets used. The model can be used for both within and cross-project bug prediction
2019	Thi Phuong Ha et al.	Machine learning algorithms (LR, SVM, NB, KNN, DT, RF, and multilayer perceptron) with GridSearch feature selection [17]	<p>The GridSearch technique was used for feature selection, and then, seven algorithms of machine learning were utilized to build the prediction model.</p> <p>Finally, 10-fold cross-validation was used for evaluating the techniques implemented</p>	<p>Multilayer perceptron gave best prediction in method-level datasets (AUC = 0.91, accuracy = 91%, F1-value = 0.59)</p> <p>For class-level dataset, SVM is best technique (F1-value = 0.48, accuracy = 63%, AUC = 0.58)</p>

(continued)

Table 2 (continued)

Year	Authors	Algorithm used	Algorithm description	Results
2019	Hoa Dam et al.	Long short-term memory (LSTM) network [18]	First, the source code is parsed to generate ASTs. ASTs are then embedded into AST nodes. All AST nodes form the embedding matrix. This matrix is applied as input to the LSTM unit. Backpropagation is used for optimization. Then, the result of LSTM was applied to LR and random forest algorithm to detect defects in the software module	The performance of the method was calculated in terms of F-measure, recall, AUC, and precision. Random forest with LSTM gave better results (all values above 0.9)
2018	Turabieh et al.	A layered recurrent neural network with iterative feature selection using the wrapper method [19]	The algorithm is iterative in nature. SFP dataset is applied as input, and then, the wrapper feature selection algorithm is implemented. There are three feature selection algorithms: ACO, genetic programming, and particle swarm optimization technique. Anyone is selected at random. After feature selection, the dataset is split into train and test dataset. Now, L-RNN method is used to predict bugs	The algorithm performed well for all datasets used, with an average value of 0.84 for AUC. The problem of this method is that it takes high execution time for large datasets

(continued)

Table 2 (continued)

Year	Authors	Algorithm used	Algorithm description	Results
2019	P. Lingden et al.	Two-layer (bagging followed by stacking) ensemble technique with modified under-sampling method [20]	<p>The algorithm starts with feature extraction and then normalization using z-score. After that modified under-sampling technique is applied that helps in overcoming the problem of class imbalance.</p> <p>The fault prediction model is built that is based on the ensemble technique. It consists of three phases. First is the feature subset selection using the correlation feature selection (CFS) method to reduce computing time and complexity of the algorithm. Then, there is bagging using random forest trees and finally stacking</p>	<p>The model was tested for ten open-source project datasets. It provided an improved accuracy of 0.68 on average. It also provided an improved processing time of 6.3 s</p>

Numerous studies have been done in the software defect prediction paradigm, but still, there exist many research gaps. Areas still open for research are as follows: Processing of class imbalance problem in the dataset is required, an adequate mechanism to deal with noisy data needs to be developed, more systematic and unbiased methods for comparing the performance of models are required. A generalized model that performs well for all types of datasets like Android projects, public datasets, and open-source software projects is still an open research area. Most of the studies concentrate on classification problems, and other issues viz. the number of defects, severities of faults, possible causes of defects, and methods to fix the detected faults are not much explored. A best metric suite for software fault prediction covering all possible parameters needs to be discovered.

In the future, we intend to find solutions to the problems defined above to develop better fault prediction models for detecting faults in software systems with object-oriented methodology.

References

1. Bibi S, Tsoumakas G, Stamelos I, Vlahavas I (2006) Software defect prediction using regression via classification. In: IEEE international conference on computer systems and applications, 2006(May 2014):330–336
2. Mahanti R, Antony J (2005) Confluence of six sigma, simulation, and software development. *Manag Auditing J* 20(7):739–762
3. Aziz SR, Khan T, Nadeem A (2019) Experimental validation of inheritance metrics' impact on software fault prediction. *IEEE Access* 7:85262–85275
4. Fan G (2018) Software defect prediction based on fourier learning. In: 2018 IEEE international conference on progress in informatics and computing (PIC), pp 388–392
5. Wahono RS (2015) A systematic literature review of software defect prediction: research trends, datasets, methods, and frameworks. *J Softw Eng* 1(1):1–16
6. Kamei Y, Shihab E (2016) Defect prediction: accomplishments and future challenges (March), 33–45. <https://doi.org/10.1109/saner.2016.56>
7. Kaur A, Kaur I (2018) An empirical evaluation of classification algorithms for fault prediction in open source projects. *J King Saud Univ Comput Inf Sci* 30(1):2–17
8. Viet AP (n.d.) (2019) Transfer learning for predicting software faults. In: 2019 11th international conference on knowledge and systems engineering (KSE), pp 1–6
9. Rizwan M, Nadeem A, Sindhu MA (2019) Analyses of classifier's performance measures used in software fault prediction studies. *IEEE Access* 7:82764–82775
10. Borandağ E, Ozcift A, Kiliç D, Yucalar F (2018) Majority vote feature selection algorithm in software fault prediction. *Comput Sci Inf Syst* 39–39. <http://doi.org/10.2298/CSIS180312039B>
11. Rathore SS, Kumar S (2015) Predicting number of faults in software system using genetic programming. *Proced Comput Sci* 62(Scse):303–311. <https://doi.org/10.1016/j.procs.2015.08.454>
12. Erturk E, Akcapinar Sezer E (2016) Iterative software fault prediction with a hybrid approach. *Appl Soft Comput J* 49:1020–1033
13. Panda M (2018) DBBRBF-Convalesce optimization for software defect prediction problem using hybrid distribution base balance instance selection and radial basis Function classifier
14. Wang Y, Zhang R, Chen X, Jia S, Ding H, Xue Q, Wang K (2019) Defect prediction model for object oriented software based on particle swarm optimized SVM. *J Phys Conf Ser* 1187(4). <https://doi.org/10.1088/1742-6596/1187/4/042082>

15. Rhmann W, Pandey B, Ansari G, Pandey DK (2019) Software fault prediction based on change metrics using hybrid algorithms: an empirical study. *J King Saud Univ Comput Inf Sci* (xxxx):4–9
16. Hailpern B, Santhanam P (2001) Software debugging, testing, and verification. *IBM Syst J* 41:4–12. <https://doi.org/10.1147/sj.411.0004>
17. Minh T, Ha P, Tran D H, Thi LE, Hanh M, Binh NT (2019) Experimental study on software fault prediction. In: 2019 11th international conference on knowledge and systems engineering (KSE), pp 1–5
18. Grundy J, Kim T, Kim C (2019) Lessons learned from using a deep tree-based model for software defect prediction in practice. In: 2019 IEEE/ACM 16th international conference on mining software repositories (MSR), pp 46–57. <https://doi.org/10.1109/MSR.2019.00017>
19. Turabieh H, Mafarja M, Li X (2018) Iterated feature selection algorithms with layered recurrent neural network for software fault prediction iterated feature selection algorithms with layered recurrent neural network for software fault prediction. *Expert Syst Appl* 122(December):27–42
20. Alsadoon PLA (2019) A novel modified undersampling (MUS) technique for software defect prediction (June), 1–18. <https://doi.org/10.1111/coin.12229>
21. Malhotra R, Bansal AJ (2012) Fault prediction using statistical and machine learning methods for improving software quality. *JIPS* 8:241–262
22. Immaculate SD (2019) Machine learning algorithms. In: 2019 International conference on data science and communication (IconDSC), pp 1–7

Tunable Transmittance Using Temperature Dependence ZnS-Based ID Photonic Crystals



Sanjeev Sharma, Vipin Kumar, and Shradha Gupta

Abstract Temperature-dependent ZnS-based optical properties of ID photonic crystal for TE mode at a particular angle of incidence with defect mode layer have been investigated. The defect layer ZnS has been tuned by varying the temperature of the semiconductor material. Here, the refractive index of the material ZnS is a function of temperature and frequency (or wavelength), respectively. It is clear that when the temperature of the material increases, the defective layer displaced towards the shorter frequency range of spectrum. Moreover, when the temperature increases, the efficiency of the layer also increases up to 96.4%.

Keywords Photonic crystal · Transmittance filter · Defect layer

1 Introduction

Photonic crystals are extremely interesting topic in the past two decades due to the existence of bandgap. Photonic crystals have bandgap structures which have multi-layer structures formed by using alternate layers of dielectric materials. Generally, these photonic bandgaps play an important role in photonic crystals and this photonic bandgap effected when the refractive index, temperature, and angle of incidence of the material change [1, 2]. The photonic bandgap of the structure changes by keeping constant temperature.

If we introduce a defect layer in these photonic structure, the bandgaps are broken and propagation of light can be localized in the photonic bandgap region. Recently, many photonic crystal-based optical devices such as channel drop filter, power splitters, multiplexer, switches, bandpass filters, and ODR mirror have been

S. Sharma (✉) · S. Gupta
Department of Physics, GLBITM, Greater Noida, UP, India
e-mail: sanjeevsharma145@gmail.com

V. Kumar
SPC Degree College, Baghpat, UP 250101, India

© Springer Nature Singapore Pte Ltd. 2021
R. Agrawal et al. (eds.), *Advances in Smart Communication and Imaging Systems*,
Lecture Notes in Electrical Engineering 721,
https://doi.org/10.1007/978-981-15-9938-5_31

proposed theoretically and experimentally [3–7]. In 2012, Suthar et al. [8] theoretically studied temperature-dependent tunable photonic channel filter. In 2018, B. K. Singh et al. proposed a tenability of temperature dependent THz photonic bandgaps in 1D photonic crystal which is composed of graded index dielectric and semiconductor materials [9]. Gharaati et al. [10] theoretically studied the effect of temperature on 1D double defects nanometallic photonic crystals.

In the present paper, we design a defect mode tunable THz filter using one-dimensional photonic crystal layer. Here, we consider a proposed structure of semiconductor materials ZnS/Ge in which the refractive index of ZnS layer depends on both temperature and frequency [11, 12]. Here, we observed that when temperature is increased up to 300–700 K; the defective layer tuned towards the lower frequency ranges with maximum transmission efficiency. Using this material, we also design a tunable channel filter for optical communications. But, in this paper, we focus the tunability of the material at a particular angle of incidence with variation of temperature from 300 to 700 K.

2 Theoretical Modal

The proposed 1D photonic crystal structure of Ge/ZnS is shown in Fig. 1. Here, the defective layer is introduced between the alternate layers of semiconductor photonic crystals and the incident EM rays is launched from the air ($n_0 = 1$).

Applying the transfer matrix method (TMM), the coefficient of reflection and the reflectance of the structure is given by,

$$r(\omega) = \frac{(m_{11} + m_{12}p_0)p_0 - (m_{21} + m_{22}p_0)}{(m_{11} + m_{12}p_0)p_0 + (m_{21} + m_{22}p_0)} \tag{1}$$

$$R = |r(\omega)|^2 \tag{2}$$

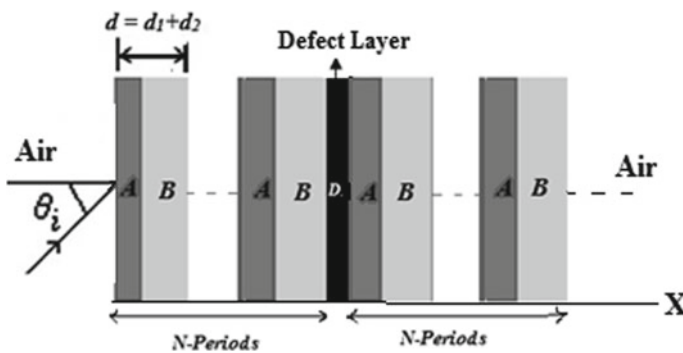


Fig. 1 Structure of one-dimensional photonic crystals

Also, the transmittance of the structure is given by,

$$T = |1 - R| \quad (3)$$

Here, $p_0 = n_0 \cos \theta_0$.

In 1D photonic crystal, the semiconductor materials A and B denote the layers of ZnS and Ge, respectively. The complete structure of 1D photonic crystal is [air/(ZnS/Ge)³ZnS/(ZnS/Ge)³/air]. In this structure, the refractive index of ZnS material depends on wavelength and temperature of the materials. For ZnS materials, the range of refractive index and temperature varies from 1.2–1.4 μm and 293–700 K, respectively [13]. It is given by,

$$n^2(\lambda, T) = \varepsilon(T) + \frac{G(T)}{\lambda^2 - \lambda_1^2} + \frac{H(T)}{\left(\frac{\lambda^2}{\lambda_2^2}\right) - 1}$$

where $\lambda_1 = 0.23979 + 4.841 \times 10^{-5}T_1$, $\lambda_2 = 36.525 + 4.75 \times 10^{-3}T_1$, and $T_1 = T - 293$.

$$\varepsilon(T) = 8.34096 + 1.29107 \times 10^{-3}T_1 + 4.68388 \times 10^{-7}T_1^2 - 1.31683 \times 10^{-9}T_1^3 - 6.64356 \times 10^{-12}T_1^4$$

$$G(T) = 0.14540 + 1.13319 \times 10^{-5}T_1 + 1.05932 \times 10^{-8}T_1^2 + 1.06004 \times 10^{-10}T_1^3 + 2.27671 \times 10^{-13}T_1^4$$

$$H(T) = 3.23924 + 1.096 \times 10^{-3}T_1 + 4.20092 \times 10^{-7}T_1^2 + 1.1135 \times 10^{-9}T_1^3 + 7.2992 \times 10^{-12}T_1^4$$

for $293 \text{ K} \leq T \leq 700 \text{ K}$

3 Result and Discussion

In this paper, we have taken the refractive index of Ge material to be 4.23 and the refractive index of ZnS semiconductor material depends on temperature. For ZnS materials, the range of refractive index and temperature varies from 1.2–1.4 μm and 293–700 K, respectively. Also, the thicknesses of Ge and ZnS semiconductor layers to be $a = 1606 \text{ nm}$, $b = 628 \text{ nm}$ and for defect layer it is $d = 395 \text{ nm}$. The transmittance of the proposed structure is shown in Fig. 2. In this Figure, it is clear that at a particular angle of incident says 0° , the bandgap as well as defect layer shifted towards lower

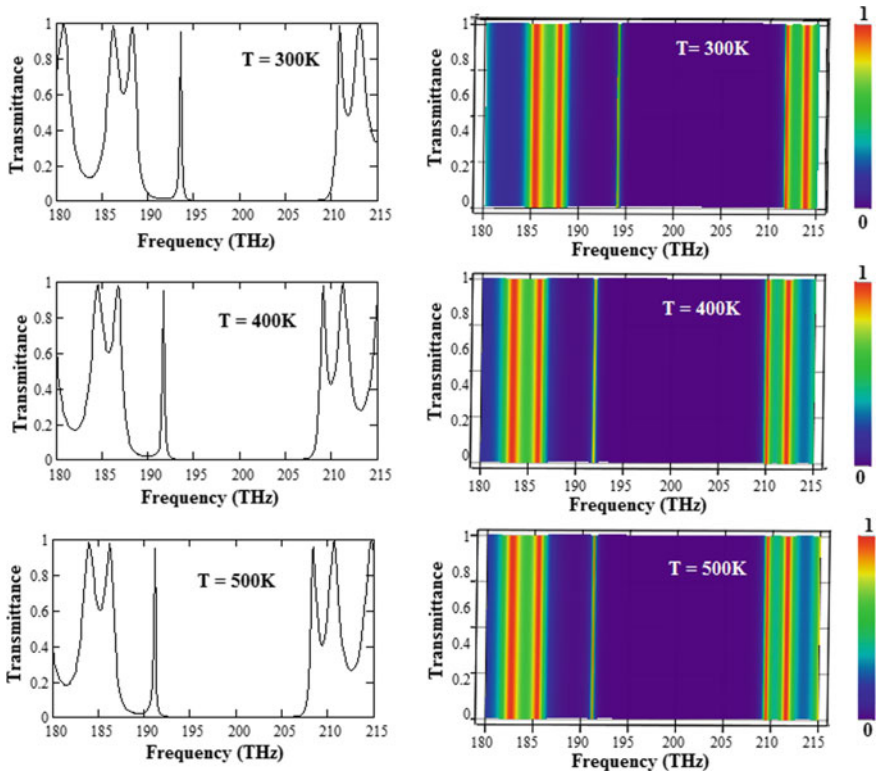


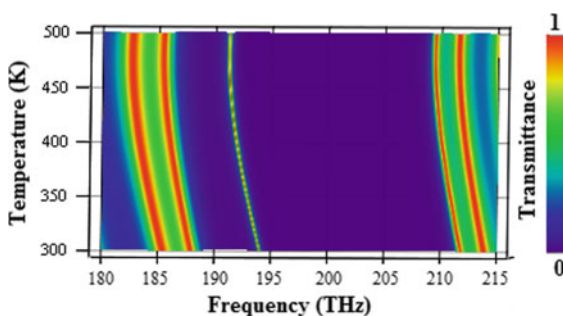
Fig. 2 Defect-mode spectrum of 1D photonic crystals at different temperatures $T = 300$ K, $T = 400$ K and $T = 500$ K

frequency range of the spectrum when temperature varies from 300 K to 500 K. The width of photonic bandgap occurs (209.94–190.83) 19.11 THz without using of defect layer; when defect layer is introduced in this photonic bandgap, the peak of defect layer is observed at frequency 193.42 THz. From Fig. 2, at temperature 300 K, 400 K, and 500 K, the defect mode layer has been tuned and observed at frequency 193.42 THz, 191.56 THz, 190.95 THz with transmittance of 0.93, 0.95, and 0.964. It is clear that when temperature increases, the defect mode layer shifted towards the lower frequency range of spectrum. When the temperature increases, the efficiency of the layer also increases and at temperature 500 K, we get 96.4% transmission efficiency which is shown in Table 1.

The 3D view of this structure is shown in Fig. 3. In this figure, the transmission peak is shifted towards the lower frequency range of the spectrum when temperature increases from 300 to 500 K. It is observed that the transmission efficiency is also improved with temperature.

Table 1 Bandgap and transmission efficiency of 1D photonic crystal

S. No.	Temperature (K)	Bandgap (THz)	Transmission efficiency %
1	300	193.42	93
2	400	191.56	95
3	500	190.95	96.4

**Fig. 3** 3D views of defect mode layer with respect to temperature and frequency

4 Conclusion

In this paper, the effect of temperature on 1D Ge/ZnS photonic crystals with defective layer ZnS was studied using TMM method. Theoretical result shows that when temperature increases, the defect mode layer shifted towards the lower frequency range of spectrum and efficiency of the layer also increases. In this work, at high temperature 500 K, we get maximum efficiency up to 96.4%. By tuning the frequency, we design a wavelength division multiplexer or filter which is used in optical fibre communication.

Acknowledgements I am thankful to Prof. R. K. Agarwal, Director and Dr. Amit Sehgal, Head department of GLBIC, GLBITM, Greater Noida (UP) for their valuable cooperation.

References

1. Kumar V, Suthar B, Arunkumar, Singh KS, Bhargava A (2013) The effect of temperature and angle of incidence on photonic band gap in a dispersive Si-based one dimensional photonic crystal. *Physica B* 416:106–109
2. Suthar B, Kumar V, Kumar A, Singh KS, Bhargava A (2012) Thermal expansion of photonic bandgap for 1-D photonic crystals. *Progress Electromagn Res Lett* 32:81–90
3. Talebzadeh R, Bavaghar M (2017) Tunable defect mode in one-dimensional ternary nanophotonic crystal with mirror symmetry. *J Optoelectron Nanostruct* 2(3):83–92

4. Barati M, Aghajamali A (2016) Near-infrared tunable narrow filter properties in a 1D photonic crystal containing semiconductor metamaterial photonic quantum-well defect. *Phys E: Low-Dimens Syst Nanostruct* 79:20–25
5. Chang TW, Wu CJ (2013) Analysis of tuning in a photonic crystal multichannel filter containing coupled defect. *Optik* 124:2028–2032
6. Banerjee A, Awasthi SK, Malaviya U, Ojha SP (2006) Design of a nano-layered tunable optical filter. *J Mod Opt* 53(12):1739–1752
7. Ghasemi F, Entezara SR, Razi S (2019) Graphene based photonic crystal optical filter: design and exploration of the tunability. *Phys Lett A* 383(21), 2551–2560
8. Suther B, Bhargava A (2012) Temperature dependent Tunable photonic channel filter. *IEEE Photonic Technol*. <https://doi.org/10.1109/lpt.2011.2178401>
9. Singh BK, Pandey PC, Rastogi V (2018) Tenability of temperature dependent THz photonic bandgaps in 1D photonic crystals composed of graded index materials and semiconductor InSb. *AIP Conf Proc* 1953:060038. <https://doi.org/10.1063/1.5032769>
10. Gharaati A, Zare Z (2017) The effect of temperature on one-dimensional nano metallic photonic crystals with coupled defects. *Pramana-J Phys* 88(75):1–6
11. Malitson IH (1963) A redetermination of some optical properties of calcium fluoride. *Appl Opt* 2:1103–1107
12. DeVore J R (1951) Refractive index of rutile and sphalerite. *J Opt Soc Am* 41:416
13. Li H (1984) Refractive index of ZnS, ZnSe and ZnTe and its wavelength and temperature derivatives. *J Phys Chem Ref Data* 13:103

Design and Analysis of UWB-Multiband Notch Antenna Loaded with CSRR and U-Shaped Slot for Wireless Applications



Madan Kumar Sharma, Suryadeep Singh, Tanishq Thakur,
Syed Md. Moazzam Sajjad Razi, and Shubham Tiwari

Abstract In this study, an ultra-broad band antenna (UWB) with a multiband notch function is designed, simulated, and analyzed. The five notch band characteristics are obtained by loading the rectangular radiating patch with complementary split ring resonator (CSRR) and U-shaped slot inserted in the feed line. Partial ground plane is adopted to offer the passband in the desired frequency range. The proposed antenna has a wide range of operating frequencies from 0.5 to 20 GHz, which can make the proposed antenna useful for many UWB applications. The planner antenna has $30 * 35 \text{ mm}^2$ compact size. The antenna rejects five-bands and these are: network 50 (Pentium 1–1.8), S-band (2–4 GHz), microwave access with Wi-MAX frequency (3.3–3.8), wireless local area network WLAN (5.1–5.9 Microsoft) x-band (8–12 cores). The proposed antenna is offered maximum gain of 5.2 dBi in the passband frequency range. However, in stopband region, gain has attained a negative peak with a value of -10 dBi . The multiband rejection capability of the antenna is achieved by the CSRR technique and the U-shaped slot developed in the transmission.

Keywords UWB · Notch band · WLAN · Microstrip · CSRR · U-slot

M. K. Sharma (✉) · S. Singh · T. Thakur · S. Md. Moazzam Sajjad Razi · S. Tiwari
Department of ECE, Galgotias College of Engineering and Technology, Greater Noida, India
e-mail: madan.kumarsharma@galgotiacollege.edu

S. Singh
e-mail: s.suryadeep2222@gmail.com

T. Thakur
e-mail: tanishqthakur17021999@gmail.com

S. Md. Moazzam Sajjad Razi
e-mail: moazzam.razi1196@gmail.com

S. Tiwari
e-mail: shubham.t.31@gmail.com

1 Introduction

Ultra-wideband (UWB) radio technology is based on IEEE 802.4a-IEEE802.4z, which was originally developed by the USA for military applications [1]. Later on, technology found its application in industry and also became a hot topic of research for the wireless communication industry. UWB uses extremely low energy while having high data transmission rates. On the press released by the Federal Communication Commissions (FCC) [2]. UWB became a freely accessible technology. Antennas are an important part of wireless systems. The compact size is a big problem when designing a UWB antenna and must have a wide impedance band and one direction for the whole working group.

However, along with the UWB performance of the antenna, several narrowband are also interfere with an interesting wideband operating range. Stopping networks are the wireless local area network (WLAN), Wireless Access to a Microwave (Wi-Max), Industrial Scientific Medical Band (ISM), Radar, and Satellite bands. To eliminate these bands, we require additional hardware in terms of band-stop filter circuits [3], and therefore, the size and cost of the system are increased. If the UWB antenna itself has inherent band-stop characteristics, the size and cost both will be reduced. Recent research into the UWB antenna architecture focuses mainly on optimizing and implementing the compact size UWB antenna with multiple band rejection capabilities [4].

Several types of researches have been carried out in the UWB antenna design. A major goal of the carried out research is to include more rejection bands in the UWB antenna as well as to extend the passband capability. In this direction, recent carried out research is well described in [5–14].

Reported in [5] was a truncated rectangular patch with U-slot and partial ground. The fabrication of the antenna was achieved by cutting the type U cut into the electric field. The WLAN band with a frequency of 5.15 GHz can be rejected. The antenna has an overall size of $13 \times 2 \text{ m}^2$ and a gain of 6.1 dBi. The UWB antenna loaded with step impedance split ring resonator (SISRR) and an integrated impedance resonator (SIR) has been reported in [6]. This antenna is capable of rejecting WLAN band and X band. In [7], a circular ring radiating element-based antenna was developed. The antenna has a partial rectangular ground plane and two small slots have been etched near to feed line. The reported antenna has held the WLAN and WIMAX band rejection property. The overall dimensions of the antenna were $35 \times 30 \text{ mm}^2$ and it was offered the gain of 4–9 dBi in the UWB frequency range. The size reduction and resonance matching technique were represented in [8]. The impedance matching was accomplished by a quarter-wave transformer. Notch band characteristic was achieved for the WLAN band. The circular patch UWB antenna has overall dimensions $30 \times 40 \text{ mm}^2$ and it was operated between 2.4 and 13.8 GHz range and the gain was 10 dBi. The band notch characteristic was included in [9] using a nested ring resonator (NSRR) and a stepped impedance resonator (SIR). The ability to repel the belt is

obtained by forming the NSRR in the radiant part and injecting the SIR with a pair of T-shaped holes in the supply line. The antenna has to be provided notch band in C and WLAN range.

An antenna was reported in [10] which was constructed with a circular radiating element and fed by a coplanar waveguide (CPW). A single notch is obtained in the stated structure through the integration of a single ring resonator under a CPW structure. To obtain a double notch, triple notch, and multiple notches, the cascade structure of ring resonator has been used. The reported antenna was assisted by the 2.5–12 GHz bandwidth, which primarily covers the range of UWB as approved by FCC. A circular radiating patch was loaded with a $\lambda/4$ slot line resonator was implemented in [11]. In the feed line near the symmetry plane, a pair of spur-lines was created which produce a notched band around 5.5 GHz. The antenna has a size of $29.38 \times 28.25 \text{ mm}^2$ with varied gain from 3 to 11 dBi. A semi-ellipsoid radiator with a microwave strip transmission line antenna was developed in [12]. In the developed prototype, resonance matching was achieved by etching rectangular slot over the ground plane. However, band-stop property was attained by an E-shaped stub and two L-shaped open-ended stubs, and a notched band was acquired at 7 GHz. The open J-shaped frames and asymmetrical T-shaped open main parts hit many bands stop. The frequency of these stop bands was 5.2 GHz, 5.8 GHz, and 3.5 GHz. Their varactor diode has been used for tuning purposes. This antenna was offered a gain of more than 3 dB over the pass band.

A UWB planer antenna was successfully developed in [13]. In this antenna, a sharp roll-off band notch has been achieved by fragment-type-etched pattern. The band rejection can be accomplished by embedding an L-shaped or square ring resonator with the adjusted ground plane. The antenna has an overall size of $24 \times 30 \text{ mm}^2$. A novel structure of the UWB antenna was implemented in [14]. The design consists of four integrated Fibonacci in the radiating element. Most of the antennas discussed so far do not cover the 900 MHz bands. Nevertheless, the configuration of the recorded antenna was beneficial since it includes a lower band of Global Systems for Mobile (GSM) along with the UWB. The multiple notches were obtained with the desired performance parameters of the antenna. The gain of the antenna was varied from -1.42 to 10.2 dBi while gain was reduced in the rejected band. The efficiency of the GSM band is 98% given by the reported antenna. The possible interference with 3.3–3.6 GHz, 5.15–5.35 GHz, and upper WLAN (6.4 GHz) was eliminated from the antenna. The CSRR loader circular microstrip antenna was developed with the LR Tape Engine (CSMA) at [15]. CSRR is performed as a two-part annular valve. The antenna shows large reduction with greater gain and directivity. The U-slot short wave antenna was implemented in the form of a short wavelength (USSPA) with a layer of foam as a substrate in [16]. The antenna operating frequency is changed with the use of PIN diode. The width plays an crucial role in the antenna's resonance frequency.

Using the Computer Simulation Tool (CST), the UWB notch antenna is modeled and tested in this article. For the operations of the UWB bands, structure of the rectangular antenna element and ground plane is modified. The CSRR and U-shaped structures are etched in the radiating element and feed line for penta-band rejection

capability. The comparative study of the presented antenna in terms of performance parameter and size is carried out and shown in Table 1. Moreover, the proposed

Table 1 Comparative study of the proposed antenna with existing antennas

References	Size of antenna in mm ²	Notch bands (GHz)	Gain (dBi)	Radiation pattern	VSWR (in stop band)
[5]	13 * 22 * 0.8	WLAN (5.1–5.9 GHz)	6.1	Symmetrical and omnidirectional	8.7
[6]	24 * 32	WLAN (5.1–5.9 GHz) and X-band (7–11 GHz)	5.2	Omnidirectional	–
[7]	35 * 30	WIMAX (3.3–3.8 GHz)	9	Omnidirectional and E-plane-bidirectional	7.5
[8]	30 * 40 * 1.6	WLAN (5.1–5.9 GHz)	10	H-plane-omnidirectional and E-plane-bidirectional	–
[9]	24 * 32	WLAN (5.1–5.9 GHz), X-band (7–11.2 GHz) and C-band (4.4–5 GHz)	5	Omnidirectional	>10
[10]	50 * 50	3.5, 5.8, 7.5 GHz	–	Omnidirectional	>10
[11]	29.38 * 28.25	WLAN (5.1–5.9 GHz)	Peak gain over 7.5	Omnidirectional	–
[12]	25 * 30	WIMAX (3.3–3.8 GHz) and WLAN (5.1–5.9 GHz)	More than 3	Omnidirectional	–
[13]	24 * 30	WIMAX (3.3–3.8 GHz) and WLAN (5.1–5.9 GHz)	4	H-plane-omnidirectional and E-plane dipole like	–
This work	30 * 35	L-band (1–2 GHz), S-band (2–4 GHz), WiMAX (3.3–3.8 GHz), WLAN band (5.1–5.9 GHz), X-band (8–12 GHz)	5.2	Directional radiation pattern	13.8

antenna is offered more band-stop property and extended passband up to 20 GHz which is covered several wireless applications. The remainder of the paper is structured as follows: The antenna architecture procedure is conducted in Sect. 2. Section 3 covers the proposed antenna outcome analysis. Eventually, the work performed is summarized in the segment on the conclusion.

2 Antenna Design

The proposed UWB antenna is designed using the FR4 substrate. The relative permittivity and the loss tangent are 4.4 and 0.02, respectively. The overall size of the substrate is $30 \times 35 \text{ mm}^2$. Figure 1 displays the system configuration and antenna dimensions. The transmission line has a width of 3.4 mm for 50Ω resonance matching. The ground plane is modified for the antenna's passband performance and is $30 * 13 \text{ mm}^2$ in size. The following six steps are followed to achieve the desired stop-band behavior and described below and evolutionary structure modification is shown in Fig. 2.

The resonating behavior of each step is analyzed using S-parameters and VSWR represented, respectively, in Figs. 3 and 4. In the first step, a simple rectangular patch with partial ground is obtained to meet the UWB performance criteria; the antenna of this step is called Ant-1. The Ant-1 has poor in-band reflection for the entire frequency range 0.5–20 GHz. However, VSWR shows a single band rejection at a frequency of

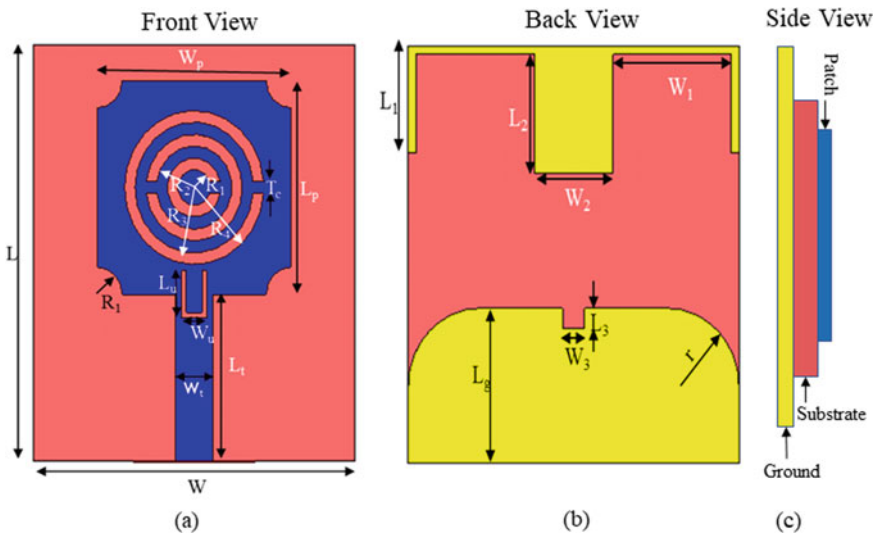


Fig. 1 Proposed penta-band notch UWB antenna with the dimensions given in mm: $L = 35, L_t = 14, L_p = 18, L_u = 4, L_g = 13, L_1 = 9, L_2 = 10, L_3 = 1.7, W = 35, W_t = 3.4, W_u = 2.4, W_p = 18, W_1 = 10.8, W_2 = 7, W_3 = 2, R_1 = 1.5, R_2 = 3.5, R_3 = 5.5, R_4 = 6.5, R_1 = 2.3, t = 6.5, T_c = 1$

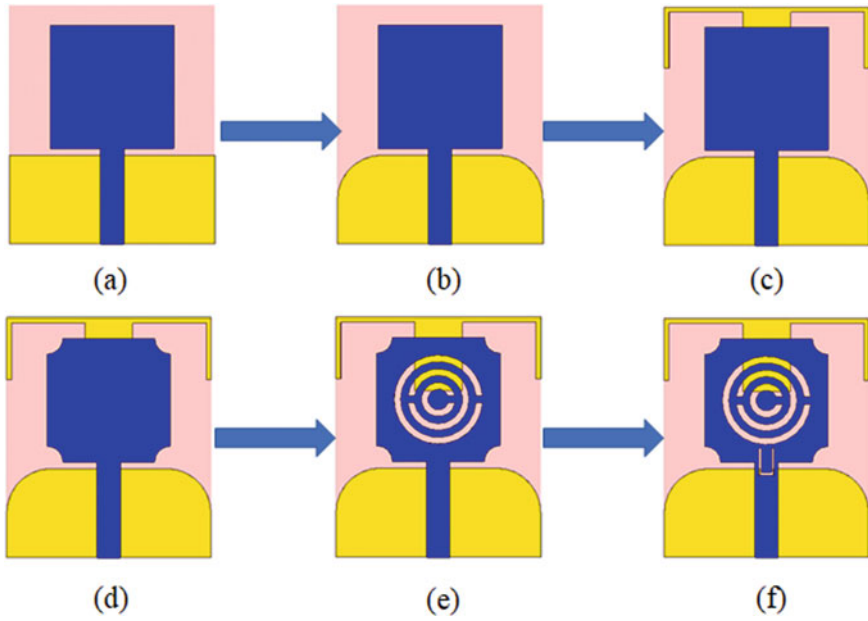


Fig. 2 Design steps for proposed antenna, **a** Ant-1; **b** Ant-2; **c** Ant-3; **d** Ant-4; **e** Ant-5; **f** Proposed antenna

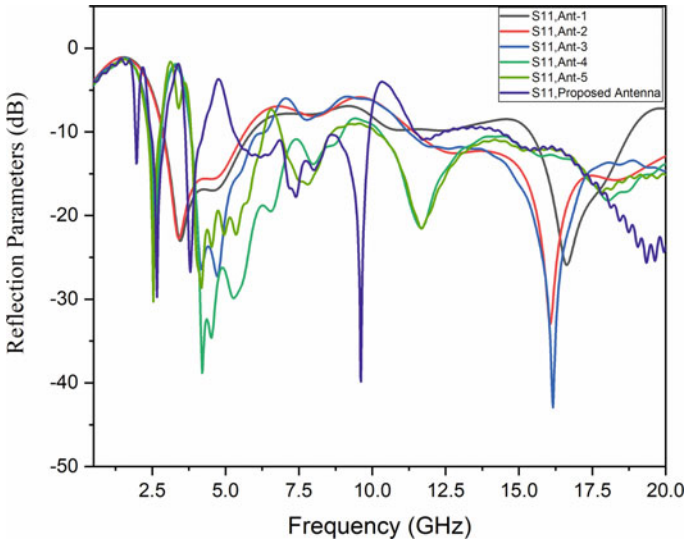


Fig. 3 S-parameter comparisons between the evolutionary steps and the proposed antenna

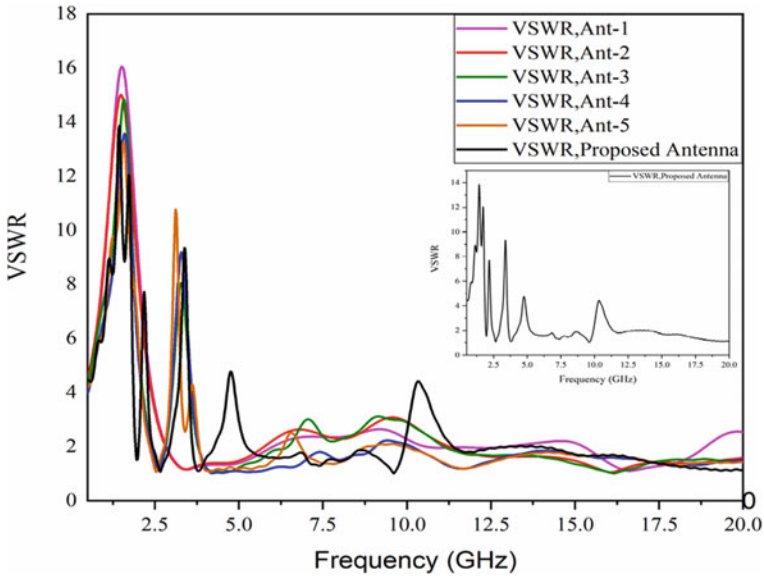


Fig. 4 VSWR comparisons between evolutionary steps and the proposed antenna

1.5 GHz. In order to attain both passband and rejected band characteristics, in the next stage, more modification in the design is performed and the antenna is called Ant-2. The Ant-2 ground plane top corner edges are chopped off in the rounded form to provide a smooth transition from one resonant mode to another. From the results of the S-parameter of Ant-2, it is clearly indicated that the in-band reflection is improved at the frequency of 12.5–20 GHz, whereas, VSWR for Ant-2 is represented single band rejection at 1.5 GHz frequency. Furthermore, in Ant-3, the M-shaped rectangular slots are suspended over the ground plane which produced 12.5–20 GHz similar to Ant-2 in-band reflection. Nevertheless, an additional stopband with a frequency of 2.1 GHz is provided in the M-shaped ground slot. In the next step, Ant-4 modified with circular slots cut at the edges of the radiating patch which helps in stabilization of the gain. A CSRR structure is developed in step-5 and antenna is named as Ant-5. In the Ant-5, we introduced three rings of CSRR at equal spacing is by which the two-notch band is achieved in a frequency range of 2.009–2.43 GHz and 4.198–5.15 GHz. In the final step, Ant-6 is updated with U-shaped slots is inserted and carved at the junction of the transmission line and the radiation patch of the proposed antenna by which another rejected band is obtained within the 9.9–11.3 GHz range.

3 Result Analysis

The proposed effects of the antenna are tracked and evaluated with respect to S-parameters, VSWR, surface current intensity, directivity, gain and radiation patterns and their detailed discussion is conducted as follows:

The effects of the proposed antenna's voltage standing wave rate are given in Fig. 5. VSWR is indicated that the proposed antenna offered five-stop band at the frequency of 1.4 GHz, 2.1 GHz, 3.3 GHz, 4.7 GHz, and 10.3 GHz.

Furthermore, validation of the proposed antenna's notch bands is authenticated with the density of the surface current. The surface current density is analyzed at the obtained stop band frequency and shown in Fig. 6. The current is fed through the transmission line and is concentrated at the transmission line below the U-shaped slot at a frequency range of 2.1 GHz, 3.3 GHz, and 10.3 GHz; the maximum current density appears in the patch around the CSRR, M-shaped in the ground plane, and U-shaped slot, respectively, as shown in the corresponding figure. The radiating element is coupled with and the remaining portion of the minimum surface current at the desired stop band frequency. Therefore, the proposed antenna band-stop characteristic is verified accordingly.

The result of the antenna is shown in Fig. 7. The antenna achieved a gain of more than 5 dBi in the frequency of the bandwidth and fell significantly below 0 dBi in the notch frequencies.

The presented antenna's radiation pattern is characterized by the 2 axes, i.e., E-plane and H-plane which correspond, respectively, to $\phi = 0^\circ$ and 90° . The radiation patterns are observed at the frequency of 3.7 GHz, 6 GHz, and 7.24 GHz. The results

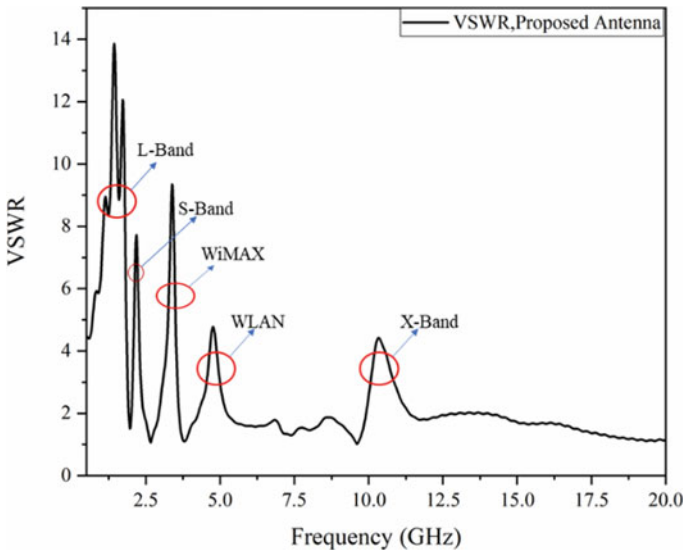


Fig. 5 Simulated VSWR of the proposed antenna

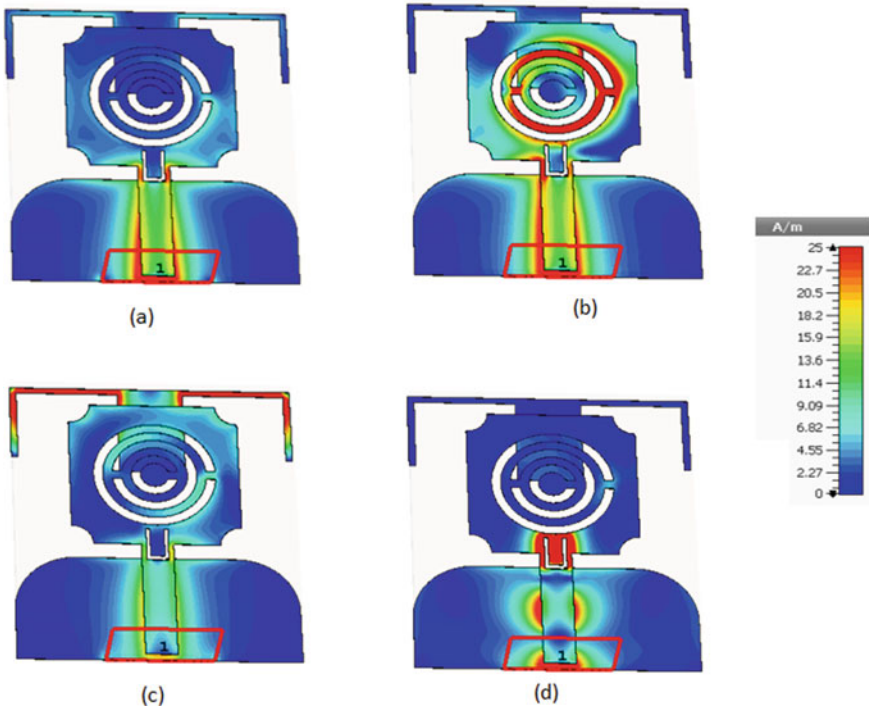


Fig. 6 Current density distribution at frequencies, a 1.4, b 2.1 GHz, c 3.3 GHz, d 10.3 GHz

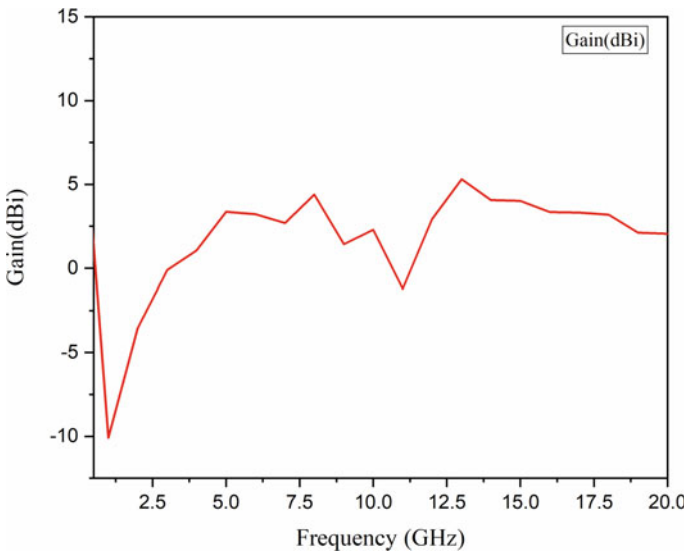


Fig. 7 Variation in the gain of the antenna with frequencies

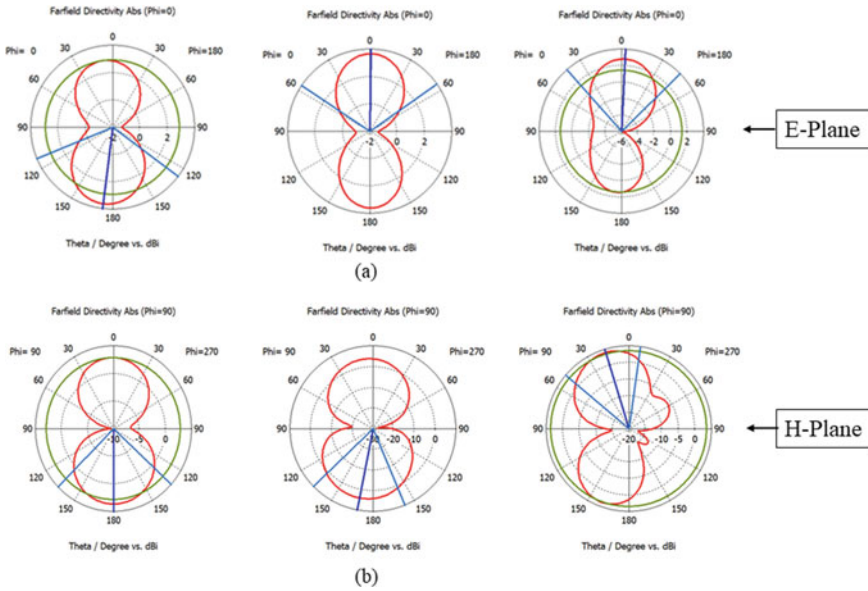


Fig. 8 Radiation pattern of the proposed antenna in **a** E-plane and **b** H-plane at frequencies 3.7 GHz, 6 GHz, and 7.24 GHz

are shown in Fig. 8. The presented UWB antenna has been found to have spatial radiation patterns with good stability within the frequency range of the passband.

The antenna directivity is defined in Fig. 9. The presented antenna is offered poor directivity in the stopbands region while in the passband frequency the directivity is more stable with a peak value of 6.9 dBi.

4 Conclusion

In this article, a compact ultra-wideband antenna with multiband notch capabilities has been successfully simulated and analyzed for next-generation wireless applications. The design has a rectangular radiating patch with concave cut edges and CSRR, U-shaped slot cut, respectively, in the radiating rectangular patch and the junction of the transmission line. By increasing the order of the concentric circular ring of the CSRR structure, multiple notch bands have been accomplished in the presented antenna design. The antenna built has a wide functioning range from 0.5 GHz to 20 GHz. The band rejection capabilities are obtained in the L-band, S-band, WLAN, Wi-Max band, and X-band. In the passband, the antenna achieved a peak gain of 5.2 dBi whereas the minimum value of the gain in the notch band is -7.2 dBi. The stable and directional radiation characteristics have been achieved in the propounded antenna. The comparative research of the proposed work is also carried out with

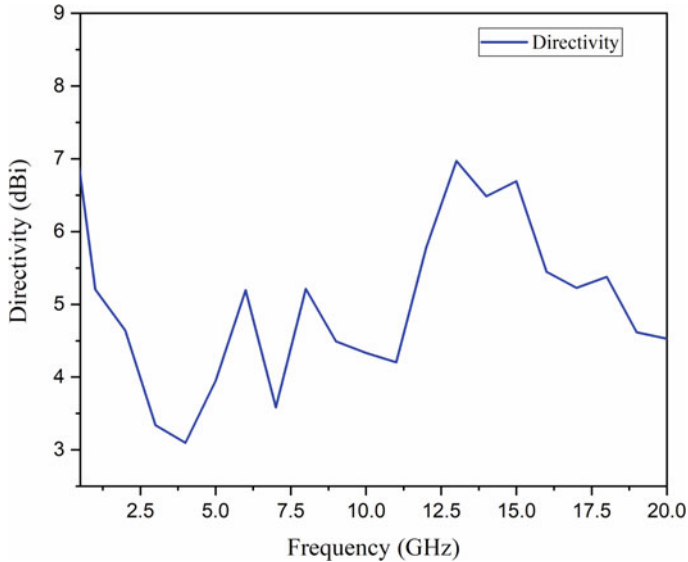


Fig. 9 Variation in the directivity of the antenna over frequencies

existing literature. In addition, the presented antenna is out-performed as compared to the current literature. In the future, the UWB-MIMO antenna configuration can be implemented using the proposed radiating element.

References

1. Saeidi T, Ismail I, Wen WP, Alhawari ARH, Mohammadi A (2019) Ultra-wideband antennas for wireless communication applications. *Int J Antennas Propag* 2019
2. Webster EM (1950) Federal communications commission. *Navigation* 2(6):189–191
3. Chiu L, Xue Q (2012) A simple microstrip band stop filter using cross-coupling stubs. *Int J Microw Sci Technol*
4. Choi SH, Lee HJ, Kim JK (2008) Design of a ultra-wideband antenna with band notch characteristic. In: 2008 IEEE international symposium on antennas and propagation and USNC/URSI national radio science meeting, APSURSI
5. Hussain N, Jeong M, Park J, Rhee S, Kim P, Kim N (2019) A compact size 2.9-23.5 GHz microstrip patch antenna with WLAN band-rejection. *Microw Opt Technol Lett* 61(5):1307–1313
6. Li Y, Li W, Yu W (2013) A compact CPW-fed wide-slot ultrawideband antenna with sharp frequency rejection functions for wlan band and X-band. *Microw Opt Technol Lett* 55(12):2972–2976
7. Srivastava G, Dwari S, Kanaujia BK (2015) A compact triple band notch circular ring antenna for UWB applications. *Microw Opt Technol Lett* 57(3):668–672
8. Mishra G, Sahu S (2016) Compact circular patch UWB antenna with WLAN band notch characteristics. *Microw Opt Technol Lett* 58(5):1068–1073

9. Li Y, Li W, Ye Q (2013) A compact UWB antenna with dual band-notch characteristics using nested split ring resonator and stepped impedance resonator. *Microw Opt Technol Lett* 55(12):2827–2830
10. Vendik IB, Rusakov A, Kanjanasit K, Hong J, Filonov D (2017) Ultrawideband (UWB) planar antenna with single-, dual-, and triple-band notched characteristic based on electric ring resonator. *IEEE Antennas Wirel Propag Lett* 16:1597–1600
11. Lee CH, Wu JH, Hsu CIG, Chan HL, Chen HH (2017) Balanced band-notched UWB filtering circular patch antenna with common-mode suppression. *IEEE Antennas Wirel Propag Lett* 16:2812–2815
12. Kingsly S et al (2019) Tunable band-notched high selective UWB filtering monopole antenna. *IEEE Trans Antennas Propag* 67(8):5658–5661
13. Du Y, Wu X, Siden J, Wang G (2018) Design of sharp roll-off band notch with fragment-type pattern etched on UWB antenna. *IEEE Antennas Wirel Propag Lett* 17(12):2404–2408
14. Srivastava K et al (2018) Integrated GSM-UWB Fibonacci-type antennas with single, dual, and triple notched bands. *IET Microwaves Antennas Propag* 12(6):1004–1012
15. Pandey GP, Kanaujia BK, Gupta SK, Gautam AK (2014) CSRR loaded tunable L-strip fed circular microstrip antenna. *Wireless Pers Commun* 74(2):717–730
16. Singh DK, Kanaujia BK, Dwari S, Pandey GP, Kumar S (2015) Complementary split ring resonator based compact wideband microstrip antenna with tunable bands. *Wireless Pers Commun* 80(2):635–645

Gray-Version Invariant Reversible Data Hiding Scheme Based on 2D Histogram Modification for Color Images



Aruna Malik, Samayveer Singh, Shashank Awasthi, and Piyush Yadav

Abstract In this paper, a new color image-based reversible data hiding scheme for gray-version invariance using two-dimensional histogram modification is proposed. The proposed scheme first decomposes the color images into its components, i.e., R, G, and B and then secret data is embedded into its two components, namely G and B using proposed embedding strategy. The proposed embedding strategy basically uses prediction error expansions and pairwise embedding for secret data hiding. To maintain the same grayscale version as of actual colored cover image, the pixel intensity values of R component are adjusted according to the modification done in the G and B channels. Therefore, the proposed scheme embeds an impressive amount of data and also result in better image quality while retaining the gray pixel intensities. The experimental results also prove that the proposed technique has shown greater embedding enactment than the existing interrelated arrangements in terms of visual quality at different embedding capacities.

Keywords Reversible data hiding · Gray-version invariance · Color image · Histogram modification · Pairwise prediction error expansion

A. Malik · S. Singh (✉)

Department of Computer Science and Engineering, Dr B R Ambedkar National Institute of Technology Jalandhar, Jalandhar, Punjab, India
e-mail: samayveersingh@gmail.com

A. Malik

e-mail: arunacsrke@gmail.com

S. Awasthi

Department of Computer Science and Engineering, G L Bajaj Institute of Technology and Management, Greater Noida, Uttar Pradesh, India
e-mail: shashanklbitm@gmail.com

P. Yadav

Department of Electronics and Communication Engineering, G L Bajaj Institute of Technology and Management, Greater Noida, Uttar Pradesh, India
e-mail: piyushyadav1985@gmail.com

© Springer Nature Singapore Pte Ltd. 2021

R. Agrawal et al. (eds.), *Advances in Smart Communication and Imaging Systems*,
Lecture Notes in Electrical Engineering 721,
https://doi.org/10.1007/978-981-15-9938-5_33

343

1 Introduction

Due to increase in the transmission of digital content over Internet, there is a need to address the challenges related to information security. In information sensitive domains, security compromises are not tolerated, thereby giving rise to the advent of various security mechanisms. The proliferated transmission of information over insecure channels has gathered attention of various attackers who attempt to harm the valuable data of users. Cryptography and steganography are the two important mechanisms that provide protection to valuable information [1, 2].

Cryptography refers to conversion of the intelligible information into some unintelligible form so that an adversary cannot understand the actual meaning of original data. The encrypted information looks meaningless; therefore, granting protection to the actual data. Thus, the encrypted data is communicated over the insecure media. At receiver side, decryption is performed to get the original data. Cryptography may be either symmetric or asymmetric key cryptography depending on the possession of secret keys. A major shortcoming of cryptography is that the conversion of data to its encrypted form conveys that some security mechanism has been applied on that data, and it attracts the malicious intruders to attempt security attacks on the encrypted data. Cryptography does not hide the presence of information, but its actual meaning is protected.

Steganography, on the other side, refers to concealing the secret data within cover medium. The cover medium can be anything like images, audios, or videos. In steganography, the presence of secret data hidden in the cover medium is not visible. The cover medium looks like an ordinary piece of digital content. So, steganography achieves information hiding in such a way so that no one could detect its existence. A prominent research work is proposed in the direction of hiding secret data into the cover medium. These methods can be either reversible or irreversible information hiding methods. In irreversible data hiding, permanent damage to the cover medium may be there after the secret data retrieval. The user is only concerned with the restoration of the secret data, and the cover medium just use as transportation channel. Such methods can be used in applications where the cover medium is just used as a channel to hide the secret content, such as secret communication. Although these data hiding methods do some alterations to the cover image pixels which are visually imperceptible to human eyes, in some information sensitive domains such as medical imagery, satellite imagery, biometrics, etc., both the cover medium as well as the secret data are important [3]. For such sensitive images, even a slight modification to the pixel values is not tolerable. In such domains, the conventional data hiding methods are not suitable because they cause permanent distortions to the cover medium. So, we need reversible data hiding methods in these application areas to make sure that a sensitive cover image is successfully restored after data extraction [4]. Reversible data hiding (RDH) methods allow complete restoration of cover medium after freeing it from the hidden secret data [5]. As these methods yield the original cover medium as well as the secret data as output, they are also called lossless data hiding methods. In the previous years, there has been tremendous

investigation in RDH field including spatial domain [3, 4, 6, 7], compression domain [8–12], transform domain [13] schemes. The compression domain-based reversible hiding approach have been used extensively for real-time communication scenarios, such that the network resources are utilized efficiently. However, the RDH schemes working in spatial domain have least complexity. These methods directly manipulate the pixel's intensities of the cover image, hence providing reasonably good performance both with regard to payload carrying capacity and the marked image's quality.

In the past few decades, various reversible data hiding methods have been presented that guarantee lossless data hiding into cover images. Such methods are histogram shifting based [14], compression based [4], and expansion based [6, 7]. In compression-based reversible data hiding, the cover image is losslessly compressed and the secret data is embedded into it. Difference expansion (DE) along with prediction error expansion (PEE) constitute expansion-based approaches. In difference expansion, a pixel pair is used to hide single data bit, where the pixels are modified such that their difference is expanded but their average remains the same. In prediction error expansion, the pixel value is predicted from its neighborhood and the prediction errors are used to hide data. In histogram shifting, the cover image histogram is generated, and the peak bin is used for information hiding.

In this paper, we propose a novel RDH technique taking inspiration from grayscale invariance concept that hides sufficiently large quantities of secret data in color images. The scheme exploits pairwise embedding and PEE for data hiding by forming a pair of pixels of two color components, i.e., G and B so that caused distortion can be limited. Further, the proposed scheme corrects the pixel values of red component so that invariance of gray-version can be maintained.

The roadmap of the manuscript is given as follows. Section 2 deals with the literature review. In Sect. 3, proposed method is discussed. Section 4 discusses the experimental result and their deliberations. Finally, Sect. 5 winds up the paper.

2 Literature Review

In this section, some of the related work and existing reversible data hiding methods are briefly reviewed. There have been developed several reversible data hiding schemes which are divided into many categories like lossless compression [3], difference expansion [6], histogram shifting [14], prediction error expansion [5, 7], pixel value ordering [15], and transform-based methods [13].

Expansion-based reversible data hiding has been in use quite extensively due to different reasons. The first successful version of expansion-based data hiding was put forward by Tian [6] known as difference expansion, in which a pixel pair is used as an embedding element. The difference among two consecutive pixels is expanded to accommodate secret data. Thodi et al. [7] extended this idea of expansion by replacing the difference value with prediction errors. They calculated the prediction error using the neighboring context of the pixel, and then expand the prediction errors for data

hiding. Prediction error expansion (PEE) is a popular and widely used reversible data hiding method due to its high potential in aspects of embedding capacity along with visual quality. Prediction error expansion generates smaller prediction errors thereby adding to its performance. Sachnev et al. [16] further amalgamated the concept of prediction error expansion and sorting of pixels. The pixels are sorted according to their local variance, that ultimately lead to bring correlated pixels closer to each other to stimulate embeddable prediction errors. They also introduced a new predictor known as rhombus predictor for effective utilization of pixel context. In this approach, the neighboring four pixels of a pixel are regarded as its context, and they represent the likelihood of generating embeddable prediction errors. Some other sorting-based methods have also made their ways to bring improvements in this field of RDH. To further enhance the embedding performance, Ou et al. [17] proposed pairwise PEE, updating a pair of prediction errors simultaneously to embed secret data. They proposed a 2D-prediction error histogram (PEH) modification strategy to expand and shift the prediction error pairs. According to this scheme, the error pair (0, 0) can embed $\log_2 3$ data bits by expanding itself to (0, 0), (0, 1), and (1, 0). However, the pair (1, 1) is exploited separately to accommodate 1-bit secret data by expanding to itself and (2, 2). The distortion level is brought down significantly, hence providing high-fidelity way of data hiding. The idea of pairwise embedding has been further incorporated with pixel value ordering [15], that is itself a high-fidelity mechanism for data hiding. Several other improvements such as [9, 10, 18, 19] have been proposed to enhance the performance achieved by prediction error expansion. These schemes differ in the pairwise mapping styles while taking inspiration from Ou et al. [17].

The above-discussed RDH approaches are primarily deployed for grayscale cover images, and they have not accounted the importance of color images in today's scenarios. In the advanced digital age, the presence of high-quality colored digital content is unavoidable, so the reversible data hiding methods that consider colored cover images also need to be studied and designed. Additionally, there is one more parameter related to robustness and security. As the presence of noise in the digital transmission is inevitable, various sensitive domains like military, etc., may pose challenges in accurate object recognition, or precise data extraction from the stego images. As most of the image processing is done on grayscale versions of images due to cost concerns, Hou et al. [20] introduce a new RDH method that do not alter the grayscale version of the color images. This work, named as grayscale invariant reversible data hiding, retains the grayscale invariant version while embedding secret data into colored images. The secret data is concealed into R and B color components, adjusting G component accordingly to maintain grayscale values. This scheme attains a reasonable EC along with high quality of the stego images. Kumar et al. [19] prolonged the work of Hou et al. [20] in the compression domain, to maintain original gray-version of the cover image. Though this method was proposed under category of irreversible data hiding, yet it focused on retaining the grayscale equivalent of the colored image with significant embedding capacity and high visual quality.

In this paper, we suggest extension of [20] by incorporating high-fidelity nature of pairwise embedding. It conceals the secret data into colored images by forming a pair of pixels of two-color components, i.e., G and B so the caused distortion is

minimized. Further, the R component is adjusted so that invariance of gray-version can be maintained. Thus, this scheme offers high-quality stego image at some defined embedding capacities while retaining the original grayscale version of colored cover image.

3 Proposed Method

This section introduces the proposed gray-version invariant RDH method based on pairwise PEE realized using 2D mapping for histogram shifting for colored cover images. First, decomposition of color image into its color components, namely R, G, and B is performed and then the Green (G) and Blue (B) components are utilized in the proposed embedding strategy. The intensity values of Red (R) components are adjusted to resist the embedding changes of G and B components so that invariant color image can be generated. The corresponding extraction procedure follows reverse steps to retrieve data and restore image. The algorithms to present the embedding phase is provided as follows.

3.1 Embedding Algorithm

Input: I: cover image of size $W \times H$ pixels, S: secret information bit stream.

Output: Stego-Image I' .

Step 1: Decompose cover image into its color components, namely R, G, and B.

Step 2: Scan the G & B components in chessboard like pattern leaving the border pixels as defined in [18].

Step 3: Calculate the prediction error using rhombus context of each pixel of both the planes.

Step 4: Form a pair of prediction errors from each component G and B and embed the secret data using [17].

Step 6: Adjust the pixels of red channel according to the changes done in the green and blue channels using the same strategy defined in [19].

Step 7: Combine all three channels, i.e., RGB to form the stego-color image.

Thus, after embedding complete secret data, the resultant stego-image I' is achieved.

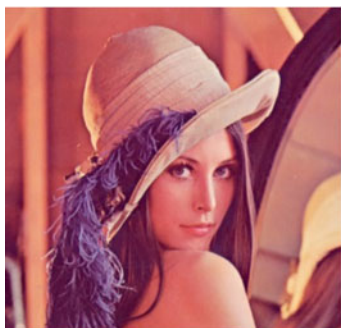
3.2 *Extraction and Restoration of Image*

The extraction and recovery procedure begins at decoder's side. The colored stego-image containing secret data is received by the decoder. The decoder first of all decomposes the image into its R, G, B color components as in the embedding phase. Here, the decoder can also convert the image into gray-version if he/she needs it. For secret data retrieval, the receiver will apply the reverse process followed at sender side on the both the planes, i.e., G and B to retrieve back the hidden secret data and the original color planes as per [17]. Next, the original pixel intensities values of the red components are restored using the gray-image and the recovered green and blue components as in the [19, 20]. Now, the composition of all the obtained/restored color components will provide the original cover image. Following this, the decoder would obtain precisely the extracted data along with restored pixel values. Further, he/she would be able to use the stego-color image for its applications like fingerprint matching without any additional processing.

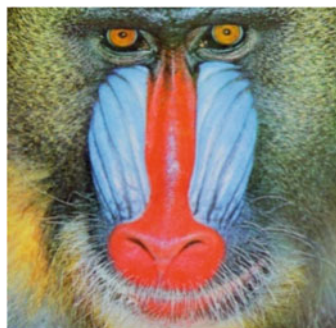
4 **Experimental Results and Their Discussions**

In this section, we discuss experimental outcomes of proposed reversible data hiding method and their discussions and comparisons with some existing schemes such as Hou et al. [20] and Kumar et al. [19]. The evaluation and experiment work are done using MATLAB environment running on the Intel(R), Core (TM)-i5 processor, 3.20-GHz with 4-GB RAM hardware specifications. To-be-embedded data is generated using arbitrary number generators. The experimental results of Hou et al. [20] and Kumar et al. [19] are occupied from their respective papers. The experiments have been performed on different colored 512×512 cover image, namely Baboon, Lena, Airplane, Barbara, Peppers, and Boat taken from the USC-SIPI image dataset [21]. Hou et al.'s work [20] is RDH approach for colored images with grayscale invariance, in the spatial domain category. Their work is recorded to be a pioneer grayscale invariant reversible data hiding scheme designed specifically for colored images. Kumar et al.'s scheme [19] is an AMBTC compression-based steganography method for color image providing gray-invariant images. For the assessment of performance, two parameters, i.e., embedding capacity (in bits) and peak signal to noise ratio (PSNR) are taken into consideration. PSNR is measured in dB (Fig. 1).

For an extensive evaluation of the presentation of the proposed scheme, the experimental outcomes, their comparison at 50,000 bits, and 100,000 bits embedding capacity are provided Tables 1 and 2, respectively. It is experimental states from the tabular results that the proposed scheme demonstrates higher PSNR values for all cover images. The explanation behind the superior embedding performance is the employment of rhombus context for prediction error calculation and the pairwise embedding which limits the caused distortion. Additionally, the proposed scheme



(a) Lena



(b) Baboon



(c) Airplane



(d) Peppers



(e) Barbara



(f) Boat

Fig. 1 Cover images

Table 1 PSNR comparison at EC of 50,000 bits

Cover images	Kumar et al. [19]	Hou et al. [20]	Proposed scheme
Lena	38.2	44.9	45.8
Baboon	31.8	38	38.52
Airplane	39.8	50.2	51.87
Peppers	38.21	41.12	43.65
Barbara	35.12	47.35	49.52
Boat	34.21	40.12	42.15

Table 2 PSNR comparison at EC of 100,000 bits

Cover images	Kumar et al. [19]	Hou et al. [20]	Proposed scheme
Lena	38.21	41.12	43.12
Baboon	31.02	32.5	33.56
Airplane	39.78	42.21	44.15
Peppers	37.89	37.56	39.56
Barbara	35.01	44.12	46.23
Boat	33.86	35.87	36.89

also maintains the same grayscale version of the as of the original colored cover image.

5 Conclusion

In this paper, a novel technique for RDH in color images ensuring grayscale invariance using a 2D-PEH modification is presented. The proposed method is basically an extended-work of Hou et al.'s scheme [20] that attains invariant grayscale image. The following points validate the superiority of proposed method: (1) It can maintain the same gray-version as of the original image, (2) It improves the visual quality of the stego-image, (3) It can reversibly embed the secret information inside the cover image. In the future work, an adaptive prediction error expansion-based approach can be utilized for further improving the image quality. Additionally, the encrypted domain can also be explored to secure the contents of the original images.

References

1. Kumar R, Saini KK, Chand S (2013) A new steganography technique using snake scan ordering strategy. *Int J Image Graph Sign Process* 6:25–32
2. Kumar R, Chand S (2013) A new image steganography technique based on similarity in secret message. In: *IEEE confluence 2013: the next generation information technology summit (4th international conference)*, pp 376–379
3. Malik A, Singh S, Kumar R (2018) Recovery based high capacity reversible data hiding scheme using even-odd embedding. *Multimed Tools Appl* 77:15803–15827
4. Kumar R, Chand S (2017) A novel high capacity reversible data hiding scheme based on pixel intensity segmentation. *Multimed Tools Appl* 76:979–996
5. Kumar R, Kim DS, Lim SH, Jung KH (2019) High-fidelity reversible data hiding using block extension strategy. In: *ITC-CSCC 2019. IEEE*, pp 74–77
6. Tian J (2003) Reversible data embedding using a difference expansion. *IEEE Trans Circuits Syst Video Technol* 13:890–896
7. Thodi DM, Rodriguez JJ (2007) Expansion embedding techniques for reversible watermarking. *IEEE Trans Image Process* 16:721–730
8. Kumar R, Chand S, Singh S (2019) An optimal high capacity reversible data hiding scheme using move to front coding for LZW codes. *Multimed Tools Appl* 78:22977–23001
9. Kumar R, Malik A, Singh S, Kumar B, Chand S (2016) Reversible data hiding scheme for LZW codes using even-odd embedding strategy. In: *International conference on computing, communication and automation (ICCCA2016)*, IEEE, pp 1399–1403
10. Malik A, Kumar R, Singh S (2016) Reversible data hiding scheme for LZW codes using LSB flipping strategy. In: *AICTC '16: Proceedings of the international conference on advances in information communication technology & computing*, pp 1–5
11. Kumar R, Kim DS, Jung KH (2019) Enhanced AMBTC based data hiding method using hamming distance and pixel value differencing. *J Inf Secur Appl* 47:94–103
12. Kumar R, Kumar N, Jung K (2019) A new data hiding method using adaptive quantization & dynamic bit plane based AMBTC. In: *6th international conference on signal processing and integrated networks (SPIN)*, pp 854–858
13. Kamstra LHJ, Heijmans AM (2005) Reversible data embedding into images using wavelet techniques and sorting. *IEEE Trans Image Process* 14:2082–2090
14. Ni Z, Shi YQ, Ansari N, Su W (2006) Reversible data hiding. *IEEE Trans Circuits Syst Video Technol* 16:354–362
15. Li X, Li J, Li B, Yang B (2013) High-fidelity RDH scheme based on pixel-value-ordering and prediction-error-expansion. *Sig Process* 39:198–205
16. Sachnev V, Kim HJ, Nam J, Suresh S, Shi YQ (2009) Reversible watermarking algorithm using sorting and prediction. *IEEE Trans Circuits Syst Video Technol* 19:989–999
17. Ou B, Li X, Zhao Y, Ni R, Shi Y-Q (2013) Pairwise prediction-error expansion for efficient reversible data hiding. *IEEE Trans Image Process* 22:5010–5021
18. Kumar R, Jung KH (2019) Robust reversible data hiding based on two layer embedding. *Inf Sci* 512:96–107
19. Kumar R, Kumar N, Jung K (2020) Color image steganography scheme using gray invariant in AMBTC compression domain. *Multidimens Syst Signal Process* 31:1145–1162
20. Hou D, Zhang W, Chen K, Lin SJ, Yu N (2018) Reversible data hiding in color image with grayscale invariance. *IEEE Trans Circuits Syst Video Technol* 29:363–374
21. SIPI: The USC-SIPI Image Database. (Online). Available: <http://sipi.usc.edu/database/>

Resonant Frequency Prediction of Patch Antenna in the Presence of Inserted Airgap Using Machine Learning



Mahima Soni, Kanhaiya Sharma, Ganga Prasad Pandey,
and Surendra K Gupta

Abstract This article presents an application of the machine learning approach to predict the resonant frequency of microstrip antenna in the presence of an inserted airgap in the band of 1.07-2.6 GHz. At a fixed overall height of 1.6 mm and by the varying thickness of FR-4 material and inserted airgap, a total of 50 data samples were collected through simulation using CST microwave studio 2019. An artificial neural network (ANN) model is developed from the simulated dataset and was used for the resonant frequency prediction. The predicted outcome is compared with simulated data, and it is determined that the model relying on ANN offers very close results with the simulated dataset. The proposed method can be applied to predict the resonant frequency of the patch antenna in the presence of an inserted airgap for regular and nonregular shapes.

Keywords Microstrip antenna · Airgap · Resonant frequency · ANN

1 Introduction

In the last four decades, the growth of information communication and technology (ICT) industries is continuously high as compared to other industries, and they demand low profile antennas, with dual polarization, multi-band in nature, low cost, and easy to fabricate for various applications like Internet of things (IoT). The continuous research shows that microstrip antenna has greater advantages and high

The work was supported by Office of Research and Sponsored Programs(ORSP) with the project no ORSP/R&D/2019/JAGP/042, Pandit Deendayal Petroleum University Gandhinagar, Gujarat 382007, India

M. Soni · K. Sharma · G. P. Pandey (✉)
Pandit Deendayal Petroleum University, Gandhinagar, Gujarat 387002, India
e-mail: gangaprasad.pandey@sot.pdpu.ac.in

S. K. Gupta
Ambedkar Institute of Technology, Shakarpur, Delhi 110092, India

© Springer Nature Singapore Pte Ltd. 2021
R. Agrawal et al. (eds.), *Advances in Smart Communication and Imaging Systems*,
Lecture Notes in Electrical Engineering 721,
https://doi.org/10.1007/978-981-15-9938-5_34

prospects over other types of antenna to fulfill the demands of industries and became a good choice. While having distinct advantages, microstrip antenna has copious disadvantages like high cross-polarization, low power handling ability, high conduction, and dielectric losses, radiated from feed structures. From the last four decades, researchers are trying to compensate these disadvantages by engineering design of microstrip antenna [1], gain improvement [2, 7, 12], bandwidth improvement [2], efficiency improvement [3], reduce cross-polarization [6, 9]. Airgap introduced to improve the bandwidth, gain, efficiency, and other parameters of patch antenna with the high dielectric substrate and its theoretical and experimental study investigated in the literature [5]. To calculate various parameters of the antenna, different analytical methods like cavity model, method of moment (MoM), and finite-difference time-domain (FDTD) models are existing and recommended by researchers, but they need antenna expertise. There is a necessity to develop a method to quickly and accurately predict various parameters of the antenna. ML is one of the solutions for it. Researches have effectively used the machine learning approach to design antenna [10], and ANN is predicting various parameters of antenna [8, 11].

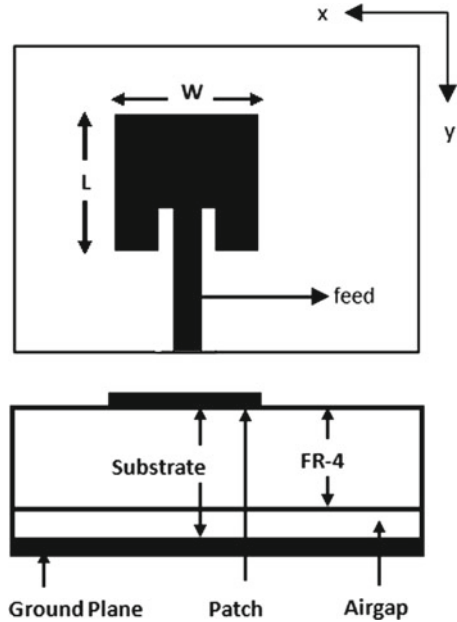
2 Antenna Design and Simulation

To design patch antenna, Fr-4($\epsilon_r = 4.4$) substrate material and inserted airgap is used and simulated using CSTTM Microwave Studio 2019 software. To improve various performance parameters of antenna like bandwidth and gain without changing the overall thickness of the 1.6mm with Fr-4($\epsilon_r = 4.4$) material, the airgap is inserted in between substrate and ground plane; hence, airgap also acts as a substrate. By inserting airgap in between FR-4 and ground plane, the overall performance of antenna is improved due to change in the value of effective ϵ_r . The copper material of 0.035 mm is used for patch and ground plane. To design antenna, $41.32 \times 49.38 \times 1.6\text{mm}^3$ dimensions are taken and inset feed is used to match 50Ω impedance value. The size of the ground plane $50.92 \times 58.98\text{mm}^2$ taken. The design structure of RMSA with the front and back view is shown in Fig. 1.

3 Machine Learning

ANN is a subset of machine learning (ML), and ML is a part of artificial intelligence(AI). The learning machine is a key concept behind ML. Based on learning, it will develop a model, and that model is used to predict new data. To train machine learning-based algorithms, we need enough data and then divide data into three parts called training, validation and testing; most preferred divisions of data are for training 70%, validation 15% and for testing 15%. Still, this combination may change according to a problem. Some optimized methods on how to divide data for ANN are investigated in [4]. In this investigation, a sufficient amount of data is collected

Fig. 1 Front and side view of rectangular microstrip antenna



through simulation for predicting the resonant frequency of patch antenna in the presence of inserted airgap.

3.1 Data Generation and Training Process of the ANN Model

A 1.6mm constant thickness of the substrate, by varying airgap and FR-4 material thickness, a total of 50 data samples is simulated using CSTTM. The details of simulated data samples are given in Table 2. For building the ANN model to predict the resonant frequency of RMSA, out of 50 data samples, 40 data samples have used to train the ANN-based Levenberg–Marquardt algorithm and build a model for prediction for the new dataset. In the training process of model again, 40 data samples are internally divided into 70%, 15%, 15% for training, validation, and testing, respectively. The architecture of the proposed ANN model is shown in Fig. 2 and detail parameter list is given in Table 1.

3.2 Testing Process of the ANN Model

To test the proposed model, randomly 10 data samples were selected from the dataset and kept to check the authenticity and reliability of the proposed ANN model. Test

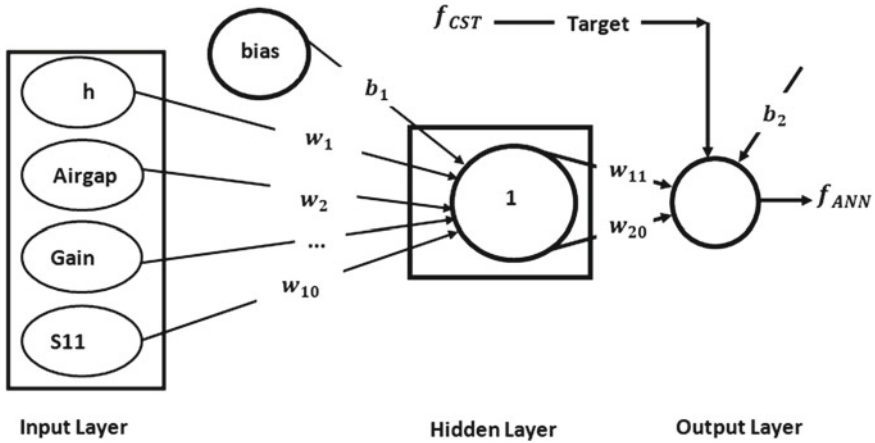


Fig. 2 Proposed model

Table 1 ANN model parameters

Parameter	Value	Parameter	Value
Input parameter	h, Airgap, Gain and S11	Validation check	6
Target parameter	Resonant frequency	Hidden layer	1
Training function	Levenberg-Marquardt	Neurons	10
Adaptive Learning function	Gradient decent	Training time	1.24 s
	With momentum weight and bias	MSE (training)	4.20696e-7
Transfer function	PURELIN	MSE (validation)	4.33737e-6
Epoch	16	MSE (testing)	6.07236e-6
Performance	2.57e-07	R (training)	9.9991e-1
Gradient	7.06e-02	R (validation)	9.99939e-1
Mu	1.00e-03	R (training)	9.99919e-1
Validation check	6	Overall Network performance	
Hidden layer	1	MSE	1.95163e-6
Neurons	10	R	9.99960e-1

Table 2 Dataset of 50 simulated RMSAs

RMSA	f_r(GHz)	Air Gap(mm)	FR-4 height h(mm)	Gain(dBi)	S11(dB)
1	1.705	0.1	1.5	5.7738	-13.2
2	1.995	0.2	1.4	5.9522	-27.333
3	2.115	0.3	1.3	5.761	-28.637
4	2.06	0.256	1.344	6.2713	-30.343
5	2.23	0.4	1.2	6.265	-21.566
6	1.99	0.5	1.1	5.3936	-23.721
7	2.056	0.25	1.35	6.3564	-33.38
8	2.28	0.45	1.15	6.7053	-18.35
9	2.228	0.4	1.2	6.4696	-20.775
10	2.055	0.255	1.345	6.1926	-32.815
11	2.312	0.48	1.12	6.9141	-17.414
12	1.956	0.175	1.425	5.7907	-28.223
13	2.055	0.255	1.345	6.1926	-32.815
14	1.989	0.2	1.4	6.038	-30.8632
15	2.049	0.25	1.35	6.2932	-34.004
16	2.079	0.275	1.325	5.9926	-29.594
17	2.223	0.4	1.2	6.2285	-18.974
18	2.274	0.45	1.15	6.3166	-17.091
19	2.384	0.55	1.05	6.4453	-15.34
20	2.049	0.25	1.35	6.2932	-34.005
21	2.274	0.45	1.15	6.497	-17.091
22	2.328	0.5	1.1	7.027	-15.666
23	2.286	0.46	1.14	6.5454	-16.96
24	2.316	0.49	1.11	7.0396	-15.94
25	2.38	0.54	1.06	6.3404	-15.97
26	2.388	0.56	1.04	6.2933	-14.106
27	1.96	0.176	1.424	6.2657	-26.107
28	2.19	0.37	1.23	5.2469	-20.465
29	2.244	0.42	1.18	6.1227	-18.31
30	2.312	0.48	1.12	6.9141	-17.414
31	2.376	0.54	1.06	6.4775	-15.503
32	2.136	0.32	1.28	6.5944	-25.906
33	2.228	0.4	1.2	6.4696	-20.775
34	2.312	0.478	1.122	6.9496	-17.447
35	2.312	0.48	1.12	6.9141	-17.413
36	2.396	0.56	1.04	6.4046	-14.997
37	2.604	0.78	0.82	6.5743	-11.408

(continued)

Table 2 (continued)

RMSA	f_r (GHz)	Air Gap(mm)	FR-4 height h(mm)	Gain(dBi)	S11(dB)
38	2.049	0.25	1.35	6.2932	-30.005
39	2.196	0.375	1.225	6.6305	-20.276
40	2.055	0.255	1.345	6.1926	-32.816
41	2.332	0.5	1.1	6.7187	-16.707
42	2.073	0.27	1.33	6.0129	-30.261
43	2.392	0.559	1.041	6.4075	-15.044
44	2.244	0.42	1.18	6.1227	-18.316
45	2.18	0.35	1.25	6.2815	-23.49
46	2.148	0.329	1.271	6.5082	-25.968
47	2.148	0.329	1.271	6.5082	-25.968
48	2.064	0.261	1.339	6.1271	-33.863
49	2.13	0.316	1.284	6.1145	-24.053
50	2.19	0.37	1.23	6.7275	-20.465

Table 3 Test dataset of RMSA's

f_r (GHz)	Air Gap (mm)	h (mm)	Gain (dBi)	S11 (dB)
2.073	0.27	1.33	6.0129	-30.261
2.312	0.48	1.12	6.9141	-17.413
2.19	0.37	1.23	5.2469	-20.465
2.384	0.55	1.05	6.4453	-15.34
2.286	0.46	1.14	6.5454	-16.96
2.055	0.255	1.345	6.1926	-32.815
2.06	0.256	1.344	6.2713	-30.343
2.055	0.255	1.345	6.1926	-32.815
2.079	0.275	1.325	5.9926	-29.594
2.148	0.329	1.271	6.5082	-25.968

datasets were used to predict the resonant frequency in the presence of airgap of RMSA. The details of test data samples are given in Table 3.

4 Resonant Frequency Calculation

In this paper, the authors have proposed a machine learning-based model to predict the resonant frequency of RMSA with the inserted airgap. The comparison of simulated and predicted resonant frequency by the proposed modes has been compared and the

Table 4 Comparison of simulated and predicted resonant frequency

RMSA	Simulated	Predicted (ANN)	Percentage error (%)
1	2.073	2.0921	0.921369995
2	2.312	2.3131	0.047577855
3	2.19	2.1867	-0.150684932
4	2.384	2.3862	0.092281879
5	2.286	2.2874	0.061242345
6	2.055	2.0549	-0.00486618
7	2.06	2.0572	-0.13592233
8	2.055	2.0549	-0.00486618
9	2.079	2.0999	1.005291005
10	2.148	2.1464	-0.074487896
		least % error	0.1506849
		Most % error	1.005291005
		Average % error	0.1756936

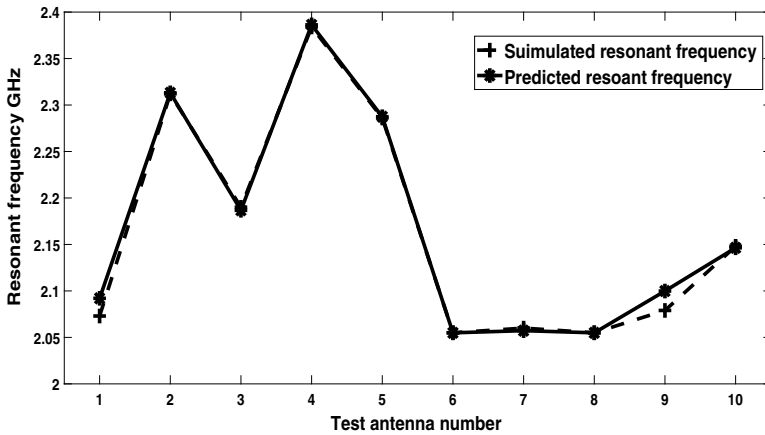


Fig. 3 Simulated and predicted resonant frequency comparison

details of comparison are given in Table 4 and its graphical representation is shown in Fig. 3.

4.1 Result and Discussion

In the present investigations, the authors proposed the ANN-based model to predict the resonant frequency of RMSA in the presence of air gap. It is clear from Table 4 that the predicted and simulated resonant frequencies are very close to each other.

The absolute least % error is 0.1506849, absolute most % is 1.005291005, and absolute average % error is 0.1756936. By observing minimum, maximum, and average absolute error is clear that the model performance of predicting resonant frequency is approximately 99% accurately.

4.2 Conclusion

For nonregular shapes, the existing analytical methods are tedious, time-consuming, and need a lot of expertise. Machine learning-based methods for calculating the resonant frequency of the patch antenna are fast and highly accurate. In this investigation, the authors proposed an ANN-based model to predicted the resonant frequency of RMSA with the inserted airgap. The predicted and simulated resonant frequencies are compared and found that simulated and predicted resonant frequencies are very closed to each other. The proposed model can be used to predict the resonant frequency of regular and nonregular shapes of the microstrip antenna in the presence of inserted airgap.

References

1. Agale T, Khanapurkar MM (2017) A review on design approach for performance enhancement techniques of microstrip patch antenna. In: 2017 Third international conference on Advances in Electrical, Electronics, Information, Communication and Bio-Informatics (AEEICB), pp 436–440
2. Ahmad H (2018) Abdelgwad: microstrip patch antenna enhancement techniques. *Int J Electronics Commun Eng* 12(10):703–710
3. Belekar VM, Mukherji P, Pote M (2017) Improved microstrip patch antenna with enhanced bandwidth, efficiency and reduced return loss using dgs. In: 2017 international conference on Wireless Communications, Signal Processing and Networking (WiSPNET), pp 2471–2474
4. Crowther PS, Cox RJ (2005) A method for optimal division of data sets for use in neural networks. In: Khosla R, Howlett RJ, Jain LC (eds) Knowledge-based intelligent information and engineering systems. Springer, Heidelberg, pp 1–7
5. Dahele JS, Lee KF (1985) Theory and experiment on microstrip antennas with airgaps. *IEE Proc H-Microwaves Antennas Propag* 132(7):455–460
6. Ghorbani K, Rowe WST (2007) A technique to reduce the cross-polarization levels of a microstrip patch fed horn antenna. In: 2007 IEEE antennas and propagation society international symposium, pp 2301–2304
7. Ineneji CN, Kusaf M (2015) Gain enhancement in microstrip patch antenna using the multiple substrate layer method. In: 2015 23rd signal processing and communications applications conference (SIU), pp 560–560
8. Khan T, De A, Uddin M (2013) Prediction of slot-size and inserted air-gap for improving the performance of rectangular microstrip antennas using artificial neural networks. *IEEE Antennas Wireless Propag Lett* 12:1367–1371
9. Khouser H, Choukiker YK (2017) Cross polarization reduction using dgs in microstrip patch antenna. In: 2017 International Conference on Microelectronic Devices, Circuits and Systems (ICMDCS), pp 1–4

10. Kim Y (2018) Application of machine learning to antenna design and radar signal processing: a review. In: 2018 International Symposium on Antennas and Propagation (ISAP), pp 1–2
11. Kushwah VS, Tomar GS (2017) Design and analysis of microstrip patch antennas using artificial neural network. In: Chattopadhyay S (ed) Microstrip antennas, Chap. 3. IntechOpen, Rijeka
12. Saravanan M, Geo VB, Umarani S (2018) Gain enhancement of patch antenna integrated with metamaterial inspired superstrate. *J Electrical Syst Information Technol* 5(3):263–270

Impact of K-Nearest Neighbour on Classification Accuracy in KNN Algorithm Using Machine Learning



Abhishek Srivastava

Abstract Classification accuracy of the KNN algorithm is affected by the number of nearest neighbour for predicting points. The idea behind nearest neighbour classification consists in finding a number, i.e. the ' k '—of training data point nearest in distance to a predicting data, which has to be labelled. The label of the new predicting data will be defined from these neighbours. Using a machine learning approach, the value of k will be fixed for model creation. In this paper, I analyse different numbers of neighbour so that classification accuracy can be maximized. Different distance metrics (Euclidean, Manhattan and Minkowski) can be used to measure the distance from the nearest data point.

Keywords Supervised machine learning · K-nearest neighbour

1 Introduction

Similarity measures play an important role while making classification using supervised machine learning. Similarity measures also create an important role while analysing some pattern of any class in the data set. KNN algorithms work on these patterns and check the new predicting data point match with which similarity based on its neighbour. Number of neighbours also plays an important role while classifying new data neighbour points. Majority of closely located neighbours help to classify new data points.

K-nearest neighbour uses different kind of distance metric to find distance between new data point with previously classified data point. These distance metrics are different in nature. Some of distance metric are used to calculate distance between coordinate points for example Euclidean some of distance metric uses distance been labelled data like yes and no like Hamming distance.

A. Srivastava (✉)

Department of Computer Science and Engineering, Sanskriti Institute of Management and Technology, Mathura, India

e-mail: mr.abhishk@gmail.com

© Springer Nature Singapore Pte Ltd. 2021

R. Agrawal et al. (eds.), *Advances in Smart Communication and Imaging Systems*,

Lecture Notes in Electrical Engineering 721,

https://doi.org/10.1007/978-981-15-9938-5_35

Decision of number of nearest neighbour also plays an important role because by changing the nearest neighbour may invert the classification. With the help of supervised machine learning model can be train with the data set. With exploratory data analysis, we can also find some insight of data which can be further analysis.

2 Related Work

Thirunavukkarasu et al. [1] proposed a method based on KNN algorithm and finding its classification accuracy. He also found the training accuracy and testing accuracy. He also divided the data set into training and testing data in a ratio of 60% and 40%. In paper, misclassification rate is 0, while classification is shown with 100%. Kulkarni et al. [2] done image-based work on iris flower, he used grey level co-occurrence matrix to find region of interest, then classification is done based on KNN on fuzzy KNN algorithm. This is a new approach where images are used rather than textual data.

Tan [3] proposed a method for text categorization. He also proposed that each neighbour which has small class should have assigned a higher weight in comparison with each neighbour which has big class should have assigned a little weight. By using that approach, balancing is done between training samples, and this approach is named as neighbour weighted K-nearest neighbour (NWKNN).

Hastie and Tibshirani [4] proposed a K-nearest neighbour-based method which used discriminant adaptive nearest neighbour. Using training data set, he created a centroid and then find the decision line to classify the object after centroid. Formation object can be classified based on neighbourhood. Weinberger and Saul [5] proposed a new distance metric Mahalanobis distance for KNN classification. They also proposed that Euclidean distance does not play an important role in face recognition as for gender identification, that is why here Mahalanobis distance plays an important role in classification.

3 Proposed Model

KNN algorithm calculates distance between new data point and its neighbour of training data point. It arranges the distance in increasing order. Once the distances are arranged in increasing order, then predecided k-nearest neighbour can be found. Out of these K, the majority of votes are considered of different classes. The dominant class is labelled assigned to new data points.

Step 1: Select any value of nearest neighbour for classification.

Step 2: Calculate distance between the new point and its K neighbour.

Step 3: Sort the calculated distance.

Step 4: Count the data point with category wise among k neighbours.

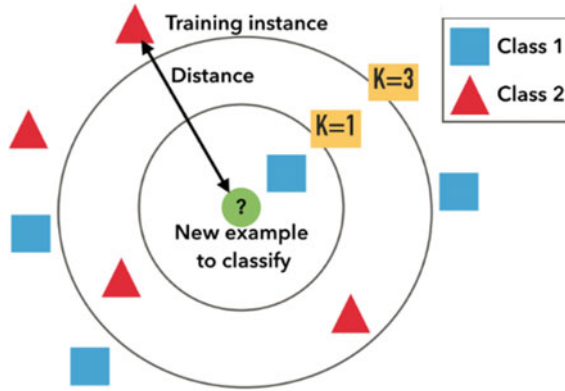


Fig. 1 Showing training data with different K values

Step 5: New data points will belong to the class that has the most neighbours (Fig. 1).

As shown in Figure, there are two classes blue square and red triangle, and we have to classify the green circle, lets first take $k = 1$ then green circle classify as blue circle while if we decide the $k = 3$ in that case one blue square and two red triangle. So, one conclusion we draw is that in the case of an odd number of neighbours there will never be a tie [1, 2].

4 Different Distance Metric Used in KNN

4.1 Minkowski Distance

Minkowski distance is used to calculate the distance between two points. Minkowski formula can be converted in Manhattan and Euclidean distance by changing the value of p , if $p = 1$, then this formula is considered as Manhattan distance, if $p = 2$, this formula is considered as Euclidean distance [6].

$$\text{Distance} = \left(\sum_{i=1}^n |x_i - y_i|^p \right)^{1/p} \tag{1}$$

4.2 Manhattan Distance

Manhattan distance can be calculated by putting $p = 1$ in Minkowski distance. Manhattan distance is basically usual when a grid-like structure is given and a distance

to be calculated between two points [6].

$$\text{Distance} = \sum_{i=1}^n |x_i - y_i| \quad (2)$$

4.3 Euclidean Distance

Euclidean distance formula can be obtained by putting $p = 2$ in Minkowski distance formula. Euclidean distance is a very popular distance metric to calculate displacement (displacement).

$$\text{Distance} = \sqrt{\sum_{i=1}^n (x_i - y_i)^2} \quad (3)$$

5 KNN Model Using Machine Learning Approach

To build a model using KNN algorithm using machine learning approach, anaconda navigator and Jupyter notebook are used. Different Python libraries are also used to build the model whose description is given below [7].

- **Pandas:** To read the data set, Python panda's library is used.
- **Matplotlib:** This Python library is used for creating different kinds of visualization like bar charts, line charts, etc.
- **Seaborn:** This Python library is used for creating different kinds of visualization with statistical approach.
- **Scikit-Learn:** This Python library is used for creating different models. This library has a very efficient model based on classification, regression and clustering.

Implementation of any model in machine learning required seven basic steps:

1. Collection of data set
2. Data preprocessing
3. Data visualization
4. Model creation
5. Prediction
6. Model validation.

5.1 Collection of Data Set

Here, iris data set is used for KNN classification download for UCI machine learning repository. Download URL is <https://archive.ics.uci.edu/ml/datasets/iris>. Total 150 observations are given in the data set with four features (sepal length, sepal width, petal length, petal width) and one target variable that is iris species. Classification of iris flowers is done on the basis of its sepal and petal. By measuring its sepal length, sepal width, petal length and petal width, iris flower is classified into its three species: 1. *Iris Setosa*, 2. *Iris Versicolour*, 3. *Iris Virginica* (Figs. 2 and 3).



Fig. 2 Iris flower

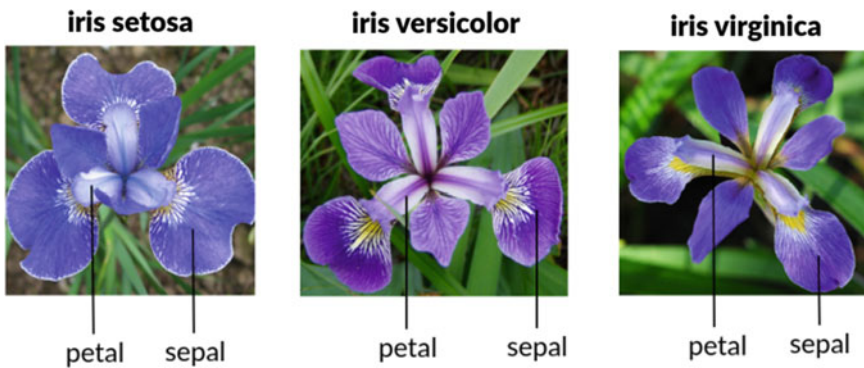


Fig. 3 Different species of iris flower

5.2 Data Preprocessing

Data preprocessing is the first step while adopting machine learning approaches. In data preprocessing, all relevant columns (features) can be considered. Each feature is further analysis for null value. If any null value is there, it should be removed [8]. Data set may not contain all columns in numeric form, there may be categorical variables, for example, male, female, but machine is not accepting these kinds of categorical variables. So, these categorical variables will be changed in numeric form [8–11].

Data normalization is another step in data preprocessing. Data is normalized around the mean value with standard deviation 1. This data normalization is also known as standard scalar.

5.3 Data Visualization

As shown in Fig. 4, we can see that each iris species is clearly separable based upon petal length, with just a bit of potential overlap in the *Iris-versicolor* and *Iris virginica*, while *Iris-setosa* is completely separable from the other two. It had been observed that statistically *Iris-setosa* is different from others too, while checking its parameters on mean median and mode value.

As shown in Fig. 5, we can see that each iris species is not clearly separable based upon sepal width, with huge overlap in the *Iris-versicolor*, *Iris virginica* and *Iris-setosa*. It had been observed that statistically iris species are very similar too, while checking its parameters on mean median and mode value.

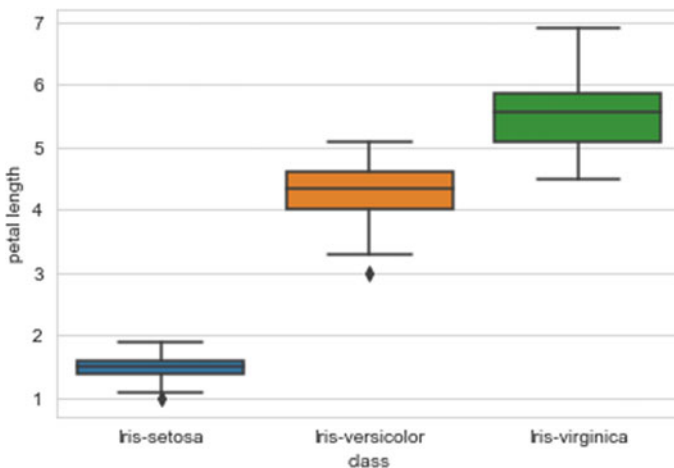


Fig. 4 Box plot between iris classes and petal length

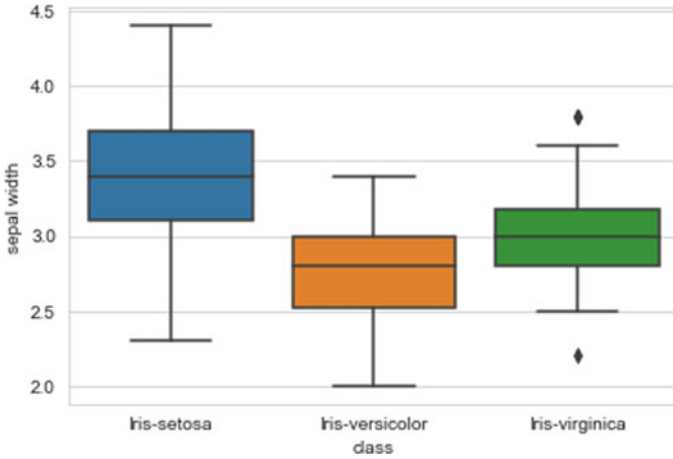


Fig. 5 Box plot between iris classes and sepal width

As shown in Fig. 6, we can see that each iris species is not clearly separable based upon sepal length, with just overlap in the *Iris-versicolor*, *Iris virginica* and *Iris-setosa*. It had been observed that statistically iris species are very similar too, while checking its parameters on mean median and mode value.

As shown in Fig. 7, we can see that each iris species is clearly separable based upon sepal length, with just overlap in the *Iris-versicolor*, *Iris virginica* and *Iris-setosa*, while *Iris-setosa* is completely separable from the other two.

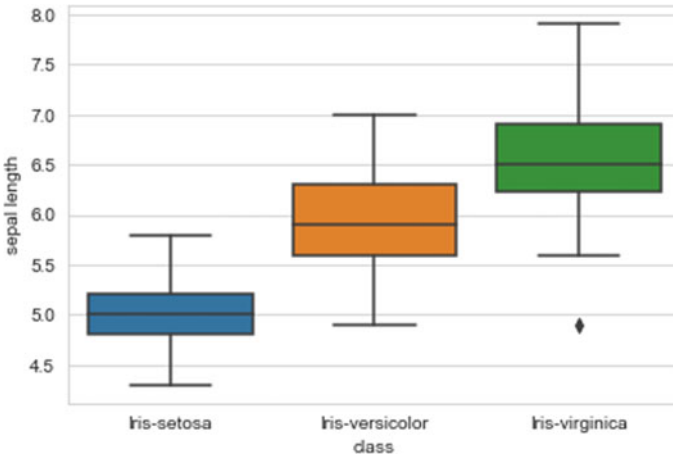


Fig. 6 Box plot between iris classes and sepal length

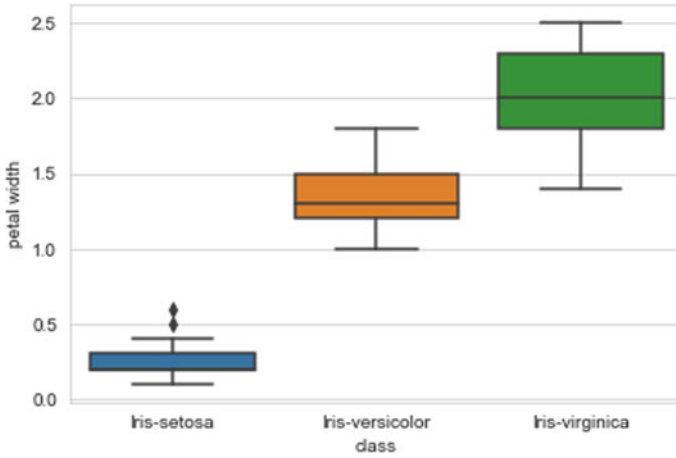


Fig. 7 Box plot between iris classes and petal width

Count plot in Fig. 8 is used to showing the total instance associated with each iris species *Iris-versicolor*, *Iris virginica* and *Iris-setosa*. In our data set, 50 data samples belong to each class.

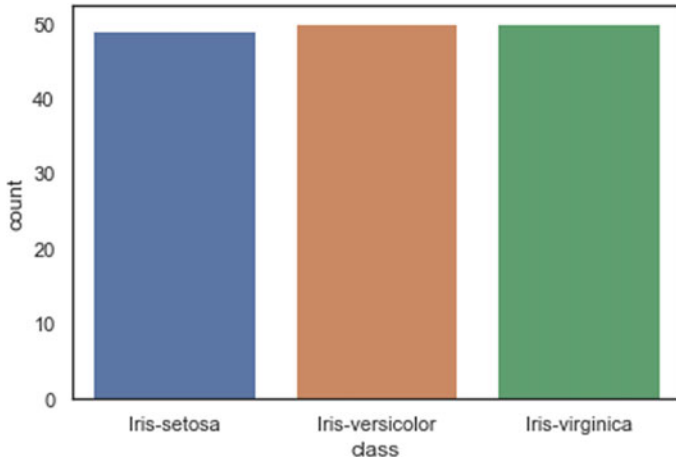


Fig. 8 Count plot between iris classes and total count of each species

Table 1 *K*-value and classification accuracy

<i>k</i> -value	Classification accuracy in %
1	95.0
2	95.0
3	95.0
4	98.3
5	96.6
6	98.3
7	98.3
8	98.3
9	98.3
10	98.3
11	98.3
12	98.3
13	95.0
14	96.0

5.4 Model Creation

For creating KNN model, Scikit-learn library is used. Data shuffling is an important step, so before fitting data to our algorithm, data is shuffled so that training on important features is distributed equally. With the help of training shuffled data, it is fit to the KNN model using fit() method. Once data gets fitted or the model gets trained, this will start prediction. The KNN model will predict the label for new data [12].

5.5 Prediction

Prediction is obtained from the KNN model by taking a different number of *k* values with distance metric as Euclidean. It is observed that initially classification accuracy is constant ($k = 1$ to 3) but after increasing the value of *k* it increases and maximizes ($k = 4$ to 12) after that classification accuracy is decreased [3–5] (Table 1; Fig. 9).

5.6 Model Validation

When performing model validation using training and testing accuracy, a fact is found out regarding number of neighbours that is accuracy is stable at $k = 10$ to 12

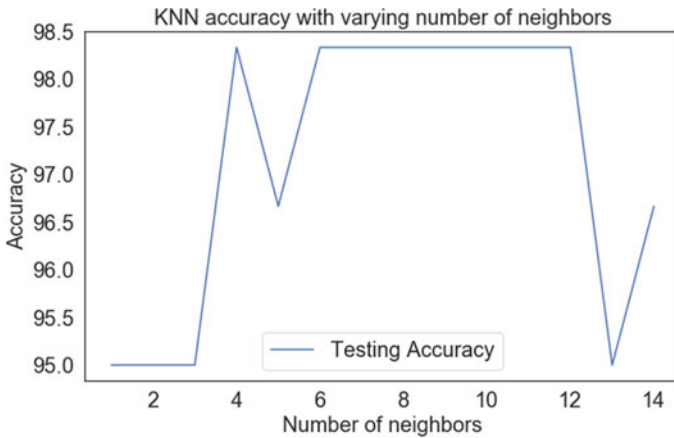


Fig. 9 Classification accuracy versus number of neighbour

in both cases training and testing. So for iris data set when performing K-nearest neighbour algorithm using machine learning approach, 10–12 number of neighbour give best/stable accuracy.

6 Conclusion

Iris data set is tested on K-nearest neighbour algorithm to find different number of neighbour value. Different number of K-nearest neighbour had been passed to model to check impact on classification accuracy. Besides this, ideally there must be an odd value of k in the range which gives maximized classification accuracy. In our result, set k value be 11 (get an odd number of neighbours). These values are odd and give maximized classification accuracy for our iris data set. These K value may be different from data set to data set, but in each data set case, iteration of K -value must be performed to find model accuracy.

References

1. Thirunavukkarasu K, Singh AS, Rai P, Gupta S (2018) Classification of IRIS dataset using classification based KNN algorithm in supervised learning. In: 4th international conference on computing communication and automation. <https://doi.org/10.1109/CCAA.2018.8777643>
2. Kulkarni SB, Kulkarni RB, Kulkarni UP, Hegadi RS (2014) GLCM-based multiclass iris recognition using FKNN and KNN. *Int J Image Graph* 14(3):1450010 (27 pages). <https://doi.org/10.1142/S0219467814500107>
3. Tan S (2005) Neighbor-weighted k-nearest neighbor for unbalanced text corpus. *Expert Syst Appl* 28:667–671

4. Hastie T, Tibshirani R (1996) Discriminant adaptive nearest neighbor classification. *IEEE Trans Pattern Anal Mach Intell* 18:607–616
5. Weinberger KQ, Saul LK (2009) Distance metric learning for large margin nearest neighbor classification. *J Mach Learn Res* 10:207–244
6. <https://towardsdatascience.com/machine-learning-basics-with-the-k-nearest-neighbors-algorithm-6a6e71d01761>
7. <https://www.javatpoint.com/k-nearest-neighbor-algorithm-for-machine-learning>
8. <https://www.analyticsvidhya.com/blog/2018/03/introduction-k-neighbours-algorithm-clustering/>
9. Sharma KP, Poonia RC, Sunda S (2019) Map matching algorithm: curve simplification for Frechet distance computing and precise navigation on road network using RTKLIB. *Cluster Comput* 22(6):13351–13359
10. KP Sharma, RC Poonia (2018) Review study of navigation systems for Indian regional navigation satellite system. (IRNSS) *Soft Comput Theor Appl* 735–742
11. Sharma KP, Poonia RC, Sunda S (2017) Map matching approach for current location tracking on the road network map matching approach for current location tracking on the road network. In: *International conference on infocom technologies and unmanned systems*, pp 573–578.
12. <https://medium.com/capital-one-tech/k-nearest-neighbors-knn-algorithm-for-machine-learning-e883219c8f>

Low-Energy-Based Multi-hop Cluster Head Selection for IoT Applications Using Super Nodes



Hardika Raman and B. Mohapatra

Abstract Energy utilization is brought about by three exercises: detecting, information handling, and interchanges. Correspondence energy establishes the significant piece of the devoured energy in the wireless gadget, though energy enhancement centers around the radio module working modes. The correspondence energy is characterized as the whole of the information transmission energy (i.e., handset energy) and the information preparing energy. Internet of things (IoT) ought to work with ideal energy to build the lifetime of the sensor hubs, at the same time guaranteeing network availability and accessibility. Due to the shortage of energy in IoT, energy streamlining is expected to limit the energy devoured by the sensor hubs to drag out network lifetime. In this way, energy proficiency must be considered in each part of network structure and activity, for the two tasks of the individual sensor hubs and correspondence of the general network. In this work, a novel method has been proposed to improve the network lifetime of the currently existing IoT nodes based on LEACH protocol for wireless sensor network (WSN) by incorporating the concept of super nodes and advanced nodes in a multi-hop framework. In the proposed algorithm, the first dead node round number is significantly increased by approximately 52% which improves the network lifetime of the IoT-based wireless sensor network.

Keywords LEACH · IoT · WSN · Multi-hop · MATLAB

1 Introduction

Internet of things (IoT) have been generally viewed as one of the most significant advancements of the twenty-first century. These sensors can impart either among one another or straightforwardly to the sink. In any case, gadgets have constrained energy

H. Raman · B. Mohapatra (✉)

School of Electrical, Electronics and Communication Engineering, Galgotias University, Greater Noida 201310, India

e-mail: writetobm@gmail.com

H. Raman

e-mail: hardikajuhi@gmail.com

© Springer Nature Singapore Pte Ltd. 2021

R. Agrawal et al. (eds.), *Advances in Smart Communication and Imaging Systems*,

Lecture Notes in Electrical Engineering 721,

https://doi.org/10.1007/978-981-15-9938-5_36

assets that speak to the greatest test for IoT. The energy productivity, hearty self-association, clustering, and steering conventions are significant parts of moderating energy and drawing out network lifetime, while guaranteeing appropriate activities of the network. Besides, IoT present a few shortcomings in view of their constrained buffering highlights and computational assets. The fundamental issue in WSNs is controlling energy utilization over the entire network.

Wireless sensor nodes have a wide scope of utilizations in different fields. One of the latest developing applications is in the realm of IoT domains, which allows between association of various articles or gadgets through the Internet. Be that as it may, restricted battery power is the significant worry of WSNs when contrasted with portable specially appointed network, which influences the life span of the network. Henceforth, a ton of research has been centered around to limit the energy utilization of the WSNs. Planning of a progressive clustering calculation is one of the various ways to deal with limit the energy of the WSNs. In this current investigation, the current low-energy adaptive clustering hierarchy (LEACH) clustering convention is altered by presenting an edge limit for group head choice at the same time exchanging the force level between the hubs.

2 Literature Review

In a WSN, the scientist mostly centers around two significant perspectives which incorporate decrease of energy utilization and dragging out the network lifetime. Considering LEACH convention [1] as an essential calculation, numerous adjustments have been done based on different applications. An overview of LEACH protocol and its derived protocols are appeared in [2]. Traditionally, four significant parameters are considered to evaluate the performance, for example, clustering strategy, information accumulation, versatility type, and adaptability. In LEACH protocol convention, haphazardly chooses cluster head (CH), and no information about the leftover energy of the network is recorded at the base stations (BS). So as to address this issue, LEACH-C [3, 4] convention was proposed. Filter C is an incorporated LEACH convention where all the choice forces are given to the BS. Every hub is outfitted with a GPS to send its position and leftover energy data to the BS for each round. The fundamental restriction of this convention is the utilization of GPS which depletes the colossal measure of energy just as is not practical. In LEACH deterministic cluster head selection [5] and improved-LEACH [6], the creators proposed another limit by altering the crude edge equation. An inclusion safeguarding CH determination calculation (CPCHSA) for the LEACH convention is proposed in [7], to expand the network detecting inclusion. One of the confinements of these conventions is that the quantity of CHs picked is not sure in each round. In LEACH-H [8, 9], the CHs are chosen through an iterative procedure and are consistent in each round and means to improve the network lifetime. The convention cannot be executed in huge scale networks and furthermore experiences huge overhead. In [10], the creators have broadened the CH choice calculation by adjusting

the likelihood of sensor hub to become CH dependent on the rest of the energy of the network. In Fig. 1, basic WSN framework and Internet model is shown with reference to Internet of things is shown. The figure shows the traditional data flow from sensor node to the end user through Internet. Figure 2 shows the LEACH protocol working phases. Here, in round 1, cluster head selection is done, and then, the cluster

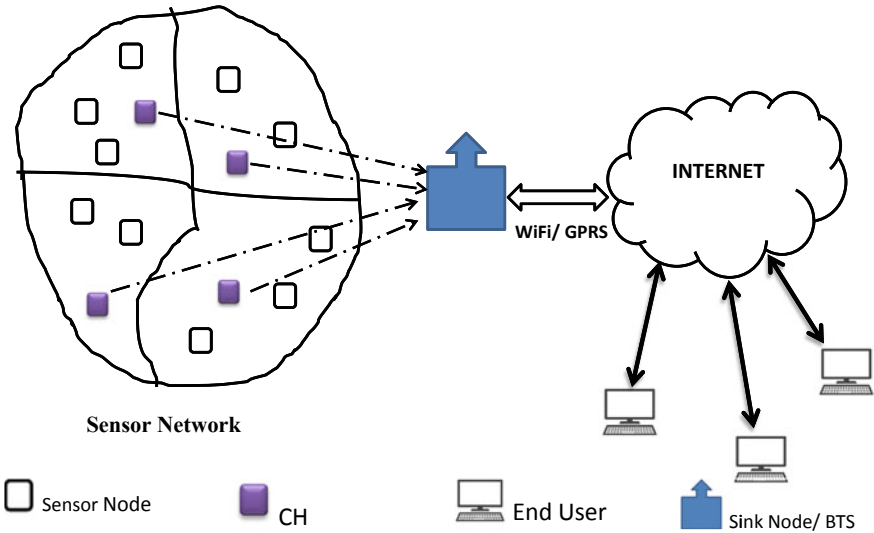


Fig. 1 Basic WSN framework and internet model [1]

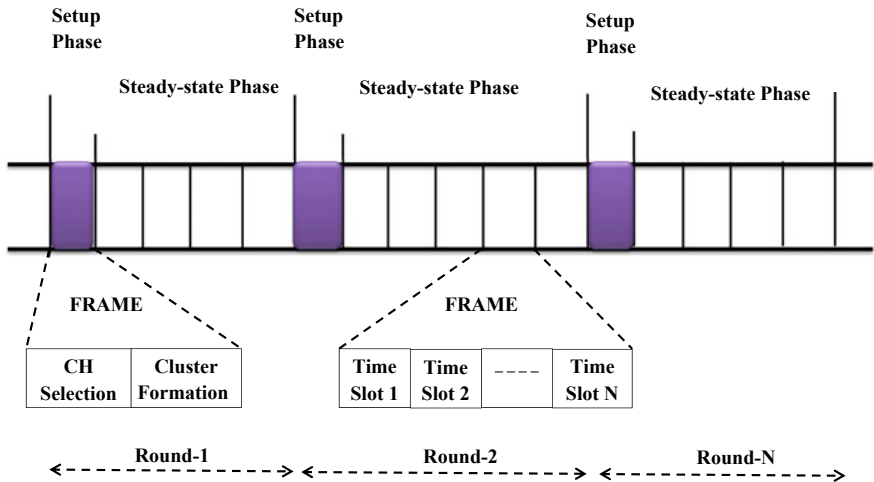


Fig. 2 LEACH protocol working phase in WSN [1]

formed. Other routing and cluster formation algorithms can be found in [11] and [12] for wireless sensor networks.

3 Implementation

Brief proposed algorithm modifications in existing IoT LEACH are described below: In initial step, random node position is derived in x - and y -axis direction. In second step, percentage of normal, super, and advanced nodes is assigned. Third step comprises setting up the transmitter and receiver parameters, assigning different initial energy levels to normal nodes, super nodes, and advanced nodes for IoT devices. In fourth step, election of cluster heads from intermediate nodes or super nodes of IoT devices and broadcast messages to find its neighbor nodes. Cluster formation is done by selecting a random value of threshold energy. In fifth step, communication link is established from normal nodes to cluster head.

Distance between cluster head and base station and also from advanced node to base station is calculated. Then, routing path is calculated based on shortest path or minimum hop distance to send data to the base station. Multi-hop communication is established accordingly, and the energy consumed in communication process is subtracted from the initial energy. The above process is repeated until the complete rounds. Figure 3 shows the flowchart of the proposed algorithm and its process.

4 Results

In this section, the results of MATLAB-based implementation in modified LEACH protocol IoT-based framework for wireless sensor network are shown. Advance nodes (AN) and super nodes concept are added in the traditional LEACH protocol. This is being done by calculating the threshold energy and subsequently elects from the advanced nodes and super nodes as cluster heads. The results are shown below: In Figs. 4, 5, 6, 7, 8, 9, 10, 11 and 12, the results for the same for various instances are shown.

Figure 4 shows the average energy consumption and transmissions. Figure 5 shows the energy consumption per transmissions of single bit.

In Fig. 6, the operational IoT nodes show that the transmissions are upto 13,000 bits which is much higher than that of the existing results.

In Fig. 6, operating nodes in round number are shown up to 30,000 rounds which is much better than the existing work.

Following results show the random nodes deployment scenario of proposed algorithm.

Now in proposed system, multi-hop (MH) communication is implemented in order to improve the network efficiency and lifetime. The results for the same are shown below. Figures 9, 10 and 11 show the results of proposed algorithm.

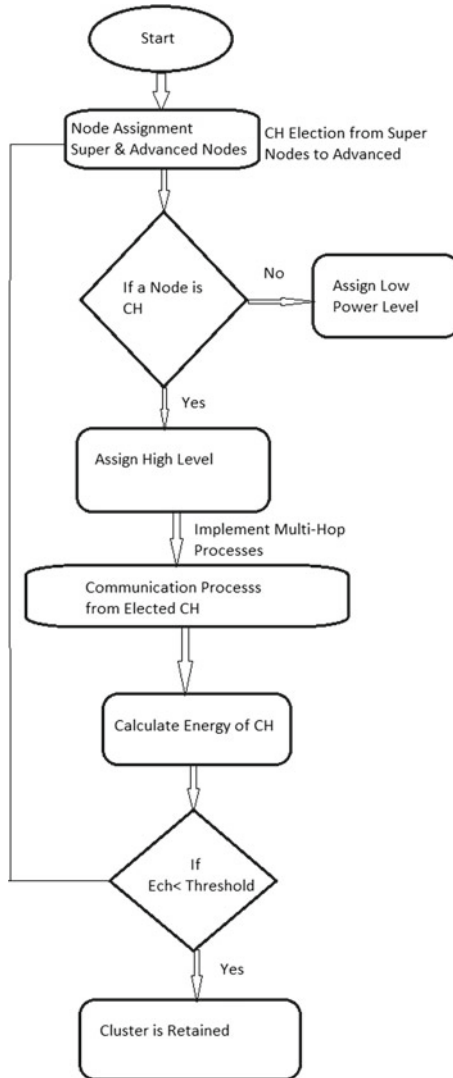


Fig. 3 Flowchart of the proposed algorithm

Figure 9 shows the average energy consumption versus transmission graph, and Fig. 10 shows energy consumed in the transmissions.

In Fig. 11, operation of IoT nodes shows that about 6500 transmissions take place.

In Fig. 12, the operational nodes are active till about 12,000 round number. In Fig. 13, random node arrangement is shown for proposed algorithm.

In Table 1, the result comparison for outputs is shown. The better techniques are the proposed IoT LEACH with AN and MH.

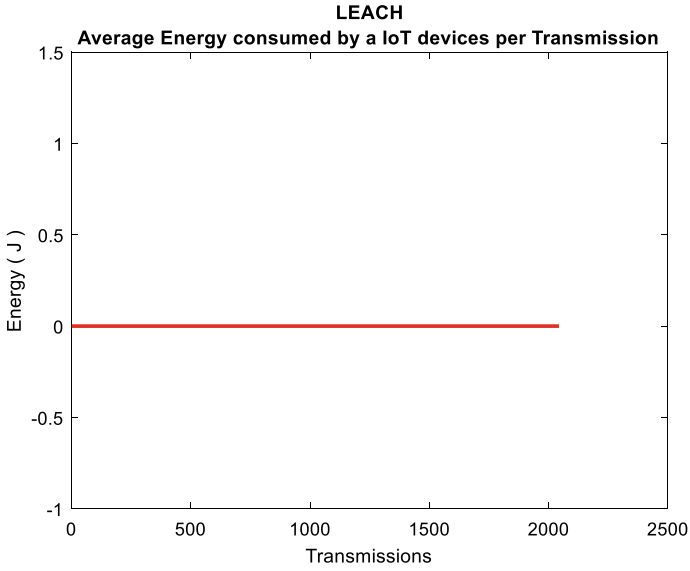


Fig. 4 Average energy consumption versus transmission for proposed system with advanced nodes

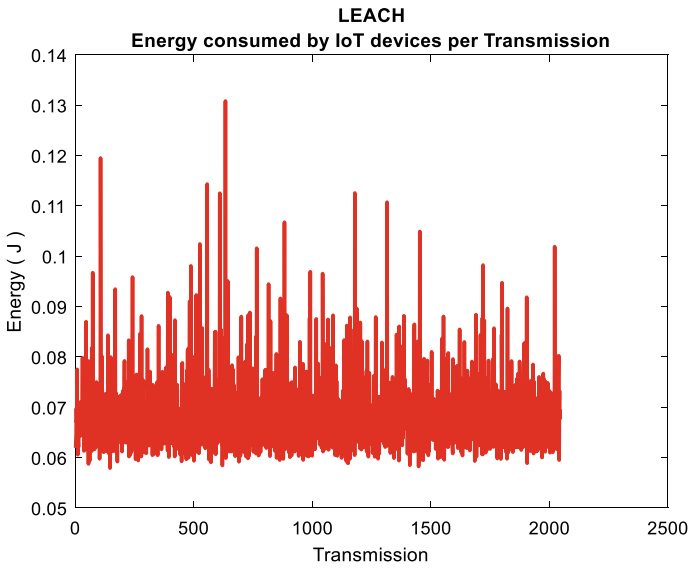


Fig. 5 Energy consumption versus transmission for proposed system with advanced nodes

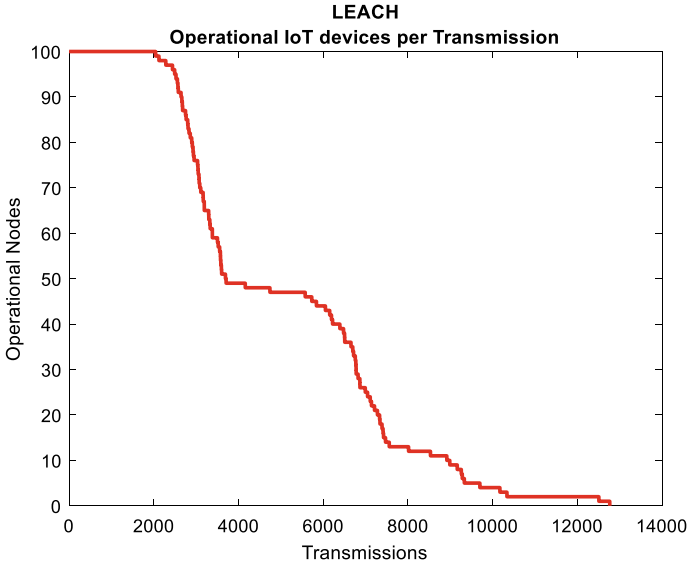


Fig. 6 Operational IoT nodes versus transmission for proposed system with advanced nodes

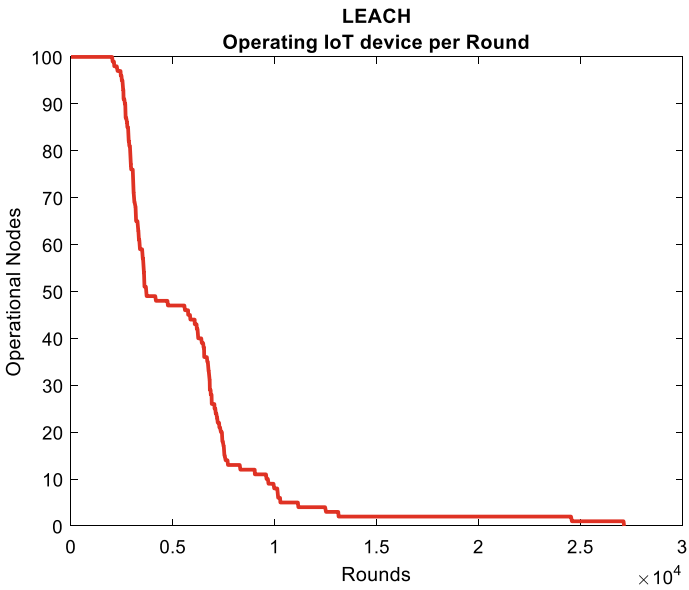


Fig. 7 Operational IoT nodes versus rounds for proposed system with advanced nodes

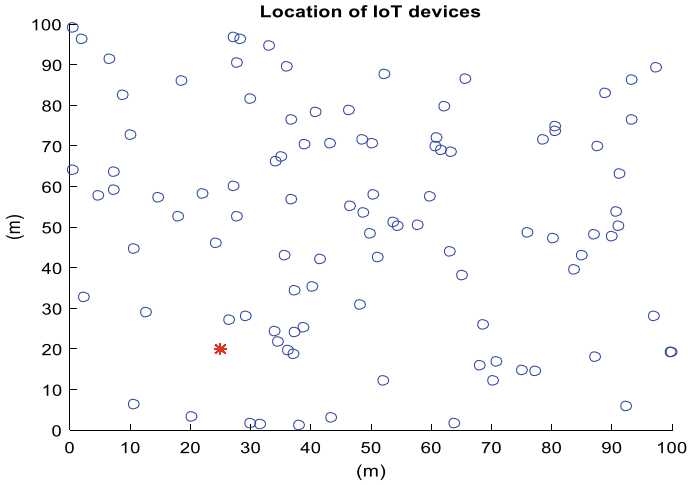


Fig. 8 IoT device final random nodes scenario for proposed system with advanced nodes

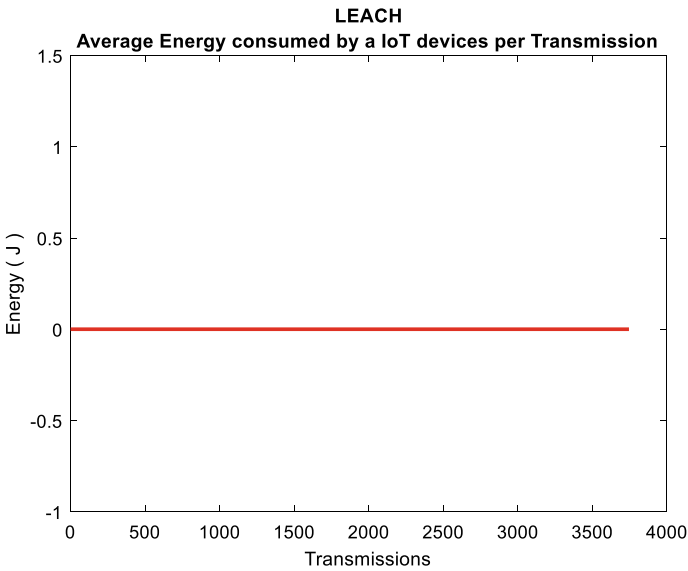


Fig. 9 Average energy consumption versus transmission for proposed system with advanced nodes and multi-hop communication

The results are compared in the Figs. 14 and 15. The lowest average energy consumption is in proposed IoT LEACH with AN MH.

The highest round number in first dead node is for proposed IoT LEACH with AN and MH.

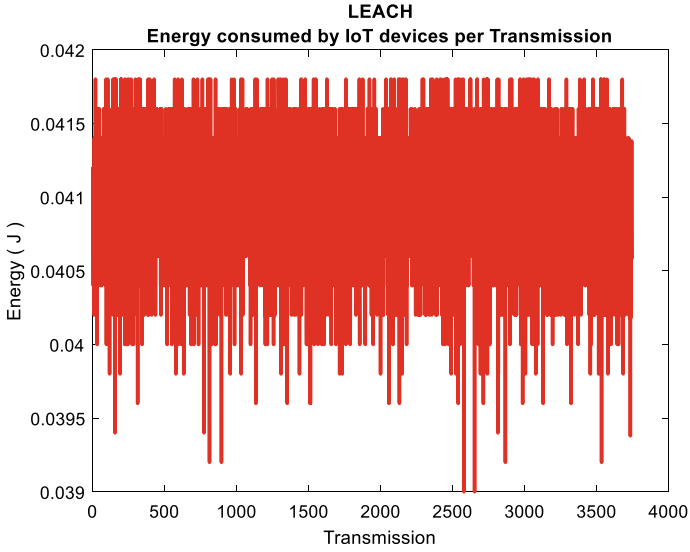


Fig. 10 Energy consumption versus transmission for proposed system with advanced nodes and multi-hop communication

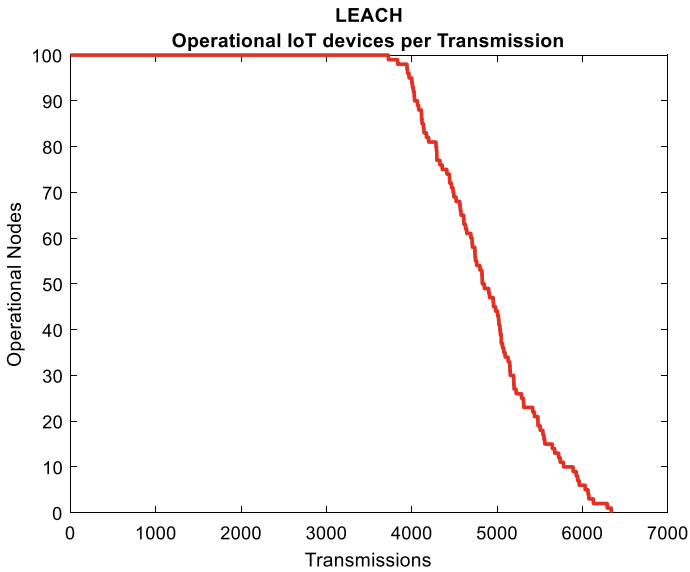


Fig. 11 Operational IoT nodes versus transmission for proposed system with advanced nodes and multi-hop communication

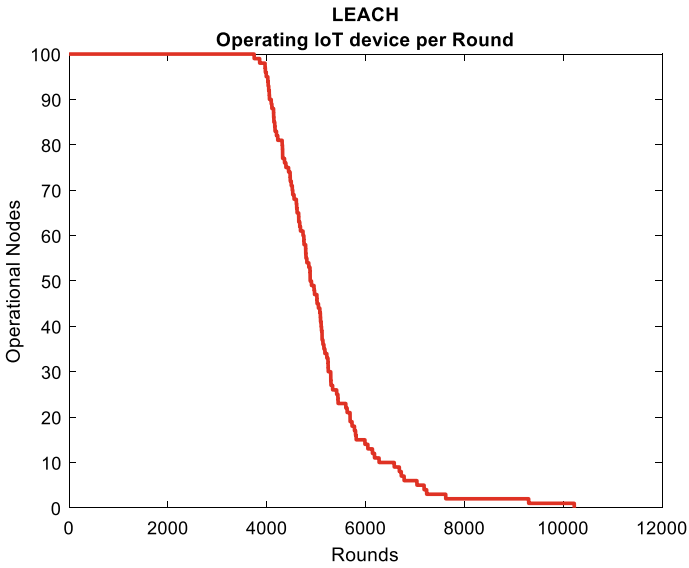


Fig. 12 Operational versus transmission for proposed system with advanced nodes and multi-hop communication

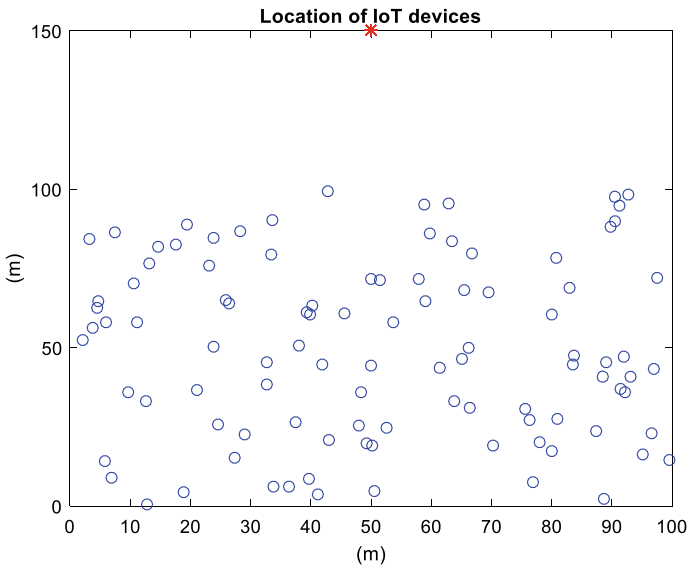


Fig. 13 IoT device final random nodes scenario proposed system with advanced nodes and multi-hop communication

Table 1 Result comparison for existing and proposed work

Network parameters	IoT LEACH	Proposed IoT LEACH with AN	Proposed IoT LEACH with AN MH
Average energy consumption	2.29E-04	3.55E-04	2.20E-04
First dead node round number	1857	2225	3902

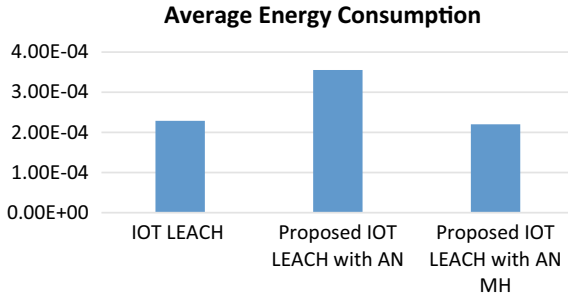


Fig. 14 Average energy consumption comparison for proposed IoT LEACH

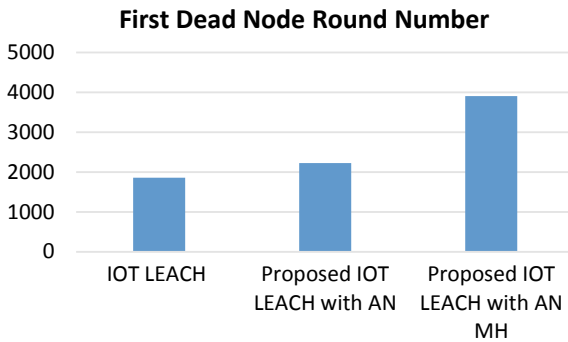


Fig. 15 First dead node comparison for proposed IoT LEACH

5 Conclusions

Improvement in the network lifetime of the currently existing Internet of things-based LEACH protocol for wireless sensor network by adding concept of super nodes and advanced nodes in multi-hop algorithm for LEACH protocol. In the proposed algorithm, the first dead node round number is significantly increased by approximately 52% which improves the network lifetime of the IoT-based wireless sensor network. The average energy consumption is minimum in the proposed system. The proposed

system network lifetime is increased to about 12,000–16,000 round numbers. In this paper, the proposed work is implemented using MATLAB and successfully simulated. In future, soft computing skills like optimization techniques can be applied like genetic algorithm, particle swarm optimization, ant colony optimization, or ANFIS in IoT based applications.

References

1. Behera TM, Samal UC, Mohapatra SK (2018) Energy-efficient modified LEACH protocol for IoT application. *IET Wirel Sens Syst* 8(5):223–228
2. Behera TM, Mohapatra SK, Samal UC, Khan MS, Daneshmand M, Gandomi AH (2019) Residual energy based cluster-head selection in WSNs for IoT application. *IEEE Internet Things J* 6(3):5132–5139
3. Wang Z, Wu R, Sa Q, Li J, Fan Y, Xu W, Zhao Y (2016) An improved cluster routing structure of IOT. In: International conference on communications, information management and network security (CIMNS 2016)
4. Rana AK, Sharma S (2019) Enhanced energy-efficient heterogeneous routing protocols in WSNs for IoT application. *Int J Eng Adv Technol (IJEAT)* 9(1). ISSN: 2249-8958
5. Ashwini M, Rakesh N (2017) Enhancement and performance analysis of LEACH algorithm in IOT. In: International conference on inventive systems and control (ICISC-2017)
6. Rani N, Kumar P (2019) Energy efficient hierarchical routing protocols for IoT. *Int J Eng Adv Technol (IJEAT)* 8(6). ISSN: 2249-8958
7. Mudasser AW, Rasool SM, Gafoor SAAA (2019) An energy efficient routing protocol for WSN assisting IoT. *Int J Innovative Technol Exploring Eng (IJITEE)* 8(7S2). ISSN: 2278-3075
8. Liu Y, Wu Q, Zhao T, Tie Y, Bai F, Jin M (2019) An improved energy-efficient routing protocol for wireless sensor networks. *Sensors* 19:4579. <https://doi.org/10.3390/s19204579>. www.mdpi.com/journal/sensors
9. Thilagavathi N, Swetha V, Aishwariya A (2019) A novel QB leach based heterogeneous wireless sensor network using IOT. *IOSR J Eng (IOSRJEN)* 9(5):12–18. www.iosrjen.org. ISSN (e): 2250-3021, ISSN (p): 2278-8719. S (III)
10. Murdan AP, Pranishtha (2018) Optimisation of the wireless sensor network with the multi-hop LEACH protocol for the smart grid. *J Electr Eng Electron Control Comput Sci JEECCS* 4(14):1–6
11. Mishra A, Choudhary S, Vats M, Sachan S (2020) LEACH with pheromone energy efficient routing in wireless sensor network. *Intell Comput Eng* 91–98. ISSN 978-981-15-2779-1. https://doi.org/10.1007/978-981-15-2780-7_12
12. Sachan S, Vats M, Mishra A, Choudhary S (2020) Comparative analysis of clustering algorithm for wireless sensor networks. In: Solanki V, Hoang M, Lu Z, Pattnaik P (eds) *Intelligent computing in engineering. Advances in intelligent systems and computing*, vol 1125. Springer, Singapore

Dynamic Wireless Charging for Electrical Vehicles



Harsh Agarwal, Vikrant Vashistha, Shohrab Alam, Pallavi Choudekar, and Ruchira

Abstract The limited supply of fuels has driven us towards the development of electrical vehicles across the globe. As of now the plugging in type of charging system is being used to charge the batteries of EVs. For such system, user has to carry cables and needs to keep waiting to get the batteries charged. Also, the operation is not effective in snow and during rains. So, in this paper, we have implemented the method of inductive power transfer to charge the batteries of EV even when they are moving which can completely reduce the range anxiety problems with the help of road/track electrification for dynamic charging of electrical vehicles.

Keywords Inductive and resonant power transfer · Road electrification · Electrical vehicles · Wireless charging

1 Introduction

Wireless power transmission is not a new technological trend, and it was already introduced in 1914 by N. Tesla and the research are still being done on the wireless power transmission system in order to improve its efficiency, power level, maximum charging distance and charging tolerance [1]. As we all know, world of engineering

H. Agarwal (✉) · V. Vashistha · S. Alam · P. Choudekar · Ruchira
Department of Electrical and Electronics Engineering, Amity University, Noida, Uttar Pradesh, India

e-mail: harsh.agarwal10000@gmail.com

V. Vashistha

e-mail: vikrantvashistha297@gmail.com

S. Alam

e-mail: shohrabalam01@gmail.com

P. Choudekar

e-mail: pallaveech@gmail.com

Ruchira

e-mail: er.ruchiragarg@gmail.com

© Springer Nature Singapore Pte Ltd. 2021

R. Agrawal et al. (eds.), *Advances in Smart Communication and Imaging Systems*,

Lecture Notes in Electrical Engineering 721,

https://doi.org/10.1007/978-981-15-9938-5_37

is going through huge transformation in automobile sector. We have all experienced the internal combustion engines (ICE) vehicles. Now it is time to switch to the electrical vehicles where they can be charged wirelessly, and even at the time, they are moving on the road, which is only possible through electrification of road by using the inductive or resonant power transfer for dynamic charging.

1.1 Literature Review

At present, charging used for EVs is plug-in connection type where the user or driver has to connect a plug into a receptacle on the electrical vehicle in order to charge the battery of their vehicle. Although, there are some pros and cons. Firstly, the cable and the connector are able to deliver 2–3 times more power than the normal plug-in systems used at home, but this increases hazard of electrocution particularly in showery and hostile situations [2]. Second, the length wire system possesses a tripping hazard and gives rise to poor aesthetics for these systems. Thirdly, in harsh weathers that frequently have snowing and icing, the plug-in charge point may develop freezing layers onto the vehicle charger. Hence, we need some alternative method like dynamic wireless charging and hence eliminating the disadvantages inherent to plug-in vehicles.

1.2 System Classification

Based on the application, wireless charging systems for EV can be classified into the two major categories,

- Static(rest) wireless charging
- Dynamic wireless charging.

1.2.1 Static Wireless Charging System

As the name specifies, the vehicle is charged when it is in rest. So here, we just park or place our electrical vehicle on charging station or our personal garage which is already modified for wireless transfer. For that, we fix the transmitter in the ground, while the receiver is present on the lowest point of the electrical vehicle. For proper charging, proper orientation of the transmitter and the receiver coil is necessary. The time taken to charge the electrical vehicle depends upon the AC power supplied, the coil size in transmitter and the receiver coil as well as the air gap distance between them [3, 4].

This type of system is suitable when the electrical vehicle is parked at some place for some time.

1.2.2 Dynamic Wireless Charging System

As the name suggests, here electrical vehicle is charged when it is in motion. The transfer of power occurs through air as medium. Here, our transmitter pad is stationary (laid out on roads), while the receiving pad which is fitted in electrical vehicle is moving (fitted in the vehicle). By using dynamic charging method for electrical vehicle, the range problem can be significantly improved, and the battery size required for the electrical vehicle can also be reduced. So, large amount of energy storage is no more needed with this method [3, 4].

1.3 Advantages and Disadvantages

Dynamic charging of electrical vehicles offers several advantages. Just consider about a situation in future where the self-driving cars are out there and they are taking us to the destinations without a need to stop to charge their batteries. Additionally, the power generated from nearby solar or wind sources is directly used to charge the vehicles. So, it offers innumerable advantages and vanishes the problem of range anxiety for the driver.

But this system faces certain challenges also like issue with electromagnetic compatibility, limited range of power transferring capacity, efficiency reduction and bulky and expensive equipment.

2 Dynamic Charging

2.1 Techniques Used in Wireless Transfer

2.1.1 Inductive Wireless Charging System

The basic principle used in inductive transfer is Faraday's law of induction. In this technique, power is transferred wirelessly by mutual induction due to the magnetic field which is developed between transmitting and receiving coil pads [5]. When the transmitter coil is applied with AC mains, an AC magnetic field is generated which passes through the receiving coil pads, this AC field is responsible for the movement of electrons and development of AC power across the receiving pads across the connected load (battery). Before feeding this generated output to the load (battery) it has to be rectified as well as filtered as per the load requirements of the charging system. In this system, the amount of power transferred depends on the choice of frequency, the coil parameters (self and mutual inductance) and the air gap present between the two coil pads. Operating frequency is 19–50 kHz.

2.1.2 Resonant Inductive Wireless Charging System

Resonators are used to obtain a higher quality factor. So, with the better Q-factor even if the generated magnetic fields are not that strong, the same amount of power can be transferred as that in inductive power transfer. So, this technique is preferred over normal inductive charging system [6]. Here, the air gap maintained for wireless transfer provides flexibility, and power can be transferred for wider air gaps. So, for this technique, the transmitter as well as the receiver coils must be tuned at resonant frequency for the transfer of maximum power through the medium.

To get the desired resonating frequencies, we need to use additional compensation networks in series and parallel the coil pads. Operating frequency is 10–150 kHz. There are other techniques used in wireless power transfer like capacitive coupling, microwave transfer, light wave transfer and magneto dynamic coupling transfer. But due to range, directivity, frequency and application in electrical vehicles, resonant and inductive coupling is used.

2.2 The Proposed System

We can understand the proposed system with the help of this diagram.

Figure 1 illustrates a method where an electrical vehicle is charged with transmitter

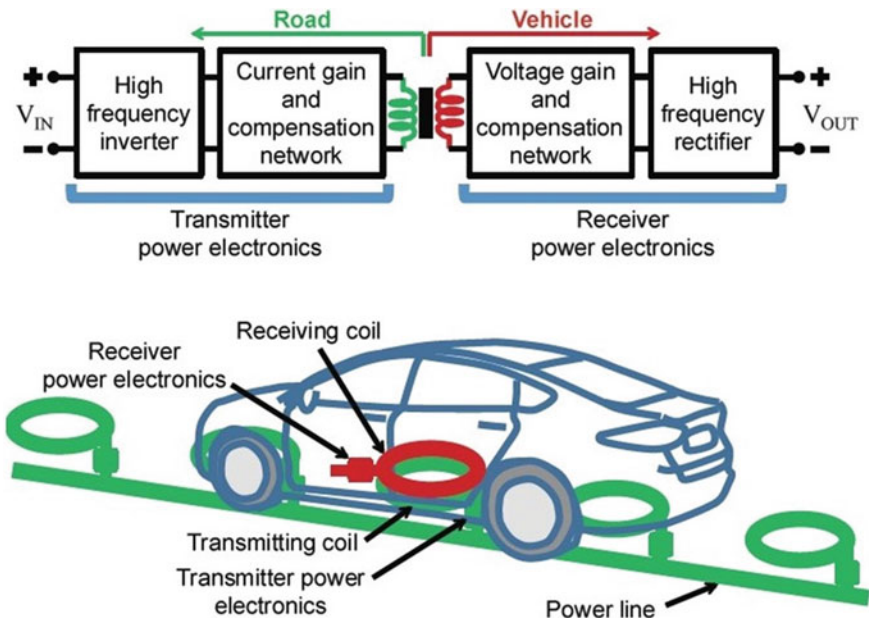


Fig. 1 Representation for the dynamic wireless charging system of an electrical vehicle

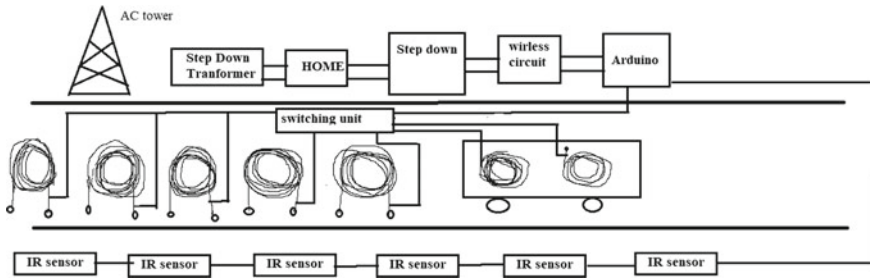


Fig. 2 Control scheme with addition of sensors and relays for switching and sensing vehicle position

and receiver coil pads installed. Firstly, the input supply will develop high frequency current in the transmitter (primary) coil-pad that transfers power through air to the receiver coil-pad [7]. When power at high frequency is received at the receiver end, the power is then converted to the DC as per the requirements of the battery needed to be charged.

Till now, we only discussed how the power is wirelessly transferred to the receiver pad in static case. The updated scheme is shown in Fig. 2

Above system depicts upgraded system, we have used additional relays and sensor devices with the proposed network. Sensors are added to the system to sense the location of the electrical vehicle over the transmitter coil, and relays control the switching of the circuitry. So, the power is transmitted only when electrical vehicle is aligned with the transmitter coil for very less time and is switched off when receiving coil changes its position.

2.3 Performance Parameters

- **Power Level**—It determines that how much power can be transmitted. So, it indirectly defines the time taken to charge the battery [8].
- **Maximum Charging Distance**—Tells us about the air gap between transmitter and receiver coil [8].
- **Efficiency**—It is the overall efficiency from AC mains to the battery terminal [8].
- **Charging Tolerance**—It is defined as the error in alignment between transmitting and the receiving coils [8].

2.4 Coil Sizing and Formula Used

The optimal coil size as per the load requirement and air gap maintained is designed using the finite element analysis Maxwell software. The coil parameters (L , C , R and Q -factor) can be calculated using Eqs. (1) to (4) [9–11].

$$L(H) = \frac{N^2(D_o - N(w + p))^2}{16D_o + 28N(w + p)} \times \frac{39.37}{10^6} \quad (1)$$

$$C(F) = \frac{1}{(2\pi f)^2 L} \quad (2)$$

$$R = \sqrt{\frac{f\pi\mu_o}{\sigma}} \times \frac{N(D_o - N(w + p))}{w} \quad (3)$$

$$Q = \frac{1}{R} \sqrt{\frac{L}{C}} \quad (4)$$

where

- D_o outer diameter,
- N number of turns N ,
- p spacing between each turn p ,
- w wire diameter w of the coil,
- f frequency used (tuned frequency).

2.5 Circuit Implementation

Above work is implemented to design a prototype of dynamic wireless charging system for electrical vehicle.

In the prototype, total eight transmitting coils (fixed in the road) and one receiver coil (fitted in vehicle) were designed. With the help of IR sensors and relays, coils were switched ON when the receiving coil of the electrical vehicle was aligned with the transmitter coil. A coil size of 60 mm (outer diameter) with 20 turns each in transmitting coil and 30 turns in receiver coil. A 24 kHz tuned frequency was used for charging the battery of electrical system. The detailed circuitry used in the prototype is depicted in Figs. 3 and 4. Further works are being done to study the effect of the air gap between the two coil pads and how to increase the power level that be transferred within lowest possible frequency range.

Parameters are given in Table 1.

Figure 4 depicts the overall scheme of the project. IR sensors are used to sense and detect the position of the electrical vehicle on the road. The relays are connected through a programming platform which works with sensor output and allows the relay for switching. It handles whether the relay should allow the power transmission or not. So, the power is flown only in case when primary coils are aligned with the secondary coils fixed in the electrified road. Further, the relays are connected to the coils, and the wireless transmission is done which we have already discussed earlier.

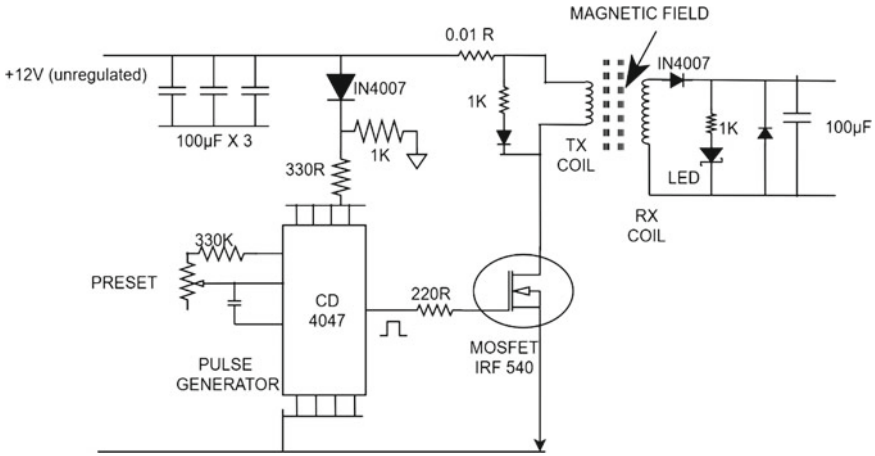


Fig. 3 Circuit diagram implemented for wireless transmission for the vehicle

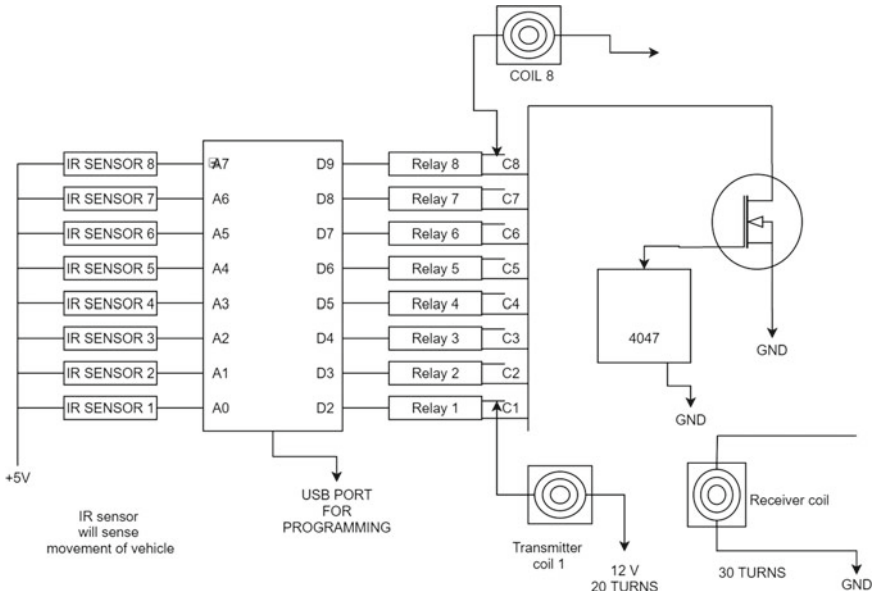


Fig. 4 Switching control through sensors and relays and detection of vehicle position

3 Conclusion

The work includes implementation of simple formulae for the calculation of different parameters and is just an upgrade of static charging system which is a wider concept these days in field of wireless transfer. Here, we developed a prototype as per the

Table 1 Working parameters

Parameters	Value
Source voltage	12 V
Working frequency	24 kHz
Turns (primary)	20
Turns (secondary)	30
Transmission distance	10 cm
Inductance (primary coil)	74.4 μ H
Capacitance (primary coil)	0.59 μ F

design developed, and after this project, further studies are needed to be done in order to increase the air gap between the primary and the secondary coil without reduction in efficiency and how the higher power ranges can be transferred using the minimum possible frequency range.

References

1. Tesla N (1914) Apparatus for transmitting electrical energy. US patent number, 119,732
2. Society of Automotive Engineers (SAE) (2017) Wireless power transfer for light-duty plug-in/electric vehicles and alignment methodology. <https://standards.sae.org/j2954201711/>
3. Choi SY, Gu BW, Jeong SY, Rim CT (2015) Advances in wireless power transfer systems for roadway powered electric vehicles. *IEEE J Emerg Sel Top Power Electron* 3(1):18–36
4. Lukic S, Pantic Z (2013) Cutting the cord: static and dynamic inductive wireless charging of electric vehicles. *IEEE Electr Mag* 1:57–64
5. Covic GA, Boys JT (2013) Modern trends in inductive power transfer for transportation applications. *IEEE J Emerg Sel Top Power Electron* 1:28–41
6. Zhu Q, Wang L, Liao C (2014) Compensate capacitor optimization for kilowatt-level magnetically resonant wireless charging system. *IEEE Trans Ind Electron* 61(12):6758–6768
7. Green AW, Boys JT (1994) 10 kHz inductively coupled power transfer: concept and control. In: Proceedings of the IEE international conference on power electronics and variable-speed drives, Oct 26–28, London
8. Wu HH, Gilchrist A, Sealy K, Israelsen P, Muhs J (2011) A review on inductive charging for electric vehicles. In: 2011 IEEE international electric machines & drives conference (IEMDC), p 2
9. Ferreira J (1990) Appropriate modelling of conductive losses in the design of magnetic components. In: 21st annual IEEE power electronics specialists conference, PESC '90 record, pp 780–785
10. Grover F (2004) Inductance calculations, Dover Phoenix editions. Dover Publications Incorporated, USA
11. Senjuti S (2013) Design and optimization of efficient wireless power transfer links for implantable biotelemetry systems. Master's thesis, University of Western Ontario

Economic Benefits of Implementing Demand Response in Congested Network of Deregulated Power Market



Anjali Agrawal, Ragini Malviya, Seema N. Pandey, and Laxmi Srivastava

Abstract Congestion management has become a vital issue within power systems and can hurdle to trade of electricity if not properly implemented. In market-driven environment, suppliers are more concerned for maximizing their profit and minimizing the financial risk. Strategies involved by market players may lead to cancel the scheduled transactions or create financial disputes among the participants. In this competitive environment, only technical aspects are incapable of managing congestion. By reducing or shifting the demand from peak hours to off peak hours, end user consumer can take part in market operations for reducing the congestion more effectively and efficiently. This paper proposes demand response program (DRP) for congestion management. DRP is the financial tool for congestion management, and the effectiveness of this method is tested on IEEE-14 bus system.

Keywords Deregulated power market · Congestion management · Demand response (DR)

1 Introduction

Restructuring in the electric power market has created competition among the market participants. The problem of congestion is more frequent and crucial in competitive environment of deregulated power market. The transmission congestion cannot be permitted due to various reasons like thermal limit of transmission lines, operating parameter limits, cascade outage of loss of load, noncompliance of power transactions, increment in market price and possibility of creation of monopoly like market

A. Agrawal · L. Srivastava
Madhav Institute of Technology and Science, Gwalior, India

R. Malviya (✉)
Noida Institute of Engineering and Technology, Greater Noida, India
e-mail: ragini.malviya@gmail.com

S. N. Pandey
Dr. Bhim Rao Ambedkar Polytechnic College, Gwalior, India

power [1, 2]. Due to congestion system, operator is unable to dispatch economic generators from specific locations. Management of congestion can permit the use of full capacity of network system. System operator will have the flexibility to accommodate all the available transaction and ensures the efficient, economic and safe operation of power system. A number of congestion management methods have been developed and are being currently used around the world [3–5]. These methods can be classified in two categories non-market-based and market-based. Several non-market-based congestion management methods are available in the literature. The which methods can reduce the congestion in a limited manner because this based on physical availability of transmission path are market based CM methods. These methods may be first come first serve, prorated rationing curtailment methods [6, 7]. Flexible alternating current transmission systems (FACTS) devices by controlling the power flows in the network can help to reduce the over flow in transmission lines. Different types of FACTS devices are available for improving congestion from transmission path by reducing losses [8]. Generation and distribution companies are not involved in these methods. Congestion is not only a simple problem of physical transmission path, but also it has become a market management issue. Market-based CM methods can eliminate it very effectively. Optimal nodal pricing approach for congestion management has been recommended by many researchers including Federal Energy Regulatory Commission (FERC) as it provides crucial market signals in case of congested transmission corridors, and hence, their continuous monitoring and accurate estimation are very useful for congestion management [9, 10]. Locational marginal price (LMP) contains three components energy price, cost of congestion and loss cost component. In competitive environment, market players submit their strategic bids into the pool in such a manner of getting maximum profit or optimally self-schedule in response to prices [11]. To survive in this environment, seller has to operate not only safely but also competitively. In case of congestion or bottleneck at a particular location of transmission network, only particular generators or sellers can supply the electric energy. They create a monopoly and control the total output to raise the energy prices up to a maximum level for maximizing their profit, exercise market power [12]. Different strategic bidding optimization techniques for reducing congestion from transmission corridors effectively are presented [13, 14]. Strategic behavior and market power-based different CM schemes are compared and presented using an agent base simulation models [15]. Under the new era of rapidly changing demands, traditional congestion management methods or rescheduling the generators are not efficient to avoid overloading of transmission system. DGs provide the electric energy at the specified location near the load point that reduces the overloading of transmission network [16, 17]. The size and location of DGs strongly affect the congested network system operation. A number of methods for siting and sizing of DGs are proposed [18–20]. Renewable energy sources wind and solar are also implemented at the optimal location for CM but create new technical issues and penetration. To resolve the problem of congestion more effectively, involvement of demand side participants has become necessary. In DR program system, operator provides information about transmission congestion, price fluctuations and incentives for end user consumers to take part in CM program. To take the advantage of

this opportunity, load with elastic demand reduces or shifts their demand from peak hours to off peak hours. This paper proposes demand response-based financial tool for congestion management.

1.1 Demand Response-Based Congestion Management

In early deregulated power market, consumers were isolated from the market operations they do not have knowledge about the fluctuations of energy prices and risks. Only generators, independent power producers and regulatory bodies were involved in market operations. Due to lack of information, consumers were not motivated to shift or reduce their demands at the peak hours. This can led to higher energy prices and more congested network [21, 22]. System operator having information about the transmission network and retail energy providers (REP) provides the bridge of proper information gap between system operator and with end user consumers. Because REP has direct contacts with end use consumers [23]. Loads with elastic demand provide more effective and efficient market solutions for secure system operation and CM [24]. Demand response-based CM methods can provide more economic solutions than rescheduling of generators for CM [25]. Some challenges for implementation of DR and potential solutions for congestion management are addressed [16]. Involvement of customer response results in smaller price spikes and can lead to lower LMPs [26]. A pool-based DR exchanges were proposed [27] in which DR exchange operator collects the bid from buyers and sellers and clears the market for economic benefit for all players under network security consideration. When price-based load reduction method fails at the time of peak hours, transfer agent can handle the problem by maintaining the household load under a prescribed limit [28]. DRs manage energy consumption from load side directly and therefore can mitigate congestion without any fuel cost and finally reduce the system operation cost.

2 Problem Formulation

The main object of the proposed method is to eliminate the congestion of transmission system with DR. Objective function having following three sections. First part is minimization of generation cost of thermal power generators, second part is incentive given to end user consumers for adjusting their loads, and third one is the minimum transmission congestion cost. The objective function is given by the following equation

$$\text{minimize} \left(\sum_{G_i=1}^n a_{G_i} (P_{G_i})^2 + b_{G_i} (P_{G_i}) + c_{G_i} + \sum_{m=1}^{N_{DR}} \text{INC}^m + \sum_{k_i=1}^{T_L} \text{TCC}_{k_i} \right). \quad (1)$$

2.1 Minimum Generation Cost

Cost of thermal generators can be represented by the following equation. Where abc are the generator coefficients, n is the number of generators and P_{G_i} is the power generated by the respective generators.

$$C_{G_i}(P_{G_i}) = a_{G_i}(P_{G_i})^2 + b_{G_i}(P_{G_i}) + c_{G_i}. \quad (2)$$

2.2 Minimum DR Cost

End user consumers reduce energy consumption under the DR in two cases. First when electric energy prices are changing at the consumer level, second satisfactory incentives are provided to consumers. In both cases, consumer wants to get maximum profit for adjusting or reducing their demands. For CM, set of loads are selected for implementing DR on the basis of transmission network configuration. Penalty and incentive-based elastic load model is proposed for CM. The demand adjustment at m th response bus can be shown by the following equation.

$$\Delta D^m = D^{0m} - D^m. \quad (3)$$

The total incentives given to the consumers at m th response bus can be shown by Eq. (3). Incentive coefficient is considered from 0.1 to 10 times of electricity prices.

$$INC^m = INC[D^{0m} - D^m]. \quad (4)$$

Once consumers are participating in DR, they have to reduce their load at the required minimum demand, if they do not response, they have to pay a penalty for that. Penalty function can be shown by the equation.

$$PEN^m = PEN[LR^m - \Delta D^m]. \quad (5)$$

Minimum load reduction requested by the system operator is shown by LR. Linear responsive load modal is proposed in this paper is shown by the equation.

$$D^m = D^{0m} \left[1 + \epsilon \frac{\sigma - \sigma^0 + INC - PEN}{\sigma^0} \right]. \quad (6)$$

where ϵ is the load elasticity σ and, σ^0 are the electricity prices after and before.

2.3 Equality Constraints

The system network has equality constraints in terms of active and reactive power available at all nodes. Sum of active and reactive power at each will be zero, respectively. Power balance equations at each node:

$$P_i - P_{G_i} + P_{D_i} + P_{DG} = 0, \quad i = 1, 2, \dots, N_i. \quad (7)$$

$$Q_i - Q_{G_i} + Q_{D_i} = 0, \quad i = 1, 2, \dots, N_i. \quad (8)$$

2.4 Inequality Constraints

Generator and transmission line constraints.

Generator having voltage, active and reactive power limitations, transmission lines having power flow limitations and DR having incentives limitations

$$V_i^{\text{Min}} \leq V_i \leq V_i^{\text{Max}}, \quad i = 1, 2, \dots, N_i. \quad (9)$$

$$P_{G_i}^{\text{Min}} \leq P_{G_i} \leq P_{G_i}^{\text{Max}}. \quad (10)$$

$$Q_{G_i}^{\text{Min}} \leq Q_{G_i} \leq Q_{G_i}^{\text{Max}}. \quad (11)$$

$$T_{k_i} \leq T_{k_i}^{\text{Max}}, \quad k = 1, 2, \dots, T_L. \quad (12)$$

$$\text{INC}_{\text{min}}^m \leq \text{INC}^m \leq \text{INC}_{\text{max}}^m. \quad (13)$$

3 Result and Analysis

Optimal power flow is simulated on IEEE-14 [18] bus system under MATLAB software environment. Bus system having five generators, nine load buses and 20 transmission lines is simulated in two cases. First is base case simulation, and DR program is simulated for CM in second case. In both the cases, generation dispatch, generation cost, DR cost and congestion costs are compared in Table 1, and power flow on transmission lines is shown in Fig. 1.

1. Base case simulation
2. DR program-based simulation.

3.1 Base Case Simulation

Base case optimal power flow is simulated that results in the generator dispatch, generation cost, congestion cost and power losses which are shown in Table 1. Active power flows on 20 transmission lines are shown in Fig. 1. It is clear from the figure that line no. 1 connected between bus no. 1 and 2 line no. 3 connected between bus

Table 1 Generator dispatch, generation cost, congestion cost and power losses

Gen/cost/losses	Base case	DR-based
PG1 (MW)	88.774	79.3089
PG2 (MW)	43.5863	42.36
PG3 (MW)	47.2047	50.4716
PG4 (MW)	92.0895	86.3295
PG5 (MW)	58.4617	57.8194
DR4 (MW)	56.05	50.4659
DR11 (MW)	39.68	35.712
DR14 (MW)	33.91	30.519
TPD (MW)	323.5	310.5569
TPG (MW)	330.1162	316.604
DR cost (Rs)	00	38.00
Total cost (Rs)	11,513	11,119
Congestion cost (Rs)	213	00
Power losses (MW)	6.6161	5.7327

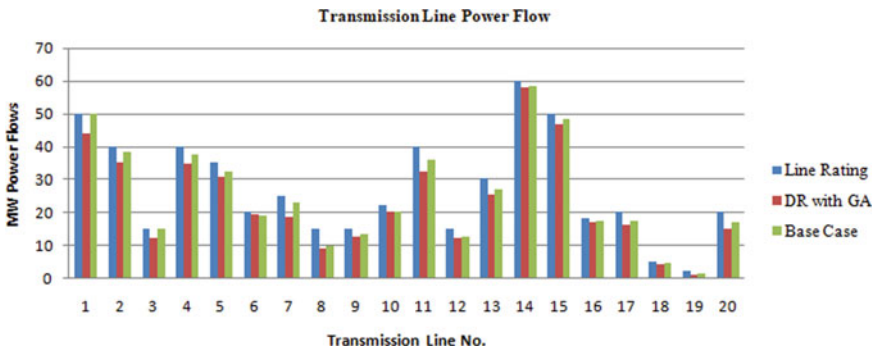


Fig. 1 Transmission line power flow in both cases

no. 2 and 3 having power flow just equal to their ratings. This situation leads to overloading of transmission system and insecure operation of power system.

3.2 DR Program-Based Simulation

For reducing congestion of transmission line, bus system is simulated with DR program. Simulation is carried out, and load bus no. 4, 11 and 14 participate in DR program for reducing the elastic load. Consumers can reduce load up to 10%. In this case, load elasticity is considered -0.1 and incentive 10% of energy price, respectively. Generator dispatch, generator cost, DR cost loads after demand response at load buses 4, 11 and 14 are shown in Table 1. Now, it is clear from Table 1 that the addition of generation cost and demand response cost is lesser than total generation cost in base case. And power flows in this case are shown in Fig. 1. It is clear from the figure that now power flow on line no. 1 and 3 is within range as well as power flows on other transmission lines are also reduced. With DR program, congestion on power system is eliminated, and system operation cost is reduced. DR program is market-based tool for CM. This method of CM saves fuel cost also.

4 Conclusions

In competitive environment of deregulated power market in most of the CM methods, only generator side entities take part. End user consumers were not aware about congested network that was the main cause congestion. Under DR program, end user consumer gets the opportunity to take part in market operation for CM. Consumers are motivated by incentives for reducing or shifting their elastic demands from peak hours to off peak hours. This paper proposes a GA-based DR for congestion management which is implemented on IEEE-14 bus system. After implementation, DR transmission system becomes congestion free, and it reduces the system operating cost also. Hence, under market-oriented competition environment of deregulated power system, DR provides a financial tool of CM for the system operator.

References

1. Kumar A, Mittapalli RK (2014) Congestion management with generic load model in hybrid electricity market with FACTS devices. *Int J Electr Power Energy Syst* 57:49–63. ISSN 0142-0615
2. Singh AK, Parida SK (2013) Congestion management with distributed generation and its impact on electricity market. *Int J Electr Power Energy Syst* 48:39–47
3. Kumar A, Srivastava SC, Singh SN (2005) 13-congestion management in competitive power market: a bibliographical survey. *Electr Power Syst Res* 76:153–164

4. Pandey SN, Verma S, Srivastava L (2006) Congestion management in restructured power system scenario: an overview. Presented at international conference on challenges and strategies for sustainable energy efficiency and environment held at UPTU, 10–11 June 2006, pp 410–421
5. Agrawal A, Pandey SN, Srivastava L (2020) A review and study on market based congestion management techniques in restructured power market. In: International conference on advances in systems, control & computing (AISCC-2020), Sponsored by Springer under TEQIP-III, 27–28 Feb 2020
6. Fang RS, David AK (1999) Transmission congestion management in an electricity market. *IEEE Trans Power Syst* 14(3):877–883
7. Amjady N, Hakimi M (2012) Dynamic voltage stability constrained congestion management framework for deregulated electricity markets. *Energy Convers Manage* 58:66–75
8. Taher SA, Besharat H (2008) Transmission congestion management by determining optimal location of FACTS devices in deregulated power systems. *Am J Appl Sci* 5(3):242–247
9. Pandey SN, Tapaswi S, Srivastava L (2008) Nodal congestion price estimation in spot power market using artificial neural network. *IET Proc Gener Trans Distrib* 2(2):280–290
10. Pillay A, Prabhakar Karthikeyn S, Kothari DP (2015) Congestion management in power systems. *Electr Power Syst Res* 70:83–90
11. Rajaraman R, Alvarado F (2003) Optimal bidding strategy in electricity markets under uncertain energy and reserve prices. Power Systems Engineering Research Centre, Apr 2003. Available at: <https://www.pserc.wisc.edu>
12. Wu C, Bose S, Wierman A, Moheseni-Rad H (2013) A unifying approach to assessing market power in deregulated electricity markets. In: IEEE Power and Energy Society general meeting (PES), 21–25 July 2013. IEEE, pp 1–5
13. Modi NS, Prakash BR (2009) Transmission network congestion in deregulated wholesale electricity market. In: Proceedings of the multiconference of engineers & scientists, vol 2
14. Zhang G, Zhang G, Ya G, Lu J (2011) Competitive strategic bidding optimization in electricity markets using bi-level programming and swarm technique. *IEEE Trans Industr Electron* 58:2138–2146
15. Tanaka M, Chen Y (2012) Market power in emissions trading: strategically manipulating permit price through fringe firms. *Appl Energy* 96:203–211
16. Rahimi F, Ipakchi A (2010) Demand response as a market resource under the smart grid paradigm. *IEEE Trans Smart Grid* 1:82–88
17. Singh K, Padhy NP, Sharma JD (2011) Influence of Price responsive demand shifting bidding on congestion and LMP in pool-based day-ahead electricity markets. *IEEE Trans Power Syst* 26:886–896
18. Gautam D, Mithulanathan N (2007) Optimal DG placement in deregulated electricity market. *Electr Power Syst Res* 77:1627–1636
19. Agrawal A, Pandey SN, Srivastava L (2020) Genetic algorithm based sizing & siting of DG for congestion management in competitive power market. In: International conference on advances in systems, control & computing (AISCC-2020), Sponsored by Springer under TEQIP-III, 27–28 Feb 2020
20. Singh K (2013) Congestion management considering optimal placement of distributed generator in deregulated power system networks. *Electr Power Compon Syst* 42(1):13–22
21. Singh S, Kumar A (2017) Congestion management using demand response program. In: International conference on power and embedded drive control (ICPEDC), Chennai, pp 83–88
22. Zaeim-Kohan F, Razmi H, Daogou-Mojarrad H (2018) Multi-objective transmission congestion management considering demand response programs and generation rescheduling. *Appl Soft Comput* 70:169–188
23. Babar M et al (2017) Learning technique for real-time congestion management in an active distribution networks. In: 2017 IEEE Manchester Power Tech, Manchester, pp 1–6
24. Liu W, Wu Q, Wen F, Ostergaard J (2014) Day-ahead congestion management in distribution systems through household demand response and distribution congestion prices. *IEEE Trans Smart Grid* 5:2739–2747

25. Shayesteh E, Parsa Moghaddam M, Taherynejhad S, Sheikh-El-Eslami MK (2008) Congestion management using demand response programs in power market. In: IEEE Power and Energy Society general meeting—conversion and delivery of electrical energy in the 21st century, Pittsburgh, PA, pp 1–8
26. Aazami R, Aflaki K, Haghifam MR (2011) A demand response based solution for LMP management in power markets. *Int J Electr Power Energy Syst* 33:1125–1132
27. Nguyen DT, Negnevitsky M, de Groot M (2011) Pool-based demand response exchange—concept and modeling. *IEEE Trans Power Syst* 26:1677–1685
28. Haque ANMM, Nijhuis M, Ye G, Nguyen PH, Blik FW, Slootweg JG (2019) Integrating direct and indirect load control for congestion management in LV networks. *IEEE Trans Smart Grid* 10:741–751

An Overview of the Intelligent Control-Based Optimization Methods for Integrated Renewable Energy Sources



Akanksha Sharma, H. P. Singh, R. K. Viral, and Naqui Anwer

Abstract In developing countries like India, the demand of energy has been increasing remarkably due to the generalization of the agricultural, industrial as well as domestic activities. The rising global warming phenomena and an increase in the depletion of fossil fuels have been the most vital driving force towards the attention to exploitation of renewable energy sources. Along with various advantages of these sources, there comes a lot of complexities attached to them due to their intermittent and variable nature. Therefore, to avoid these uncertainties, it is necessary to provide these resources with proper planning and optimization methods. This paper deals with a detailed study of many optimization techniques which can be applied to the renewable energy sources including the classical as well as the Artificial Intelligence and hybrid techniques which can offer a clear vision for the researchers in this field. The main focus has been laid on the fuzzy logic-based and adaptive intelligent-based techniques for renewable energy sources. Certain recommendations considering the challenges in renewable energy development are also been provided.

Keywords Optimization techniques · Renewable energy sources · Integrated renewable energy system · Hybrid energy system

A. Sharma (✉) · H. P. Singh · R. K. Viral
Department of Electrical and Electronics Engineering, Amity School of Engineering and Technology, Amity University, Noida, Uttar Pradesh, India
e-mail: akanksha.sharma2610@gmail.com

H. P. Singh
e-mail: hpsingh2@amity.edu

R. K. Viral
e-mail: rviral@amity.edu

N. Anwer
Teri School of Advanced Studies, New Delhi, India
e-mail: naquianwer@gmail.com

1 Introduction

As we know that the natural capacity of earth for supplying fossil energy is not ever lasting. So, in addition to the increasing energy demands, several factors like: The vast increase in oil pricing, reduction of conventional sources of energy, and most importantly global warming have been redirecting the awareness for the proper utilization as well as of renewable energy sources (RESs) [1]. For satisfying the basic needs such as cooking, lighting, heating, etc., all the societies need energy services. For a secured sustainable development of the country, these energy services need to be safe with low environmental impacts. Such social development requires energy security and an easy access to the energy resources which are very crucial for the promotion of sustainable environment [2]. The main step towards this sustainable environment is the use of RESs for both large scale energy production and standalone systems [3].

RESs are the most important solution for the increasing global warming and because of the fact that these sources are abundant and clean, various researches are being carried out for the optimization of these systems. Apart from several advantages, there are many problems caused due to the variable nature of these sources. Fortunately, the problems which are caused by the variable nature of these resources can be overcome to a certain extent by integrating the two resources in proper combination by using the strengths of one of the sources to overcome the weakness of the other [4]. The hybrid systems that combines solar and wind generating units with battery backup is able to attenuate their individual fluctuations and reduce energy storage requirements significantly. However, some problems stem from the increased complexity of the system in comparison with single energy systems especially when it is backed by an efficient storage system [5]. This complexity, brought about by the use of two different resources combined, makes an analysis of hybrid systems more difficult.

Several authors have evaluated the main renewable energy technologies taking into account sustainability indicators, such as Evans et al. [6] who compared wind power, hydropower, photovoltaic, and geothermal energy taking into account the price of generated electricity, greenhouse gas emissions during the full life cycle of the technology, availability of renewable sources, efficiency of energy conversion, land requirements, water consumption, and social impacts. Evans et al. concluded that wind power has the lowest relative greenhouse gas emissions, the least water consumption demands and the most favorable social impacts, but it requires more land and has high relative capital costs [6]. Lund [7] analyzed strategies for a sustainable development of renewable energy taking into account three major technological changes: energy savings on the demand side, efficiency improvements in energy production, and the replacement of fossil fuels with various sources of renewable energy.

The improvement of renewable energy technologies (RETs) will assist sustainable development and provide a solution to several energy related environmental problems. In this sense, optimization techniques constitute a suitable tool for solving

complex problems in the field of renewable energy systems. In this paper, various optimization techniques suitable for renewable energy sources integration have been discussed along with their merits and demerits.

1.1 Various Integration Structures

Different RESs have different operating characteristics; therefore, it is much needed to provide them with a standard integrating procedure. For the integration of different RES, there are basically three possible structures [8–10]:

- 1. DC Coupled Structure
- 2. AC Coupled Structure
- 3. Hybrid Structure.

DC Coupled Structure

A DC configuration consists of a single DC bus upon which all the RESs are being connected by the related power electronics circuits. This type of structure is able to supply power to a DC load as well as AC load by the use of an inverter. It is a very simple structure as no synchronization is required [10]. The basic DC coupled structure for a solar–wind integrated system is shown in Fig. 1 [10].

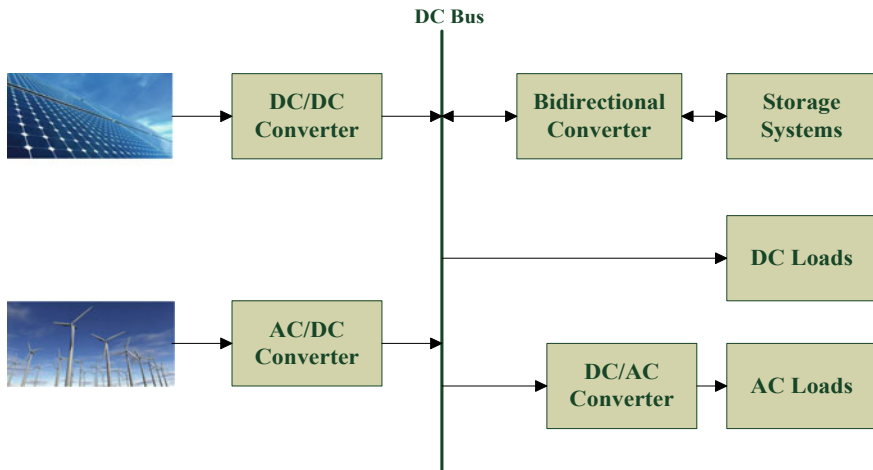


Fig. 1 DC coupled structure of solar–wind integrated system

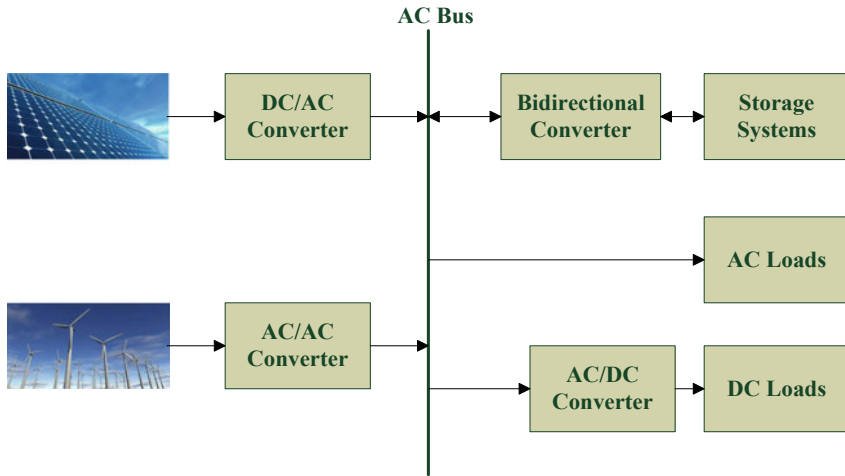


Fig. 2 AC coupled structure of solar–wind integrated system

AC Coupled Structure

In an AC coupled structure, various RESs are connected with the help of a power frequency AC bus using appropriate power electronics circuits. The AC loads can be directly connected to the bus but the DC loads can be only connected via an AC/DC converter. This type of structure is basically used for high frequency loads [11]. The basic AC coupled structure for a solar–wind integrated energy system has been shown in Fig. 2 [10].

Hybrid Structure

A hybrid structure consists of both AC and DC bus. In this particular structure, the DC sources like the solar energy source are coupled via DC bus and the DC loads are directly connected to the DC bus with the use of proper interfacing circuits. The AC sources are being connected directly without the use of any interfacing circuit. The hybrid type DC–AC structure is of comparatively high efficiency and lower cost [10]. The basic hybrid DC–AC coupled structure for a solar–wind—small hydro integrated system is shown in Fig. 3 [10].

2 Need for Optimization

There is still a huge percentage of population in the country residing in the rural areas and not getting the benefits of suitable developments through electrification. In India, there are a number of villages which cannot be connected to the electricity grid due to their remote location. So, there is a need to provide electrification to

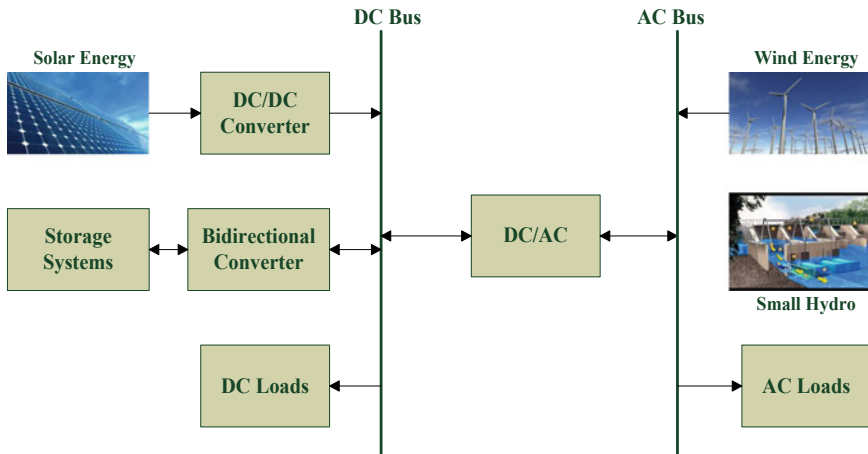


Fig. 3 Hybrid DC–AC coupled structure for a solar–wind—small hydro integrated system

such areas through the RESs. Using these sources in isolated mode will not be an effective solution due to various factors like the cost, reliability, and efficiency. Therefore, the best possible method is to use these sources as HRES or IRES. In order to make an efficient and economical solution of such system, their strategic planning becomes an important task. An inappropriate planning of these sources can lead to create diverse challenges, thereby degrading the system performance and need to overcome. The basic planning focuses on the performance of the components of the system. However, through the optimal modeling of such system, an optimal performance can be achieved in least cost [12, 13].

3 Modeling and Optimization Techniques Used for RESs

The research area of RESs planning is vast and consequently, the available reforms in this area are also extensive. Keeping this fact in mind; this section aims to provide a state of art on various aspects of RES planning such as resource load estimation, sizing and siting, socio- economic planning, etc.

Aforementioned, aspects of RESs can be achieved by optimal planning. Researchers have applied various approaches and optimization techniques for solving RES planning problems. A detailed review of various types of methodologies, which are incorporated in RESs, has been carried out. The different approaches and technologies are well described in Fig. 4. These methodologies have been grouped under following categories:

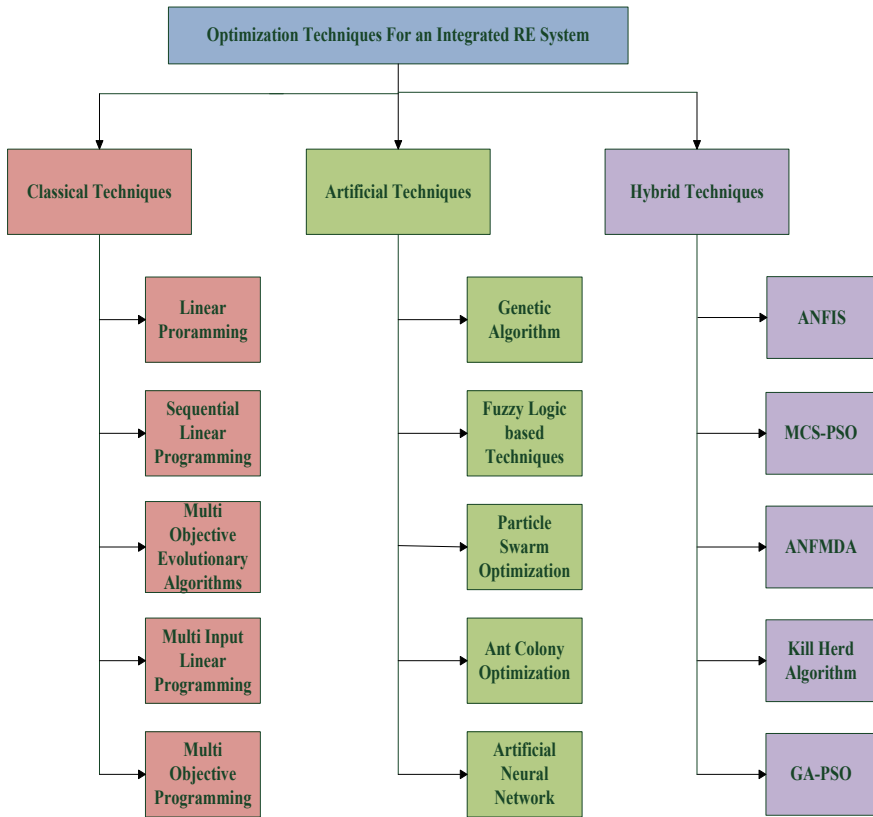


Fig. 4 Various optimization techniques for integrated renewable energy system

1. Classical Techniques
2. Artificial Intelligence-Based Techniques
3. Hybrid and other approaches.

3.1 Classical Techniques

To facilitate an ideal solution for a continuous and differential function, the optimization based on the classical techniques is generally used. These techniques use the differential calculus techniques for the construction of optimum energy models. The basic classical techniques used for the RES-based systems are the dynamic

programming (DP), linear programming (LP) model, sequential linear programming (SLP), non-linear programming (NLP), multi-objective evolutionary algorithms (MOEA), analytical approaches, multi-objective programming (MOP), multi-input linear programming (MILP), various graphical user interface (GUI) software, and optimization tools [14]. Some of the notable studies are discussed here.

Ramakumar et al. [15] designed an IRES model using a LP method for meeting up the energy-based requirements for the developing nations. The objective function, which is related to the annual cost of the system, has been worked out, resulting into energy sets and constraints of power. Devadas [16] designed a LP-based model for the maximization of production of energy as well as the crop revenue with various constraints of the system. The revenue which is generated by the rural energy system proposed is used for reducing commercial energy cost, fertilizer, labor wages and animal feed. Hennes and Samarakou [17] minimized the total life-cycle cost (LCC) of wind conversion system and the optimal capacity of the battery storage system. Fang [18] developed a LP-based optimization model using several equations for the variation in the rural energy system and supply demands. Nagabhushana et al. [19] developed a cost function-based model for minimization of the equipment cost of HRES. Ashok [20] designed a hybrid model based on the numeric iterative algorithm for the rural electrification in some areas of Kerala. For optimization of sizing of solar, wind, micro-hydro hybrid system, an objective function was designed. Ho et al. [21] designed a model for minimizing the cost components of the HES like the biogas, biomass, battery storage, solar photovoltaic, etc. The MILP-based techniques have been proposed to estimate the availability of resources and the operation of an inverter with binary constraints. Joshi et al. [22] developed a model incorporating a technology mix for lighting, irrigation, and cooking need using RESs which are available locally. Iqbal et al. [23] developed few linear as well as non-linear equation based for the electricity need of small units. Vaccari et al. [24] used SLP method to develop an optimization tool which can generate an operating plan over specified time horizon of the given set points for meeting up the basic requirements with the minimum operating costs. Wang et al. [25] developed a multi-objective model for the optimization of the size of a stand-alone HRES. The model also considers economy, reliability, and the environment aspect and also optimizing the number as well as the type of RES used along with their height and installation angle. Diemuodeke et al. [26] presented an optimal mapping of the HES considering the energy storage and a backup diesel generator for the households in Nigeria. This system is able to meet 7.23 kWh/day of a household's energy demand. Jafari et al. [27] developed a magnetically coupled HRES for the residential applications.

3.2 Artificial Intelligence-Based Techniques

Artificial intelligence (AI)-based approach is implementation of science along with engineering for making an intelligent computer program. They do not require the availability of the weather data for the sizing of the integrated energy system in

the remote areas. These techniques provide better optimization results due to fast convergence rate and ease of implementation [28, 29]. There are many AI techniques which are being reported in the literature for the problems of size and cost optimization of the HES such as genetic algorithms (GA), particle swarm optimization (PSO), ant colony optimization (ACO), harmony search (HS), fuzzy logic (FL), evolutionary particle swarm optimization (EPSO), artificial neural network (ANN), and also the hybridization of such techniques. These AI techniques can also deal with the non-linear variation of RESs.

Hakimi and Moghaddas-Tafreshi [30] developed a hybrid system configuration using a PSO-based approach with wind units, anaerobic reactor, fuel cells, electrolyzer, reformer, and hydrogen tank for the sizing problem in the hybrid system for meeting residential area demand. Amer et al. [31] used the PSO technique to develop a hybrid system for the satisfaction of the load demand. The technique was used for reduction in the cost of energy and consideration of losses between the production and demand side. Fetanat and Ehsan [32] developed a PV-wind HES for the optimization of size using the ACO technique. The objective function minimizes the sum of maintenance and capital cost. Koutroulis et al. [33] used the GA technique with an objective function to minimize the total system cost for the investigation of system components type and an optimal number. Arabali et al. [34] used the GA technique for cost minimization and increase of efficiency of a solar PV-wind system along with a battery storage device. Maximum storage capacity and the energy excess of the storage system for the percentage of load shifting was calculated. Paliwal et al. [35] developed the relation between size of the storage units, number of cycles, and the replacement over the life time of the project by optimizing the PV-wind-diesel system for the fulfilment of the techno-socio-economic criterion. Abdelkader et al. [36] used a multi-objective GA (MOGA) approach for the sizing of the system considering the storage dynamics. Different economic analysis was considered for the optimal system configuration. Li et al. [37] designed a sustainable HRES with RO desalination system using recurrent neural networks (RNN). Multi-area optimization was also conducted using an extended mathematical programming (EMP) to minimize total annual costs and greenhouse gas emission. Murugaperumal and Raj [38] validated an optimal design of HRES for a remote village in Pondicherry, India using artificial neural network (ANN-BP) feedback propagation and Levenberg-Marguardt (LM) data training technique. The work shows that HRES in a remote location is a cost-effective solution for the sustainable development of the rural areas. Ghiasi [39] developed a system for providing an extensive analysis about the new AC and DC structures, determining the capacity as well as the capital designing using HRES for increasing the availability and reducing costs of the network with the use of PSO. Magdy et al. [40] used model predictive control (MPC) technique for the frequency stabilization of RES with inherent nonlinearities. An Egyptian power system (EPS) was used to prove the effectiveness of the proposed system, and the performance is compared with the PSO algorithm under varying load profiles and uncertainties. Singh and Fernandez [41] used a new algorithm named Cuckoo search algorithm (CSA) for the problem of hardware failure in PV panels during modeling. A concept based on random number generation has been adopted to calculate the actual hourly

available PV power. Mohammed et al. [42] designed a system to satisfy a stand-alone area in Brittany, France, as an example of load demand using PSO for minimization of energy cost. Wagh and Kulkarni [43] presented certain combinations RES for satisfying the thermal demand of a region. A Microsoft excel optimizer software and PSO algorithm were used is used to solve the constraint optimization problem.

3.2.1 Fuzzy Logic Based Techniques

Fuzzy logic controller (FLC) is an intelligent controller, the concept of which was conceived by Lotfi Zadeh, professor at the University of California at Berkeley. Fuzzy logic (FL) is basically a problem solving control system methodology which can be implemented into systems ranging from small, embedded micro controllers to large, networked or workstation-based data acquisition systems [a]. FL provides simple way for a conclusion based upon ambiguous, imprecise and noisy or any missing output information. It can be implemented both in hardware as well as software. The main approach behind FL is based upon a person's behavior while making any decision and that too much faster. It considers some numerical parameters to operate the significant error and the rate of change of error.

3.3 Hybrid Techniques

The combination of two or more optimization techniques is known as hybrid techniques which are used to overcome the problems and limitations of the single algorithm. There are various such techniques including artificial neural fuzzy interface system (ANFIS), artificial neural network/GA/monte carlo simulation, hybrid iterative/GA, monte carlo simulation (MCS)—PSO, simulation optimization—MCS. Khatib et al. [44] developed a hybrid optimization technique for creating the set of possible configurations for the desired system using the GA. Rajkumar et al. [45] developed a technique based on ANFIS to benefit with the ANN learning abilities by the performance of an intelligent system. This technique allows the fuzzy inference system to track the input/output data. Bashir and Sadeh [46] used the PSO/MCS hybrid technique for the system capacity determination for the wind, PV cell and battery for the supply of specific load. PSO is used for the optimal sizing of the system and the MCS for the assessment of uncertainties in wind and PV power. Maleki and Pourfayaz [47] used the evolutionary algorithms (EA) for the optimum sizing of the HES with a reliability index in terms of LPSP. Fadaee and Radzi [48] used the multi-objective approach using the EA for the overview of the optimization methods. Shilaja and Ravi [49] presented a hybrid metaheuristic optimization method including Dragonfly algorithm (DA) with aging particle swarm optimization (APSO) for handling the optimal power flow problem. The main objective of this work is fuel cost minimization, voltage profile deviation, and power loss minimization. Murugaperumal and Raj [50] proposed a hybrid technique using ANFIS and

modified dragonfly algorithm (MDA), termed as ANFMDA for the modeling and optimal energy management of the micro grid with a low cost. Kaabeche and Bakelli [51] used four algorithms namely-ant lion optimizer algorithm (ALO), grey wolf optimizer algorithm (GWO), krill herd algorithm (KH), and JAYA algorithm for the establishment of rules and the tools for energy management optimization and also the sizing of a wind and solar production system using an electrochemical storage device. Sawle et al. [52] presented an optimal planning of PV-wind-biomass hybrid energy system including the backup power sources like battery bank and diesel generator. GA and PSO are used for the cost of energy minimization.

The comparison of these various optimization techniques for RESs is described in Table 1.

4 Recommendations

In countries like India, which are rich in renewable resources, the power generation using RES will be on high demand because of the declining fossil fuels and it becomes important to pay attention to various challenges attached to these resources and depending on these challenges there are certain recommendations which can be kept in mind:

1. Technical constraints like—power quality, stability, voltage, and power fluctuations should be considered properly due to the complexity of the system.
2. Various optimization techniques like—ANFIS, ANN, GA, FL should be used to find an optimal solution to the complexity involved with the process.
3. For maintaining the stability of IRES, the transient analysis of system should be carried out in a proper manner by step changes in the variable parameters like solar radiation, wind speed, load demand, etc.
4. For the improvement of system components in IRES, nanotechnology is a very important and crucial subject.

5 Conclusion

The paper provides a comprehensive study of the latest research developments in the field of optimization of renewable energy sources. The overview provides about various optimization techniques involved and used in the planning, design, and control of renewable energy. Different optimization techniques are discussed including the classical techniques like: dynamic programming (DP), linear programming (LP) model, sequential linear programming (SLP), non-linear programming (NLP), multi-objective evolutionary algorithms (MOEA), multi-objective programming (MOP), etc., the artificial intelligence techniques like: algorithms (GA), particle swarm optimization (PSO), ant colony optimization (ACO), harmony search (HS), fuzzy logic (FL), evolutionary particle swarm optimization (EPSO), artificial

Table 1 Comparison of various optimization techniques used for RESs

S. No.	Problem type	Technique/approach	Objective function	Merits	Demerits	References
A. Classical techniques						
1	Linear programming optimization problem	<ul style="list-style-type: none"> Linear programming (LP) approach 	<ul style="list-style-type: none"> Minimization of total cost 	<ul style="list-style-type: none"> Applicable under wide variety of conditions Utilized locally available resources 	<ul style="list-style-type: none"> Trial design to be done for different seasons 	[15]
2	Linear programming optimization problem	<ul style="list-style-type: none"> Two pronged approach 	<ul style="list-style-type: none"> Minimization of energy cost Maximization of energy production 	<ul style="list-style-type: none"> Use of energy sources 	<ul style="list-style-type: none"> Proper examination required 	[16]
3	Non-linear programming problem	<ul style="list-style-type: none"> Sequential LP algorithm 	<ul style="list-style-type: none"> Minimization of operating cost 	<ul style="list-style-type: none"> Tool can be used for pre-existing HRES 	<ul style="list-style-type: none"> Work over a specified time horizon 	[24]
4	Linear programming optimization problem	<ul style="list-style-type: none"> System dynamics (SD) model Linear programming model 	<ul style="list-style-type: none"> Least cost of energy supply 	<ul style="list-style-type: none"> Reasonable use of energy sources Increased efficiency 	<ul style="list-style-type: none"> Require proper examination of oil and electricity supply 	[18]
5	Sizing optimization problem	<ul style="list-style-type: none"> Numeric iterative algorithm 	<ul style="list-style-type: none"> Minimum life-cycle cost 	<ul style="list-style-type: none"> Reliability Economic power supply to the village Applicable to any village area 	<ul style="list-style-type: none"> Require diesel generator backup for peak hours 	[20]

(continued)

Table 1 (continued)

S. No.	Problem type	Technique/approach	Objective function	Merits	Demerits	References
6	Optimal mapping problem	<ul style="list-style-type: none"> Multi-area criteria decision making algorithm 	<ul style="list-style-type: none"> Minimum life-cycle cost 	<ul style="list-style-type: none"> Able to meet household's electricity needs Good environmental impact 	<ul style="list-style-type: none"> High cost of energy of HES 	[26]
7	Magnetically coupled HRES	<ul style="list-style-type: none"> Real-time control techniques Off-line 2D dynamic programming 	<ul style="list-style-type: none"> Minimization of total energy cost 	<ul style="list-style-type: none"> Can operate in large number of grid connected and off grid operation modes 	<ul style="list-style-type: none"> Special consideration to be given to characteristics of each energy source 	[27]
B. Artificial intelligence techniques						
1	Optimal sizing problem	<ul style="list-style-type: none"> PSO 	<ul style="list-style-type: none"> Minimization of total cost 	<ul style="list-style-type: none"> High reliability Depends on the performance of the system and system costs 	<ul style="list-style-type: none"> Sensitivity of system costs to the capital costs of wind turbine is higher 	[30]
2	Size optimization problem	<ul style="list-style-type: none"> Ant colony optimization (ACO) bases integer programming 	<ul style="list-style-type: none"> Minimization of total design cost 	<ul style="list-style-type: none"> High convergence speed, performance, and accuracy 	<ul style="list-style-type: none"> System provided high operating costs 	[32]
3	Multi-objective optimization problem	<ul style="list-style-type: none"> GA Discrete fourier transform algorithm 	<ul style="list-style-type: none"> Minimum LPSP Minimization of cost of energy 	<ul style="list-style-type: none"> High reliability 	<ul style="list-style-type: none"> Improvement in simulation program needed to find a very significant solution 	[36]

(continued)

Table 1 (continued)

S. No.	Problem type	Technique/approach	Objective function	Merits	Demerits	References
4	Multi-criteria optimization problem	<ul style="list-style-type: none"> Recurrent neural networks (RNN) 	<ul style="list-style-type: none"> Minimization of total costs Minimization of greenhouse gas emission Minimization of power of LPSP 	<ul style="list-style-type: none"> Advantageous to predict future uncertainties Decrease in greenhouse gas emission 	<ul style="list-style-type: none"> Takes large time as compared to classical method 	[37]
5	Optimal design of HRES	<ul style="list-style-type: none"> Artificial neural network feedback propagation (ANN-BP) algorithm 	<ul style="list-style-type: none"> Minimization of total cost 	<ul style="list-style-type: none"> Estimate load forecasting 	<ul style="list-style-type: none"> No practical system used 	[38]
6	Multi-objective optimization problem	<ul style="list-style-type: none"> Particle swarm optimization (PSO) 	<ul style="list-style-type: none"> Minimization of total cost 	<ul style="list-style-type: none"> Reduce losses Increased efficiency 	<ul style="list-style-type: none"> Risks related to renewable sources uncertainty 	[39]
7	Optimization of power	<ul style="list-style-type: none"> PSO Multi-objective PSO 	<ul style="list-style-type: none"> Minimization of energy cost Total net present cost (TNPC) 	<ul style="list-style-type: none"> High speed and accuracy 	<ul style="list-style-type: none"> Not applicable for complex and non-linear problems 	[42]
8	Multi-objective optimization problem	<ul style="list-style-type: none"> PSO Optimizer software 	<ul style="list-style-type: none"> Minimization of life-cycle cost Minimization of CO2 emission 	<ul style="list-style-type: none"> Less greenhouse gas emission 	<ul style="list-style-type: none"> The method applicable only to a certain area 	[43]

(continued)

Table 1 (continued)

S. No.	Problem type	Technique/approach	Objective function	Merits	Demerits	References
C. Hybrid techniques						
1	Multi-objective optimization problem	<ul style="list-style-type: none"> GA Hybrid iterative technique 	<ul style="list-style-type: none"> Minimization of system cost Loss of load probability (LPSP) 	<ul style="list-style-type: none"> Lowest cost optimization 	<ul style="list-style-type: none"> Applicable only when average wind speed is available 	[44]
2	Techno economical optimization problem	<ul style="list-style-type: none"> Artificial neuro fuzzy inference system (ANFIS) technique 	<ul style="list-style-type: none"> Minimization of total cost Loss of power supply probability 	<ul style="list-style-type: none"> Long power supply Accurate power output 	<ul style="list-style-type: none"> Depends on solar-wind data, load profile, unit cost 	[45]
3	Optimal sizing problem	<ul style="list-style-type: none"> PSO MCS 	<ul style="list-style-type: none"> Minimization of cost 	<ul style="list-style-type: none"> Considers the uncertainty of wind and PV 	<ul style="list-style-type: none"> Lifetime of project is limited 	[46]
4	Optimal sizing problem	<ul style="list-style-type: none"> PSO TS Simulated annealing (SA) Improved PSO (PSO) Improved harmony search (IHS) Improved harmony search-based simulated annealing (IHSBSA) Artificial bee Swarm optimization (ABS0) 	<ul style="list-style-type: none"> Minimization of total cost Maximum LPSP 	<ul style="list-style-type: none"> Accurate results Robustness 	<ul style="list-style-type: none"> Due to many techniques involved takes large time 	[47]

(continued)

Table 1 (continued)

S. No.	Problem type	Technique/approach	Objective function	Merits	Demerits	References
5	Non-linear optimization problem	<ul style="list-style-type: none"> Dragonfly algorithm (DA) Ageing PSO (APSO) 	<ul style="list-style-type: none"> Minimization of fuel cost Minimization of power loss Voltage profile deviation 	<ul style="list-style-type: none"> Reduced time of computation 	<ul style="list-style-type: none"> Further fuel reduction can be done 	[49]
6	Multi-objective optimal energy management problem	<ul style="list-style-type: none"> Artificial neural fuzzy inference system and modified dragon fly algorithm (ANFISMDA) 	<ul style="list-style-type: none"> Minimization of fuel cost Minimization of total cost 	<ul style="list-style-type: none"> Prediction of load demand No wastage of available energy sources Reduced computational time 		[50]
7	Energy management optimization and sizing problem	<ul style="list-style-type: none"> Ant lion optimizer (ALO) Grey wolf optimizer (GWO) Krill Herd algorithm (KH) JAYA algorithm 	<ul style="list-style-type: none"> Minimization of energy cost 	<ul style="list-style-type: none"> Reliability Reduction in cost 	<ul style="list-style-type: none"> Does not have a much optimal solution 	[51]
8	Optimal sizing optimization problem	<ul style="list-style-type: none"> GA PSO 	<ul style="list-style-type: none"> Minimization of energy cost 	<ul style="list-style-type: none"> Reliability Low greenhouse gas emission 		[52]

neural network (ANN), etc., and also the hybrid techniques like: artificial neural fuzzy interface system (ANFIS), artificial neural network/GA/MCS, hybrid iterative/GA, MCS—PSO, simulation optimization—MCS, etc. The study shows that some researchers have used heuristic optimization methods and others have solved multi-objective problems using Pareto optimization methods. Therefore, it can be concluded that multi-objective optimization methods using various hybrid techniques is a promising field in renewable energy development.

References

1. Kajela D, Manshahia MS (2017) Optimization of renewable energy systems: a review. *IJSRST* 3(8)
2. Erdinc O (2017) Optimization in renewable energy systems: recent perspectives. Butterworth-Heinemann, UK
3. Martiskainen M, Coburn J (2010) The role of information and communication technologies (ICTs) in household energy consumption/prospects for the UK. *Energy Effi*. <https://doi.org/10.1007/s12053-010-9094-2>
4. Abdulkarim A, Abdelkader SM, Morrow DJ (2017) Model for optimal design of standalone hybrid renewable energy microgrids. *J Fundam Appl Sci* 9(2):1074–1101
5. Maleki A, Gholipour M, Ameri M (2016) Electrical power and energy systems optimal sizing of a grid independent hybrid renewable energy system incorporating resource uncertainty and load uncertainty. *Int J Electr Power Energy Syst* 83:514–524
6. Evans A, Strezov V, Evans TJ (2009) Assessment of sustainability indicators for renewable energy technologies. *Renew Sustain Energy Rev* 13(5):1082–1088
7. Lund H (2007) Renewable energy strategies for sustainable development. *Energy* 32(6):912–919
8. Lasseter R, Abbas A, Marnay C, Stevens J, Dagle J, Guttromson R et al (2003) Integration of distributed energy resources: the CERTS microgrid concept. California Energy Commission. P500-03-089F
9. Farret FA, Simões MG (2006) Integration of alternative sources of energy. Wiley, Hoboken, NJ
10. Chauhan A, Saini RP (2014) A review on integrated renewable energy system based power generation for stand-alone applications: configurations, storage options, sizing methodologies and control. *Renew Sustain Energy Rev* (38):99–120
11. Sood PK, Lipo TA, Hansen IG (1988) A versatile power converter for high-frequency link systems. *IEEE Trans Power Electron* 3(4):383–390
12. Deshmukh MK, Deshmukh SS (2008) Modeling of hybrid renewable energy system. *Renew Sustain Energy Rev* 27:235–249
13. Bernal-Agustin JL, Dufo-Lopez R (2009) Simulation and optimization of stand-alone hybrid renewable energy systems. *Renew Sustain Energy Rev* 13:2111–2118
14. Rajanna S, Saini RP (2016) A review on planning, configurations, modeling and optimization techniques of hybrid renewable energy systems for off grid applications. *Renew Sustain Energy Rev* 58:376–396
15. Ramakumar R, Shetty PS, Ashenayi K (1986) A linear programming approach to the design of integrated renewable energy systems for developing countries. *IEEE Trans Energy Convers* 1(4):18–24
16. Devadas V (2001) Planning for rural energy system: part I. *Renew Sustain Energy Rev* 5(3):203–226
17. Hennem JC, Samarakou MT (1986) Optimization of a combined wind and solar power plant. *Energy Res* 10(2):181–188

18. Fang Z (1983) A model of the energy-supply and demand system at the village level. *Energy* 18(4):365–369
19. Nagabhushana AC, Rohini R, Raju AB (2011) Economic analysis and comparison of proposed HRES for stand-alone applications at various places in Karnataka state. In: *Proceedings of IEEE PES innovative smart grid technologies*
20. Ashok S (2007) Optimized model for community-based hybrid energy system. *Renew Energy* 32:1155–1164
21. Ho WS, Hashim H, Lim JS (2014) Integrated biomass and solar town concept for a smart eco-village in Iskandar Malaysia (IM). *Renew Energy* 69:190–201
22. Joshi B, Bhatti S, Bansal NK (1992) Decentralized energy planning model for a typical village in India. *Energy* 17(9):869–876
23. Iqbal M, Azam M, Naeem M, Khwaja AS, Anpalagan A (2014) Optimization classification, algorithms and tools for renewable energy: a review. *Renew Sustain Energy Rev* 3:640–654
24. Vaccari M, Mancuso GM, Riccardi J, Cantu M, Pannocchia G (2019) A sequential linear programming algorithm for economic optimization of hybrid renewable energy systems. *J Process Control* 74:189–201
25. Wang R, Li G, Ming M, Guohua Wu, Wang L (2017) An efficient multi-objective model and algorithm for sizing a stand-alone hybrid renewable energy system. *Energy* 141:2288–2299
26. Diemuodeke EO, Addo A, Oko COC, Mulugetta Y, Ojapah M (2019) Optimal mapping of hybrid renewable energy systems for locations using multi-criteria decision-making algorithm. *Renew Energy* 134:461–477
27. Jafari M, Malekjamshidi Z (2020) Optimal energy management of a residential-based hybrid renewable energy system using rule-based real-time control and 2D dynamic programming optimization method. *Renew Energy* 146:254–266
28. Rajkumar V, Khatod DK (2012) Optimal planning of distributed generation systems in distribution system. *Renew Sustain Energy Rev* 16:5146–5165
29. Binayak B, Kyung-Tae L, Gil-Yong L, Young-Man C, Hoon AS (2015) Optimization of hybrid renewable energy power systems: a review. *Int J Precis Eng Manuf Green Technol* 2:99–112
30. Hakimi SM, Moghaddas-Tafreshi SM (2009) Optimal sizing of a stand-alone hybrid power system via particle swarm optimization for Kanauji area in South-East of Iran. *Renew Energy* 34(7):1855–1862
31. Amer M, Namaane A, M'Sirdi NK (2013) Optimization of hybrid renewable energy systems (HRES) using PSO for cost reduction. *Energy Procedia* 42:318–327
32. Fetanat A, Ehsan K (2015) Size optimization for hybrid photovoltaic-wind energy system using ant colony optimization for continuous domains based integer programming. *Appl Soft Comput* 31:196–209
33. Koutroulis E, Dionysian K, Antonis P, Kostas K (2006) Methodology for optimal sizing of stand-alone photovoltaic/wind-generator systems using genetic algorithms. *Sol Energy* 80(9):1072–1088
34. Arabali A, Ghofrani M, Amoli ME, Fadali MS, Baghzouz Y (2013) Genetic algorithm based optimization approach for energy management. *IEEE Trans Power Deliv* 28(1):162–170
35. Paliwal P, Patidar NP, Nema RK (2014) Determination of reliability constrained optimal resource mix for an autonomous hybrid power system using particle swarm optimization. *Renew Energy* 63:194–204
36. Abdelkader A, Rabeh A, Ali DM, Mohamed J (2018) Multi-objective genetic algorithm based sizing optimization of a stand-alone wind/PV power supply system with enhanced battery/super capacitor hybrid energy storage. *Energy* 163:351–363
37. Li Q, Loy-Benitez J, Nam K, Hwangbo S, Rashidi J, Yoo C (2019) Sustainable and reliable design of reverse osmosis desalination with hybrid renewable energy systems through supply chain forecasting using recurrent neural networks. *Energy* 178:277–292
38. Murugaperumal K, Raj PADV (2019) Feasibility design and techno-economic analysis of hybrid renewable energy system for rural electrification. *Solar Energy* 188:1068–1083
39. Ghiasi M (2019) Detailed study, multi-objective optimization, and design of an AC-DC smart microgrid with hybrid renewable energy resources. *Energy* 169:496–507

40. Magdy G, Shabib G, Elbaset AA, Mitani Y (2018) Frequency stabilization of renewable power systems based on MPC with application to the Egyptian grid. *IFAC-Papers OnLine* 51(28):280–285
41. Singh SS, Fernandez E (2018) Modeling, size optimization and sensitivity analysis of a remote hybrid renewable energy system. *Energy* 143:719–731
42. Mohammed OH, Amirat Y, Benbouzid M (2019) Particle swarm optimization of a hybrid wind/tidal/PV/battery energy system. Application to a remote area in Bretagne, France. *Energy Procedia* 162:87–96
43. Wagh MM, Kulkarni VV (2019) Thermal energy demand fulfilment of Kolhapur through modelling and optimization of integrated renewable energy systems. *Renew Energy Focus* 29:114–122
44. Khatib T, Mohamed A, Sopian K (2012) Optimization of a PV/wind microgrid for rural housing electrification using a hybrid iterative/genetic algorithm: case study of Kuala Terengganu, Malaysia. *Energy Build* 47:321–333
45. Rajkumar RK, Ramachandaramurthy VK, Yong BL, Chia DB (2011) Techno economical optimization of hybrid PV/wind/battery system using neuro fuzzy. *Energy* 36(8):5148–5153
46. Bashir M, Sadeh J (2012) Optimal sizing of hybrid wind/photovoltaic/battery considering the uncertainty of wind and photovoltaic power using Monte Carlo simulation. In: *Proceedings of IEEE international conference*
47. Maleki A, Pourfayaz F (2015) Optimal sizing of autonomous hybrid photovoltaic/wind/battery power system with LPSP technology by using evolutionary algorithms. *Sol Energy* 115:471–483
48. Fadaee M, Radzi MAM (2012) Multi-objective optimization of a stand-alone hybrid renewable energy system by using evolutionary algorithms: a review. *Renew Sustain Energy Rev* 16:3364–3369
49. Shilaja C, Ravi K (2017) Optimal power flow using hybrid DA-APSO algorithm in renewable energy resources. *Energy Procedia* 117:1085–1092
50. Murugaperumal K, Raj PADV (2019) Energy storage based MG connected system for optimal management of energy: an ANFMDA technique. *Int J Hydrogen Energy* 44(16):7996–8010
51. Kaabeche A, Bakelli Y (2019) Renewable hybrid system size optimization considering various electrochemical energy storage technologies. *Energy Convers Manag* 193:162–175
52. Sawle Y, Gupta SC, Bohre AK (2017) Optimal sizing of standalone PV/wind/biomass hybrid energy system using GA and PSO optimization technique. *Energy Procedia* 117:690–698

Bit Error Rate Analysis for Indoor Optical Wireless Communication System



Mansi Gupta, Gagan Agrawal, Namrata Kumari, and Rekha Rani

Abstract For this paper, we use visible light spectrum (380–740 nm wavelength) for indoor optical wireless communication which is an emerging technology and new way for indoor communications. It uses the already built-in LED infrastructure which is being used for illumination, to transmit signals and photodiode for receiving signals. This paper contains BER analysis for indoor visible light communication for indoor communication. The system model consists of one LED and one photodiode which form a classic point-to-point indoor visible light communication system. The Lambertian emission-based channel model is used along with On–Off Keying modulation. The effect of various parameters on BER is studied and plotted.

Keywords VLC · BER · Lambertian emission-based channel model · Detection threshold

1 Introduction

Visible light communication is gaining popularity in the past few years. The data traffic in the RF spectrum is increasing and so is the demand for data; hence, the RF spectrum is saturating [1]. In VLC, LEDs are used for transmitting while photodiodes for receiving signals. An LED transmitter used for illumination can also be used for communication.

M. Gupta (✉) · G. Agrawal · N. Kumari · R. Rani
Department of Electronics and Communication Engineering, Galgotias College of Engineering and Technology, 1, Knowledge Park, Greater Noida, India
e-mail: mansigup123@gmail.com

G. Agrawal
e-mail: gagan.agrawal@gmail.com

N. Kumari
e-mail: naky1499@gmail.com

R. Rani
e-mail: rekha.rani@galgotiacollege.edu

Implementation of VLC can be done for both indoor and outdoor scenarios, but most of the research is focused on indoor scenarios. Visible light communication has many advantages over other methods of communication, like an unlicensed spectrum that is free to use, exempt from RF interference, and a better rate of data transmission. Hence, VLC will be a favourable method for indoor wireless communications in the upcoming 5G era [2].

A fundamental scenario of indoor VLC is explored by research. A comparison between the Lambertian model and the results of empirical data is done in [3]. However, received optical power is measured only up to 10 m.

Various modulation techniques like pulse amplitude modulation [4], colour shift keying (CSK) [5], phase shift keying (PSK) [6], orthogonal frequency division multiplexing (OFDM) [7, 8] have been explored. In this paper, only Gaussian noise (both noise dependent on input and noise not dependent on input) is considered.

For this paper,

- Channel gain is plotted for various orders of the Lambertian emission (m)
- The power emitted by the LED varies with m .

2 System and Channel Models

For this paper, an indoor VLC system (single input single output) is considered as shown in Fig. 2. The LED used for transmitter converts electrical signals to VLC signals. (x, y, z) are the coordinates of the LED. At the receiving end, PIN photodiode is used to convert VLC signals back to electrical signals. The coordinates of the photodetector are (p, q, r) . The LED is fixed, while the photodetector can move on the receiving plane and can be tilted at an angle. The size of the room is fixed (Fig. 1).

The major sources of noise in this paper Gaussian noise dependent on input and Gaussian noise not dependent on the input.

2.1 Transmitter

White light LED is used as a transmitter. Let X be the transmitted signal. Since On-Off Keying (OOK) modulation is used, X is either 0 or $2P$. P is the average power emitted by the LED and λ is the irradiance angle. At the transmitting end, the radiant

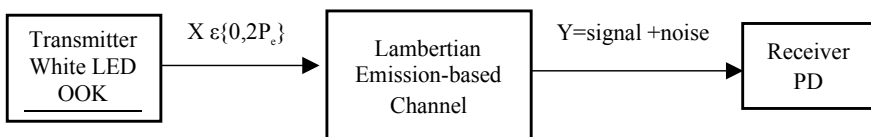
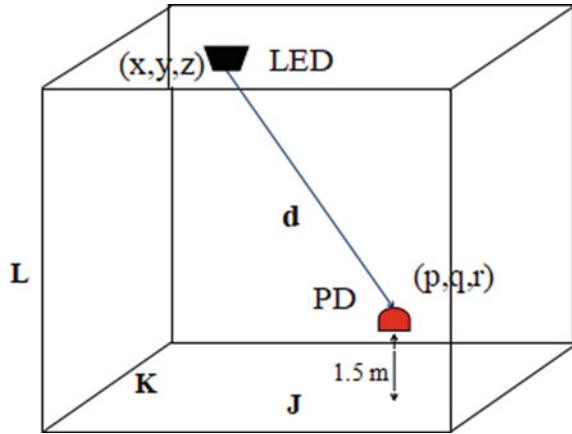


Fig. 1 Flow diagram for VLC system

Fig. 2 System model for indoor VLC



intensity of LED can be written as in [9],

$$R(\lambda) = \left[\frac{(m + 1)}{2\pi} \right] \cos^m(\lambda) \tag{1}$$

Here m equals,

$$m = \frac{-\log_e 2}{\log_e (\cos(\Omega_{1/2}))} \tag{2}$$

$\Omega_{1/2}$ is the semi-angle at the half-power emitted by the LED. The power transmitted (P_t) can be given as,

$$P_t = P * R(\lambda) \tag{3}$$

2.2 Channel Model

Lambertian emission-based channel model h can be defined as [10],

$$h = R_0(\lambda) * \frac{A}{d^2} \cos(\varphi) \tag{4}$$

φ is the incidence angle of the photodiode, d is the scalar distance between the transmitter (LED) and the receiver (PD), A is the physical area of photodiode.

$\cos(\lambda)$ and $\cos(\varphi)$ are given below,

$$\cos(\varphi) = \frac{z - r}{d} \quad (5)$$

$$\cos(\lambda) = \frac{\langle V_{\text{nor}}, V_{\text{rs}} \rangle}{\|V_{\text{nor}}\| \cdot \|V_{\text{rs}}\|} \quad (6)$$

where V_{rs} is the vector from the PD to the LED and V_{nor} is the unit normal vector of the receiver plane,

Therefore,

$$\begin{aligned} V_{\text{nor}} &= [x, y, z] - [p, q, r] = [x - p, y - q, z - r] \text{ and} \\ V_{\text{rs}} &= [\cos \alpha \sin \theta, \sin \alpha \sin \theta, \cos \theta] \end{aligned}$$

where θ is the angle of inclination that is calculated by the coordinates of the PD and the projection angle of LED on the XY -plane. The azimuth angle (α) equals to

$$\alpha = \tan^{-1} \left| \frac{y - q}{x - p} \right| \quad (7)$$

For the first quadrant of the XY -plane.

Furthermore, (6) can be written as

$$\cos \varphi = [(x - p) \cos \alpha \sin \theta + (y - q) \sin \alpha \sin \theta + (z - r) \cos \theta] / d \quad (8)$$

Hence after substituting Eqs. (1), (5) and (8) in Eq. (4), the channel gain (h) becomes

$$h = \frac{(m + 1)A}{2\pi d^2} [(x - p) \cos \alpha \sin \theta + (y - q) \sin \alpha \sin \theta + (z - r) \cos \theta] \quad (9)$$

2.3 Receiver

Photodiodes are used for receiving the electrical signal propagated by the transmitter and the noise added by the channel. Various noises added to the signal are shot noise, thermal noise, etc. They are modelled by Gaussian distributions [11]. Y represents the received signal.

$$Y = ohX + Z_0 + \sqrt{ohX}Z_1 \quad (10)$$

In Eq. (10), $Z_1 \sim N(0, \zeta^2\sigma^2)$ is the Gaussian noise dependent on input and $Z_0 \sim N(0, \sigma^2)$ is the Gaussian noise independent of the input. σ is the standard noise variance of input independent Gaussian noise, and $\zeta^2 \geq 0$ is the ratio of the variance of Z_1 to the variance of Z_0 assuming both to be independent. o denotes the optoelectronic conversion factor of the photodiode.

3 BER Performance Analysis

The bit error rate for the indoor VLC communications system with OOK can be calculated as,

$$\text{BER} = \text{Pr(off)}\text{Pr(off|on)} + \text{Pr(on)}\text{Pr(on|off)} \tag{11}$$

where Pr(on) is the probability of transmitting bit 1 and Pr(off) is the probability of transmitting bit 0, and both are equal to 1/2 and Pr(off|on) and Pr(on|off) are the conditional bit error probabilities for transmitted bit equals 0 and 1, respectively.

The conditional PDF ($f_{Y|X}(y|x)$) is,

$$f_{Y|X}(y|x) = \frac{1}{\sqrt{2\pi(1+rhx\zeta^2)}\sigma} e^{-\frac{(y-rhx)^2}{2(1+rhx\zeta^2)\sigma^2}} \tag{12}$$

According to (12), $\text{Pr}(0|1)$ and $\text{Pr}(1|0)$ can be derived as

$$\begin{aligned} \text{Pr}(0|1) &= \int_{-\infty}^{\eta} \frac{1}{\sqrt{2\pi(1+\chi\zeta^2)}\sigma} e^{-\frac{-(y-x)^2}{2(1+\chi\zeta^2)\sigma^2}} dy \\ &= Q\left(\frac{\chi - \eta}{\sqrt{1 + \chi\zeta^2}\sigma}\right) \end{aligned} \tag{13}$$

$$\begin{aligned} \text{Pr}(1|0) &= \int_{\eta}^{\infty} \frac{1}{\sqrt{2\pi}\sigma} e^{-\frac{y^2}{2\sigma^2}} dy \\ &= Q\left(\frac{\eta}{\sigma}\right) \end{aligned} \tag{14}$$

Therefore, (11) can be written as,

$$\text{BER}_{\zeta^2>0} = \frac{1}{2} \left[Q\left(\frac{\chi - \eta}{\sqrt{1 + \chi\zeta^2}\sigma}\right) + Q\left(\frac{\eta}{\sigma}\right) \right] \tag{15}$$

η is the threshold value for detection of signal at the receiver’s end and is presumed to be a random number.

4 Results and Discussion

Figure 3 shows channel gain versus $\Omega_{1/2}$ and it can be observed that the maximum channel gain is observed when $\Omega_{1/2}$ is 54° . Figure 4 shows channel gain versus order of the Lambertian emission where $\zeta = 2$. It is observed that the channel gain reaches its maximum value when the value of $m = 5$. Since BER is inversely proportional to the channel gain, it is observed that BER will be least at these values (Table 1).

Figure 5 shows BER versus channel gain where $P = 55$ dBm. Figure 5 shows an initial decrease in BER as the channel gain increases, but BER stabilizes with a further increase in channel gain.

For $h = 8 \times 10^{-6}$.

Considering the values in Table 2, it can be noted that for a constant channel gain (h), BER is directly proportional to ζ .

Table 3 shows the values of BER for ζ for $\eta = 2$. It is noted that BER is directly proportional to ζ just as the observation in Table 2. Figure 6 shows BER versus η , where the coordinates of the photodiode (p, q, r) are (2 m, 2 m, 1.5 m), and the coordinates of LED (x, y, z) are (2.5 m, 2.5 m, 3 m). It can be observed that BER reaches a valley value for a particular η . This is known as the optimum detection threshold (η^*).

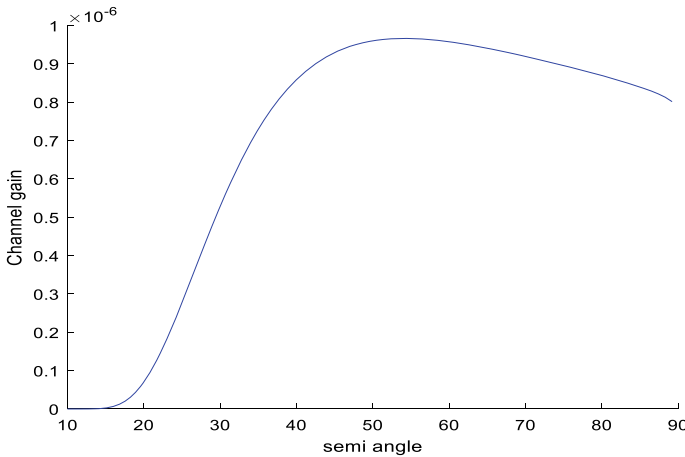


Fig. 3 Channel gain versus $\Omega_{1/2}$

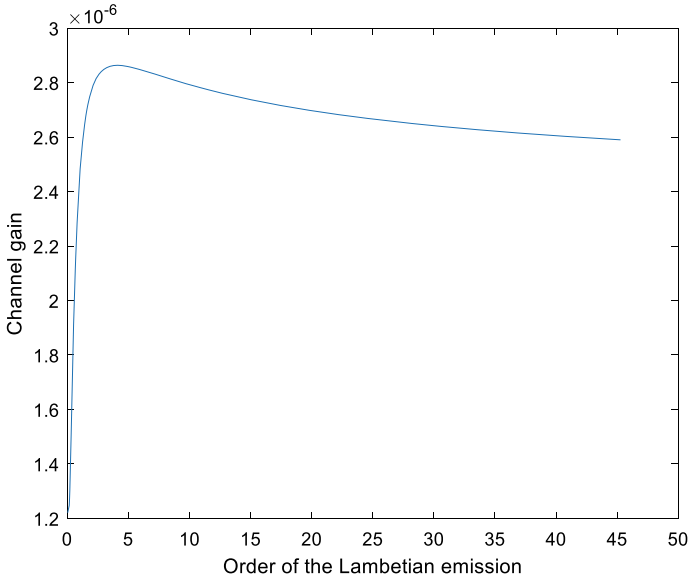


Fig. 4 Channel gain versus m

Table 1 Parameters used

Parameters	Symbol	Value
Room size	$J \times K \times L$	$5 \times 5 \times 3$ m
Physical area of PD	A	0.1 cm^2
Standard noise variance	σ	1
Opto-electronic conversion factor	o	0.9

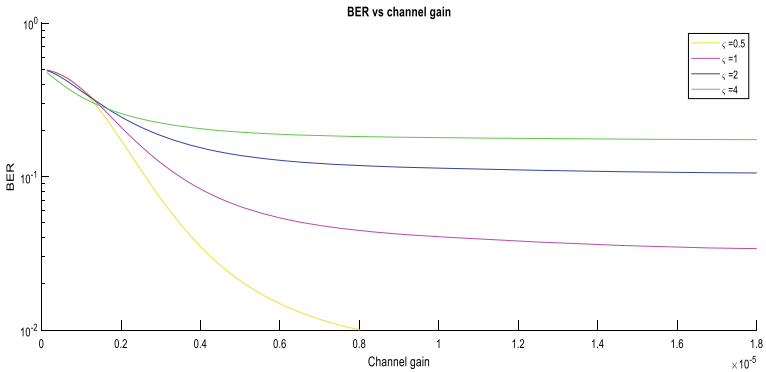


Fig. 5 BER versus channel gain (h)

Table 2 BER values for various ζ

σ	BER
0.5	0.0010
1	0.0444
2	0.1177
4	0.1821

Table 3 BER values for various ζ keeping $\eta = 2$

ζ	BER
0.5	0.0313
1	0.0789
2	0.1502
4	0.2033

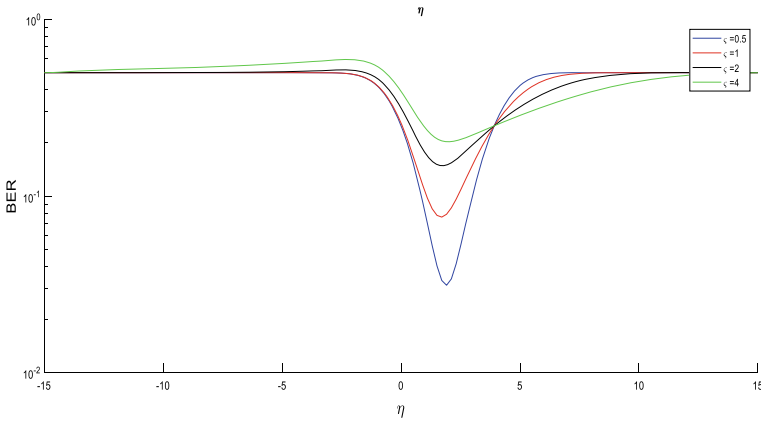


Fig. 6 BER versus η

5 Conclusion

In this paper, it is observed that the value of the Lambertian emission between 0 and 5 gives the highest channel gain and hence the minimum BER. Thus, the value of the semi-angle at half power of the LED ($\Omega_{1/2}$) is found to be 54° .

References

1. Rajagopal S, Roberts RD, Lim SK (2012) IEEE 802.15. 7 visible light communication: modulation schemes and dimming support. *IEEE Commun Mag* 50(3):72–82
2. Idris S, Mohammed U, Sanusi J, Thomas S (2019) Visible light communication: a potential 5G and beyond communication technology. In: 2019 15th international conference on electronics, computer and computation (ICECCO). IEEE, pp 1–6
3. Viriyasitavat W, Yu SH, Tsai HM (2013) Short paper: channel model for visible light communications using off-the-shelf scooter taillight. In: 2013 IEEE vehicular networking conference. IEEE, pp 170–173
4. Wu L, Shen Y, Zhang Z, Dang J, Liu H, Wang J (2019) Receiver algorithms for single-carrier OSM based high-rate indoor visible light communications. *IEEE Trans Wireless Commun* 19(2):1113–1126
5. Tzikas AE, Sahinis A, Tsvlakis SE, Tegos SA, Diamantoulakis PD, Karagiannidis GK (2019) 3-color shift keying for indoor visible light communications. *IEEE Commun Lett* 23(12):2271–2274
6. Pathak PH, Feng X, Hu P, Mohapatra P (2015) Visible light communication, networking, and sensing: a survey, potential and challenges. *IEEE Commun Surv Tutor* 17(4):2047–2077
7. Nauryzbayev G, Abdallah M, Elgala H (2018) On the performance of NOMA-enabled spectrally and energy efficient OFDM (SEE-OFDM) for indoor visible light communications. In: 2018 IEEE 87th vehicular technology conference (VTC Spring). IEEE, pp 1–5
8. Ji H, Qiao S, Zhang T (2019) A MISO-VLC system based on LACO-OFDM and superposed constellation demodulation. In: 2019 9th international conference on information science and technology (ICIST). IEEE, pp 294–298
9. Zeng L, O’Brien D, Le-Minh H, Lee K, Jung D, Oh Y (2008) Improvement of data rate by using equalization in an indoor visible light communication system. In: 2008 4th IEEE international conference on circuits and systems for communications. IEEE, pp 678–682
10. Lin SH, Liu C, Bao X, Wang JY (2018) Indoor visible light communications: performance evaluation and optimisation. *EURASIP J Wirel Commun Netw* (1):228
11. Lapidoth A, Moser SM, Wigger MA (2009) On the capacity of free-space optical intensity channels. *IEEE Trans Inf Theory* 55(10):4449–4461

An Automatic Self-sufficient Irrigation System Using Microcontrollers



Varun Singh Chauhan, Ruchira Singla, and Pallavi Choudekar

Abstract Irrigation system has a big contribution in the development of horticultural yields, landscape development, and revegetate dismayed soils in dry zones or during poor rainfall. Water system likewise has different uses in crop creation, including frost protection, stifling weed development in grain fields and preventing soil erosion. This paper proposes an automatic irrigation system which senses the content of moisture in the soil and accordingly turns the pump motor ON/OFF for a certain period of time. The proposed system reduces the water wastage and reduces the human intervention. To develop the prototype, the 8051 microcontrollers have been programmed, and it receives input signal from the sensor of varying moisture conditioning of the soil. The system uses a electrical energy generated by the photovoltaic panel to energize the devices. After receiving the signal, the microcontroller gives an output that drives a relay which is used for operating the water pump for a fixed period. This is linked directly to the timer section of microcontroller. The status of the soil and water pump is displayed on the LCD which is interfaced to the microcontroller

Keywords Renewable energy sources · Solar panel · Microcontrollers · Resource optimization · Moisture sensor · Arduino

V. S. Chauhan (✉) · R. Singla · P. Choudekar
Electrical and Electronics Engineering Department, Amity University Noida, Noida, Uttar Pradesh, India

e-mail: volk.4197@gmail.com

R. Singla

e-mail: er.ruchiragarg@gmail.com

P. Choudekar

e-mail: pallaveech@gmail.com

1 Introduction

The farming sector of Indian economy provides roughly 70% of all employment in the Indian economy while only accounting for less than 30% of GDP of the whole country, compared to the farming employment rates in developed countries, the employment provided is very less for roughly the same percentage of GDP. Also, all developed countries have higher produce per person than Indian farmers. They achieve it by a combination of both biotechnology and automation. They use harvesters to harvest the crops and bio-engineered crops resistant to pests while providing higher produce. Such automation may not be possible in India currently due to lack of capital, but some sectors where automation is feasible must be pursued so as to ease every bit of strain on the farmers as possible. In this paper, simplistic automation of irrigation of crops by using a automatic irrigation system is done that is cheap and self-sufficient by means of a solar tracking solar panel that is used to power the electronics and batteries for the pump.

The automatic irrigation system is designed and accomplished by using a moisture sensor that tests the level of moisture of soil and relays the info to the Arduino board. This Arduino board compares it to a pre-set threshold value and accordingly decides to turn pump or solenoid valve in case of sprinklers ON. The entire setup is very cheap and very flexible; the pre-set value can be changed according to the crop to be irrigated.

The system is made self-sufficient by use of a solar tracking solar panel that reduced the heavy cost of a larger solar panel by increasing the efficiency of a cheaper smaller solar panel by orienting it according to the direction of sun.

The main goals of this project are to:

- Propose, design and construct a system that automates the tedious and continuous task of irrigation.
- Make the system cost effective and flexible to accommodate needs of various crops and farmers.
- Make it feasible in the rural areas where the supply of power may not be guaranteed at all times.
- Make the system self-sufficient and not too tacky such that an average farmer might be intimidated by it.
- To be able to make use of systems already in place for irrigation.

2 Literature Review

In [1], the authors have designed a solar tracking device which can harvest more power and provides better efficiency by keeping the panel at a right angle to the sun rays. The work presented in [2] defines the method used in traditional irrigation system. The proposed system not only provides a low-cost solution but is very effective in the

sense that it saves water up to 80% as compared to the traditional irrigation practices applied in the agriculture.

The design in [3] presents an automated irrigation system by using different controlling parameters such as temperature, soil moisture and air humidity. These are the important parameters which need to be controlled especially in case of precision agriculture. A simple four-electrode conductivity sensor is used in [4] for the automatic logging of soil water.

In [5], the work is done on automatic irrigation system in which the sensor senses the soil moisture content, and there is an automated mechanism to turn ON or OFF the pumping motor. Arduino board ATmega328 microcontroller collects the input signal of changeable moisture circumstances of the soil via moisture detecting system. In [6], an automatic plant irrigation system using ATMEGA microcontroller is discussed.

3 System Operation

The automatic irrigation system comprises mainly of a moisture sensor that is buried deep in soil which is the target area of irrigation. This soil sensor's output is connected to the analog in pin (A0) of the programmed Arduino board that compares it to the pre-set value for desired moisture provided. If the received input for moisture content is lower than the threshold pre-set, it turns the pump motor ON, or in case of sprinkler system, solenoid valve operates that begins the watering process until the moisture level is of desired quantity. Schematic is shown in Fig. 1.

The Arduino board is powered by a 5 V solar tracking solar panel to ensure self-sufficiency of electronics, but if the motor needs to be operated too, a bigger solar panel may be used or a different panel may be utilized for charging battery of motor or solenoid valve.

The solar tracking solar panel (supply unit for AIM) utilizes two LDR sensors that are placed such that they have very little overlap area where they both receive equal amount of light. When both the LDR receive same amount of light, their resistance becomes same. Based on this concept, this voltage through each LDR is sent to the L293D IC that compares them and acts it by sending signal to the 555IC on the side of LDR receiving less light to actuate the motor to rotate in the direction that it gets just enough light to maintain the balance between the two LDR, and this is used to orient the solar panel towards the sun. Solar tracking schematic is shown in Fig. 2.

4 Components

1. Light-Dependent Resistor

These are variable resistors whose resistance can range from Mega ohms to just several ohms depending on the amount of light they receive and in different

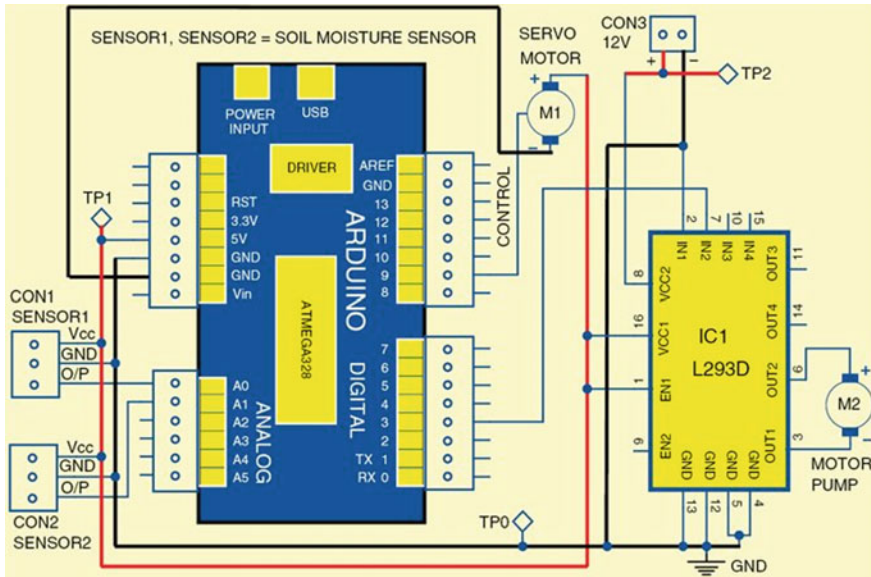


Fig. 1 Schematics of irrigation module

cases the wavelength of the light they receive. When light falls on the LDRs, the electrons from the outermost shell get enough energy to cross the energy gap and go from valence bond to conduction bond, thus becoming available for conduction; this forms holes and electrons in the medium, thereby lowering resistance. It can be said as a sub-type of photocell. Some examples include cadmium sulphide cells, etc.

2. Moisture Sensor

These sensors are moisture sensors typically employed to measure the volumetric content of water in soil without the lengthy process of physical tests on soil sample. They measure it live and using properties of soil like soil resistivity, etc. More complex soil sensors can utilize microwaves to measure moisture content or using soil water as an electrolyte in a galvanic cell-type phenomenon.

3. IC L293D

L293D is a typical motor driver or motor driver IC which allows DC motor to drive on either directions. L293D is a 16-pin IC which can control a set of two DC motors simultaneously in any direction.

4. 555 timer IC

The 555 timer IC is an integrated circuit chip used in a variety of timer, pulse generation and oscillator applications. The 555 can be used to provide time delays, as an oscillator, and as a flip-flop element.

5. Arduino Microcontroller

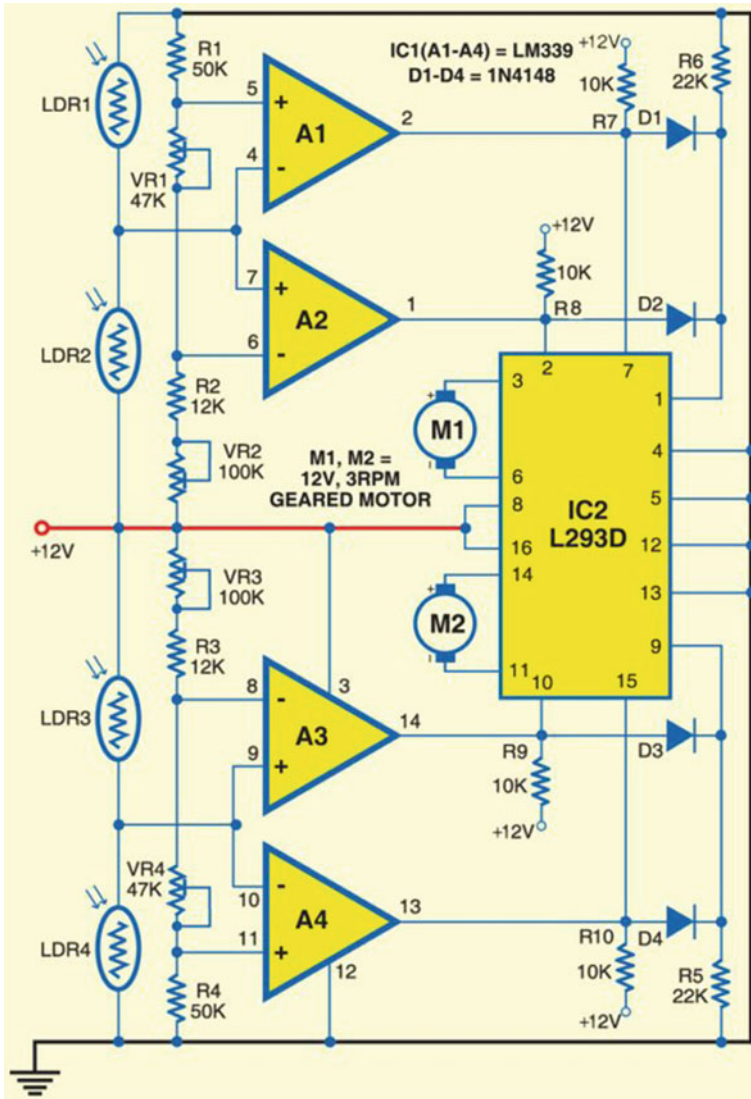


Fig. 2 Solar tracking schematics

It is an open-source, relatively cheap and very versatile atmega382p microcontroller-based chip system that can be programmed within the pre-installed boot loader using Arduino IDE software. The programming language being a derivative of C and C++ is easy to learn for beginners and makes the Arduino to become very versatile. It can accept both digital and analog inputs and can interface with a wider range of electronics that can further add to its versatility. The Arduino accepts the inputs from the soil moisture sensor and

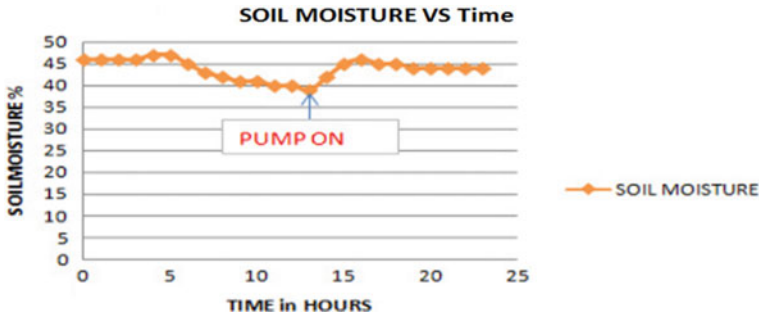


Fig. 3 Operation of pump

compares it the present interval of moisture levels and then accordingly turns water supply ON or OFF via motor pump or solenoid valve.

5 Results

The solar panel tracks the sun and powers the automatic irrigation system that senses the moisture and soil and operates the pump if the moisture content is below the threshold value (Fig. 3).

Its main advantages over the traditional watering systems are as given below

- It can prevent over watering that can cause plants to die
- It increases efficiency of irrigation per volume of water used
- It can check soil erosion caused by extreme over watering
- It can ensure uniformity in irrigation by use of multiple moisture sensors or distributed moisture sensors spread evenly across a field
- It can monitor rate of drying of soil and be used in DAQ systems
- It can reduce labour costs and labour requirement for irrigation.

6 Conclusion

This research paper proposes designs and constructs an automatic irrigation system powered by a solar tracking solar panel that can reduce the wastage of water and is self-sufficient to be installed in rural areas. Its threshold value can be set according to irrigation requirements of various plants.

While the common fixed solar panel has an efficiency of about 39%, the use of solar tracker can increase the amount of power collected by the solar panel to about 70% and more than that in case of solar panels that track the sun in more than one axis. Therefore, this project utilizes this clean source such that the smaller size of panel thus required can be used to power the automatic irrigation system sufficiently

while also reducing the heavy cost of a larger panel that is fixed for same amount of energy. Solar tracking was made possible with use of PIC16F84A microcontroller. The PIC based on the information received about the area of maximum illumination in form of increased power flow through light-dependent resistor moves the panel to face that direction completing the process of solar tracking by using components and gear DC motors, which allow for a dependable and accurate movement to face the sun. This methodology for solar tracking was adopted because of the bell curve nature of solar energy which was unsuitable and weak compared to requirement of pump. The energy that would be required to run pump based on solar panel directly would require a larger solar panel; hence, a rechargeable battery is used as an intermediate to run pump motor.

The Arduino upon being powered up receives the information from soil moisture sensor about the amount of moisture in soil and compares it to the threshold value; if it is less than the said value, it activates the pump motor to water the plant until it exceeds threshold value set by the user as required by needs of various crops. The entire system is self-sufficient and optimizes the irrigation of plants which is considered a labour-intensive and meticulous task and accomplishes it a low cost with enough flexibility to accommodate a wide range of irrigation situations. Solar power is used as it does not need to operate at night when there is no photosynthesis and during rainy days when irrigation is not required, besides its availability in remote areas.

References

1. Rizk J, Chaiko Y (2008) Solar tracking more efficient use of solar panels. *World Acad Sci Eng Technol* 41
2. Haikwad PS (2018) Advancing in agro industrial field. *Int J Comput Appl Eng*, April 2018. ISSN 2321-3469
3. Chikankar PB, Das S, Mehtre D (2015) Automatic irrigation system using Zigbee in wireless sensor network. In: *ICPC 2015*
4. Skinner AJ, Lambert MF (2011) An automatic soil pore-water salinity sensor based on wetting front detector. *IEEE Sens J* 11(1):245–254
5. Branam RV, Karthikeyan M, Sasikala V (2016) Automatic irrigation system on sensing soil moisture content. *IRJET* 3(03)
6. Ganesh S (2013) CS efficient automatic plant irrigation system using ATMEGA microcontroller. *IJETEE* 7(1)

Performance Analysis of Smart PMSM Drive Using SVM Based 3-Level Neutral Point Clamped Inverter



Ratan Raju Ravela, Dharmendra Kumar Singh, and Jay Singh

Abstract In this paper, a different switching sequences using Space Vector Pulse Width Modulation (SVPWM)-based 3-level Neutral Point Clamped Inverter (NPCI) for permanent magnet synchronous motor (PMSM) drive is proposed. The proposed technique decreases the switching sequences number of converter compared to existing strategy. This method provides less THD and good dynamic response when it is put in to PMSM drive. Nowadays, 3-L NPCI has renowned influence in area of medium voltage high-power requirement. The various waveforms are compared with SPWM. The analysis of speed and torque for PMSM drive are simulated in MATLAB simulink.

Keywords Neutral point clamped inverter · Permanent magnet synchronous motor · SVPWM · Sinusoidal pulse width modulation · THD

1 Introduction

Multi-level inverters emerged as an interesting choice for high power and medium voltage applications [1]. Figure 1 shows inverter classification based on different topologies. For recent years, multi-level inverter is widely used because of better harmonic spectrum and high attainable voltage [2]. It reduces high voltage and current change rate due to peak voltages and other short comings in conventional inverter. The structure of 3-L NPCI topologies gives desirable characteristics such as lower

R. R. Ravela · D. K. Singh (✉)
Department of Electrical and Electronics Engineering, Noida Institute of Engineering & Technology, Greater Noida, UP, India
e-mail: er.dksingh1994@gmail.com

R. R. Ravela
e-mail: ratnamwait@gmail.com

J. Singh
Department of Electrical and Electronics Engineering, GL Bajaj Institute of Technology & Management, Greater Noida, UP, India
e-mail: jaysinghism@gmail.com

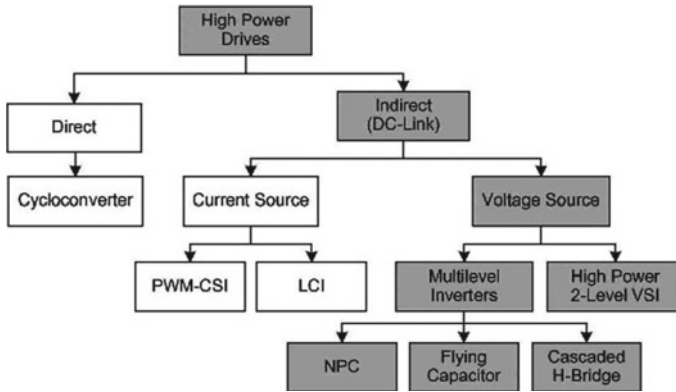


Fig. 1 High power converter classification

switching losses, higher efficiency, and negligible electromagnetic interference [3]. Therefore, it is widely used in industry and become hot spot of power electronic drives [4].

For variable speed drives, SVPWM is the most popular among other pulse with modulation (PWM) techniques. SVPWM leads in digital realization and stronger utilization of dc bus [5]. This implementation involves identification of sector, time of switching calculation, and optimum switching sequence of voltage vectors for inverter [5, 6]. This can be achieved by coordinate transformation and look up table.

The main aspect of variable frequency drive (VFD) used in industrial application is PMSM, which run by 3-L NPCI due to its high reliability and productivity [7]. Because of the advancement in power electronic technology, high performance smart digital processor enhances new application to PMSM. internet of things (IOT)-based PMSM are getting popular nowadays. Smart PMSM is used in exhaust gas recirculation, electric throttle control, and variable nozzle turbine. Nowadays smart PMSM used in motion control are designed with SVPWM, field orientation control methods [8]. In this paper SVPWM-based 3-L NPCI PMSM drive analyzed over SPWM scheme of 3-L NPCI.

1.1 Neutral Point Clamped Inverter

In high-power application, 3-L NPC voltage source inverter has significant advantage over 2-L voltage source inverter in two ways [7]. One is it double the power rating, second improves the quality of output by reducing harmonics [9]. The conventional 3-L NPCI topology structure is shown in Fig. 2 [4]. It has two capacitors C_1 , C_2 which provide two identical DC voltages and diodes will provide clamp level. The three level output of each bridge arm is $+V_{dc}/2$, 0 , $-V_{dc}/2$, where $V_{dc}/2$ is DC voltage [10, 11]. The three types of potentials on DC side, respectively, are P, O, and N. In

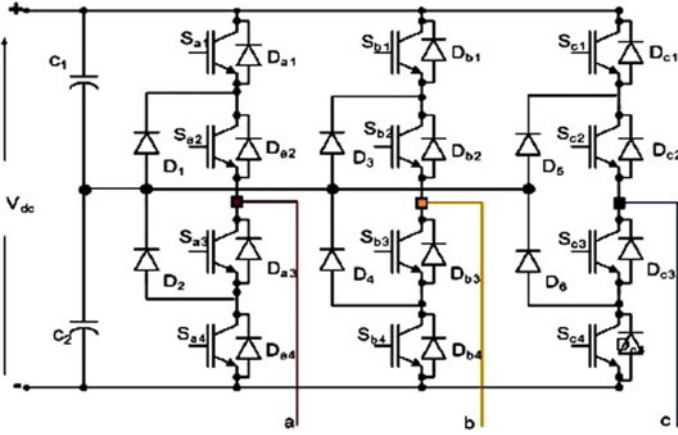


Fig. 2 3-L NPC inverter circuit diagram

2-level conventional inverter has eight ($n^3 = 2^3$ where n is number of level) switching states where as 3-L inverter has twenty-seven ($3^3 = 27$ where n is number of level) switching states with 19 voltage vectors which decides their output is shown in Fig. 3 [12].

Voltage vectors are partitioned into four groups per their magnitude. Figure 3 shows three zero voltage vector, twelve small voltage vectors, six medium voltage vectors, and six long voltage vectors. The long voltage vectors with V_{dc} magnitude responds to vertices of outer hexagon, the medium voltage vector with $2 V_{dc}/\sqrt{3}$ locates an angle bisector of each 60° sector. The short vectors with $V_{dc}/2$ magnitude

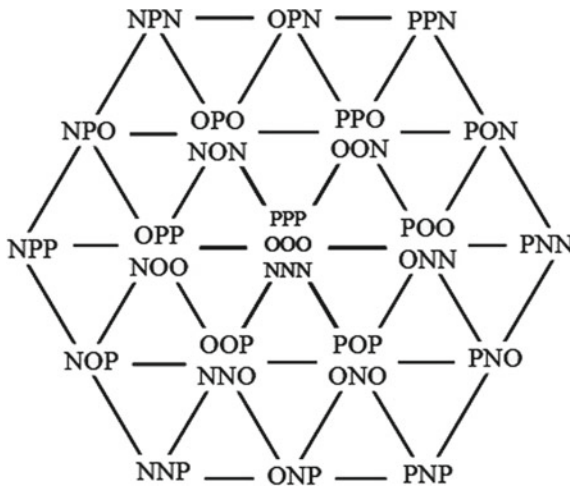


Fig. 3 Space vector diagram of three levels inverter

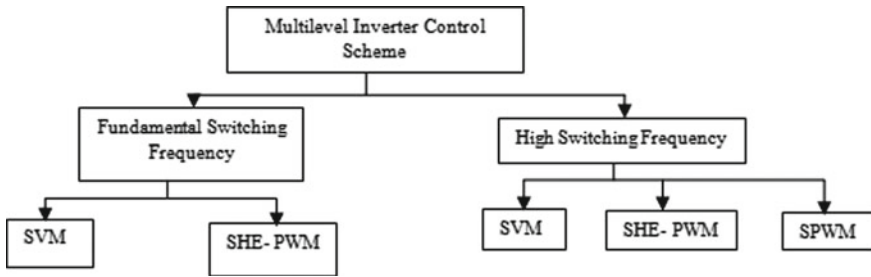


Fig. 4 Classification of multilevel inverter modulation techniques

are in inner vertices of inner hexagon. Neutral point current does not affect by both long and zero vectors. Symmetry of space vectors compensate the voltage imbalance created by medium vectors [12].

1.2 PWM Techniques

The PWM technique is the most superior to control the inverter voltage. From fixed DC voltage, we can obtain controlled output voltage by proper switching periods of 3-L NPC inverter. Energy delivered to motor by PWM inverter is achieved by controlling the train of PWM control circuitry [12]. Figure 4 shows classification of modulation techniques used in multilevel inverter. The quality of PWM techniques depends on many parameters such as harmonic content in inverter output and amplitude of fundamental components [13]. To control output voltage, reduce harmonic content most useful methods are SPWM and SVPWM.

1.3 Sinusoidal Pulse Width Modulation

For 3- ϕ PWM inverter, switching pulses are created after comparing balanced 3-phase sinusoidal reference voltages having high frequency common triangular with carrier voltage signal in SPWM [14]. Turn on and turn off times are decided by intersection of reference voltage signals with triangular carrier signals. A better sinusoidal output can be obtained by either varying amplitude, frequency of reference voltage, or by high switching frequency [15, 16]. SPWM scheme is more flexible and simple to implement, however, it has fundamental component maximum peak is restricted to 50% of DC link voltage. Further extension of the SPWM method is difficult due to over modulation range.

1.4 Space Vector Pulse Width Modulation (SVPWM)

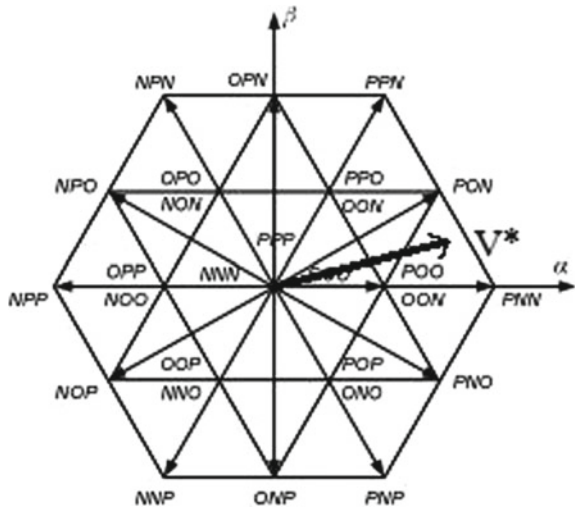
The SVPWM provides more fundamental voltage and reduces harmonic over SPWM method. This method is most suitable for adjustable speed drives. The output of SVPWM is 27.3% greater than SPWM in terms of its fundamental values [17]. It uses a rotating synchronous reference frame. In order to implement SVPWM reference frames from abc to $\alpha\beta$ transformation to be done [18]. Nowadays research work is directing towards simplification of modulation methods, reduction of capacitor voltage of dc link.

3-L NPCI PMSM with SPWM scheme is discussed first in the second section of this paper, section-III dealt with SVM technique. Three levels NPCI PMSM drive with SVM has better dynamic performance with change in load conditions over SPWM employed drive due its robustness [19].

2 Working Principle of SVM Method

SVM method uses volt-time balance to calculate duty cycles for different switching state vectors. Primary task is to determine the reference voltage vector V_{ref} which lies in small triangles of a big sector. As mentioned earlier, switching state for three levels has 27 ($n^3 = 3^3$ where n is number of level), which generates 19 different voltage vectors [20]. Figure 5 shows the closet vector from where reference vector is generated as below.

Fig. 5 Space vector modulator for 3-L inverter



$$v^* = \vec{v} = \frac{1}{T_s} [V_1 t_1 + V_7 t_7 + V_{13} t_{13}] \tag{1}$$

$$T_s = t_1 + t_7 + t_{13} \tag{2}$$

where v^* (or) \vec{v} is mean value of load voltage, T_s is the modulation period, V_1, V_7 and V_{13} are application vectors with time t_1, t_7 and t_{13} , respectively. By calculating these times with the help of volt-time balance we will get below equation [21]

$$\vec{V} = \frac{1}{T_s} [V_{aN} + aV_{bN} + a^2V_{cN}] \tag{3}$$

where $a = e^{j2\pi/3}$, V_{xN} = Phase voltage.

These vectors generate pulses for 3-L inverter. Some have redundant switching states so can generate more than a single switching state [22]. Switching timing of each vector in sector-1 are shown in Table 1. Figure 6 shows sequence of switching patterns in each sub sector based on arrow head direction.

Table 1 States of switching of 3-L inverter

Switching symbols	Switching states				Output voltage
	S11	S12	S13	S14	
P	ON	ON	OFF	OFF	$+V_{dc}/2$
O	OFF	ON	ON	OFF	0
N	OFF	OFF	ON	ON	$-V_{dc}/2$

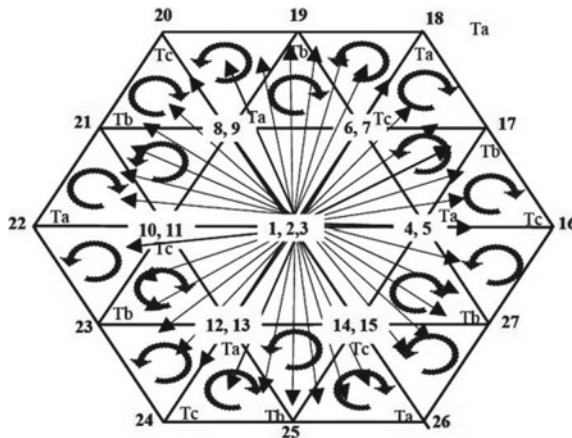


Fig. 6 Switching patterns of 3-L inverter

3 Simulation Results

PMSM is used in industrial drives widely because of its high efficiency, high reliability, and dynamic performance. 3-L NPCI is very effective for medium voltage and high-power applications. So, in this paper, dynamic behavior of PMSM for SPWM and SVPWM with load variations are discussed (Fig. 7).

The simulation results of NPC inverter controlled PMSM drive for both SVPWM and SPWM are presented that results in good dynamic response for SVPWM method when load and speed variations applied. Figure 8 shows MATLAB Simulink diagram of PMSM with SVM algorithm.

3.1 Sinusoidal PWM

For 3-L NPC inverter permanent magnet synchronous motor phase as well as line voltages are shown in Figs. 9 and 10, when load torque is changed from 2 N-m to 22 N-m at 0.6 s in SPWM method was applied. With more distortions at starting and the THD values for line to line and phase voltage of PMSM drive are 36.61% and 55.44%, respectively. For same load torques changes, Fig. 11 shows rotor speed, rotor angle and electromagnetic torque variations.

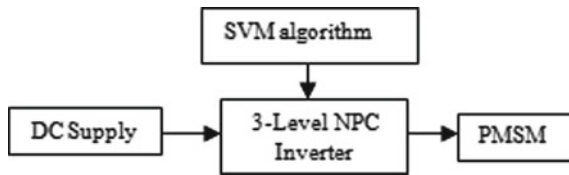


Fig. 7 Block diagram of PMSM controlled by 3-L NPC inverter

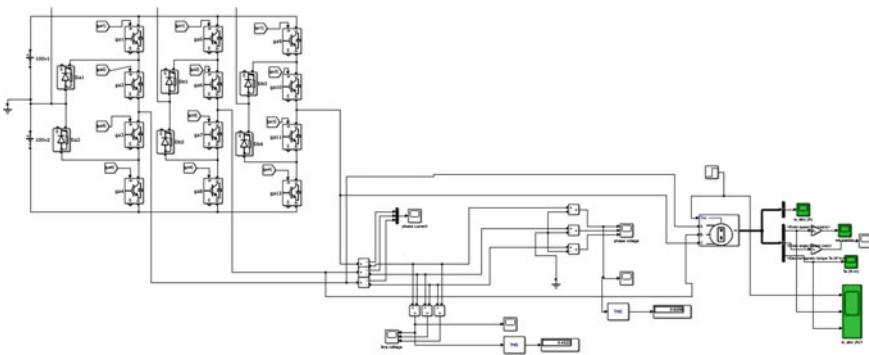


Fig. 8 Simulation diagram of proposed work

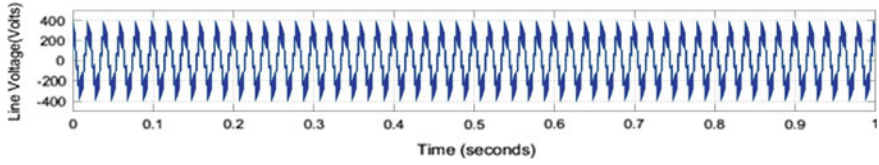


Fig. 9 Line to line voltage of 3-L NPC PMSM drive

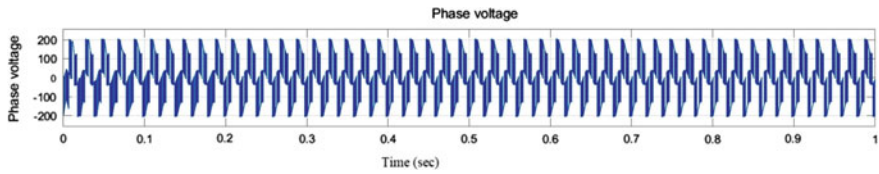


Fig. 10 Phase voltage of 3-L NPC PMSM drive

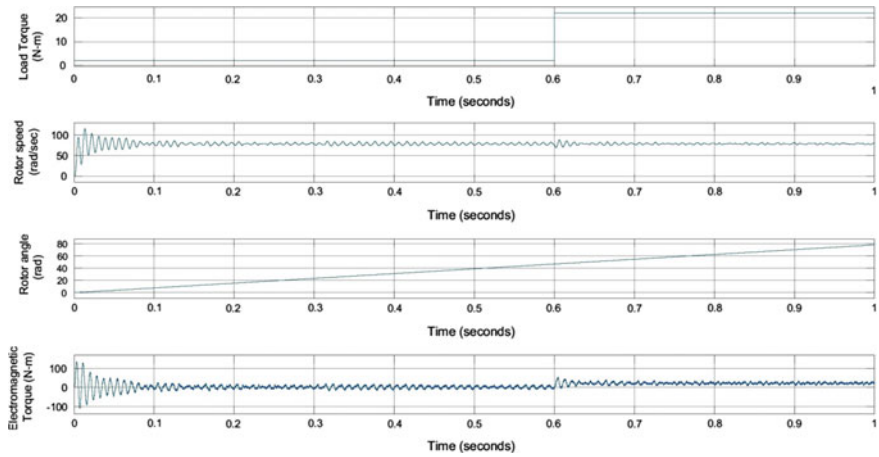


Fig. 11 Load torque, rotor speed, rotor angle, and electromagnetic torque of PMSM

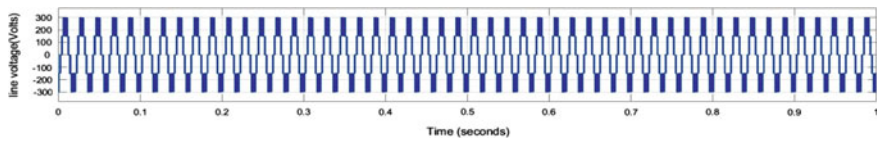


Fig. 12 Line voltage waveform of PMSM drive for SVM scheme

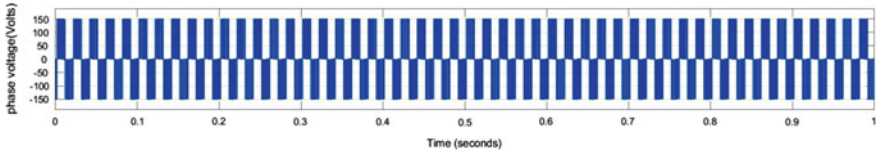


Fig. 13 Phase voltage waveform of PMSM drive for SVM scheme

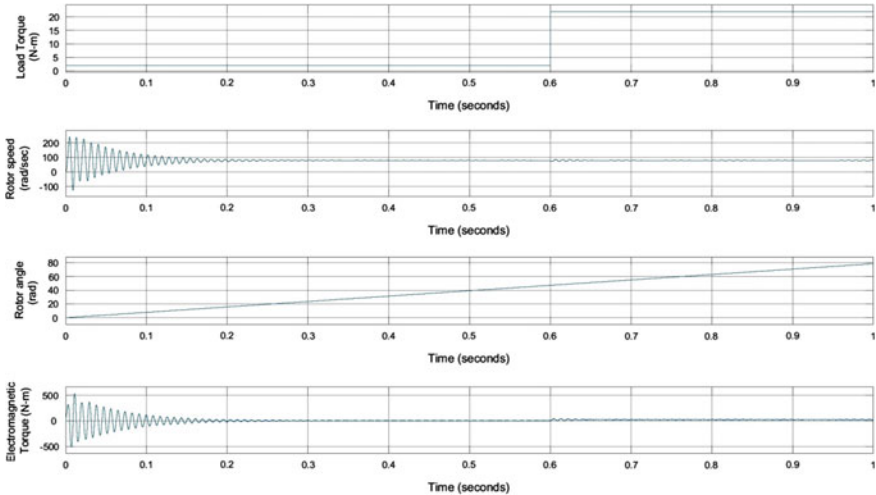


Fig. 14 Load torque, rotor speed, rotor angle, and electromagnetic torque of PMSM with SVM scheme

3.2 Space Vector PWM

Line to line as well as phase voltages of 3-L NPCI PMSM are shown in Figs. 12 and 13, when load torque varied from 2 N-m to 22 N-m at 0.6 s in SVM method was applied. The THD values for line to line, phase voltage of PMSM drive are 31.56% and 52.45%, respectively. It has fewer distortions at starting over SPWM method. For same load torques changes, Fig. 11 shows rotor speed, rotor angle, and electromagnetic torque variations (Fig. 14).

4 Conclusion

This paper provides control strategy and mathematical model of smart PMSM drive with SVPWM-based 3-level neutral point clamped inverter. The dynamic response corresponding to speed and torque are very important for any industrial and automation applications. The PMSM is the best suitable for automation because of its good

speed control feature even at variable load, therefore the speed and torque variations are relatively less corresponding to load change. From MATLAB Simulink results, we observed that SVPWM method shows better performance compared to PWM both dynamically as well as steady state conditions. This topology result in a good dynamic response and less THD with less number of converter switching sequences applied to 3-L NPC inverter PMSM drive.

References

1. Rodriguez J, Bernet S, Steimer PK, Lizama IE (2010) A survey on neutral point clamped inverters. *IEEE Trans Ind Electron* 57(7):2219–2230
2. Lai JS, Peng FZ (2002) Multilevel inverters: a survey of topologies, controls, and applications. *IEEE Trans Ind Electron* 49(4):724–738
3. Bose BK (2002) *Modern power electronics and AC drives*. Prentice-Hall, Upper Saddle River
4. Yamanaka K, Hava AM, Kirino H, Tanaka Y, Koga N, Kume T (2002) A novel neutral point potential stabilization technique using the information of output current polarities and voltage vector. *IEEE Trans Ind Electron* 38:1572
5. Gupta AK, Khambadkone AM (2006) A space vector, PWM scheme for multilevel inverters based on two-level space vector PWM. *IEEE Trans Ind Electron* 53(5)
6. Seo JH, Hyun DS (2001) A new simplified space-vector PWM method for three-level inverters. *IEEE Trans Power Electron* 16(4)
7. Chen C, Ye Y (2012) Research on vector control of PMSM based on three-level NPC inverter. *IEEE Trans Ind Electron* 58(4):854–858
8. Marchland C, Razek A (1993) Optimal torque operation of digitally controlled, permanent magnet synchronous motor drives. *Proc IEEE Control Theory Appl* 140(3):232–240
9. Singh B, Chandra A, Al Haddad K, Power quality: problems and mitigation techniques, 1st edn. Wiley, Hoboken
10. Celanovic N, Boroyevich D (2000) A comprehensive study of neutral-point voltage balancing problem in three-level neutral-point-clamped, voltage source PWM inverters. *IEEE Trans Power Electron* 15
11. Nabae A, Takahashi I, Akagi H (1981) A new neutral-point-clamped PWM inverter. *IEEE Trans Ind Appl* 17:518–523
12. Zhu C, Zeng Z, Zhao R (2017) Comprehensive analysis and reduction of torque ripples in three-phase four-switch inverter-fed PMSM drives using space vector pulse-width modulation. *IEEE Trans Power Electron* 32(7), 5411–5424
13. Pou J, Pindado R, Boroyevich D, Rodriguez P (2008) Evaluation of the low-frequency neutral-point voltage oscillations in the three-level inverter. *IEEE Trans Ind Electron*
14. Hari M, Verma A, Halakurki RR, Ravela RR, Kumar P (2018) A dynamic analysis of SVM based three-level, NPC for a 3-phase, induction motor. In: 2018 International conference on power energy, environment and intelligent control (PEEIC)
15. Zou Y-Y, Hsu H-J (1997) FPGA realization of space-vector PWM control IC for three-phase PWM inverters. *IEEE Trans Power Electron*
16. Jahns TM, Soong WL (1996) Pulsating torque minimization techniques for permanent-magnet ac motor drives—a review. *IEEE Trans Ind Electron* 43
17. Steinke JK (1992) Switching frequency optimal PWM control of a three level inverter. *IEEE Trans Power Electron* 7
18. Holmes DG, Lipo TA (2003) *Pulse width modulation for power converters, principles and practice*. Wiley-Interscience and IEEE Press
19. Abu-Rub H, Holtz J, Rodriguez J, Baoming G (2010) Medium voltage multilevel converters—state of the art, challenges, and requirements in industrial applications. *IEEE Trans Ind Electron* 57(8):2581–2596

20. Xia C, Shi T (2013) A novel direct torque control of matrix converter-fed PMSM drives using duty cycle control for torque ripple reduction. *IEEE Trans Ind Electron* 61(6):2700–2713
21. Rodriguez J, Franquelo LG, Kouro S, Leon JI, Portillo RC, Prats MA, Perez MA (2009) Multilevel converters: an enabling technology for high-power applications. *Proc IEEE* 97(11)
22. Zhang J (1995) High performance control of a three-level IGBT inverter fed ac drive. In: *Proceedings of the IEEE IAS conference*, pp 22–28

Performance Analysis of Indoor Visible Light Communication System Using NRZ-OOK Modulation Technique



Mohd Faheem, Indra Kumar Verma, Prakhar Nag, Shivam Goswami, and Vinay Singh

Abstract Visible light communication (VLC) is one of the key areas in wireless communication. It has recently been acknowledged as an alternate to RF communication due to increased bandwidth and avoiding health-related impact of RF waves. In the paper, performance of Indoor visible light communication system is analyzed using NRZ-OOK as modulation technique on optisystem 16.1.0. The performance of indoor VLC system is improved using NRZ-OOK modulation in comparison with RZ OOK modulation. Simulation results depict that NRZ-OOK modulation provides optimized data rate of 1 Gb/s up to 6 m distance. BER is also reduced on applying the technique to 1.64851×10^{-15} bits per sequence.

Keywords Bit error rate (BER) · On–off-keying non-return to zero (OOK-NRZ) · Line of sight (LOS) · Visible light communication (VLC)

1 Introduction

Visible light communication system utilizes the wavelength spectrum from 380 to 780 nm, i.e., VLC spectrum. It is able to utilize for indoor wireless data transmission system with very high data rates. Indoor VLC system can be used for both illumination and communication [1]. VLC system uses LED as a transmitter, air as a transmission medium and photodiode uses as receiver. The main key benefit of visible light communication is that it does not interfere with radio frequency signals. This made visible light communication to be used at hospitals, airplanes, underwater communication vehicular-to-vehicular communication and space stations. The main features that increase the usage of visible-light communication for different applications are security, simple implementation procedures, and license free band characteristics [2].

M. Faheem · I. K. Verma (✉) · P. Nag · S. Goswami · V. Singh
Department of Electronics and Communication Engineering, Galgotias College of Engineering and Technology, 1, Knowledge Park II, Greater Noida, Uttar Pradesh 201306, India
e-mail: indraverma1304@gmail.com

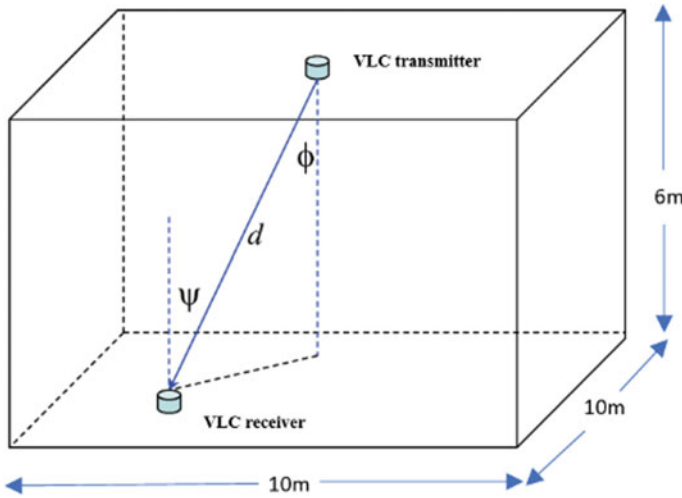


Fig. 1 LOS propagation model

The paper consists of the following segments. A brief introduction to VLC system is mentioned in Sect. 1. Indoor system model is mentioned in Sect. 2. Block diagram of the proposed system is mentioned in Sect. 3. The proposed simulation setup of the system along with results and discussion is included in Sect. 4.

2 Indoor VLC System Model

The specific room model with dimension of $10 \times 10 \times 6 \text{ m}^3$ is shown in Fig. 1 where single LED transmitter and photodetector are shown below. LOS signal is transmitted from LED source and received by the photodetector. Path d is for LOS channel [3].

3 Block Diagram of the Proposed System

The proposed system includes three blocks like transmitter block, LOS channel, and receiver block as shown in Fig. 2.

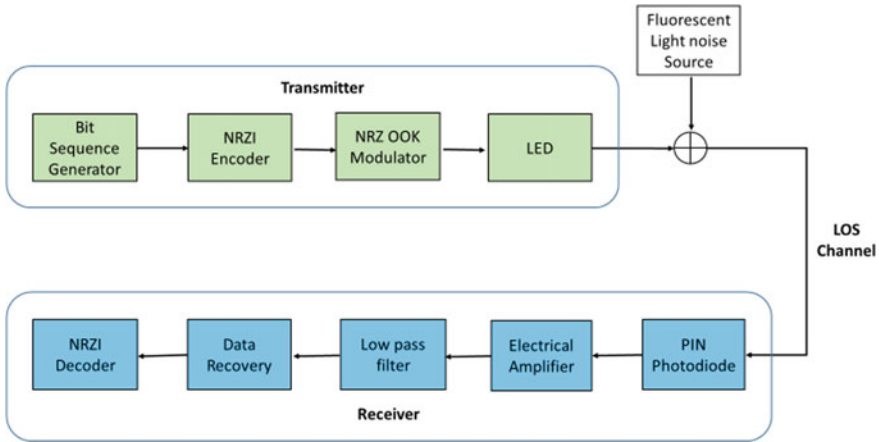


Fig. 2 Block diagram of the proposed indoor VLC system with optical back ground noise

3.1 VLC Transmitter

VLC transmitter utilizes white LED for the data transmission. The key advantages of white LEDs are consume less power, more brighter, low cost, less complexity, and long life duration over 50,000 h [4]. Mainly, two types of white LEDs are available in market, RGB LEDs and yellowish phosphor [5]. In this proposed work, phosphor-based white LED is used, which emits more light per watt.

3.2 Channel Modeling

The transmitter LED transmits the data in the form of light. The light transmitted over LOS channel model and the photodetector is used to receive the light from the LOS channel. The LOS channel model is used to achieve the higher data rate, lowest path loss, and dispersion. The total power of received optical signal from the transmitting LED source is shown by the equation below [3].

$$Pr = [H_{LOS}(0)]Pt + \sigma_{noise}^2 \tag{1}$$

where the direct gain (DC) is represented by $H_{LOS}(0)$ of LOS channels, the total power of receiver noise is represented by σ_{noise}^2 , which involves thermal noise, and shot noise is shown by the following equation below [3].

$$\sigma_{noise}^2 = \sigma_{shot}^2 + \sigma_{thermal}^2 \tag{2}$$

The shot noise variance induced by the fluorescent light source and signal, which is described in [6], is shown by the following equation below.

$$\sigma_{\text{shot}}^2 = 2qR(\text{Pr} + \text{Pn})B \quad (3)$$

where the charge on electron is represented by q , the responsivity of photodetector is represented by R , the power of received noise is represented by Pn , the total power of received optical signal is represented by Pr , and bandwidth of the receiver is represented by B .

$$\sigma_{\text{thermal}}^2 = 4KT/BR_f \quad (4)$$

where Boltzmann's constant is denoted by K , absolute temperature is denoted by T , and feedback resistance is represented by R_f [7]. LOS channel components have been used to design the FSO propagation model of indoor communication system. On the basis of half-angle of transmitter (source), the following equation is used to calculate the Lambertian order [3].

$$m = \frac{-\log_2}{\log[\cos(\varnothing_{1/2})]} \quad (5)$$

where the half power semi-angle of LED is represented by $(\varnothing_{1/2})$. The LOS channel DC gain is shown by the following equation below [8]

$$H_{\text{LOS}}(0) = \frac{A_r(m+1)}{2\pi d^2} \cos^m(\varnothing) \cos(\varphi) g(\varphi) \quad (6)$$

where active area of the receiver is represented by A_r and irradiance angle of LOS channel is represented by the angle \varnothing . The incidence angle of LOS channel at the receiver is represented by the angles φ , and the receiver's optical gain is represented by the $g(\varphi)$ which is shown by the following equation below [3].

$$g(\varphi) = \frac{n^2}{\sin^2(\varphi_{\text{FOV}})} \quad (7)$$

where refractive index of concentrator is represented by n .

3.3 VLC Receiver

At receiver side, signal is received by the photodetector. Generally, two types of photodiodes are used to receive optical signal such as PIN photodiode and avalanche photodiode. It converts detected light signal into electrical signal [5]. VLC receiver consists of electrical amplifier, low-pass filter, and data recovery. The received signal

is very weak. To amplify the received signal, an electrical amplifier is utilized; to eliminate undesired frequency components, low-pass filter is used, and to recover back the transmitted signal, data recovery is used [9].

4 Simulation Setup

The proposed VLC system simulation is done on optisystem 16.1.0 software. The optisystem is a tool which is used to simulate the system of optical communication and analyze the practical modeling of the optical components [10].

The transmitter consists of pseudo-random bit sequence generator operating at 1Gbit/sec, NRZI sequence encoder converts data one format to another format, and NRZ-OOK modulation is a simplest on-off-keying modulation. The operating wavelength of LED is 500 nm, and the bandwidth of modulation is 0.4 THz. The proposed system includes optical back ground noise. Thus, optical signal from transmitting LED source and optical back ground noise from fluorescent light source are received by the photodetector. To calculate the bit errors, BER analyzer is utilized. To define the interferences and signal distortion, eye diagram analyzer is utilized. Thus, the performance of indoor VLC system results obtained by simulation are analyzed.

Table 1 includes list of the parameter of components with values used for the optisystem simulation of the proposed indoor VLC systems using NRZ-OOK modulation. It contains the major parameters such as bitrate, size of the room, line of sight channel (channel distance, detection surface area, irradiance angle and incidence angle), LED wavelength, photodiode (responsivity, wavelength and bandwidth), gain of the electrical amplifier and cutoff frequency of the low-pass Bessel filter. The operating power of optical background light noise source is 22 W, and the frequency is 450THz. Thermal noise and shot noise are induced by transmitted optical signal and optical background light. The operating wavelength of LED is 500 nm, and bandwidth of the LED is 400 GHz. In this model to receive optical signal, silicon PIN photodiode is used having wavelength of 500 nm, bandwidth of 400 GHz, and responsivity of 0.2 A/W. Fluorescent lamp is used to generate optical background light noise having frequency of 450 nm, and power is 22 W. The simulated indoor visible light communication system using OOK-NRZ modulation technique is proposed as shown in Fig. 3.

4.1 Results and Discussion

We have designed and simulated the indoor VLC system with and without optical background light noise source by using the parameter values listed in Table 1. We have analyzed the output results by using different types of analyzer such as BER analyzer, eye diagram analyzer, optical spectrum analyzer, and oscilloscope visualizer. The optical power of transmitting LED is 1.215 W which added with the optical

Table 1 List of the parameter of components with values used for the optisystem simulation of the proposed indoor VLC systems

Parameters	Value
Room size	$10 \times 10 \times 6 \text{ m}^3$
Bit rate	1 Gbit/s
Modulation	OOK-NRZ
Encoder	NRZI sequence encoder
Optical source (LED)	Wavelength—500 nm Bandwidth—400 GHz Electron life time—0.01 ns RC time constant—0.01 ns
LOS channel	Distance—6 m Transmitted half-angle— 45° Irradiance angle— 6° Incidence angle— 6° Detection surface area— 10 cm^2
Silicon PIN photodiode	Wavelength—500 nm Bandwidth—400 GHz Responsivity—0.2 A/W
Electrical amplifier	Gain—102 dB
Low-pass Bessel filter	Cutoff frequency— $0.75 * \text{Bit rate}$
Optical light noise source (fluorescent lamp)	Power—22 W Frequency—450 THz

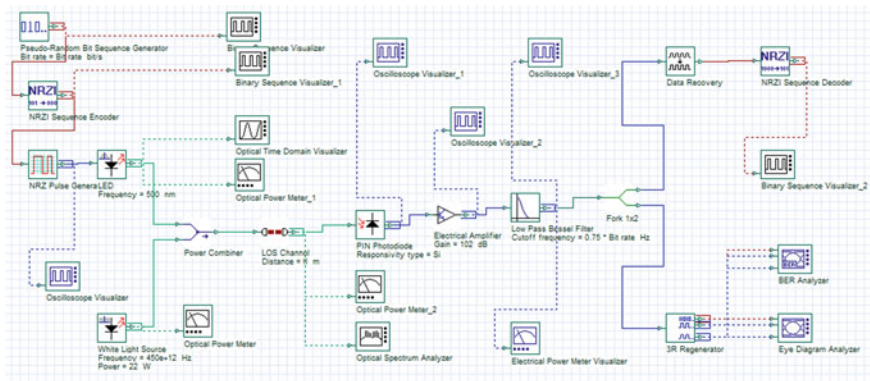


Fig. 3 An optisystem simulation of the proposed system with optical background noise

background light noise source power of $56.315 \text{ E}12 \text{ W}$; when the transmitted light signal propagates through the LOS channel, then the received optical signal power is $826.522 \text{ E}6 \text{ W}$ which is obtained for the distance of 6 m, and the achieved electrical power at the photodetector is $87.754 \text{ E}-12 \text{ W}$ (Figs. 4, 5, 6, 7 and 8).

From Figs. 6 and 9, it has been observed that the waveform of received signal at

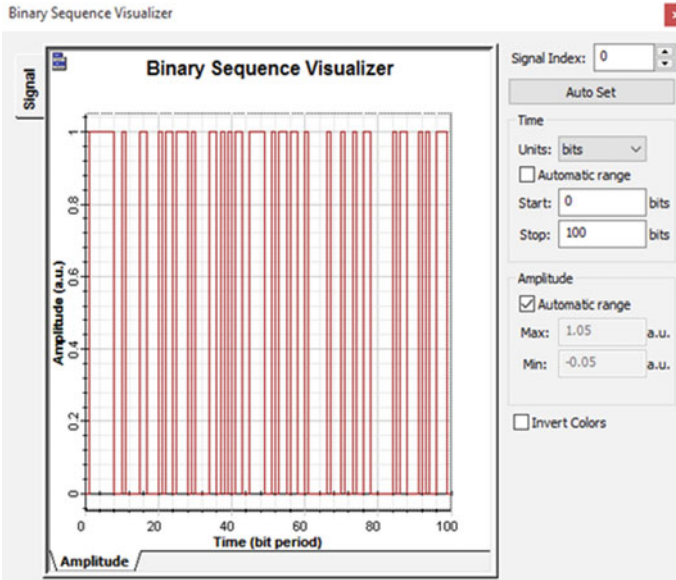


Fig. 4 Binary sequence visualizer output of PRBS generator

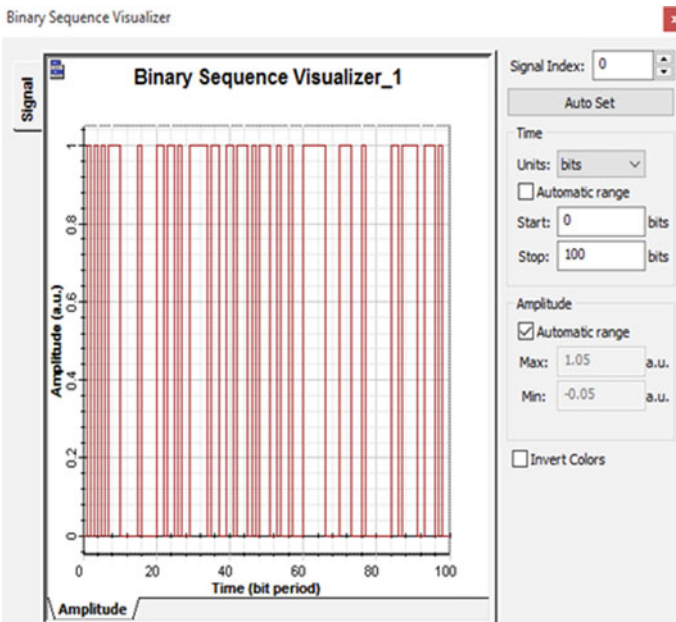


Fig. 5 Binary sequence visualizer_1 output of NRZI encoded signal

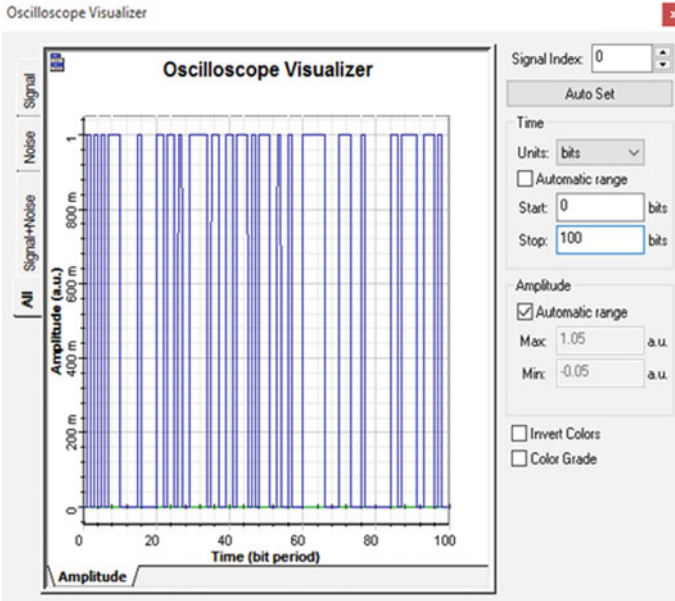


Fig. 6 Output of oscilloscope visualizer for 1 Gb/s OOK-NRZ signal

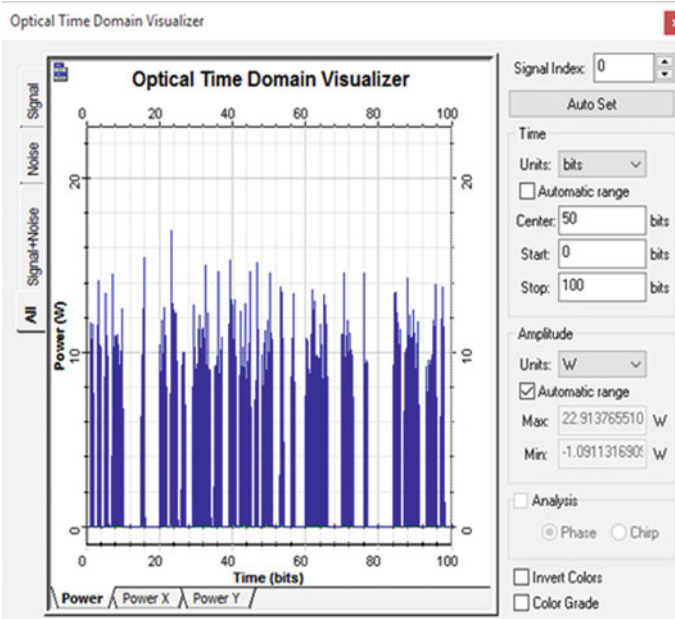


Fig. 7 Output of optical time domain visualizer for signal modulated by LED

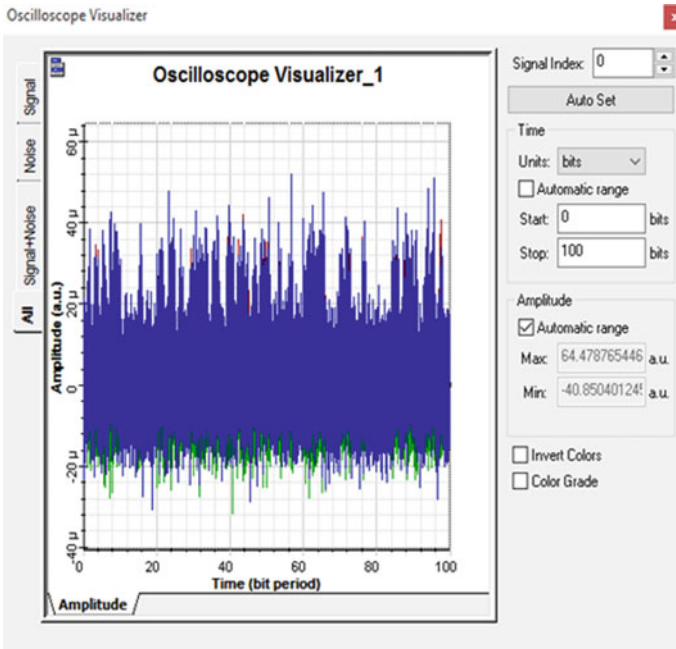


Fig. 8 Output of oscilloscope visualizer_1 at the PIN photodiode with optical background noise

the photodetector is same as the transmitted signal and the bit sequences both of the signals are same.

From Figs. 4 and 10, it has been observed that the decoded signal and the information signal are same, and the bit sequence of both of the signals is same.

From Fig. 11, it has been observed that the minimum BER of 1.64851×10^{-15} is obtained for the distance of 6 m between transmitter and receiver.

From Fig. 12, it is noticed that the output of eye diagram analyzer for 1 Gb/s OOK-NRZ signal having minimum BER of 1.64851×10^{-15} , max Q factor of 7.87816, and the eye height of 0.553761 au is achieved for 6 m distance between transmitter and receiver.

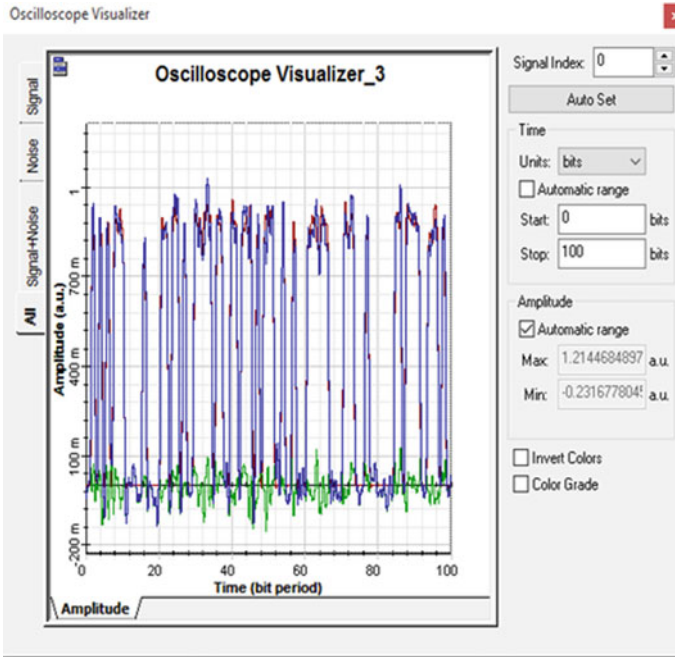


Fig. 9 Output of oscilloscope visualizer_3 at low-pass Bessel filter

The electrical power on the photodetector linearly reduces for different distances between the transmitting LED and the photodetector, which is shown by the graph given in Fig. 13.

From Fig. 14, it has been seen that the eye height reduces linearly for different distances between transmitter and receiver.

It is noticed that the minimum BER of 1.64851×10^{-15} is achieved for 6 m distance between transmitter and receiver, and the BER also increases as distance increases, which is shown by Fig. 15.

5 Conclusion

In this paper, the indoor VLC system using OOK-NRZ modulation and NRZI sequence encoding and decoding technique with optical background noise is analyzed. The performance analysis of key parameters like bit error rate, eye height, optical to electrical power conversion, etc., is presented which conclude that an improved performance regarding BER and data rate up to 6 m. A low-pass Bessel filter is employed to further minimize thermal noise and shot noise. It is also observed

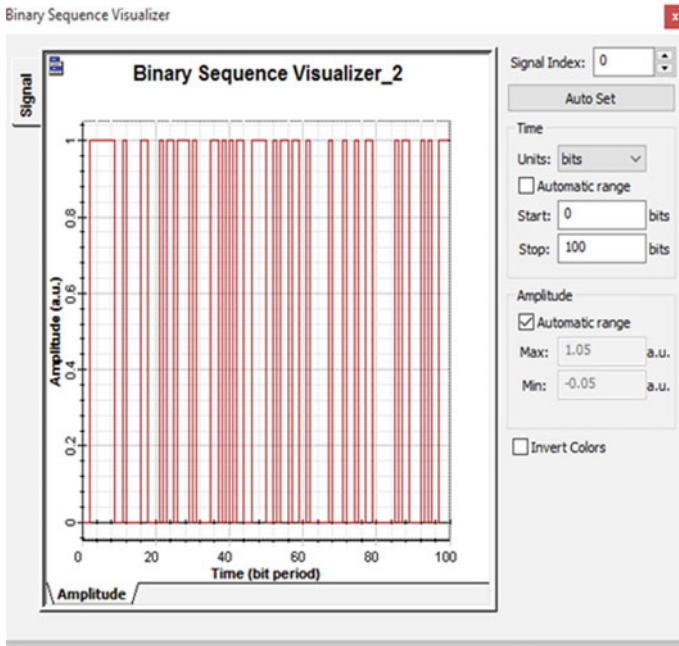


Fig. 10 Output of binary sequence visualizer_2 for recovered information signal by using NRZI decoder

that the BER performance of the NRZ-OOK modulation is enhanced under the influence of optical background noise. Thus, the VLC in indoor application is set up for the data rate of 1Gbps and the distance up to 6 m which will provide additional supplements to extant RF communication.

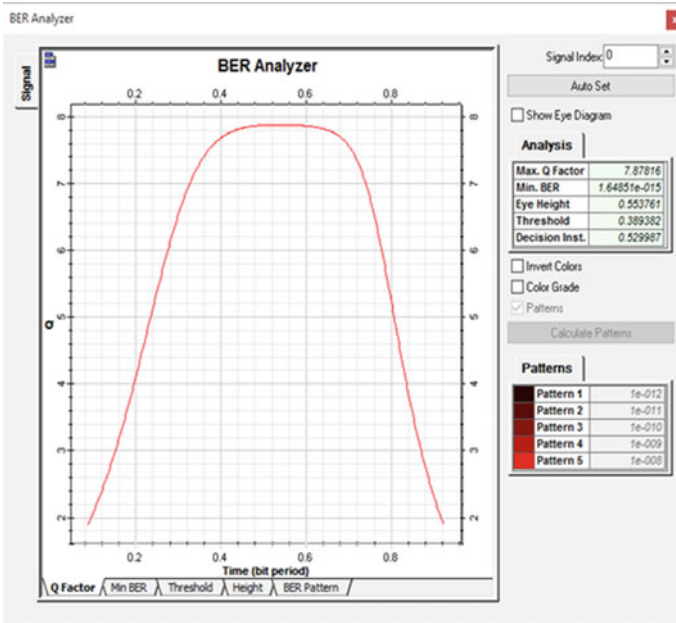


Fig. 11 Output of BER analyzer for 1 Gb/s OOK-NRZ signal

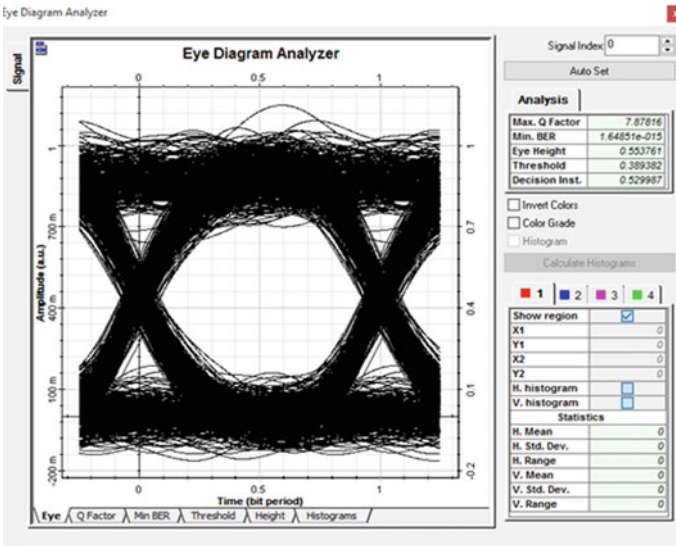


Fig. 12 Output of eye diagram analyzer for 1 Gb/s OOK-NRZ signal

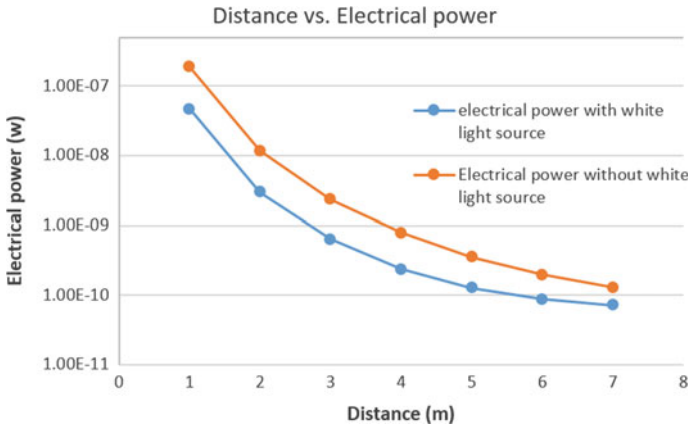


Fig. 13 Distance versus electrical power on the photodiode for 1 Gb/s signal

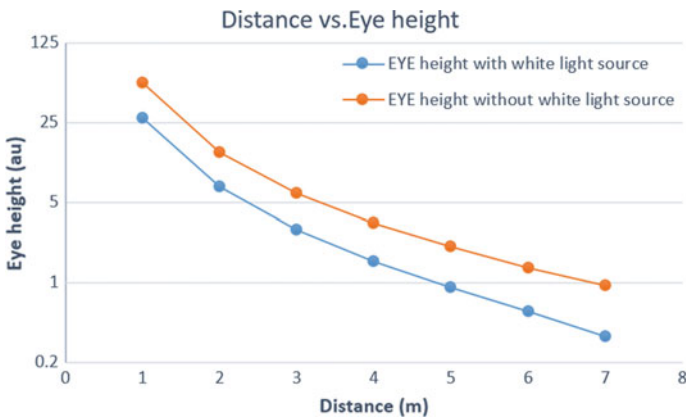


Fig. 14 Distance versus eye height for 1 Gb/s signal

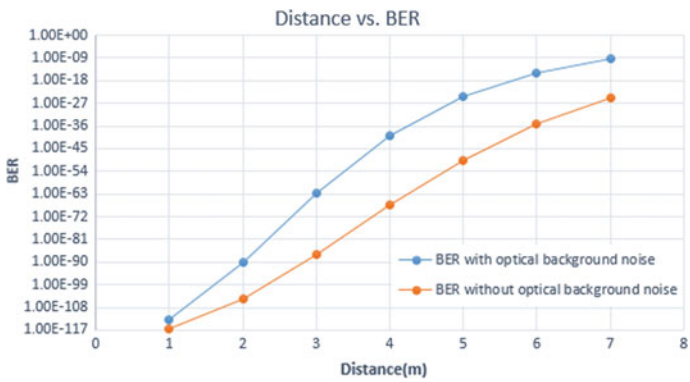


Fig. 15 Distance versus min BER for 1 Gb/s data signal

References

1. Lee K, Park H, Barry JR (2011) Indoor channel characteristics for visible light communications. *IEEE Commun Lett* 217–219
2. Karunatilaka D, Zafar F, Kalavally V, Parthiban R (2015) LED based indoor visible light communications. *IEEE Commun Surv Tutor* 1649–1678
3. Kumar A, Ghorai SK (2018) BER performance analysis of indoor MIMO-VLC system for multipath reflection. In: *Technologies for smart-city energy security and power (ICSESP)*. IEEE, pp 1–5
4. Sindhubala K, Vijayalakshmi B (2015) Design and performance analysis of visible light communication system through simulation. In: *International conference on computing and communications technologies*. IEEE, pp 215–220
5. Saadi M, Wattisuttikulij L, Zhao Y, Sangwongngam P (2013) Visible light communication opportunities, challenges and channel models. *Int J Electron Inf* 1–11
6. Zeng L, O'Brien D, Le-Minh H, Lee K, Jung D, Oh Y (2008) Improvement of data rate by using equalization in indoor visible light communication system. In: *4th IEEE International conference on circuits and systems for communications* 678–682
7. Kahn JM, Barry JR (1997) Wireless infrared communications. *Proc IEEE* 265–298
8. Nuwanpriya A, Ho SW, Chen CS (2015) Indoor MIMO visible light communications: novel angle diversity receivers for mobile users. *IEEE J Sel Areas Commun* 1780–1792
9. Manivannan K, Raja AS, Selvendran S (2016) Performance investigation of visible light communication system using optisystem simulation tool. *Int J Microwave Opt Technol India*
10. Sindhubala K, Vijayalakshmi B (2017) Simulation of VLC system under the influence of optical background noise using filtering technique. *Mater Today Proc* 4239–4250

A 73% PAE, Highly Gain Inverse Class-F Power Amplifier for S-Band Applications



Jatoth Deepak Naik, Pradeep Gorre, Rajesh Kumar, Sandeep Kumar,
and Hanjung Song

Abstract This paper proposes a continuous-mode inverse Class F power amplifier (PA) achieving wide bandwidth, high output power, and high efficiency. This work includes transmission line-based output/input matching networks and single-ended topology. The main focus of the work is to achieve a high gain with wide bandwidth. The proposed structure incorporates a termination of even and odd harmonics to deliver voltage and current waveform isolation with minimal matching network (MN) design complexities. The analyses simulated in Keysight Technologies Advanced Design System (ADS), which results in a wideband PA design. The results are quantified by using high power-added efficiency (PAE) and output power. PAE of 72.6% and output power more than 41 dBm obtained over wide bandwidth 2–4.2 GHz at –3 dB gain compression. The proposed PA could overcome the traditional performance and utilize for green communication.

Keywords Green communication · Continuous-mode PA · Harmonic tuning · Inverse class F · S-band

J. D. Naik (✉) · P. Gorre · S. Kumar

Department of Electronics and Communication, National Institute of Technology, Surathkal, Karnataka, India

e-mail: jatothdeepaknaik@gmail.com

P. Gorre

e-mail: pradeepgorre@gmail.com

S. Kumar

e-mail: fedrer.engg@gmail.com

R. Kumar

Department of Electronics Engineering, Indian Institute of Technology Dhanbad, Dhanbad, India

e-mail: rajeshict42@gmail.com

H. Song

Department of Nanoscience and Engineering, Centre of Nano-Manufacturing, Inje University, Gimhae, South Korea

e-mail: hjsong@inje.ac.kr

© Springer Nature Singapore Pte Ltd. 2021

R. Agrawal et al. (eds.), *Advances in Smart Communication and Imaging Systems*,

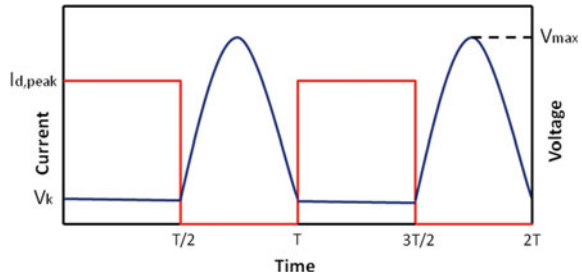
Lecture Notes in Electrical Engineering 721,

https://doi.org/10.1007/978-981-15-9938-5_44

1 Introduction

The growing consequences of environmental awareness and global warming of information and Communications Technology (ICT), researchers have continued exploring ideas to drop energy dissipation. Mobile networks play a significant impact on energy dissipation, which drawn considerable attention to academia, researchers, and industry. Due to rapid changes in climate with counting the economic interests of network operators, green communication has become an attractive research area. The energy can be saved by making use of renewable energy resources or modifying the hardware design, which makes the design more efficient and cost-effective. Moreover, a new component installation, heavy manpower, disturbances to basic operations, and heavy transportation are prohibited. The design approaches are compared with different works that operate on system protocols, and a new network architecture implementation is demanded to achieve economical and simpler construction [1, 2]. The modern wireless communications system demands high efficiency, large bandwidth in addition to optimum linearity for a power amplifier (PA), which remains a critical ingredient inside the architecture of radio frequency (RF) transmitter. To realize the broadband applications, the PA design strategies transferred from the tuning load to harmonic tuning designs [3]. In the harmonic tuning PAs, the overlapping of drain voltage and current is minimized by tuning the load harmonic components, which in turn reduces the power dissipation of the device [4–6]. In general, this is achieved by canceling the harmonics at either open or short (e.g., Class F-1, Class F). Although the harmonic tuning strategies result in highly complex matching networks, they assure a high PA efficiency performance [7]. Nonetheless, these design strategies primarily focus on individual frequency applications due to the restraint on particular harmonic terminations. To realize wideband operation and to overcome this, the recommended design technique is continuous-mode PA. With the growing demand in industries, especially for S-band (i.e., 2–4 GHz), power amplifiers (PAs) achieve optimum gain and efficiency. Gallium nitride (GaN) device is found to be suitable for satellite commutations and radar applications. Classes F, E, and F-1 PAs employ switch-mode techniques on model voltage and current waveforms. The ability to produce excellent linearity and high output power of Class F-1 and Class F PAs enables them to operate at high input power levels. Class F-1 topology can be obtained using a harmonic control model, giving the drain current a rectangular waveform with high efficiency. In these PAs, a half-sine voltage waveform and a rectangular current waveform are produced odd harmonics by a short circuit and even harmonics by an open circuit. The work is organizes as follows: Sect. 2 describes the analytical modeling of inverse class F PA. The circuit implementation is described in Sect. 3. Section 4 presents the discussion and results of the stated Inverse class F PA. Finally, the conclusion does follow during Sect. 5.

Fig. 1 Ideal inverse Class-F voltage and current waveforms



2 Analytical Model of Inverse Class F PA

Figure 1 illustrates the typical time-domain current and voltage characteristics of the inverse Class F PA, where the fundamental output power is equal when the drain voltage is the same. Class F-1 amplifiers have square current wave and half sinusoidal voltage wave signals. The DC power dissipation, output power, fundamental impedance of load examined with the help of the Fourier series expansion.

A Class-F⁻¹ amplifier parameters are estimated by applying the subsequent equations from (1) to (4) equations.

$$P_{dc} = I_{dc} * V_{dc} = \frac{I_{dp}}{2} * V_{dc} \quad (1)$$

$$P_{fo} = \frac{I_{dp}}{2} * (V_{dc} - R_{on} * I_{dp}) \quad (2)$$

$$R_{i,f0} = \frac{-V_{fo}}{I_{f0}} = \frac{\pi^2 * (V_{dc} - R_{on} - I_{dp})}{4 * I_{dp}} \quad (3)$$

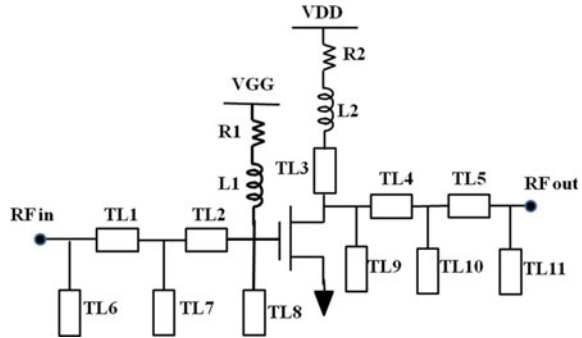
$$R_{on} = \frac{V_k}{I_{dp}}$$

$$\text{Efficiency}(\eta) = \frac{(V_{dc} - R_{on} * I_{dp})}{V_{dc}} * 100 \quad (4)$$

3 Circuit Implementation

Figure 2 presents the schematic of proposed continuous-mode Class F⁻¹ PA, which is designed in S-band to work at 3.5 GHz employing a Nitronex GaN HEMT NPTB00004 design technology. GaN device is biased within Class AB and Class B to exhibit excellent performance. The termination of even harmonics at the drain

Fig. 2 Schematic of proposed Class F^{-1} PA



retains the shape of the output current. Drain voltage waveform is shaped by controlling the odd harmonics to diminish overlap with the current waveform. The matching network of the circuit is a combination of stubs and microstrip lines to maintain a flat gain over the desired frequency band. The impedance matching strip lines are modeled using TLY5 with a substrate thickness of 0.7 mm at permittivity $\epsilon = 2.2$.

The parasitic capacitances of the transistor influence impedance of the amplifiers at the input, thus restricting the load network modulator at the bandwidth. The only possible way to overcome this effect is to consider the transistor with parasitic capacitances into the impedance network by diminishing the length of the transmission line. To determine the optimum load impedance, a load-pull test set up is incorporated at the drain of the transistor. By tuning the load matching network, the optimum impedance at the source will vary slightly, enabling the necessity to control the matching impedance to obtain the feasible result. To limit the bandwidth, the power splitter impedance matching network should be matched for large C_{gs} to the impedance of the transistors. The phase alignment network and input power splitter bandwidth are diminished because of the gate-source capacitance C_{gs} . The C_{gs} nonlinearity, especially for the Class-C biased peaking transistor, leads to dependency. Table 1 shows the lengths and widths of microstrip lines and stubs.

4 Results and Discussions

The simulation experiments are carried to analyze the representation of inverse Class F^{-1} PA by odd and even tuneful conclusions at the drain. The comparison of output matching networks with power efficiency and the simulation experiments were made to generate odd harmonics as well as even harmonics in the voltage waveform. The conclusions were obtained by simulating in the Keysight Technologies Advanced Design System (ADS). The simulated S-parameters of the proposed continuous-mode Class F^{-1} are shown in Fig. 3 with a maximum forward gain (S_{21}) of 15 dB at 3.5 GHz frequency and a functional return loss (S_{11}) over the S-band frequency.

Figure 4 presents the power gain analysis simultaneously, including the simulated

Table 1 Components value of transmission line used in PA

Dimensions	W (mm)	L (mm)
TL1	2	8.3
TL2	5	12.8
TL3	0.6	10
TL4	2.4	5.6
TL5	0.2	3
TL6	3	4.3
TL7	5	1.3
TL8	5.1	1.6
TL9	1.5	3
TL10	1.5	1.5
TL11	1.2	2.8

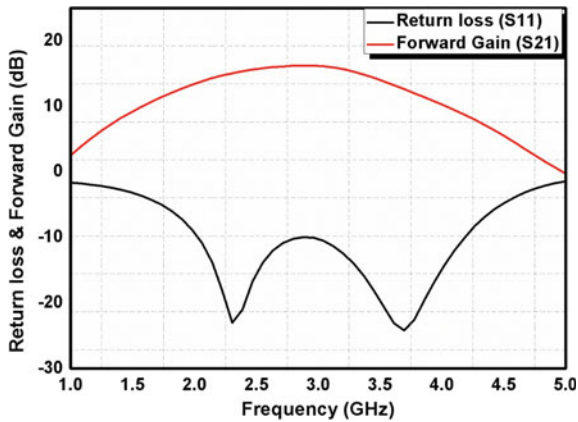


Fig. 3 S-parameter of proposed Class F^{-1} PA

outcomes. The ideal value deviates insignificantly, and the total appearance of the gain development employing gate adaptation is established, as Fig. 4 intimates.

Figure 5 shows the simulated output power variation with input power. Initially, output power modified linearly, including input power saturated to 36.2 dBm. Class F^{-1} amplifier outwardly, a shaping process, remits an output power of 40.1 dBm. Input power as a function of Simulation of power-added efficiency is conferred in Fig. 6, and a % PAE of 72.3 is observed at 16 dBm input power. The realization of load power with respect to input power is also conferred in Fig. 7. The layout of the proposed PA is shown in Fig. 8. The layout is done using nano-manufacturing Modelithics exemplar library.

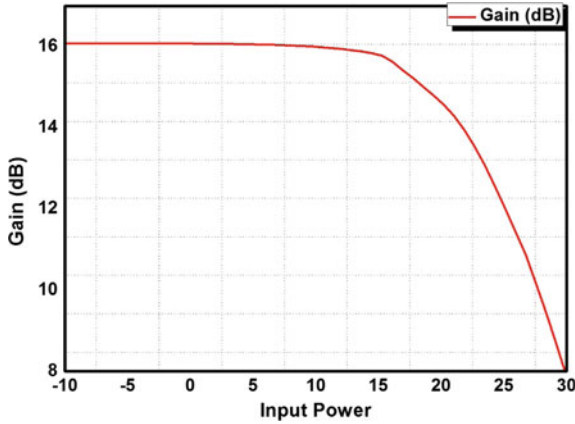


Fig. 4 Power gain versus input power

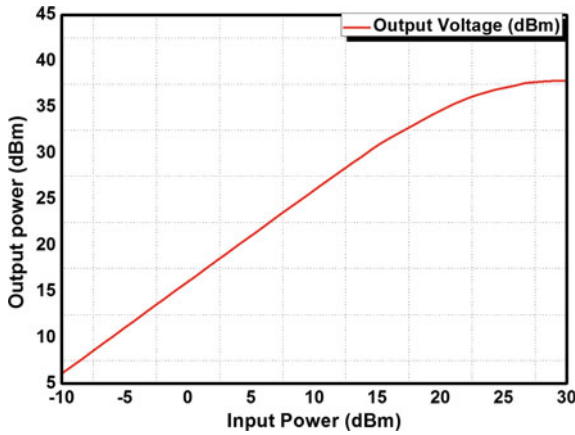


Fig. 5 S-parameter simulation of proposed Class F⁻¹ PA

5 Conclusion

This paper discusses a detailed analysis of GaN HEMT continuous-mode Class F⁻¹ PA for S-band frequency. Table 2 performs the estimate of suggested Class F⁻¹ PA with state-of-art work and present work results a high PAE (%) of 72.6 and high output power of 41.1 dBm with acceptable performance of other parameters. Analytical analysis shows second and third harmonics at source and drain reduces the gain by -3 dB for Continuous-mode Class F⁻¹ PA by examining data nonlinearity. This work presents an even and odd harmonics cancellation for broadband PA operation. Hence, the proposed Class F⁻¹ PA design minimizes matching network design complexities for wideband operation.

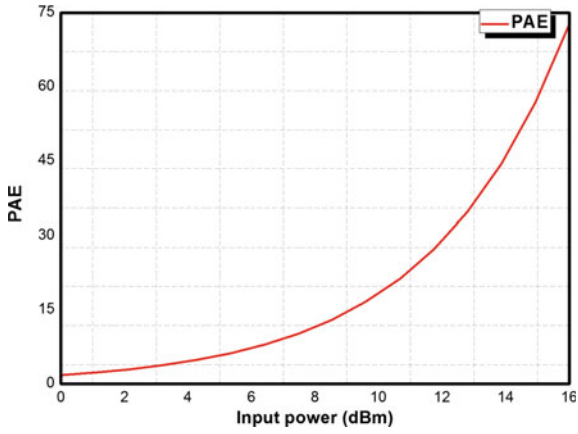


Fig. 6 Power added efficiency as a function of input power

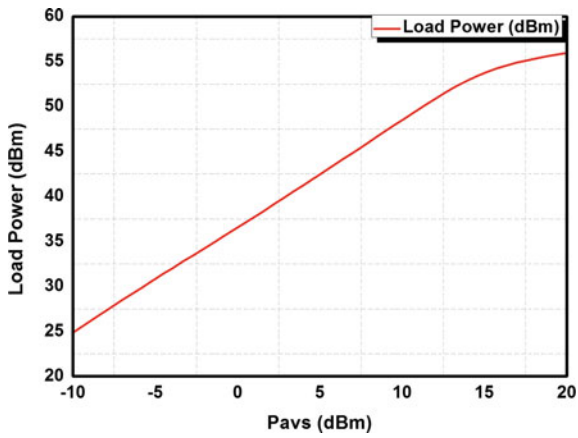


Fig. 7 Simulated load power versus average power

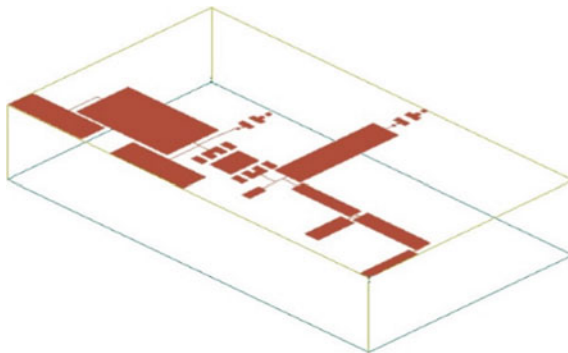


Fig. 8 Layout of proposed PA

Table 2 Performance comparison of proposed PA with other reported papers

References	Frequency (GHz)	Device technology	PAE (%)	Output power (dBm)
[8]	2.29	GaN HEMT	63	42
[9]	1.6	GaN HEMT	60	37.7
[10]	2.14	GaN HEMT	40	39.3
[11]	2.4	GaN HEMT	54	42.3
This work	2–4.2	GaN HEMT	72.6	41.1

Acknowledgements This research was supported by the “Modelithics models utilized under the University License Program from Modelithics, Inc., Tampa, FL.” 2019–2020.

References

1. GreenTouch. (Online). Available <http://www.greentouch.org/>
2. International Telecommunication Union (2011) ITU Green Standards Week. Geneva, Switzerland
3. Colantonio P, Giannini F, Limiti E (2009) High efficiency RF and microwave solid state power amplifiers. Wiley, Hoboken
4. Raab FH (1997) Class-F power amplifiers with maximally flat waveforms. *IEEE Trans Microw Theory Technol* 45:2007–2012
5. Colantonio P, Giannini F, Leuzzi G, Limiti E (2011) Multiharmonic manipulation for highly efficient microwave power amplifiers. *Int J RF Microw Comput-Aided Eng* 11:366–384
6. Raab FH (2001) Maximum efficiency and output of Class-F power amplifiers. *IEEE Trans Microw Theory Technol* 49:1162–1166
7. Colantonio P, Giannini F, Leuzzi G, Limiti E (2003) Theoretical facet and experimental results of harmonic tuned Pas. *Int J RF Microw Comput-Aided Eng* 13:459–472
8. Aliparast P (2016) Design and implementation of a high efficiency RF power amplifier for S-band telemetry subsystems. *Int J Electron Commun (AEÜ)*. 20:1311–1320
9. Kryzhanovskiy R (2011) The output circuit of inverse class F power amplifier with slot resonators in microstrip line ground plane. In: 21st international crimean conference microwave & telecommunication technology (CriMico), pp 141–142
10. Bathich K, Markos AZ, Boeck G (2011) Frequency response analysis and bandwidth extension of the Doherty amplifier. *IEEE Trans Microw Theory Tech* 59:934–944
11. Kim J (2019) Analysis and design optimisation for inverse Class-F GaN Doherty amplifier. *IET Microw Antennas Propag* 13:448–454

Performance Analysis of Stationary and Moving V2V Communications Using NS3



Divyanshu Gupta, Aditi Uppal, Ayushi Walani, Devanshi Singh, and Amanpreet Singh Saini

Abstract Vehicle-to-vehicle communication is prime focus of major studies concerning road safety as it can ensue an efficient traffic flow with fewer accidents. It is expected to exhibit a flexible routing method as vehicles enter and leave rapidly. Both proactive and reactive modes are used in hybrid wireless mesh protocol; thus, it is expected to give optimum results. To analyse that, in this paper, we have used IEEE 802.11p and IEEE 802.11s for static and moving vehicles working under mesh topology. The performance evaluation is accomplished by simulation on network simulator 3 (NS-3) followed by visualizing the model on NetAnim and measuring the performance of network protocols in FlowMonitor. Throughput, packet delivery function (PDF) and packet sizes are parameters that have been evaluated.

Keywords V2V · Mesh · 802.11p · 802.11s · ITS · NS3

1 Introduction

The recent advancements in intelligent transport system (ITS) provide a way towards more efficient, safe and comfortable driving. For this purpose, it has been seen over

D. Gupta (✉) · A. Uppal · A. Walani · D. Singh · A. S. Saini
Department of Electronics and Communication Engineering, Galgotias College of Engineering and Technology, Greater Noida, India
e-mail: divyanshu4760@gmail.com

A. Uppal
e-mail: uppaladiti.au@gmail.com

A. Walani
e-mail: ayushi.main@gmail.com

D. Singh
e-mail: deva.vashi@gmail.com

A. S. Saini
e-mail: aps.saini@galgotiacollege.edu

the past few years, V2V communication systems have come into limelight which is a vital part of the ITS [1].

The amendment of IEEE 802.11 which deals with the mesh topology is IEEE 802.11s. Also, the routing capabilities at the MAC layer has been introduced which has been described by the wireless mesh network (WMN) concept in 802.11s [2]. The dedicated short-range communication (DSRC) spectrum has a bandwidth of 75 MHz in 5.9-GHz band which was projected and licensed to support the vehicle-to-vehicle (V2V) and vehicle-to-infrastructure (V2I) communications. It is being standardized as IEEE 802.11p. Vehicular safety communication through wireless networks can be provided by 802.11p which proves to be an emerging standard in V2V communication. It is an extended version of the standard IEEE 802.11 for high-speed vehicular environment. Throughput, packet loss and end-to-end delay metrics are some of the important performance metrics for vehicular safety communication. The key is to determine the effects of varying vehicle's speed and different packet sizes on the performance metrics. The vehicles act as the nodes when their performances are to be considered in the highway scenario. They are fully managed with the short-range wireless communication technology, in general dedicated short-range communications (DSRC) [3, 4].

IEEE 802.11s enables a pairwise master key (PMK) within two mesh stations which can be used to encrypt each other's frame, whereas in IEEE 802.11p, with the help of wireless networks vehicular safety communication can be optimized and the main concern of IEEE 802.11p is to broadcast messages reception performance [5].

The data packets to be sent of those of non-safety applications can be successfully directed by wireless access for vehicular network (WAVE) which operates in the range of dedicated short-range communication (DSRC). Various ITS applications are supported by WAVE technology which aims to support car-to-car communications [6].

A typical routing protocol enhances the performance of the network in a great way. A hybrid routing protocol can be formed by combining reactive and proactive routing protocols [7].

The NS-3 is being greatly used for the simulation purpose and optimization of certain values and graphs. Hence, NS-3 is a type of networking simulator which is used to implement network protocols [8]. The study and evaluation of network protocols can be effectively done with the help of network simulators.

The rest of the paper is described as follows: Sect. 2 presents the system model which analyses the performance of HWMP with standards IEEE 802.11p and IEEE 802.11s and presents the parameters considered for the same. Section 3 and 4 provide the result and conclusion, respectively.

2 System Description

This section illustrates the traffic scenario and intervehicle communication, respectively, and indicates the specific metrics and assumptions of the proposed VANET

model. The paper discusses the performance being analysed using simulation performed on NS3. As vehicular communications are based on safety message broadcasting between neighbouring vehicles, performance is measured in terms of broadcast message reception rate. IEEE 802.11p as well as IEEE 802.11s is the standards used for message delivery. The performance in terms of following metrics is being measured and compared:

1. Packet delivery function (PDF)
2. Throughput

where PDF is calculated as percentage quantity of packets received at the final destination with respect to the number of packets originated for the duration of simulation time and throughput is calculated as the rate at which data frame bytes are received in comparison with the total information conveyed in the network.

As per IEEE 802.11p standard, the vehicle first checks for the transmission medium. For a precise duration of time if the channel is observed to be free, the vehicle begins to transfer the packet. Else, if further the channel is not observed to be idle, it arbitrarily selects a value from a given set of numbers also known as the Contention Window. A backoff counter is then set taking any random value from the Contention Window and is decremented with every idle slot detected. Channel's access is given to the node when the counter drops to zero [9]. The vehicles within the broadcasting range establish a multi-hop communication with other vehicles which improves data transmission reliability [10].

Thus, proceeding with model development—two scenarios are considered for respective simulations. For the rest of the paper, each node represents each vehicle. Nodes are set to broadcasting mode. Receivers never acknowledge broadcast frames. The distributed technique of cluster formation is used as per which the nodes form the cluster themselves. This technique offers reliability and consumes less time [11]. In the first scenario, all the nodes are static; i.e. the vehicles remain stationary. In static, the cluster formation is firm and it lasts for the duration. In the second scenario, all the nodes are in motion; i.e. all the vehicles move freely in either direction within their specified range of speed. In dynamic, clusters are formed time after time, sporadically. The nodes in the cluster as modelled offer an efficient communication for study. The setup of both the scenarios are the same; i.e. a V2V communication system is modelled in a grid area of $300 \times 300 \text{ m}^2$. Initial positions of the nodes are set as per the position allocator model, and the distance between each vehicle is 50 m. The scenario is then represented as shown in Figs. 1 and 2.

The position of static nodes is allocated through simulation code using *Grid Position Allocator* which allocates position to nodes in a rectangular 2D grid, whereas the position of the moving vehicles is allocated using *Random Rectangle Position Allocator* which is used to allocate random positions within a rectangle according to a pair of random variables [12, 13]. To deploy the changes in node position during simulation, *Constant Velocity Mobility Model* is used according to which nodes move with a constant speed, set at the start, in a straight line [14]. The nodes have a variable speed within the range of 60–80 km/h, and a backoff interval of 0.1 s is provided to restrain simultaneous transmission from multiple devices.

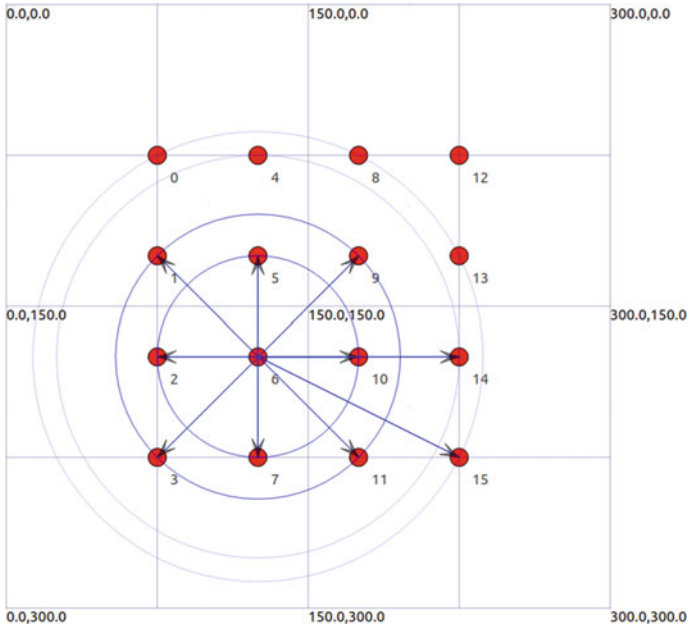


Fig. 1 System scenario for static 16 nodes

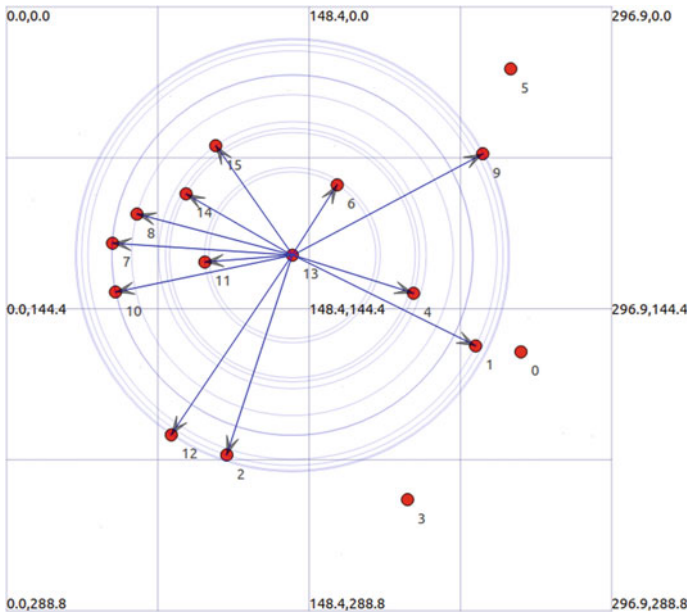


Fig. 2 System scenario for moving 16 nodes

Table 1 Simulation parameters

Parameters	Value
Total simulation time	60 s
Packet frequency	10 Hz
Data rate	6 Mbps
Packet size	64–2048 Bytes
Transmitter power	21.5
Transmitter gain	2
Receiver gain	2
Energy detection threshold	−83.0
propagation loss model	Nakagami propagation loss model
Mac address of mesh point	“ff:ff:ff:ff:ff:ff”

In order to study the impact of the increase in information required to be delivered, the packet size is varied from 64 to 2048 bytes/s in increasing power of 2. For the propagation modelling, we have utilized *Nakagami Fading Channel model*. The parameters used in NS3 VANET simulations are mentioned in Table 1.

The wireless connectivity is established using WMN. Mesh networks allow properties to be installed into IEEE 802.11 standard. In wireless mesh networks, nodes share their topological and routing information. And the paper [15] suggests, we can use a protocol with different network routing algorithms to grant for multipoint-to-multipoint network implementation. Thus, we make use of a mesh networking algorithm with IEEE 802.11s as well as IEEE 802.11p protocols as it characterizes the increase in range of the network till the radio range of the node which is farthest connected. The category of mesh networking used is hybrid wireless mesh protocol (HWMP). HWMP is implemented using two classes: *HwmpProtocol* and *HwmpProtocolMac*. HWMP, here, is also responsible for filtering broadcast data frames and adding/parsing mesh control header apart from routing. *HwmpProtocol* and *HwmpProtocolMac* are managed as defined by standard [16]. For HWMP, the dependency of throughput and packet delivery ratio with respect to varying speed is done in [17] but so far, no work has been done to check the dependency of these parameters with respect to varying packet sizes.

NS-3 simulator provides a realistic environment, and its source code is well organized. Tracing facilities for output and small units of information are attached to each packet [18].

3 Results and Discussion

After thorough simulations on NS-3 simulator along with NetAnim—to animate the simulations and flowmonitor—to measure the performance of network protocols, a total of four comparison graphs are obtained where the comparison is done between IEEE 802.11s and IEEE 802.11p for static and moving vehicles, separately. To compare, we have monitored each scenario for their overall throughput and packet delivery function (PDF) with respect to varying packet sizes.

Figures 3 and 4 contain plots for static scenario having a total of 16 nodes, respectively, whereas Figs. 5, 6 contain plots for moving scenario having 16 nodes. Each figure has two plot lines in it: dotted line represents performance of IEEE 802.11p and straight line represents the performance of IEEE802.11s. Comparison done in plots are packet size vs throughput and packet size versus PDF with packet size in their x-axis. It can be observed that in all cases a directly proportional relationship

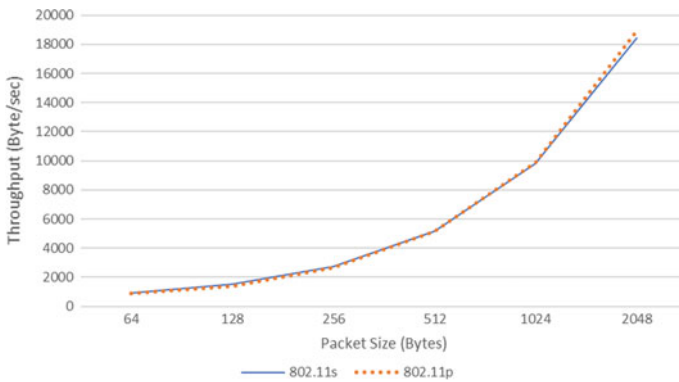


Fig. 3 Throughput versus packet size for static 16 nodes

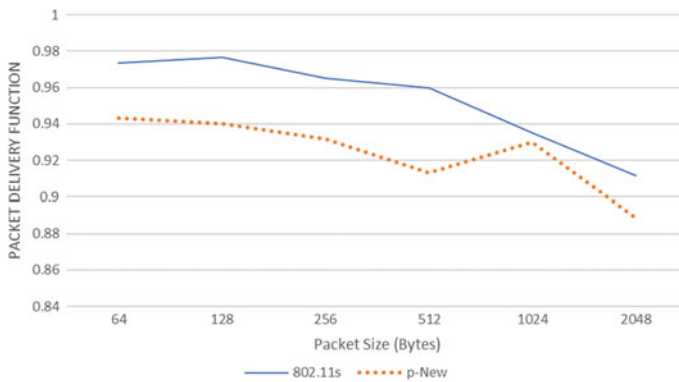


Fig. 4 PDF versus packet size for static 16 nodes

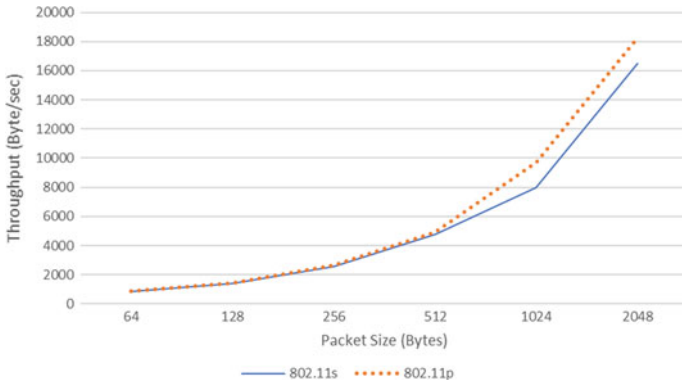


Fig. 5 Throughput versus packet size for moving 16 nodes

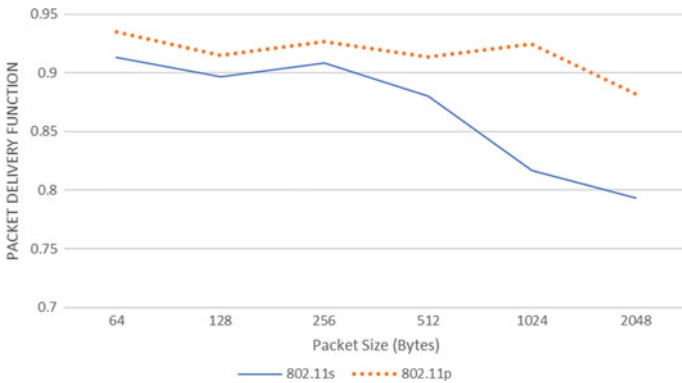


Fig. 6 PDF versus packet size for moving 16 nodes

is obtained between packet size and throughput, whereas in case of packet size and PDF all the scenarios show an inversely proportional relationship.

Performance of IEEE 802.11p and IEEE 802.11s when compared with respect to throughput is nearly same in every scenario. IEEE 802.11p starts to perform slightly better when the packet size is increased the difference observed here also increases; i.e. the difference is 180 kb/s at 512 Bytes to 1833.8 kb/s at 2048 Bytes.

When performance of both protocols is compared with respect to PDF, a dissimilarity can be observed. When the nodes are in static condition; i.e. with zero mobility, 802.11s performs marginally better but when the nodes are in mobility, IEEE 802.11p surpasses IEEE 802.11s in performance and gives much better result.

4 Conclusion and Future Scope

In this paper, we have examined the performance of IEEE 802.11p and IEEE 802.11s for stationary as well as moving vehicles. Parameters evaluated were throughput and PDF. It can be observed from the plots obtained from simulations that IEEE 802.11s performs better when the vehicles are stationary, whereas IEEE 802.11p performs better when the vehicles are in motion.

In future, we plan to design and inspect the performance of hybrid model which uses IEEE 802.11p when the vehicles are in motion and IEEE 802.11s when vehicles are stationary.

References

1. Figueiredo L, Jesus I, Machado JT, Ferreira JR, De Carvalho JM (2001) Towards the development of intelligent transportation systems. In: ITSC 2001. 2001 IEEE intelligent transportation systems. Proceedings (Cat. No. 01TH8585). IEEE, pp 1206–1211
2. Yahiabadi SR, Berekatain B, Raaheimifar K (2019) TIHOO: an enhanced hybrid routing protocol in vehicular ad-hoc networks. *EURASIP J Wireless Commun Network* 2019(1):192
3. Yao Y, Rao L, Liu X (2013) Performance and reliability analysis of IEEE 802.11 p safety communication in a highway environment. *IEEE Trans Veh Technol* 62(9):4198–4212
4. Jafari A, Al-Khayatt S, Dogman A (2012) Performance evaluation of IEEE 802.11 p for vehicular communication networks. In: 2012 8th international symposium on communication systems, networks & digital signal processing (CSNDSP). IEEE, pp 1–5
5. Chbib F, Khoukhi L, Fahs W, Khatoun R, Haydar J (2019) Wave performance analysis and enhancement for safety applications in vehicular networks. In: 2019 10th IFIP international conference on new technologies, mobility and security (NTMS). IEEE, pp 1–7
6. Hafeez KA, Zhao L, Ma B, Mark JW (2013) Performance analysis and enhancement of the DSRC for VANET's safety applications. *IEEE Trans Veh Technol* 62(7):3069–3083
7. Eltahir AA, Saeed RA, Alawi MA (2013) An enhanced hybrid wireless mesh protocol (E-HWMP) protocol for multihop vehicular communications. In: 2013 international conference on computing, electrical and electronic engineering (ICCEEE). IEEE, pp 1–8
8. Bu J, Tan G, Ding N, Liu M, Son C (2014) Implementation and evaluation of wave 1609.4/802.11 p in ns-3. In: Proceedings of the 2014 workshop on ns-3, pp 1–8
9. Vinel A, Molinaro A, Koucheryavy Y (2011) Modeling broadcasting in IEEE 802.11 p/WAVE vehicular networks
10. Choudhary S, Sharma L, Kaushik AK, Mishra A (2019) Novel approach to reduce the replication of information and to increase the reliability of end to end data transmission in WSN. In: 2019 2nd international conference on intelligent communication and computational techniques (ICCT). IEEE, pp 83–86
11. Sachan S, Vats M, Mishra A, Choudhary S (2020) Comparative analysis of clustering algorithm for wireless sensor networks. In: *Intelligent computing in engineering*. Springer, Singapore, pp 63–71
12. https://www.nsnam.org/doxygen/classns3_1_1_random_rectangle_position_allocator.html
13. https://www.nsnam.org/doxygen/classns3_1_1_grid_position_allocator.html
14. https://www.nsnam.org/doxygen/classns3_1_1_constant_velocity_mobility_model.html
15. Beckman P, Verma S, Rao R (2003) Use of mobile mesh networks for inter-vehicular communication. In: 2003 IEEE 58th vehicular technology conference. VTC 2003-Fall (IEEE Cat. No. 03CH37484), vol 4. IEEE, pp 2712–2715

16. Katkar PS, Ghorpade DVR (2016) Comparative study of network simulator: NS2 and NS3. *Int J Adv Res Comput Sci Softw Eng* 6(3)
17. Goswami S, Joardar S, Das CB, Kar S, Pal DK (2017) Performance analysis of three routing protocols in manet using the ns-2 and anova test with varying speed of nodes. *Ad Hoc Networks* 126–138
18. Andreev K, Boyko P (2010) IEEE 802.11s mesh networking NS-3 model. In: *Workshop on ns3*, vol 43

COVID-19 Pandemic and Post-pandemic: Impact and Technical Threats in India



Aastha Tyagi and Madhu Sharma Gaur

Abstract World Health Organization declared Coronavirus as a pandemic. More than 6 million confirmed cases of COVID-19 have been found leading to more than 367166 deaths till May 31, 2020. With every passing day, the number of cases and deaths is expanding. The widespread of this epidemic has not only threatened human health but also production, economy, social functioning, education, etc. In this critical pandemic situation, a large number of the population are fighting for their lives and economic challenges for survival. Although digital health would not be the main contributor in combating COVID-19, it could play a very important supporting role in control and prevention work. During this isolation period, various digital applications are needed to ensure a normal life for most of the people. Artificial intelligence, machine learning, data analytics, big data, cloud computing, Internet of things (IoT) and other digital technologies are playing a vital role in managing routine activities through work from home, online education, remote patient treatment, citizen protection, risk communication, and medical supplies. On the downside, various technical threats like online fraud and cyber-attacks are rising and increasing challenges in the COVID-19 pandemic. The objective of this paper is to explore the available COVID-19 statistics and understand the impacts with technical threats to relief measures in India caused in the current pandemic. To realize social responsibility and comprehend response capacity in foreseeing COVID-19 extortions and foster the community awareness toward population and public health allocation where upholding local health with technical risk prevention is alarming. In the winding up, post-pandemic open challenges are also discussed.

Keywords Corona virus · COVID-19 · Cyber threats · Cyber security · Cyberspace · Impacts · Pandemic opportunities · Post-pandemic challenges

A. Tyagi (✉) · M. S. Gaur
G.L. Bajaj Institute of Technology and Management, Greater Noida, GautamBudh Nagar, UP,
India
e-mail: aasthatyagi90561@gmail.com

M. S. Gaur
e-mail: madhu14nov@gmail.com

© Springer Nature Singapore Pte Ltd. 2021
R. Agrawal et al. (eds.), *Advances in Smart Communication and Imaging Systems*,
Lecture Notes in Electrical Engineering 721,
https://doi.org/10.1007/978-981-15-9938-5_46

1 Introduction

In the month of December 2019, in China Wuhan City, a mysterious pneumonia killed many people and also infected more than seventy thousand individuals. As per World Health Organization (WHO), the virus that causes this disease “Severe Acute Respiratory Syndrome Coronavirus-2 (SARS-Cov-2)”, disease was named as novel Coronavirus or COVID-19. It belongs to the family of Coronaviridae. The disease COVID-19 was named by the combination of two words (Corona + Virus) where Corona means a part of body resembled to be a crown-like spike found on the outer surface of the virus. The virus is contagious and rapidly spreading through human-to-human transmission. Initially, it was reported in the people who had travel history being transmitting. As the year 2020 starts, the virus spread worldwide and COVID-19 was announced and from the January 2020 to till now virus infection transmission continues and has huge impact on the worldwide society. On March 11, 2020, World Health Organization (WHO) classified this virus as pandemic [1]. Around 8098 individuals were infected around the world by SRAS-CoV (2003) [2], on the other hand, COVID-19 infected 6 M individuals leading to 367 K deaths around the world, till date of this writing.

2 Related Work

Some researchers have been made considering threats and relief measures from COVID-19 so far. Different authors have suggested different measures to control and prevent people. In [1], Mouton and Coning, talk about various areas which create a larger impact from cyber security perspective on COVID-19 like misinformation, fear mongering (panic buying), fake URLs and malicious Web site. It talks about only two measures, i.e., node VPN and cyber measure. According to International Criminal Police Organization (INTERPOL) [3], in order to take advantages of online behavior and trends (COVID-19 outbreak), cyber threats are constantly evolving. It talks about the three types of cyber-attacks in COVID-19 like malicious domain, malware, ransomware. It also provides some recommendation and tips to prevent from these threats as by keeping information safe, securing email gateways, performing regular scans on computer and mobile devices.

Analysis of malware that supersedes the system master boot record was done by Trend Micro in [4], analyzed (April 24) about a malware based on coronavirus theme, making it unbootable. It also mentioned about some other type of threats using COVID-19 such as spam, mobile ransomware (CovidLock) an android application that helps to track COVID-19 cases but actually locks the phone of victims. A cloud app security by Trend Micro provides solution to defense against these threats in which it finds unknown malware using machine learning. As per the recent Technical Analysis report by VMware [5], COVID-19 has generated a “substantial

uptick” in cyber security attacks, leading to “high-level risk for both personal security as well as corporate security”. According to this report, phishing emails are the primary source of attack where unauthorized users use techniques like fake links in emails and attachments to deliver malicious software to recipients. In [6], Matt J Keeling discussed the ability to produce intended result through contact tracing. It mentioned about the main advantage of contact tracing as it is an effective and robust technology, which can identify the person before severe symptoms emerge and can prevent onward transmission.

3 COVID-19 Epidemic

Since December 2019, Coronavirus has spread rapidly nationwide in China and now by the month of January 2020 it reached worldwide. Everyday number of positive cases are being confirmed and deaths being reported of less immune and aged people. As per available sources, in India, on January 30, 2020, first Corona positive case was reported in Kerala in a student who came for vacation from China. The student was studying in Wuhan University, China, returned to India and was found Corona positive. Although in the month of February 2020, the virus transmission was very slow, as by the end of February only three Corona positive cases were confirmed. Figure 1 shows confirmed cases in India from January 30, 2020–February 29, 2020.

But due to certain events like Tablighi Jamaat event, panic buying, escaping of suspected people, misinformation and discrimination, there is a sudden increase in the number of individuals affected by it. In March, these cases rise from few to 1 K as shown in Fig. 2.

By April 29, 2020, the Ministry of Health and Family Welfare has confirmed 31,332 cases, leading to 1007 deaths and 7797 recoveries (1 migration), in India [2] which increased as shown in Fig. 3.

On May 18, 2020, some zones were being unlocked. On May 19, 2020, the cases reached to 100 K. As on May 31, 2020, there were 182,143 active cases being reported as shown in Fig. 4. In the coming month, there will be the hype in these cases.

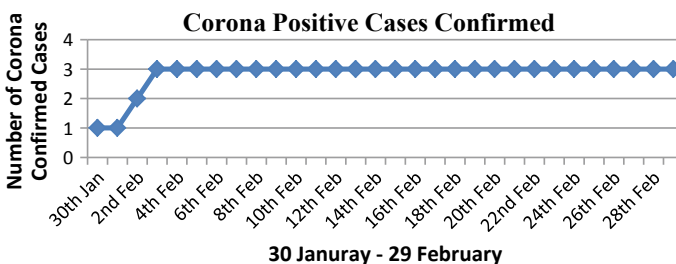


Fig. 1 Corona positive cases confirmed in India, January 30–February 29, 2020 [7]

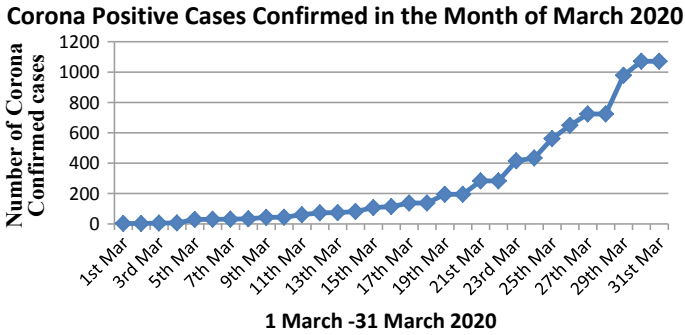


Fig. 2 Sudden increase of confirmed cases in India (March report) [7]

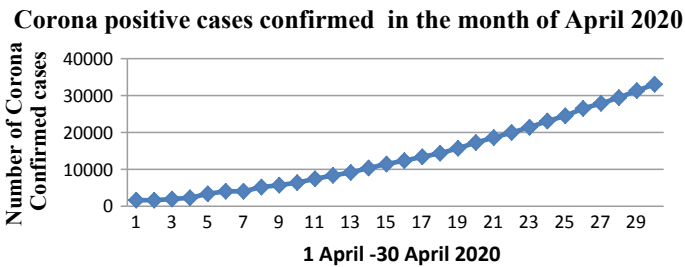


Fig. 3 Worse situation due to the increased number of cases (April report) [7]

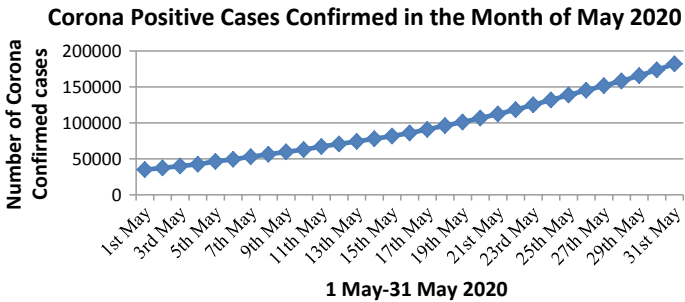


Fig. 4 Cases in India have crossed 1,00,000 (May report) [7]

Since January 31 (when the first case was identified in India) till May 31, the cases are being increased leading to 5164 deaths. Figure 5 shows the confirmed cases from January–February to May 2020 with the linear increase.

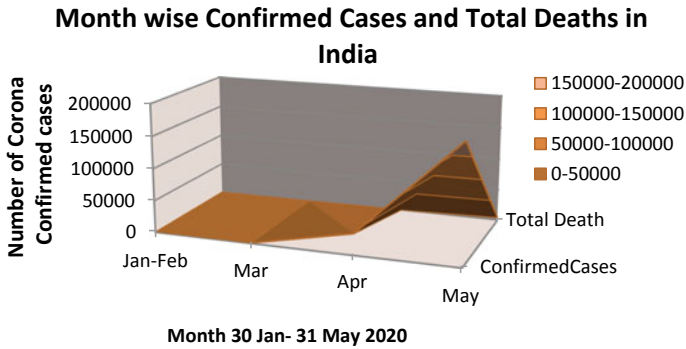


Fig. 5 Month wise (January–May 2020) confirmed cases and total death in India by the end of month

4 COVID-19 Rise and Outbreak in India

4.1 Top Seven Indian States Where Rising Corona Cases

In India, the cases of COVID-19 are going to reach 200 K leading to more than 5 K deaths [7]. Table 1 shows seven states of India where the cases are increasing gradually.

When the first case was detected in India, since then lots of actions are being taken by Indian government to control the increase in the cases. To maintain social distancing, lockdown has been imposed in the whole country. Various applications are being launched to fight against COVID-19. Following is the chronological list of COVID-19 rise and what India has gone through the period when first case was detected on January 30, 2020 to March 31, 2020.

Table 1 List of top seven states of India where Corona cases increased rapidly [8]

S. No.	Indian state	Number of Corona confirmed cases (in Thousands—K)
1	Maharashtra	70 K
2	Tami Nadu	23 K
3	Delhi	20 K
4	Gujarat	17 K
5	Rajasthan	8980
6	Madhya Pradesh	8283
7	Uttar Pradesh	8075

Table 2 Chronological list of rising COVID-19 outbreak in India

Year	Date	Event
2019	?	Mysterious phenomenon in Wuhan, Hubei, China
	December	First confirmed case in Wuhan
2020	January 30	First case in India (Kerala)
	March 5	Sudden increase in the number of confirmed cases (29 confirmed case) in India
	March 25	21 days lockdown(25 March 2020–14 April 2020)
	March 30	More than 1000+ confirmed cases identified in India
	April 2	Launching of AarogyaSetu (application to fight against COVID-19) app in India
	April 14	The confirmed increases from 1 to 10 k leading to 339 deaths Lockdown 2.0 till May 3, 2020
	April 28	First update of AarogyaSetu
	April 30	33,050 (confirmed cases), 1074 (deaths) in India
	May 18	Lockdown 4.0
	May 19	101,139 (confirmed cases), 3163(deaths)in India
	May 30	Lockdown 5.0 in containment zone till June 30, 2020 173,763 (confirmed cases), 4971 (deaths) in India

4.2 Events in COVID-19 Outbreak

See Table 2.

5 Threats Caused Due to COVID-19 and Relief Measure Taken

5.1 Technical Threats

Due to the shift of remote work (work from home), organizations are more vulnerable to rising cyber-attacks. In the mid of the month of March, rapidly number of Corona cases being rising and by the Govt. complete lockdown was declared in India on March 24. On the same time, many Indian companies noticed a massive number of attacks too. There are many types of technical threats using COVID-19 [1, 4, 6, 9].

Cyber Threats during COVID-19 lockdown: During lockdown work from home, online business, online study increasing cyber threats and other technical challenges.

As India was facing spike in COVID-19 cases, there is also an increase of COVID-19 information emails. Some emails are related to charity, researches or some claims to provide essentials to the one in need. Due to this situation, there is a threat of becoming

cybercrime target is rising by opening those emails. Many offices have provided their own laptop to their workers which are on the target of being attacked and hence leading to attacking the online meeting being organized. [10]. Some common attacks are as follows:

Phishing: It is one of the easiest forms of cyber-attack for an attacker to carry out; through it, they can invade every important thing of their target's lives. Most of the time, phishing has been witnessed in the wild in emails. More than 900 k threats are there across email, URL and file according to data collected by smart protection network. Certain phishing Web sites were being remarked and are now blocked:

- adaminpomes[.]com/em/COVID-19/index-2[.]php
- bookdocument[.]in/Covid-19/COVID-19/index[.]php
- glofinance[.]com/continue-saved-app/COVID-19/index[.]php
- laciewinking[.]com/Vivek/COVID-19/

Malicious Web Site: It is a Web site created when a scammer links a user to a Web site that looks exactly like a familiar site but is actually the scammer's site. Increase impact of COVID-19 results in the threat caused by two Web sites; "antivirus-covid19[.]php" and "corona-antivirus[.]com" which is now inaccessible. According to Trend Micro, there were more domains that were also found malicious as given below:

- Accorona[.]com
- beatingcoronavirus[.]com
- bestcorona[.]com
- coronadatabase[.]com
- corona-crisis[.]com and many more.

Fake Maps: This was developed to silently steal passwords, crypto wallets and other sensitive information. The cyber-attackers made a "fake" version of the map provided by Johns Hopkins University named as deadly Coronavirus map.

Mobile Threats: CovidLock(mobile ransomware) tracks COVID-19 cases. Actually, this malicious android application locks the phone of victims and demand for some ransom from the victim to gain access to their phone. Otherwise, they might delete the victim's important data or might leak social media account details. As per VMware Carbon Black, the fake android Coronavirus app was discovered as follows:

- COVI (com.droobihealth.corona)
- Corona Virus Status (com.arumcomm.coronavirusstatus)
- Coronavirus (coronavirus.tracker.news)
- COVID-19 Alert (corona.report).

Sextortion Scam: Sextortion is an attempt to extort money or get victims do something against their will by threatening the victim to release their personal images and videos. The images may be fake imagery such as sextortion scams. According to certain sources, in this scam the victim gets email with respect to danger that

Table 3 List of data breaches, ransomware, malicious insiders and miscellaneous incidents (March 2020)

Entity	Records	Method	Ref
Tesco	600,000	Credential stuffing attack	[11]
Boots Advantage Card	150,000	Hacking	[12]
Hammersmith Medicines Research (attack on COVID-19, former patients record)	Unknown	Maze ransomware attack	[13]
Vijay Sales (India)	Unknown	Data breaching	[14]
Henry Mayo Newhall hospital	1	Snooping medical record	[15]

scammer knows every one of their mysteries, their passwords, their whereabouts and different subtleties identified with individual exercise (Table 3).

5.2 COVID-19 Frauds in India

EMI moratorium fraud: Reserve Bank of India (RBI) first declared the moratorium on loan EMI for next 3 months (from March 1 to May 31, 2020) and now it has been further extended to 3 month (June 1 to August 31, 2020) [16]. It means in this duration, the borrowers will not have to pay EMIs and other loan. Due to this, cyber-criminals get the chance to trick people. In EMI moratorium fraud, attacker calls the borrower as their bank representative and asks for OTPs or passwords to gain access to the bank detail of the customer by offering them extend their EMI payment. The borrower loses money when they share their details with the fraudsters.

Fraud in PM CARES FUND: In the Prime Minister’s Citizen Assistance and Relief in Emergency Situation Fund, the national fund is raised for endangering situation like COVID-19 pandemic. Main objective of this PM CARES FUND is to provide relief and render financial assistance to enhance the critical healthcare facilities, etc. [17]. Basically in PM CARES Fund fraud, fake Unified Payment Interfaces (UPIs) are being used. The correct UPI ID is “pmcares@sbi”. Generally, the fake UPI IDs are omitting the letter “s” from PM CARES. The fake UPIs mentioned by CERT-in (Indian Computer Emergency Response Team) are pmcare@sbi, pmcares@pnb, pmcare@yesbank and pmcare@icici [18].

Fake E-commerce Web site: During this pandemic, the customer usually prefers to purchase product online by keeping them safe, and it is also easy to use. Therefore, cybercriminals take a huge advantage of it by developing fake e-commerce Web site selling essentials. The site is similar to the original site in which you can select item, provide your address details and make payment. After that the site is shut and your item never gets delivered [19].

Malware installation: According to some resources, many domains with name containing Corona, COVID, virus and many more were being registered for phishing attacks. The most well-known video conferencing application during nowadays is Zoom, and there is an abrupt increment in the new area enlistment with names including Zoom. These domains contain malware, once the user clicks on it, which leads to malware attack on their device [20].

5.3 *Technical Relief Measures*

Contact Tracing: It is the process of identification of undiscovered individual who may have come into contact with a tainted individual. This helps to reduce infection in the population. The purposes of contact tracing are as follows:

- To reduce spread of the infection by interrupting this transmission.
- To aware, alert and prevent people from contacting to the possibility of infection.
- To offer diagnosis to those who are infected.

Certain mobile applications are designed for preventing 2019–20 Coronavirus pandemic to aid contact tracing like:

- *AarogyaSetu* (launched by Government of India): This app uses GPS location and Bluetooth to track users. It also guides for self-isolation and is also aware about COVID-19 symptoms and precautions [21].
- *BeAware Bahrain* (developed by iGA (The information of eGovernment authority)): This app went through BETA testing, and it is compulsory for all the quarantine cases to register in it, whereas other can register by their valid IDs or passport number [22].
- *CoronaApp* (developed by the Colombian Government): It helps to detect nearby areas and individuals infected by COVID-19. It also contain technologies developed by Government of Singapore, Government of South Korea and Apple [23].
- *eRouška application* (launched in Czech Republic): It is based on Bluetooth technology. If the permission is granted by user, then the phone with active Bluetooth will help to know about both infected and non-infected person as they meet [24].

India takes action against the prevention of COVID-19 by launching many mobile applications. These applications are as in Table 4.

Table 4 Action against the prevention of COVID-19

Application name	Launched by developed by	Different features
AarogyaSetu	Government of India	<ul style="list-style-type: none"> • This app tells about the low, moderate or high risk when a non-infected person meets an infected person • Works on Bluetooth proximity • Available in 11 languages
COVA Punjab	Government of Punjab (India)	<ul style="list-style-type: none"> • Works on real-time dashboard for Punjab stats • Traveler and shop registration feature(updated on April 29)
CG COVID-19 ePass	Government of Chhattisgarh	<ul style="list-style-type: none"> • Issue state wise and intra-district wise e-pass for vehicular movement to transport essential commodities • e-pass generated by photograph, valid ID proof and business proof
Test Yourself	Government of Goa/Innovanccer Inc.	<ul style="list-style-type: none"> • Self-evaluation assessment for risk identification
Quarantine Watch	Revenue Department, Government Of Karnataka	<ul style="list-style-type: none"> • Self-reporting by home quarantine persons

Certain features to be added in an application for combating against COVID-19

1. Travel history of the person should also be recorded if he travels from hotspot area to green area. (Hotspot areas are those areas where more than six people have been tested positive of Coronavirus)
2. Alert message while entering in the red zone, i.e., hotspot zone.
3. Map of area with zone highlighted (low, moderate, high risk zone) nearby the individual location.
4. COVID-19 prevention-related games for children which should be aware of them and also productively passes their quarantine time.
5. Some healthy tasks and videos should be available on the app so that individual can utilize their time.
6. Aware every individual about cyber-attacks which is also creating a huge impact on lives.

Things to keep in mind:

- Not to reveal your information to strangers whether they claim they are from your bank, company or any government organization.
- Do not open attachments from unknown sources.
- Avoid using unauthorized applications or software.
- Check the details correctly while transferring money digitally.

- There are many known and well-established Web sites, therefore buy items from them only otherwise prefer buying items locally.
- Better to verify the identity of the receiver before helping them.

5.4 Impact of COVID-19

On Information Technology: These days major problem faced by the IT industry is because of the economic fall, due to the public health concern companies tell their employees to work from home (remotely). Therefore, there is a huge loss. For example: Due to the unpredictability caused by the outspread of Coronavirus, Apple's stock rises and falls widely. In the mid of February, Apple stock hits a high closing price and by the end of February it dropped. Furthermore, in March, it has also fallen [25]. The Indian IT sector depends upon international clients like Europe and USA, where there is a worse impact of this pandemic. Due to which there may be a worse impact on the Indian IT sector leading to huge losses [26].

On Education: As everything has moved online from education to teaching, this creates an immense revelation on student's social life and learning also [27]. Due to network failure and many uncertainties, many assessments and exams are being canceled or postponed. This is not only an issue for school-going children but it is also affecting many universities as there is a slowdown in student placements and internships.

Internet of Things (IoT): The interest of IoT gadgets has been diminished as clients are staying at home, increased unemployment and lack of income, there is a decrease in the acquisition of IoT gadgets. In India in complete lockdown, due to the decline in budgets of technology, many ongoing projects are being paused. Not only the ongoing projects are being paused as well as the new projects are also declined. Many companies freeze their hiring in IoT firms [28, 29].

Drones: The doctors, the policemen, the security guards, the sanitary workers all are playing a major role in combating COVID-19 similarly technologies like artificial intelligence, big data, GIS and location technology are also playing a vital role in combating COVID-19. The drones also play a key role in helping people and authorities through:

- Surveillance
- Broadcast
- Disinfectant spraying
- Monitoring traffic and lockdown violators.

In many parts of India, drones are being used like in New Delhi, and it is used to enforce social distancing on roads, to keep watch on places where there is a crowd like grocery shops, banks and religious places. In some part of India, it is being

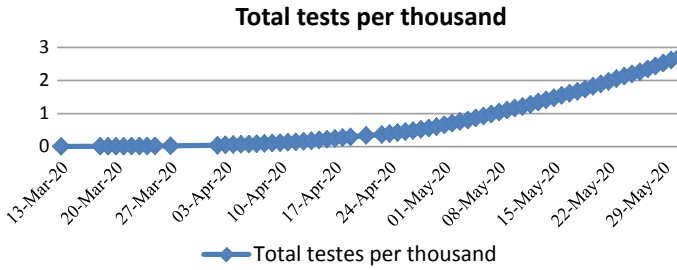


Fig. 6 Total tests per thousand have done in India by May 31, 2020

used for creating awareness among people about the restrictions implemented by administration [30].

Machine learning: Major problem in this pandemic is the lack of testing done. Testing is important to know how many people are infected with this virus. In many countries including India, the limit with regard to COVID-19 testing is still low. Figure 6 shows the total tests done per thousand in India. Machine learning is a significant tool in fighting the current pandemic. In this time, if we take the opportunity to gather information, pool our insight and combine our abilities, we can then save much information—both now and later on.

Through machine learning, we can categorize the population based on gender, age, symptoms and their travel history which can be used further for processing and combating COVID-19 [31].

Blooming opportunities: To fight with this virus, we require three things to cooperate which is primarily focused on better understanding of pandemic challenges and public health risks prevention for population awareness and to get learning from this pandemic and give a social call for preparedness for such future outbreaks. Technology enabled services to contribute in promoting public advisory and guidelines. Here are some opportunities for people during this pandemic:

- Although the information technology is suffering a lot with this outbreak, there are some opportunities opened in IT industry like 5G technology, ecommerce, epayments, Telehealth, etc.
- Students should explore digital learning platforms on their own.
- Lot of internship programs and research projects are available online.
- Support communities should be made for teachers and students for queries.

5.5 Post-pandemic Challenges

The future is never an exact replica of the past, and the universe will see further tragedies, but they are not going to grow just as COVID-19 did. It is necessary to

think beyond this current virus to develop a system that can provide an effective solution to the wider range of future threats, and post-pandemic sustainability imposed many open challenges like reinventing remote health monitoring, telemedicine and teleconsultation, public health and elderly care.

Technological shift and assessing the emerging technical risks with new strategies will be another major challenge for technology leaders working in different domains. Recognizing new world of work with upgrading skills and learning will be the basic course of action remote access, virtual laboratories, virtual business with virtual collaborative space secure accessibility, online education and community events with security and privacy will be a big concern, whether it is a cyber-attack, climate change-fueled disasters or some other possibilities.

Furthermore, the world's battle with the coronavirus is highlighting how risk will spread and intensify one another. Scenarios for the post COVID-19 can be defined as the economic powers may lead to panic and conflicts, exacerbate economic harm (economic reconstruction had to deal with massive debts, broken global trading and investment system), increase in cyber-attacks/cyber threats (cyber-attackers will use this pandemic situation and may cause more harm in future), technology shift in the domain (as everything is moving online people who are facing problem in business, education, online shopping) and decimate the hope of growing out of this crisis.

6 Conclusion

COVID-19 pandemic is increasing day by day. There are many steps taken by the Govt., administrative and healthcare warriors but we can delay the increasing number in India rather than fully control the social, economic and general life-threatening problems. There are social and technical threats have been explored and presented in this paper. A social call is still open to protect our lives from this virus, and on the other side many opportunistic withering minds who are involved in creating technical threats. By being aware of the cybercrimes and growing threats in this pandemic as well as post pandemic can contribute in the race of fighting against COVID-19 with new normal opportunities. Self-care awareness, healthcare best practices and strictly following advisories with better realization of technological threats and opportunities are the best tools to overcome from this pandemic crisis. In every sector, a proper planning and leadership qualities are to be taken to prevent various attacks. As the government is taking action to prevent the people of their countries from pandemic impacts and consequences. Being a socially sensitive community contributor it is also every one's responsibility to keep them safe and beware to challenges and opportunities with countersign impact of open and connected technological inferences to countersign impact and open and connected technological inferences.

References

1. Mouton F, de Coning A (2020) COVID-19 impact on the cyber-security threat landscape, March 2020
2. Adnan Shereen A, Khan S, Kazmi A, Bashir N, Siddique R (2020) COVID-19 infection: Origin, transmission, and characteristics of human coronaviruses, March 2020
3. INTERPOL: International Criminal Police Organization. <https://www.interpol.int/en/Crimes/Cybercrime/COVID-19-cyberthreats>.
4. Trend Micro Inc. [US], Developing story: Covid-19 used in malicious campaigns. © 2019 Trend Micro. Updated on 24 April 2020
5. VMware Carbon Black, Technical analysis: hackers leveraging COVID-19 pandemic to launch phishing attacks, fake apps/maps, Trojans, Backdoors, Cryptominers, Botnets & Ransomware. ©2020 Carbon Black
6. Keeling MJ, Deirdre Hollingsworth T, Read JM (2020) The efficacy of contact tracing for the containment of the 2019 Novel Coronavirus (COVID-19). February 2020
7. WHO Coronavirus disease (COVID-19) situation reports. <https://www.who.int/emergencies/diseases/novel-coronavirus-2019/situation-reports>
8. HomeMinistry of Health and Family WelfareGOI. <https://www.mohfw.gov.in/>. Accessed on 29 April 2020
9. CRN Team, PwC India's Threat Analysis_COVID-19|Significant rise in cyber incidents as hackers exploit the Covid-19 crisis
10. Saran J, Cyber threat in times of COVID-19 outbreak. 8 April 2020. <https://www.financialexpress.com/opinion/cyber-threat-in-times-of-coronavirus-outbreak/1921878/>
11. Kleinman Z, Tesco sends security warning to 60,000,000 Clubcard holders. <https://www.bbc.com/news/technology-51710687>
12. Wharton J (2020) Boots Advantage Card hit by cyber attack, 5 March 2020
13. Goodwin B, Cyber gangsters hit UK medical firm poised for work on coronavirus with Maze ransomware attack. 22 March 2020
14. India's Vijay, Sales leaks private information through exposed Amazon backup server. 20 March 2020
15. HIPPA Journal, Henry Mayo Newhall hospital fires employees for Snooping on medical records, 13 March 2020
16. ET Online, RBI extends EMI-moratorium for another 3-month on term loans. Here's what it means for borrowers. 23 May 2020
17. PMINDIA, About PM CARES Fund. <https://www.pmindia.gov.in/en/about-pm-cares-fund/>. Accessed on 25 May 2020
18. CERT-In, Alert people about fake UPI IDs seeking donations towards PM-CARES Fund." Updated on 3 April 2020
19. India's ecommerce growth propelled due to COVID might come at the cost of more online frauds. Published on 18 May 2020
20. COVID-19 Impact: cyber criminals Target Zoom domains. Accessed on 25 May 2020. <https://blog.checkpoint.com/2020/03/30/covid-19-impact-cyber-criminals-target-zoom-domains/>
21. MyGov [IN], Government of India. <https://www.mygov.in/aarogya-setu-app/>
22. MGZN Startup, BeAwareBahrain' app officially launched by iGA (31 March 2020)
23. CoronaApp, <https://coronaviruscolombia.gov.co/test/aislamiento-saludable/coronapp.html>
24. Holzman O (2020) V Česku se spouští aplikace Rouška. Staví na ochraně soukromí a upozorní, pokud jste přišli do kontaktu s nakaženým (in Czech), 11 April 2020. (The eRouška application is launched in the Czech Republic. It builds on privacy and alerts you if you come in contact with an infected person (English translation))
25. Clover J (2020) COVID-19 Coronavirus impact on Apple's iPhoneMax and WWDC. 14 May 2020. <https://www.macrumors.com/guide/covid-19-coronavirus/>
26. Raja Simhan TE, Indian IT sector may take a heavy hit as Covid batters US and Europe. Updated on 8 April 2020. <https://www.thehindubusinessline.com/info-tech/indian-it-sector-may-take-a-heavy-hit-as-covid-batters-us-and-europe/article32289747.ece>

27. Burgees S, Sievertsen HH, Schools, skills, and learning: the impact of COVID-19 on education. 1 April 2020
28. LasseLueth K, The impact of COVID-19 on the (IoT) Internet of Things-now and beyond the Great Lockdown: Part-I. 16 April 2020
29. LasseLueth K, The impact of COVID-19 on the (IoT) Internet of things-now and beyond the Great Lockdown: Part 2. 22 April 2020
30. Chandola S, Drones emerged as go to technology partners to combat COVID-19 India. 13 April 2020
31. Burhanuddin Bhopalwala, COVID-19 and machine learning. 26 March 2020

IoT-Based Automation Irrigation System



Rahul Thakur and Jay Singh

Abstract In the development of agricultural country like Asian nation, agriculture plays a crucial role. Numerous ancient strategies that were used for irrigation, like Moat, Chain pump, Dhekli, Rahat, drip system and overhead mechanical device, is not that abundant economical. They finish in loads of wastage of water and should conjointly promote diseases like flora formation, and the only resolution to the current downside is smart agriculture by modernizing present ancient strategies of agriculture. Thence, the projected ancient strategies of agriculture aim at creating agriculture sensible victimization automation and IoT techniques. In this paper an IoT platform supported ThingSpeak and Arduino has been developed and tested as well where the goal is that the farmer can control the irrigation by employing a PC or smartphone from anywhere within the world, can monitor the flow of pump and soil moisture level and reduce his efforts to optimize the utilization of water.

Keywords IoT platform · ThingSpeak · Irrigation · Arduino · Centrifugal pump · Soil moisture sensor

1 Introduction

The water dearth in major cities of India, mainly Chennai, brought some public attention again to the problem of water dearth in India. Though consultants, ecologist and other committees had been crying aloud as they are concerned with India's water crisis for an extended time, until and unless the taps went dry in major cities they did not garner public attention. In fact, the govt. discharged a report, in this, it acknowledged in history the country was full of the worst water crisis and regarding six hundred million folks or about forty fifth of the India's population suffer from water crisis [1].

R. Thakur (✉) · J. Singh
Electrical and Electronics Engineering Department, G. L. Bajaj Institute of Technology and Management, Greater Noida, U.P., India
e-mail: rahulthakur12123434@gmail.com

© Springer Nature Singapore Pte Ltd. 2021
R. Agrawal et al. (eds.), *Advances in Smart Communication and Imaging Systems*,
Lecture Notes in Electrical Engineering 721,
https://doi.org/10.1007/978-981-15-9938-5_48

Technology development has played an important role in the agricultural field and especially in the irrigation where it contributed to solving the problem of water shortage and the development of various irrigation system. In this context, many works are realized, a Web application is developed and connected to Arduino via Wi-Fi shield for monitoring the greenhouse and controlling the temperature and the soil moisture, and an automatic irrigation system based on IoT is realized which allows the optimal remote control of the water consumption. An interesting control and monitoring result has been achieved has allowed the preservation of water in agriculture using a low-cost system. Many others works based on IoT and phone are created to help in an automated irrigation system [2].

Mainly, it focuses on attaining a technological answer supported IoT and Arduino to facilitate the task of monitoring plant, control the irrigation process, to help the farmer and reduce its efforts. Here, we used C++ programming language for automation. A ThingSpeak channel is created and connected to Arduino by using ESP8266 Wi-Fi module to sending and receiving data using the cloud, where the user can access the channel via username and password to remotely monitor and control. The test result shows the efficacy of the system.

2 Proposed System

A fully automated irrigation system supported cloud and Arduino is planned to optimize the employment of water for farmland and assist the farmer to monitor his field. The structure of the projected system is illustrated in Fig. 1, this system includes a soil wet detector that measures the soil moisture level and sends to the ThingSpeak cloud via the Wi-Fi module ESP8266 to monitor the soil condition. An algorithm

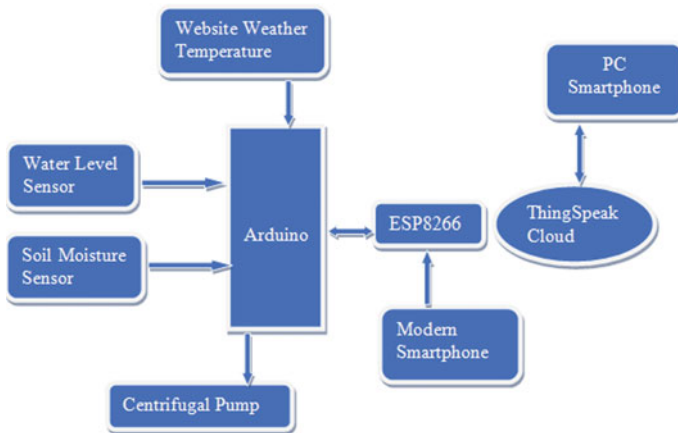


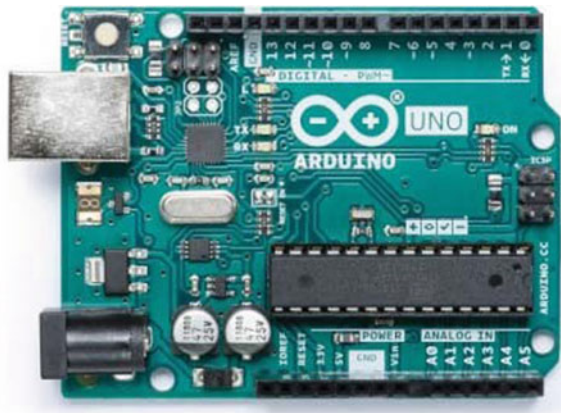
Fig. 1 Proposed system diagram

has been developed with soil moisture intervals that have been programmed into an Arduino to make a decision to irrigate or not, the latter is done provided that the tank is not empty. For this, we have a tendency to use a water level detector that is employed to observe the water level within the tank [3]. This system also offers the ability to detect the outside temperature imported from a weather Web site as (this is an advantage, where we do not need to use a sensor to measure the temperature, we retrieve the information directly via the Web site). If the humidity level is at well-defined intervals, you can know the state of the soil if it is dry or wet, which opens the solenoid valve and thus provides water to irrigate the soil.

To build this system, we used the following hardware and software components:

- **Arduino uno:** It acts as the microcontroller board for the project. Arduino is an open-source electronics platform based on easy-to-use hardware and software. It is combination of microcontroller-based Arduino board, Arduino program language and Arduino software for development and compilation. Arduino has evolved from just being an embedded environment to helping build advanced products for IoT applications, wearables, 3D printing, etc. Also being an open-source platform, the hardware design schematics, PCB files and the code for the software are freely available. This gives user the flexibility to adapt and develop the design for their own projects (Fig. 2).
- **ThingSpeak platform:** Is an IoT analytics platform service that can you view and analyze live data in the cloud and also give you the ability to execute MATLAB code.
- **Wi-Fi module ESP8266:** Is a leading low-cost platform for IoT. The prominence of ESP8266 is primarily due to its dual functionality. It can be used as a self-contained Wi-Fi networking solution that can carry and drive the entire application. It can be used as a Wi-Fi adapter to control other microcontroller units that can host more complex applications than supported by ESP8266. It acts as the Wi-Fi adapter for the IoT projects. It has multiple general purpose input output pins which can be used to interface sensors directly to the MCU.

Fig. 2 Arduino Uno



- Soil Moisture Sensor: The soil wet sensor is employed to live the wet level of soil. The YL-69 probes are used to measure the resistance of current in soil. As the moisture level increases the resistance to the flow of current will decrease [4–9].
- Centrifugal Pump: Is a mechanical device designed to maneuver a fluid from cistern to the individual field space wherever water is needed by means that of the transfer of motion energy from driven rotors, known as impellers (Figs. 3, 4, 5 and 6).

Fig. 3 ESP8266

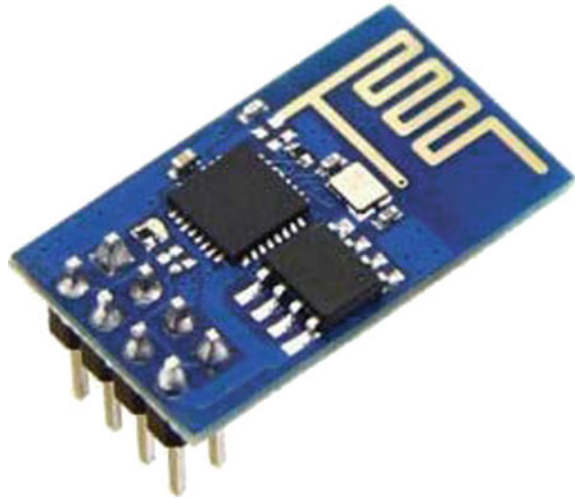


Fig. 4 ThingSpeak platform [2]

A person's hands are holding a tablet displaying the ThingSpeak IoT dashboard. The screen shows several data visualization widgets, including a bar chart, a line graph, and a 3D surface plot. The background of the image is a blurred outdoor setting with green foliage.

ThingSpeak for IoT Projects

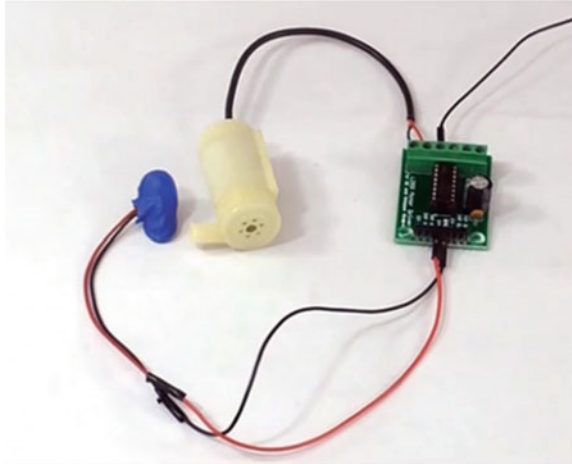
Data collection in the cloud with advanced data analysis using MATLAB

Get Started For Free

Fig. 5 Soil moisture sensor



Fig. 6 Centrifugal pump



3 Implementation

The realization of this work is illustrated below. First a MathWorks account is created that allows us to create a ThingSpeak account (Fig. 7). Then, a channel named smart irrigation system using IoT associated with an ID and a password is also created. For the exchange of data, we must first connect to our Wi-Fi and then connect the Wi-Fi module to the channel that was created through its API key (Fig. 8).

4 Test Results

The setup of an automatic irrigation system is completed. If soil wet level goes below a definite threshold price (i.e., moisture level below 50), then the water pump will “TURN ON”. If the soil is wet (i.e., moisture level above 50), then the water pump will automatically “TURN OFF”. All the information will be sent to the Arduino through the server via Wi-Fi. The visualization in the system is performed at the field level to display the soil moisture values in diagrams, or the values are taken at well-defined times in order to monitor the soil condition like illustrate in Fig. 9

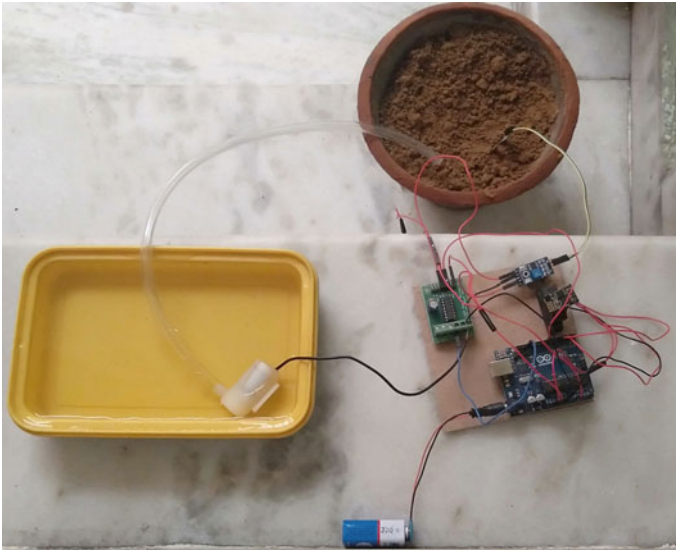


Fig. 7 System prototype

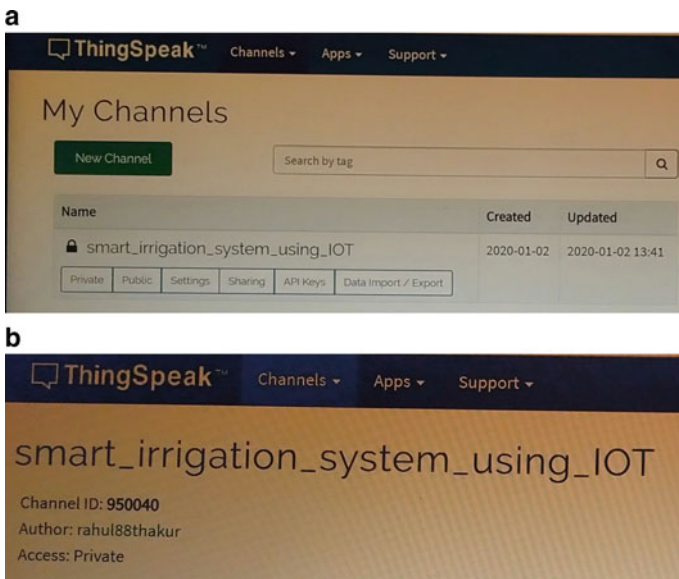


Fig. 8 ThingSpeak channels

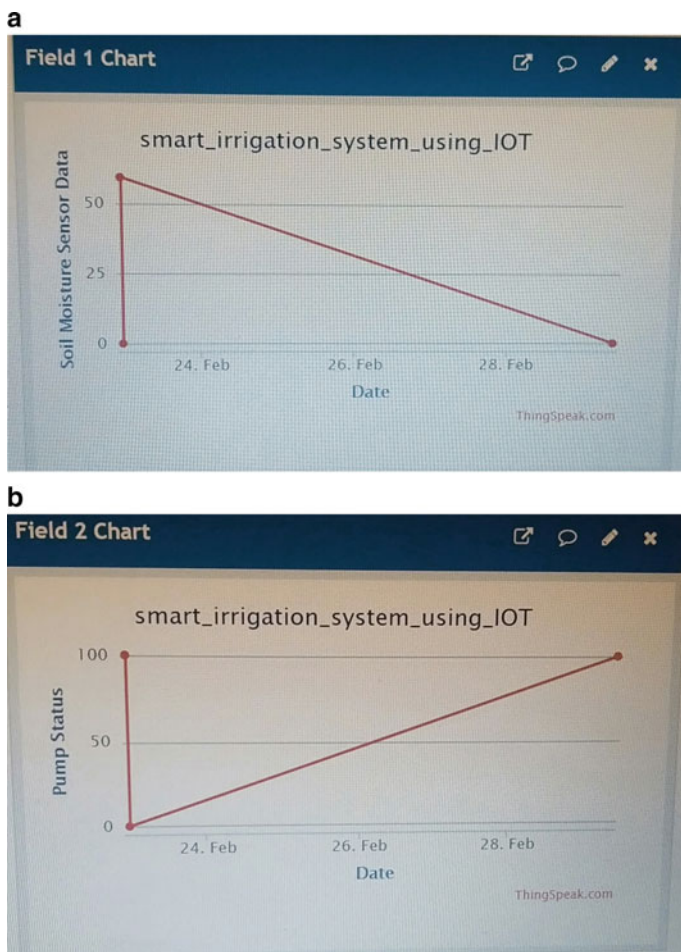


Fig. 9 Soil moisture and water pump display in different times

(Table 1).

Table 1 Soil moisture content

Moisture content	Time (s)	Pump status
100	1	ON
85	3	ON
65	2	ON
50	3	ON
30	4	OFF
20	1	OFF
11	3	OFF
8	2	OFF
0	4	OFF

5 Conclusion

In this paper, an associate intelligent irrigation system primarily based within the cloud is enforced successfully. A channel is made in an associate ASCII text file IoT platform that is created to save lots of and show the soil wetness data and conjointly to manage the irrigation by the net.

This system options a custom detector style for power potency, value effectiveness, low-cost elements, further as measurability finish simple use. In the future, there are some tasks that need to be done like creating this technique work on renewable sources corresponding to solar power which might facilitate in low consumption of fossil fuels.

References

1. Hamza B, Mounir B, Khaoula D, Amina S (2018) Smart irrigation system based Thingspeak and Arduino. In: ICASS, Nov 2018, Médéa, Algeria
2. Vaishali S, Suraj S, Vignesh G, Dhivya S, Udhayakumar S et al (2017) Mobile integrated smart irrigation management and monitoring system using IOT. In: ICCSP, 2017, pp 2164–2167
3. Sepaskhah AR, Ahmadi SH (2010) A review on partial root zone drying irrigation. IJPP
4. Song Y, Wang J, Qiao X, Zheng W, Zhang X (2010) Development of multi-functional soil temperature measuring inst. JAMR 9(1):80–84
5. Gawali YG, Chaudhari DS, Chaudhari HC (2016) Automated irrigation system using wireless sensor network. IJARECE 5(6). ISSN: 2278-909X
6. Viani F, Bertolli M, Salucci M, Polo A (2017) Low-cost wireless monitoring and decision support for water saving in agriculture. IEEE Sens J 17(13):4299–4309
7. Learn More - ThingSpeakIoT. [En ligne]. Disponiblesur: https://thingspeak.com/pages/learn_more. [Consulté le: 03-aôût- 2018].

8. Ning W, Naiqian Z, Maohua W (2006) Wireless sensors in agriculture and food industry—recent development and future perspective. *Comput Electron Agric* 50:1–14
9. Muthunpandian S, Vigneshwaran S, Ranjitsabarinath RC, Kumar Reddy YM (2017) IOT based crop-field monitoring and irrigation automation, vol 4, Special Issue 19

Leaky Wave Antenna for Wide Angle Beam Scanning and High Directivity



Ruchi Agarwal, Prakhar Pratap Singh, Suresh Kumar, Umang Singh, and Vipul Agarwal

Abstract A periodic leaky wave antenna having series fed 7-unit cell structure is proposed here. The design of the proposed antenna is mirrored E-shaped antenna. In this work, directivity and efficiency of the antenna are improved by etching rectangular-shaped patch added with small triangular patch and loading of balanced sorting pins. Antenna is working efficiently in range 21.1 GHz to 26 GHz having center frequency of 24 GHz. It is having a high scanning range 70° (from -30° to 40°) and improved directivity. Efficiency is the ratio of conversion of power of accepted RF signals into radiated signals, and efficiency of the designed antenna is 90%. Gain of the proposed antenna is 15.1 dBi. Circular polarization is also obtained at different frequencies, i.e., 21.1 GHz and 24.5 GHz. The working of proposed antenna is effective as well as efficient, and radiation is circularly polarized.

Keywords LWA (leaky wave antenna) · Periodic LWA (PLWA) · RF signal · SIW circular polarization

1 Introduction

Leaky wave antenna or LWA is a traveling wave antenna, in this, waves generally propagate along the structure of the antenna [1–4]. Substrate integrated waveguide (SIW) structures are used in industries due to its several advantages including cost-efficient, simple construction, and ease of fabrication with other circuits [5].

Leaky wave antennas or LWAs are classified based on their behavior as uniform and periodic LWAs [6]. In uniform LWAs, they generally have structures which is wave guiding which helps in supporting fast waves in the fundamental mode. In fundamental mode, uniform LWAs help to obtain better scanning range in the forward

R. Agarwal · P. P. Singh (✉) · S. Kumar · U. Singh · V. Agarwal
Department of Electronics & Communication Engineering, Galgotia College of Engineering & Technology, Greater Noida, India
e-mail: singhpratap.pps01@gmail.com

R. Agarwal
e-mail: ruchi.agarwal1987@gmail.com

direction region [7, 8]. Periodic LWAs can be formed by periodically addition of unit cells along with the length of the non-radiating structure. PLWAs are used for beams steering or scanning frequency in both forward and backward directions, and they are used for obtaining narrow beams having high directivity [9]. Leaky waves are generally called as fast waves as they travel with faster speed and surface wave as slow waves as they travel slower comparatively [4]. Properties of the LWA like different radiation pattern can be modified by merely changing structure of the antenna. LWAs have received high development due to its important properties like high gain and ease of integration with other devices and circuits [10–12]. LWAs have been developed for various transmission lines and have received high interest throughout the decade. LWAs can be categorized as uniform, quasi-uniform, or periodic depending upon the radiation characteristics. To increase the directivity of the antenna at the cross-plane, an array is formed by a combination of unit antennas in a particular order. LWAs are now used extensively in various fields like wireless communication systems, radar systems, etc., they are in heavy demand because of low profile structure, scanning beams, and high directivity [13].

A uniform LWA has a uniform guiding shape along the length or a periodic structure with a period much less than a wavelength, which commonly works at the fundamental mode of a fast-wave guiding structure (like metallic waveguide and substrate integrated waveguide [14, 15]). Various methods for enhancement of the performance of leaky wave antennas have already been done in past few decades, a few of them are (i) impedance match optimization in microstrip patch antenna by using plates, shorting pins [16], (ii) polarization of microstrip antenna and tuning the operating frequency by using shorting pins [17], (iii) huge amount of bandwidth are required for the operation of conventional LWAs which is having low scanning rate and low directivity [18]. For the suppression of unwanted frequency modes and enhancement of the excitation efficiency of other modes, the stopband in unwanted frequency mode was exploited [19].

The main challenge faced during the antenna designing was to modify the structure to allow proper scanning of the proposed antenna through broadside, and different strategies have been applied to obtain radiation through broadside. In this paper, LWA has been designed by removing a rectangular patch and adding a small triangular patch and on combination with suitable balance shorting pins, scanning range, as well as directivity of the antenna, is increased. To reduce the cross-polarization effect and to improve the band performance, the rectangular patch is truncated, and a small triangular patch at both the wings of the antenna is added. Suppression of open stopband at broadside is achieved by choosing the suitable dimensions as well as by proper positioning of the shorting pins. The antenna proposed here is having higher directivity, and scanning range of the antenna is large.

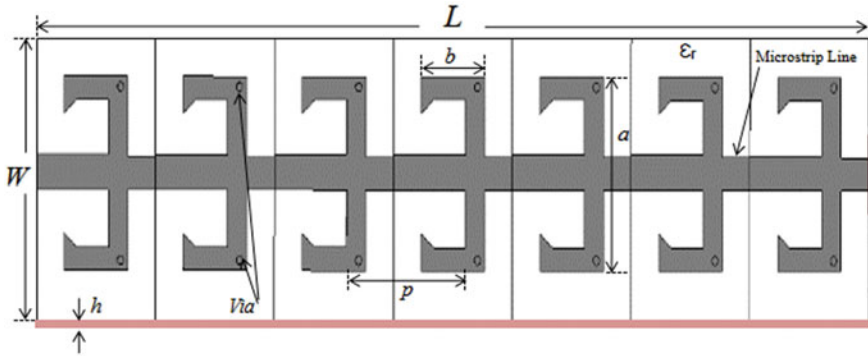


Fig. 1 Antenna dimensions are $L = 105$, $W = 60$, $p = 15$, $a = 16.8$, $b = 8$, $h = 1.575$ (mm)

2 Antenna Structure

The structure of the antenna is a mirrored E-shaped antenna having rectangular patch, added with a small triangular patch at the wings which is overall integrated with balanced sorting pins as shown in Fig. 1. In unit cell structure, leaky mode leakage rate is varied by using metallic vias. Also, by clearly defining the position of vias, SLL (side lobe level) has been reduced effectively. The antenna array is a combination of seven unit cells interconnected by 50Ω series line. These unit cells are added uniformly to get high directivity. Two waveguide ports are added at the extreme ends of the antenna. Substrate used in the antenna is Rogers RT5880 (lossy) having epsilon 2.2 and height 1.575 mm. Rogers RT5880 has a low dielectric constant (Dk), low dielectric loss and can be easily cut, sheared, and easily machined to shapes, making them suitable for broadband and various communication purposes. The designed antenna is microstrip periodic LWA having forward to backward scanning capability which is enabled by perturbations. CST versus 16 is used for the simulation of the proposed antenna. CST studio suite is a simulation software which can solve all electromagnetic problems from low frequency to microwave.

3 Unit Cell Characteristics and Dispersion Diagram

The unit cell structure of antenna is shown in Fig. 2. Two small rectangular shapes are etched, and two small triangular patches are added to form the required antenna design. There are two balanced shorting pins near wings of the radiating corners of the antenna. These etched portions are symmetrical with central feed line which means upper and lower portion of the antenna are similar to each other. The diameter of shorting pin is taken as 0.8 mm (or radius 0.4 mm). These shorting pins are used for integration of ground, substrate and patch and helpful in enhancing the radiation capability of antenna. The unit cell dispersion diagram of the antenna is calculated

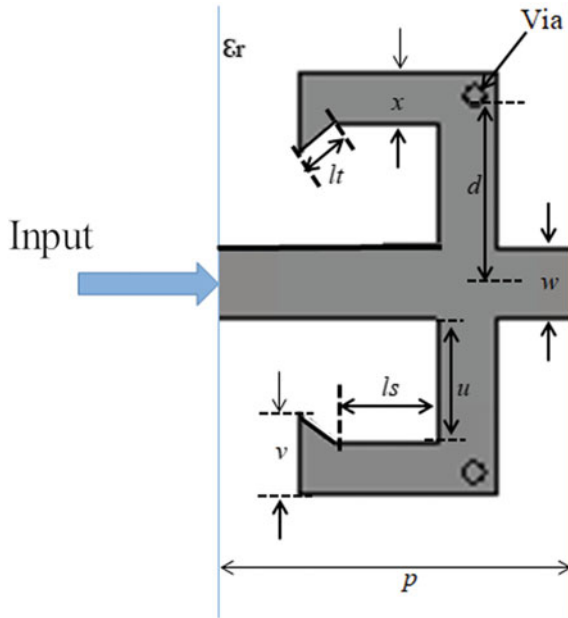


Fig. 2 Unit cell structure of antenna: $p = 15$, $w = 2.8$, $lt = 1.98$, $ls = 4$, $u = 4.8$, $v = 3.20$, $x = 2$ (mm)

and is depicted in Fig. 3. We can observe from the diagram that the parameter phase constant varies from forward direction to backward direction as frequency increases.

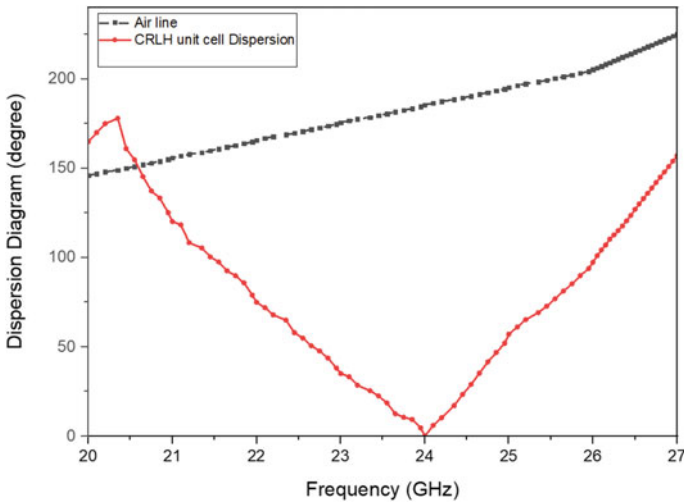


Fig. 3 Dispersion diagram of proposed antenna (center frequency at 24 GHz)

It is clearly depicted in the figure that the center frequency of the proposed antenna is obtained at 24 GHz as CRLH line is decreasing to 0 at the same frequency. The etching of rectangular patches and addition of triangular patches at the end position resulted in wide band performance and reduces cross-polarization. Further, open stopband is removed by using suitable dimensions of the rectangular patch. The material for ground and patch used in proposed antenna designing is perfect electric conductor (PEC). PEC is used to improve aperture efficiency and hence higher gain. The dimensions of the wings can be adjusted to obtain the suitable results.

$$\beta_{\text{eff}} = \frac{1}{p} \text{Re} \left[\cos^{-1} \left(\frac{1 - S_{11}S_{22} + S_{21}S_{12}}{2S_{21}} \right) \right] \quad (1)$$

$$\text{airline} = \left(2p \times \frac{\text{freq}}{C_0} \right) \quad (2)$$

where

β_{eff} is the effective phase constant
 p is unit cell length.

4 Result and Discussion

The S parameters are used to describe the relationship between different ports of the antenna (currently two ports in antenna are applied). The S parameters of proposed work are depicted Fig. 4. The result of S11 parameter shows it is matched to central feed line between the frequency range (21.1 GHz and 26 GHz). It tells how radio waves travel in a multi-port network. S11 result shows the bandwidth of the antenna and can be observed that the antenna is working efficiently between frequency range 21.1 GHz and 26 GHz.

Far-field pattern or beam steering of the antenna is shown in Figs. 5, 6, 7, 8 and 9. The radiation patterns are continuously varying with the change in the frequency of the antenna. In two-dimensional antenna, reciprocity is used to find the far-field radiation patterns in periodic leaky wave antennas [16, 17]. It shows how the main lobe changes its direction from backward to forward and hence beam steering is obtained with the variation in the frequency.

Beam steering is observed at various continuous frequencies and can be noted that the normalized pattern of the radiation of far-field directivity at 21 GHz, 22 GHz, 24 GHz, 24.5 GHz, 25 GHz is sequential and hence antenna is radiating backward to forward. The broadside is observed at 24 GHz frequency. Main lobe direction can be calculated by using the below formula.

$$\theta = \arccos(\beta_{-1}/k_0) \quad (3)$$

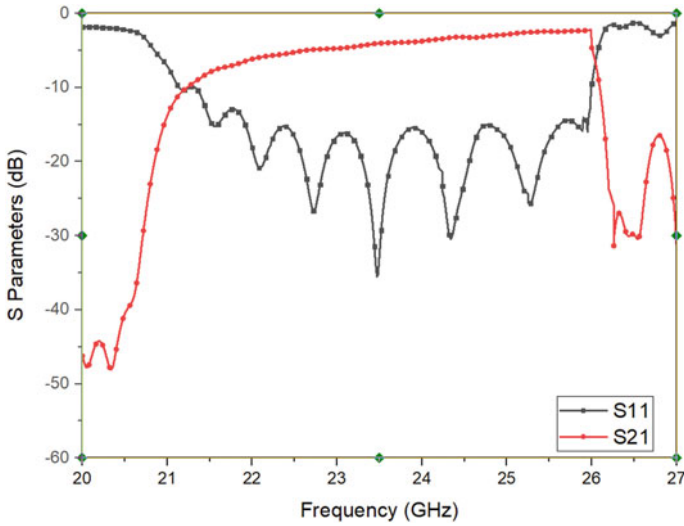


Fig. 4 S parameter of the antenna

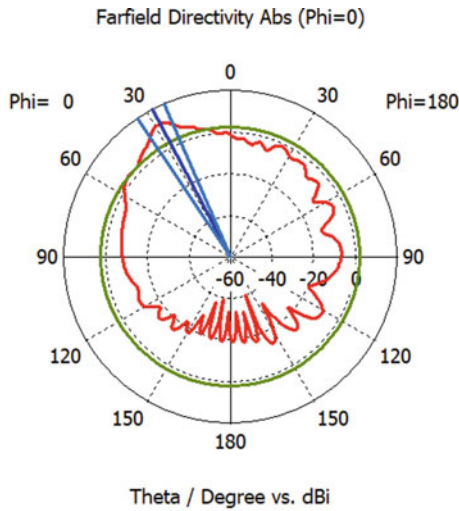


Fig. 5 Far-field directivity at frequency (21 GHz)

The relationship HPBW and the main beam scan angle can be obtained by using the formula (θ_{max}) [3]

$$\Delta\theta \approx (\alpha/k0)/0.183 \cos \theta_{max} \tag{4}$$

Fig. 6 Far-field directivity at frequency (22 GHz)

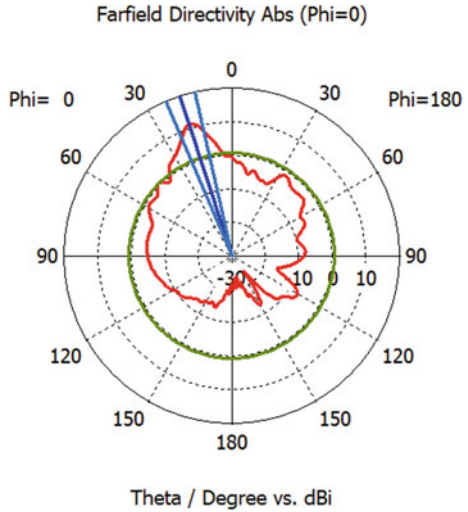
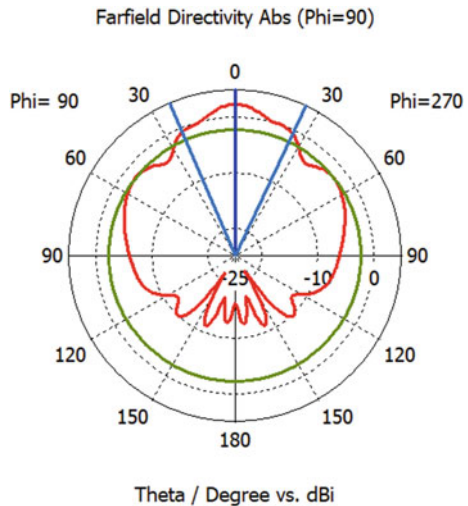


Fig. 7 Far-field directivity at frequency (24 GHz)



It is observed that the antenna shows broad beam patterns at lower frequencies. Half power beam width or HPBW increases when main beam starts scanning toward the direction of end fire.

Efficiency is the ratio of conversion of power of accepted radio frequency signals into radiated signals. At higher frequencies, high radiation efficiency is observed, and as the frequency decreases, radiation capability decreases. Efficiency of the antenna is observed to be 90%. The simulated total efficiency present in the antenna is depicted in Fig. 10. The maximum gain over frequency of the antenna is shown in Fig. 11. It

Fig. 8 Far-field directivity at frequency (24.5 GHz)

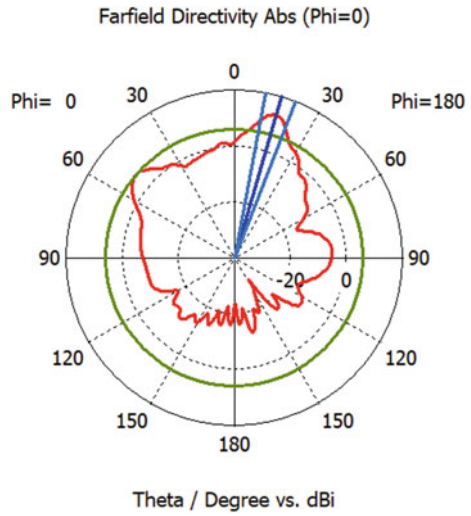
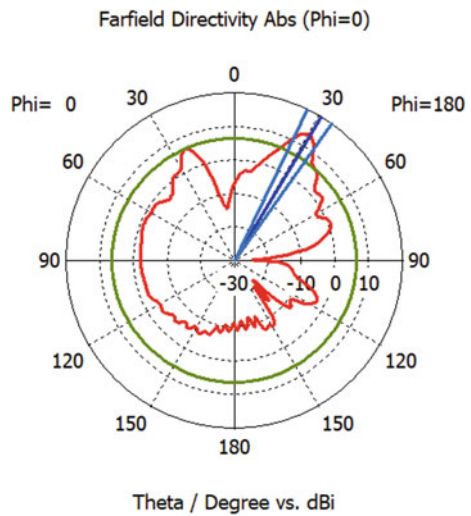


Fig. 9 Far-field directivity at frequency (25 GHz)



can be observed from the figure that maximum gain is 15.1 dBi in the antenna and the maximum gain is obtained at 24 GHz.

The designed antenna is circularly polarized at different frequencies, i.e., 21.1 GHz and 24.1 GHz. The antenna is multi-functional, circularly polarized antenna which could be used at various base station or at communication system of radio detection and ranging (RADAR). These circular polarization patterns are of great importance, and presently, they are used at various antenna stations in various parts of the world. Circular polarization of the simulated antenna is shown in Figs. 12 and 13.

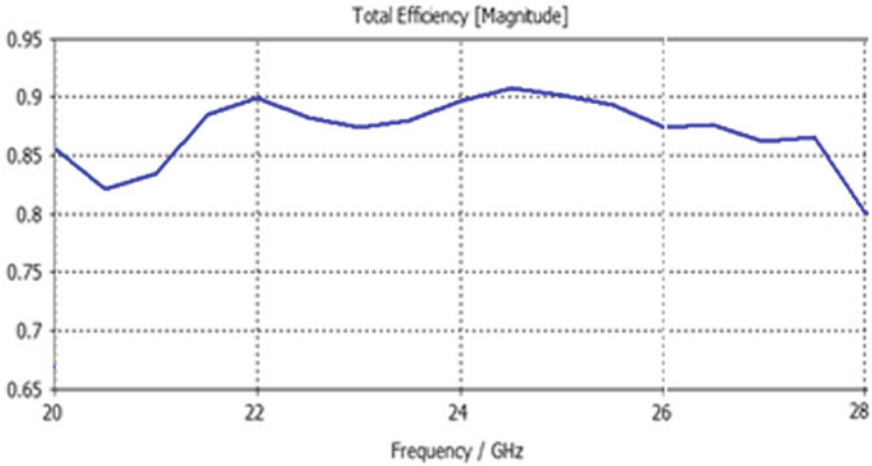


Fig. 10 Total efficiency of the antenna

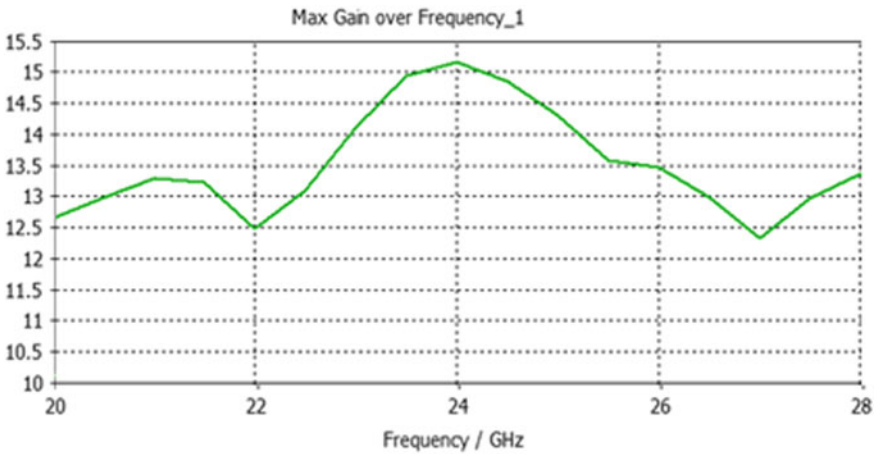


Fig. 11 Max. gain over frequency of the antenna

We have focused on LWA system to achieve effective as well as efficient antenna. Major problem was associated with broadside beam, which was achieved by truncation of rectangular patch and proper positioning of balanced sorting pins. Although there are papers which has broadside radiation pattern but efficiency of antennas in those papers are low comparatively. Also, in this paper we have used 7 unit cell structures hence the size of the antenna is not large. A complete comparison of proposed antenna and other antennas is made in Table 1. It is seen that proposed antenna here when compared with these reference LWAs is superior as well as overall effective in various parameters mentioned. The antenna is smaller in size, having circular

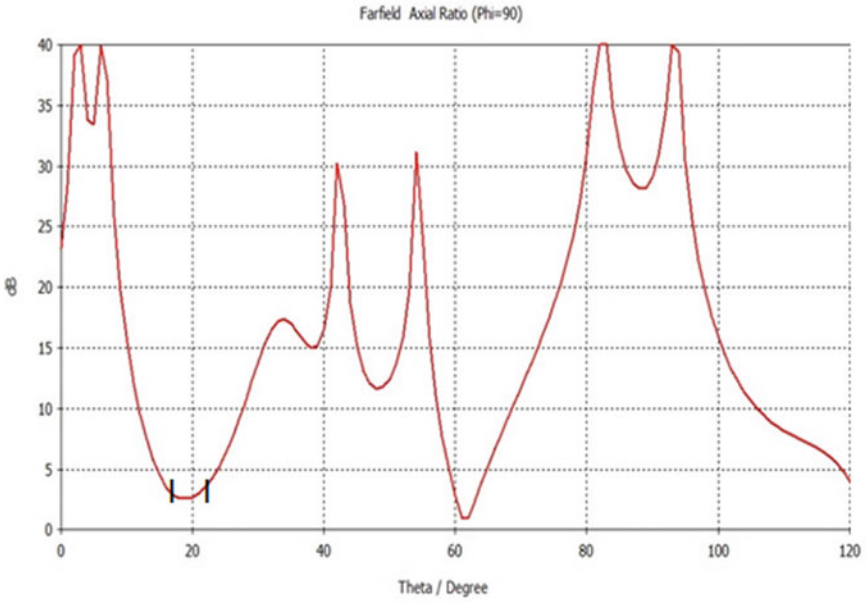


Fig. 12 Circular polarization at frequency 21.1 GHz

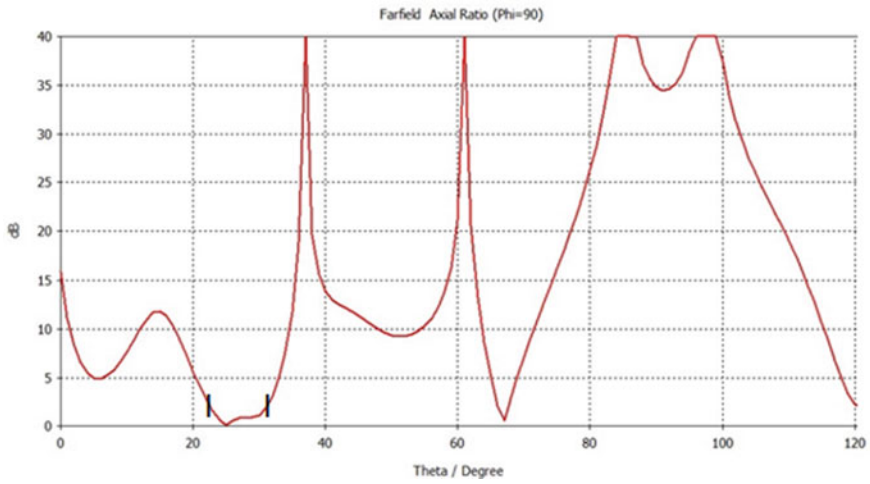


Fig. 13 Circular polarization at frequency 24.5 GHz

Table 1 Proposed antenna and recent reported works on LWAs comparison table

Property	Ref. [1]	Ref. [7]	Ref. [17]	Proposed antenna
Number of unit cell structure	8	9	5	7
Bandwidth range (GHz)	10–18	57–64	9–14	21.1–26
Circular polarization	Not reported	Circularly polarized radiation	Not reported	Circularly polarized radiation
Efficiency (%)	91	85	Not reported	90

polarization at various frequencies and is highly efficient when compared with other antennas.

5 Conclusion

Leaky wave antenna has been designed which is having a wider beam scanning capability of 70°. The designing of the antenna is very simple and compact resulting in reducing cost of manufacturing. The efficiency of antenna is found to be 90%, i.e., it is highly efficient and shows circular polarization at various frequencies and has total gain of 15.1 dBi. It is simple in designing and is easy to manufacture. Rogers RT 5880 (lossy) is used as a substrate, and PEC is used for designing of ground and patch. Various methods are proposed for the elimination of open stopband, and attenuation loss in the antenna resulting in design having less attenuation loss and eliminated open stopband. The antenna is radiating at various frequencies sequentially from forward to backward including broadside radiation.

References

1. Tiwari AK, Awasthi S, Singh RK (2018) A leaky-wave antenna with improved directivity and scanning range. In: 2018 5th IEEE Uttar Pradesh Section international conference on electrical, electronics and computer engineering (UPCON). IEEE, pp 1–5
2. Vashishtha A, Yadav A, Chaudhary D (2016) A review of 1-dimensional and 2-dimensional leaky wave antenna and recent advancements in LWAS. *Int J ComputAppl* 155(9)
3. Jackson DR (2013) Recent advances in leaky-wave antennas. In: 2013 international symposium on electromagnetic theory. IEEE, pp 9–12
4. Jackson DR, Caloz C, Itoh T (2012) Leaky-wave antennas. *Proc IEEE* 100(7):2194–2206
5. Sengupta S, Jackson DR, Long SA (2018) Modal analysis and propagation characteristics of leaky waves on a 2-D periodic leaky-wave antenna. *IEEE Trans Microw Theory Tech* 66(3):1181–1191
6. Emami M, Rahmani MH, Deslandes D (2018) A LTCC ultra-wideband periodic leaky-wave antenna with wide scanning range at 60 GHz. In: 2018 IEEE-APS topical conference on antennas and propagation in wireless communications (APWC). IEEE, pp 916–919

7. Wei DJ, Li J, Liu J, Yang G, Zhang W (2019) Dual-band substrate-integrated waveguide leaky-wave antenna with a simple feeding way. *IEEE Antennas Wirel Propag Lett* 18(4):591–595
8. Scattone F, Ettorre M, Eddo B, Sauleau R, Fonseca NJ (2018) Truncated leaky-wave antenna with cosecant-squared radiation pattern. *IEEE Antennas Wirel Propag Lett* 17(5):841–844
9. Li Z, Zhang S, Wang J, Li Y, Chen M, Zhang Z, Guo YJ (2019) A method of generating radiation null for periodic leaky-wave antennas. *IEEE Trans Antennas Propag* 67(6):4241–4246
10. Bozzi M, Georgiadis A, Wu K (2011) Review of substrate-integrated waveguide circuits and antennas. *IET Microwaves Antennas Propag* 5(8):909–920
11. Wang H, Fang DG, Zhang B, Che WQ (2009) Dielectric loaded substrate integrated waveguide (SIW) H -plane horn antennas. *IEEE Trans Antennas Propag* 58(3):640–647
12. Chen S-L et al (2019) Circular-polarized substrate-integrated-waveguide leaky-wave antenna with wide-angle and consistent-gain continuous beam scanning. *IEEE Trans Antennas Propag* 67(7):4418–4428
13. Liu J, Jackson DR, Long Y (2011) Substrate integrated waveguide (SIW) leaky-wave antenna with transverse slots. *IEEE Trans Antennas Propag* 60(1):20–29
14. Mohsen MK, Isa MM, Isa AAM, Zin MSIM, Saat S, Zakaria Z, Ibrahim IM, Abu M, Ahmad A, Abdulhameed MK (2018) The fundamental of leaky wave antenna. *J Telecommun Electron Comput Eng (JTEC)* 10(1):119–127
15. Kossifos KM, Antoniadis MA (2018) A NRI-TL metamaterial leaky-wave antenna radiating at broadside with zero beam-squinting. *IEEE Antennas Wirel Propag Lett* 17(12):2223–2227
16. Zhang X, Zhu L (2016) Gain-enhanced patch antennas with loading of shorting pins. *IEEE Trans. Antennas Propag.* 64(8):3310–3318
17. Zhang X, Zhu L (2016) Patch antennas with loading of a pair of shorting pins toward flexible impedance matching and low cross polarization. *IEEE Trans Antennas Propag* 64(4):1226–1233
18. Rahmani MH, Deslandes D (2017) Backward to forward scanning periodic leaky-wave antenna with wide scanning range. *IEEE Trans Antennas Propag* 65(7):3326–3335
19. Liu J, Li Y, Long Y (2017) Fundamental even leaky mode in microstrip line loaded with shorting vias. *IET Microw Antenna Propag* 11(1):129–135
20. Xie D, Zhu L, Zhang X (2017) An EH₀-mode microstrip leaky-wave antenna with periodical loading of shorting pins. *IEEE Trans Antennas Propag* 65(7):3419–3426

Modelling and Simulation of Advance Charging for Electric and Solar Assisted Vehicles



Pushpendra Kumar Singh, M. A. Ansari, Nidhi Singh Pal, Jay Singh, and Nivedita Singh

Abstract The need for quick charging of an EV becomes a major issue that is projecting to mitigate the range uneasiness hazardous of EV drivers and understand the restricted activity. This paper introduced a charging methodology for an EV battery which is dependable and strong for a lithium-ion battery, here we have designed a bidirectional charger in MATLAB (Simulink). Changes in ready converters applied to electric vehicles for better charging, and furthermore for finding the better method to charge a lithium battery ion, an onboard circuit is intended for charging station for EV's and sunlight-based electric vehicle so that there is just need of simply plug into an AC power source as utilized in the different application the thought process behind structuring the charger is make charging in a simpler manner with the goal that it gives a positive effect on the headway of electric vehicle in future.

Keywords Charging · Electric vehicle · Controller · Battery

1 Introduction

Electric vehicle is a rising idea in the field of transportation part. Due to such a large number of advantages for example useful for the condition because of less ecological contamination, less expensive method of transportation, utilization of less oil, EV turns out to be a lot of famous nowadays [1]. There are essentially three classifications of the electric vehicle offered in overall plug-in hybrid electric vehicle (PHEV). These vehicles are using electric machine, the motor to run these

P. K. Singh (✉) · M. A. Ansari · N. S. Pal · N. Singh
Department of Electrical Engineering, Gautam Buddha University, Greater Noida, Uttar Pradesh, India
e-mail: pushpendrakumarsingh59@gmail.com

M. A. Ansari
e-mail: ma.ansari@gbu.ac.in

J. Singh
Department of Electrical and Electronics Engineering, GL Bajaj Institute of Technology & Management, Greater Noida, Uttar Pradesh, India

© Springer Nature Singapore Pte Ltd. 2021
R. Agrawal et al. (eds.), *Advances in Smart Communication and Imaging Systems*,
Lecture Notes in Electrical Engineering 721,
https://doi.org/10.1007/978-981-15-9938-5_50

vehicles with the electrical power provided by the batteries. The EV has various advantages over the standard internal combustion electric vehicle (ICEV), because of no surges of gases, high efficiency, self-governance from oil, and tranquil and smooth movement. hybrid electric vehicle (HEV) and battery electric vehicle (BEV) [2]. EV concept establishes a good market attention over time due to the degradation of petroleum leads to rise the EV market greatly. EV also gives a positive impact on the society due to clean energy operated vehicle. Secondly, mostly various grid is powered by digging materials, i.e. the fossil fuels like coal. Most obvious advantage is of any electric vehicle over combustion engine is the zero emission, no noise pollution and simple in use, electric vehicles replaces many of manual transmission units of an internal combustion engine such as clutch and consists of just very few moving parts.

2 Power Electronics in Field of Electric Vehicle

Nowadays, power electronics play a energetic role in new findings of EVs. The evolution of power electronic converter made devices to accomplish high efficiency, high power density and robust converters like DC chopper (DC-DC converters), and inverters (DC-AC converter) are designed for different operations of motors. Power converters also provide high-speed switching, where resonant DC-link inverters is a kind of battery fed applications [3]. Several resonant inverters connected in series or in parallel by which they provide zero-current-switching (ZCS) or zero-voltage-switching (ZVS). Due to low heat dissipation, zero switching losses, high power density, very small acoustic noise, they are very advantageous. And hence they are used in propulsion of EV.

3 Methods for Charging

3.1 Unidirectional Battery Charger

To quickly charge an EV battery, there is a fast EV charging method which is most preferable nowadays; i.e. a constant current voltage/constant current (CV/CC) charging is a good approach for the fast charging facility of the EV battery. For Initially, high current is supplied to the battery so that it gets charged rapidly as the battery electrical pressure (voltage) reaches to its extreme value than to avoid the risk of damage and due to overvoltage charger shifts to constant voltage mode, a normal CV mode, it typically takes three times longer to complete charging than CC. Unidirectional charger works on two stages in which firstly conversion of provided AC to DC by a converter and then a DC-DC converter with high frequency and also do the job of power factor correction [4]. Also, there is need of high electric power

chargers for electric vehicles batteries for the separation of wellbeing reasons. The detachment is given to the high-frequency transformer since it operates at some kHz frequencies. The inverter changes DC voltage to high-frequency AC so that transformer behaves well and not be destroyed due to DC input as it is being converted into AC via inverter. Further, a voltage level is made perfect with the use of step-down transformer, which is suitable for the good life of the battery. This movement isn't performed by the chopper since it is less capable. Voltage of secondary side transformer is adjusted by the diode rectifier circuits [5]. Furthermore, finally corrected DC voltage is supplied to the electric vehicles battery for charging of the battery as well, the DC chopper works in current control mode; as soon as the ostensible estimation of the battery is reached, the chopper movements to voltage control mode and finishes the charging of the battery [6].

3.2 Bidirectional Battery Charger

Demand of market needed to be fulfilled by the V2G leads to the need of researchers to give their responses over this topic than needed to research a bidirectional EV chargers are main element in the V2G network, which is the result of grid connected EVs [7], i.e. charging and discharging. A bidirectional EV charger has two switches DC/DC buck–boost converter, and charging and discharging currents are handle by this switch.

Thus, the whole game-plan is known as bidirectional. In the primary stage, a totally controlled rectifier is utilized as it can works as a bidirectional stream to cure the rectifying power factor as required. Another side, in optional way a full controlled converter is utilized as conflicting to the diode circuit, the essential scaffold converter in the adjustable/flexible side has full control on power factor and DC voltage furthermore improved power stream. The other two extension converters related to the high-frequency transformers play out the primary parts of such kind of charger. Both the converters run with the output producing square wave voltage and frequency in the range of kHz [8]. An inductor is used for soft switching and the energy storage for a small-time exchange and furthermore for impermanent vitality stockpiling. An improved structure of converters and segments can prompt less exchanging misfortunes and productive since there are two controlled converters [9].

4 Integrated Chargers

Due to charging and traction are different except in case of regenerative braking, there is need of thing known as integrated charger. Integrated chargers have the capabilities of minimizing the various issues such as voltage fluctuation and harmonics reduction. They utilize the electric drive framework segments likewise at the hour of

charging. This prompts an important abatement in volume, weight and cost [10]. This coordination likewise has galvanic isolation because of which info power circuit is segregated from the output power circuit; however for the reconfiguration of electric drive frameworks both force gadgets and control circuit are to be planned [11].

Charging voltage, reduction in harmonics, unwanted magnetomotive force developed during charging, hardware/software complexity needed to be further improved. Modelling of the integrated charger is to design a model that can understand relationships and linkages between the components that form the system. Here, an approach is taken to design the charger which has two inputs either by an AC power source or by DC power source, it is essential to understand that a system. In modelling complex systems, the general methodology is the following: First, the system is divided into smaller subsystems according to their function [12]. These are described by independent models [6].

5 Electric Vehicle and Solar

Due to zero emission of CO₂ the use of electric vehicle charging facility become more advantageous when the charging infrastructure is derived from the renewable energy sources. Now a days charging of an EV from a grid connected charger is a reliable option because of no weather disturbances continuous power supply, but the petroleum or other fuels of power plants is decaying with time so there is need of a power source like solar PV and a charging facility which works as better as grid connected chargers do, so an on board chargers are employed [12]. Basically, EV charging based on DC both PV and EV are fundamentally DC in nature, so there is need of conversion between AC and DC which leads to additional losses. To overcome these integrated multiport converters are used.

6 Mathematical Modelling

$$i = \frac{1}{L} \int_0^t V dt + i_0 \quad (1)$$

$$\Delta i = \frac{(V_{\text{out}} - V_{\text{in}} + V_D)T_{\text{off}}}{L} \quad (2)$$

where, V_{out} = output voltage, V_{in} = input voltage, V_D = voltage drop across diode, D = duty cycle.

Peak inductor current	i_{pk}
Min inductor current	i_o
Ripple current	$\Delta i = (i_{pk} - i_o)$
Ripple current ratio to average current	$r = \Delta i / i_{ave}$
Off duty cycle	$1 - D = T_{off} / T$
Switch off time	$T_{off} = (1 - D) / f$
Average and load current	$i_{ave} = \Delta i / 2 = i_{load}$
RMS current for a r Wave	$i_{rms} = \sqrt{i_o^2 + (\Delta i)^2 / 12}$

See Figs. 1 and 2.

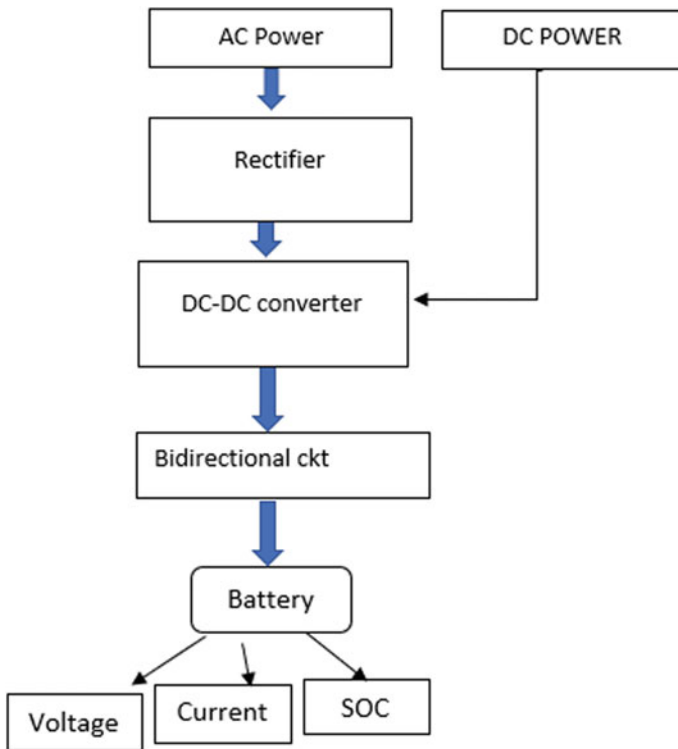


Fig. 1 Diagrammatic representation of designed model working

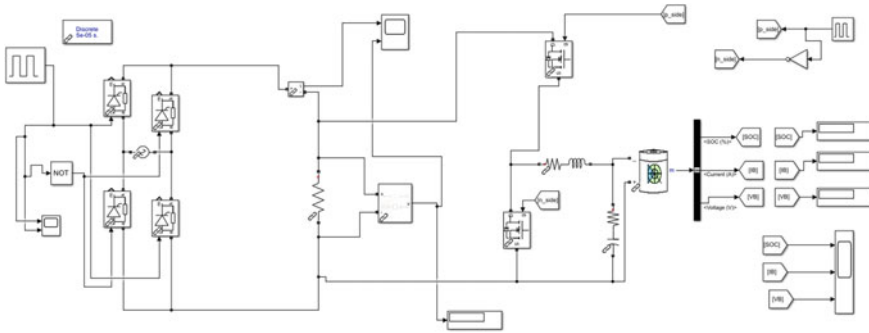


Fig. 2 Simulink model designed

7 Challenges and Solution

The main challenge is to improve charging time by use of different ways to achieve a goal of best charging made some limitation on the EV's.

- Build models of multilevel converters programs statically from base components.
- Use configurable subsystem to switch between different converter architectures.
- Analyze harmonic signature to verify the correctness of model authors and affiliations.

8 Simulation Results and Discussion

See Figs. 3, 4, 5, 6, 7 and 8.

Simulation to verify that the model designed to provide charging facility for a electric vehicle is accomplish from a AC power source so that it is more convenient for the person to charge with a AC power source just by plugging in to the AC port, in this a projection of actual model is made to define the charger the project is designed in three parts in one part a AC to DC converter is designed and in another one boost

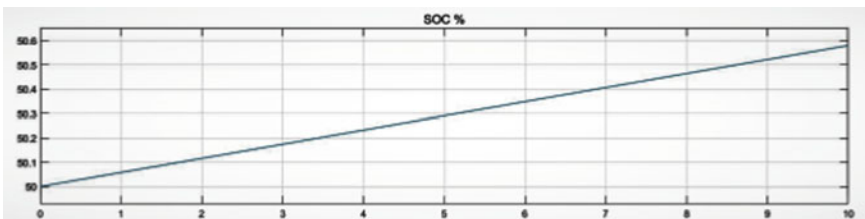


Fig. 3 State of charge when battery is charging by the designed model, initially battery SOC taken is 50 percent increasing graph shows charging

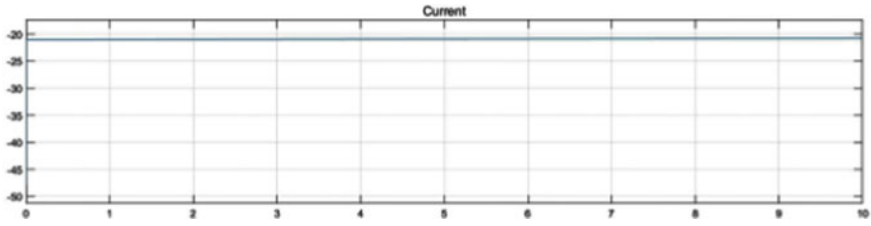


Fig. 4 Graph showing the current at the time of charging

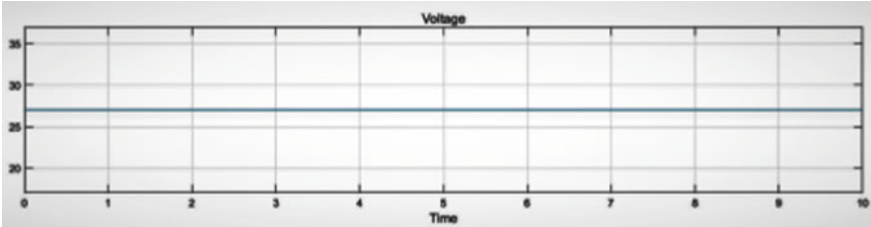


Fig. 5 Graph showing the voltage at the time of charging



Fig. 6 Graph showing the current at the time of discharging

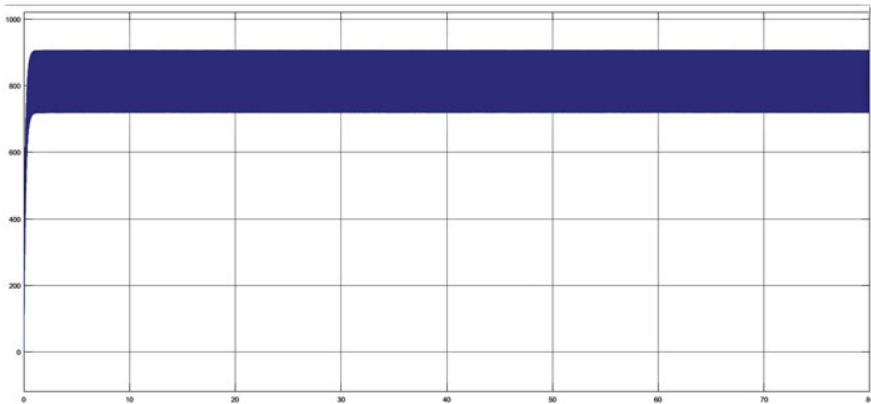


Fig. 7 Simulation result of Boost converter designed

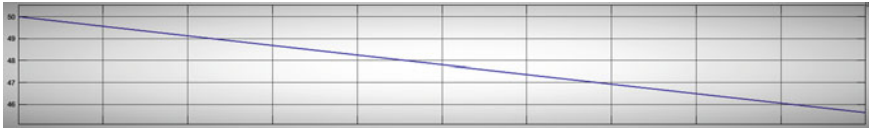


Fig. 8 Graph showing the discharging of battery SOC is decreasing with time

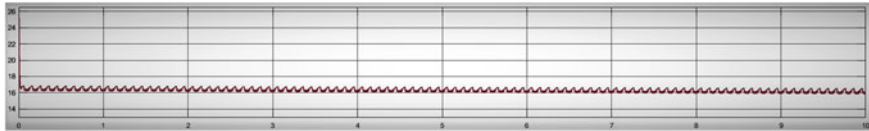


Fig. 9 Graph showing voltage at the time of discharging

converter is designed [13], than a lithium-ion battery is charged by designed model, various tables [Tables 1 and 2] of readings are also incorporated for the precise results so the state of charge, voltage and current are demonstrated battery used for this project is lithium ion. There are several graphs which are obtained by this project, i.e. charging versus time, voltage versus time, current versus time, which is showing how the Simulink model works on the given parameters. As in Fig. 3, state of charge goes on increasing with time this shows that the model is working perfectly for charging a lithium-ion battery taken, Fig. 8 shows discharging graph, Figs. 5 and 9 show the voltage at the time of charging and discharging, Figs. 4 and 6 show current at the time of charging and discharging. So we can say that the results are as per desired values this model is working smoothly for charging of lithium-ion battery which is fastly growing need for electric vehicles; in this project, we take a survey of various charging methods and models for making it better and developed a new model which consists of various converters like boost converter, AC to DC converter and a direct DC supply is also a means of power charge battery so this working model designed on Simulink has the ability to take both AC and DC supply for charging purpose. When firstly an AC supply is provided than the AC to DC converter converts into DC which consists of thyristors of appropriate quantities and than a boost converter is incorporated to increase the output so that it can further used to charge the lithium-ion battery, the readings of boost converter is shown in [Table 3] and charging by the designed model; initially, battery SOC taken is 50 percent increasing graph shows charging.

9 Conclusion

We have discussed the use of various charging methods and designed a charger that convert AC power into a charge an electric vehicle the designed model of a charger is also shown which consists of different converter as per the need as boost converter

Table 1 Battery parameters taken or charging

S. No.	Lithium-ion battery	
	Parameter	Reading
1	Nominal voltage (V)	24 V
2	Rated capacity	10 Ah
3	State of charge	50%
4	Cut-off voltage (V)	18
5	Nominal discharge current (A)	4.24
6	Full charge voltage (V)	27.93

Table 2 Boost converter parameters

S. No.	I/p o/p voltages	
	Input	Output
1	20	850
2	30	1000
3	50	1300
4	60	3520

Table 3 Power flow in various methods

S. No.	Power flow	
	Unidirectional	Bidirectional
1	Exclusively provide EV charging	Provide EV charging
2	Less complicated structure	Complex structure
3	Unidirectional power flow only	Allow bidirectional power flow
4	Less initial investment	Require high initial investment

and rectifier and a bidirectional converter so a design of on board charger for an electric vehicle is made, and all the results are shown state of charge (SOC), voltage, current with respect to time.

References

1. Mastanamma Y (2017) Electric vehicle mathematical modelling and simulation using MATLAB Simulink. IOSR J Electr Electron Eng (IOSR-JEEE) 12(4)
2. International Conference on Electrical, Computer and Communication Engineering (ECCE), 7–9 February 2019
3. Future of electric vehicle charging. In: 19th international symposium power electronics Ee2017, October 19–21, 2017, Novi Sad, Serbia

4. Smart charging of electric vehicles according to electricity price. In: 2019 international conference on innovative trends in computer engineering (ITCE'2019), Aswan, Egypt, 2–4 February 2019
5. Kumar P, Srivastava KN, Dhar A (2017) Role of electric vehicles in future road transport. In: Sustainable energy and transportation. Part of the Energy, Environment, and Sustainability book series. Springer, Singapore
6. Kumar K, Ansari MA (2017) Integration of fuel cell to reduce capacity of battery bank in hybrid system. *Front Energy* (2017)
7. Yilmaz M, Krein PT (2018) Review of battery charger topologies, charging power levels, and infrastructure for plug-in electric and hybrid vehicles. *IEEE Trans Power Electron* 28(5):2151–2169
8. Pantic Z, Lee K, Lukic SM (2015) Receivers for multi frequency wireless power transfer: design for minimum interference. *IEEE J Emerg Selected Topics Power Electron* 3(1):234–241
9. Jape SR, Thosar A (2017) Comparison of electric motors for electric vehicle application. *JRET: Int J Res Eng Technol* 06(09). eISSN: 2319-1163 | pISSN: 2321-7308. Available @ <https://www.ijret.org>
10. Emadi A, Lee YJ, Rajashekara K (2008) Power electronics and motor drives in electric, hybrid electric, and plug-in hybrid electric vehicles. *IEEE Trans Industr Electron* 55(6):2237–2243
11. Aryanezhad M (2017) Optimization of grid connected bidirectional V2G charger based on multi-objective algorithm. In: Proceedings of IEEE power electronics, drive systems & technologies conference (PEDSTC), pp 519–524
12. Pennycott A, De Novellis L, Gruber P, Sorniotti A, Goggia T (2013) Enhancing the energy efficiency of fully electric vehicles via the minimization of motor power losses. In: 2013 IEEE international conference on systems, man, and cybernetics
13. Rafajdus P, Peniak A, Diko M, Makarovic J, Dubravka P, Hrabovcova V (2015) Efficiency and losses analysis in switched reluctance motors for electric vehicles. *IEEE*. 978-1-4763-7239-8/15/
14. <https://www.smmmt.co.uk/industry-topics/uk-automotive/the> Society of Motor Manufacturers and Traders (SMMT) is one of the largest and most influential trade associations in the UK

Design and Performance Analysis of the Ghost-Shaped Antenna for Extremely High-Frequency Applications



Madan Kumar Sharma, Nitin Kumar Gautam, Gagan Walia, Ankit Sharma, Nikhil Sachan, and Deepak Kumar

Abstract In this paper, a ghost-shaped antenna is presented for extremely high-frequency applications. The structure is implemented with ghost-shaped radiating element and staircase partial ground plane. The antenna has overall size of $15 \times 20 \times 1.5 \text{ mm}^3$ and designed on the RO 5880 substrate with relative permittivity of 2, permeability $\mu = 1$, and 0.0009 loss tangent. The thickness of the antenna substrate is 1.5 mm. The extended impedance bandwidth 163.63% (30–300 GHz) of resulted antenna (magnitude of $S_{11} < -10 \text{ dB}$) is accomplished by stepping the size of the feed line and placed inverted C-shaped slot etched near to feed line. The gain of the resulted antenna is 15 dBi. Omnidirectional radiation pattern is observed in the entire frequency range. However, all these properties of the proposed antenna are suitable for remote sensing (57–59.3 GHz), automotive RADAR systems, IEEE802.16 (10–66 GHz) and Imaging security and other wireless communication applications.

Keywords EHF · Antenna efficiency · Return loss · Gain · Ghost-shape

M. K. Sharma (✉) · N. K. Gautam · G. Walia · A. Sharma · N. Sachan · D. Kumar
Department of Electronics and Communication, Galgotias College of Engineering and
Technology, 201306 Greater Noida, India
e-mail: madansharma12@gmail.com

N. K. Gautam
e-mail: 2298.gautam@gmail.com

G. Walia
e-mail: Gagan1.gw@gmail.com

A. Sharma
e-mail: ankit.deli@gmail.com

N. Sachan
e-mail: Sachann51@gmail.com

D. Kumar
e-mail: Deepakpal2227@gmail.com

1 Introduction

The demand of the wireless communication has high-data rate networks, high spectral efficiencies, and stronger mitigation over extremely wide band increased sharply from last few decades. By the Edholm's law, wireless data levels continue to be double in each 18 months [1]. All these demands are fulfilled easily with the implementation of terahertz communication system for which EM spectrum lies between microwave and mid-infrared region. Extremely high frequency in this range supports higher data rate [2] and good penetration strength in the human body in case of biomedical sensing applications [3–5]. International Telecommunication Union (ITU) has designated the extremely high-frequency (EHF) band of 30–300 GHz frequency. This frequency band has advantages of high data rate up to 10 Gbits/s, high frequency range, lower interference with other existing wireless bands. This wide spectrum has many applications in scientific research, telecommunications, weapons system, security screening, thickness gauging, medicine, police speed radar, etc.

Thin triangular and circular antennas on graphene were analyzed and compared [6]. The combined geometrical structure of circular patch and triangular substrate at 7.32 THz gives the best possible results to return loss S_{11} of -50.78 dB, 7.899dBi directivity, 6.338 dB gain, and very high bandwidth. A graphene-based hexagonal-shaped dual-band antenna fed by microstrip feed line was implemented in [7]. The plus-shaped slot is used in hexagonal patch, and the antenna has fed by the microstrip feed line which results to returns loss less than -10 dB at frequencies 2.14 THz and 5.41 THz. The obtained gains at the resonating frequency were 4.71 dB and 5.61 dB for the 2.14 THz and 5.41 THz frequency, respectively. However, antenna has narrow bandwidth of 658 GHz (10.97%) and 1.023 THz (17.05%). In [8], a novel linear-scaling technique was used for development of the THz antenna from a GHz antenna. This technique works as a bridge between micro-strip-slot antennas in GHz frequency and THz antennas. The reported antenna was operated from 4.9 THz to 5.9 THz range. All the dimensions of the antenna have been linearly scaled to produce a THz range. Thus, novel idea of dimension reduction was novel, and the antenna of THz bandwidth was produced from a GHz bandwidth antenna. A novel high-efficiency micro-strip patch antenna was introduced in [9]. Due to fractal structure of the antenna, all the results are suitable for THz frequency applications such as reflection parameters, 118% bandwidth (0.434–1.684 THz), efficiency, and gain (maximum 5.72 dBi), the Size $15 \times 150 \times 9.6 \mu\text{m}^3$, and very low cost. In [10], developed antenna was used for biomedical sensing application which was operated in the THz range. The wave THz characteristic of absorption and propagation in metallic meshes built for terahertz sensing and used in biomedicine linked samples. In [11], ultra-wide-band THz application-based antenna has been presented with elliptical patch and microstrip feed line. The rectangular ground plane has been converted into partial ground plane which results to enhance impedance bandwidth of the antenna. Although, existing literature have been reported several antennas in the frequency range of THz, still is a scope to develop a novel antenna which has small size, fabricated on the low cost substrate and has THz operating range.

Table 1 Comparison of the proposed work with existing literature

Reference	Size	Operating bandwidth	Gain	Radiation pattern	Substrate material used
[6]	$11.2 \times 11.2 \times 2 \mu\text{m}^3$	371 GHz	6.338 dB	Bi-directional	RO 4003C
[7]	$25.8 \times 34 \times 40 \mu\text{m}^3$	658 GHz for 2.14 THz 1.023 THz for 5.41 THz	4.71 dB for 2.14 THz 5.61 dB for 5.41 THz	–	Novel substrate
[8]	$25 \times 30 \times 16 \text{ mm}^3$	1 THz (4.9–5.9 THz)	3 dB	Bi-directional	FR4-epoxy
[9]	$150 \times 150 \times 9.6 \mu\text{m}^3$	0.434–1.684 THz	5.72 dBi	–	FR4
[10]	$600 \times 800 \times 7 \mu\text{m}^3$	0.46–5.46 THz	12 dB	Omnidirectional	Polyamide
In this work	$15 \times 20 \times 15 \text{ mm}^3$	30–300 GHz	15 dBi	Omnidirectional	RO 5880

In this paper, stair-case micro-strip-fed multiple circular slot cut circular antenna is presented with partial ground. The resulted antenna has a size of $15 \times 20 \times 1.5 \text{ mm}^3$ and fabricated on RO 5880 substrate with loss tangent of 0.0009. The impedance bandwidth is 163.3% (30–300 GHz) of proposed antenna (magnitude of reflection coefficient $S_{11} \leq -10 \text{ dB}$). The proposed antenna is simulated on microwave studio CST software. Moreover, proposed antenna is small in size and developed on the low-cost RO 5880 substrate. Comparisons of the proposed antenna in terms of size, substrate material used, achieved gain and pattern stability are carried out, and data is shown in Table 1.

The presented antenna is designed and simulated on the RO5880 substrate, and optimized structure of the antenna has overall size $15 \times 20 \times 1.5 \text{ mm}^3$. The geometrical structure of the resulted antenna is shown in Fig. 1. It is constructed with ghost-shaped radiating element which is fed by a stepped size feed line. The evolution steps of the proposed antenna are initiated with the modification of the geometry of the reference antenna developed in [12].

The evolution procedure of the resulted antenna is shown in Fig. 2. The reference antenna has ultra-wideband width 2–12 GHz.

Initially, the reference antenna is simulated for in-band reflection, and the reflection coefficient of each step is shown in Fig. 3. It is covered only 2–12 GHz band as quoted by authors. In the first modification step, the ground plane is etched with multiple stair-case structure to alter current path and to improve the antenna resonance. In this step, reflection coefficient is above -10 dB for whole range of the frequency 30–300 GHz. In second step, radiating element is modified from circular shape to ghost-shaped radiating element; now design is simulated for reflection coefficient analysis. In this step, the in-band reflection ($S_{11} \leq -10 \text{ dB}$) is also poor and resulting for zero impedance bandwidth. Further, feed line is converted into stepped

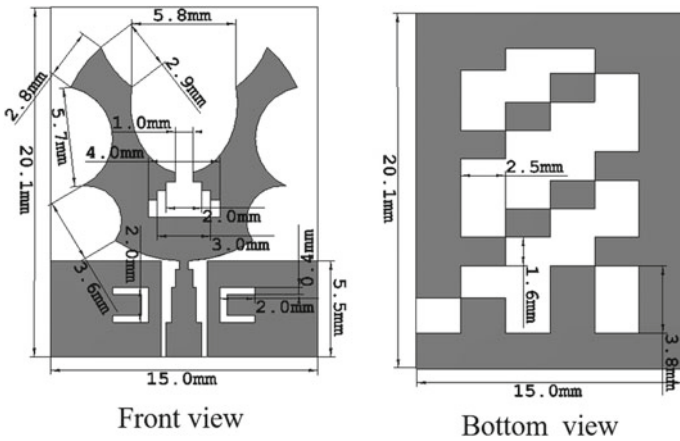


Fig. 1 Front and bottom views of the resulted antenna

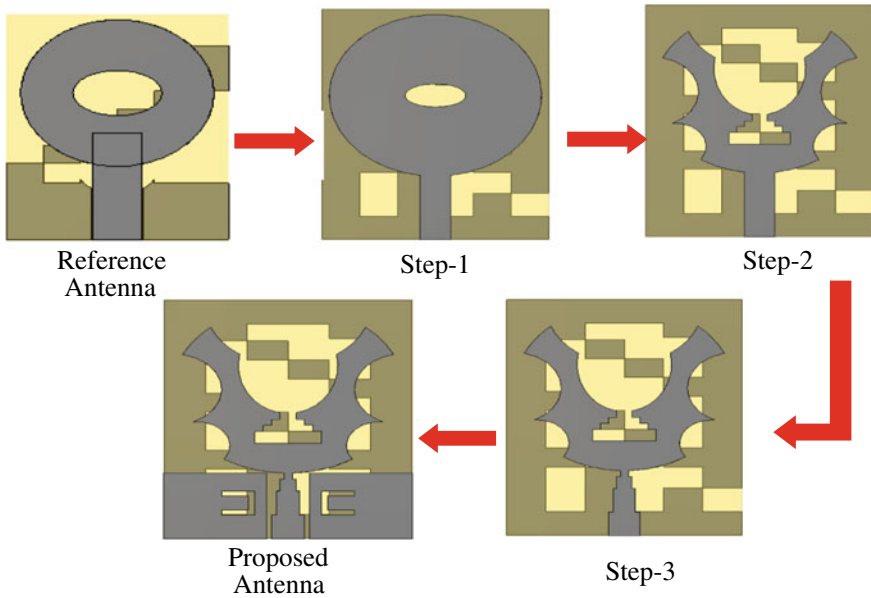


Fig. 2 Evaluation steps of the resulted antenna

size structure for impedance bandwidth improvement. In this case, antenna offered poor impedance bandwidth and reflection coefficient above -10 dB for entire range of frequency. However, good resonance match is accomplished with inverted C-shaped slot etched near to feed line which acts as impedance transformer and resulting for in-band reflection ($S_{11} \leq -10$ dB) for entire frequency 30–300 GHz. The antenna developed in this stage is known as proposed antenna.

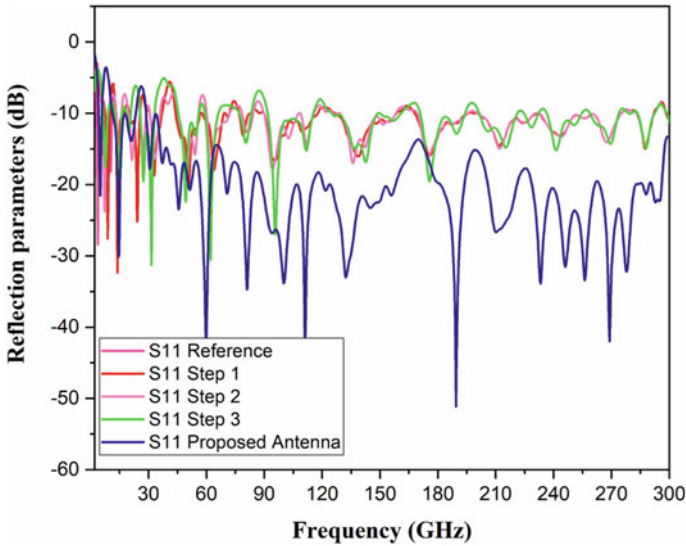


Fig. 3 Simulated reflection parameters of the reference antenna, step-1, step-2, step-3, and proposed antenna

1.1 Parametric Study of the Proposed Antenna

To obtain the desired performance results, the proposed antenna components are studied. Therefore, antenna is modeled using different kind of substrate. The return loss comparison of proposed antenna with different substrate materials (plexiglass, polyimide, RO 5880, teflon, quartz and FR4) is shown in Fig. 4. By changing the substrate material, different frequency bands are observed with or without in-band reflection. It is observed that the reflection coefficient for substrate with (plexiglass, polyimide, RO 5880, teflon, quartz) material is less than -10 dB for the bandwidth range 30–180 GHz. However, FR4 has well in band reflection, and S11 is less than -10 dB for entire interested frequency range of 30–300 GHz.

Another parametric analysis is carried out with the variation of the thickness of the RO 5880, teflon and FR4 substrate-based antenna. Results of reflection parameters for thickness of 0.5 mm, 1.0 mm and 1.5 mm for all three type of substrate are shown in Figs. 5, 6, and 7 respectively. At the substrate thickness 0.5 mm results of the reflection coefficient is below -10 dB except some peaks above -10 dB at the frequencies 60 GHz, 75 GHz, 190 GHz, 210, and 225 for RO5880, Teflon and FR4 substrate as depicted from Figs. 5 and 6. However, at the thickness of 1.5 mm for all three types of the substrate antenna is simulated, and reflection coefficient is depicted in Fig. 7. The reflection coefficient for all three substrate has in-band reflection ($S_{11} \leq -10$ dB) for interested frequency range 30–300 GHz. However, FR4 has better results of in-band reflection than RO 5880 and teflon, but FR4 is exhibited high dielectric loss comparatively.

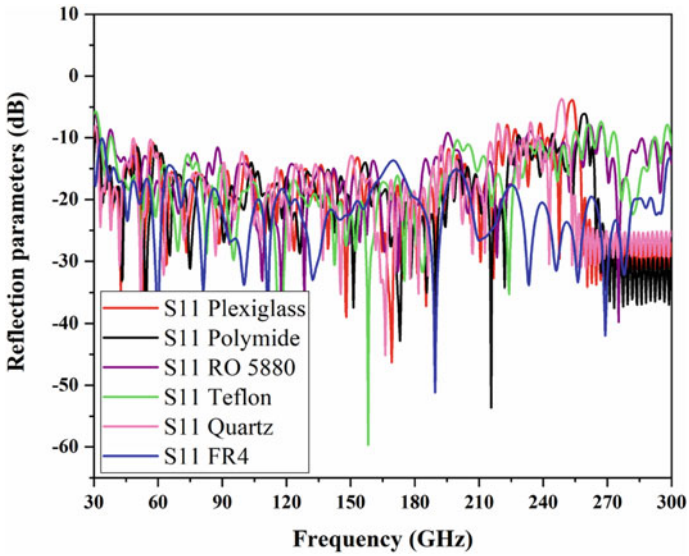


Fig. 4 Simulated return loss comparison of the antenna with different substrate (plexiglass, polyamide, RO 5880, teflon, quartz, and FR4)

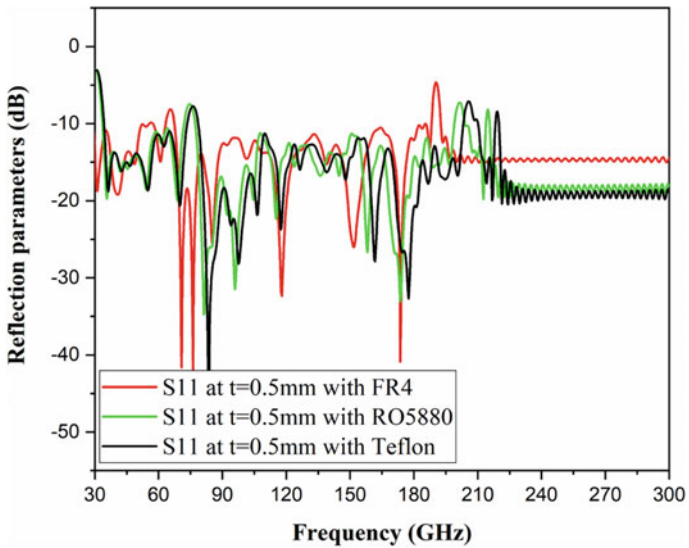


Fig. 5 Simulated reflection parameters for thickness of 0.5 mm of the antenna with different substrate (FR4, RO5880, and teflon)

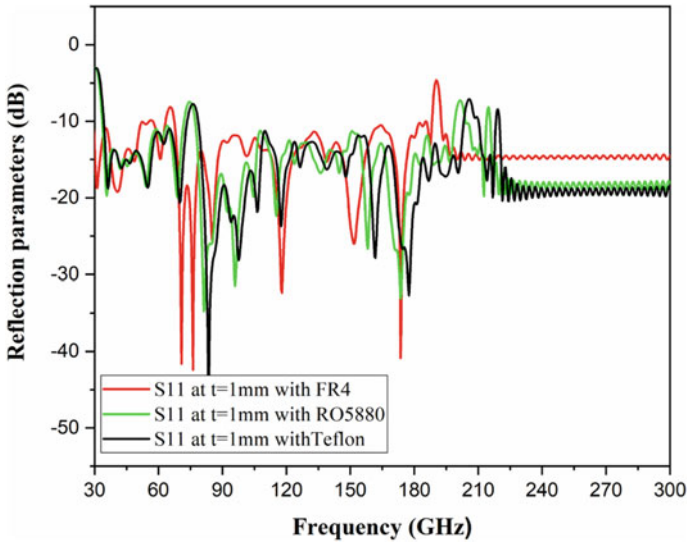


Fig. 6 Simulated reflection parameters for thickness of 1.0 mm of the antenna with different substrate (FR4, RO5880, and teflon)

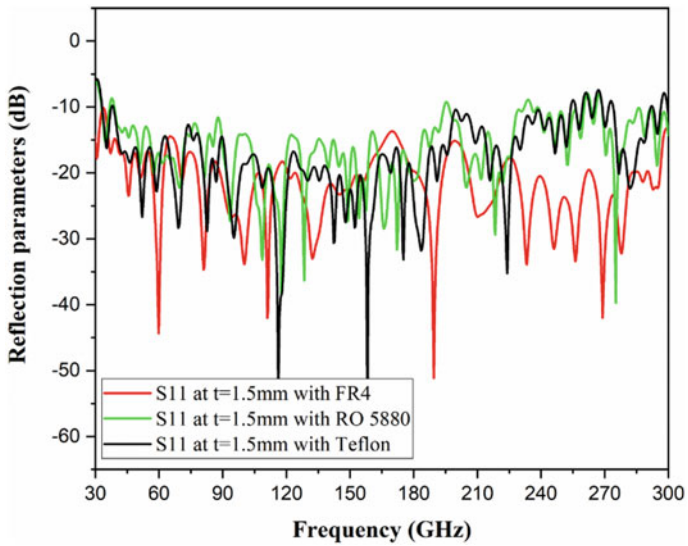


Fig. 7 Simulated reflection parameters for thickness of 1.5 mm of the antenna with different substrate (FR4, RO5880, and Teflon)

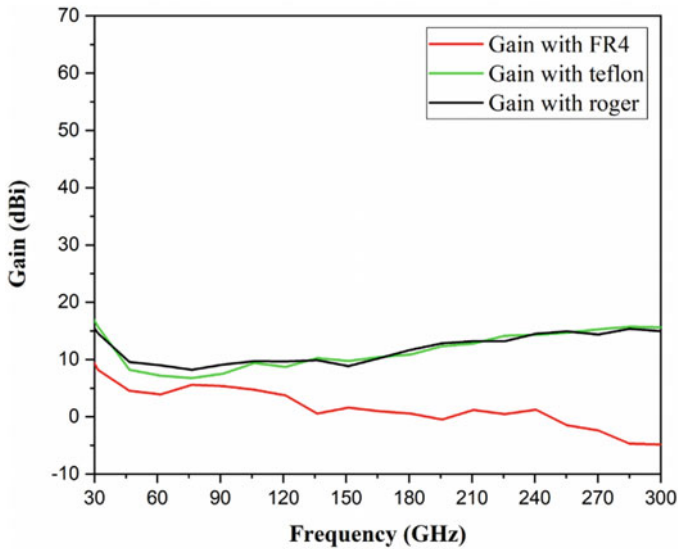


Fig. 8 Simulated gain of the antenna with different substrate (FR4, teflon and RO5880)

Therefore, gain analysis of RO 5880, teflon, and FR4-based antenna is also carried out. Results of the gain with all different substrate are shown in Fig. 8. These results are shows that FR4 substrate-based antenna has very poor gain due to more dielectric loss occurred in that substrate. However, Roger 5880 and teflon substrate-based antenna have closely matched results with the constant value of 15 dBi for frequency of 100–300 GHz. However, teflon-based antenna has poor and unstable gain for 40–90 GHz frequency. Finally, Roger 5880 substrate with thickness of 1.5 mm is selected for development of the proposed antenna which has more stable gain with an average value of 15 dBi.

2 Results and Discussion

The proposed antenna performance results are simulated and analyzed in terms of impedance bandwidth, gain, surface current, and radiation patterns. The impedance bandwidth is shown in Fig. 9. Result is indicated that antenna covered the extremely high frequency range 30–300 GHz. Simulated gain of the antenna is depicted in Fig. 10 which is almost constant with a value 15 dBi over the entire frequency range. Surface current analysis of the antenna is carried out to measure distributed current density across the radiating element. The current density is observed at 30 GHz, 50 GHz, 70 GHz, and 85 GHz.

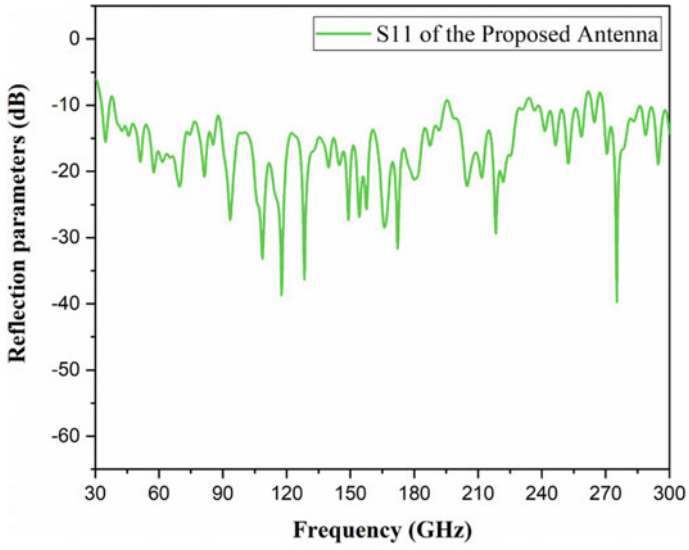


Fig. 9 Simulated return loss of the antenna

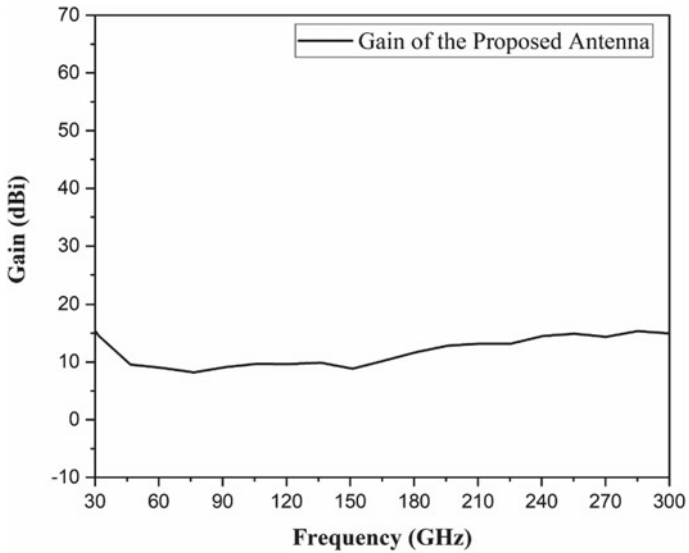


Fig. 10 Simulated gain of the antenna

The surface current distribution at the given frequency is shown in Fig. 11. The radiating element has accumulated maximum charge at this frequency, and results exhibited low dielectric loss across the substrate.

The radiation patterns are also evaluated using CST to determine the orientation of the radiated energy from the antenna. The results are evaluated at the frequency 50 GHz, 150 GHz, 250 GHz, and 280 GHz frequency for $\varnothing = 0$ and $\varnothing = 90$ and shown in Fig. 12a, b respectively. Obtained radiation patterns are stable and omnidirectional at the operating frequency of the antenna.

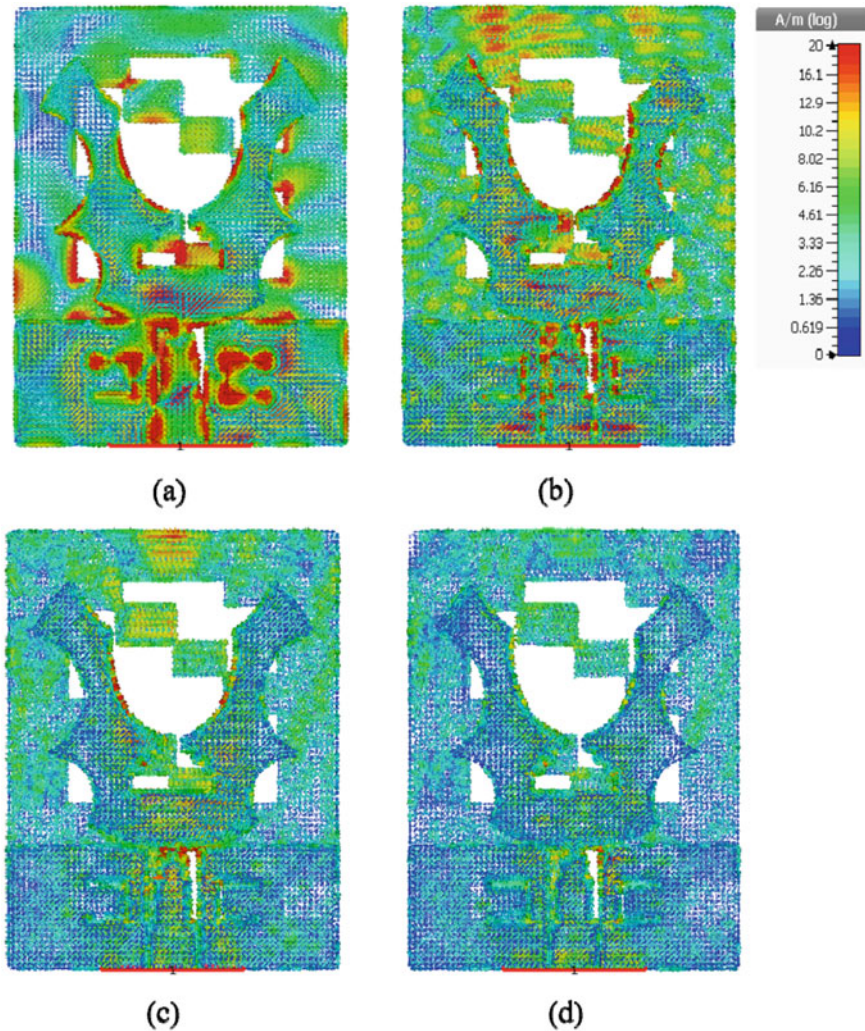


Fig. 11 Surface current distribution of the antenna at **a** 30 GHz, **b** 50 GHz, **c** 70 GHz, and **d** 85 GHz

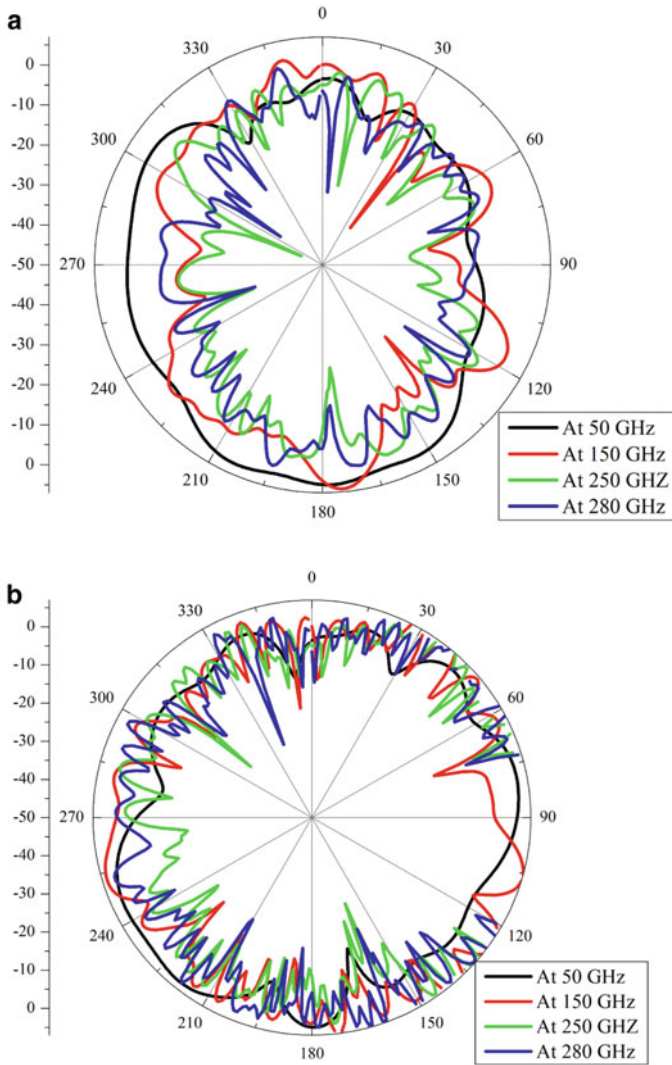


Fig. 12 **a** Simulated radiation patterns of the antenna at (a) 50 GHz, (b) 150 GHz, (c) 250 GHz, and (d) 280 GHz for $\theta = 0$. **b** Simulated radiation patterns of the antenna at (a) 50 GHz, (b) 150 GHz, (c) 250 GHz, and (d) 280 GHz for $\theta = 90$

3 Conclusion

A ghost-shaped antenna with staircase etched ground plane and stepped size feed line is successfully implemented in this study. The substrate-based analysis is carried out for improved results. The proposed antenna has wide impedance bandwidth 30–300 GHz which covers various extremely high-frequency applications, constant gain

of 15 dBi, and stable omnidirectional patterns. The proposed antenna is compared with existing literature and offered better results than existing one.

References

1. Webb W (2006) Laying down the law [technological development]. *Commun Eng* 4(1):18–23
2. Khan F, Pi Z (2011) mmWave mobile broadband (MMB): unleashing the 3–300GHz spectrum. In: 34th IEEE Sarnoff Symposium. IEEE
3. Dawoud MM (2003) High frequency radiation and human exposure. In: Proceedings of the international conference on radiation at UNITEN (ICNIR 2003)
4. Sharma MK et al (2020) Experimental investigation of the breast phantom for tumor detection using ultra-wide band–MIMO antenna sensor (UMAS) probe. *IEEE Sen J* (2020)
5. Sharma MK, Kumar M, Saini JP (2015) UWB-MIMO antenna with enhanced isolation for breast cancer detection. In: 2015 international conference on computing for sustainable global development (INDIACom). IEEE
6. Khan MAK, Shaem TA, Alim MA (2020) Graphene patch antennas with different substrate shapes and materials. *Optik* 202:163700
7. Badr NS, Moradi G (2020) Graphene-based microstrip-fed hexagonal shape dual band antenna. *Optik* 202:163608
8. Bhattacharyya K et al (2019) A linear-scaling technique for designing a THz antenna from a GHz microstrip antenna or slot antenna. *Optik* 199:163331
9. Davoudabadifarahani H, Ghalamkari B (2019) High efficiency miniaturized microstrip patch antenna for wideband terahertz communications applications. *Optik* 194:163118
10. Tabata H (2015) Application of terahertz wave technology in the biomedical field. *IEEE Trans Terahertz Sci Technol* 5(6):1146–1153
11. Singhal S (2019) Ultrawideband elliptical microstrip antenna for terahertz applications. *Microw Opt Technol Lett* 61(10):2366–2373
12. https://www.academia.edu/38573901/Acompact_ultrawide_band_planar_antenna_with_corrugated_ladder_groundplane_for_multiple_applications

Design and Comparative Analysis of Photovoltaic Battery Charge Control Techniques in Simulink Environment



Santosh Kumar Yadav, Nidhi Singh, M. A. Ansari, and Rohit Kumar

Abstract In this paper, the methods for battery charging controller are structured as consistent current (CC) charging, steady voltage (CV) and two-phase consistent current steady voltage (CC-CV) charging procedure. We can accomplish a high-yield voltage and high increase by controlling the obligation pattern of switches by utilizing a controller. Interface the battery with DC-DC converter and controller, which improves the proficiency, decreases misfortunes and improves execution. In this paper, the procedures for battery charging controller are structured as steady current (CC) charging, consistent voltage (CV) and two-phase steady current steady voltage (CC-CV) charging strategy.

Keywords Lithium-ion battery · Controller · Battery energy storage · State of charge · DC/DC converter

1 Introduction

Nowadays, technology is progressing at breakneck pace, and our traditional energy sources are reduced and depleting day by day due to deforestation, small reserves of fossil fuels, global warming, etc. Even if they are used constantly, there will be no traditional energy sources in the future. The reason for thinking about generating power on site is the economic and environmental problems. The customary vitality emergency and the developing occurrence of ecological unsettling influence, for

S. K. Yadav (✉) · N. Singh · M. A. Ansari · R. Kumar
Department of Electrical Engineering, Gautam Buddha University, Greater Noida 201308, India
e-mail: Santosh.ky97@gmail.com

N. Singh
e-mail: Nidhi@gbu.ac.in

M. A. Ansari
e-mail: Ma.ansari@gbu.ac.in

R. Kumar
e-mail: Rohitkumarhu@gmail.com

example, air contamination and an Earth-wide temperature boost; bring about a consistently rising rate of use of non-traditional or sustainable power sources since they are perfect and liberated from numerous hurtful impacts. Sun-powered vitality is one of the most encouraging of sustainable power sources [3]. This paper is structured according to the following; Sect. 1 includes paper presentation. Section 2 includes battery made from lithium-ion. Section 3 comes with DC-DC converter. Section 4 contains schematic diagrams and MATLAB/Simulink models, Sect. 5 consists of a comparative study using simulation results of all techniques, Sect. 6 contains the paper conclusion, and the paper references are included at the end.

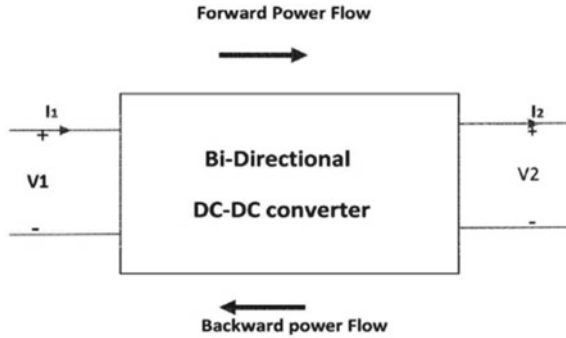
2 Lithium-Ion Battery

It got obvious throughout the most recent couple of years that not all mercury, silver or soluble manganese dioxide frameworks could gracefully a higher vitality thickness gadget from hermitically fixed cells at a sensible expense, henceforth the requirement for the presentation of lithium battery framework. Lithium batteries contain natural electrolyte lithium and can offer up to 330 Wh/kg of gravimetric vitality thickness, right around multiple times that of mercury and silver batteries and multiple times that of antacid manganese batteries, among different points of interest. Lithium particle (Li-particle) batteries are the most well-known kind of lithium batteries while the further developed sorts incorporate lithium polymer (Li-Po), lithium-molybdenum disulfide and lithium (aluminum) iron monosulfide batteries [10].

3 DC-DC Converter

The DC converters are also used as regulators for switching mode to convert a normally uncontrolled DC voltage to a controlled DC output voltage. PWM usually achieves control at a static frequency, and the switching driver is typically BJT, MOSFET or IGBT as well. The power regulator is often based on an inductor, a charging pump single condenser, switch-mode power converter or a linear regulator. What regulator has its own advantages and disadvantages, but it is the requirements of operation that decide which type of power regulator is best suited. Bidirectional DC-DC converters allow power flow, in either direction, between two DC sources. They can switch the heading of current stream and subsequently power while holding the voltage extremity at the two finishes unaltered and are accordingly progressively being utilized in applications, for example, DC persistent force supplies, battery charger circuits, circuits with battery chargers, power supplies for telecoms, and electronic control systems [1]. Here bidirectional converter is utilized as an interface in this exposition to charge and release the battery. The generic circuit structure of the directional converter is illustrated in Fig. 1.

Fig. 1 Illustration of bidirectional power flow



3.1 Simulink Model for Isolated Bidirectional DC-DC Converter

Attributable to the changing natural circumstance, yield varies in the force creation by windmills and sun based force frameworks. As a result of the huge varieties in yield such vitality frameworks are not adequate to take care of the force as an independent framework, and along these lines these vitality frameworks are regularly associated with vitality stockpiling gadgets, for example, batteries and super capacitors. These vitality stockpiling gadgets store the overflow vitality during low burden request and give reinforcement when a framework disappointment happens and when the vitality framework yield changes because of climate.

This converter is well designed for uninterruptible power supply (UPS) battery charging and discharge circuits in DC. The basic circuit of isolated bidirectional DC-DC converter is shown in Fig. 2.

The Simulink model for bidirectional DC-DC converter is shown in Fig. 3.

The bridge consists of four switches; MOSFET is used for high-power applications here. The first H-bridge supplies AC voltage in square wave to the transformer's main

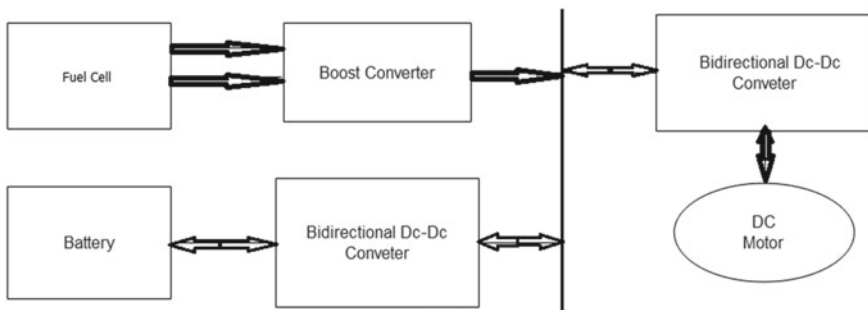


Fig. 2 Basic circuit diagram of isolated bidirectional DC-DC converter

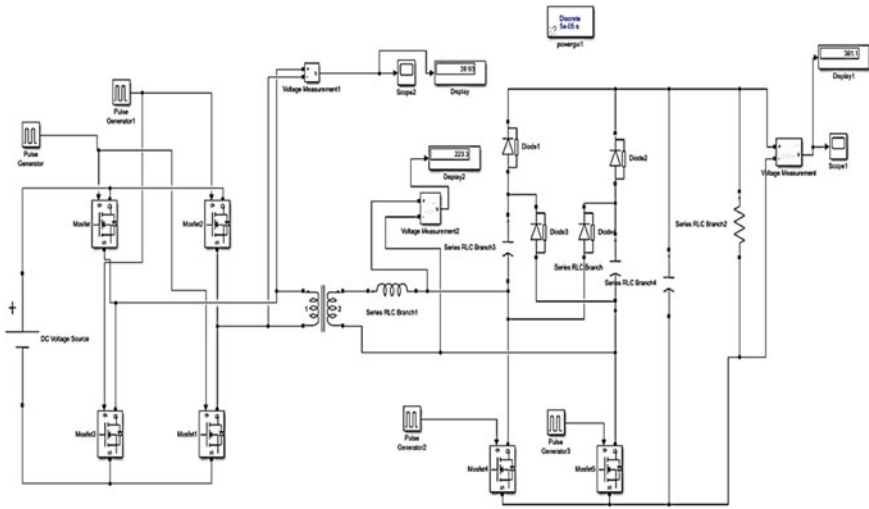


Fig. 3 Simulink model of bidirectional DC-DC converter

winding. The second H-bridge provides DC voltage output for many applications, such as charging the PV batteries.

3.2 Simulink Model for Battery Charging with Half-Bridge Converter

One of the main features of a PV system is that power is only produced when the sunlight is available. In the system which the photovoltaic is the sole source of generation, the supply of power all the time is not possible. Utilizing legitimate battery charging/releasing control procedures which accomplish high battery charging (SOC) can diminish generally speaking framework cost (Fig. 4).

System description

Input DC voltage-48 V.

Lithium-ion battery rating

Nominal voltage-24 V.

Full-charge voltage-27.93 V.

Internal resistance-0.024 Ω.

Battery output- SOC (50.37%), current (13.09 A),

Voltage (26.59 V).

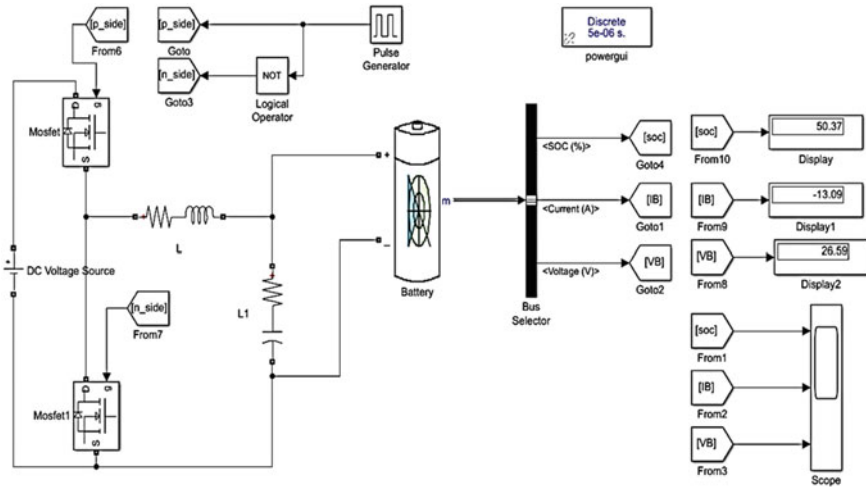


Fig. 4 Simulink model for battery charging with half-bridge converter

4 Simulink Models of the Three Charge Control Techniques

4.1 Constant Current Charging Technique

In steady current charging method, the converter gives the battery a consistent charging current which implies whatever variety of the current the PV board supplies as indicated by various degrees of sun-oriented insolation, is taken care of to the converter and the charging controller at that point gives the converter the required PWM sign to gracefully the battery with consistent current all through the charging procedure. Consistent current is a basic sort of battery charging, with the present level set at about 10% of the most extreme battery esteem. Charge times are genuinely long with the disadvantage that whenever over-burden, the battery can overheat, prompting untimely substitution of the battery. Hence, this approach will prevent the issue of intermittent charging current [5]. The schematic of this charging topology is given in Fig. 5.

The Simulink model for constant current charging technique is shown in Fig. 6.

In Fig. 6 the battery is accused of a steady present until a specific limit estimation of V_{OC} is reached at the battery terminal voltage. The PI controller sensed the voltage of the battery terminal ($V_{Battery}$) and gave the output to PWM which gave the switch converter signal. When the battery voltage arrives at the limit estimation of V_{OC} , the charging cycle is terminated and the reference charging current is shown in the control logic at zero.

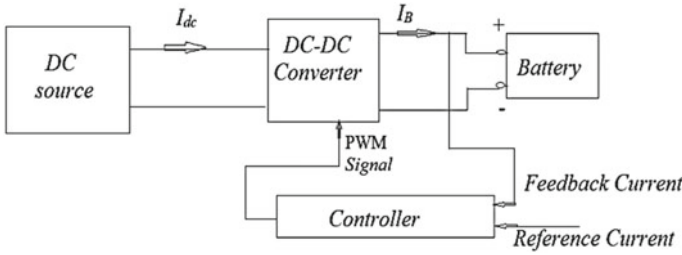


Fig. 5 Diagram for constant current (CC) charging

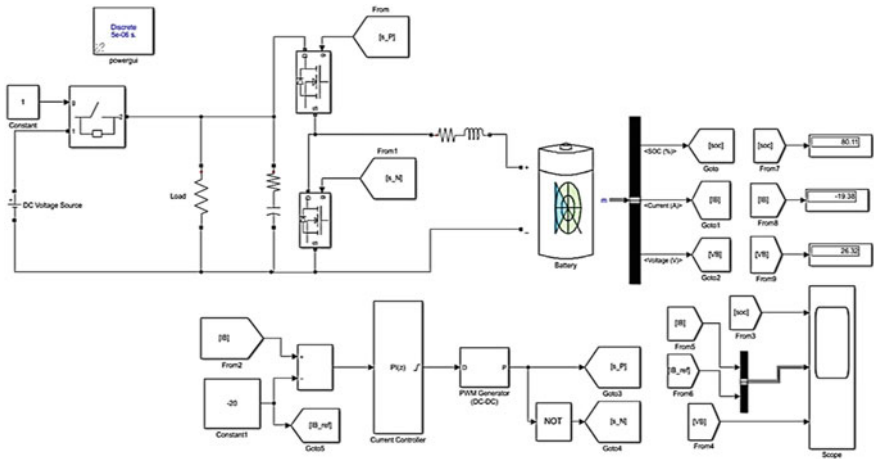


Fig. 6 Simulink model for constant current charging

4.2 Constant Voltage Charging Technique

Steady voltage lets the charger’s full current stream into the battery until the force flexibly arrives at its pre-set voltage. At the point when the voltage point is reached, the present will at that point tighten to a base worth. The battery will remain connected to the charger until it is prepared for use and will remain at the “coast level,” stream charging to make up for standard self-release of the battery. The customary steady voltage charging strategy (CC-CV) is utilized to get away from the consistent current charging method impediments as depicted previously. Here the entire charging cycle is part into two stages, one being consistent present mode and the other being steady voltage mode. In predictable current mode, before the preset over-voltage limit is shown up at the battery is given a high charge current called mass current. The mode changes to consistent voltage mode when reached after this edge estimation of voltage, where the upper limit voltage is held in the battery until the present abatements to a preset, little worth called coast. On the off chance that the present

drops over the level, at that point the charging cycle will be ended. Figure 7 shows the topology of this charging cycle.

Figure 8 shows the Simulink model for the consistent voltage charging framework. The control rationale for the calculation for persistent voltage charging is additionally appeared. In the event that the voltage of the battery is not exactly the limit of over-voltage, at that point the charging of steady current is empowered. For charging the battery, a high-charge current (mass current) is provided. The PI controller limits the mistake between the genuine charging voltage and the ideal charging voltage and produces the obligation cycle important for setting off the converter. In the event that the condition is wrong, implying that the voltage of the battery is more prominent than or equivalent to the V_{OC} then the method of consistent voltage is incapacitated. By and by, the PI controller delivers the essential obligation cycle for the converter to screen the ideal consistent charge voltage of 25.98 V for the thought about battery.

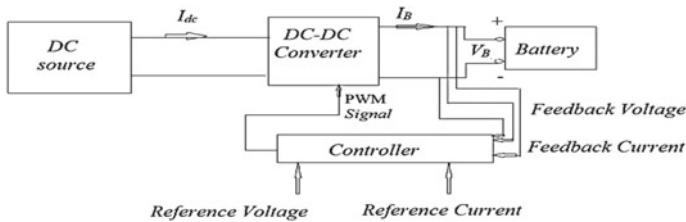


Fig. 7 Diagram for constant voltage (CV) charging

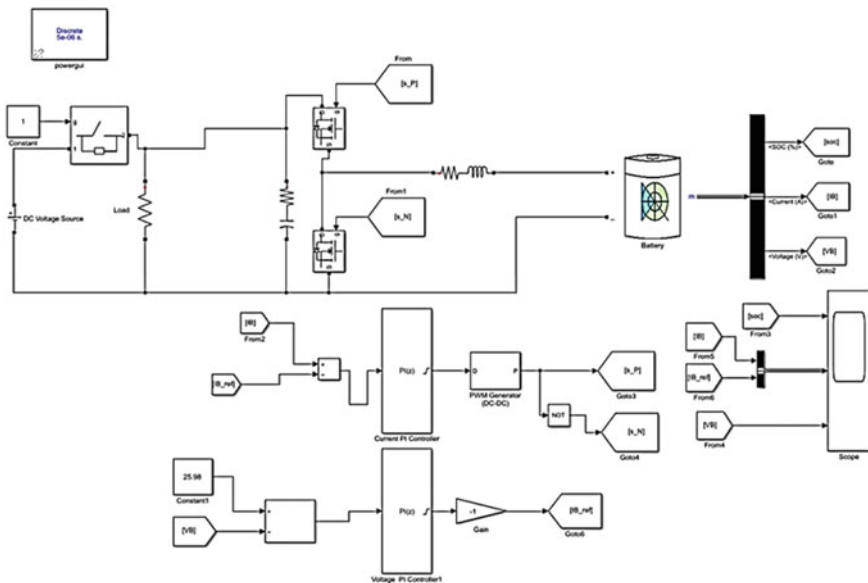


Fig. 8 Simulink model for constant voltage charging

In the event that the condition is genuine that implies the charging is more prominent than reference current 16 A. At that point, the steady voltage of V_{OC} is kept up by the converter over the battery terminal. In the event that the condition is inaccurate, it infers that the charging current falls beneath the 16 A edge. The PI controller produces zero obligation cycle for the converter and ends battery charging.

4.3 Constant Voltage/Constant Current (CV-CC) Technique

It is a mixture of the two strategies set out above. The charger confines the measure of current to a pre-set level before a pre-set voltage level is reached. The current then decreases as the battery is charged to the maximum. The lithium-ion battery employs the charging process of constant current fixed voltage (CC/CV). A controlled current increases the terminal voltage before reaching the upper charge voltage limit, so all in all the present drops because of immersion. The charging procedure for the three-phase battery is an altered two-phase steady current consistent voltage (CC-CV) charging framework. It does have three charging stages instead of two charging stages. The circuit topology used to actualize this charging calculation is like the two-phase CC-CV charging strategy, as shown in Fig. 9.

The Simulink model of CC-CV charging technique is shown in Fig. 10. At the start of the charging cycle, the discharged battery terminal voltage is initially compared with the trickle charge voltage threshold. If the voltage of the battery is less than the threshold of the stream charge voltage (specified by the battery producer) at that point, the stream charge stage is permitted. Here in Fig. 7, the transfer condition called $V < V_{Trickle}$ decides whether or not to supply the charging current in stream mode. In the event that this condition is substantial, the capitalized (16 A) is permitted and on the off chance that this is off base, at that point the following state of the switch becomes effective. The PI controller is developed so as to limit the blunder between the genuine and wanted/reference value of the charging current and according to which the DC-DC buck converter is given the pulse width modulation (PWM) signal. Buck converter then fills the battery with the preset trickle current. If the voltage of the battery exceeds $V_{Trickle}$ then the charging stage for the bulk is triggered. At this

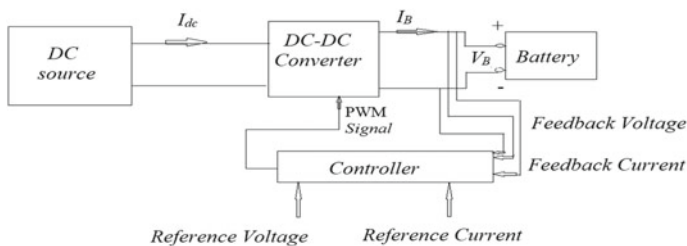


Fig. 9 Diagram for constant current constant voltage (CC-CV) charging

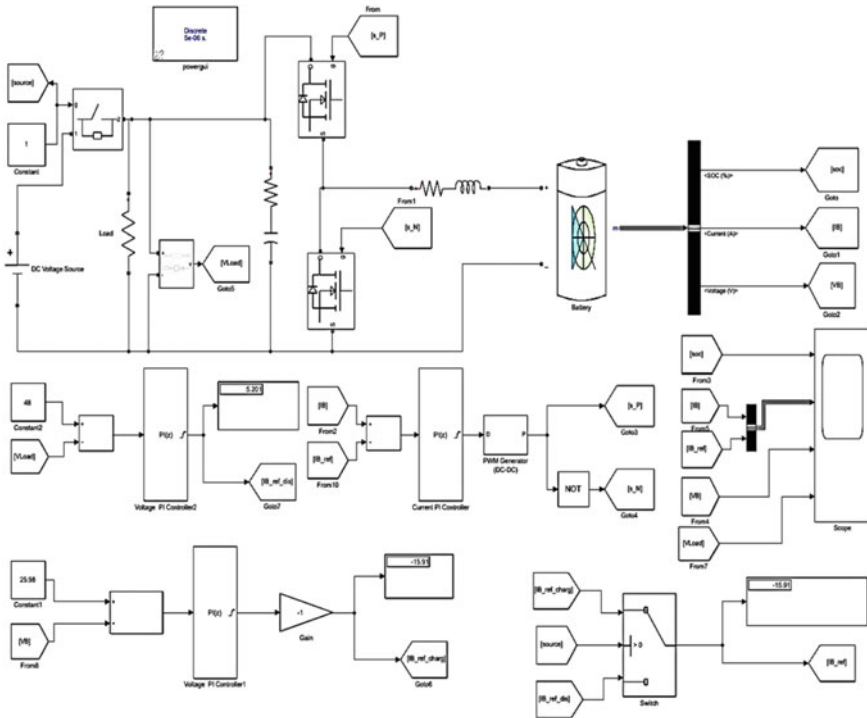


Fig. 10 Simulink model of constant current-constant voltage (CC-CV) charging technique

point, a higher-current I_{Bulk} charges the battery until the battery voltage is lower than its V_{OC} edge overvoltage.

5 Results and Discussion

5.1 Simulation Results of Bidirectional DC-DC Converter

See Figs. 11 and 12.

5.2 Simulation Results of Battery Charging with Half-Bridge Converter for SOC, Current and Voltage

See Fig. 13.

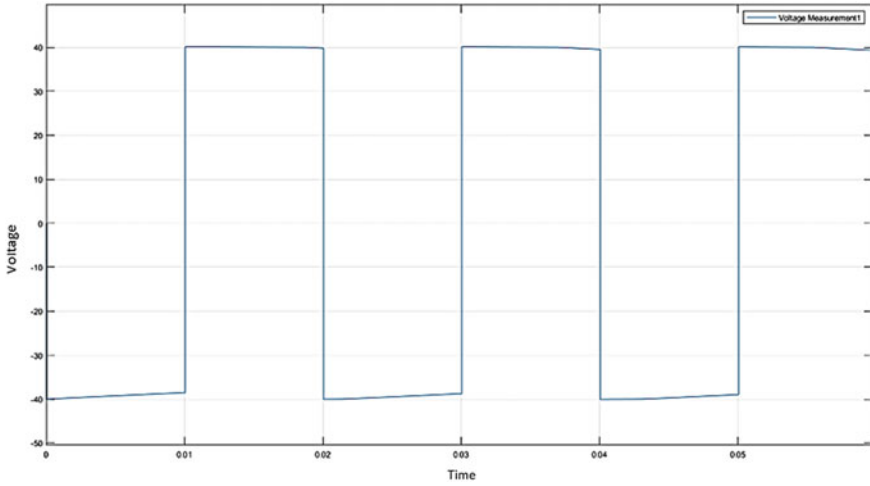


Fig. 11 Input square wave

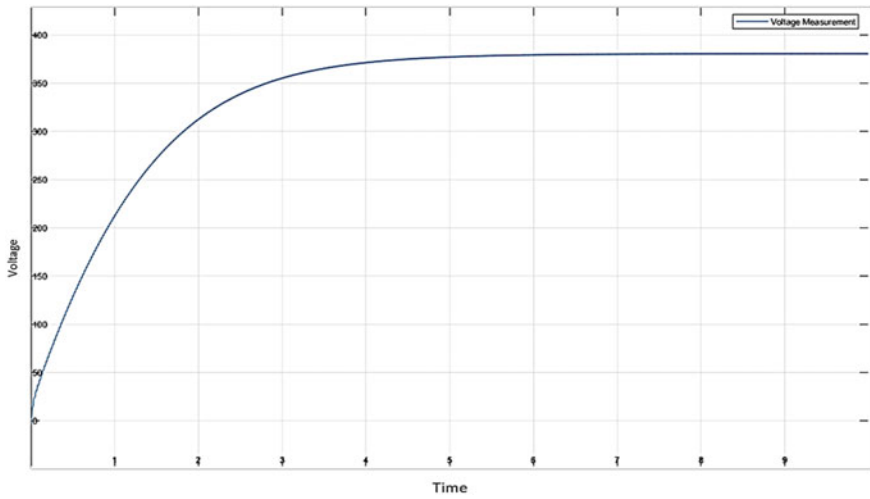


Fig. 12 Output DC voltage

5.3 Simulation Results of Constant Current Technique for SOC, Current and Voltage

See Fig. 14.

System description

Input DC voltage-48 V.

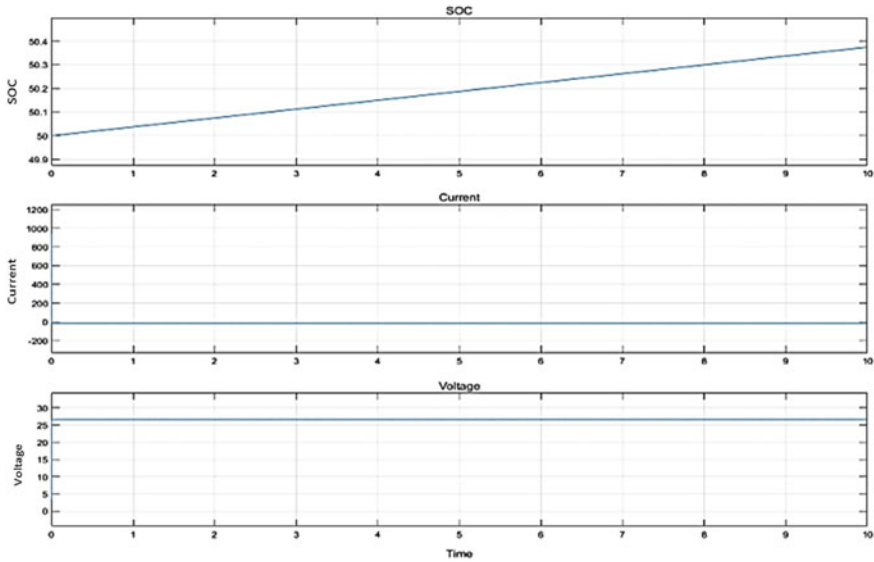


Fig. 13 Output of the battery in charging process

Constant current-($-5, -10, -15, -20$ A).

Lithium-ion battery rating

Nominal voltage-24 V.

Full-charge voltage-27.93 V.

Internal resistance-0.024 Ω .

Battery output-SOC (80%), current (-19.38 A), voltage (26.32).

5.4 Simulation Results of Constant Voltage Technique for SOC, Current and Voltage

See Fig. 15.

System description

Input DC voltage-48 V.

Constant voltage-25.98.

Lithium-ion battery rating

Nominal voltage-24 V.

Full-charge voltage-27.93 V.

Internal resistance-0.024 Ω .

Battery output-SOC (45%), current (-16 A), voltage (25.98).

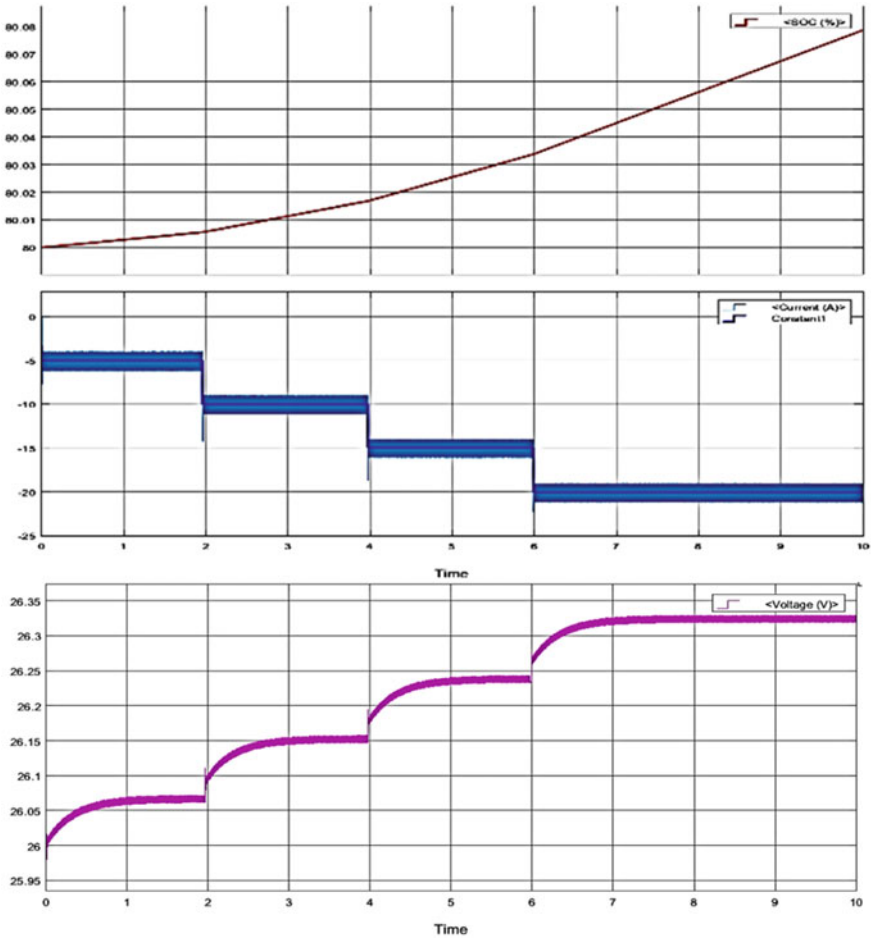


Fig. 14 Simulation results for SOC, current and voltage

5.5 Simulation Results of (CC-CV) Charging Technique for SOC, Current and Voltage

See Fig. 16.

5.6 Comparative Study of All the Three Charging Techniques

From Figs. 14 and 16, in the proposed CC-CV charge controller, from the outset the battery is blamed for a current of 16 A however in the consistent current charging

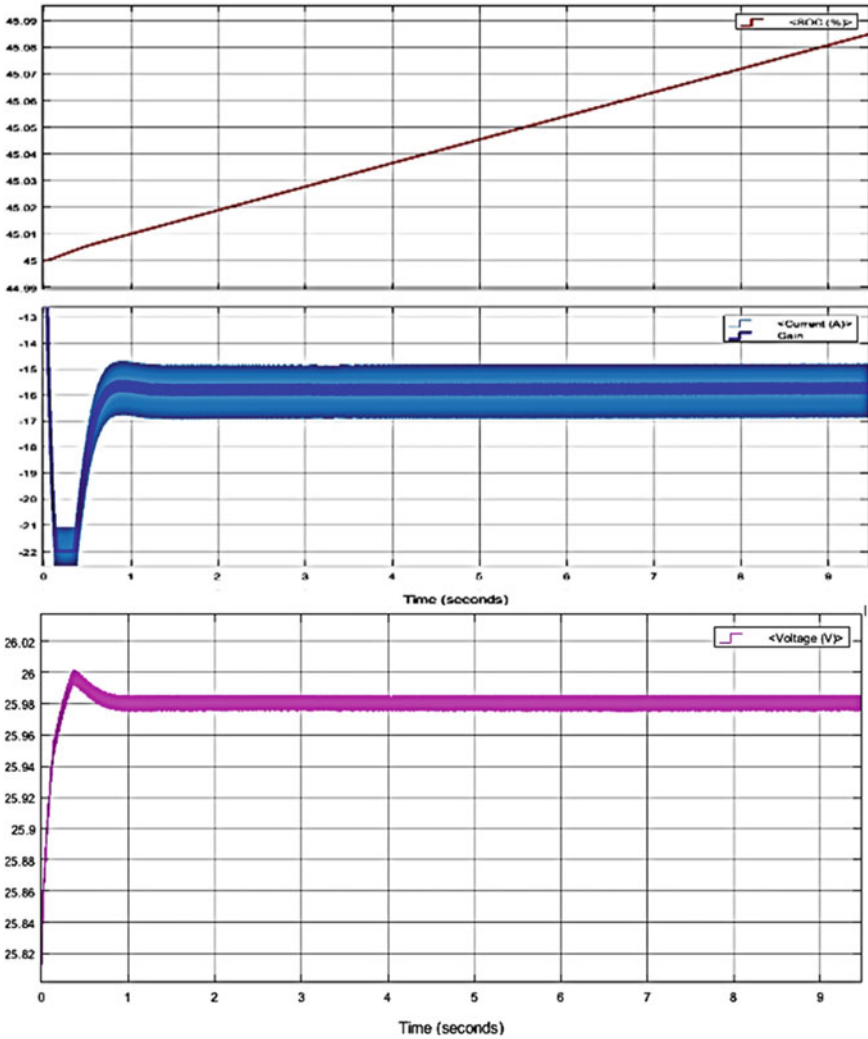


Fig. 15 Simulation results for SOC, current and voltage

strategy if the battery is charged by a predictable current of 1 A and the consistent current is given even in the mass charging stage as depicted in the proposed estimation where the battery is charged by 20 A current. Subsequently, the proposed CC-CV charging sets aside altogether less exertion to charge the battery in this mass accusing stage when differentiated of the consistent current charging procedure. Another essential issue is that the battery encounters lacking charging in consistent current charging method. From Fig. 15 and Fig. 16, the charging current of consistent voltage charging is high from the start when the battery is charged from totally

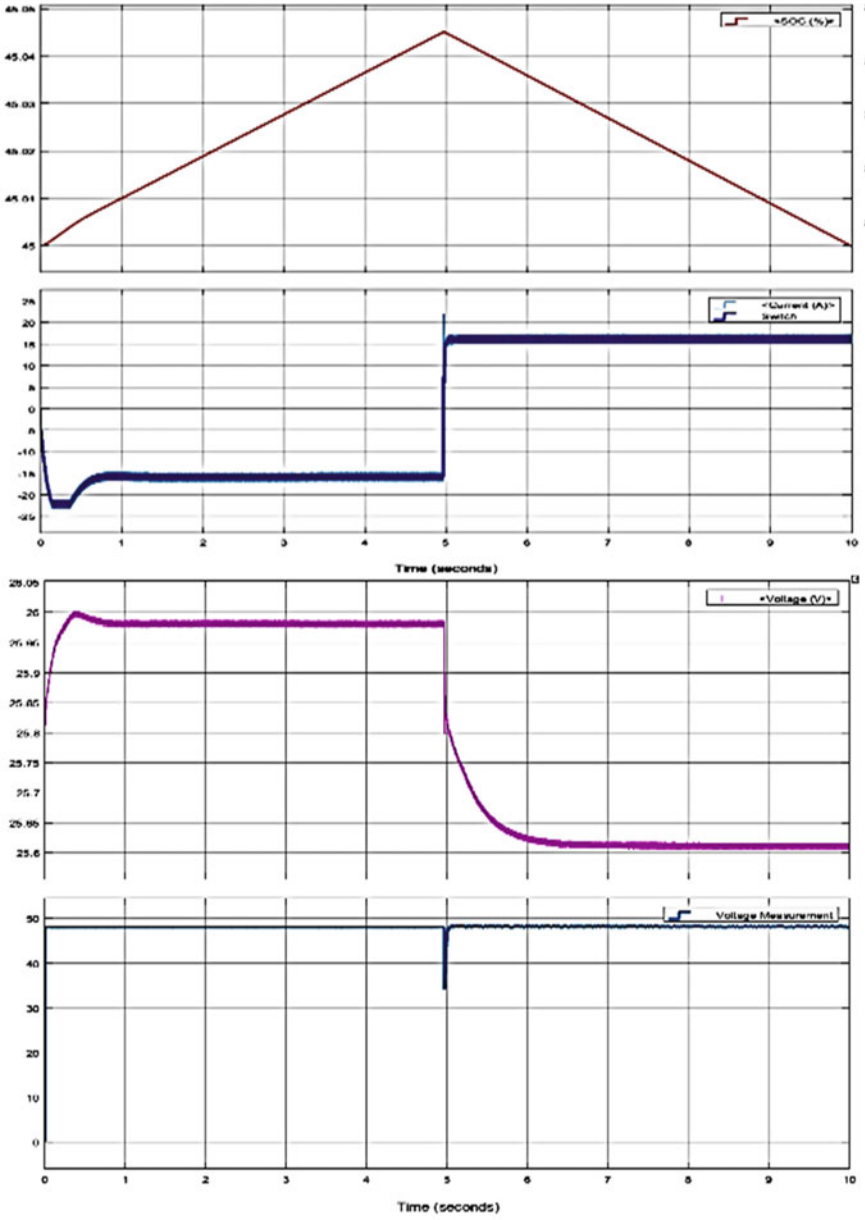


Fig. 16 Simulation results for SOC, current and voltage

Table 1 Comparison of three-charging technique

Criteria	PV battery charging algorithm		
	Constant current charging	Constant voltage charging	Constant current-Constant voltage charging
1. Charging time	Depends upon constant current charging	Lesser time is required	Longer
2. Incomplete charging	Suffers from phenomena	Overcomes this phenomena	Overcomes this phenomena
3. Battery life	Affected	Affected	Remains unaffected

discharged condition. Henceforth, the battery terminal voltage shows up at the over-voltage edge V_{oc} a ton sooner than the CC-CV charging methodology as shown in Fig. 10 where the battery terminal voltage is kept up at V_{oc} until the seeking after current goes to the I_{Float} regard. Regardless, in the CC-CV charging estimation, the battery is from the outset blamed for somewhat present and the battery voltage rises to a particular cutoff called stream voltage and subsequently a high charging current of 5 A of the charging current is given to the battery (Table 1).

6 Conclusion

Normally, when the charger is connected to the charger, the charger will automatically charge the battery pack, but it will continue to charge even though the battery is fully charged. That situation can cause damage to the battery itself. A successful charging system will improve battery life. The structure, essential parts and working guideline of the disconnected bidirectional DC-DC converter are portrayed in this section. Additionally, the Simulink model of IBDC has been proposed to show the two-sided stream of intensity. The waveforms of the model show the stage move of 180° which permits the most extreme capacity to be moved between the two DC sources. The stage move between the two DC voltages decides the bearing and the measure of intensity move between two DC transports. By altering the stage move, full control on the force move is conceivable. In the three charge control techniques of battery, the PI controller can regulate the output voltage from the charger to satisfy a desire value by regulating the rise time of the current, over-shooting and error occurring during charging phase. The proportional (P) action reduces the time of increase and increases error while the Integral (I) action removes the error. Pulse width modulation (PWM) is the most effective means of achieving constant voltage charging of batteries by switching the power devices of the solar system controller. The current from the solar array tapers according to the condition of the battery and the recharging requirements when in PWM regulation. The CC-CV charging is frequently contrasted with the CV charging, and it tends to be surmised that the time

taken by the CC-CV charging is more than the CV charging yet the CC-CV charging strategy is better for the security of the battery than the CV charging procedure in light of the fact that the battery is accused of high beginning current in the CV charging in the CC-CV charging method, the battery is at first provided with a little current called stream current up to a specific voltage limit, called stream voltage, and afterward high charging current is provided in the next stage.

References

1. Tariq M, Maswood AI, Madishetti S et al (2015) Battery integration with more electric aircraft DC distribution network using phase shifted high power bidirectional DC-DC converter. In: Power and Energy Engineering Conference (APPEEC), 2015 IEEE PES Asia-Pacific, pp 1–5
2. Chiang YH, Sean WY, Ke JC (2011) Online estimation of internal resistance and open-circuit voltage of lithium-ion batteries in electric vehicles. *J Power Sources* 196:3921–3932
3. Chun WN (2011) Study on characteristics of photovoltaic cells based on MATLAB simulation. IEEE
4. Rashid MH (2007) Power electronics hand book, 2nd edn, pp 246–251, 661–671
5. Schmid J (2002) Charge controllers and monitoring systems for batteries in PV power systems, pp 864–875
6. Salas V, Manzanas MJ, Lazaro A, Barrado A, Olias E (2002) The control strategies for photovoltaic regulators applied to stand-alone systems. IEEE, pp 3274–3279
7. Duryea S, Islam S, Lawrance W (1999) A battery management system for stand-alone photovoltaic energy systems. In: Proceedings of the 34th annual meeting of the IEEE industry applications conference, Phoenix, USA, vol 4, pp 2649–2654
8. Colak I, Tuncay N (2008) High current, low voltage modular power converter for lead acid battery charging. In: International conference on sustainable energy technologies. IEEE, pp 1042–1046
9. Armstrong S, Glavin ME, Hurley WG (2008) Comparison of battery charging algorithms for stand-alone photovoltaic systems. In: IEEE Power Electronics Specialists Conference, pp 1469–1475
10. Crompton TP, Battery reference book: Newnes

High Impedance Fault Analysis of Distributed Power System Network Using Discrete Wavelet Transform



Abrar Ul Qadir Bhat, Anupama Prakash, Vijay Kumar Tayal, and Pallavi Choudekar

Abstract When an energetic primary conductor comes into contact with a quasi-insulating surface, such as a tree, equipment, or structure or it falls to the ground, the occurrence of the high impedance fault becomes quite high. The importance of these previously unnoticeable flaws is that they pose a significant threat to public safety as well as the risk of ignition by arcing fire. The high impedance failure is categorized by a sufficiently high impedance that traditional safety, such as fuses and current relays, does not detect it. Unlike short circuits with low impedance, which involves relatively large fault currents and are easily detectable by conventional over-current protection, these HIFs constitute a small threat to the power system equipment damage. High impedance failures generate current rates approximately in the range from 0 to 85 Amperes. Typically, a HIF shows flashing and arcing at the point of contact. In this paper, high impedance fault is modelled in the MATLAB/Simulink environment and are classified using discrete wavelet transform to implement proper safety scheme in the distribution system.

Keywords Distribution network · Fault detection · HIF modelling · High impedance fault circuit · Discrete wavelet transform

A. Ul Qadir Bhat (✉) · A. Prakash · V. K. Tayal · P. Choudekar
Department of Electrical and Electronics Engineering, AMITY University, Noida, Uttar Pradesh, India

e-mail: erabrar17@gmail.com

A. Prakash

e-mail: aprakash1@amity.edu

V. K. Tayal

e-mail: vktayal@amity.edu

P. Choudekar

e-mail: pachoudekar@amity.edu

© Springer Nature Singapore Pte Ltd. 2021

R. Agrawal et al. (eds.), *Advances in Smart Communication and Imaging Systems*,

Lecture Notes in Electrical Engineering 721,

https://doi.org/10.1007/978-981-15-9938-5_53

1 Introduction

Power system engineers need to carefully design and calibrate the protective devices as safety and reliability of power systems is of utmost importance. Some of the anomalies that exist in distributed power system networks are line failures, high impedance failures, condenser switching, and unexpected charging rejection. Amid these disruptions, the most complicated phenomena faced by utilities is the determination of HIF fault in distributed power system network [1]. The standard protection schemes designed to identify the fault in the network over the years are based on over-current principle and are therefore suited only for low impedance faults, where the fault currents are extremely higher than load current. In case of HIF fault, the magnitude of fault current is comparable to that of load current and is therefore undetected by the over-current relays. The HIF, if not detected and taken care off by the protection system leads to the flash and arc at the point of contact and can be dangerous to the living beings in the vicinity [1, 2]. In order to mitigate such a crisis, traditional schemes such as system current and voltage trends, minimal reaction approach, and the transients linked to these waves were used to identify system failures [3–6].

It is difficult to determine high impedance fault present in medium voltage distribution networks using various ground fault and over-current relays [7]. This form of failure is difficult to detect by monitoring equipment since its existence results in just a small increase in phase to ground voltage, so it may be confused with regular increases in load [8]. HIF is characterized as unwanted electrical contact with a high impedance surface like sand, asphalt road, tree or grass [9]. The HIF fault has a low magnitude of current (few mA) or tens of amperes [10]. Failure to detect HIFs leads to serious danger to human beings in electric shock and possible fire hazards [11]. HIF is a very dynamic phenomenon and is strongly nonlinear [12]. Detecting high impedance faults is definitely challenging [13]. There are various ways to detect and treat high impedance earth faults such as direct measurement of the power system's electrical quantities, randomness and energy algorithms, harmonic analysis, neural networks, chaotic pattern and discrete wavelet analysis [14].

2 System Modelling

The distribution network which is shown in Fig. 1 has been used for the analysis of different types of faults which occur in the power system distributed network. The system has been modelled in MATLAB/Simulink environment. High impedance fault is introduced such as symmetrical (HLLLG) and unsymmetrical (HLG, HLL and HLLG). It has grid source (100 MVA/11 kV), two transformers each of 100 MVA, transformer 1 and transformer 2 of 11 kV/33 kV and 33 kV/400 V, respectively, three distribution line 1, 2 and 3 of 30 km, 30 km and 40 km, respectively, with integration of load facility.

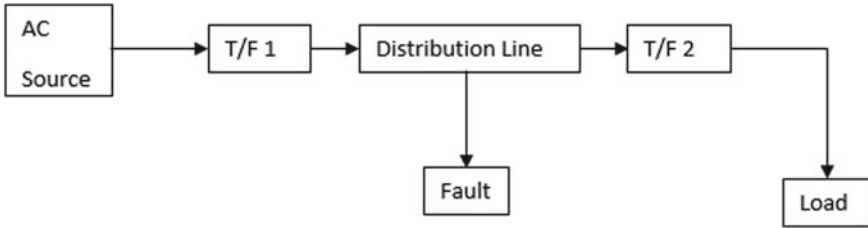


Fig. 1 Block diagram of distribution network

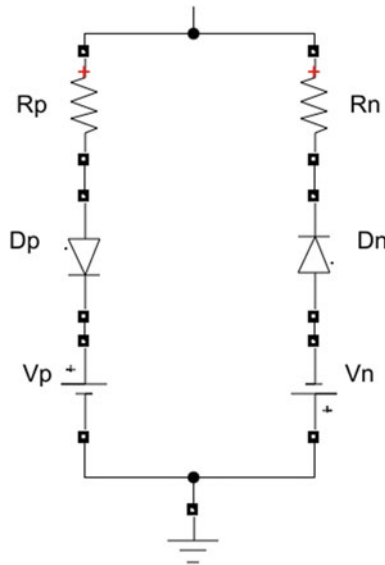


Fig. 2 High impedance fault model

The high impedance fault model proposed in this paper as shown in Fig. 2 comprises of two DC sources (DC1 and DC2) with voltages (V_p and V_n) representing arcing voltage values of 5500 V and 2750 V, respectively; two resistances (R_p and R_n) between the diodes representing resistance having values of 300 Ω and 1000 Ω , respectively.

3 Discrete Wavelet Transform

Discrete wavelet transform has been an effective application in numerous fields, for example, acoustics, sign and picture preparing, power system analysis, discourse separation and optics. Its application in power system analysis has been widely

accepted by the researchers worldwide. Typical implementations include power device protection [15], power system transient analysis [16], control condition identification and classification [17], etc. Unlike conventional Fourier transform, the transition of the wavelet is capable of supplying period and frequency details at the same period, it then provides different frequency and time resolutions which may be of benefit to the study of transient signals comprising both low- and high-frequency components together. Discrete wavelet transform (DWT) analysis is a tool of signal processing in which the signal is interpreted at various frequency levels following a sequence of decompositions.

Protection experts and scholars have been searching for approaches to this long-standing issue for several years. This search culminated in the creation of many HIF detection techniques. In addition, as being defined as low current fault, these fault classes continue to show erratic actions with unpredictable and large variations in current rates. These are often distinguished by the inclusion of high-frequency elements and harmonics. Much of the high impedance fault work centered on designing flexible detectors to identify these faults reliably. Some of the methods include Fourier transform, neural networking, fuzzy logic [18, 19], relay logic, Kalman filtering, wavelets and others.

The effective method for processing information about the time–frequency signal is discrete wavelet transform. This produces non-redundant signal restoration and allows sampling of the signal with localized transients. This also provides improved spatial and spectral signal localisation. Such sophisticated, efficient tool has been used in recent decades to develop protective relays. In discrete wavelet transform analysis, fault current $x(t)$ is broken down into twofrequency components, i.e. high and low such as accurate coefficients (D) and approximation (A) as shown in Eqs. (1)–(4) [20–23].

$$\begin{aligned} x(t) &= \sum_k cA_0\vartheta_{j,k}(t) \\ &= \sum_k cA_1\vartheta_{j-1,k}(t) + \sum_k cD_1\vartheta_{j-1,k}(t) \\ x(t) &= A_1(t) + D_1(t) \end{aligned} \tag{1}$$

To derive the correct details from the lower part of frequency,

$$x(t) = A_2(t) + D_2(t) + D_1(t) \tag{2}$$

$$x(t) = A_3(t) + D_3(t) + D_2(t) + D_1(t) \tag{3}$$

Therefore, signal can be shown as,

$$x(t) = A_N(t) + D_N(t) + D_{N-1}(t) + \cdots + D_1(t) \tag{4}$$

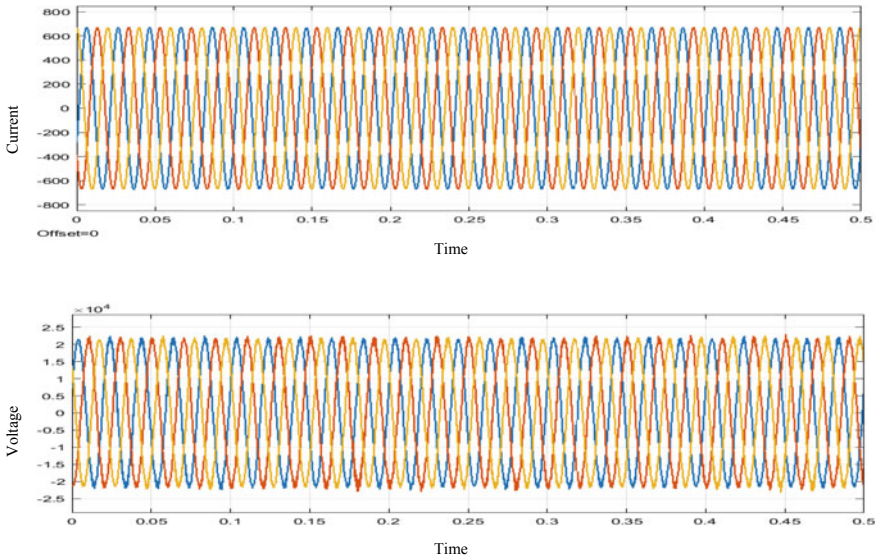


Fig. 4 Current and voltage waveform under normal case/no fault

and their respective DWT waveform are shown in Figs. 4, 5, 6, 7, 8, 9, 10 and 11. It is found that the magnitude of current in case of normal remains same for all the phases. But in case of HLG, HLLG and HLLLG fault, the magnitude of faulted current is of having little difference. For example, in case of HLG fault of phase-A, the magnitude of fault current of phase-A is 487.78 A which is almost high as compared to other two phases i.e. phase-B (473.48 A) and phase-C (474.20 A). While in case of DWT analysis, the magnitude of noise present in levels d1 to d3 is seen to be high and d4 to d5 levels are full of transients. Standard deviation values are found using Eq. (5) shown in Sect. 3 and is listed in Table 1.

Figure 4 shows current and voltage waveform under normal case. Here the current and voltage remain the same throughout the time period for all the phases.

The high impedance A-G fault was simulated from 0.15 to 0.2 s. The current and voltage waveforms captured at bus1 for this fault are as shown in Fig. 5. Since this is HAG fault, the current in phase-A has increased slightly as compared to the rest of the phases, and voltage for the same phase has decreased slightly from 0.15 to 0.2 s. The change in current and voltage is not only significant enough to be detected by conventional protection schemes but similar changes in current and voltage can be seen during the increase in load.

The high impedance AB-G fault was simulated from 0.15 to 0.2 s. The current and voltage waveforms captured at bus1 for this fault are as shown in Fig. 6. Since this is HABG fault, the current in phase-A and phase-B has increased slightly, and voltage for phase-A and phase-B has decreased slightly during the fault period. The change in current and voltage is not significant enough to be detected by conventional protection schemes.

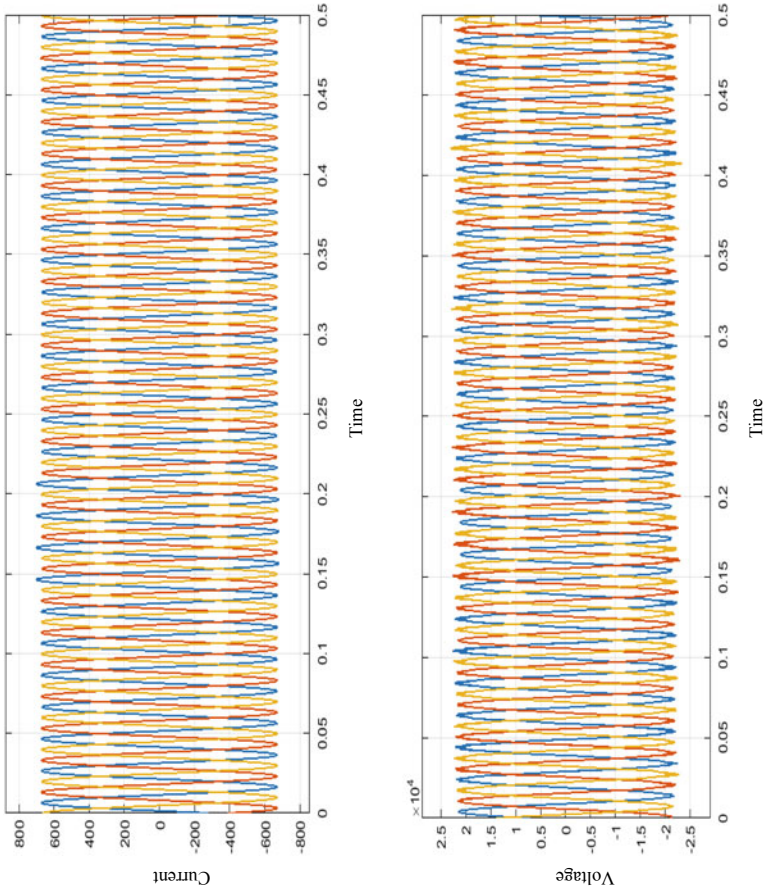


Fig. 5 HIF current and voltage waveform for LG fault (HAG)

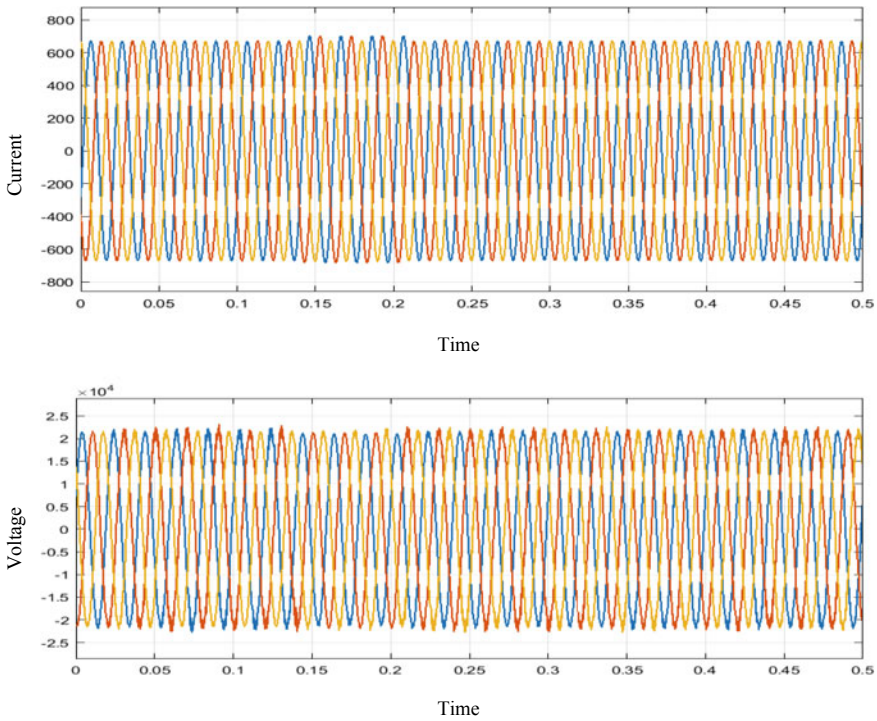


Fig. 6 HIF current and voltage waveform for LLG fault (HABG)

Figure 7 shows the HIF current and voltage waveform for LLLG fault (which is also represented as HABCG Fault). The current and voltage waveforms captured at bus1, for this fault are as shown in Fig. 7 Since this is HABCG fault, the current in all the phases has increased, and voltage for all the phases has decreased from 0.15 to 0.2 s.

Figure 8 shows the DWT waveform of HIF for Normal case/No Fault.

Figure 9 shows the DWT waveform of HIF for LG fault (which is also represented as HAG Fault).

Figure 10 shows the DWT waveform of HIF for LLG fault (which is also represented as HABG Fault).

Figure 11 shows the DWT waveform of HIF for LLLG fault (which is also represented as HABCG Fault).

Table 1 shows the values of standard deviation values of different types of fault listed above. The variation in standard deviation will help in identifying the HIF which was not detected by conventional protection schemes as the fault current levels are comparable to load currents.

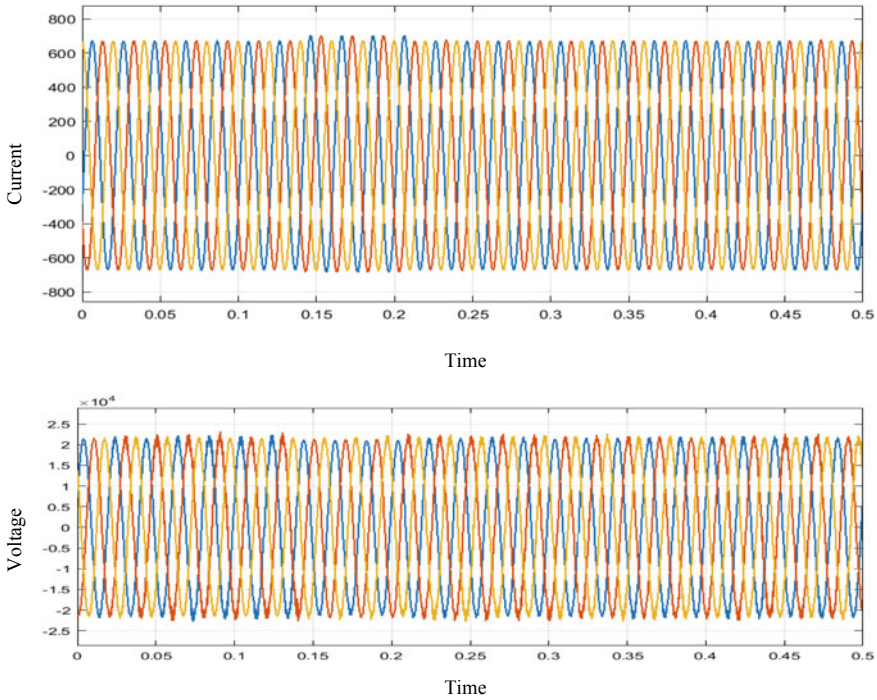


Fig. 7 HIF current and voltage waveform for LLLG fault (HABCG)

5 Conclusion

In this paper, 11 kV medium voltage distribution network has been designed in MATLAB/Simulink environment by applying different types of the fault in the power system distributed network. The main aim of this paper was to create a model that detects and classifies the high impedance fault. High impedance fault model consisting of both active and passive components (outlet voltages, resistors and diodes) provides a very satisfactory description of the arc characteristics and has been used in this work. The current waveform obtained in each case of HIF fault has been analysed using the discrete wavelet transform (DWT). The DWT could detect the HIF fault in the distribution network.

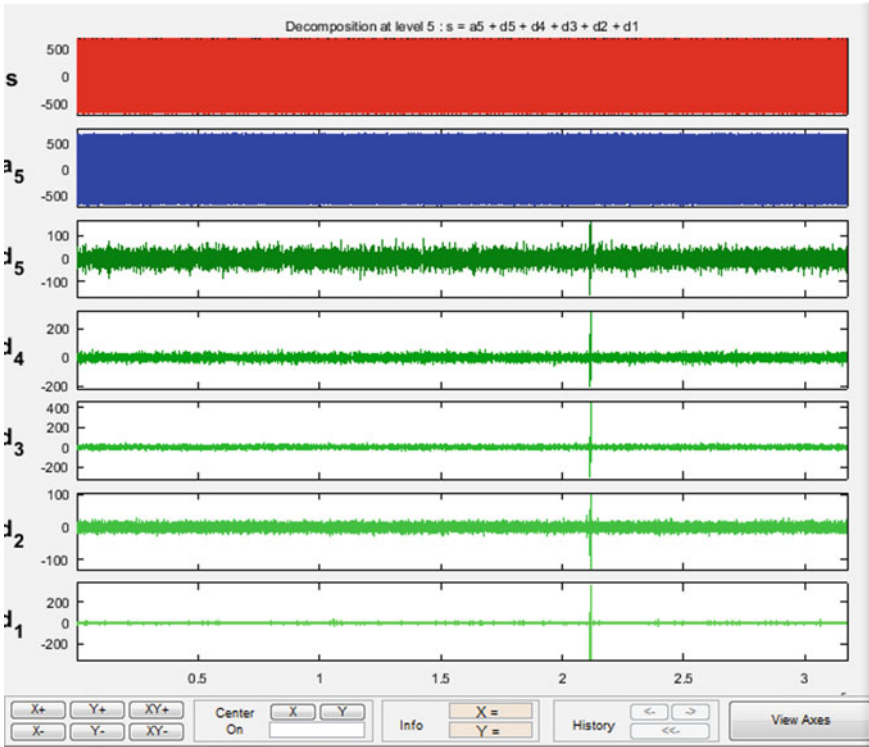


Fig. 8 DWT analysis under normal case

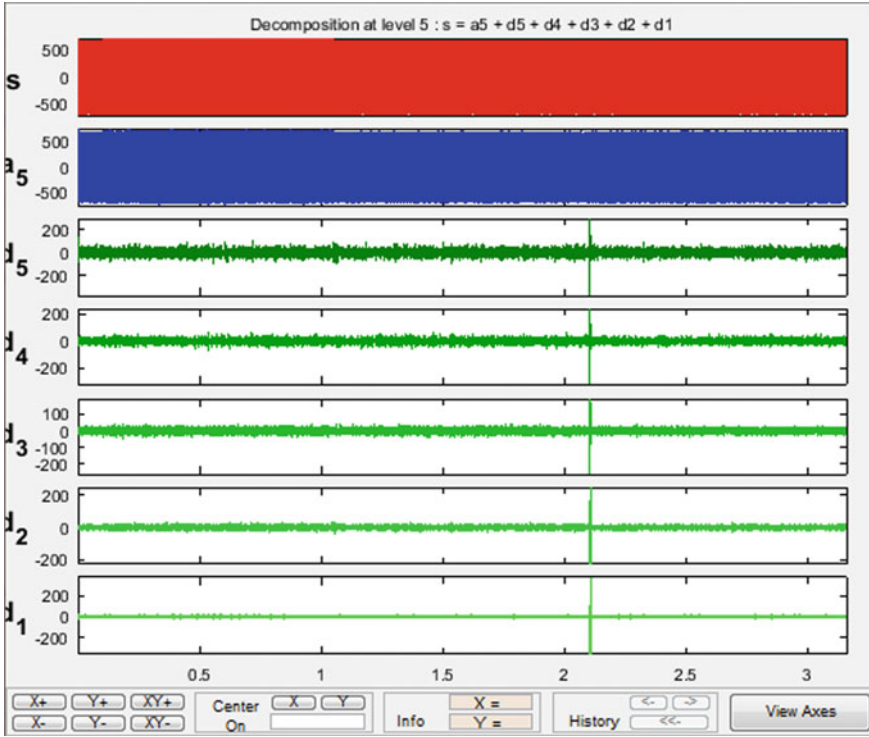


Fig. 9 DWT waveform of HIF for HLG fault (HAG)

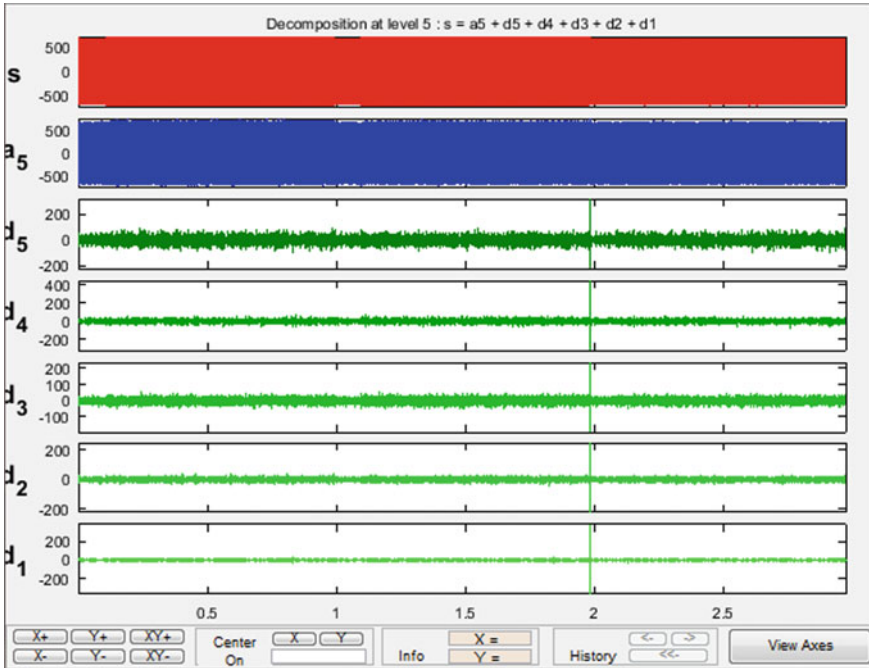


Fig. 10 DWT waveform of HIF for HLLG fault (HABG)

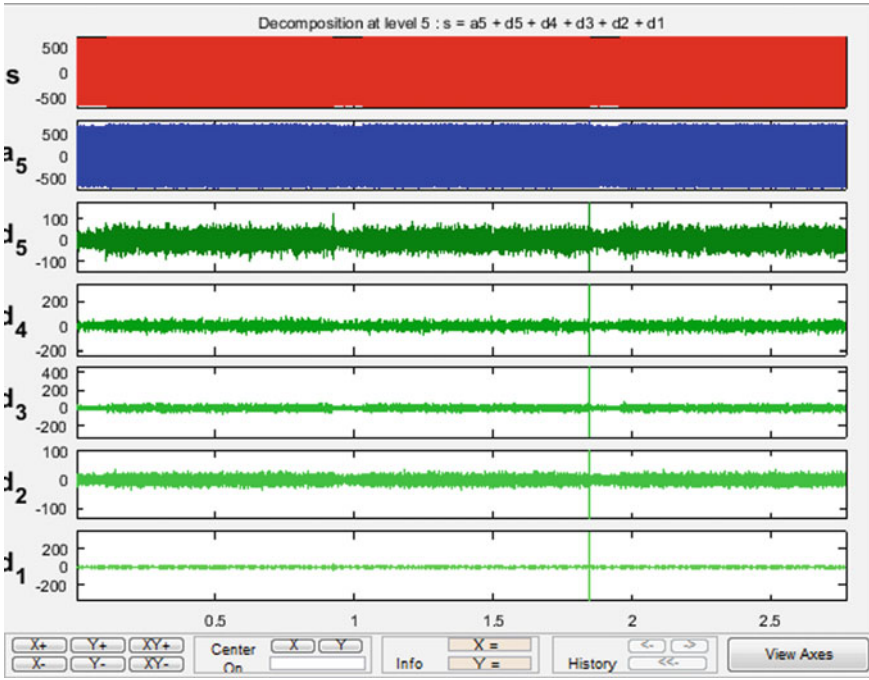


Fig. 11 DWT waveform of HIF for HLLG fault (HABCG)

Table 1 SD values for current signal for different faults

Cases	Fault type	Fault name	I_a (A)	I_b (A)	I_c (A)	V_a (V)	V_b (V)	V_c (V)	SD values of I_f
1	Normal case	No fault	473.26	472.79	473.01	15,123.87	15,123.19	15,107.43	475
2	HLG fault	HAG	487.78	473.48	474.20	15,013.39	15,283.88	15,029.32	479.7
		HBG	474.29	487.97	473.57	15,023.17	15,015.96	15,291.92	479.7
		HCG	473.41	474.43	487.72	15,266.68	15,007.83	15,016.62	479.7
3	HLLG fault	HABG	488.62	488.88	475.31	14,905.19	15,177.53	15,181.36	484.6
		HBCG	475.29	488.89	488.80	15,169.80	14,906.07	15,170.52	484.6
		HACG	489.19	475.24	488.74	15,171.61	15,170.26	14,901.25	484.6
4	HLLLG fault	HABCG	490.05	489.60	489.35	15,070.31	15,069.40	15,066.35	489.6

References

1. Wang B, Geng J, Dong X (2018) High-impedance fault detection based on nonlinear voltage-current characteristic profile identification. *IEEE Trans Smart Grid* 9(4):3783–3791
2. Baqui I, Zamora I, Mazon J, Buigues G (2011) High impedance fault detection methodology using wavelet transform and artificial neural networks. *Electr Power Syst Res* 81:1325–1333
3. Prasad A, Edward B (2015) Classification of faults in power transmission lines using fuzzy-logic technique. *Indian J Sci Tech* 8:1–6
4. Narasimha Rao G (2012) High impedance fault detection and classification of a distributed system. *Int J Eng Res Tech*, 1–6
5. Chang GW, Shih M-F, Chen Y-Y, Liang Y-J (2014) A hybrid wavelet transform and neural-network-based approach for modelling dynamic voltage-current characteristics of electric arc furnace. *IEEE Trans Power Delivery* 29:815–824
6. Homaei M, Moosavian SM, Ilias HA (2014) Partial discharge localization in power transformers using neuro-fuzzy technique. *IEEE Trans Power Delivery* 29(5):2066–2076
7. Samantaray SR, Dash PK (2010) High impedance fault detection in distribution feeders using extended kalman filter and support vector machine. *Eur Trans Electr Power* 20(3):382–393
8. Uriarte FM (2003) Modeling: detection and localization of high impedance faults in low-voltage distribution feeders. Master of science thesis, Virginia Tech Polytechnic Institute and State University, Blacksburg, VA (2003)
9. Zhang Y, Wang Z, Zhang J (2011) Universal characteristics of faults in complex power system. *Int Rev Electr Eng (IREE)* 6(3):1474–1482
10. Eldin AH, Abdallah E, Mohamed N (2013) Detection of high impedance faults in medium voltage distribution networks using discrete wavelet transform. In: 22nd International Conference on Electricity Distribution, Stockholm, Sweden Session 3, 10–13 June 2013
11. Tawafan AH, Sulaiman MB, Ibrahim ZB (2002) Adaptive neural subtractive clustering fuzzy inference system for the detection of high impedance fault on distribution power system. *Int J Artif Intell* 1(2):63–72
12. Ravlić S, Marušić A (2015) Simulation models for various neutral earthing methods in medium voltage systems. *Procedia Eng* 100(12):1182–1191
13. Sagastabestia KJ, Zamora I, Mazón AJ, Aginako Z, Buigues G (2011) Phase asymmetry: a new parameter for detecting single-phase earth faults in compensated MV networks. *IEEE Trans Power Delivery* 26(4):2251–2258
14. Hanninen S, Lehtonen M (1999) Method for detection and location of very resistive earth faults. *Eur Trans Electr Power* 9(5):285–291
15. Robertson DC, Camps OI, Mayer JS, Gish WB (1996) Wavelets and electromagnetic power system transients. *IEEE Trans Power Delivery* 11(2):1050–1056
16. Gaouda AM, Salama MMA (1999) Power quality detection and classification using wavelet multi-resolution signal decomposition. *IEEE Trans Power Delivery* 14(4):1469–1475
17. Wan EA (1993) Finite impulse response neural networks with applications in time series prediction. Ph.D. dissertation, Department of Electrical Engineering, Stanford University
18. Tayal VK, Lather JS (2015) PSO based robust Fuzzy power system stabilizer design for single machine infinite bus system. In: Annual IEEE India Conference (INDICON), New Delhi, pp 1–6
19. Tayal VK, Lather JS, Sharma P, Sinha SK (2014) Power system stability enhancement using fuzzy logic based power system stabilizer. In: Proceedings of the third international conference on soft computing for problem solving, advances in intelligent systems and computing (Springer), vol 258, pp 55–68
20. Deekshit KKC, Chaitanya Kumar AN, Supraja B, Sumanth M (2015) Comparison of DWT and WPT to detect bearing faults in 3 phase Induction Motor using Current Signature analysis. *J Electr Eng*, 1–9
21. Sedighi AR, Haghifam MR, Malik OP, Ghassemian MH (2005) High impedance fault detection based on wavelet transform and statistical pattern recognition. *IEEE Trans Power Delivery* 20(4):2414–2421

22. Ghaderi A, Mohammadpour HA, Ginn HL, Shin Y (2015) High-impedance fault detection in the distribution network using the time-frequency-based algorithm. *IEEE Trans Power Delivery* 30(3):1260–1268
23. Haghifam MR, Sedighi AR, Malik OP (2006) Development of a fuzzy inference system based on genetic algorithm for high-impedance fault detection. *IEE Proc-Gener Transmission Distrib* 153(3):359–367

Implementation of Secured Wired and WLAN Network Using eNSP



Amanpreet Singh Saini, Pallavi Gupta, and Harshita Gupta

Abstract WLAN is a key component of computer networking courses. For a better understanding of the WLAN concept, this paper plans the implementation of a secured wired and wireless LAN network on the eNSP modeling platform where an experimental environment is created, network connections are implemented through AC and AP configurations, and cellular users can also travel in wireless network coverage. At the same moment, we configure firewall for security purposes, configure, and analyze principles of networking protocols (LACP, MSTP, DHCP, VRRP, BFD, OSPF, IS-IS, CAPWAP, and WLAN802.11b), use Wireshark to intercept protocols, and check the wireless terminal roaming. This implementation also enhances the basic principle and data analysis capabilities of WLAN technology.

Keywords Computer networking · Firewall · Network connectivity · WLAN

1 Introduction

Amidst that accelerated growth of wireless technologies, the usage of WLAN is increasing. WLAN extends the network to end-users. Wireless LAN is a popular way to offer network connectivity without having to distribute fixed cables to the workplace [1]. WLAN toward our quotidian times commits to the restricted interpretation

A. S. Saini · P. Gupta (✉) · H. Gupta
Department of Electronics and Communication Engineering, Galgotias College of Engineering and Technology, 201310 Greater Noida, Uttar Pradesh, India
e-mail: guptapallavi0202@gmail.com

A. S. Saini
e-mail: aps.saini@galgotiacollege.edu

H. Gupta
e-mail: harshitagupta0542@gmail.com

of WLAN. The standards of 802.11 series have enhanced WLAN's leading technological standards because of its comparatively manageable implementation technology, secure connection, tremendous adaptability, and comparably cheap implementation price. Besides this, these standards become interchangeable with wireless LAN technological standards [2]. To ensure the enhancement of data capabilities, WLAN 802.11b is used. Since WLAN 802.11b, transmission speed can be 0 to 11 Mbps. This makes it faster than the original IEEE standard 802.11 (transmit data at 2 Mbps) [3].

The campus network is often part of a network infrastructure that provides access to telecommunications services as well as the capabilities of users and devices that span the entire area. The connected campuses are much more than just a series of connected devices. The most difficult and important part of this is the planning and design method, where it is necessary to take into account the various rules of technology and technology products, which can affect the products choice and its design. Besides this, IP addressing is also one of the challenging tasks in networking. In this paper, the unique arrangement of IP addresses is done according to ASN to decrease the number of IP addresses to be compared [4].

As good design is quintessential for network performance measurement. Here, we solve complex network design problems and design a smaller, more manageable model with the help of eNSP.

A simulation platform, eNSP, is used by network designers for experimenting simulations and configurations. It is very much similar to the package stressors of cisco devices. It has a collection of devices like routers, switches, wireless LAN, firewall, cloud, and connection links. It has features like GUI, used to analyze processes within complicated networking and help users to inspect equipment designs. A high simulation degree along with distributed deployment makes it convenient for deployment on various servers building a complex network and allow flexible networking by implementing connections among real devices and simulated devices [5].

The main contribution of this paper is as follows:

- We designed a secured wired and WLAN with the help of eNSP simulator which is based on a large-sized network, interconnects two campuses and provides Internet connection and security to the staff members and students.
- We analyzed the performance of every existing protocol in the designed network with the help of "Wireshark."
- From the simulation results, we observed that all the devices established their connections within the network successfully and a wireless coverage area can be seen within the network where mobile users can roam easily.
- Finally, this secured wired and WLAN topology can be connected to the real network adapter of the physical computers, switches, routers, access controller, access point and firewall.

Despite some interesting and challenging research problems in the design of these networking protocols, we restrict our focus in this paper to the design of interconnecting two campuses by configuring networking protocols (LACP, MSTP, DHCP, VRRP, BFD, OSPF, IS-IS, CAPWAP, and WLAN 802.11b). This means that we have

Table 1 Summary of acronyms

Acronym	Full-form
WLAN	Wireless Local Area Network
LAN	Local Area Network
IP	Internet Protocol
ASN	Autonomous System Number
eNSP	Enterprise Network Simulation Platform
GUI	Graphical User Interface
LACP	Link Aggregation Control Protocol
MSTP	Multiple Spanning Tree Protocol
DHCP	Dynamic Host Configuration Protocol
VRRP	Virtual Router Redundancy Protocol
BFD	Bidirectional Forwarding Detection
OSPF	Open Shortest Path First
IS-IS	Intermediate System to Intermediate System
CAPWAP	Control and Provisioning of Wireless Access Points

done our entire implementation with the help of these networking protocols and have created a successful network. A summary of acronyms used in this paper is outlined in Table 1.

2 Network Implementation

2.1 Objectives

The design objectives of secured wired and WLAN include the following:

- To interconnect two campuses, as well as the communication between the campuses and the Internet.
- The whole setup needs to deploy a firewall and a wired and WLAN at the campus to ensure network security and provides a mobile office for staff members as well as students.

The purpose is also to understand the basics of wired and wireless LAN, the architecture of the network and the process of creating GRE tunnel session, using the method of distribution, and understand the configuration process of AC, switches, routers, and firewall in manageable secured wired and wireless LAN, and follow the roaming status of cellular users.

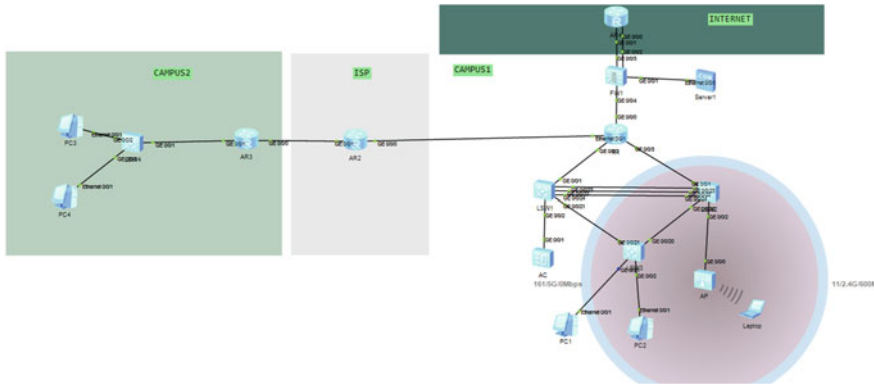


Fig. 1 Secured wired and WLAN topology

2.2 IP Module

The following section describes the devices that are used in the test environment:

There is one USG6530 firewall, four AR2200E routers, four S5720-36C-PWR-E1 switches, one AC6005 wireless controller, one AP4030DN wireless access point, four wired clients, and one wireless client. These devices are referred to as FW1, AR1-4, LSW1-4, AC, AP, PC1-PC4, and laptop, respectively. The secured wired and WLAN network topology is shown in Fig. 1, and the devices’ addresses are shown in Table 2 [6].

3 Implementing Simulation Procedures

3.1 Configuring Networking Protocols

LACP: In switch 1, Loopback 0 IP address configured which applied as the local loopback interface. Configured the IP address of VLANIF 10, 20, 30, and 1 to implement Inter-VLAN Communication. Similarly, to switch 1, the Loopback 0 IP address configured which applied as the local loopback interface in Switch 2. Configured the IP address of VLANIF 10, 20, and 1 to implement Inter-VLAN Communication.

To implement IEEE 802.3ad, i.e., LACP, bundled the interfaces connecting LSW1 and LSW2 into a Layer 2 logical interface. To increase throughput and to provide redundancy, bundled the multiple physical interfaces into a logic one named Eth-Trunk, which also implements load balancing and higher reliability [7].

Table 2 IP address planning

Device Name	Interface/VLAN/VLANIF	IP Address
AR1	Loopback 0	1.1.1.1 32
	Tunnel 0/0/0	10.1.13.1 30
	GE 0/0/0	10.1.1.1 30
	Eth 0/0/1	200.1.1.1 30
	GE 0/0/2	10.1.11.1 30
	GE 0/0/3	10.1.12.1 30
AR2	GE 0/0/0	200.1.1.2 30
	GE 0/0/1	200.1.2.2 30
AR3	GE 0/0/0	200.1.2.1 30
	Tunnel 0/0/0	10.1.13.2 30
	GE 0/0/1	10.2.1.1 30
AR4	Loopback 0	100.100.100.1 32
	GE 0/0/0	100.1.1.2 30
	GE 0/0/1	100.1.2.2 30
LSW1	Loopback 0	4.4.4.4 32
	VLANIF 10	192.168.10.253 24
	VLANIF 20	192.168.20.253 24
	VLANIF 30	192.168.30.254 24
	VLANIF 1	10.1.11.2 30
LSW2	Loopback 0	5.5.5.5 32
	VLANIF 10	192.168.10.252 24
	VLANIF 20	192.168.20.252 24
	VLANIF 1	10.1.12.2 30
LSW4	VLANIF 40	192.168.40.254 24
	VLANIF 50	192.168.50.254 24
	VLANIF 1	10.2.1.2 30
AC1	VLANIF 30	192.168.31.254 24
FW1	Loopback 0	7.7.7.7 32
	GE 0/0/4	10.1.1.2 30
	GE 0/0/1	192.168.100.1 24
	GE 0/0/2	100.1.1.1 30
	GE 0/0/3	100.1.2.1 30

Configured LSW1 as the actor by setting the priority of 100, and configured GE0/0/22 and GE0/0/23 as active interfaces with a priority of 100. Therefore, interfaces with higher priority will become active upon link failure [7]. To enable the functioning of the interface having the highest LACP priority as an active interface. Enabled the LACP preemption function. Set the preemption delay to 10 s which is the period when an inactive interface switches to active.

MSTP: As AC S-Series switches keep up all STP versions of the IEEE standard, including IEEE 802.1W RSTP, IEEE 802.1S MSTP, and IEEE 802.1D STP [8]. Configured STP to prevent Layer 2 loops between LSW1, LSW2, and LSW3.

Firstly, configured the switch interfaces as trunk and then added the allowed VLAN on this trunk interfaces.

Secondly, set the STP mode to MSTP and the MSTP domain name to GALGOTIA.

Thirdly, added VLAN 10 and VLAN 30 to MSTI 1, and added VLAN 20 to MSTI 2. Then, activated the MST region configuration with an “active region-configuration” command.

Lastly, in MSTI 1, configured LSW1 as the primary root bridge and LSW2 as the secondary root bridge. In MSTI 2, configured LSW2 as the primary root bridge and LSW1 as the secondary root bridge.

VRRP: Configured VRRP on LSW1 and LSW2 to ensure the continuity and reliability of service network segments and communication services. Thus, VRRP prevents network interruptions in case of any of the link failure [9].

To both the switches, LSW1 and LSW2, assigned VRRP group 1 to VLAN 10, and set a virtual IP address for VRRP group 1 to 192.168.10.254. In VRRP group 1, configured LSW1 as the master device, and set its priority to 120 and the preemption delay to 20 s; configured LSW2 as the backup device and retained the default priority for LSW2.

Assigned VRRP group 2 to VLAN 20, and set a virtual IP address for VRRP group 2 to 192.168.20.254. In VRRP group 2, configured LSW2 as the master device, and set its priority to 120 and the preemption delay to 20 s; configured LSW1 as the backup device and retained the default priority for LSW1.

BFD: The Hello Packets Detection on Layer 3 network will not detect errors for all routes, such as static routes. That means that it is difficult to track any fault between interconnected networking system. Configured BFD for VRRP to implement fast switchover in the event of a VRRP link failure [10].

Firstly, enabled BFD globally on LSW1 and LSW2.

Secondly, configured a single-hop BFD session by setting the local discriminator of the BFD session on LSW1 to 1 and that on LSW2 to 2.

Lastly, set the interval for sending or receiving BFD packets to 100.

DHCP: Enabled DHCP service based on the global IP address pool on LSW1 and LSW2 to facilitate unified management and reduce manual configuration costs [11].

Configured an IP address pool named VLAN10 on LSW1, and set a gateway address to 192.168.10.254 and a DNS server address to 8.8.8.8. PC1 needs to dynamically acquire the IP address of the IP address pool VLAN10 through the DHCP server.

Configured an IP address pool named VLAN20 on LSW2, and set a gateway address to 192.168.20.254 and a DNS server address to 8.8.8.8. PC2 needs to dynamically acquire the IP address of the IP address pool VLAN20 through the DHCP server.

OSPF: Configured OSPF to implement Layer 3 interconnection within campus1 network.

Enabled OSPF between LSW1 (VLANIF 1 and Loopback 0), LSW2 (VLANIF 1 and Loopback 0), AR1 (GE 0/0/0, eth 0/0/1, GE 0/0/2, GE 0/0/3 and Loopback 0), and FW1 (GE 0/0/4, GE 0/0/1 and Loopback 0), created an OSPF process with the ID 1, and created an OSPF area with the ID 0. The network command needed to

be used for accurate advertisement of routes to ensure that all 32 bits of interface IP addresses are exactly matched [12].

Enabled OSPF on LSW1 (VLANIF 10, VLANIF 20, and VLANIF 30) and LSW2 (VLANIF 10 AND VLANIF 20) created an OSPF process with the ID 1 and created an OSPF area with ID 1. The network command needed to be used for accurate advertisement of routes.

Implemented security within the whole network, configured area authentication for all OSPF devices, set the authentication mode to md5 authentication, and set the cipher text password type to cipher and the password to GALGOTIA@2020.

IS-IS: Configured IS-IS to implement Layer 3 interconnection with Campus2 [13].

Created an IS-IS process with the ID 1, and set the area ID to 49.0001. Set the system IDs of AR3 and LSW4 to 0000.0000.0003 and 0000.0000.0004. Configured AR3 and LSW4 as Level-2 routers.

Enabled IS-IS on GE0/0/1 and Loopback 0 of AR3 and VLANIF 1, VLANIF 40, and VLANIF 50 of LSW4.

To ensure the security of the campus-2 network, configured domain authentication on all IS-IS devices, and set the authentication mode to md5 authentication and password to GALGOTIA@2020.

GRE: Deployed GRE VPN (Virtual Private Network) to allow interconnection between campus1 and campus2. The campus1 and campus2 are connected through an ISP (Internet Service Provider) network.

Established a GRE tunnel between Tunnel 0 interfaces of AR1 and AR3. Established an OSPF neighbour relationship between AR1 and AR3 over the GRE tunnel. Set the OSPF process ID to 1, and advertised the IP addresses of Tunnel0 interfaces on AR1 and AR3 into OSPF area 0 using the network command.

To implement security within the enterprise network, configured area authentication for all OSPF devices, set the authentication mode to md5 authentication, set the ciphertext password type to cipher and the password to GALGOTIA@2020.

3.2 *Configuring Firewall*

In order make the network secure, firewall is configured. Security zones are implemented. On FW1, added GE0/0/4 to the trusted zone, GE0/0/1 to the DMZ (Demilitarized Zone), add GE 0/0/2 as well as GE 0/0/3 to the trusted zone.

FW1 is connected to the Internet through two links. Configured two default routes on FW1 for Internet access ensured that the links where GE 0/0/2 and GE 0/0/3 reside are the active and standby links, respectively, and set priority of default route for standby link to 100.

3.3 Configuring ACL (Access Control List)

Managed the Campus2 network, the Campus1 core router LSW1 can remotely manage the Campus2 core switch LSW4 through Telnet. Configured an ACL to allow only Loopback 0 of LSW1 to access LSW4 [14].

Set authentication mode to a authentication, and set user name to GALGOTIA and the password to GALGOTIA@123.

3.4 Configuring WLAN

Enabled Layer 2 communication between AP and AC. Configured the AC as DHCP server and allocate IP addresses to wireless device and AP.

Added GE0/0/1 that connects the AC to LSW1 to vlan 4000. Configured AC so that AP and AC can transmit CAPWAP packets [15].

Configured WLAN service parameters. Created security profile as Security_GALGOTIA and set the security policy in the profile. Created SSID profile SSID_GALGOTIA and set the SSID name to GALGOTIA_HW. Created VAP profile VAP_GALGOTIA, set the service VLAN, and applied the security profile and SSID to the VAP profile. Bounded VAP profile VAP_GALGOTIA to the AP group and applied the profile to radio 0 and radio 1 of the AP group.

4 Results and Discussion

To find out the establishment of protocols successfully, we start capturing the packets on “Wireshark” and find out the results which are as follows-

4.1 LACP

LACP was performed between LSW1 and LSW2, i.e., Switch1 and Switch2, respectively. We had captured packets on the connection between LSW1 and LSW2. Then, we filtered out the packets in the state of “LACP.” We can examine the information of LACP protocol and get the outcomes which are as follows

- LACP packets are enabling the switch to assign an automated package to the match.
- These packages offer a successful configuration of the connection aggregation between LSW1 and LSW2 on the same actor port (Fig. 2).

No.	Time	Source	Destination	Protocol	Length	Info
1	0.000000	HuaweiTe_0a12f:02	Slow-Protocols	LACP	124	v1:ACTOR 4c1f:cc:0a:34:15 P: 24 K: 305 **DCS07A PARTNER 4c1f:cc:0a:34:15 P: 24 K: 305 **DCS07A
2	0.050000	HuaweiTe_0a12f:02	Slow-Protocols	LACP	124	v1:ACTOR 4c1f:cc:0a:34:15 P: 24 K: 305 **DCS07A PARTNER 4c1f:cc:0a:34:15 P: 24 K: 305 **DCS07A
3	0.100000	HuaweiTe_0a12f:02	Slow-Protocols	LACP	124	v1:ACTOR 4c1f:cc:0a:34:15 P: 24 K: 305 **DCS07A PARTNER 4c1f:cc:0a:34:15 P: 24 K: 305 **DCS07A
4	0.150000	HuaweiTe_0a12f:02	Slow-Protocols	LACP	124	v1:ACTOR 4c1f:cc:0a:34:15 P: 24 K: 305 **DCS07A PARTNER 4c1f:cc:0a:34:15 P: 24 K: 305 **DCS07A
5	0.200000	HuaweiTe_0a12f:02	Slow-Protocols	LACP	124	v1:ACTOR 4c1f:cc:0a:34:15 P: 24 K: 305 **DCS07A PARTNER 4c1f:cc:0a:34:15 P: 24 K: 305 **DCS07A
6	0.250000	HuaweiTe_0a12f:02	Slow-Protocols	LACP	124	v1:ACTOR 4c1f:cc:0a:34:15 P: 24 K: 305 **DCS07A PARTNER 4c1f:cc:0a:34:15 P: 24 K: 305 **DCS07A
7	0.300000	HuaweiTe_0a12f:02	Slow-Protocols	LACP	124	v1:ACTOR 4c1f:cc:0a:34:15 P: 24 K: 305 **DCS07A PARTNER 4c1f:cc:0a:34:15 P: 24 K: 305 **DCS07A
8	0.350000	HuaweiTe_0a12f:02	Slow-Protocols	LACP	124	v1:ACTOR 4c1f:cc:0a:34:15 P: 24 K: 305 **DCS07A PARTNER 4c1f:cc:0a:34:15 P: 24 K: 305 **DCS07A
9	0.400000	HuaweiTe_0a12f:02	Slow-Protocols	LACP	124	v1:ACTOR 4c1f:cc:0a:34:15 P: 24 K: 305 **DCS07A PARTNER 4c1f:cc:0a:34:15 P: 24 K: 305 **DCS07A

Link Aggregation Control Protocol	
LACP Version:	0x01
TLV Type:	Actor Information (0x01)
TLV Length:	0x14
Actor System Priority:	100
Actor System ID:	HuaweiTe_0a12f:02 (4c1f:cc:0a:34:15)
Actor Key:	305
Actor Port Priority:	100

Fig. 2 Data flow process for LACP

No.	Time	Source	Destination	Protocol	Length	Info
2	0.700000	HuaweiTe_0a12f:02	Spanning-tree (For- STP)	551	1551	1551 Root = 32768/0/4c1f:cc:0a:34:15 Cost = 0 Port = 0/0/0/1
7	2.000000	HuaweiTe_0a12f:02	Spanning-tree (For- STP)	551	1551	1551 Root = 32768/0/4c1f:cc:0a:34:15 Cost = 0 Port = 0/0/0/1
11	3.300000	HuaweiTe_0a12f:02	Spanning-tree (For- STP)	551	1551	1551 Root = 32768/0/4c1f:cc:0a:34:15 Cost = 0 Port = 0/0/0/1
20	7.500000	HuaweiTe_0a12f:02	Spanning-tree (For- STP)	551	1551	1551 Root = 32768/0/4c1f:cc:0a:34:15 Cost = 0 Port = 0/0/0/1
21	9.050000	HuaweiTe_0a12f:02	Spanning-tree (For- STP)	551	1551	1551 Root = 32768/0/4c1f:cc:0a:34:15 Cost = 0 Port = 0/0/0/1
29	14.150000	HuaweiTe_0a12f:02	Spanning-tree (For- STP)	551	1551	1551 Root = 32768/0/4c1f:cc:0a:34:15 Cost = 0 Port = 0/0/0/1
33	16.350000	HuaweiTe_0a12f:02	Spanning-tree (For- STP)	551	1551	1551 Root = 32768/0/4c1f:cc:0a:34:15 Cost = 0 Port = 0/0/0/1
40	18.550000	HuaweiTe_0a12f:02	Spanning-tree (For- STP)	551	1551	1551 Root = 32768/0/4c1f:cc:0a:34:15 Cost = 0 Port = 0/0/0/1
43	20.750000	HuaweiTe_0a12f:02	Spanning-tree (For- STP)	551	1551	1551 Root = 32768/0/4c1f:cc:0a:34:15 Cost = 0 Port = 0/0/0/1
48	23.050000	HuaweiTe_0a12f:02	Spanning-tree (For- STP)	551	1551	1551 Root = 32768/0/4c1f:cc:0a:34:15 Cost = 0 Port = 0/0/0/1
55	25.250000	HuaweiTe_0a12f:02	Spanning-tree (For- STP)	551	1551	1551 Root = 32768/0/4c1f:cc:0a:34:15 Cost = 0 Port = 0/0/0/1
55	27.450000	HuaweiTe_0a12f:02	Spanning-tree (For- STP)	551	1551	1551 Root = 32768/0/4c1f:cc:0a:34:15 Cost = 0 Port = 0/0/0/1


```

3 Frame 21: 151 bytes on wire (1208 bits), 151 bytes captured (1208 bits) on Interface -, Id 0
3 IEEE 802.3 Ethernet
3 Logical-Link Control
3 Spanning Tree Protocol
  Protocol Identifier: Spanning Tree Protocol (0x0000)
  Protocol Version Identifier: Multiple Spanning Tree (3)
  BPDU Type: Rapid/Multiple Spanning Tree (0x02)
  BPDU Flags: 0x0c, Agreement, Forwarding, Learning, Port Role: Designated

```

Fig. 3 Data flow process for MSTP

4.2 MSTP

MSTP was performed between LSW1, LSW2, and LSW3 which are Switch1, Switch2, and Switch3, respectively. We capture packets on LSW3 (interface GE0/0/20). Then, we start filtering the packets in the condition of “STP.” The results from the messages of STP protocol are as follows-

- One or more further VLANs can be assigned to an individual MSTI.
- Bit 4 to 7 conveys the learning flag, forwarding flag, and agreement flag for this MSTI.
- The captured messages show that we are successful in preventing the loop path between LSW1, LSW2, and LSW3 (Fig. 3).

4.3 VRRP

VRRP was conducted on LSW1 and LSW2, i.e., Switch1 and Switch2. To capture messages that show the performance of the protocol successfully, we started capturing packets on the interface GE0/0/22 of LSW1. The captured messages indicate the following results

No.	Time	Source	Destination	Protocol	Length	Info
1	0.000000	192.168.10.252	224.0.0.18	VRRP	64	Announcement (v2)
5	0.985000	192.168.20.252	224.0.0.18	VRRP	64	Announcement (v2)
7	1.000000	192.168.10.252	224.0.0.18	VRRP	64	Announcement (v2)
14	1.985000	192.168.20.252	224.0.0.18	VRRP	64	Announcement (v2)
15	2.000000	192.168.10.252	224.0.0.18	VRRP	64	Announcement (v2)
17	2.985000	192.168.20.252	224.0.0.18	VRRP	64	Announcement (v2)
18	3.000000	192.168.10.252	224.0.0.18	VRRP	64	Announcement (v2)
19	3.985000	192.168.20.252	224.0.0.18	VRRP	64	Announcement (v2)
20	4.016000	192.168.10.252	224.0.0.18	VRRP	64	Announcement (v2)
22	5.000000	192.168.20.252	224.0.0.18	VRRP	64	Announcement (v2)
23	5.016000	192.168.10.252	224.0.0.18	VRRP	64	Announcement (v2)
26	6.000000	192.168.20.252	224.0.0.18	VRRP	64	Announcement (v2)
27	6.032000	192.168.10.252	224.0.0.18	VRRP	64	Announcement (v2)
28	7.000000	192.168.20.252	224.0.0.18	VRRP	64	Announcement (v2)


```

Virtual Rtr ID: 1
Priority: 100 (Default priority for a backup VRRP router)
Addr Count: 1
Auth Type: No Authentication (0)
Adver Int: 1
Checksum: 0xaf55 [correct]
[Checksum Status: Good]
IP Address: 192.168.10.254
    
```

Fig. 4 Data flow process for VRRP

- Messages start sending announcements. As we can see, the advertisements come from 192.168.10.252 and 192.168.20.252, which are LSW1 and LSW2, respectively. This means that as soon as the current assistant has lost multiple announcements, another router starts advertising and receives the highest priority (Fig. 4).

4.4 OSPF

OSPF was implemented within Campus1. We capture packets on LSW1 (GE0/0/22). Then, we filtered out the packets in the state of “OSPF” and get the results as follows

- We can recognize “Hello Packet” messages among several source addresses.
- Detect other OSPF routers in the shared subnet.
- It checks the bidirectional clarity among the routers (Fig. 5).

4.5 IS-IS

IS-IS was implemented within Campus2. We capture packets on LSW4 (interface GE0/0/1). Then, we filtered out the packets in the state of “ISIS” and the results are as follows-

- These “Hello” packets discover their neighbors by reference.
- Because there are three types of channels indicating the type of router. The secondary router involves 10 channels.
- The originator of the Hello packet is 0000.0000.0003.

No.	Time	Source	Destination	Protocol	Length	Info
66	3.016000	192.168.10.253	224.0.0.5	OSPF	102	Hello Packet
78	3.563000	10.1.12.2	224.0.0.5	OSPF	94	Hello Packet
94	4.297000	192.168.20.253	224.0.0.5	OSPF	102	Hello Packet
120	5.422000	192.168.30.254	224.0.0.5	OSPF	98	Hello Packet
173	7.906000	192.168.10.252	224.0.0.5	OSPF	102	Hello Packet
186	8.484000	10.1.11.2	224.0.0.5	OSPF	94	Hello Packet
214	9.828000	192.168.20.252	224.0.0.5	OSPF	102	Hello Packet
290	13.359000	10.1.12.2	224.0.0.5	OSPF	94	Hello Packet
298	13.688000	192.168.10.253	224.0.0.5	OSPF	102	Hello Packet
312	14.266000	192.168.20.253	224.0.0.5	OSPF	102	Hello Packet
332	15.141000	192.168.30.254	224.0.0.5	OSPF	98	Hello Packet
377	17.250000	192.168.10.252	224.0.0.5	OSPF	102	Hello Packet
413	18.922000	10.1.11.2	224.0.0.5	OSPF	94	Hello Packet
451	20.656000	192.168.20.253	224.0.0.5	OSPF	102	Hello Packet

```

> Frame 66: 102 bytes on wire (816 bits), 102 bytes captured (816 bits) on interface -, id 0
> Ethernet II, Src: HuaweiTe_ba:34:15 (4c:1f:cc:ba:34:15), Dst: IPv4mcast_05 (01:00:5e:00:00:05)
> 802.1Q Virtual LAN, PRI: 6, DEI: 0, ID: 10
> Internet Protocol Version 4, Src: 192.168.10.253, Dst: 224.0.0.5
> Open Shortest Path First

```

Fig. 5 Data flow process for OSPF

No.	Time	Source	Destination	Protocol	Length	Info
1	0.000000	HuaweiTe_S3:7F:60	3255-411-Level-2-15_3255_M_	1534 I2 HELLO, System-ID: 0000.0000.0000		
2	0.422000	HuaweiTe_S3:7F:60	3255-411-Level-2-15_3255_M_	319 I2 CSMP, Source-ID: 0000.0000.0000, Start LSP-ID: 0000.0000.0000-00-00, End LSP-ID: FFFF.FFFF.FFFF.FF-FF		
4	1.378000	HuaweiTe_S3:7F:60	3255-411-Level-2-15_3255_M_	1534 I2 HELLO, System-ID: 0000.0000.0000		
5	3.344000	HuaweiTe_S3:7F:60	3255-411-Level-2-15_3255_M_	1534 I2 HELLO, System-ID: 0000.0000.0000		
7	8.403000	HuaweiTe_S3:7F:60	3255-411-Level-2-15_3255_M_	1534 I2 HELLO, System-ID: 0000.0000.0000		
12	8.344000	HuaweiTe_S3:7F:60	3255-411-Level-2-15_3255_M_	1534 I2 HELLO, System-ID: 0000.0000.0000		
14	10.344000	HuaweiTe_S3:7F:60	3255-411-Level-2-15_3255_M_	319 I2 CSMP, Source-ID: 0000.0000.0000, Start LSP-ID: 0000.0000.0000-00-00, End LSP-ID: FFFF.FFFF.FFFF.FF-FF		
19	11.673000	HuaweiTe_S3:7F:60	3255-411-Level-2-15_3255_M_	1534 I2 HELLO, System-ID: 0000.0000.0000		
18	11.308000	HuaweiTe_S3:7F:60	3255-411-Level-2-15_3255_M_	1534 I2 HELLO, System-ID: 0000.0000.0000		
20	15.204000	HuaweiTe_S3:7F:60	3255-411-Level-2-15_3255_M_	1534 I2 HELLO, System-ID: 0000.0000.0000		

```

> Frame 9: 1534 bytes on wire (12112 bits), 1534 bytes captured (12112 bits) on interface -, id 0
> IEEE 802.3 Ethernet
> Logical-Link Control
> ISO 10589 IS-IS InTRA Domain Routing Information Exchange Protocol
v IS-IS HELLO
....-10 = Circuit type: Level 2 only (0x2)
0000 00.. = Reserved: 0x00
SystemID (Sender of PDU): 0000.0000.0000

```

Fig. 6 Data flow process for IS-IS

- Figure 6 shows 30 ms, which is the time a neighbor must wait for a Hello packet before declaring the neighbor dead.

4.6 DHCP

We captured the DHCP packets on AC, and the results are as follows

- DHCP discover message (lease request traffic) indicates that the AP receives an IP address and default gateway via DHCP and receives AC’s IP address (Fig. 7).

4.7 CAPWAP

We started capturing CAPWAP on AC, and the results are as follows

No.	Time	Source	Destination	Protocol	Length	Info
45	43.8128000	0.0.0.0	255.255.255.255	DHCP	342	DHCP Discover - Transaction ID 0x2905cfc4
52	71.8590000	0.0.0.0	255.255.255.255	DHCP	342	DHCP Discover - Transaction ID 0x2905cfc4
55	77.8900000	0.0.0.0	255.255.255.255	DHCP	342	DHCP Discover - Transaction ID 0x2905cfc4
70	181.8900000	0.0.0.0	255.255.255.255	DHCP	342	DHCP Discover - Transaction ID 0x4099fc10
73	189.2030000	0.0.0.0	255.255.255.255	DHCP	342	DHCP Discover - Transaction ID 0x4099fc10
80	215.2400000	0.0.0.0	255.255.255.255	DHCP	342	DHCP Discover - Transaction ID 0x4099fc10
90	111.9500000	0.0.0.0	255.255.255.255	DHCP	342	DHCP Discover - Transaction ID 0x4099fc10
130	168.5620000	0.0.0.0	255.255.255.255	DHCP	342	DHCP Discover - Transaction ID 0x2d37d1e
133	172.8590000	0.0.0.0	255.255.255.255	DHCP	342	DHCP Discover - Transaction ID 0x2d37d1e
142	180.7500000	0.0.0.0	255.255.255.255	DHCP	342	DHCP Discover - Transaction ID 0x2d37d1e
157	197.2340000	0.0.0.0	255.255.255.255	DHCP	342	DHCP Discover - Transaction ID 0x2d37d1e
184	235.6870000	0.0.0.0	255.255.255.255	DHCP	342	DHCP Discover - Transaction ID 0x8ff4376c
189	240.6720000	0.0.0.0	255.255.255.255	DHCP	342	DHCP Discover - Transaction ID 0x8ff4376c

Fig. 7 Data flow process for DHCP

No.	Time	Source	Destination	Protocol	Length	Info
43	36.9028000	10.10.10.11	255.255.255.255	CAPWAP	393	CAPWAP-Control - Discovery Request
44	37.6720000	10.10.10.1	10.10.10.11	CAPWAP	236	CAPWAP-Control - Discovery Response
53	42.0000000	10.10.10.11	10.10.10.1	CAPWAP	674	CAPWAP-Control - Join Request
54	42.4070000	10.10.10.1	10.10.10.11	CAPWAP	593	CAPWAP-Control - Join Response
55	42.4090000	10.10.10.11	10.10.10.1	CAPWAP	93	CAPWAP-Control - Configuration Status Request
56	42.4090000	10.10.10.1	10.10.10.11	CAPWAP	74	CAPWAP-Control - Configuration Status Response
57	42.5150000	10.10.10.11	10.10.10.1	CAPWAP	65	CAPWAP-Control - Change State Request
60	42.5160000	10.10.10.1	10.10.10.11	CAPWAP	118	CAPWAP-Control - Change State Response
62	42.5790000	10.10.10.11	10.10.10.1	CAPWAP	72	CAPWAP-Control - Unknown Message Type (0x7db51)
63	43.4300000	10.10.10.1	10.10.10.11	CAPWAP	74	CAPWAP-Control - Unknown Message Type (0x7db71)
64	43.5000000	10.10.10.11	10.10.10.1	CAPWAP	118	CAPWAP-Control - Unknown Message Type (0x7db65)
65	43.6570000	10.10.10.1	10.10.10.11	CAPWAP	402	CAPWAP-Control - Unknown Message Type (0x7db64)
66	43.6570000	10.10.10.1	10.10.10.11	CAPWAP	74	CAPWAP-Control - Unknown Message Type (0x7db52)

Fig. 8 Data flow process for CAPWAP

- These messages show a discovery request sent by the AP to the AC and an AC discovery response. In its answer, it will inform AP the number of APs online.
- Messages 54–55 are a join request and a response to join.
- Messages 55–56 are modifications of status messages and responses (Fig. 8).

4.8 WLAN 802.11b

We captured the wireless packets on AP, and the results are as follows

- Messages 8–9 show the 802.11 beacon frames sent systematically by the AP (Fig. 9).

For security aspects, we had configured the network coverage area with a password. Therefore, we must enter the password we have configured earlier. Until the password is correctly configured, we can immediately connect laptop within the range of the network movement. In Fig. 1, we can see the relevant data network, such as channels, radiofrequency, and radio signal range to the right.

We have configured so many networking protocols in our single model. And it is also connecting one device to another device successfully, as we saw by capturing the protocols from with the help of Wireshark. Even if a link fails, then in that case our second device is ready to auto-connect. In this way, with the help of a simulator,

The screenshot shows a Wireshark packet capture with the following details:

No.	Time	Source	Destination	Protocol	Length	Info
1	0.000000	HuaweiTe_Sci7f:70	Broadcast	802.11	131	Beacon frame, Sh=0, Fm=0, Flags=....., B1=100, SSID=HUAWEI_MU
2	0.000000	HuaweiTe_Sci7f:80	Broadcast	802.11	131	Beacon frame, Sh=0, Fm=1, Flags=....., B1=100, SSID=HUAWEI_MU[Malformed Packet]
3	2.515000	0.0.0.0	255.255.255.255	DHCP	446	DHCP Discover - Transaction ID 0x4c9f
4	4.515000	0.0.0.0	255.255.255.255	DHCP	446	DHCP Discover - Transaction ID 0x4c9f
5	7.515000	HuaweiTe_Sci7f:70	Broadcast	802.11	131	Beacon frame, Sh=0, Fm=0, Flags=....., B1=100, SSID=HUAWEI_MU
6	7.515000	HuaweiTe_Sci7f:80	Broadcast	802.11	131	Beacon frame, Sh=0, Fm=1, Flags=....., B1=100, SSID=HUAWEI_MU
7	8.515000	0.0.0.0	255.255.255.255	DHCP	446	DHCP Discover - Transaction ID 0x4c9f
8	14.000000	HuaweiTe_Sci7f:70	Broadcast	802.11	131	Beacon frame, Sh=0, Fm=0, Flags=....., B1=100, SSID=HUAWEI_MU[Malformed Packet]
9	14.000000	HuaweiTe_Sci7f:80	Broadcast	802.11	131	Beacon frame, Sh=0, Fm=1, Flags=....., B1=100, SSID=HUAWEI_MU[Malformed Packet]
10	17.515000	0.0.0.0	255.255.255.255	DHCP	446	DHCP Discover - Transaction ID 0x4c9f
11	19.515000	0.0.0.0	255.255.255.255	DHCP	446	DHCP Discover - Transaction ID 0x4c9f
12	21.015000	HuaweiTe_Sci7f:70	Broadcast	802.11	131	Beacon frame, Sh=0, Fm=0, Flags=....., B1=100, SSID=HUAWEI_MU[Malformed Packet]
13	21.015000	HuaweiTe_Sci7f:80	Broadcast	802.11	131	Beacon frame, Sh=0, Fm=1, Flags=....., B1=100, SSID=HUAWEI_MU[Malformed Packet]

Summary statistics at the bottom of the capture:

- Frame 10: 446 bytes on wire (3568 bits), 446 bytes captured (3568 bits) on interface -, id 0
- IEEE 802.11 Data, Flags:T
- Logical-Link Control
- Internet Protocol Version 4, Src: 0.0.0.0, Dst: 255.255.255.255
- User Datagram Protocol, Src Port: 68, Dst Port: 67
- Dynamic Host Configuration Protocol (Discover)

Fig. 9 Data flow process for WLAN802.11b

we have set up a secured network that is on a large scale. Finally, our network is ready to connect to the real network adapter.

5 Conclusion

This paper considers WLAN architecture as well as network security. As we know that campus networking is an important lifestyle for campuses, network security is important for campuses. Therefore, we monitor the hierarchical design of our network. The network is scalable, performance and security are improved, and network maintenance is easier. This work proposed a compact, economical and secure campus network design based on the working environment and the required adaptability, security and other aspects. This prevents devices from being left alone because all devices are properly connected via network protocols. By analyzing the packets of the networking protocols with Wireshark, we can conclude that the goal has been achieved and is now fully functional.

References

1. Hamid RA (2003) Wireless LAN: security issues and solutions. GIAC Security Essentials Certification (GSEC) Practical Assignment Version. 2003;1
2. Cao X, Meng W, Chen R (2017) WLAN experimental design and implementation based on Ensp. Res Explor Lab 36(7)
3. Gierłowski K, Kostuch A, Woźniak J, Nowicki K (2011) Testbed analysis of video and VoIP transmission performance in IEEE 802.11 b/g/n networks. Telecommun Syst 48(3–4):247–260
4. Garcia-Jimenez S, Magana E, Izal M, Morato D (2009) IP addresses distribution in Internet and its application on reduction methods for IP alias resolution. In: 2009 IEEE 34th conference on local computer networks, 20 Oct 2009. IEEE, pp 1079–1086
5. Bin Y (2017) Simulation experiment of spanning tree protocol principle based on ENSP. Software 38(2):125–129
6. Wang D (2018) Huawei Switchboard learning guide. Beijing: People’s Posts and Telecommunications Publishing House, 2016.07

7. Irawati ID, Hadiyoso S, Hariyani YS (2017) Link aggregation control protocol on software defined network. *Int J Electr Comput Eng* 7(5):2706
8. de Sousa A, Soares G (2007) Improving load balance and minimizing service disruption on ethernet networks with IEEE 802.1 S MSTP. In: *Workshop on IP QoS and traffic control 2007*, pp. 25–35
9. Srikanth A, Onart AA (2002) VRRP: increasing reliability and failover with the Virtual Router Redundancy Protocol. Addison-Wesley Longman Publishing Co., Inc.
10. Cirkovic S, Shah CA, Rajagopalan B, Karuppiyah A (2011) Methods and apparatus for improving network communication using BFD and VRRP tracking system. United States patent US 7,990,852. 2011 Aug 2
11. Subramanian R (2014) Prioritization based on IP pool and subnet by DHCP. United States patent application US 13/535,693. 2014 Jan 2
12. Sidhu D, Fu T, Abdallah S, Nair R, Coltun R (1993) Open shortest path first (OSPF) routing protocol simulation. *ACM SIGCOMM Comput Commun Rev* 23(4):53–62
13. Lakhmir MN, Qureshi AA, Channa MI (2015) Performance evaluation of link state routing protocol in an enterprise network. *Bahria University Journal of Information & Communication Technologies (BUJICT)*. 2015 Apr 6;8(1)
14. Shaffi AS, Al-Obaidy M (2012) Effective implementation Of VLAN and Acl in local area network. Faculty of Computing Studies, Gulf College Muscat, Sultanate of Oman
15. Chen J, Zheng X, Zhang L, Peng L, Liu X (2019) WLAN simulation experiment based on ENSP. *J Phys Conf Ser* 1325(1):012046

Performance of X-Band CMOS LNA with Broadband Approach for 5G Wireless Networks



Srihith Kumar Pottem, Raghavendra D. Kabade, T. N. Nikith, Saptarshi Mondal, and Sandeep Kumar

Abstract This paper presents a CMOS low noise amplifier (LNA) for X-band range of communication for 5G wireless networks. The proposed LNA consists of three stages of casade–cascode CS topology. A Chebyshev filter T-network stage is employed for broadband input impedance matching while cascode–cascode stage is followed for a higher gain. The current mirror topology is used to provide bias current and active load to the LNA. The LNA is designed and simulated using 180 nm UMC Taiwan process in cadence platform. The proposed schematic simulation achieved a gain higher than 15 dB for the range of 8 GHz to 12 GHz (X-Band) and a minimum noise figure (NF) of 4.2 dB at 12 GHz. The proposed differential LNA operates under 2 V power supply and layout using metal–insulator–metal layers. The design and layout are verified using DRC and LVS rules.

Keywords Complementary metal oxide semiconductor (CMOS) · LNA · X-band · Chebyshev filter · Cascode–cascode · 5G

S. K. Pottem · R. D. Kabade · T. N. Nikith · S. Mondal · S. Kumar (✉)
Department of Electronics and Communication, National Institute of Technology, Surathkal,
Karnataka, India
e-mail: sandeep@nitk.edu.in

S. K. Pottem
e-mail: srihith99@gmail.com

R. D. Kabade
e-mail: raghavendrakabade98@gmail.com

T. N. Nikith
e-mail: 16ec158.nikith@nitk.edu.in

S. Mondal
e-mail: 16ec124.saptarshi@nitk.edu.in

Table 1 5G features for different spectrum

Frequency band	C	X	Ku	Ka
Weatherproof	Yes	Yes	No	No
High-throughput	No	Yes	Yes	Yes
On-chip antennas, low cost (extreme high MHz-Mbps efficiency)	No	Yes	No	No
High link availability	Yes	Yes	No	No
Low probability of interference/fewer users	No	Yes	No	No
Military and government purpose	No	Yes	No	No

1 Introduction

There is a rapidly rising demand for the improvement of the wireless communication systems with the arrival of 5G. Many challenges such as low data rate, limited cover areas, and high-power consumptions are encountered by the mm-wave wireless systems. Table 1 is shown 5G features of different spectrums. LNA has considerable effect on performance of the system as a whole in specific the receiver's sensitivity and signal noise ratio [1, 2].

An LNA is an active block after the antenna and the filter of RF receiver system. LNA has a primary objective is to achieve high-power gain and low noise for an over a desired frequency range simultaneously. There are many fundamental LNA topologies for narrowband design such as common source resistive termination, common gate, common source shunt series feedback, common source inductive degeneration, source degeneration of cascode inductors [3–6]. A cascode configuration involving feedback for matching of noise and input impedance simultaneously to the inductive degenerated common source amplifier bases the design [7]. This paper describes the operation of the LNA for X-band range of frequencies and simulation of gain and noise figure using UMC 180 nm CMOS process. The organization of work is as follows: Sect. 2 describes importance of LNA and X-band for 5G communication while Sect. 3 explain design and consideration of X-band LNA. Section 4 includes results and discussion, and finally, Sect. 5 is followed by conclusion.

2 Importance of X-band LNA for 5G

A high gain and low noise of amplifier is necessary to amplify this signal before it is sent to other parts of the communication system. Since it amplifies the input signal and yields a better noise performance, it is named as low noise amplifier (LNA). A LNA is essential component in any RF integrated circuit. The first step in the receiver setup configuration is the low-noise amplifier stage. Since LNA operates at radio frequencies, the circuit has to be very much simpler in order to achieve low noise. For additional precautions, if the circuit is complex, the amplified received

signal may be worthless by the parasitic effects caused by the circuit. Hence, there are various LNA topologies to overcome the parasitic. There would always be a trade-off between system integration, cost and performance in all these designs. Gain measure in cascade amplifiers is large but the stability is smaller, and also, it occupies a lot of space. Low noise and high gain are achieved using inductive source degeneration design fashion but there are stability issues due to the undesirable feedback in the ground [8, 9]. The X-band is the EM spectrum identity for the frequency band within the microwave radio region. In radar engineering the frequency range of 8–12 GHz is defined as X-band by the Institute of Electrical and Electronic Engineers (IEEE). The benefits of X-band over other frequency ranges are summarized in Table 1.

3 LNA Design and Performance Evaluation

3.1 Narrowband LNA

For LNA topologies, gain can be obtained by using a single transistor which contains three terminals. One terminal serves as an input while the remaining terminals are reserved for output and AC RF. A common source stage as a cascode connection to achieve high gain, whereas CC stage has high impedance at the input and low impedance in output and hence well suitable as buffers. The topology loads can be made by using resistor for broadband applications or by using tuned resonators for applications with narrow band [10]. The input-matching network decision protocol is similar to the load option procedure. For narrowband applications, tuned resonators can be used, whereas for broadband applications, a resistor can be used as the loads for different networks. Due to the resistances in the circuit input, an LNA with resistive input matching has high noise figures and hence not advisable. Since resistors can be implemented using inductors, these can be placed at the input side at the cost of size as inductors are bulky compared to other components. The topology of choice in this work is “emitter-degenerated cascode” or can be defined as LNA degenerated by common source inductive and whose schematic is shown in Fig. 1.

Figure 2 shows schematic of common source degeneration LNA in cascode connection along with current mirror topology. A high gain could provide by the cascode amplifier in addition to the low noise and stability. The transistor M_1 supplies the amplifier gain and must be cautiously selected from the hardware catalog. We are only allowed to change the length of the emitter, thus changing the M_1 's effective emitter region. The length of the emitter specifically changes the capacitance of the C and the transistor input impedance. The latter one carries greater significance because C can be compensated by tuning the L_s value when the transistor's emitter length increases, the transistor M_1 impedance at the input reduces, becoming harder to match to the source impedance. Table 2 shows components value used for narrowband LNA.

Figure 3 depicts S-parameter and noise figure plot of narrowband LNA. The S-

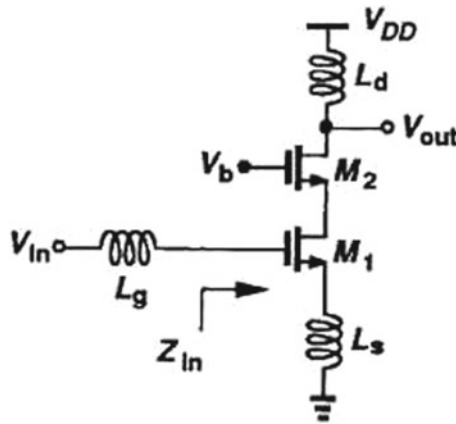


Fig. 1 Inductive degenerated LNA

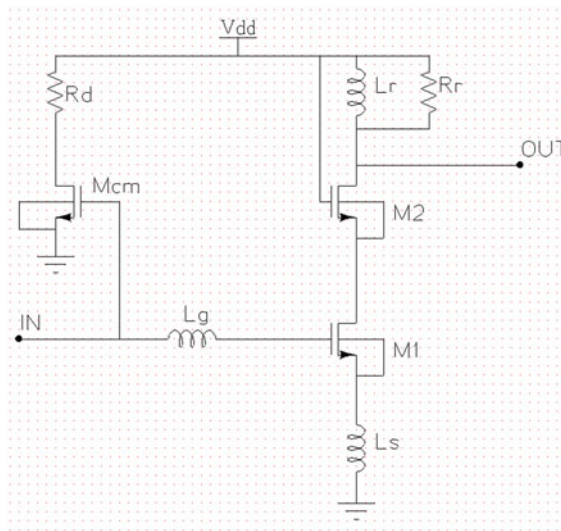


Fig. 2 Proposed schematic of narrowband LNA

parameters such as return loss and forward gain are simulated and achieve 10 GHz operating frequency with maximum gain of 12 dB. While the noise figure of 3.16 dB is achieved over 9.5 GHz to 10.5 GHz, Table 3 summarizes simulated values of S-parameter and noise figure.

Table 2 Components values of narrowband LNA

Components	Value
L_g	10 nH
L_s	0.9 nH
M_1	11.9 μm
M_2	30 μm
L_r	0.495 nH
R_r	5.5 $\text{k}\Omega$
R_d	350 Ω
M_{cm}	5 μm

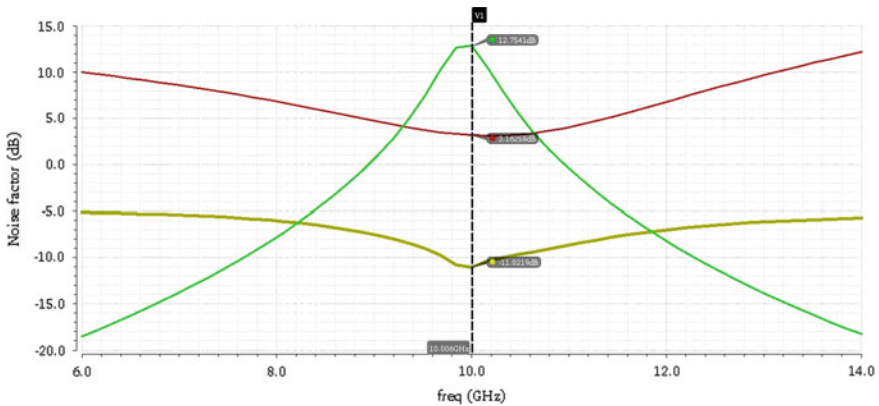


Fig. 3 S-Parameter and NF Plot of narrowband LNA

Table 3 Values of S11, S21, and noise figure

Parameters	Value (10 GHz)
Gain (S21)	12.7541 dB
Return loss (S11)	-11.021 dB
Noise figure	3.162 dB

3.2 Wide Band LNA

The performance parameters such as low-power and high-data rates over a wide band (WB) frequency range can be achieved using multi-stage system. A CMOS technology is a good option for WB systems due to scaling high-frequency CMOS devices and also helps the processing of large and low power analog bandwidth signals. The numbers of topologies have been reported for the wideband of operation. A resistive terminated common source amplifier, common gate amplifier, resistive shunt

feedback amplifier, inductively degenerated amplifier, cascode degenerated amplifier with corresponding LC ladder network are regularly used topologies. Different LNAs therefore have different circuit areas and thus trade-off between efficiency and minimal design. Below are the LNA schemes which yielded the best results. A third section consists of the series RLC network generated by the transconductance stage of the filter, whose R is $\omega_T L_s$ series resistance in the source of transistor. The input impedance of the inductive degenerating MOS transistor is calculated as:

$$Z_{in}(s) = 1/(s(C_{gs} + C_p)) + s(L_s + L_g) + \omega_T L_s \tag{1}$$

where $\omega_T = g_m / C_{gs} + C_p$ and C_p parasitic capacitance. Figure 4 is shown Chebyshev filter network. The input matching is made by adding this network into the Chebyshev structure. There is parallel resonance between L_s and C_{gs} . The amplifier's voltage gain can be found by $R_s/W(s)$, where $W(s)$ is a transfer function of the Chebyshev filter. Chebyshev filter transfer function is unity in-band, and out-of-band tends to zero. So, the impedance that looks into the amplifier is R_s in-band, and very high in out-of-band, the overall gain is

$$\frac{V_{out}}{V_{in}} = -g_m W(s) \cdot R_L (1 + sL_L/R_L) / sC_t R_s \cdot (1 + sR_L C_{out} + s^2 L_L C_{out}) \tag{2}$$

The real part of Z_{in} is considered to be 50Ω . The network impedance at the input is equal to $R_s/W(s)$, where $W(s)$ is the transfer function of the Chebyshev filter network. The current flowing into M_1 is $V_{in} W(s) / R_s$ [1]. A MOSFET acts as a current amplifier at high frequencies with the current gain. Hence, the output current is $V_{in} W(s) / sC_t R_s$ (Assuming ideal cascode operation). The overall gain is given above. Choosing the input network structure is the primary step in designing any LNA. An input reflection coefficient lesser than 10 dB in-band gives a ripple of 0.46 dB [1]. The values of several components of the original filter are calculated by demoralization, by setting the bandwidth to be between 8 to 12 GHz and center frequency approximately as 10 GHz. Since there is a compromise between component values and size of the filter, a three-section structure is chosen. Figure 5 shows reported schematic of the cascode wideband topology. While the proposed schematic of wideband LNA is

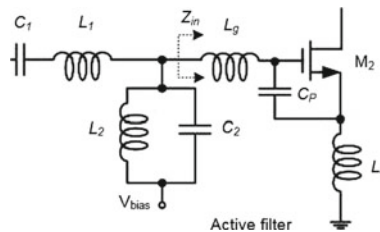


Fig. 4 Chebyshev active filter [2]

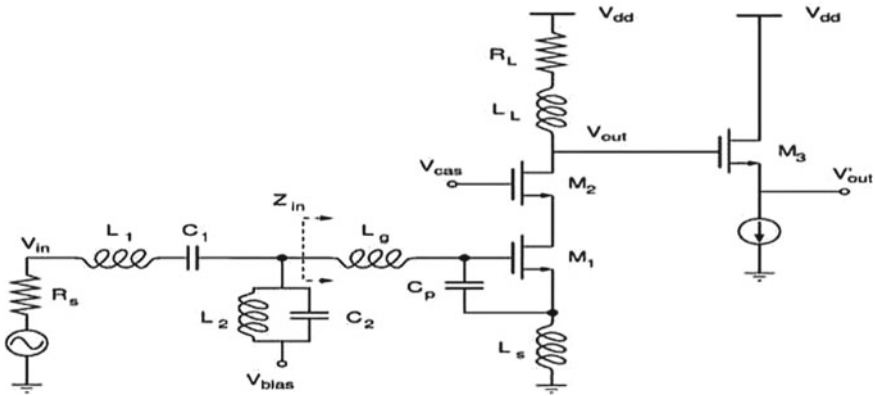


Fig. 5 Simplified schematic of wideband LNA [1]

shown in Fig. 6, the width of the cascode device should be very low to yield better noise performance as it has parasitic effects. Hence, the selected value is $60 \mu\text{m}$ for the width of the cascode MOSFET M_1 and M_2 are chosen to be of minimum length. Constant gain is configured for the load over the entire bandwidth. A current mirror is used here for biasing LNA. MOSFET M_1 is biased through one AC ground point of the filter. Noise figure mainly depends on the ω_T , transistor width (W), and frequency of the drain current. Topology for inductive degeneration provides the lowest amount

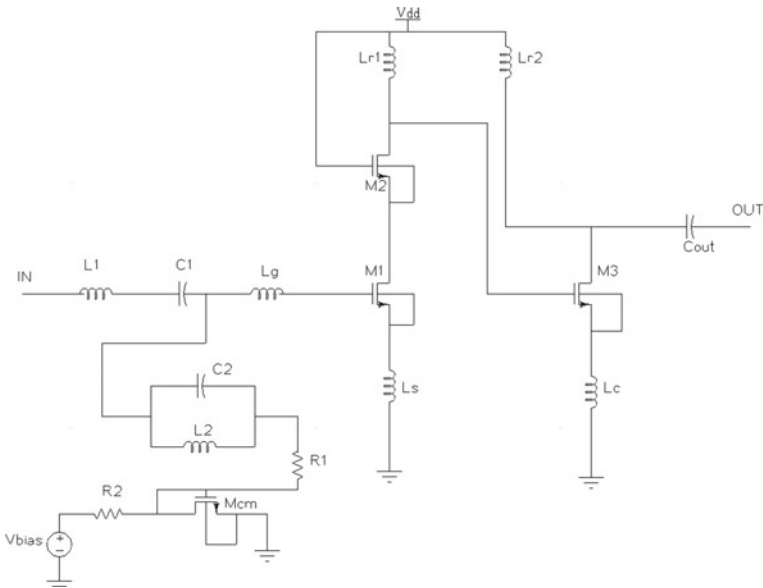


Fig. 6 Proposed schematic of wideband LNA

Table 4 Components value of wideband LNA

Components	Value	Components	Value
L_1	0.991 nH	L_{r2}	0.733 nH
C_1	421.04 fF	L_c	100 pH
L_2	0.776 nH	M_1	400/0.018 μm
C_2	537 fF	M_2	72/0.018 μm
R_1	5 K	M_{cm}	85/0.018 μm
R_2	1 K	M_3	137/0.018 μm
L_g	0.627 nH	C_{out}	912 fF
L_s	1.304 nH	V_{bias}	1.8 V
L_{r1}	0.75 nH	V_{dd}	2 V

of noise as inductors are used in place of resistors. L_s inductor is degenerated to the source of the MOSFET M1 and it offers a negative feedback to the MOSFET and hence the name inductive degeneration. All the necessary stability requirements to the circuit will be taken care of by the negative feedback connection.

The noise performance can be better, provided the width of the MOSFET M1 should be anywhere between 250 and 450 μm [1]. In this design, we have chosen MOSFET width to be $W = 400 \mu\text{m}$. Note that the quantitative findings apply only to M_1 's contribution to noise. The NF is therefore predicted to be weaker in actual LNA implementation due to the contribution of the noise by the cascode device, contribution of noise by the load resistance as well as the output buffer and mostly because of the losses in the input network [1]. Use of inductive local series feedback has many advantages as it enables the synthesis of a specified real part for the impedance at the input side which is equal to that in a broadband fashion, where the transistor's cutoff frequency is ω_T . The carrier frequency is resonated at, by the reactive portion of the input impedance in a narrowband configuration. Better noise figure can be obtained by this at that frequency [6]. Chebyshev filter network is used in the proposed wideband design, shown below, to propagate the reactive portion of the impedance at the input from 8 to 12 GHz over the entire band (Table 4).

Figure 7 shows S-parameters analysis with respect to frequency. The return loss of LNA achieves wide impedance bandwidth ranging from 8 to 12 GHz with maximum peak gain of 24 dB. The plot of third intercept point (IIP3) with respect to input power is shown in Fig. 8. The IIP3 shows -11dBm of output power while input power is -5 dBm .

Figure 9 shows 1-dB compression point at -12.08 dBm . The layout of the proposed LNA is plotted in Fig. 10. Table 5 summarizes the analysis of wideband LNA while comparison performance of LNA with other reported papers is shown in Table 6.

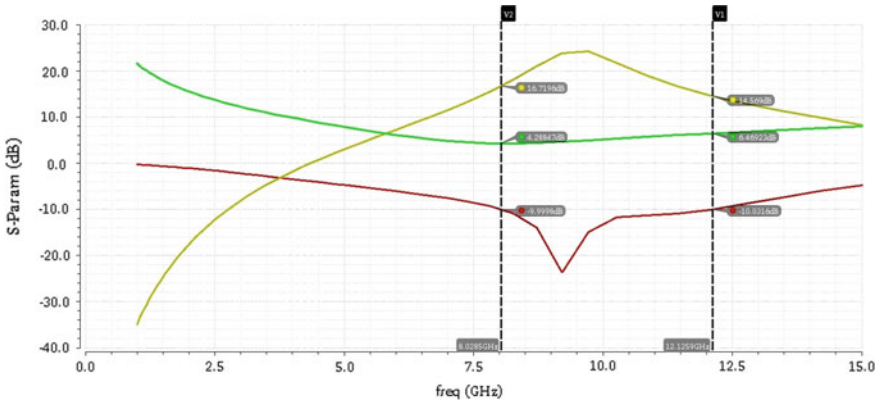


Fig. 7 S-Parameter and NF Plot of Wideband LNA

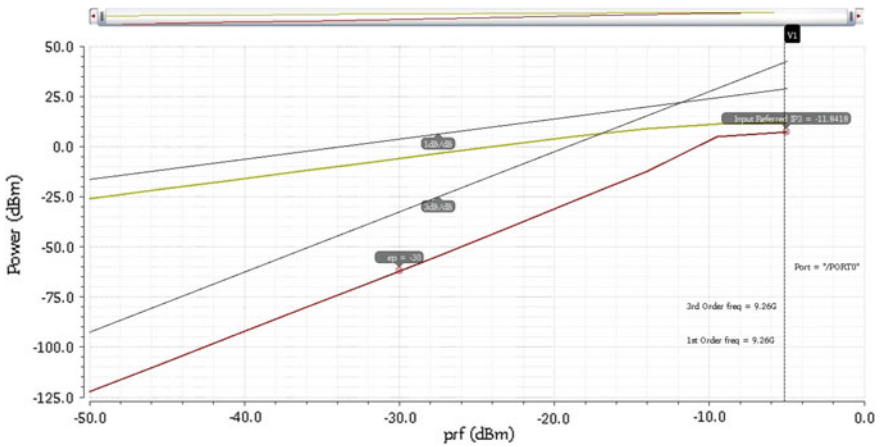


Fig. 8 Plot of IIP3 versus input power

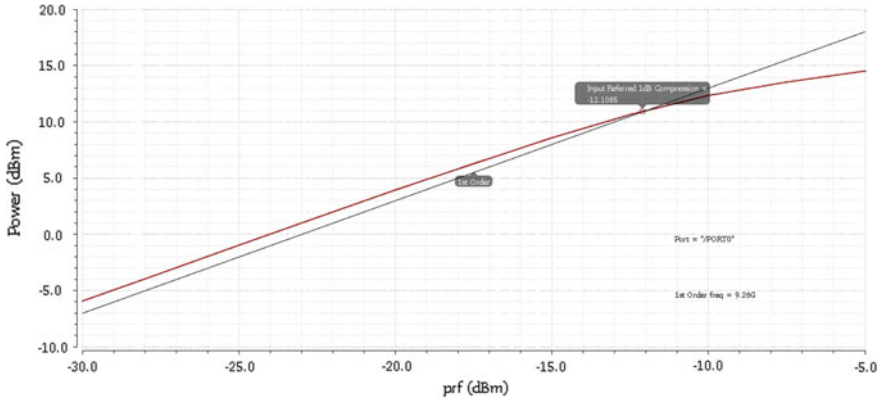


Fig. 9 Plot of 1 dB compression point

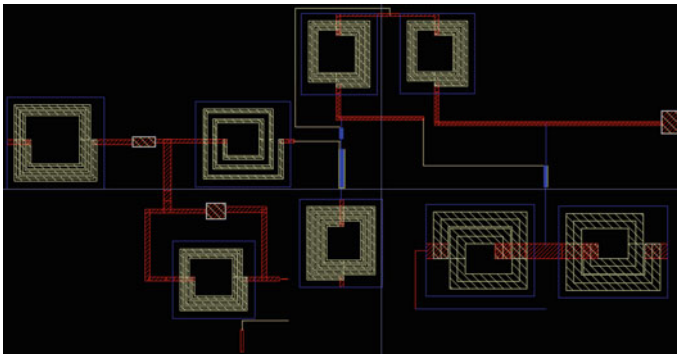


Fig. 10 Layout picture of LNA

Table 5 Summarize the analysis of LNA

Parameters	Value	Max/Min Value
Gain (S21)	16.7196 dB to 14.569 dB	24.16 dB at 9.22 GHz
Return Loss (S11)	-9.99 dB to -10.031 dB	-23.9 dB at 9.26 GHz
Noise Figure (NF)	4.288 dB to 6.469 dB	4.288 dB at 8 GHz
IIP3 (Third-Order Intercept Point)	-	-11.8418 dBm
1 dB Compression Point	-	-12.1085 dBm

Table 6 LNA performance comparison with reported ones

	[1]	[11]	[12]	This work
Frequency (GHz)	2.4–9.5	2–10	3–10	8–12
S11 (dB)	<–9.9	<–10	<–8.28	<–10
S21 (dB)	9.3–6.3	21–17	14.5–15.3	14.57–24.16
NF _{min} (dB)	4–9	2.5–4.5	3.57–4.27	4.28–6.46
Supply (V)	1.8	3	1.8	2
Technology (nm)	180 CMOS	180 SiGe	180 CMOS	180 CMOS
IIP3 (dBm)	–6.7	–5.5	3.43	–11.84
Topology	Chebyshev filter-based(CS)	LC ladder filter-based(CE)	Butterworth filter-based(CG)	Chebyshev filter network-based CS LNA

Reference

1. Bevilacqua A, Niknejad AM (2004) An ultra-wide band CMOS low-noise amplifier for 3.1–10.6GHz wireless receivers. *IEEE J Solid-State Circuits* 39(12):2259–2268
2. Shekhar S, Walling J, Allstot D (2006) Bandwidth extension techniques for CMOS amplifiers. *IEEE J Solid-State Circuits* 41:2424–2439
3. Razavi B (2006) A 60 GHz CMOS receiver front-end. *IEEE J Solid-State Circuits* 41(1):17–22
4. Baki RA, Tsang TKK, El-Gamal MN (2006) Distortion in RFCMOS short-channel low-noise amplifiers. *IEEE Trans Microwave Theory Tech* 54(1):46–56
5. Xiao J et al (2016) A 180 mW multi-standard TV tuner in 28 nm CMOS. In: *Proceedings of the IEEE symposium VLSI circuits*, pp 1–2
6. Lee TH (1998) *The design of CMOS radio-frequency integrated circuits*, 1st edn. Cambridge University Press, New York
7. Janisha F (2016) *Int J Eng Res Appl* 6(11)(Part 1):43–47. ISSN: 2248-9622
8. Ehrampoosh S, Hakimi A (2010) High gain CMOS low noise amplifier with 2.6 GHz Bandwidth. In: *International conference on communication Engineering*
9. Ellinger F (2007) *Radio frequency integrated circuits and technologies*. Springer, New York
10. Kaynak M, Tekin I, Bozkurt A, Gurbuz Y (2006) Low noise amplifier design using 0.35 μm SiGeBiCMOS technology for WLAN/WiMAX applications. In: *2006 IEEE Long Island systems, applications and technology conference*
11. Ismail A, Abidi AA (2004) A 3–10 GHz low-noise amplifier with wideband LC-ladder matching network. *IEEE J Solid State Circuits* 39(12):2269–2277
12. Fan X, Sanchez-Sinencio E, Silva-Martinez J (2005) A 3 GHz–10 GHz common gate ultra-wide band low noise amplifier. In: *48th Midwest symposium on circuits and systems*, Covington, KY, vol 1, pp 631–634
13. XTAR Telecommunications, Ashburn, VA

Design and Analysis of Pattern Reconfigurable MIMO Antenna Using PIFA Structure



Ranjana Kumari, Archit Kumar Jha, Anuj Sachan, Aryan Kishan, and Milky Jain

Abstract In this paper, two-element planar inverted F antenna (PIFA) structure-based pattern reconfigurable MIMO antenna is presented for WiMAX application. The antenna array is designed on (50×70) mm² ground plane and PIFA layer's height is 7 mm from the ground plane. Each element consists of PIFA layer and monopole layer. Pattern re-configurability is generated by using PIN diodes. The proposed PIFA-based MIMO antenna is operating from 2.9 to 3.5 GHz. Isolation is achieved better than 13 dB over various range of frequencies each antenna covers. The maximum simulated gain is 6.41dBi with the maximum total efficiency of 86%. Envelope correlation coefficient (ECC) value between two ports is less than 0.05, and diversity gain (DG) is 9.9 dB. High diversity gain with low ECC makes proposed antenna more efficient for wireless handheld devices.

Keywords Pattern reconfigurable · MIMO antenna · WiMAX application · PIFA

R. Kumari · A. K. Jha (✉) · A. Sachan · A. Kishan · M. Jain
Department of Electronics and Communication Engineering, Galgotias College of Engineering and Technology, Greater Noida, Uttar Pradesh, India
e-mail: archit.ashesh26@gmail.com

R. Kumari
e-mail: ranjana.kumari@galgotiacollege.edu

A. Sachan
e-mail: anujrabs@gmail.com

A. Kishan
e-mail: aryankishan28@gmail.com

M. Jain
e-mail: milkyjain95@gmail.com

1 Introduction

Multiple input multiple output plays a very important role in 4G application such as WLAN/WiMAX. MIMO is used to increase data rate, channel capacity with improved reliability of systems [1]. Over the past few years, WiMAX technology is accepted worldwide and its becoming compatible to our wireless communication. WiMAX is a very popular technology, which is used to deliver high-quality services to residential and commercial areas. Many existing MIMO systems involve fixed antennas which have fixed radiation patterns and beam angles but they are not able to adapt to changing channel spectrum. Therefore, by using pattern reconfigurable antennas satisfy our goal. Several pattern reconfigurable antennas are proposed in the literature view. In [2] pattern, reconfigurable antenna was proposed covering frequency band 5.15–5.35 GHz. In this paper, a compact design was constructed having single element ground plane size of $50 \times 50 \text{ mm}^2$ for mobile applications [3]. PIFA layer was designed at the bottom layer of structure, and monopole layer is designed at the top of the antenna in free space. To make the antenna more compact, PIFA structure is used with the two decoupling techniques.

In [2–13], reconfiguration was achieved using PIN diodes as switches, also with additional changes in integration of switches(in few). In [2, 4, 5, 7, 14, 15], these antenna were designed for WLAN/WiMax applications. In [4, 5], antenna was used for WLAN, LTE, GSM (1800, 1900) and UTMS frequency bands, here pattern reconfiguration was achieved using PIN diodes as switches in the structures. The frequencies of the working antenna's were in (1.7–2.7 GHz) bandwidth. In [6], antenna used for wireless systems in shape of a hexagonal ring of size $44 \times 42 \text{ mm}^2$ with frequency range of 1.9–2.4 GHz. 8 pin diodes were located on the hexagonal ring as switches.

In [7], slot antenna of frequency 2.4 GHz consisting of slot length half wavelength. Diodes are used to short circuit the metal patches and controlled circuits are used. In [8], two rectangular patch antennas with frequency 2.43 GHz, and size ($58 \times 100 \text{ mm}$) placed perpendicular to each other fed with a common feed line. In [9], the size of antenna was ($22 \times 22 \times 95 \text{ mm}^3$), and frequency 2.4 and 5.8 GHz. In [10], antenna of frequency 2.7–6 GHz, radiation direction is adjusted on H plane to achieve switching between $-\theta$ to $+\theta$ and pattern is changed by 4 groups of rf switches on each element. In [11], antenna of size $30 \times 40 \text{ mm}^2$ with frequency 3.4–3.8 GHz having fork-shaped identical slots feed line and beam scattering in bands. In [12], antenna is designed for working on 5.15–5.35 GHz frequency range with dipole-loop shaped structure.

Antenna is designed for 5G wireless technology at operating frequency 5.6 GHz and size $29.15 \times 29.15 \text{ mm}^2$, a technique derived upon Fabry–Perot cavity holding two surface, in accordance with antenna structure a switching pattern was derived by combining frequency selective surfaces [13]. Partially reflective surface and active selective surfaces are used in addition for pattern reconfiguration. In [16], the folded inverted L antenna is used so that size can be reduced. Antenna of size ($68 \times 130 \times 10 \text{ mm}^3$) and a return loss of -6 dB can easily be integrated in mobile devices that cover 700–960 MHz frequencies. In [17], spectral efficiency of the

MIMO system was improved using considerable numbers of multimode antennas. A horizontal azimuth pattern reconfigurable antenna is also designed. In [14] with configurable arrays, microstrip array, four parasitic elements, and conducting plate are used to achieve this goal.

In [15], frequency and pattern reconfigurable antenna is presented operating at frequency of 4.5 and 4.8 GHz. In [18], a six-order band reject filter is designed for S band. This is providing improved reflection loss and insertion loss and designed for radio space science [19] Multiband microstrip patch antenna (U slot planar patch) working on diverse frequencies (2.8, 3.1, 3.6, 4.7, and 5.4 GHz) used for WiMax/WLAN applications, frequency reconfiguration achieved by modification in each (patch and U slot).

In this paper, a pattern reconfigurable antenna is proposed whose design is based on PIFA structure. Selection of this structure is done by keeping factor in mind such as size was reduced by 50% that is adaptable for wide range of applications and hence provide stability. This proposed structure has a total height of 7 mm from ground. PIN diodes are used to achieve pattern reconfiguration by switching them in desired manner. Hence by controlling them, the antenna achieves unchanged resonant frequency of 3.1 GHz and the radiation pattern changed in four modes. Antenna is designed on FR4 substrate above the ground plane of $50 \times 70 \text{ mm}^2$.

2 Antenna Structure

The geometry and structure of single unit of proposed antenna are presented in Fig. 1. The antenna has two layers consisting PIFA structure as shown in Fig. 1b, and monopole structure is shown in Fig. 1c. The monopole structure consists a square patch of dimension ($L3 \times L3$) inscribed in a square perimeter/frame of dimension ($W2 \times W2$). The square patch is connected to the ground plane with a shorting pin, and the patch is also connected to the square frame/perimeter with P-I-N diodes (used as Switch 1). Top and lateral view of two element MIMO antenna with PIN diodes is shown in Figs. 1 and 2. PIN diode is connected as lumped element in CST 2018.

In Fig. 2, PIFA structure has a slot etched out beside the shorting wall, the patch and the shorting wall are connected with 2 P-I-N diodes (Switch 2) implemented between them. PIFA structure has a rectangular hole etched in the center of the patch of dimension ($W3 \times W4$). A via is implemented through this etched rectangular hole to avoid any direct physical connection between the top layer (monopole structure) and the PIFA structure. First, the PIFA structure is implemented with dimensions of the structure ($W1 \times L1$). In PIFA structure, the height of the shorting wall is same to that of PIFA layer from the ground plane. The diodes in the etched slots are connected opposite to each other whose combination is termed as (Switch 2).

Two element array antennas are designed on FR 4 substrate having thickness of 0.5 mm and permittivity 3.48. This is applied between the layers and ground plane for structural stability. The ground plane of dimension (50×70) mm^2 and the other structural layers is designed from copper metal of thickness 0.03 mm, and then

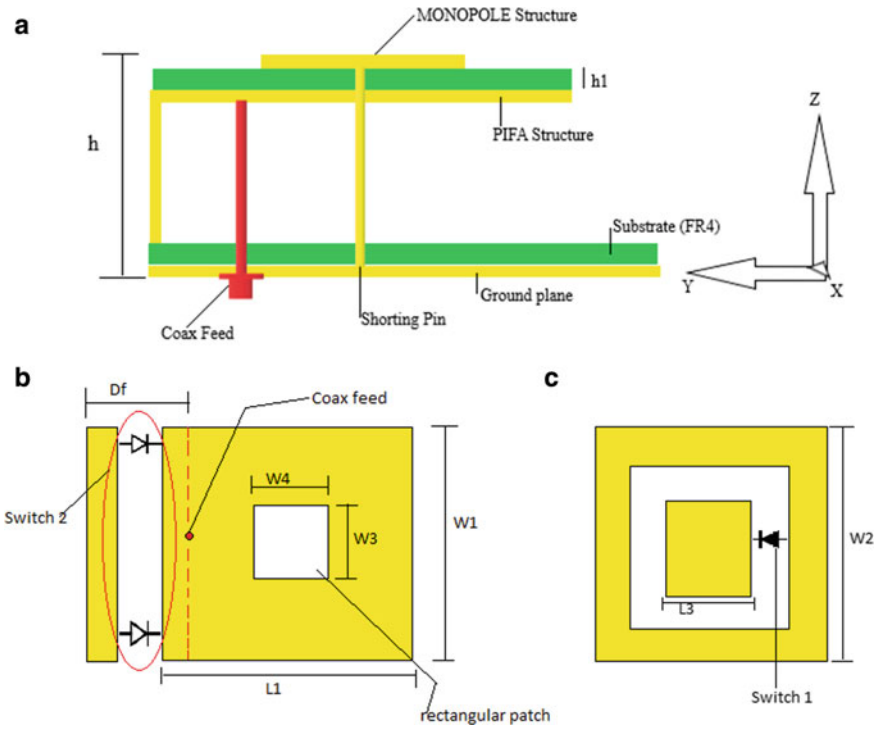


Fig. 1 a Lateral view of *single unit of proposed Antenna* with dimensions: $h = 7$ mm, $h1 = 0.5$ mm. b PIFA structure dimensions: $L1 = 16.3$ mm, $W1 = 19.3$ mm, $W3 = 4.2$ mm, $W4 = 3$ mm, $Df = 5.8$ mm. c Monopole structure dimensions: $W2 = 5$ mm, $L3 = 1.6$ mm

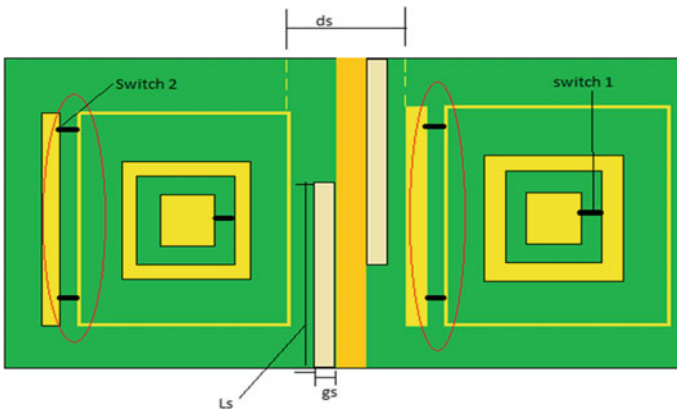


Fig. 2 Top view of proposed antenna structure. Decoupling slits: $l_s = 28$ mm, $g_s = 1$ mm, distance between the antennas: $d_s = 10$ mm

Table 1 Switching modes for proposed antenna

Modes	Antenna 1		Antenna 2	
	S 1	S 2	S1	S2
PIFA-PIFA	OFF	ON	OFF	ON
PIFA-Monopole	OFF	ON	ON	OFF
Monopole-PIFA	ON	OFF	OFF	ON
Monopole-Monopole	ON	OFF	ON	OFF

monopole structure is implemented over the PIFA structure with FR 4 in between them. ON–OFF resistance for P-I-N diodes are 0.45 kΩ for monopole structure and 10 kΩ for PIFA structure. PIFA structure, antenna is fed, the current is induced in PIFA structure the feed is then in turn coupled to the square patch in monopole structure using capacitive coupling this occurs when Switch 1 is ON and Switch 2 is OFF. When Switch 2 is ON and Switch 1 is OFF, it activates the PIFA structure as the shorting wall is connected. It is noted that all the four modes have common frequency range. P-I-N diode plays major role, i.e., switching by making them ON and OFF different modes can be observed in given Table 1.

The inductance L is kept too short and hence neglected, *when we simulate this antenna in CST Microwave Studio 2018.*

2.1 Switching Modes and Antenna Array Setup

In order to form array side-by-side placement, two antennas are preferred in same orientation. Ground plane is enlarged to 50 x 70 mm for the placement of the array, where both the antennas are 10 mm apart. PIN diode used as switch and switch will be ON when resistance is low and switch will be OFF when connecting high resistance is in kΩ. S1 (switch 1) and S2 (switch 2) are implemented as lumped element using in CST 2018 for changing modes, modes are discussed in Table 1.

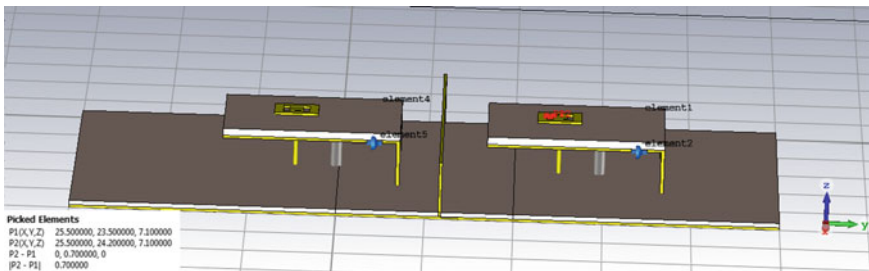


Fig. 3 Lateral view of proposed antenna structure

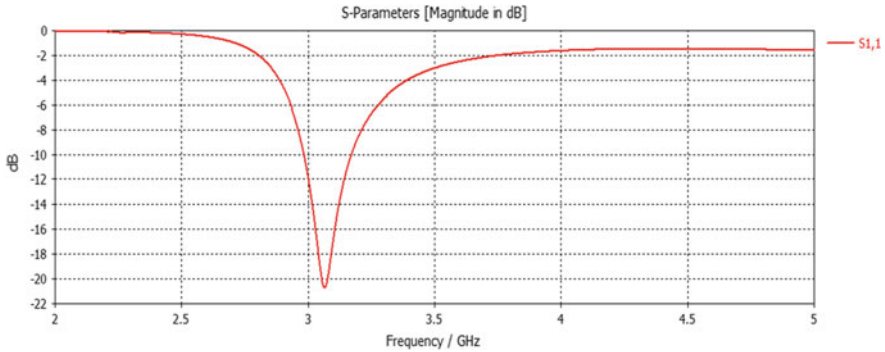


Fig. 4 S parameters of single unit of antenna (simulated)

In Fig. 3, isolation is achieved by using shielding wall and slits. This provides isolation below -12 dB. *The effect of this technique can be seen in the below results of radiation pattern in different modes.*

3 Simulation Results and Radiation Patterns

3.1 S-Parameters

Figure 4 shows simulated result of reflection coefficient S_{11} (dB) for single unit of PIFA-based antenna.

S_{11} (dB) denotes amount of power reflected back from antenna often termed as reflection coefficient. From reflection coefficient result, it is proven that single unit structure can achieve -10 dB frequency range from 2.9 to 3.5 GHz helpful to cover WiMax application. Simulated result S_{11} (dB) gets -21 dB at 3.11 GHz.

3.2 Combined Results of S_{11} and S_{22} Parameters for PIFA-PIFA Mode and PIFA-Monopole Mode

In PIFA-PIFA mode, center frequency is 3.1 GHz at which antenna is operating and it is very close to resonant frequency of single element PIFA structure. Here the isolation loss is also below -13 dB and therefore, -10 dB is the power that is reflected back from the antenna, if 3 dB power is given to it as shown in Fig. 5 and Fig. 6

Similarly, in PIFA-Monopole mode center frequency of the antenna does not change but there is an effect in radiation patterns in same mode. Hence, the purpose

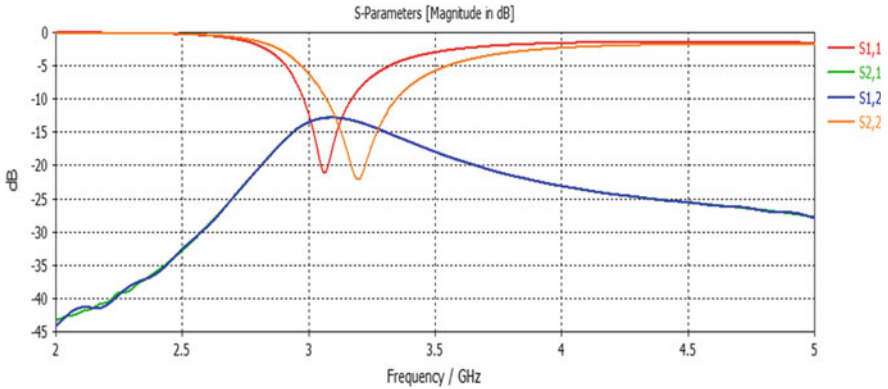


Fig. 5 Simulated S-parameters in PP mode

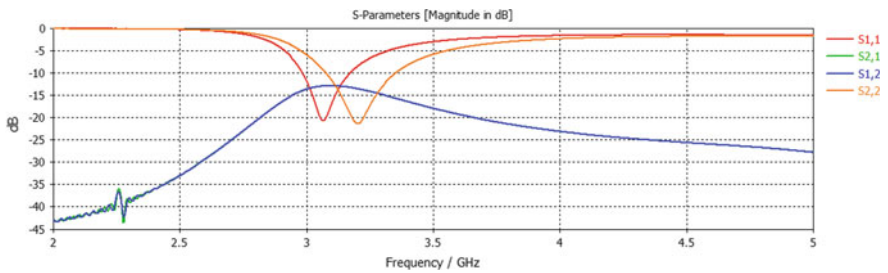


Fig. 6 Simulated S-parameters in PM mode

of working in the same frequency by changing the radiation pattern is fulfilled. In other mode, results are same, so other mode radiation patterns are shown in Table 2.

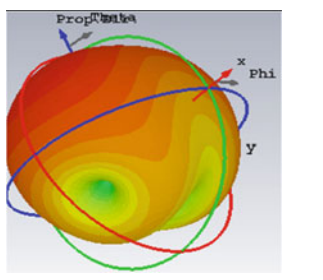
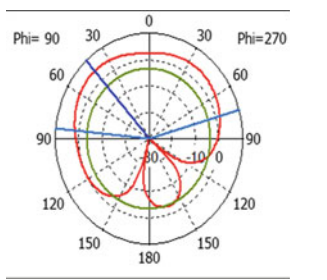
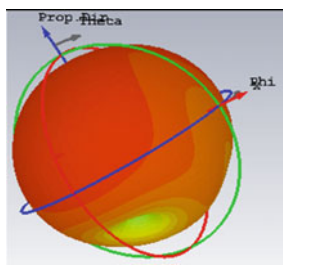
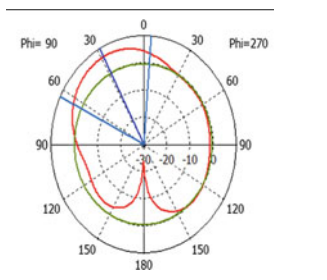
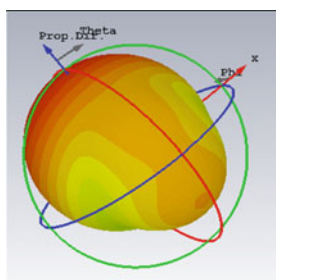
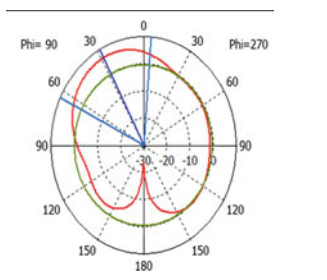
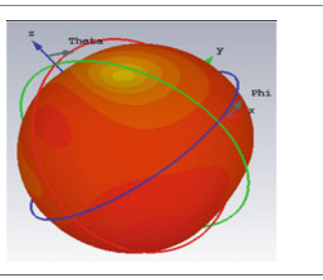
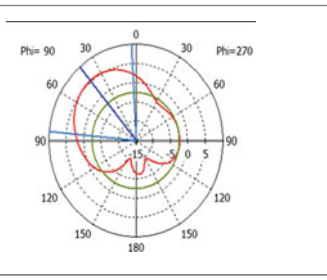
4 Efficiency

The simulated total and radiated efficiency of proposed antenna are shown in Fig. 7, and it is ratio of radiated power and supplied power of antenna. The proposed antenna has radiation efficiency 98%, and total efficiency is 86%, respectively.

5 Radiation Performance

3D view and 2D view of radiation patterns are shown in Table 2.

Table 2 3D view and 2D view of radiation patterns

S. No.	3D radiation pattern	2D radiation pattern
(a) PP mode		
<p><i>In PIFA-PIFA mode 2D radiation pattern shows, main lobe magnitude is 4.46dBi, and the main lobe direction is changed to 42°, while having the angular width of 158.3°</i></p>		
(b) PM mode		
<p><i>In PIFA-Monopole mode, 2D radiation pattern shows, main lobe magnitude is 5.26dBi, and main lobe direction is moving in 128° from 0°, while having the angular width of 61°</i></p>		
(c) MP mode		
<p><i>In the Monopole-PIFA, mode 2D radiation pattern shows, main lobe magnitude is 6.41dBi, and radiation direction is in 27°, while the angular width is 64°</i></p>		
(d) MM mode		

(continued)

Table 2 (continued)

S. No.	3D radiation pattern	2D radiation pattern
	<i>Monopole-Monopole mode, 2D radiation pattern shows, main lobe magnitude is observed to be 5.27dBi with the main lobe direction of radiation in 40°, while angular width is 81°</i>	

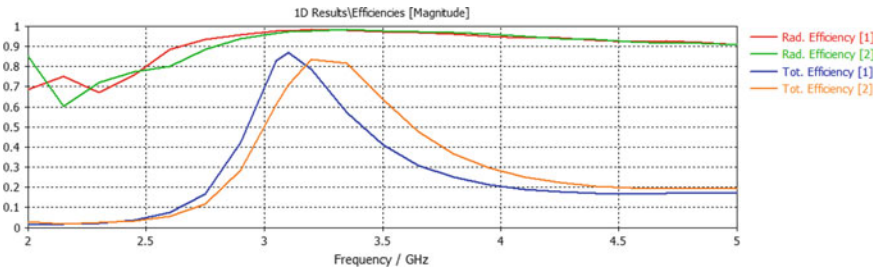


Fig. 7 Simulated radiation and total efficiency

6 MIMO Performance

Envelope correlation coefficient (ECC) and diversity gain (DG) are most important parameters to evaluate the diversity performance of MIMO system. ECC explain correlation between two elements. Ideal value of ECC should be 0.5. In Fig. 8, simulated result shows ECC value at 3.1 GHz is much less than 0.05. The ideal diversity gain should be 10 dB. Figure 9 shows simulated result of diversity gain which has 9.9 dB diversity gain at 3.1 GHz.

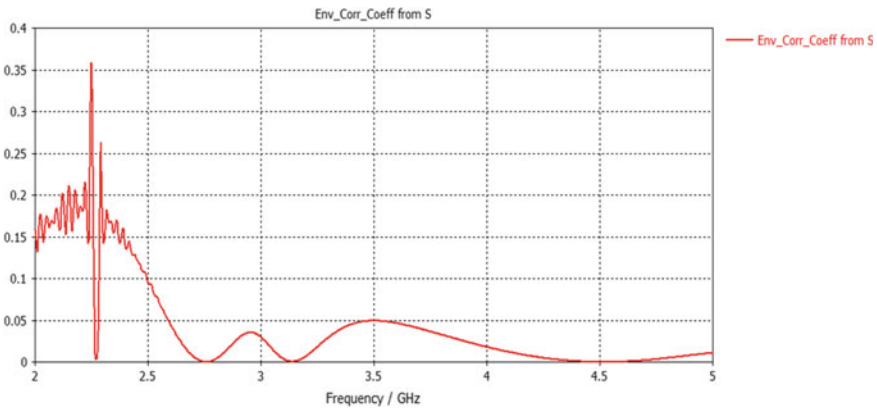


Fig. 8 Simulated result of envelope correlation coefficient (ECC)

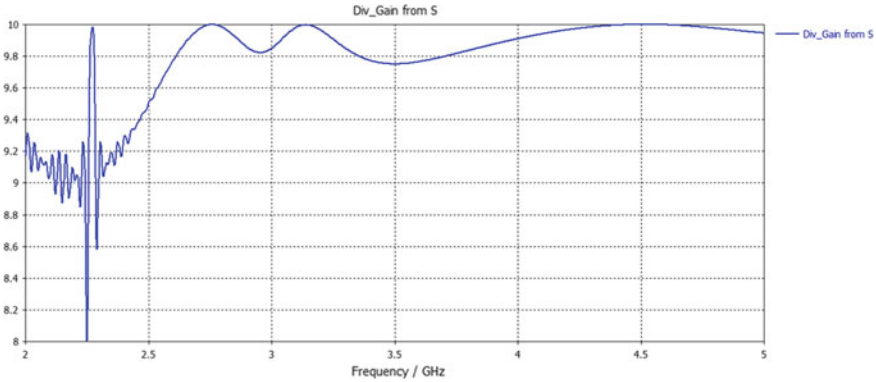


Fig. 9 Simulated result of diversity gain (DG)

7 Conclusion

A pattern reconfigurable MIMO antenna for WiMax application is proposed. It is operating at 3.1 GHz. Pattern can be changed by PIN diodes (ON/OFF) in four modes. The volume of antenna $50 \times 70 \times 7 \text{ mm}^3$ provides maximum gain 6.41dBi with 86% total radiating efficiency. MIMO antenna has good diversity performance because ECC is less than 0.05 and diversity gain is 9.9 dB. Combination of shielding wall and decoupling slits to provide isolation greater than -12 dB for all four operating modes. In future, further improvement is required to achieve isolation between in two elements but radiation patterns are changing from 27° to 128° while resonant frequency is stable. Finally, simulation results show that the proposed design is applicable for WiMax application.

References

1. Jensen M, Wallace J (2004) A review of antennas and propagation for MIMO wireless communications. *IEEE Trans Antennas Propag* 52: 2810–2824
2. Rhee C, Kim Y, Park T, Kwoun SS, Mun B, Lee B, Jung C (2014) Pattern-reconfigurable MIMO antenna for high isolation and low correlation. *IEEE Antennas Wireless Propag Lett* 13: 1373–1376
3. Li H, Lau BK, He S (2017) Design of closely packed pattern reconfigurable antenna array for MIMO terminals. *IEEE Trans Antennas Propag* 65(9): 4891–4896
4. Shoaib S, Shoaib N, Shoaib I, Chen X (2017) Design and performance analysis of pattern reconfigurable MIMO antennas for mobile smartphones. *Microw Opt Technol Lett* 59(1):148–156
5. Shoaib S, Shoaib I, Shoaib N, Chen X, Parini CG (2014) Pattern reconfigurable antenna for mobile handsets. In: *Loughborough Antennas and Propagation Conference (LAPC)* IEEE, November, pp 48–51
6. Zhu Z, Wang P, You S, Gao P (2018) A flexible frequency and pattern reconfigurable antenna for wireless systems. *Prog Electromagn Res* 76:63–70

7. Lai MI, Wu TY, Hsieh JC, Wang CH, Jeng SK (2007) A compact pattern reconfigurable antenna design for handheld wireless devices. In: IEEE antennas and propagation society international symposium, June, pp 5223–5226
8. Khan MS, Capobianco AD, Asif SM, Iftikhar A, Braaten BD, Shubair RM (2016) A pattern reconfigurable printed patch antenna. In: 2016 IEEE international symposium on antennas and propagation (APSURSI), June, pp 2149–2150
9. Ji JK (2016) Dual-band pattern reconfigurable antenna for wireless MIMO applications. *ICT Express* 2(4):199–203
10. Sun F, Zhang F, Feng C (2019) Wideband pattern reconfigurable printed-Yagi antenna array based on feed structure. *J Microw, Optoelectron Electromagn Appl* 18(2): 270–275
11. Han L, Wang C, Zhang W, Ma R, Zeng Q (2018) Design of frequency-and pattern-reconfigurable wideband slot antenna. *Int J Antennas Propag*. <https://doi.org/10.1155/2018/3678018>
12. Rhee C, Kim Y, Park T, Kwoun SS, Mun B, Lee B, Jung C (2014) Pattern-reconfigurable MIMO antenna for high isolation and low correlation. *IEEE Antennas Wirel Propag Lett* 13:1373–1376
13. Laafif K, Bouslama M, Gharsallah A (2017) Pattern reconfigurable antenna design for for 5G mobile communication systems. In: IEEE Mediterranean Microwave Symposium (MMS), November, pp 1–3
14. Yang L, Lu C, Li X, Liu L, Yin X (2019) A horizontal azimuth pattern-reconfigurable antenna using omnidirectional microstrip arrays for WLAN application. *Int J Antennas Propag* pp 1–9
15. Kingsly S, Thangarasu D, Kanagasabai M, Alsath MGN, Palaniswamy SK, Rao TR, Subbaraj S, Selvam YP, Sambandam P, Ganesan G (2019) Tunable band-notched high selective UWB filtering monopole antenna. *IEEE Trans Antennas and, Propag* 67(8):5658–5661
16. Trinh LH, Ferrero F, Staraj R, Ribero JM (2013) Mobile phone antenna for 2G, 3G and 4G standards. In: IEEE. *international conference on advanced technologies for communications*, October 2013, pp 195–202
17. Sanchez-Fernandez M, Rajo-Iglesias E, Quevedo-Teruel O, Pablo-Gonzalez ML (2008) Spectral efficiency in MIMO systems using space and pattern diversities under compactness constraints. *IEEE Trans Veh Technol* 57(3):1637–1645
18. Vats M, Sachan S, Choudhary S, Mishra A, Shukla V (2020) Designing of band reject filter for Radio Astrophysics. In: International conference on Artificial Intelligence: advances and applications, Springer, Singapore, pp 91–100
19. Lozada A, Piedrahita A, Russi G (2017) Design and study of a microstrip slot antenna operating at 2.8/3.1/3.6/4.7/5.4 GHz. In: *MATEC Web of Conferences*, Vol 125, p 3003 (EDP Sciences)

Three-Phase Fault Analysis of Distributed Power System Using Fuzzy Logic System (FLS)



Abrar Ul Qadir Bhat, Anupama Prakash, Vijay Kumar Tayal, and Pallavi Choudekar

Abstract This paper presents the fuzzy logic system (FLS) for the classification and detection of three-phase fault that occurs in the distributed power system network. An 11 kV, 50 Hz three-phase three-wire power system distributed network model is designed in MATLAB/Simulink environment and various faults such as Normal, Line to Ground (LG), Line to Line (LL) to Ground (LLG), and Line to Line to Line to Ground (LLLG) have been applied to study the performance of distribution system. Based on the results of the simulation, it has been analyzed that the proposed fuzzy logic system correctly classifies and detects the various types of the fault.

Keywords Electric Power Distribution Network (EPDN) · Three-phase fault circuit · Fuzzy logic system (FLS)

1 Introduction

The key source for the electrical utility is AC transmission, but the transmission corridors are overstressed due to excessive increase in demand. Because of fluctuating system parameters and uncertain charging conditions, the power flow in these complex transmission systems is not easy to control [1]. The important component of a power system is distribution system which is one of the parameters along with generation and transmission system. The electrical power system consists of mainly three

A. U. Q. Bhat (✉) · A. Prakash · V. K. Tayal · P. Choudekar
Electrical and Electronics Engineering Department, AMITY University, Noida, Uttar Pradesh, India
e-mail: erabrar17@gmail.com

A. Prakash
e-mail: aprakash1@amity.edu

V. K. Tayal
e-mail: vktayal@amity.edu

P. Choudekar
e-mail: pachoudekar@amity.edu

components or parameters, i.e., generation, transmission and distribution system. “For over twenty years, the subject of location of fault has been of considerable interest to electrical utility engineers and researchers” [2]. The occurrence of fault is due to the failure of distribution system insulation, accidents by bridging of energized phase conductors, objects, etc. These events have an impact on the current and voltage value of the distributed power system network that run overhead. It becomes expedient to need an accurate and reliable fault detection system. Recently, researchers have become more interested in finding solutions to the problem of fault data error, vagueness, incomplete fault information, and information redundancy [3]. “The fault detection system can use fuzzy logic to cope with uncertainties that occur while the fault is located in the electrical distribution networks” [4]. In [5], a fuzzy logic-based algorithm used the proposed fault detection technique to identify the fault type in a system.

As a result of advances in various protection schemes based on artificial neural networks [6, 7], soft computing techniques, support vector machines [8, 9], neuro-fuzzy [10], and fuzzy logic system [11, 12] have been carried out to protect the three-phase transmission lines. A fault identification approach based on current signals using a digital distance protection system fuzzy logic-based algorithm has been reported in [13]. A fuzzy logic system is presented in [14], using the phase angle between line currents to identify fault and initiate single-phase auto reclosure.

2 System Modeling

The distributed power system network shown in Fig. 1 has been used for analyzing different types of the fault. The network is designed in MATLAB/Simulink environment with the implementation of different types of fault such as symmetrical (LLLG), unsymmetrical (LG, LL, and LLG), and high impedance fault (HLG, HLLG, and HLLLG). It consists of a grid source (100 MVA/11 KV), two transformers each of 100 MVA, Transformer 1 and Transformer 2 of 11 KV/33 KV and 33 KV/400 V, respectively, three distribution lines 1, 2, and 3 of 30 km, 30 and 40 km, respectively, connected to the load.

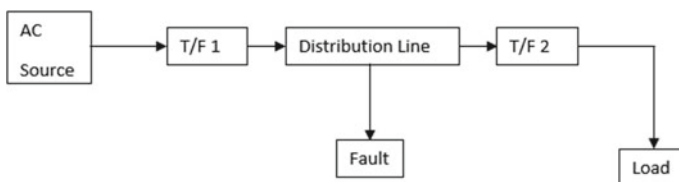


Fig. 1 Block diagram of distribution network

3 Fuzzy Logic System

In 1965, Lotfi Zadeh gave the concept of fuzzy logic system. This logic is used in many industry applications because of certain advantages: simple and quicker methodology, reduction of the design cycle, ease of implementation, reduction of hardware costs, improvement of control performance, simplification of design complexity [15].

The fuzzy logic scheme is a kind of multi-assessed logic with a collection of common-sense rules. This approach is also used to determine the sort of fault inside the network. The measures to be taken in this FLS training model are shown in Fig. 2 and are also shown below [16].

- Rule 1: Define the fuzzy sets with variable name for input and output.
- Rule 2: Define each variable of the member function.
- Rule 3: Set the rules.
- Rule 4: Building and checking the system.
- Rule 5: Tune the system and test it.

The fuzzy system has three (Ia, Ib, and Ic) inputs and one (fault) output. Two triangular membership functions were chosen for each phase (Ia, Ib, and Ic), such as normal and high. For each membership function, the selected values varies from 400 to 600 for normal and 1000 to 2000 for high. The output membership function has eleven trapezoidal membership functions named as Normal (No Fault), LG fault (AG, BG, and CG), LL fault (AB, BC, and AC), LLG fault (ABG, BCG, and ACG), and LLLG fault (ABCG).

The fuzzy rules for three-phase are framed using Ia, Ib, and Ic as input is shown in Fig. 3.

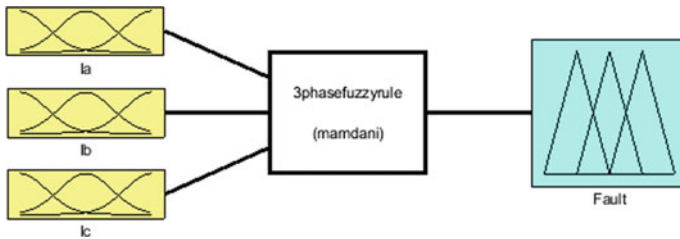


Fig. 2 FLS structure

1. If (Ia is Normal) and (Ib is Normal) and (Ic is Normal) then (Fault is No_Fault) (1)
2. If (Ia is High) and (Ib is Normal) and (Ic is Normal) then (Fault is AG) (1)
3. If (Ia is Normal) and (Ib is High) and (Ic is Normal) then (Fault is BG) (1)
4. If (Ia is Normal) and (Ib is Normal) and (Ic is High) then (Fault is CG) (1)
5. If (Ia is High) and (Ib is High) and (Ic is Normal) then (Fault is AB) (1)
6. If (Ia is Normal) and (Ib is High) and (Ic is High) then (Fault is BC) (1)
7. If (Ia is High) and (Ib is Normal) and (Ic is High) then (Fault is AC) (1)
8. If (Ia is High) and (Ib is High) and (Ic is Normal) then (Fault is ABG) (1)
9. If (Ia is Normal) and (Ib is High) and (Ic is High) then (Fault is BCG) (1)
10. If (Ia is High) and (Ib is Normal) and (Ic is High) then (Fault is ACG) (1)
11. If (Ia is High) and (Ib is High) and (Ic is High) then (Fault is ABCG) (1)

Fig. 3 Fuzzy rule for three-phase fault

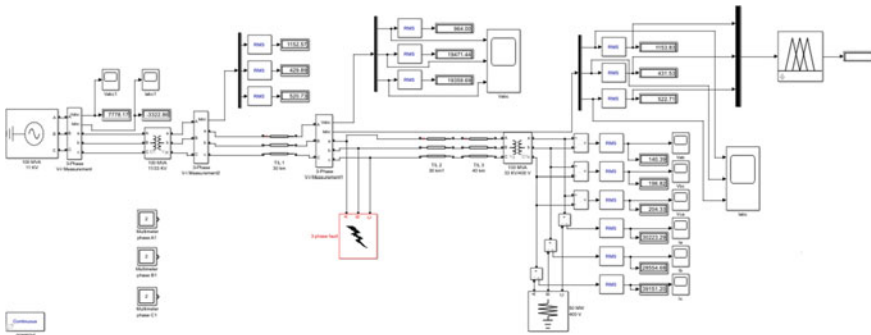


Fig. 4 Three-phase fault model

4 Results and Discussion

4.1 MATLAB/Simulation

The three-phase three-wire power system distribution network model of three-phase fault of 11 kV, 50 Hz as shown in Fig. 4 is designed in MATLAB/Simulink environment. The current and voltage waveform have been captured for the time period of 0–0.5 s to study the type of the fault in a system [17]. The switching time for all the cases is from 0.15 to 0.2 s. It has been analyzed that in case of LG, LL, LLG and LLLG; the magnitude of fault currents is very high, and their respective phase to ground voltages is very low.

4.2 FLS Analysis

The current signal analysis is carried out under different cases of fault such as Normal, LG, LL, LLG, and LLLG. The current and voltage waveforms of all phases under

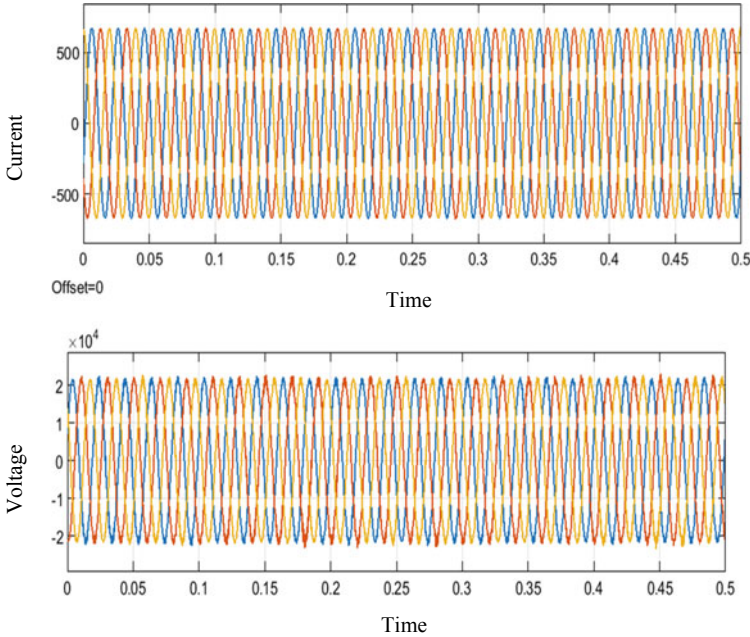


Fig. 5 Current waveform under normal case/no fault

normal as well as under faulty conditions of different faults are shown in Figs. 5, 6, 7, 8, 9 for better understanding and the detailed list of each three-phase current (I_a , I_b , and I_c) are listed in Table 1.

Figure 5 shows current waveform under normal case. Here the current and voltage remain the same throughout the time period for all the phases.

Figure 6 shows the waveform for current for LG of phase-A. The current and voltage waveforms captured at bus1 for this fault are as shown in Fig. 6. Since this is AG fault, the current in phase-A has increased as compared to the rest of the phases and voltage for the same phase has decreased from 0.15 to 0.2 s.

Figure 7 shows the waveform for current and voltage for LL fault of phase-AB. The current and voltage waveforms captured at bus1 for this fault are as shown in Fig. 7. Since this is AB fault, the current in phase-A and phase-B has increased and voltage for the same phases has decreased from 0.15 to 0.2 s.

Figure 8 shows the waveform for current and voltage for LLG fault of phase-AB. The current and voltage waveforms captured at bus1 for this fault are as shown in Fig. 8. Since this is ABG fault, the current in phase-A and phase-B has increased, and voltage for phase-A and phase-B has decreased from 0.15 to 0.2 s.

Figure 9 shows the waveform for current and voltage for LLG fault of phase-ABC. The current and voltage waveforms captured at bus1 for this fault are as shown in Fig. 9. Since this is ABCG fault, the current in all the phases has increased, and voltage for all the phases has decreased from 0.15 to 0.2 s.

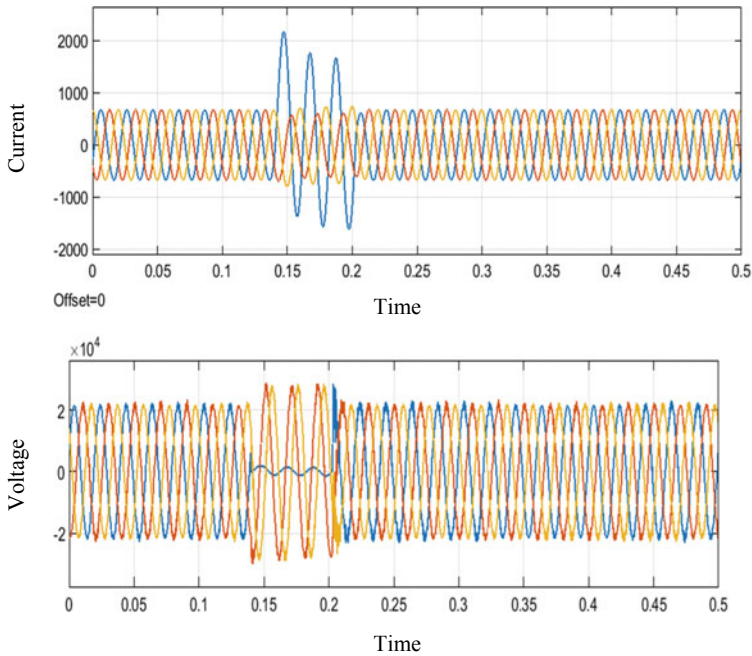


Fig. 6 Current and voltage waveform of LG fault (AG)

Table 1 shows that by doing analysis of fuzzy logic method the output of each fault comes out to be same as that of three-phase fault analysis. It has been found that the magnitude of current in case of normal remains same for all the phases. But in case of LG, LL and LLG fault, the magnitude of faulted current is too high as compared to the rest of the phases. For example, in case of LG fault of phase-A, that is AG Fault, the magnitude of fault current of phase-A is 1152.38 A which is too high as compared to phase-B (430.48 A) and phase-C (520.94 A) and voltage of phase-A is too low (964 V) as compared to phase-B (19471 V) and phase-C (19359.69 V). Same is the case for the rest of the faults. In case of LLLG fault, the magnitude of faulted current is too high in all the phases phase-A (1803.47 A), phase-B (1804.91 A), and phase-C (1807.00 A) voltage of all the phases are zero volt.

5 Conclusion

In this paper, the 11 kV medium voltage distribution network has been simulated using the MATLAB/Simulink environment by adding different types of faults in the distributed power system network. The current waveform captured in each case of normal symmetrical and unsymmetrical fault has been analyzed using the fuzzy logic method in order to locate the type of the fault in the three-phase three-wire

Table 1 Fuzzy output values for current signal for different cases of faults

Fault	State	Fault Type	Ia (A)	Ib (A)	Ic (A)	Va (V)	Vb (V)	Vc (V)	FUZZ output	Remarks
Three-phase fault	Normal	No fault	474.96	474.64	474.92	15127.45	15117.31	15118.43	No fault	✓
		AG	1153.83	431.53	522.71	964.00	19471.44	19359.69	AG	✓
		BG	523.54	1153.98	432.01	19384.48	964.17	195505.73	BG	✓
	LL Fault	CG	431.12	522.16	1153.68	19467.23	19355.95	963.82	CG	✓
		AB	1708.26	1451.67	475.22	7588.86	7588.86	15177.86	AB	✓
		BC	474.99	1704.69	1448.41	15130.76	7565.35	7565.35	BC	✓
	LLG Fault	AC	1448.35	474.87	1705.05	7569.09	15138.28	7569.09	AC	✓
		ABG	1769.22	1487.60	479.53	655.08	655.08	19715.23	ABG	✓
		BCG	479.79	1765.13	1482.71	19717.91	655.84	655.84	BCG	✓
	LLLG Fault	ACG	1483.61	479.89	1765.27	655.95	19722.57	655.95	ACG	✓
		ABCG	1806.73	1800.56	1807.75	0	0	0	ABCG	✓

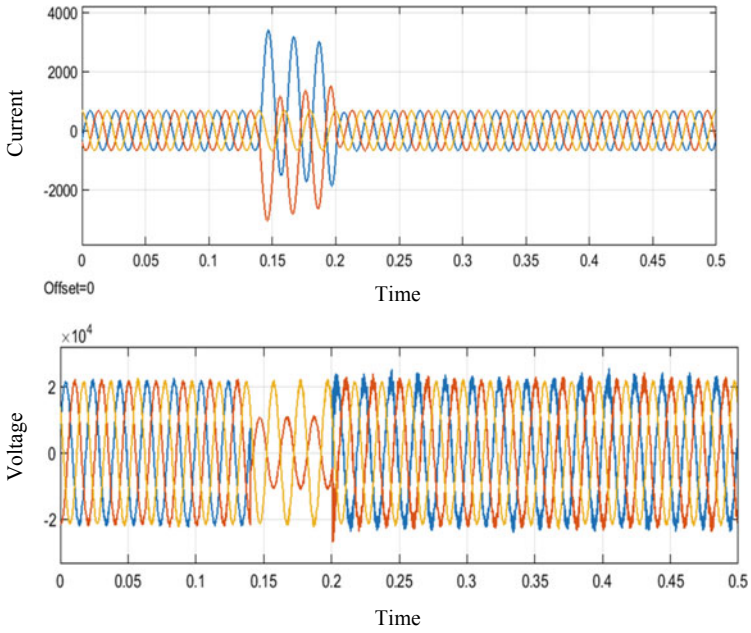


Fig. 7 Current and voltage waveform for LL fault (AB)

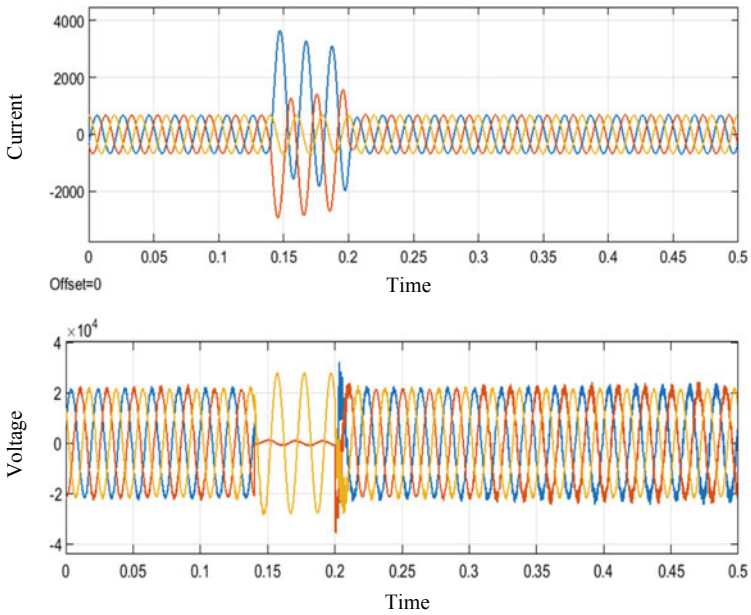


Fig. 8 Current and voltage waveform for LLG fault (ABG)

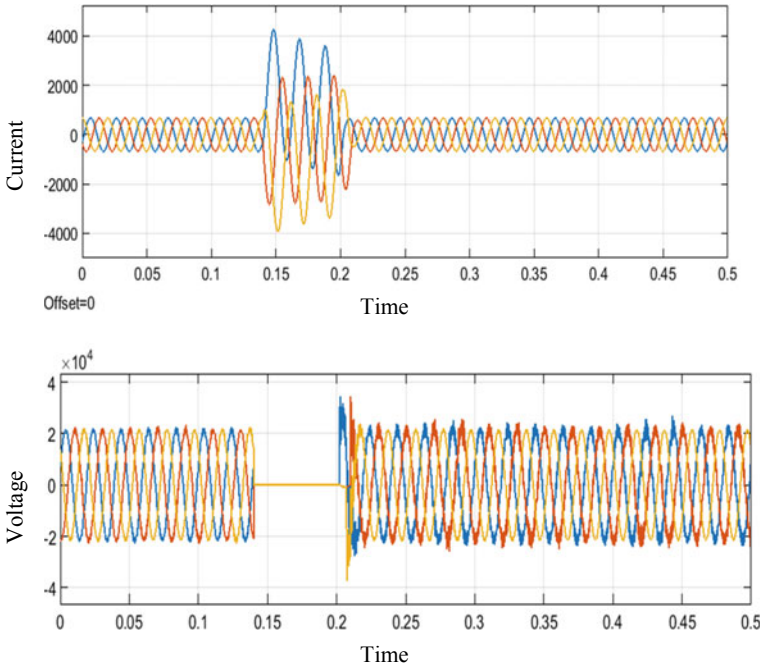


Fig. 9 Current and voltage waveform for LLLG fault (ABCG)

distribution system. It has been analyzed that the faults can occur in all the possible combinations in distribution systems; hence, the fuzzy membership function plays a main important role in capturing the various combinations.

References

1. Dwivedi Y, Tayal VK (2016) Robust control of power system using shunt FACTS controllers. In: 7th India International Conference on Power Electronics (IICPE), Patiala, pp. 1–6
2. Das B. Fuzzy logic-based fault-type identification in unbalanced radial power distribution system. In IEEE Transactions on Power Delivery, vol. 21, no. 1, pp. 278–285, January 2006
3. Jalali D, Moslemi, N (2005) Fault location for radial distribution systems using fault generated high-frequency transients and wavelet analysis. In CIRED 2005—18th International Conference and Exhibition on Electricity Distribution, Turin, Italy, pp 1–4
4. Mamdani, EH Application of fuzzy logic to approximate reasoning using linguistic synthesis. www.google.com. Viewed date: 17 March 2008
5. Naveh HS, Zadeh HK, Hosseini BT, Zadeh, AS (2010) A novel approach to detection high impedance faults using fuzzy logic
6. Koley Ebha, Kumar Raunak, Ghosh Subhojit (2016) Low cost microcontroller-based fault detector, classifier, zone identifier and locator for transmission lines using wavelet transform and artificial neural network: A hardware co-simulation approach. Int J Electr Power Energy Syst 81:346–360

7. Koley Ebha, Yadav A, Thoke AS (2015) A new single-ended artificial neural network-based protection scheme for shunt faults in six-phase transmission line. *Int Trans Electr Energy Syst* 25(7):1257–1280. <https://doi.org/10.1002/etep.1901>
8. Samantaray SR, Dash PK (2008) Transmission line distance relaying using machine intelligence technique. *IET Gener Transm Distrib* 2(1):53–61
9. Swetapadma Aleena, Yadav Anamika (2016) Directional relaying using support vector machine for double circuit transmission lines including cross-country and inter-circuit faults. *Electr Power Energy Syst* 81:254–264
10. Reddy MJB, Mohanta DK (2008) Performance Evaluation of an Adaptive-Network-Based Fuzzy Inference System Approach for Location of Faults on Transmission Lines Using Monte Carlo Simulation. *IEEE Trans Fuzzy Syst* 16(4):909–919 August
11. Das B, Reddy JV (2005) Fuzzy-logic-based fault classification scheme for digital distance protection. *IEEE Trans Power Delivery* 20(2):609–616 April
12. Samantaray SR (2013) A systematic fuzzy rule-based approach for fault classification in transmission lines. *Appl Soft Comput* 13:928–938
13. Youssef OAS (2004) Applications of fuzzy inference mechanisms to power system relaying. *IEEE PES Power Syst Conf Expo* 1:560–567
14. Youssef OAS (2004) Combined fuzzy-logic wavelet-based fault classification technique for power system relaying. *IEEE Trans Power Delivery* 19(2):582–589 April
15. Tayal VK, Lather JS, Sharma P, Sinha SK (2014) Power system stability enhancement using fuzzy logic based power system stabilizer. In: *Advances in intelligent systems and computing*, Vol. 258, Springer Verlag, Berlin, pp 55–68 (March)
16. Yi Z, Etemadi AH (2017) Fault detection for photovoltaic systems based on multi-resolution signal decomposition and fuzzy inference systems. *IEEE Trans Smart Grid* 8(3):1274–1283 May
17. Veerasamy V, Abdul Wahab NI, Ramachandran R, Mansoor M, Thirumeni M, Lutfi Othman M (2018) High impedance fault detection in medium voltage distribution network using discrete wavelet transform and adaptive neuro-fuzzy inference system. *Energies* 11(12):3330

Design and Analysis of Reconfigurable MIMO Antenna for Wireless Applications



Chirag Agrawal, Akshay Pratap Singh, Bisma Ashraf, and Ranjana kumari

Abstract This paper presents pattern reconfigurable antenna for LTE band in multiple-input multiple-output configurations. In this paper, MIMO antenna is presented which is efficient to cover frequency within the range of 2.54–2.89 GHz which cover 4G-LTE band. Two-element MIMO antenna is designed on $120 \times 65 \times 1.6 \text{ mm}^3$ with each antenna hold a neighborhood of $26.5 \times 14.5 \text{ mm}^2$ on FR-4 substrate with relative permittivity of 4.35 and loss tangent of 0.02. The pattern reconfigurability is achieved by the help of PIN diodes by connecting and disconnecting a $4 \times 1 \text{ mm}^2$ metal strip. The proposed antenna is pattern reconfigurable within the frequency range of 2.54–2.89 GHz. The isolation curve shows a value of -37 dB at center frequency of 2.67 GHz secured by every antenna. The simulated result shows the maximum gain of 2.57 dBi and maximum efficiency of 85%. The envelope correlation coefficient does not exceed 0.02 across the complete operating band.

Keywords Reconfigurable antenna · Multiple-input multiple-output (MIMO) · LTE

C. Agrawal (✉) · A. P. Singh · B. Ashraf · R. kumari
Department of Electronics and Communication Engineering, Galgotia's College of Engineering and Technology, Greater Noida, India
e-mail: chiragagrawal782@gmail.com

A. P. Singh
e-mail: akshaypratapsingh2403@gmail.com

B. Ashraf
e-mail: bismashraf97@gmail.com

R. kumari
e-mail: ranjana.kumari@galgotiacollege.edu

1 Introduction

In late years, the media transmission brought numerous difficulties inside the arranging of cell phones, particularly inside the antennas area. In current there are different frequency bands in media transmission frameworks, and multiband technology is of greatest use. Numerous investigations have presented multiband antennas for GSM, UMTS, and Wi-Fi during a portable, yet as now LTE standard is reported and being to be conveyed, new frequency bands should be secured due to the low frequency utilized by this norm, the structure of a antenna which can accomplish over a more extensive waveband and be coordinated during a versatile structure factor turns into an attest again [1]. In Ref. [2] proposed configuration direct in two configuration in which one is PIFA and other is loop mode. PIN diodes are used to exchange between the configuration. The downside of the designed structure is antenna height that spread over the base by 6 mm, which cause the arranging not appropriate for slim phone. Additionally, since the arranging of antenna shows frequency reconfigurability, it cannot be implemented to acknowledge design reconfigurable ability from a cell phone.

A design in Ref. [3] has achieved pattern reconfigurability in 700 to 960 MHz and 1700 to 2700 MHz bands respectively. The pattern reconfigurability of working band is accomplished utilizing MEMS. In spite of the fact that the arranging proposed during this work is reduced, in any case, the utilization of MEMS switches in portable handsets is not reasonable because MEMS have high insertion loss and high biasing voltage (50.0–70.0 V) and a luxurious coordinating system. In [4], designed antenna consists of two stripes and a pairing branch. Stripe one grants to the center frequency at 2 GHz, whereas stripe two grants to the center frequency of 0.98 GHz, and therefore bandwidth is improved by the help of the pairing branch. A PIN diode switch is utilized to manage the stripe for accomplishing pattern reconfigurability in working. The antenna is not appropriate for pattern reconfigurable in working band on a mobile. Antenna showed in Ref. [5] is an example of pattern reconfigurable antenna. The proposed design has introduced less area, however the coordinating frequency bandwidth is 5.150–5.350 GHz which is not reasonable for cellphones. Most of the part of the design antenna are of frequency pattern reconfigurable antennas and any plans of reconfigurable antennas were likewise examined. This was a powerful chance to create multiband pattern reconfigurable antenna for accomplishing best throughput and abundancy from a multifunction handset. In [6], the designed antenna is a compact U-slot antenna which is pattern reconfigurable. The antenna has a U-slot patch with 8 sorting posts via PIN diodes. Antenna shows three different pattern reconfigurability by the help of PIN diodes. The antenna has a center frequency of 5.32 GHz. Any additional DC bias lines are not required to the implemented design to control PIN diodes. Since the design has simple structure and it is showing pattern reconfigurability, the performance of a wireless communication system is enhanced by this design. This paper suggests to improve the gain of antenna in states 2 and 3.

In [7], the paper presents an antenna which is pattern reconfigurable having two rectangular patches that are placed at 90° to each other. The feed line is connected

to patches through same point so that they can resonate at same frequency by the help of diodes. Maximum gain has, when diode 1 is kept on patch 1 of proposed antenna, it radiates and shows a pattern having maximum gain of 5.69 dBi at 30° to the right-hand side of the y - z plane and similarly when diode 2 is kept on the patch 2, it radiates and antenna shows a pattern having maximum gain of 5.7 dBi at -30° to the left hand side of the y - z plane. This design has operating frequency of 2.43 GHz. A compact dual antenna array which is pattern reconfigurable is designed in Ref. [8] having center frequency of 2.65 GHz. This antenna is an application for laptops. The proposed antenna composed of two layers, one is monopole layer and other is PIFA layer. Pattern reconfigurability is achieved by the help of diodes. The antenna operates in four modes. The $\lambda/11$ distance between the antennas makes the structure compact. The ECC value of this antenna is below 0.05 in free space and below 0.1 in outdoors and indoors. The efficiency of the antenna is in between 68 and 85%. In [9], the paper presents a design which is novel frequency and shows pattern reconfigurability. The designed antenna has a rectangular patch with two longitudinal slits. PIN diodes make the slit to connect with patch. PIN diode makes antenna pattern reconfigurable. The antenna works at frequency 4.5 and 4.8 GHz/5.2 and 5.8 GHz, and the antenna has pattern at -30° , 0° , $+30^\circ$. The designed antenna is applicable for General Wireless Communication Service band, Telemetry and WLAN.

In [10] multiband multipolarized antenna is presented with dual bandwidth. The antenna produces three senses of polarization, and PIN diodes are used in antenna for polarization reconfigurability. In OFF state, the bandwidth of antenna is 3.99–4.42 GHz and 5.84–14.20 GHz. In ON state, the bandwidth of antenna is 7.20–11.04 GHz and 12.66–15.37 GHz. The antenna is suitable for many application like C-band communication satellite for uplink amateur satellite operations (CP1), traffic light crossing detector, and terrestrial communication (CP4). In [11], a circularly polarized capacitive feed microstrip antenna is presented. PIN diodes are used to provide the dual-band circular polarization. The proposed design give bandwidth of 66.61% (ON state) range from 4.42 to 8.80 GHz and 68.42% in OFF state in range from 4.12 to 8.91 GHz. When diode is ON, a single frequency is obtained and in OFF state dual band is obtained. The application of proposed antenna is 5 GHz WLAN and public safety WLAN at 4.9 GHz. In [12], antenna is designed for (WLAN) 802.11 a working on 5.15–5.35 GHz frequency range. Dipole loop-shaped structure is achieving pattern reconfigurability by two switches that were employed. In [13] Antenna used for 5G wireless technology of frequency 5.6 GHz and size $29.15 \times 29.15 \text{ mm}^2$, a technique derived upon Fabry Perot cavity holding two surfaces. In accordance with antenna structure, a switching pattern was derived by combining frequency-selective surfaces. Reconfigurability is achieved by using partially reflective surface and by adding active selective surface with the PIN diodes. In [14], the folded inverted L antenna is used so that size can be reduced. Antenna of size $(68 \times 130 \times 10) \text{ mm}^3$ and a return loss of -6 dB can easily be integrated in mobile devices that cover 700–960 MHz frequencies. In Ref. [15], a six-order band reject filter is designed for S band. This is providing improved reflection loss and insertion loss and designed for radio space science. In Ref. [16] with configurable arrays for

WLAN application, microstrip array, four parasitic elements, and conducting plate are used to achieve this goal.

In this paper, two directly polarized multiple-input multiple-output antennas printed corner to corner on the FR-4 substrate are introduced. Monopoles antennas are used here that are wandered to possess minimal vol^m. An extra metal strip is associated with each antenna utilizing PIN diode for changing the pattern. The pattern change is accomplished by adding and removing a $4 \times 1 \text{ mm}^2$ metal strip utilizing the PIN diode. The antennas are showing pattern reconfigurability inside the frequency scope of 2.54–2.89 GHz. The isolation curve shows that the isolation accomplished is best than -37 dB at center frequency 2.67 GHz secured by every antennas.

2 Antenna Structure

The proposed antenna is simulated and designed in CST Microwave Studio 2018. Figure 1 shows the simulated model of the proposed antenna. The size of the substrate utilized for the structure is $65 \times 120 \times 1.6 \text{ mm}^3$ with every antennas occupying a neighborhood of $14.5 \times 26 \text{ mm}^2$. Antenna is designed on FR-4 with relative permittivity of 4.35 and loss tangent of 0.02. Two metallic pieces of region $4 \times 1 \text{ mm}^2$ likewise are etched and associated with the monopoles utilizing PIN diode add as lumped component in CST 2018. When the PIN diode will be utilized in the simulated, i.e., in ON state then the resistance of lumped component will be 4.7Ω and in the OFF state the value of resistance will be $2 \text{ k}\Omega$. The value of the capacitance is 17 pF and has been chosen through PC recreations. The antenna is composed of a coupled fed meandered monopole antenna with an extended metallic branch for pattern . The extended metallic branch is connected and disconnected by using the PIN diode switch which changes the path for current flow thereby achieving pattern reconfigurability. When the PIN diode is 'ON', the metallic branch is activated and the current start flowing through it and pattern is shifted to the left. When the PIN diode is in 'OFF' state, the metallic branch is disconnected and the pattern is shifted to the right, i.e., at frequency 2.67 GHz in OFF state the main lobe magnitude of radiation pattern is 2.67 dB and in ON state the main lobe magnitude is 2.56 dB . So, the proposed antenna is showing pattern reconfigurability in Fig. 1.

3 Simulation Result

3.1 Return Loss (S11)

The return loss (S11) curve of the pattern reconfigurable multiple-input multiple-output antennas is appeared in Fig. 2. The return loss is the loss of power in signal returned by a discontinuity. Return loss (S11) curves show that the proposed antenna

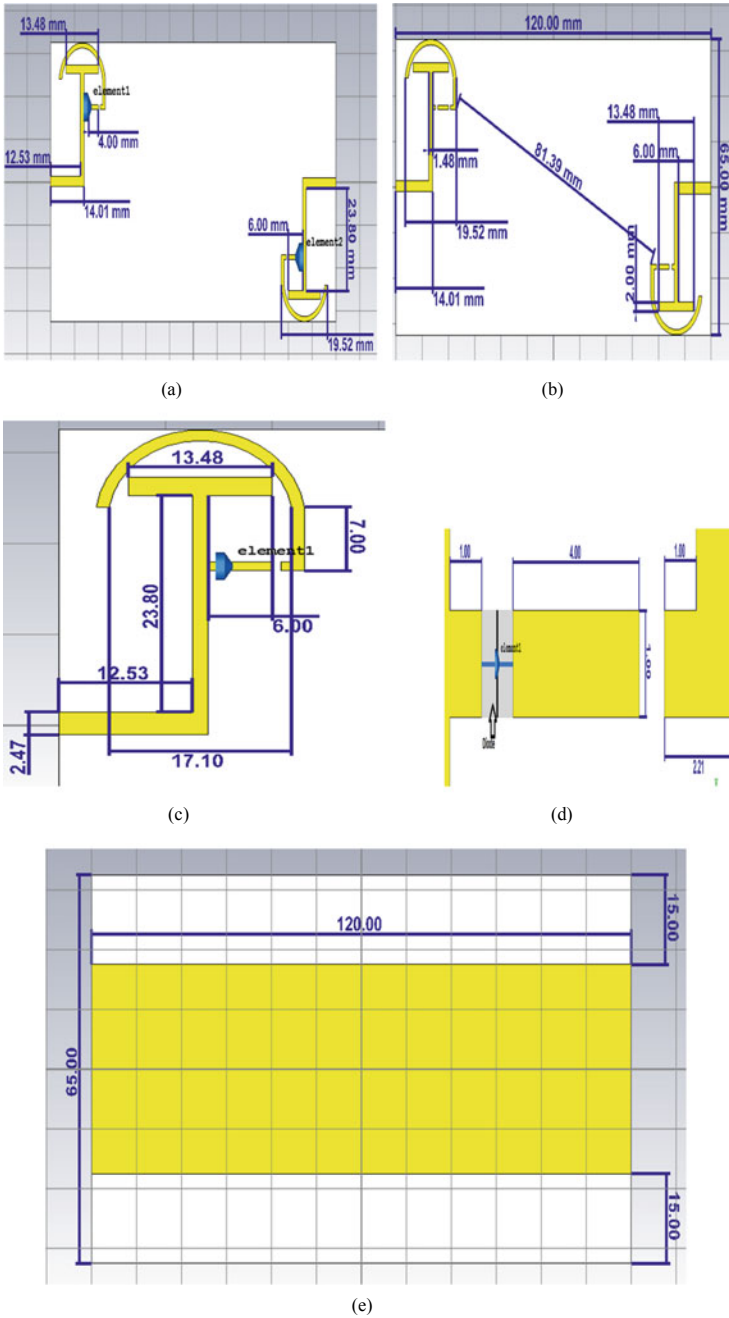


Fig. 1 Simulated model of proposed antenna [units: mm]. **a** Proposed antenna design in ON state **b** Proposed antenna design in OFF state **c** Enlarge view of single element **d** Enlarge view of metallic strip used **e** Back view

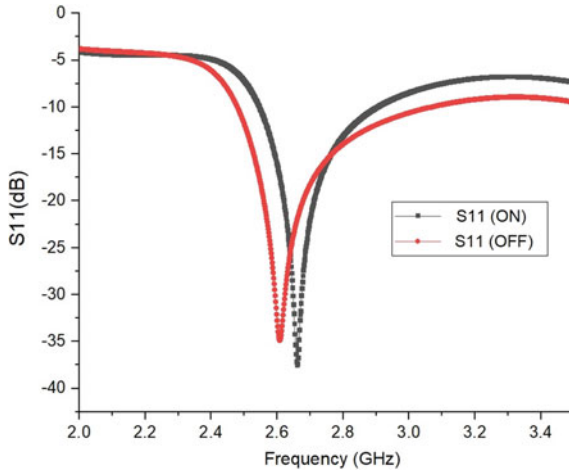


Fig. 2 Return loss of the proposed antennas (ON/OFF State)

shave return loss better than -10 dB in the frequency range of 2.48–3.06 GHz having bandwidth 580 MHz. Each antenna is thus capable to resonate at 2.67 GHz for LTE band number 7. The return loss is -37.7 dB at 2.67 GHz. According to simulated result of S11, S11 is changing very slightly when diode is ON/OFF but radiation pattern is changing [4].

3.2 Isolation (S_{21})

Isolation curve for proposed antenna is appeared in Fig. 3. The proposed antenna is showing isolation curve superior to -15 dB over the frequency band where antenna is working. The S_{21} parameter has -48.5 dB value at 2.67 GHz. This antenna is giving very high isolation comparison to other antenna.

3.2.1 2D Radiation Patterns and Result Discussion

Metal strip At frequency 2.52 GHz in OFF state, main lobe direction is -94.0° and angular width is 252.3° , and in ON state at 2.52 GHz, main lobe direction is -173.0° and angular width is 277.0° . At frequency 2.67 GHz in OFF state, main lobe direction is -97.0° and angular width is 192.1° and in ON state at same frequency main lobe direction is -164.0° and angular width is 87.9° . At frequency 2.83 GHz in OFF state main lobe direction is -114.0° and angular width is 226.1° and in ON state at same frequency main lobe direction is -159.0° and angular width is 78.9° . According to these results shown in 2D, pattern is changing at resonant frequency when diode (ON/OFF).

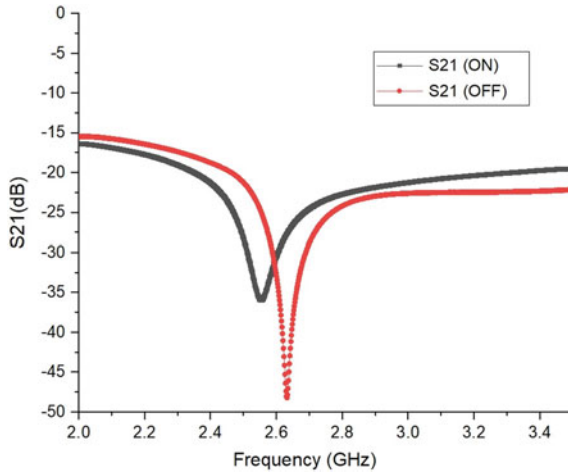


Fig. 3 Isolation curves for the proposed antenna

3.3 MIMO Performance

The simulated efficiencies with ECC and DG (diversity gain) of the proposed multiple-input multiple-output antenna at various frequencies are recorded in Table 1. Table 2 shows the gain of proposed antenna at various frequencies. The proposed antenna has the efficiency of 81% in ON state and 85% in OFF state, shown in Fig. (7). The simulated qualities confirm performance of the MIMO antenna. Envelope correlation coefficient (ECC) and diversity gain are most important parameters to evaluate the diversity performance of MIMO system. ECC explain correlation between two elements of antenna and simulated results are shown in Fig. (6). Ideal value of ECC should be less than 0.5. The ideal value of diversity gain should be 10 dB and simulated results shown in Fig. (5). From Table 1, we observed the ECC value of 0.007 and diversity gain 9.99 dB at 2.67 GHz. These simulated results prove good diversity performance of proposed reconfigurable antenna.

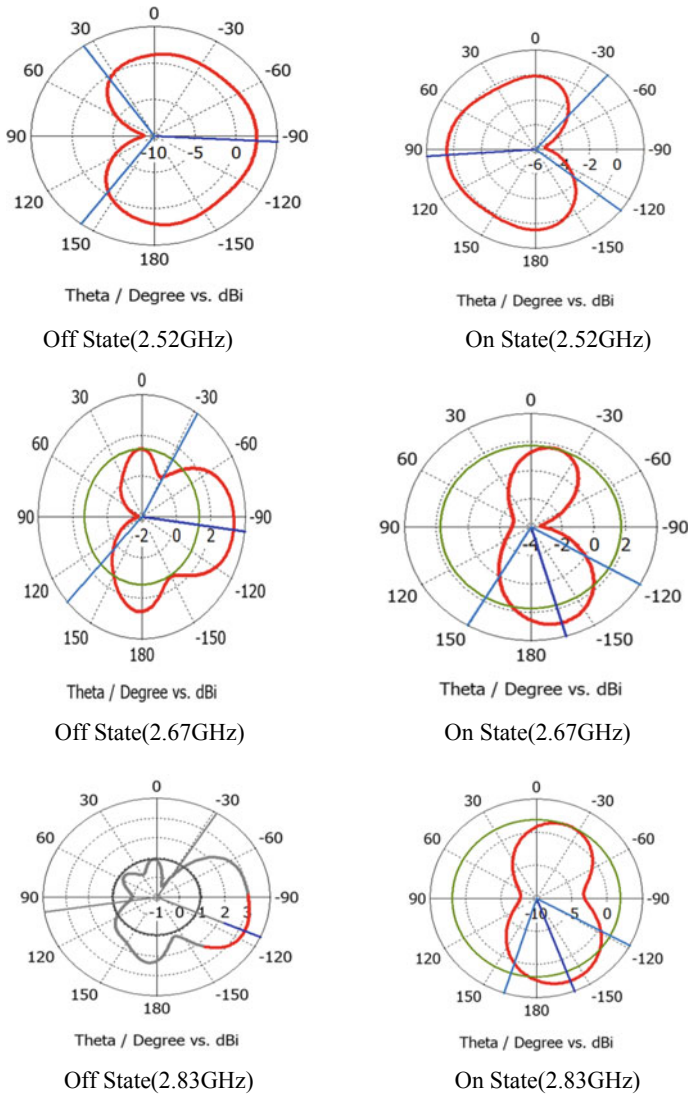


Fig. 4 Proposed antenna radiation patterns in x-z plane (2D)

4 Conclusion

A pattern reconfigurable MIMO antenna for LTE is introduced during this paper. The proposed antenna has centered frequency of 2.67 GHz. Every antenna is changing radiation pattern in frequency range of 2480–2830 MHz. The pattern reconfigurability of the antenna is accomplished by adding or subtracting the additional metal piece of $4 \times 1 \text{ mm}^2$ utilizing the PIN diode. The antenna is designed on a substrate

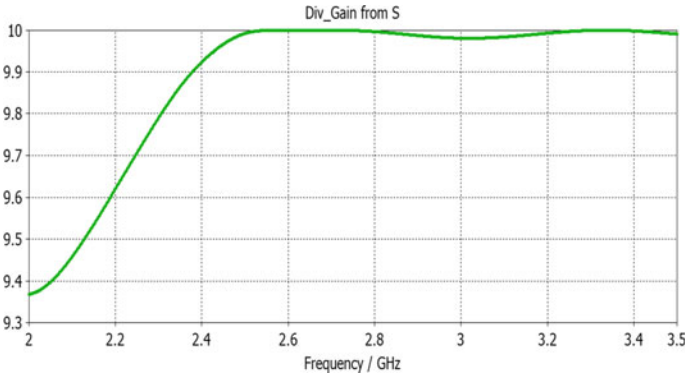


Fig. 5 Diversity gain curve for proposed antenna

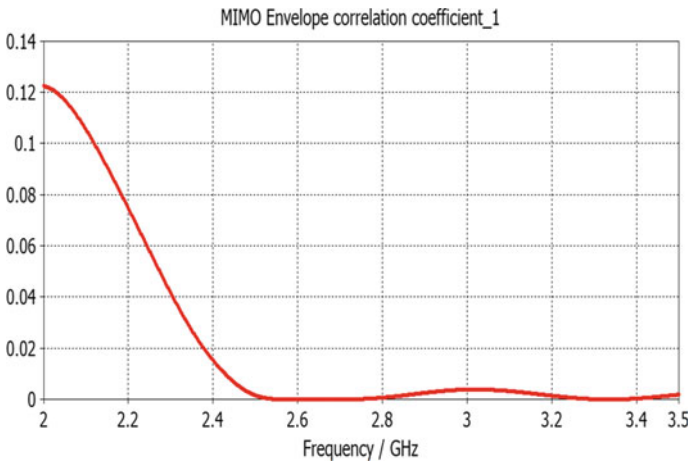


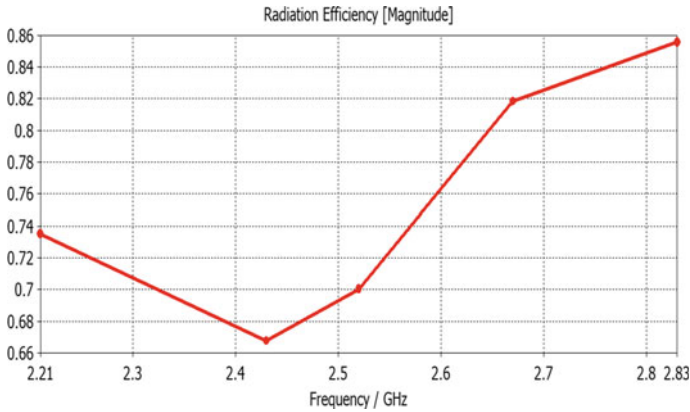
Fig. 6 ECC curve for proposed antenna

Table 1 Simulated efficiencies, diversity gain, and ECC of the proposed antennas

Frequency (GHz)	ON (Efficiency in %)	OFF (Efficiency in %)	Diversity Gain (dB)	ECC
2.48	73	72	9.98	0.002
2.55	78	78	9.99	0.005
2.67	81	85	9.99	0.007
2.71	86	85	9.99	0.007
2.83	88	87	9.99	0.001

Table 2 Stimulated gain

Frequency	Gain (ON)	Gain (OFF)
2.21	2.19	1.84
2.43	0.445	0.196
2.52	0.514	1.26
2.67	2.57	2.65
2.83	2.86	2.67

**Fig. 7** Radiation efficiency curve for proposed antenna

having volume $120 \times 65 \times 1.6 \text{ mm}^3$ every antenna having area of $26.5 \times 14.5 \text{ mm}^2$. The isolation curve shows that isolation is best than -37 dB in the frequency range where antenna is showing a good performance. The simulated result shows the maximum gain of 2.57 dBi and maximum efficiency of 85% . The envelope correlation coefficient does not exceed 0.02 across the complete operating band and proposed size of antenna can easily apply to hand held devices.

References

1. Shoaib S, Shoaib N, Shoaib I, Chen X (2017) Design and performance analysis of pattern reconfigurable MIMO antennas for mobile smartphones. *Microw Opt Technol Lett* 148–156
2. Panagamuwa CJ, Chauraya A, Vardaxoglou JC (2006) Frequency and beam reconfigurable antenna using photoconducting switches. *IEEE Trans Antennas Propag* 449–454
3. Lee JH, Sung Y (2012) A reconfigurable PIFA using a PIN-diode for LTE/GSM850/GSM900/DCS/PCS/UMTS. In: *Antennas and propagation society international symposium (APSURSI)*, pp 1–2
4. Ban Y-L, Chen Z-X, Chen Z, Kang K, Wei Li JL (2014) Decoupled closely-spaced hepta-band for WWAN/ LTE smartphone applications. *IEEE Trans Antennas Propag Lett* 13:31–34

5. Kumar Kishor K, Hum SV (2014) A pattern reconfigurable chassis mode MIMO antenna. *IEEE Trans Antennas Propag* 3290–3298
6. Qin P-Y, Jay Guo Y, Weily AR, Liang C-H, Senior Member IEEE (2012) A pattern reconfigurable U-slot antenna and its application in MIMO systems. *IEEE Trans Antennas Propag* 516–528
7. Sadeed Khan M, Capobianco AD, Asif Adnan Iftikhar SM, Braaten BD, Shubair RM (2016) A pattern reconfigurable printed patch antenna. In: *IEEE international symposium on antennas and propagation (APSURSI)*, pp 2149–2150
8. Li H, Lau BK, He S (2017) Design of closely packed pattern reconfigurable antenna array for MIMO terminals. *IEEE Trans Antennas Propag* 1–6
9. Selvam YP, Kangasabai M, Gulam Nabi Alsath M, Velan S, Kingsly S, Subbaraj S, Ramana Rao YV (2017) A low profile frequency and pattern reconfigurable antenna. *IEEE Antenna Wirel Propog Lett* 16:1–4
10. Singh DK, Kanaujia BK, Dwari S, Pandey GP (2018) Multi band multi polarized reconfigurable circularly polarized monopole antenna with simple biasing network. *Int J Electronic C (AEÜ)* 95:177–188
11. Singh DK, Kanaujia BK, Dwari S, Pandey GP, Kumar S (2016) Reconfigurable circularly polarized capacitive coupled microstrip antenna. *Int J Microw Wirel Technol* 9(4):843–850
12. Rhee C, Kim Y, Park T, Kwoun SS, Mun B, Lee B, Jung C (2014) Pattern-reconfigurable MIMO antenna for high isolation and low correlation. *IEEE Antennas Wirel Propag Lett* 13:1373–1376
13. Laafif K, Bouslama M, Gharsallah A (2017) Pattern reconfigurable antenna design for 5G mobile communication systems. In: *Mediterranean microwave symposium (MMS) IEEE*, pp 1–3
14. Trinh LH, Ferrero F, Staraj R, Ribero JM (2013) Mobile phone antenna for 2G, 3G and 4G standards. In: *International conference on advanced technologies for communications (ATC) IEEE*, pp 195–202
15. Vats M, Sachan S, Choudhary S, Mishra A, Shukla V (2019) Designing of band reject filter for radio astrophysics. In: *International conference on artificial intelligence: advances and application*, pp 91–100
16. Yang L, Lu C, Li X, Liu L, Yin X (2019) A horizontal azimuth pattern-reconfigurable antenna using omnidirectional microstrip arrays for WLAN application. *Int J Antennas Propag*

Implementation of Cyclic Reed–Muller Code for Molecular Communication



Ruchi Rai, S. Pratap Singh, M. Lakshmanan, and V. K. Pandey

Abstract Molecular communication (MC) is evolving as an innovative paradigm of communication, the application which ranges from military to biomedical and information theory to industry. Further, forward error correcting (FEC) codes control the faults in transmitted data over reliable or noisy channels of the MC system. Especially, FEC is the key method to expand transmission consistency. In our literature, cyclic Reed–Muller (C-RM) is presented to improve the performance of molecular nanocommunication (MNC). However, the VLSI implementation of C-RM is missing from the literature. So, this paper fills the gap by presenting the VLSI implementation of C-RM to improve the performance MC system. In particular, this paper processes the design and implementation of the encoder and decoder logic circuit using the CMOS logic circuit. In addition, power consumption and delay are presented. The performance of the circuit is verified through simulations using 250 nm CMOS technology in the Tanner EDA Tool.

Keywords Channel coding · FEC · MC · Noise · C-RM

R. Rai · V. K. Pandey
Noida Institute of Engineering and Technology, Greater Noida, India
e-mail: ruchirai1000@gmail.com

V. K. Pandey
e-mail: vijaygpandey@yahoo.com

S. Pratap Singh · M. Lakshmanan (✉)
Galgotias College of Engineering and Technology, Greater Noida, India
e-mail: tmlakshmanan@gmail.com

S. Pratap Singh
e-mail: drsprataps@gmail.com

1 Introduction

Molecular communication (MC) allows nanomachines to communicate over short distances (tens of micrometers) using molecules as a communication carrier [1]. Molecular communication (MC) is evolving as a novel paradigm of communication, the application which ranges from military to biomedical and information theory to industry. In a communication process applying error correction codes (ECCs) are a rapid method of reducing many errors that are caused due to noise and packet loss [2]. For enhancing the overall performance of the molecular communication system, the authors presented the Hamming code [3–5]. The result clearly shows that the Hamming code improves the performance of the MC, but work additionally considers energy costs related to the implementation of the encoding and decoding methods.

In [6], a new coding distance function is introduced for enhancing the reliability of diffusion-based molecular communication system over Hamming distance named as molecular coding distance function (MoCo). Self-orthogonal convolutional code (SOCC) with the majority logic process had been projected in the DMC scheme, and the performance of the system is compared with the Hamming code [7]. The result affirmed the novel coding technique has the largest coding gain and as well as the shortest critical distance over the hamming code.

In [8], authors proposed the Reed–Solomon (RS) code that is used as an error recovery tool to expand the consistency of transmitted data inside the diffusion-based communication system. An analytical expression is derived for the BEP of the DMC system, to count the overall performance improvement due to RS code. The bit error probability of the projected device with R-S codes can be progressed by rising the lowest distance of the codeword. ISI-free code in addition to their bit error rate (BER) approximations had been introduced for the diffusion-based molecular communication system [9]. The result associated with the uncoded system and novel ISI-free code offers better performance with judiciously low complexity for the DMC scheme. In [10], investigation and comparison among all proposed error-correcting codes based on their complication and error-correcting capability. C-RM and RS are used to expand BER and coding gain as well as EG-LDPC and Hamming codes are used for improving energy cost. Except for these codes, a new code is presented because of the high existence of inter-symbol interference among dissimilar codewords named ISI-free code. In [11], RS encoder/decoder is designed as well as its functionality are verified on FPGA. Low-density parity check and Bose, Chaudhuri, and Hocquenghen (BCH) both are error-correcting code, implemented on FPGA for finding power and area [12]. Result shows that LDPC code had less and power low area than BCH.

Reed–Muller codes are simple linear block codes, and RM codes are simply decoded with majority logic gate. Evaluating channel coding methods for MC systems, authors introduce how the Reed–Muller (RM) is converted as cyclic code to demonstrate that the C-RM codes are a subgroup of BCH [13]. C-RM code is used to increase the reliability of the transmitted data. This code is also compared

with the Hamming code. C-RM code is simply encoded/decoded with shift register and ML decoding technique. The key benefit of the above codes is from the viewpoint of energy cost, coding gain, and critical distance. In the literature, we found that C-RM outperforms over the other error-correcting code. However, the VLSI implementation of C-RM is missing from the literature. So, this paper fills the gap by presenting the VLSI implementation of C-RM to improve the performance MC system, which includes the design and implementation of encoder and decoder logic circuits using CMOS. Specifically, power consumption and delay are presented. Simulation is performed in the Tanner EDA Tool.

The rest of the paper is systematized as follows:- Section 2 defines the “FEC” for molecular communication. Section 3 describes the simulated results of C-RM logic circuits on the Tanner EDA Tool. Section 4 describes the conclusion.

2 Error Correction Code for MC: Cyclic Reed–Muller (C-RM)

Error correction is the procedure of finding errors from transmitted data in addition to recreated authentic error-free data. Error correction procedures are both the “Backward Error Correction” and the “Forward Error Correction.” In BEC, once the error is discovered, receiver appeals to the sender to transmit the whole data unit. On the other hand, receiver uses error correction code which routinely modifies error in FEC. In this paper, we use the C-RM code which is part of the forward error-correcting code.

With several error correction abilities, Reed–Muller codes are part of binary code. How they are constructed as cyclic code is discussed in [13]. The C-RM code is denoted as C-RM (j, m) with a block length $N_R = 2^m - 1$, besides, the minimum distance $D_{Rmin} = 2^{m-j} - 1$ [13] exist for any integer $m \geq 2$ and $0 \leq j < m - 1$. The message length K_R is calculated as:

$$K_R = 1 + \binom{m}{1} + \binom{m}{2} + \dots + \binom{m}{j} = N_R - \sum_{z=1}^{m-j-1} \binom{m}{z} \quad (1)$$

Figure 1a shows the encoder of C-RM code, and non-systematic encoder of C-RM code can be formed by using shift registers and two-input XOR gates. Shift register and XOR gate are formed by the CMOS logic circuit. For calculating the parity bit, two-input XOR gate is used. The two-input XOR gate is reliant on the generator polynomial of each code. Generator polynomial for C-RM (1, 3) code is $g_{(1,3)} = x^3 + x + 1$.

Figure 1b shows the decoder of C-RM (1, 3) code which can be simply decoded with a simple shift registers and two-step ML method. The four-input XOR gate is used as an input for the majority logic method. In this paper, we formed two-input MLG by using two two-input NAND gate, as well as for forming six-input MLG

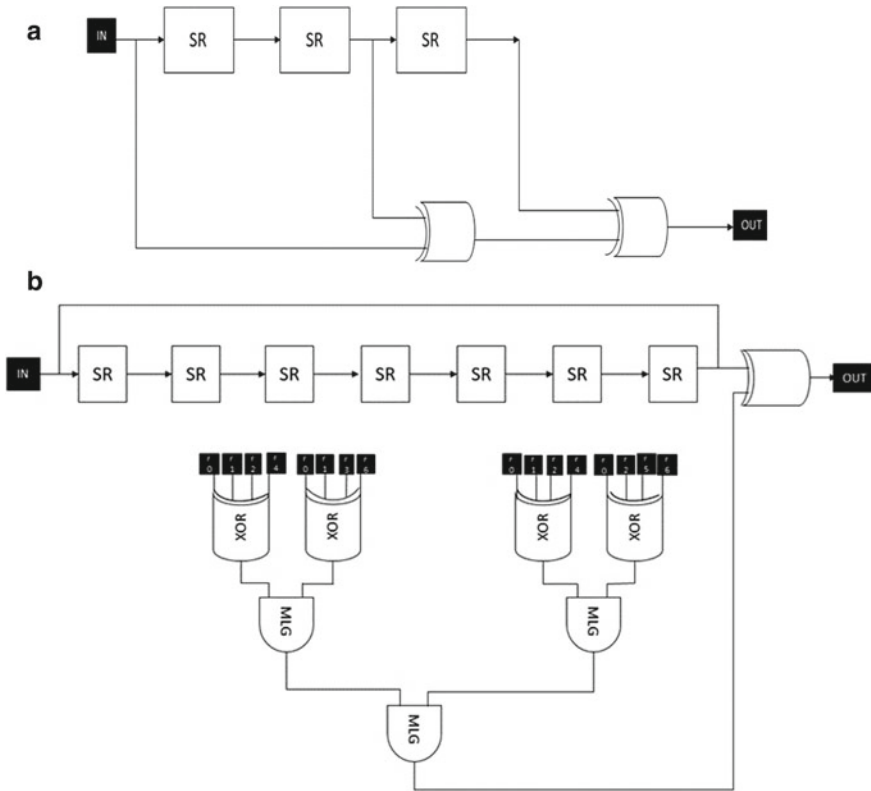


Fig. 1 a Non-systematic encoder circuit of C-RM (1, 3) [13]. b A Dual-step ML decoder circuit for C-RM (1, 3) code [13]

we can use 22 NAND gate. In this paper, we consider two-input MLG is used in C-RM (1, 3) as shown in Fig. 2. The four-input XOR gates used in the dual-step majority logic decoding method can be got with the amalgamation of several dual-input XOR gate and the number of inputs in the XOR gate can be reliant on the check polynomial. Check polynomial for C-RM is $h_{(C-RM)(1,3)} = x^4 + x^2 + x + 1$.

MLG is formed by using two NAND gates. A NAND gate used in this paper is formed by using CMOS which can be simulated on the Tanner EDA Tool. The function of the majority logic gate (MLG) includes two cases: when the majority of the inputs are 1, then the output of the MLG is 1, otherwise 0.

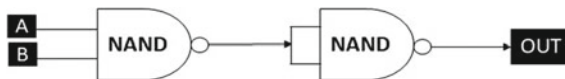


Fig. 2 Two inputs (MLG) circuit

3 Simulation Result

In this section, we have described the simulation result of the C-RM encoder and decoder. Figures [3] and [4] show that the schematic diagram and simulation result of encoder and decoder for C-RM (1, 3) codes are designed and simulated using 250 nm technology in Tanner EDA Tool first time for finding the power consumption and delay. We take a 5 V power supply for all the circuits which are used in C-RM encoder and decoder. The schematic layout of the C-RM encoder and decoder is performed in S-Edit. The simulation of C-RM encoder and decoder is with low power strategies which are executed at 250 nm technology, in T-Spice. The waveform is done in W-Edit.

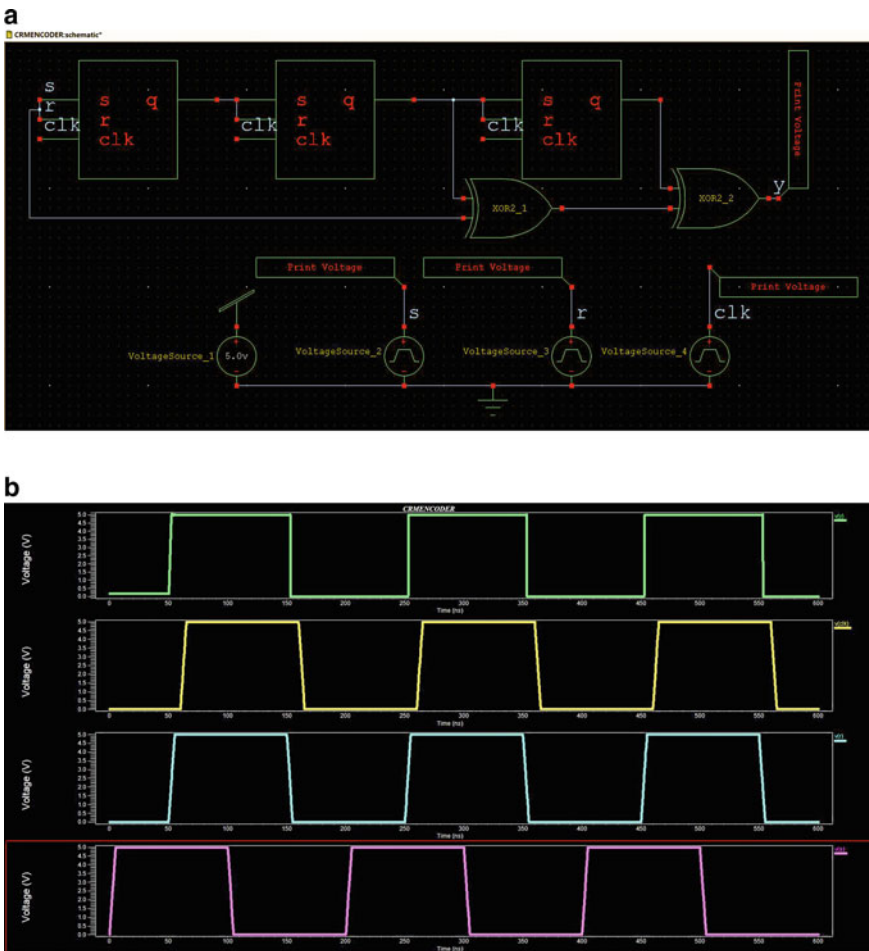


Fig. 3 a Schematic diagram of the non-systematic encoder. b Simulation result of an encoder for 5 V Vdd

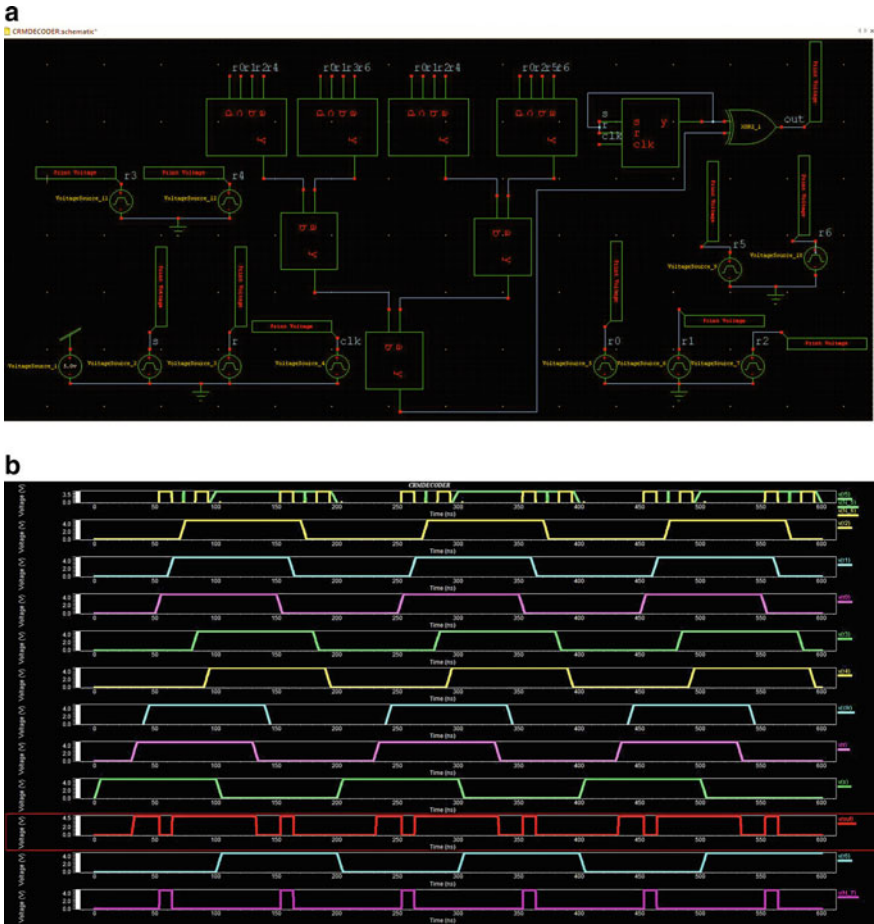


Fig. 4 a Schematic diagram of a decoder. b Simulation result of decoder for 5 V Vdd

C-RM code is simply encoded through a simple shift register. In this work, each shift register is formed by using Set-Reset flip-flop, and also individually SR flip-flop is formed by using CMOS logic. XOR gate which is used herein is also formed by using CMOS logic. XOR gate in C-RM encoder is used for calculating the parity check bits. Encoder with a shift register and XOR gate is designed and simulated using 250 nm technology on Tanner EDA. 5 V power supply is used for the C-RM encoder.

C-RM codes are simply decoded with the majority logic decoding technique. Two-input majority logic gates are formed by two two-input NAND gate, and NAND gate is formed by using CMOS logic. Decoder with SR flip-flop, XOR gate, and two input MLG is designed and simulated using 250 nm technology on Tanner EDA. 5 V

Table 1 Power and delay of encoder and decoder

C-RM	Power (W)	Delay (S)
Encoder	4.1084e-003	4.8729e-008
Decoder	6.7779e-002	2.9000e-008

power supply is used for the C-RM decoder. Power and delay of C-RM encoder and decoder with proposed MLG is given in Table 1.

4 Conclusions

In this paper, for first time, C-RM encoder and decoder is designed and simulated using 250 nm technology in Tanner EDA Tool. All the circuits are simulated using CMOS logic. In addition, power and delay are presented. It is noticeable that the C-RM code is proposed in the literature to recover the workability inside molecular communication system. However, as per our best knowledge no one of the literature has implemented in any of the VLSI tool. So, this paper fills the gap by presenting C-RM implementation in Tanner EDA Tool. Application-specific integrated circuit (ASIC) implementation can be the future scope of this work.

References

1. Hiyama S, Moritani Y, Suda T, Egashira R, Enomoto A, Moore M, Nakano T (2006) Molecular communication. *J Inst Electron Inf Commun Eng* 89(2):162
2. Blahut RE (2003). In: Algebraic codes for data transmission. Cambridge University Press
3. Lu Y, Higgins MD, Lesson MS (2014) Diffusion based molecular communication system enhancement using high order hamming codes. In: 9th international symposium on communication systems, networks & digital sign (CSNDSP), pp 438–442
4. Lesson MS, Higgins MD (2012) Error correction coding for molecular communication. In: IEEE international conference on communications (ICC), pp 6172–6176
5. Lesson MS, Higgins MD (2012) Forward error correction for molecular communication. *Nano Commun Netw* 3(3):161–167
6. Ko PY, Lee YC, Yeh PC, Lee CH, Chen KC (2012) A new paradigm for channel coding in diffusion-based molecular communications: molecular coding distance function. In: IEEE global communications conference (GLOBECOM), pp 3748–3753
7. Lu Y, Higgins MD, Lesson MS (2015) Self-orthogonal convolutional codes (SOCCs) for diffusion-based molecular communication systems. In: IEEE international conference on communications (ICC), pp 1049–1053
8. Dissanayake MB, Deng Y, Nallanathan A, Ekanayake EMN, Elkashlan M (2017) Reed Solomon codes for molecular communication with a full absorption receiver. *IEEE Commun Lett* 21(6):1245–1248
9. Shih PJ, Lee CH, Yeh PC, Chen KC (2013) Channel codes for reliability enhancement in molecular communication. *IEEE J Sel Areas Commun* 31(12):857–867

10. Darya AM, Vakani H, Nasir Q (2019) Error control codes for molecular communication channels: a survey. In: The international conference on communications, signal processing, and their applications (ICCSPA), pp 1–4
11. Parvathi P, Prasad PR (2015) FPGA based design and implementation of Reed-Solomon encoder & decoder for error detection and correction. In: Conference on power, control, communication, and computational technologies for sustainable growth (PCCCTSG), pp 261–266
12. Muthammal R, Madhane SSR (2013) Design, analysis, and FPGA implementation LDPC codes with BCH codes. In: International conference on current trends in engineering and technology (ICCTET), pp 242–244
13. Lu Y, Higgins MD, Lesson MS (2015) Comparison of channel coding schemes for molecular communication systems. *IEEE Trans Commun* 63(11):3991–4001

Design of Cascaded H-Bridge Multilevel Inverter



Nitin Pawar, Vijay Kumar Tayal, and Pallavi Choudekar

Abstract Multilevel inverters have been widely used in many applications for improving quality of output voltage and reduce harmonics content in AC output voltage. This paper presents single-phase CHB multilevel inverter design with sinusoidal pulse width modulation (SPWM) technique. This paper represents analysis of three-, five-, and seven-level cascaded H-bridge multilevel inverter (CHMLI) with minimum no. of power switching devices. Due to a smaller number of switches, switching loss is reduced and cost of the inverter is also reduced. Work has been carried out in MATLAB.

Keywords Multilevel inverter(MLI) · Cascaded H-bridge(CHB) · Sinusoidal pulse width modulation (SPWM)

1 Introduction

Inverter is a system that is used to generate AC output from a DC input. Multilevel inverter is an equipment which uses various low DC voltages as input to achieve optimal alternating voltage at the output. In multilevel inverter, the output voltage is generated at high frequency and with low switching frequency with low distortions. Different multilevel inverters are: cascaded H-bridge inverter (CHB), flying capacitor inverter (FC), and diode clamped inverter (DC). This work is related to study different topologies of CHB inverter and compare their performances [1–4]. In CHB inverter, only switches are used. This topology needs fewer switches compared with flying capacitor multilevel inverter. The arrangement of switches together with voltage

N. Pawar (✉) · V. K. Tayal · P. Choudekar
Amity University, Noida, UP, India
e-mail: nitinp91@gmail.com

V. K. Tayal
e-mail: vktayal@amity.edu

P. Choudekar
e-mail: pachoudekar@amity.edu

source is termed as H-bridge cell. H-bridge cell supplies three separate voltages, i.e., zero, positive DC, and negative DC voltages [5–8]. Each H-bridge cell has a different DC source in the inverter. Inverter is assigned a defined DC input voltage and by changing the on and off periods of switches we can obtain regulated AC output voltage. Different pulse width modulation techniques are single, multiple, and sinusoidal pulse width modulation. In this work, we use the sinusoidal PWM (SPWM) method to obtain controlled AC output voltage [9, 10]. In SPWM technique, we compared sinusoidal sample wave with a triangle carrier wave. Modulation signal used is sinusoidal and modulating signal peak is smaller than peak of carrier signal; gate signal for switches can be formed by SPWM technique [11, 12]. In previous years, multilevel inverters have been extensively used in high power applications and high voltage applications. Voltage waveform obtained at output of cascaded H-bridge multilevel inverter (CHMLI) is staircase type and it appears as a sinusoidal waveform. As compared to bipolar inverter, output voltage of multilevel inverter has less harmonics content [13–15].

Advantages of multilevel inverters are mentioned below [16–18]:

1. It is operated at high voltage.
2. Efficiency is higher than simple bipolar inverter.
3. Low electromagnetic interferences.
4. Less distorted sinusoidal output voltage.

Figure 1 shows various types of multilevel inverters (MLI). Simulation of cascaded H-bridge multilevel inverter (CHMLI) had been done in MATLAB and results and waveforms are presented in the paper [19].

Figure 2 represents the block diagram for the implementation for the multilevel inverter.

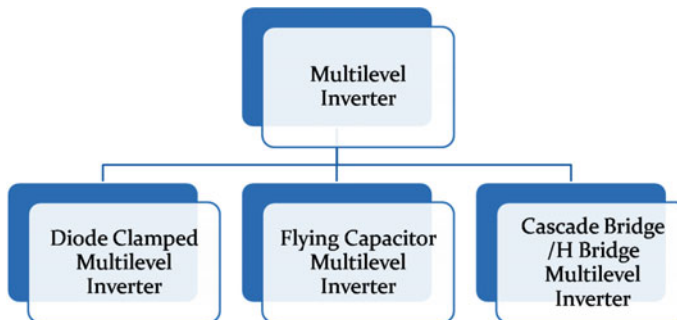


Fig. 1 Types of multilevel inverter (MLI)

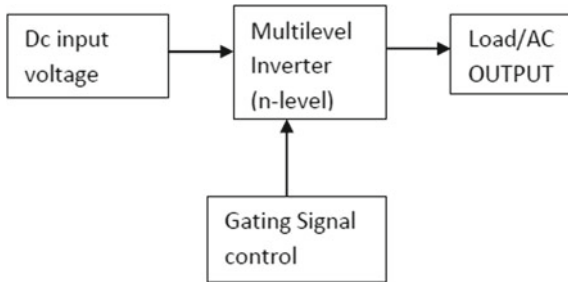


Fig. 2 Multilevel inverter block diagram

2 Modeling of CHB Multilevel Inverter

Multilevel inverters are most important devices in power electronics. Out of all categories of multilevel inverters discussed in Sect. 1, cascaded H-bridge (CHB) multilevel inverters are extensively used due to its numerous advantages and simplicity. Pulse width modulation (PWM) technique has been used for obtaining improved quality of output voltage and current waveform. Due to some limitations of two-level inverters, multilevel inverters are designed which can be used for high-power applications [8].

For n -level CHB multilevel inverter, there are $m = (n - 1)/2$ H-bridge cell required. Every H-bridge cell contains four switching devices and every H-bridge cell requires a separate DC source. Assume V_a, V_b, V_c, \dots is the voltage at the output of every H-bridge cell, then the total voltage V for n -level cascaded H-bridge is given by $V = V_a + V_b + V_c + V_d$ For n -level CHB inverter, the quantity of switches needed is $4m$ where m denotes number of H-bridge cell. Different dc source required in CHB inverter is m .

2.1 Three-Level CHB Multilevel Inverter

Figure 3 shows schematic of three-level multilevel inverter with four switching devices.

Figure 4 shows modeling of three-level CHB inverter with RL load.

2.2 Five-Level CHB Multilevel Inverter (CHBMLI)

Figure 5 shows schematic of five-level multilevel inverter with eight switching devices.

Figure 6 shows modeling of five-level CHB inverter (CHBMLI) with RL load.

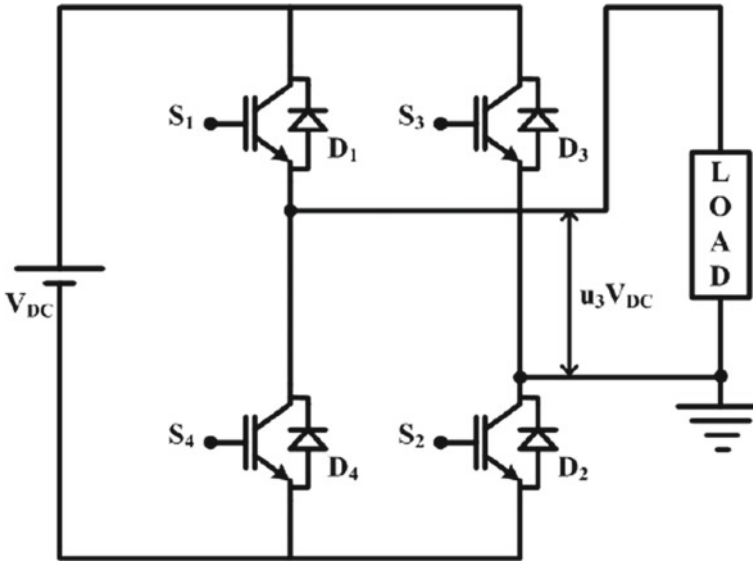


Fig. 3 Schematic of three-level multilevel inverter

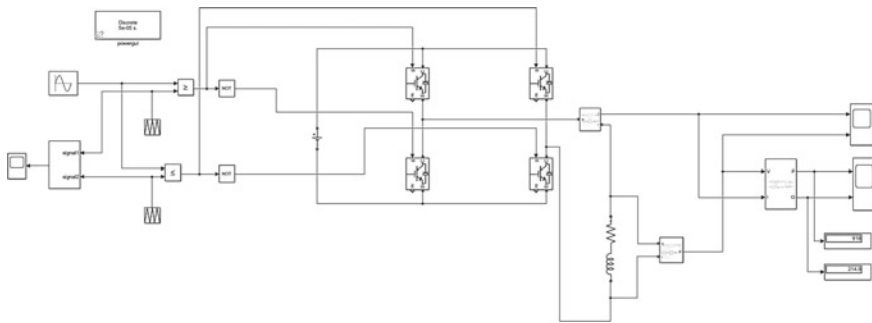


Fig. 4 Model of three-level CHB inverter

2.3 Seven-Level CHB Multilevel Inverter (CHBMLI)

Figure 7 shows schematic of seven-level multilevel inverter with 12 switching devices.

Figure 8 shows modeling of seven-level CHB inverter with RL load.

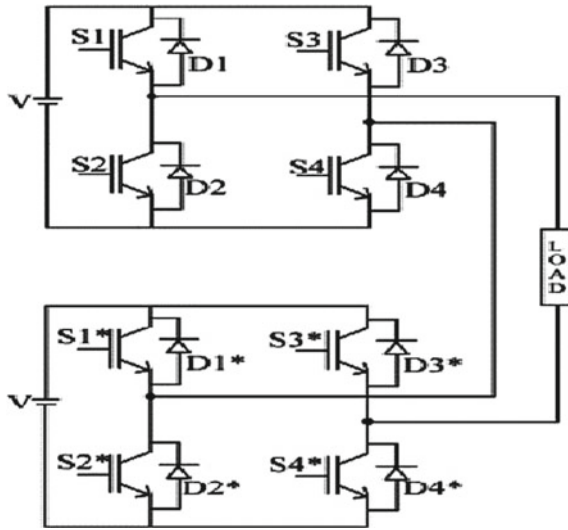


Fig. 5 Schematic of five-level multilevel inverter (CHBMLI)

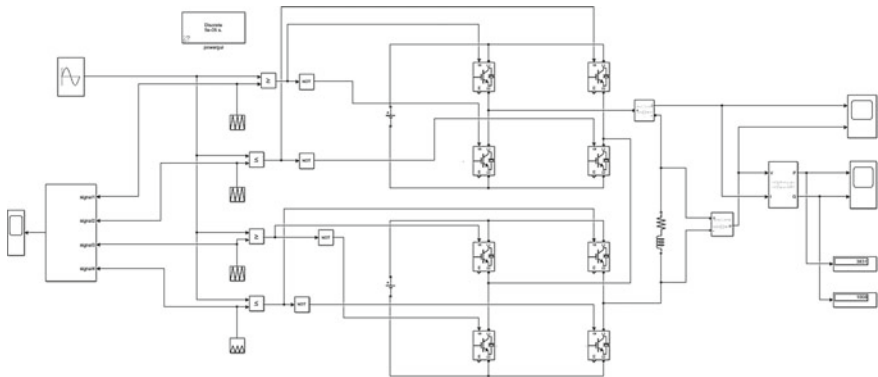


Fig. 6 Model of five-level CHB ML inverter

3 Simulation Results and Discussions

Figures 9, 10, and 11 show simulation results for three-level CHB multilevel inverter.

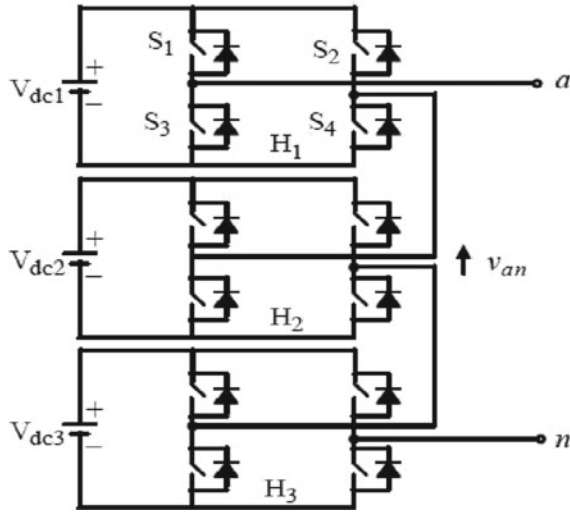


Fig. 7 Schematic of seven-level multilevel inverter (CHBMLI)

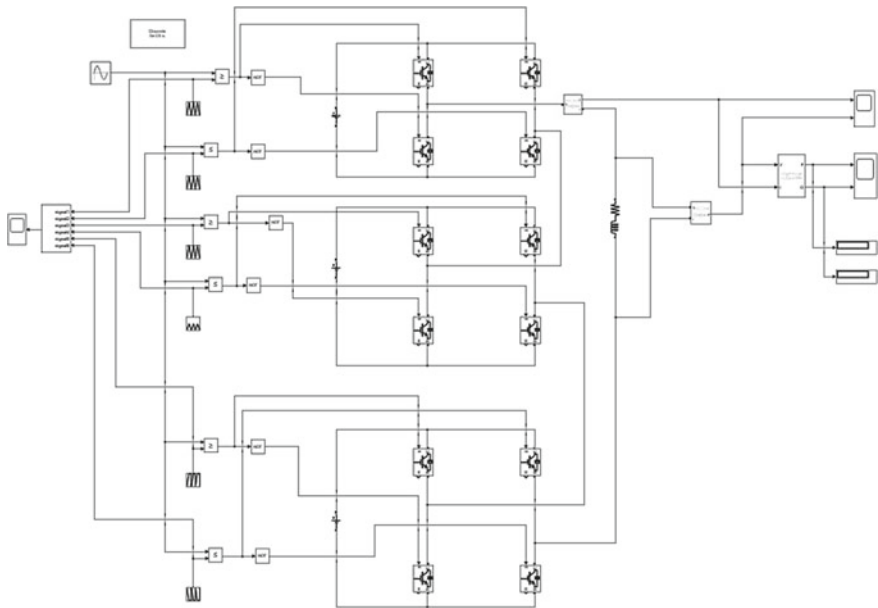


Fig. 8 Model of seven-level CHB inverter (CHBMLI)

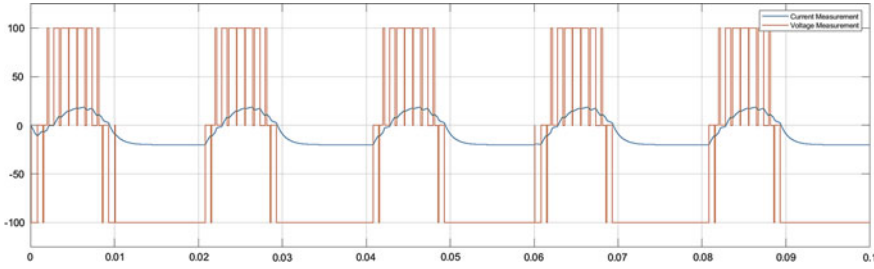


Fig. 9 Output current and voltage waveform

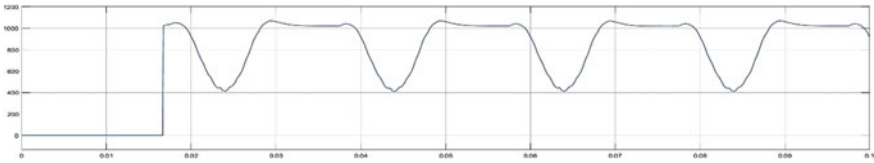


Fig. 10 Active power waveform

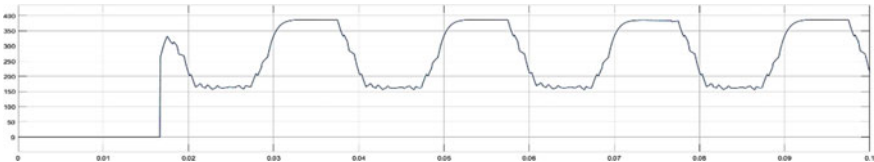


Fig. 11 Waveform of reactive power

3.1 Single-Phase Three-Level CHB Inverter

In single-phase three-level CHB inverter with inductive load, current lags inductive voltage. RMS value of current and voltage waveform is 16.14 A and 89.89 V, respectively. Active and reactive power waveform values are 918 W and 214.9 VAR, respectively. The PF of the load is 0.63 and phase angle is 50.74° .

3.2 Single-Phase Five-Level CHB ML Inverter

Figures 12, 13, and 14 show simulation results for five-level CHB multilevel inverter (CHBMLI).

In single-phase five-level CHB inverter with inductive load, current lags inductive voltage. RMS value of current and voltage waveform is 27.05 A and 146.70 V,

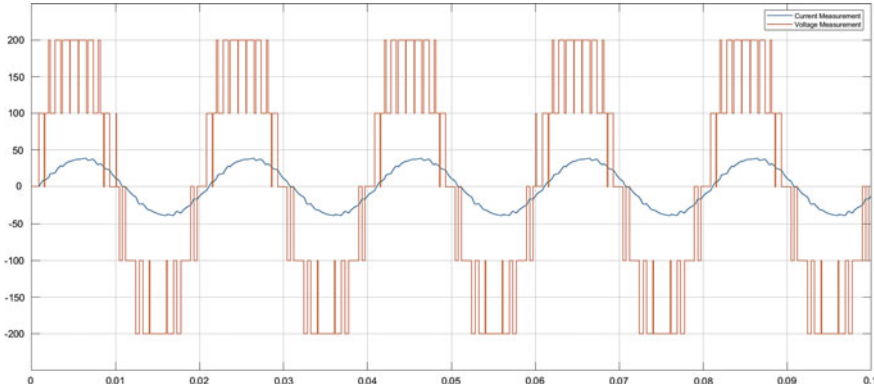


Fig. 12 Waveform of output current and voltage

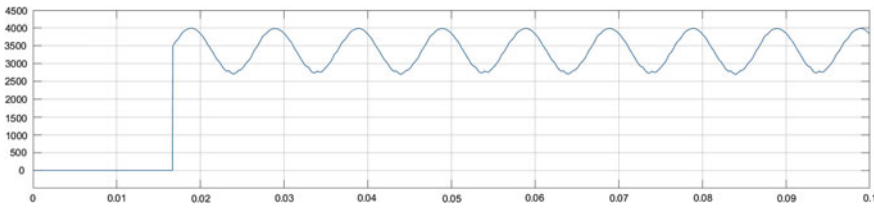


Fig. 13 Waveform of active power

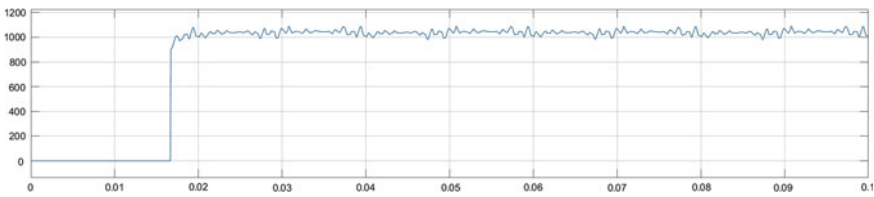


Fig. 14 Waveform of reactive power

respectively. Active and reactive power waveform values are 3831 W and 1008 VAR, respectively. The PF of the load is 0.965 and phase angle is 15.11° .

3.3 Single-Phase Seven-Level CHB Multilevel Inverter (CHBMLI)

Figures 15, 16, and 17 show simulation results for seven-level CHB multilevel inverter.

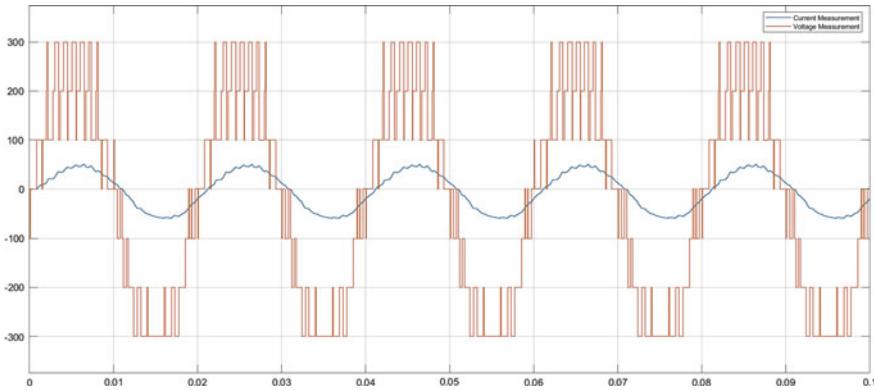


Fig. 15 Waveform of output current and voltage

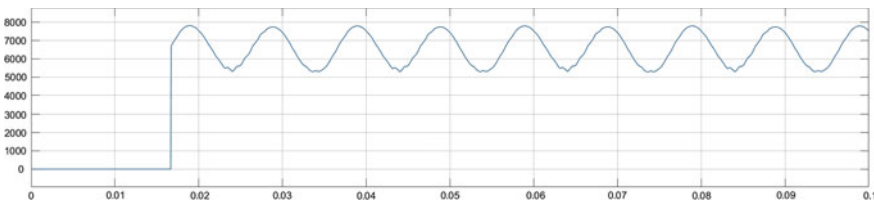


Fig. 16 Waveform of active power

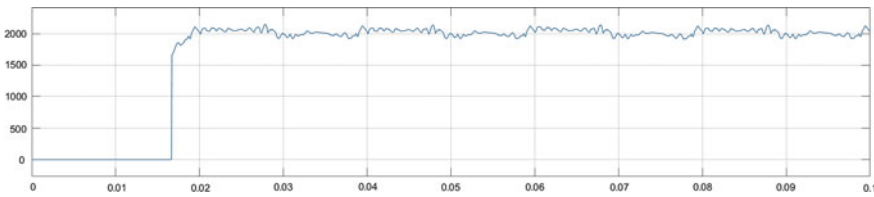


Fig. 17 Waveform of reactive power

In single-phase seven-level CHB inverter with inductive load, current lags inductive voltage. RMS value of current and voltage waveform is 38.11 A and 206.6 V, respectively. Active and reactive power waveform values are 7519 W and 2031 VAR, respectively. The PF of the load is 5 and phase angle is 17.259°.

From Fig. 18, it is clear that as levels of multilevel inverter increase, power output also increases.

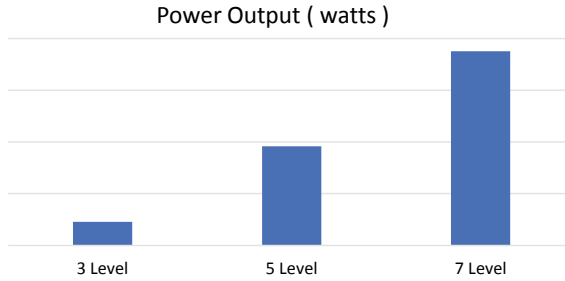


Fig. 18 Power output at various levels

4 Conclusion

Single-phase three-, five-, and seven-level CHB multilevel inverters are modeled with MATLAB–Simulink. With the rise in level of inverter, the stepped voltage waveform at output is getting close to sinusoidal voltage waveform pattern. It is observed that power factor of load improves with increase of levels of inverter, hence it is concluded that higher levels of CHB multilevel inverter show better performance as compared to lower levels of multilevel inverters. It is also observed that noise in the output side of inverter is decreased with increase in levels of CHB multilevel inverter, hence it is concluded that for DC to AC conversion higher level CHB inverter should be preferred to get sinusoidal voltage waveform.

References

1. Jayabalan M, Jeevarathinam B, Sandirasegarane T (2017) Reduced switch count pulse width modulated multilevel inverter. *IET Power Electron* 10(1):10–17
2. Azli NA, Choong YC (2006) Analysis on the performance of a three-phase cascaded H-bridge multilevel inverter. In: *Int Power Energy Conference PE Con*, pp 28–29
3. Rodriguez J, Lai J-S, Peng FZ (2002) Multilevel inverters: a survey of topologies, controls and applications. *IEEE Trans Ind Electron* 49(4):724–738
4. Holinezhad JG, Noroozian R (2012) Application of cascaded H-bridge multilevel inverter in DTC-SVM based induction motor drive, pp 46–59
5. Malinowaski M, Gopakumar K, Rodriguez J, Perez M (2005) A survey on cascaded multilevel inverters, pp 23–43
6. Babaei E, Laali S, Bayat Z (2015) A single phase cascaded multilevel inverter based on a new basic unit with reduced number of power switches, pp 28–36
7. Gobinath K, Mahendran S, Gnanambal I (2013) New cascaded H-bridge multilevel inverter with improved efficiency. *Int J Adv Res Electr Electron Instrum Eng* 2(4):54–78
8. Kuriakose M, Anooja VS (2014) Comparison of performances of switched DC sources inverter and cascaded H-bridge Inverter. *Int J Sci Eng Technol Res* 3(9)
9. Kavithal M, Arunkumar A, Gokulnath N, Arun S (2016) New cascaded H-bridge multilevel inverter topology with reduced number of switches and sources, pp 52–69
10. Peng FZ, Lai JS, Rodriguez J (2002) Multilevel inverters: a survey of topologies, controls, and applications. *Ind Electron IEEE Trans* 49(4):724–738

11. Khomfoi S, Tolbert LM (2007) Multilevel power converters. Power electronics handbook, 2nd edn. Elsevier, ISBN 978-0-12- 088479-7, Chapter 17, pp 451–482
12. Holmes DG, McGrath BP (2002) Multicarrier PWM strategies for multilevel inverters. *Ind Electron IEEE Trans* 49(4):858–867
13. Villanueva E, Correa P, Rodriguez J, Pacas M (2009) Control of a single-phase cascaded H-bridge multilevel inverter for grid-connected photovoltaic systems. *IEEE Trans Ind Electron* 56(11):4399–4406. <https://doi.org/10.1109/TIE.2009.2029579>
14. Daher S, Schmid J, Antunes F (2008) Multilevel inverter topologies for stand-alone PV systems. *IEEE Trans Ind Electron* 55(7):2703–2712
15. Rodriguez J, Lai J-S, Peng FZ (2002) Multilevel inverters: a survey of topologies controls and applications. *IEEE Trans Ind Electron* 49(4):724–738
16. Busquets-Monge S, Robolet J, Rodriguez P, Alepuz S, Bordonau J (2008) Multilevel diode-clamped converter for photovoltaic generators with independent voltage control of each solar array. *IEEE Trans Ind Electron* 55(7):2713–2723
17. Calais M, Agelidis V (1998) Multilevel converters for single-phase grid connected photovoltaic systems: an overview. *Proc IEEE ISIE* 1:224–229
18. Ertl H, Kolar J, Zach F (2002) A novel multicell DCAC converter for applications in renewable energy systems. *IEEE Trans Ind Electron* 49(5):1048–1057
19. Alonso O, Sanchis P, Gubia E, Marroyo L (2003) Cascaded H-bridge multilevel converter for grid connected photovoltaic generators with independent maximum power point tracking of each solar array. *Proc 34th Annu IEEE PESC* 2:731–735

Reliability and Energy Efficiency of Ring Frame Machine in Textile Industries: Secure, Smart, and Reliable Network



Saurabh Kumar Rajput, Sulochana Wadhvani, and Jay Singh

Abstract Improving energy efficiency is a kind of energy generation, so it also raises the per capita energy consumption. This research study is based on data collection from textile industry and identifies the scope of energy conservation in ring frame machine network. Energy savings in a selected textile industry are calculated on annual basis and a simple approach is developed for energy conservation. This study focuses to secure a smart, energy efficient, and reliable network for ring frame three-phase induction motor which is other than the conventional methods of energy savings used by Indian textile sectors.

Keywords Textile industry · Ring frame machine · Energy efficiency · Smart and reliable network

1 Introduction

In India, textile sector plays a very important role for employment generation. Presently, it is providing employment to about 35 million people, which are second largest after agriculture. Textile sector also has an impact on the economic development of country and out of total industrial production, textile industry contributes about 14% with 4% contribution in GDP and 17% contribution in earnings from exports. Indian textile sector is second in the world after china in terms of installed number of spindles (19.6%) [1]. The energy requirements of textile industries are increasing day by day because of the two main reasons. First reason is the dusty and

S. K. Rajput (✉) · S. Wadhvani
Department of Electrical Engineering, M.I.T.S, Gwalior, MP, India
e-mail: saurabh9march@gmail.com

S. Wadhvani
e-mail: sulochana_wadhvani@mitsgwalior.in

J. Singh
Department of Electrical and Electronics Engineering, GL Bajaj Institute of Technology and Management, Greater Noida, UP, India
e-mail: jaysinghism@gmail.com

© Springer Nature Singapore Pte Ltd. 2021
R. Agrawal et al. (eds.), *Advances in Smart Communication and Imaging Systems*,
Lecture Notes in Electrical Engineering 721,
https://doi.org/10.1007/978-981-15-9938-5_61

noisy environment of the mill, due to which the workers do not take interest in working with textile mills and the managements are forced to use automated machineries to compensate the shortage of workers. These modern machines require more energy for their operation. Second reason is the inefficient operation of machineries in textile industry [2]. Also, the high energy demand is increasing the concentration of greenhouse gases, which create an adverse effect on environment. The spinning textile mill mainly produces thread from cotton, where ring frame machine uses maximum part (about 37%) of total electricity. Rest of the electricity is used by open end machines, blow room, carding, drawing, combing roving, and winding [3]. The energy management is the requirement of textile industries for reducing the energy wastage and to save the environment. There are many energy conservation practices which are commonly used in Indian textile mills; spinning process include the use of automatic power factor correction capacitor bank, energy efficient motors, and synthetic flat belts in ring frames machines. Weaving process includes the use of flat belt drive instead of V-belt drives, efficient H plant fans and reduction in wastage of compressed air. Processing in Indian textile industries includes the reutilization of waste water in dyeing process [4]. Energy consumption in textile industry is high but the reduction in wastage of energy is possible through different energy conservation methodologies [5–9]. Three-phase-type induction principle-based motor is used in ring frame process of textile mills. The efficiency of this motor can be improved by proper time-to-time required testing and by providing sophisticated rewinding to the motor [10–12]. By load management and energy audits, energy should be conserved in textile mills. This is helpful in finding economic growth as well as energy efficiency [13, 14]. Figure 1 shows that the spinning process takes the highest amount of energy so there is a great opportunity of energy saving through improving the network of ring frame machine.

The present study is based on the data collection from textile industry analyzing it for improving energy efficiency of ring frame machine. In this study, some other possibilities of energy savings in ring frame machine of textile industries are investigated and that are analyzed for the selected spinning mill. These possibilities

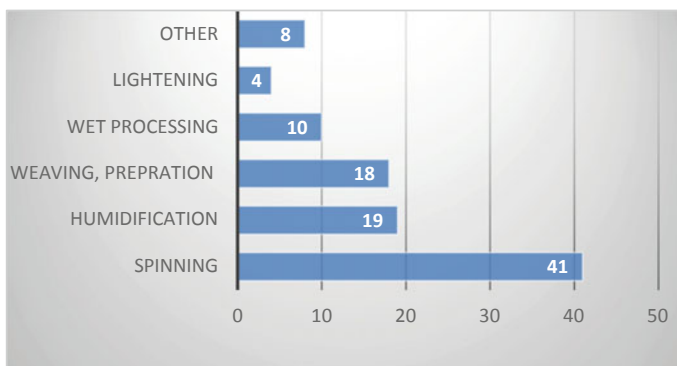


Fig. 1 Percentage breakup of electrical power in textile sector

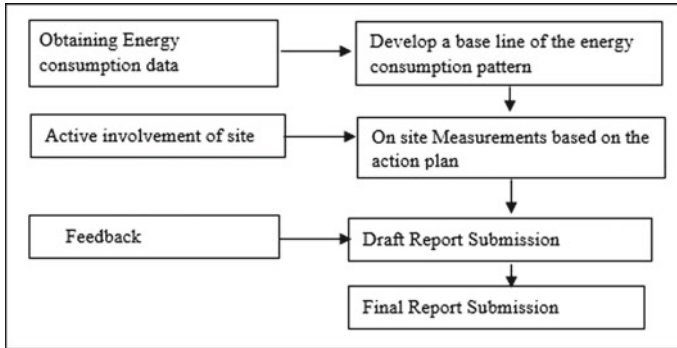


Fig. 2 Methodology for secure, smart, and reliable network of ring frame machine

include—energy saving by optimizing ring frame suction tube size and replacement of the faulty suction tube of autoconer with small diameter caps for energy conservation. In addition to this, few studies are also performed for improvements in already applied energy conservation techniques, and electrical energy savings in the industry is calculated. These studies are replacement of faulty motors by new and energy efficient motor.

2 Secure, Smart, and Reliable Network for Ring Frame Machine in Textile Industries

For secure, smart, and reliable network for ring frame machine, a methodology is developed. As shown in Fig. 2, the first step includes the development of a base line for energy consumption pattern which is followed by the energy consumption data collection. Further on site measurement of data is covered. Finally, a report is generated and submitted for improving energy efficiency.

3 Reliability and Energy Efficiency of Ring Frame Machine in Textile Industries

An energy audit is performed in an Indian textile industry and possibilities are found where the energy can be saved other than the conventional methods of energy savings.

3.1 Size Selection of Suction Tube in Ring Frame Machine for Energy Saving

During study, it has been observed that plant is using different size suction tubes in the same ring frame machine. Suction tube size affects the power consumption as well as suction pressure. It is important to ensure proper sized and similar suction tubes are installed on the machine. A study was conducted to quantify the power saving by optimizing suction tube size on ring frame machine. Following are the details of study. The pressure (Pa) and power (kW) on ring frame machine are measured which have 9 mm suction tube. The pressure on the 2nd, 251th, and 501th spindle of the machine was 353 Pa, 489 Pa, and 1153 Pa, respectively, and the total power consumption was 5.10 kW. The study was repeated on the ring frame machine which has 7 and 8 mm suction tube. In this case, the pressure on the 2nd, 251th, and 501th spindle of the machine was 421 Pa, 551 Pa, and 1196 Pa, respectively, and the total power consumption was 5.00 kW. Finally, the test was performed on the ring frame machine which has 5 mm suction tube and measured the pressure on same 2nd, 251th, and 501th spindle, now the results was 591 Pa, 781 Pa, and 1351 Pa, respectively, and the total power consumption was 4.20 kW. So by optimizing the suction tube size, there is scope of energy saving and in the present study, energy up to 1, 32,475 kWh can be saved per year in one machine.

3.2 Replacing Faulty Suction Tube of Autoconer and Using Optimum Size Caps

The mill is using Variable speed drives (VSD) on autoconer suction fan. VSD are running at more than 50 Hz frequency. Purpose of installing VSD on suction fan is to save power on part load operation of suction and frequency of 60 Hz. The same autoconer machine has suction of 41 mbar with power consumption of 3.3 kW at 50 Hz and has suction of 38 mbar with power consumption of 3.1 kW and frequency 48 Hz. It was clear from the above data that due to higher pressure drop across the machine, pressure of the suction fan is kept high. Subsequently, frequency of the VSD has been increased, that is leading to higher power consumption. Two major sources of pressure drop were identified during the study, one was the broken cover (top) of autoconer suction tubes and another was bigger size of suction tube cover (diameter). Hence, it is suggested to replace the broken caps of suction tubes and use smaller diameter suction tube caps to prevent pressure drop across the machine. Higher counts require bigger diameter of suction tube caps; hence one machine may be selected for higher counts (≥ 12 's count) and equipped with bigger diameter caps. In our audit study, the above practice lead to the saving of 22.90 kW at autoconer suction fan; which is annual power saving of 1, 89,275 kWh.

Table 1 Daily working condition of motor in plant

Working condition			
Loading (%)	50	75	100
Power (kW)	15	22	30
Operating hours per day	8	14	1

Table 2 Variation of efficiencies of motors with loading

30 kW motor	Loading (%)	50	75	100
Old motor	Efficiency (%)	85.5	86.7	84.8
Energy efficient motor	Efficiency (%)	93.8	94.1	92.9

3.3 Use of Energy Efficient Ring Frame Motors

The plant is using inefficient motors which are consuming more power. The plant has a 30 kW, 90% efficiency old IE2 (international efficiency 2) motor in ring frame. This motor can be replaced by an energy efficient IE3 (international efficiency 3) motors with ratings: 30 kW, 94% efficiency. The motor is four pole, three phase, 400 V, 50 Hz, 30 kW, which is operating for about 23 h per day and 360 days per year. Motor loading profile is as follows (Table 1).

The efficiencies of faulty motor and new motor are checked at various loading conditions as per the plant operation profile. The measured efficiencies at different loading is as follows (Table 2).

By considering the load profile and daily working hours, the annual energy demand of the above mentioned two motors are calculated. The energy demand of old motor is 191,151.43 kWh/annum, while the energy demand of new energy efficient motor is 175,512.93 kWh/annum so the energy saving is 15,638.49 kWh/annum/motor. So it is suggested to replace all the old and inefficient motors by new and efficient motors for energy saving.

4 Results and Conclusion

Increasing demand of energy in textile industries and price hiking are the two main factors which are responsible for high production cost. To reduce this cost, energy conservation is essentially required by textile industries. There are many energy conservation practices which are being implemented by industries. These techniques are either costly or require technical support. Because most of the textile mills in India, are small and medium enterprises so they have limited resources to support these methodologies (Table 3).

During energy audit visits of several textile industries, some simple methodologies of energy savings are investigated and verified. By applying these techniques,

Table 3 Electrical energy audit results

Description	Potential savings
Size selection of suction tubes in ring frame machine	1,32,480 kWh in one machine
Replacing the faulty suction tube of autoconer and optimizing diameter	1,89,280 kWh/year
Use of energy efficient ring frame motor	15,638.49 kWh/year/motor

ample amount of energy can be saved with less investments hence these are also cost effective.

Energy savings by above-said methodologies are not fixed but vary with the size of plant, its operational practices, and duration of operations per day. Therefore, in every individual textile industry, the research should continue on the basis of economic measures and plant's output product quality.

Acknowledgements The authors acknowledge to NPIU and AICTE, New Delhi for providing the support under Collaborative Research Scheme (CRS) projects of TEQIP III.

Authors are also thankful to Er. Vikas Sharma (Accredited Energy Auditor) of NITRA Ghaziabad, India for his guidance and support.

References

1. New energy and industrial technology development organization: a report on national survey on implementation of energy efficiency improvement technologies in textile sector (2009)
2. Dhayaneswaran Y, Ashokkumar L (2013) A study on energy conservation in textile industry. *J Inst Eng India Ser B* 94:53–60
3. Hasanbeigi A (2010) Energy-efficiency improvement opportunities for the textile industry. Ernest orlando lawrence berkeley national laboratory
4. Khude P (2017) A review on energy management in textile industry. *Innov Ener Res* 6
5. Goyal S (2011) Energy conservation in textile industry. Lambert Academic Publishing
6. Bhaskar M, Verma P, Kumar A (2013) Indian textile industries towards energy efficiency movement. *Int J Environ Sci Develop Monit (IJESDM)* 4:36–39
7. Hong G-B, Su T-L, Lee J-D, Hsu T-C, Chen H-W (2010) Energy conservation potential in Taiwanese textile industry. *Energy policy* 38:7048–7053
8. Hasanbeigi A, Price L (2012) A review of energy use and energy efficiency technologies for the textile industry. *Renew Sustain Energy Rev* 16:3648–3665
9. Koc E, Kaplan E (2007) An investigation on energy consumption in yarn production with special reference to ring spinning. *FIBRES TEXTILES in Eastern Europe* 15:18–24
10. Rajput SK, Singh O (2017) Energy audit in textile industry: a study with ring frame motor. *ICCCCM- 2nd IEEE Int Conf Control Comput Commun Mater*, 2–5
11. Rajput SK, Godhar P (2015) AC motors burn out in textile industry—causes and impact on motor performance. In: 56th joint technological conference SITRA, Coimbatore
12. Rajput SK, Rani P, Sadhu Pk, Sadhu M, Das N (2018) Energy conservation in textile industries by replacing rewound motors—an energy audit study. In: *Int Conf Power Energy Environ Intell Control (PEEIC)*, Greater Noida, India, pp 820–824

13. Muhammad IY, Muhammad DZ, Tahir S, Rizv H (2018) Design and development of energy audit and load management system. Bahria Uni J Inf Commun Technol 11(II)
14. Balachander K, Amudha A (2019) Energy saving measures in textile mill. Int J Innovative Technol Exploring Engg (IJITEE) 8(8), ISSN:2278-3075

Economic Load Dispatch Using Evolutionary Technique



Rohit Kumar, Nidhi Singh, M. A. Ansari, and Santosh Kumar Yadav

Abstract This paper basically presents the use of evolutionary technique for economic scheduling problems. Various evolutionary techniques like genetic algorithm (GA), particle swarm optimization (PSO) and ant colony optimization (ACO) have been implemented to solve problems of economic scheduling in which the objective function (i.e., fuel cost) is stochastic, non-differentiable and nonlinear. The effectiveness of the techniques has been performed on a test system consisting of six generation units considering the losses (i.e., transmission losses) and satisfying all its constraints. They have been compared individually with respect to each other on the basis of power allocation and convergence rate.

Keywords Economic load dispatch · Objective of ELD · Transmission losses · Genetic algorithm · ACO · PSO · Fitness function · Constraints

1 Introduction

One of the most significant issues that need to be tackled in a power system is its economic operation and is done by using economic scheduling [1]. Before doing economic scheduling, one has to do “unit commitment” which gives the scheduled of generating units that must be kept ON/OFF in the course so that load demand is satisfied all the time. Then, after that, we proceed for economic scheduling and is defined as “the sharing of the load (i.e., total load) among various units that are in a

R. Kumar (✉) · N. Singh · M. A. Ansari · S. K. Yadav
Department of Electrical Engineering, Gautam Buddha University, Greater Noida 201308, India
e-mail: rohitkumarhu@gmail.com

N. Singh
e-mail: nidhi@gbu.ac.in

M. A. Ansari
e-mail: ma.ansari@gbu.ac.in

S. K. Yadav
e-mail: santosh.ky97@gmail.com

state of ON position in such a way that the overall cost of the system (i.e., generation cost) is minimum.” The allocation is done on the basis of constraints (i.e., equality and inequality) [2]. In order to meet particular demand/load, large interconnections of the electric networks reduce the fuel consumption [3]. In load flow solutions, we have to specify all generator buses except one generator bus, i.e., slack bus, but in economic scheduling, the generations are not fixed. We have to specify the limits of generations in order to meet the required demand/load with minimal consumption of fuel [4]. By this, we conclude that the economic scheduling problem is needed as the solution of a large number of load flow problems and picking one can be the optimal solution in cost of generation.

In this paper, various evolutionary techniques like GA, ACO, PSO, etc., have been implemented so as to get the optimal generation from units with the lowest generation cost considering power transmission losses. Transmission loss coefficients are obtained using power system MATLAB toolbox. These techniques have been performed with the proposed algorithm and being compared with one another so as to get minimal fuel cost (optimal cost of generation).

The following algorithm of different techniques has been implemented by MATLAB R2018a software version. The results obtained are compared so as to get optimal cost of generation.

2 Operating Cost of Thermal (Coal) Plant

Fuel cost, generators efficiency and transmission losses are the factors that are responsible for power generation at minimum cost.

It is not mandatory that the most efficient generator in the system guarantees minimum cost as the location is such that where the fuel cost is high.

The characteristics of generating units are as follows.

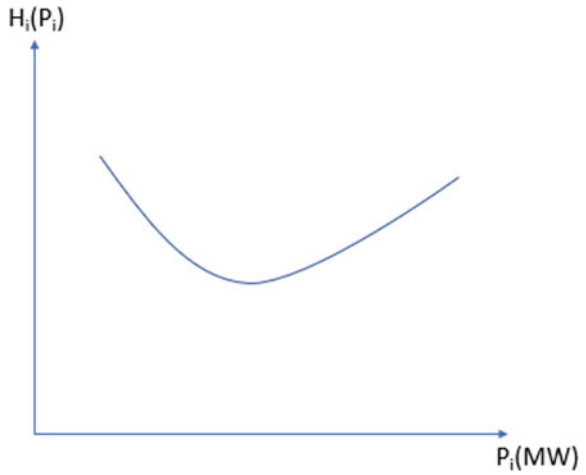
2.1 Heat Rate Curve

It is represented as:

$$H_i(P_i) = \left(\frac{\alpha}{P_i} + \beta + \gamma P_i \right) \text{Mcal/MW h} \quad (1)$$

- For the generator’s MW output, the thermal energy required per MW h is referred to be as the heat rate curve. Thus, it signifies the efficiency of the unit over its range of operation (Fig. 1).

Fig. 1 Heat rate curve



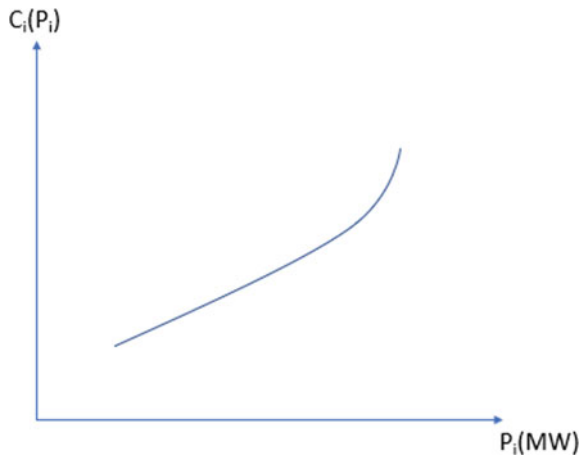
2.2 Fuel Cost Curve

It is represented as:

$$C_i(P_i) = (\alpha + \beta P_i + \gamma P_i^2) \text{ ₹/h} \tag{2}$$

- When the heat rate curve gets multiplied by fuel cost, then it is referred as a fuel cost curve.
- This curve tells us that as the power generated increases, correspondingly, the fuel cost also increases (Fig. 2).

Fig. 2 Fuel cost curve



2.3 Incremental Fuel Cost Curve

It is represented as:

$$IC(P_i) = \frac{dC_i(P_i)}{dP_i} \tag{4}$$

$$IC_i(P_i) = (\beta + 2\gamma P_i) \text{ ₹/MW h} \tag{5}$$

- The unit is the increment in the cost of the unit corresponding to 1 MW increment in the output of unit which is referred as an incremental cost (Fig. 3).

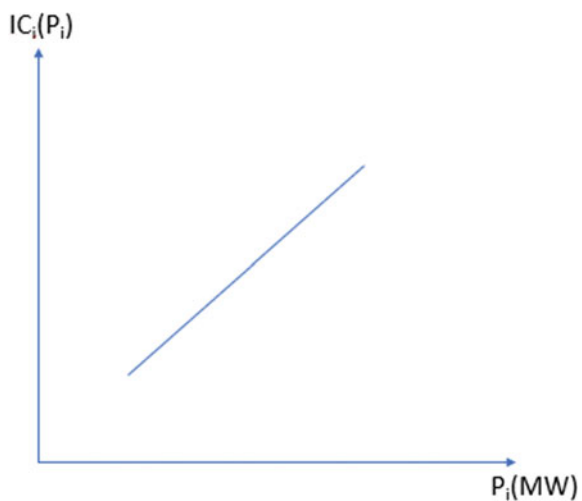
3 Objective of ELD

The objective of ELD or economic scheduling problem is to find out the optimal solution of power generation that minimizes the total generation cost, while satisfying its constraints (i.e., equality and inequality constraints). Mathematically, the cost function (fuel cost) or objective funcⁿ to be minimized is given as below:

$$C_i(P_i) = (\alpha + \beta P_i + \gamma P_i^2) \text{ ₹/h} \tag{6}$$

where α, β, γ (fuel cost coefficients) of i th generator subjected to the constraints are given below.

Fig. 3 Incremental fuel cost curve



3.1 Equality Constraint (Energy Balance Equation)

The total power generated is equal to the summation of power demand (P_D) and the transmission losses. Energy balance eqⁿ with losses (i.e., transmission losses) is given in equation below as:

$$\sum_{i=1}^n P_i - P_D - P_L = 0 \quad (7)$$

(Loss are considered)

The above eqⁿ describes that the total generation is equal to the summation of power demand and the losses during the transmission.

3.2 Inequality Constraint (Generating Capacity Limit Constraints)

Each unit should have generating output in b/w its max^m and min^m limits. Inequality constraints (boundary condⁿ) are given below as

$$P_{i \min} \leq P_i \leq P_{i \max} \quad (8)$$

With the help of Bloss-coefficient or B-coefficient method, the transmission losses can be calculated in order to achieve the economic load dispatch problem.

4 Genetic Algorithm

Genetic algorithm is an evolutionary technique which is used to find an optimal cost of generation. It was developed by John Holland. Genetic algorithm is stochastic in nature. It is inspired by Darwin's theory about evolution [5]. Both types of constrained as well as unconstrained optimization problems can be solved with the help of this technique based on natural selection. It is basically calculated using fitness value [6]. It encodes "select the best and discard the rest," i.e., the fittest individual is selected for evaluation and rest other are neglected so as to find optimal solution.

The algorithm repeatedly modifies a population by using random numbers in the form of binary strings. From these populations, the fittest parent is selected and over repeated generations, the generated population evolves over an optimal desired solution. It can also be used for nonlinear constraint problems [7]. For this, we require three very important parameters that are:

- Selection;
- Crossover;
- Mutation.

4.1 Selection

In this, we have to select individuals from their parent population whose probability is proportional to their fitness using roulette wheel.

4.2 Crossover

The new individuals are generated combining the characteristics of the fittest parents which are selected by a fitness value using roulette wheel. This can be done in three ways:

a. Single point:

$$P1 = [i\ j\ k\ l\ m\ n\ o\ p] \quad P2 = [1\ 2\ 3\ 4\ 5\ 6\ 7\ 8]$$

$$\text{Child} = [i\ j\ k\ 4\ 5\ 6\ 7\ 8]$$

b. Two point:

$$P1 = [i\ j\ k\ l\ m\ n\ o\ p] \quad P2 = [1\ 2\ 3\ 4\ 5\ 6\ 7\ 8]$$

$$\text{Child} = [i\ j\ k\ 4\ 5\ 7\ o\ p]$$

c. Scattered:

$$P1 = [i\ j\ k\ l\ m\ n\ o\ p] \quad P2 = [1\ 2\ 3\ 4\ 5\ 6\ 7\ 8]$$

If binary strings = [1 0 0 1 1 0 0 1]

$$\text{Child} = [i\ 2\ 3\ 1\ m\ 6\ 7\ p]$$

4.3 Mutation

Genetic diversification is provided by mutation operator and is used to search over a broader space for genetic algorithm. It is generally used in range of 0.01.

5 Genetic Algorithm for ELD

In genetic algorithm optimization technique, the following steps are considered:

Initialization of population, generation using random numbers, evolution of fitness function and creating new offsprings by using GA operator such as selection, crossover and mutation [8].

For maximization problem, the fitness function is taken as

$$f(X) = F(X) \quad (9)$$

and for minimization problem, the fitness function is given

$$f(X) = \frac{1}{F(X)} \quad (10)$$

where $f(X)$ denotes the fitness function and $F(X)$ describes the objective function [9].

Step 1: Initialization of population

Specify all the parameters of GA and then initialize the population size using random number generator in the form of binary strings, time limit and maximum generation and read the cost coefficients of the generating units.

Step 2: Formulation of problem

The initial population for each generator is formed by

$$P_{g_i}^j = P_{g_i}^{\min} + \left\{ \left(P_{g_i}^{\max} - P_{g_i}^{\min} \right) / (2^j - 1) \right\} * b_1^j \quad (11)$$

where g_i = number of generator and j = no of generation

Step 3: Fitness function

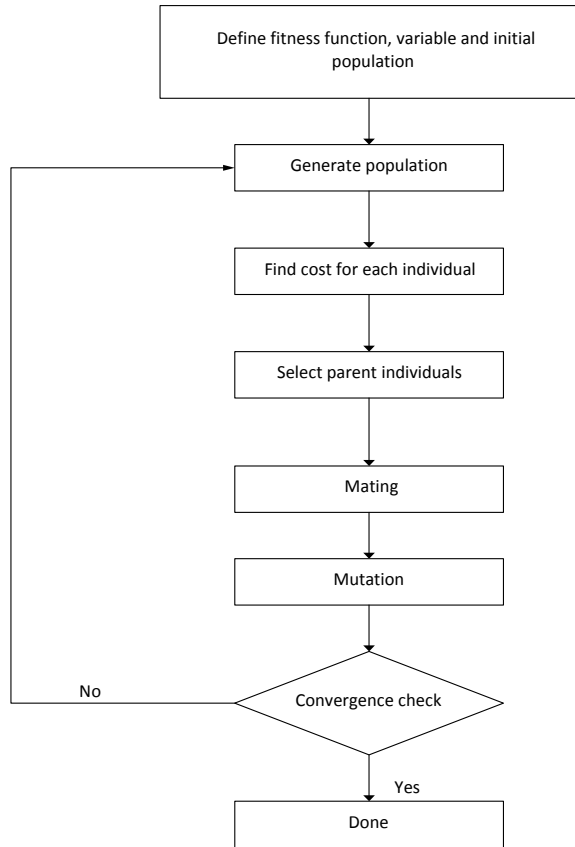
Calculate maximum and average fitness function of population strings.

Step 4: Reproduce

Select the parent using roulette wheel selection method and perform different operators like crossover and mutation.

Step 5: Exit

Repeat the above steps until the desired result is obtained (Fig. 4).

Fig. 4 Flow diagram of GA

6 Ant Colony Optimization (ACO)

ACO also known as ant colony optimization was developed by Dorigo [10]. It is also a stochastic searching algorithm. It is based on the real behavior of ants, i.e., how they are able to find the shortest path from food source to their nest. By a study, we came to know that a chemical matter/substance, called as pheromone trail by the ants on the surface when they do movement [11]. Higher the level of pheromone trail means, the way/path which ants have chosen is shortest. This is the basic principle which is used in ACO algorithm for optimization of ELD problem.

Let us take an example which will explain the real behavior of ants, i.e., how they move in search of food from their nest via shortest path.

In Fig. 5, the real behavior of ants has been shown. Let us suppose that the food source is referred as A, and on a straight line, nest is taken as E. In Fig. 5b and c, the path at B is blocked by an obstacle appearing. In Fig. 5a, ants are moving on a straight line from nest to food source and vice versa. In Fig. 5b, at B position, ants will decide whether to go from left path (BHD) or right path (BCD). Some of the ants

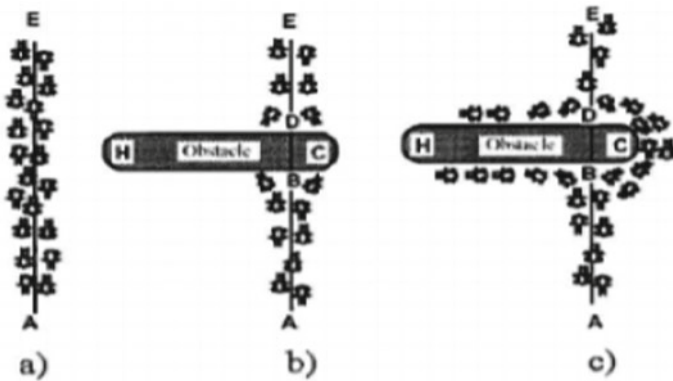


Fig. 5 Real behavior of ants

will move from path BHD and some will move from BCD. As we can see the path BCD is shorter as compared to path BHD. The amount of pheromone trail deposited on path BCD is more; therefore, all ants will take the right path as its higher level of pheromone concentration. In this way, all the ants will follow the shortest path.

7 ACO Algorithm

Ant colony optimization (ACO) is based on the real behavior/conduct of ants. In ACO, ants are being generated which are known as artificial ants which produce artificial pheromone trails [12]. Artificial ant transits from nodes to nodes. After the ant has completed its visit from one node to other node and to the last node, the pheromone level of all the paths is updated. The pheromone level is more if ants (artificial) completed its visit with a good path. To stop artificial ants from being stuck in local optima, the pheromone level of the path decreases by evaporation [13]. The following steps are considered in doing ACO algorithm.

Step 1: Initialization

First of all, the ACO parameters have to be specified during initialization process. To avoid large computational time, we have to limit the range of parameter.

- n Number of nodes
- m Number of ants
- t_{max} max. reiteration
- d_{max} max. ants visit distance
- β A constant; pheromone versus distance ($\beta > 0$)
- ρ Coefficient based on rules (heuristic) ($0 < \rho < 1$)
- α Pheromone decay constant ($0 < \alpha < 1$)
- q_0 Algorithm constant ($0 < q_0 < 1$)

τ_0 Pheromone level (initial level).

Step 2: Generation of the first node

By using random no. generator ranging from 1 to n , the node i st (first) is chosen.

Step 3: State Transition rule (S.T.)

Corresponding to every step, we have to apply the state transition rule in order to decide the next node which the ants have to visit. It is given as:

- (a) Exploitation rule: In this, the next node is selected based on the parameters that are provided.
- (b) Exploration rule: In this, the next node is randomly selected from the list nodes that are left unvisited.

Initial pheromone level is determined by a parameter known as τ which is used to determine the shortest path with high level of pheromone.

Step 4: Local Updating rule (L.U.)

- By this rule, we can update the quantity of pheromone level to the paths that are toured/visited by ants while making the solⁿ.
- Ant tours will get shuffled by applying local updating rule so that the early nodes can be traversed in other ants' visits later.
- The quantity of chemical substance trail, pheromone level, on toured paths will be decreased so that the ways/paths that are visited become less significant and probability of choosing these paths becomes less by the ants that are going to visit it in the rest of a reiteration process.
- The probabilities of selecting the same nodes become lower, when the new τ value is min^m.

Step 5: Fitness function

The evaluation based on the fitness value takes place after all of the ants finished their visits. And then, the control variable (t) is analyzed using the below given eqⁿ as:

$$t = \frac{d}{d_{\max}} * x_{\max} \quad (12)$$

where:

d Ants tour distance
 x_{\max} Maximum (max) t
 d_{\max} Ants tour max^m distance

The values obtained for variable t are assigned as the fitness values in ACO algorithm [14].

Step 6: Global Updating rule (G.U.)

- The shortest tour generated by the ant from the beginning of the tour gets updated by a method called as global updating rule (GU) by changing the quantity of pheromone level.
- The best fitness which is determined by the quantity of pheromone level is allowed to update by the one ant only.

Step 7: End condition

- The iterations get stopped by an algorithm when t_{\max} (i.e., \max^m iterations) have been implemented.
- The visit by ants should be evaluated. In case, during this process, if we found a better path, then it will be saved for the upcoming reference.
- The way which is best chosen b/w all reiterations describes the perfect solution for economic scheduling problem.
- Ants' convergence to a common path does not take place. This is experimental proven in laboratories, and it is an important feature.
- If ants traverse various ways/paths, then there is a higher chance that one of them will find an optimal and improved solution of ELD problem (Fig. 6).

8 Particle Swarm Optimization (PSO)

Particle swarm optimization (PSO) was developed by Eberhart and Kennedy in 1995 [15]. The technique is a population-based optimization algorithm and is inspired by social conduct of bird flocking or fish schooling. It is very much similar to one of the evolutionary techniques such as GA. The only difference is that it has no evolutionary operators like mutation and crossover as they are present in GA. In PSO, every single answer is a "bird" in the search space. And these potential solutions (birds) are referred to be as particles [16].

These particles fly through the problem space by following the current optimum particle. Every particle is assigned by their fitness values which are being accessed by their fitness function. In PSO, every particle remembers the previous best position on feasible search space that it has ever visited. This is termed as "pbest" value. And the best value among pbest is termed as "gbest" value [17]. In order to reach the optimum value of the problem, one needs to change the velocity and position among pbest and gbest values.

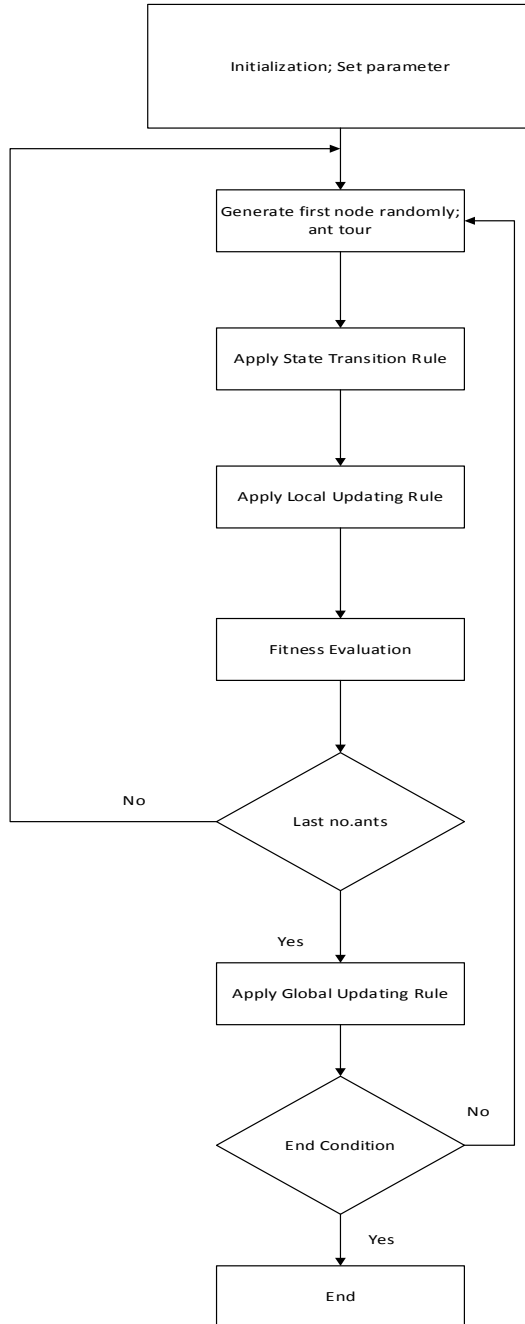


Fig. 6 Flow diagram of ACO

9 PSO Algorithm

The following steps are required while performing PSO algorithm [18]. They are as follows (Fig. 7):

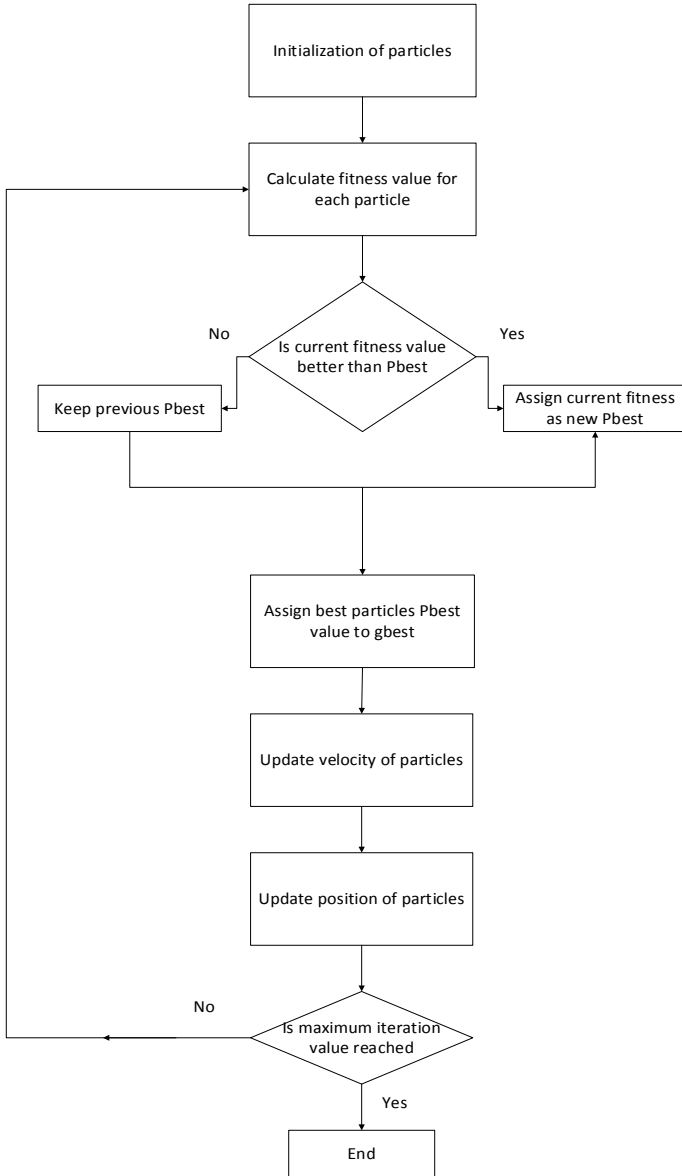


Fig. 7 Flow diagram of PSO

- **Initialization:** The velocity and position of all the particles are set using random number generator randomly.
- **Fitness Function:** Fitness of each and every particle is evaluated.
- **Velocity Update:** At each iteration, the velocity of all the particles is updated according to the following equation:

$$V_i^{k+1} = V_i^k + C1 * \text{rand}()1 * (Pbest_i - S_i^k) + C2 * \text{rand}()2 * (gbest_i - S_i^k)$$

- **Positioning Update:** The position of the particles is updated according to:

$$S_i^{k+1} = S_i^k + V_i^{k+1} \quad (14)$$

- **Memory Updating:** Update the values of pbest and gbest as:

$$Pbest = P_i \quad \text{if } P_i > Pbest$$

$$gbest = P_g \quad \text{if } P_g > gbest$$

- **End Condition:** Repeat the steps from 2 to 5 until we get our desired optimum solution.

where,

V_i^{k+1}	Velocity of particle i at iteration $k + 1$
V_i^k	Velocity of particle i at iteration k
S_i^{k+1}	Position of particle i at iteration $k + 1$
S_i^k	Position of particle i at iteration k
$C1, C2$	Constant weighing factors
$C1, C2$	Constant weighing factors
$\text{rand}()1$	Random number between 0 and 1
$\text{rand}()2$	Random number between 0 and 1
$Pbest_i$	Position of particle i
$gbest_i$	Position of the swarm i

10 Algorithm Parameters, Generation Data and Loss Matrix

The parameters involved in the algorithm for obtaining our desired optimum solution of ELD problem are given as in the form of tables [19]:

The following data for GA algorithm is given in Table 1.

The following data for ACO algorithm is given in Table 2.

The following data for PSO algorithm is given in Table 3.

Table 1 GA data

Genetic algorithm		
SI. No.	Parameters	Specifications
1.	Population size	50
2.	Chromosomes length	15
3.	Crossover rate	0.75
4.	Mutation rate	0.01
5.	Maximum iteration	40

Table 2 ACO data

ACO		
SI. No.	Parameters	Specifications
1.	Population of ants	50
2.	Length of ant junction	15
3.	Pheromone coefficients, β	5
4.	Heuristic coefficients, ρ	5
5.	Decay parameter,	0.5
6.	Maximum Iteration	40

Table 3 PSO data

PSO		
SI. No.	Parameters	Specifications
1.	Population size (particles)	50
2.	Dimension	6
3.	$C1, C2$ (acceleration constant)	2
4.	Inertia weight	0.9, 0.4
5.	Maximum iteration	40

The following data is of thermal power generator station of six (6) generating units with α, β, γ as fuel coefficients and P_{\min}, P_{\max} as minimum and maximum limit of output power is shown in Table 4.

The loss coefficient matrix data is given in Table 5.

11 Results

The following results are obtained while doing optimization of economic scheduling using various evolutionary techniques such as genetic algorithm (GA), ant colony

Table 4 Generator data of thermal power station

Generating unit	α	β	γ	P_{\min}	P_{\max}
1	0.007	7	240	100	500
2	0.0095	10	200	50	200
3	0.009	8.5	220	80	300
4	0.009	11	200	50	150
5	0.008	10.5	220	50	200
6	0.0075	12	120	50	120

Table 5 Loss coefficient matrix data

Loss coefficient matrix					
0.14	0.17	0.15	0.19	0.26	0.22
0.17	0.6	0.13	0.16	0.15	0.2
0.15	0.13	0.65	0.17	0.24	0.19
0.19	0.16	0.17	0.71	0.3	0.25
0.26	0.15	0.24	0.3	0.69	0.32
0.22	0.2	0.19	0.25	0.32	0.85

optimization (ACO) and particle swarm optimization (PSO) by using various parameters in order to get our desired optimum solution, i.e., generation with minimum fuel cost (Tables 6, 7 and 8).

The following results show the allocation of power to six generating units with their convergence rate using different evolutionary techniques. These are shown in the form of tables and figures (Figs. 8, 9 and 10, Table 9).

Table 6 Power allocation and fuel cost (GA)

Generator output	Genetic algorithm
G1 (MW)	217.5791
G2 (MW)	53.4118
G3 (MW)	82.5258
G4 (MW)	50.6033
G5 (MW)	51.2545
G6 (MW)	50.2333
Power demand (MW)	500
Total power generated (MW)	505.6078
Total power loss	5.6078
Total generation cost	6139 \$/h (368,340 ₹/h)

Table 7 Power allocation and fuel cost (ACO)

Generator output	ACO
G1 (MW)	219.2885
G2 (MW)	52.1536
G3 (MW)	80.4562
G4 (MW)	51.8361
G5 (MW)	50.1232
G6 (MW)	51.7412
Power demand (MW)	500
Total power generated (MW)	505.5988
Total power loss	5.5988
Total generation cost	6135.992 \$/h (368,159.52 ₹/h)

Table 8 Power allocation and fuel cost (PSO)

Generator output	PSO
G1 (MW)	221.2620
G2 (MW)	50.0000
G3 (MW)	84.3219
G4 (MW)	50.0000
G5 (MW)	50.0000
G6 (MW)	50.0000
Power demand (MW)	500
Total power generated (MW)	505.5839
Total power loss	5.5839
Total generation cost	6132.3 \$/h (367,938 ₹/h)

12 Conclusion

The following various evolutionary techniques like GA, ACO and PSO have been implemented on the economic scheduling problems. The proposed algorithm is able to minimize the generation cost while meeting the demand requirement which was proposed on six generating units.

The results obtained by GA, ACO and PSO are compared with each other. After comparing, we came to know that PSO is versatile, robust and efficient and has the capability to work more accurately than GA and ACO.

Hence, the convergence rate for optimized solution is better in PSO compared to GA and ACO; i.e., in minimum iteration, it achieves the optimal solution of ELD problems compared to GA and ACO. This can be seen in the above figures.

The printing area is 122 mm × 193 mm. The text should be justified to occupy the full line width, so that the right margin is not ragged, with words hyphenated as

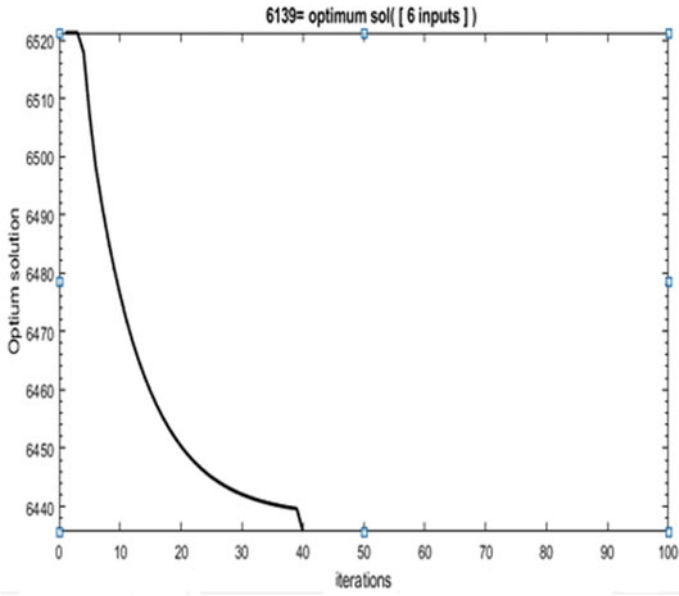


Fig. 8 Convergence rate of GA

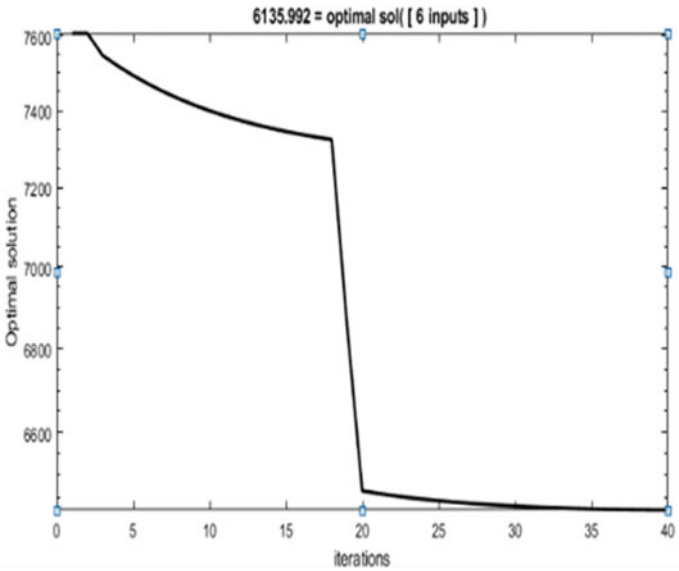


Fig. 9 Convergence rate of ACO

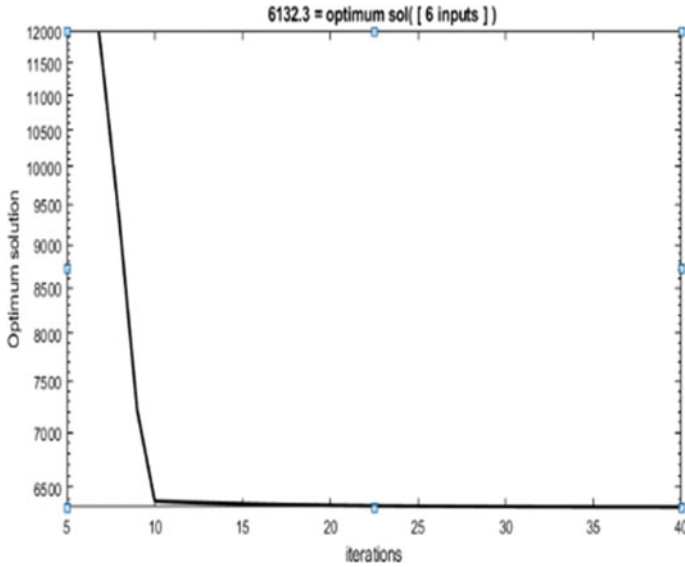


Fig. 10 Convergence rate of PSO

Table 9 Comparison of GA, ACO and PSO and fuel cost

Generator output	Genetic algorithm	ACO	PSO
G1 (MW)	217.5791	219.2885	221.2620
G2 (MW)	53.4118	52.1536	50.0000
G3 (MW)	82.5258	80.4562	84.3219
G4 (MW)	50.6033	51.8361	50.0000
G5 (MW)	51.2545	50.1232	50.0000
G6 (MW)	50.2333	51.7412	50.0000
Power demand (MW)	500	500	500
Total power generated (MW)	505.6078	505.5988	505.5839
Total power loss	5.6078	5.5988	5.5839
Total generation cost	6139 \$/h (368,340 ₹/h)	6135.992 \$/h (368,159.52 ₹/h)	6132.3 \$/h (367,938 ₹/h)

appropriate. Please fill pages so that the length of the text is no less than 180 mm, if possible.

References

1. Kothari DP, Dhillon JS (2011) Power system optimization, 2nd edn. PHI, Delhi
2. Nagrath IJ, Kothari DP (2003) Modern power system analysis. McGraw Hill, New York
3. Kirchmayer LL, Stagg GW (1952) Evaluation of methods of coordinating incremental fuel costs and incremental transmission losses. *IEEE Trans* 71(111):513–520
4. Saadat H (1999) Power system analysis. McGraw Hill, New York, pp 257–312
5. Walters DC, Sheble GB (1993) Genetic algorithm solution of economic dispatch with valve point loading. *IEEE Trans Power Syst* 8(3):1325–1332
6. Chen P-H, Chang H-C (1995) Large scale economic dispatch by Genetic algorithm. *IEEE Trans Power Syst* 10(4):1919–1926
7. Genetic Algorithm—MATLAB—Math Works
8. Pratap Singh S, Tyagi R, Goel A (2018) Genetic algorithm for solving economic load dispatch. *Int J Electron Electr Eng* 7
9. Dulton JA (2017) Economic dispatch and operations of electric utilities. *Energy Markets, Policy, and Regulation*
10. Nwohu MN, Osaremwinda OP (2017) Evaluation of economic load dispatch in power generating stations by use of Ant Colony Search Algorithms. *Int J Res Stud Electr Electron Eng*
11. Osaremwinda OP, Nwohu MN, Kolo JG (2017) A comparative study of meta-heuristics algorithms in evaluation of economic load dispatch problems in generating power station with matlab codes
12. Thakral DR, Rai HM (2008) Ant Colony Optimization: A new approach for economic load dispatch. *Int J Res Eng Appl Sci*
13. Chowdhury BH, Rahman S (1990) A review of recent advances in economic dispatch. *IEEE Trans Power Syst* 5(4):1248–1259
14. Santra D, Sarker K, Mukherjee A (2016) Hybrid PSO-ACO algorithm to solve economic load dispatch problem with transmission losses. In *IEEE transactions international conference on intelligent control power and instrumentation*, Aug 2016
15. Narayana PP, Latha K (2004) Evolutionary programming based economic power dispatch solutions with independent power producers. In *IEEE international conference on electric utility deregulation, restructuring and power technologies*, April 2004, pp 172–177
16. Mahajan M, Vadhera S (2012) Economic load dispatch of different bus system using PSO. In *IEEE international conference*, 2012
17. Al-Bahrani LT, Patra JC, Kowalczyk R (2016) Multi-gradient PSO algorithm for economic dispatch of thermal generating units in smart grid. In *Proceedings of IEEE Innovative Smart Grid Technology-Asia (ISGT-Asia)*, pp 258–263
18. Vlachogiannis JG, Lee KY (2009) Economic load dispatch—A comparative study on heuristic optimization techniques with an improved coordinated aggregation-based PSO. *IEEE Trans Power Syst* 24(2):991–1001
19. Maharana HS, Dash SK (2019) A new approach to economic load dispatch by using improved QEMA based particle swarm optimization considering generator constraints. *Int Res J Eng Technol* 06(07):3661–3667

VLSI Implementation of Hamming Code for Molecular Communication



Ruchi Rai, S. Pratap Singh, M. Lakshmanan, and V. K. Pandey

Abstract Application of molecular communication (MC) is claimed almost in every field of humanity, be it medicine, be it security, or be it industry. However, the channel is the biggest impairment of any wireless. On the other hand, forward error correction (FEC) is found as the most worth full technique to improve performance due to channel degradation. Though various literature has proposed Hamming codes for MC, none of the literature has presented the implementation of it in any of the VLSI tools. This paper, however, implements an encoder of Hamming code using CMOS logic circuits for different values of parity-check bits (m). Specifically, we have considered $m = 3$ and $m = 5$ to implement the Hamming code. Further, power and delay analysis are presented and verified through simulations in 250 nm CMOS technology using Tanner EDA Tool.

Keywords FEC · Hamming code · MC · Channel coding · Noise

1 Introduction

Molecular communication (MC) is a unique vicinity of research that extends to communication technology, nanotechnology, and biotechnology. Molecular communication permits nanomachines to communicate together using molecules as a carrier

R. Rai · V. K. Pandey
Noida Institute of Engineering and Technology, Greater Noida, India
e-mail: ruchirai1000@gmail.com

V. K. Pandey
e-mail: vijaygpandey@yahoo.com

S. Pratap Singh · M. Lakshmanan (✉)
Galgotias College of Engineering and Technology, Greater Noida, India
e-mail: tmlakshmanan@gmail.com

S. Pratap Singh
e-mail: drsprataps@gmail.com

[1]. There are many molecular communication procedures, for example, micro-tube for minimum-range communication, ion-signaling, and diffusion for minimum-range to middle-range communication, on the other hand, spore and pollen-based ideas may be used for extensive-term communications [2, 3]. In a molecular nano-communication (MNC) system, error-correcting codes (ECC) are applied to decrease the count of errors caused by interference, packet loss, noise, as well as cross-talk [4].

For enhancing the reliability of the (DMC) system, a new coding distance function is introduced named molecular coding distance function (MoCo), and this is also likened with Hamming distance [5]. Also, self-orthogonal convolutional code (SOCCs) with ML decoding scheme, Euclidean geometry low-density parity-check (EG-LDPC), and cyclic Reed–Muller (C-RM) codes are used to enhancing the transmission reliability of molecular communication system [6, 7]. All these codes are compared with the uncoded system. The result confirmed that the coding method advances the reliability of the transmitted data of the MC system.

In [8], the author proposed a novel code that is used as an error recovery device to advance the consistency of the transmission in a diffusion-based molecular communication system (DMC), name as RS code. An analytical expression is derived for the BEP of the DMC system, to quantify the performance improvement due to RS code. They further develop the simulation framework based on the particle for simulating the proposed scheme using the R-S code to confirm the accurateness of their derivative analytical results. The BEP of the anticipated scheme with R-S codes is better by increasing the codeword minimal distance. ISI-free code and their bit error rate (BER) approximations had introduced for the diffusion-based molecular communication scheme [9]. The result compared by the uncoded system and proposed ISI-free code offers better performance for the DMC system through relatively low complexity. In [10], a simple study and evaluation between all error-correcting codes is presented based on their error-correcting ability and complication. For expanding BER and coding gain, extra complex codes like C-RM or R-S code are used. Fewer complicated codes specifically EG-LDPC and Hamming codes are used for improving energy cost. Except for these codes, a new code is introduced because of the excessive existence of inter-symbol interference between dissimilar codewords named ISI-free code. Low-Density Parity Check and Bose Chaudhuri and Hocquenghen (BCH) are error-correcting codes that are implemented on FPGA for finding power and area [11]. Result shows that LDPC code had less power and low area than BCH.

The earlier papers to offer the use of error correction code (ECC) inside the molecular communication system were [12–14], which proposed the usage of HC. Hamming code is a straight linear block code that is capable of modifying one error and detecting up to dual errors. Turbo, LDPC, and BCH codes are completed in Verilog HDL and implementen on FPGA in [15] and [16]. This paper presents the design and implementation of the Hamming code on the Tanner EDA Tool. This paper also presents the power consumption and delay of the Hamming code.

The remaining paper is structured as follows: Sect. 2 defines error-correction code in the MC system. Section 3 describes the simulation results of Hamming code logic circuits in the Tanner EDA Tool. Section 4 describes the conclusion.

2 Error Correction Code for MC: Hamming Code

Error correction is the method of detecting errors from transmitted information and restored the original error-free information. Forward error-correcting (FEC) codes control the errors in transmission of data over unreliable or noisy channels of the MC system. In turn, FEC is the key procedure used to increase the reliability of transmissions. In this paper, the Hamming code is used as the performance enhancement technique inside the molecular communication scheme. Hamming code is deliberated below.

Hamming codes are linear block codes that precise single error in each block and recognize up to dual errors. Hamming codes can be denoted as (n, k) , where block length, $n = 2^m - 1$, and message length, $k = n - m$, with $m(m \geq 2)$ parity-check bits. Linear block codes can accurate ' t ' errors in individually block:

$$t = \left[\frac{(D_{\min} - 1)}{2} \right], \quad (1)$$

where D_{\min} is the minimum distance and in Hamming codes D_{\min} is equivalent to 3.

Figure 1 shows the encoder for $m = 3$ and $m = 5$ Hamming code which can be simply encoded by shift-registers as well as two-input XOR gate. In our work, set-reset flip-flop is used in every shift-register and can be built by CMOS logic. Dual-input XOR gates are also be formed by CMOS logic. For calculating the parity bit, dual-input XOR gate is used. The two-input XOR gate depends on the generator polynomial of individually code. Generator polynomial for $m = 3, 4, 5$ Hamming code is specified by: $f(X) = X^3 + X + 1$, $f(X) = X^4 + X + 1$ and $f(X) = X^5 + X^2 + 1$.

3 Simulation Result

In this section, we have defined the schematic diagram and waveform result of an encoder for $m = 3, 5$ Hamming code. Figures 2 and 3 present the schematic diagram and waveform of an encoder. The schematic of an encoder is designed and simulated using 250 nm technology in the Tanner EDA tool for $m = 3$ and 5, respectively. Further, the power consumption and delay are presented. We use a 5V power supply for all the circuits which are used in the Hamming code encoder. SR flip-flop is formed by using CMOS. As well as XOR gate is formed by using CMOS logic. The schematic diagram of the Hamming code is complete at S-Edit. The Hamming code simulation is performed at 250 nm technology, in T-Spice, with low power techniques. The waveform is occupied from W-Edit.

Encoder for $m = 3$ Hamming code with a shift-register and two two-input XOR gate can be designed and simulated using 250 nm technology on Tanner EDA. 5V power supply is used. Two-input XOR gate is used in the encoder for calculating the parity bit of each circuit.

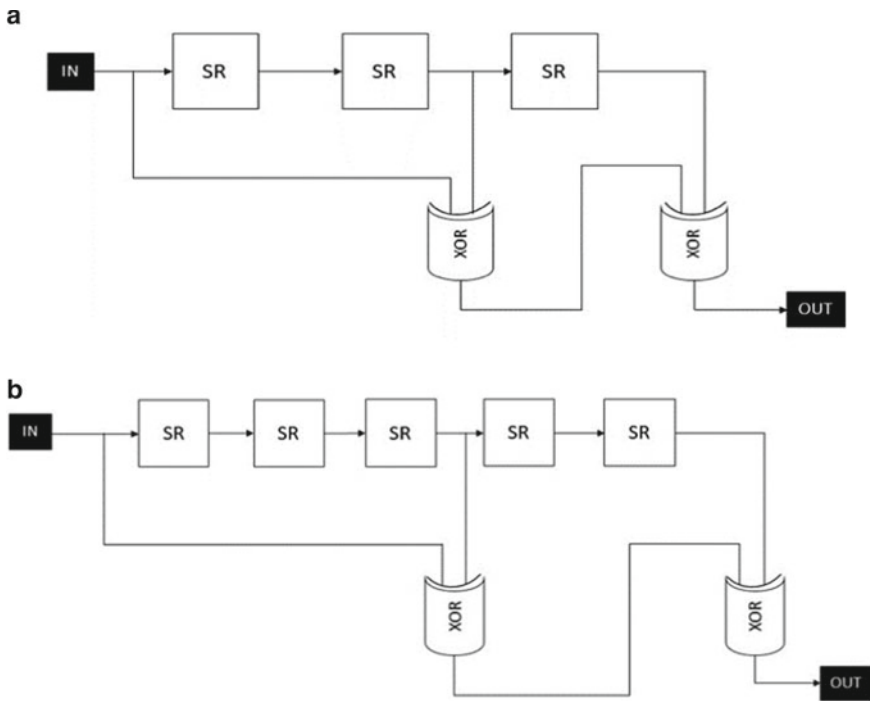


Fig. 1 **a** Non-systematic encoder for $m = 3$ Hamming code [13]. **b** Non-systematic encoder for $m = 5$ Hamming code [14]

Encoder for $m = 5$ Hamming code with a shift-register and two two-input XOR gate can be designed and simulated using 250 nm technology on Tanner EDA. 5V power supply is used. Power and delay of encoder for $m = 3$ and $m = 5$ Hamming code is given in Table 1.

4 Conclusion

In this paper, for the first time, the encoder of Hamming code is designed and simulated using 250 nm technology in Tanner EDA Tool for, $m = 3$ and $m = 5$, respectively. Power and delay are presented and analyzed. CMOS logic is used to design all the circuits. The proposed VLSI implementation of the Hamming code can be used to improve the molecular communication system’s performance, which is missing in our literature. Further, implementation of Hamming code using an application-specific integrated circuit (ASIC) can be implemented in the future.

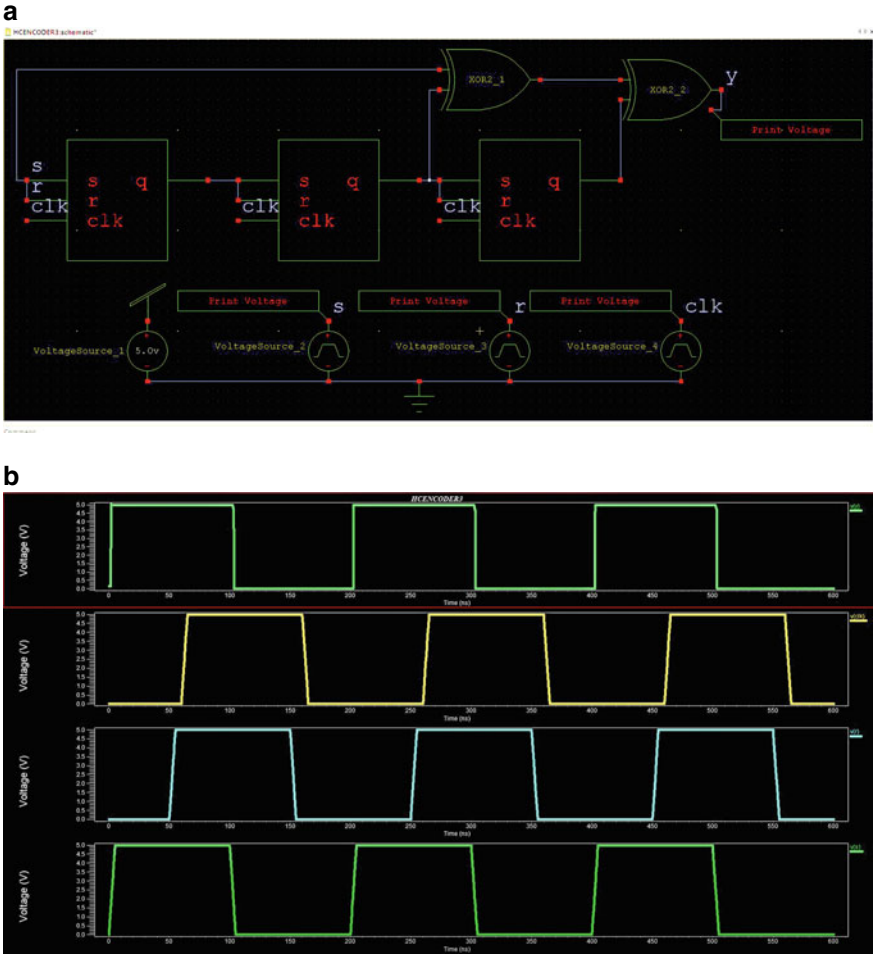


Fig. 2 **a** Schematic diagram of an encoder for $m = 3$ Hamming code. **b** Simulation result of an encoder for $m = 3$ Hamming code

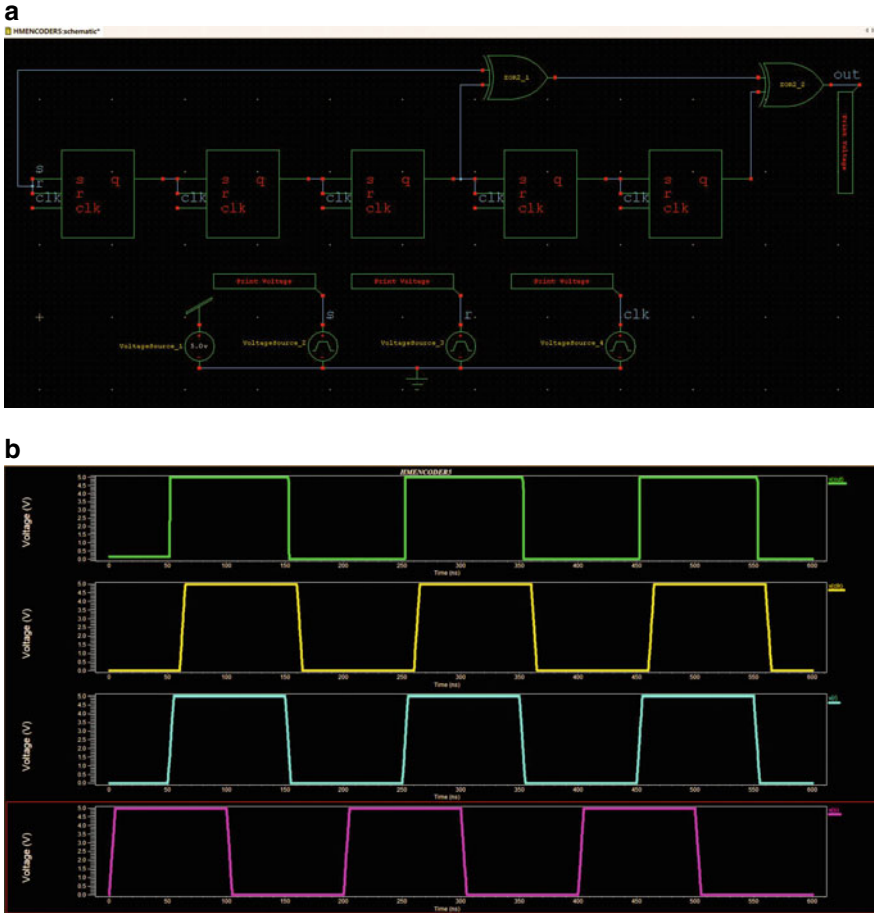


Fig. 3 **a** Schematic diagram of an encoder for $m = 5$ Hamming code. **b** Simulation result of an encoder for $m = 5$ Hamming code

Table 1 Power and delay of encoder for $m = 3$ and $m = 5$ Hamming code

Hamming code	$m = 3$ encoder	$m = 5$ encoder
Power (W)	4.7573e-004	5.1792e-003
Delay (S)	8.8239e-010	4.9020e-008

References

1. Hiyama S, Moritani Y, Suda T, Egashira R, Enomoto A, Moore M (2006) Molecular communication. IEICE 89(2):162
2. Nakano T, Suda T, Moore M, Egrashira R, Enomoto A, Arima K (2005) Molecular communication for nanomachines using intercellular calcium signaling. In: 5th IEEE conference on

- nanotechnology, vol 2, pp 478–581
3. Akyildiz IF, Gine LP (2009) Molecular communication options for long-range nanonetworks. *Comput Netw* 53:2753–2766
 4. Blahut RE (2003) Algebraic codes for data transmission. Cambridge University Press
 5. Ko PY, Lee CH, Chen KC (2012) A new paradigm for channel coding in diffusion-based molecular communication. In: IEEE global communications conference (GLOBECOM), pp 3748–3753. IEEE
 6. Lu Y, Higgins MD, Leeson MS (2015) Self-orthogonal convolutional codes (SOCCs) for diffusion-based molecular communication system. In: IEEE International conference on communication, June, pp 1049–1053. IEEE
 7. Lu Y, Higgins MD, Lesson MS (2015) Comparison of channel coding schemes for molecular communications system. *IEEE Trans Commun* 63(1):3991–4001
 8. Dissanayaka MB, Deng Y, Nallanathan A, Ekanayake EMN, El-kashlan M (2017) Reed-Solomon codes for molecular communication with a full absorption receiver. *IEEE Commun Letters* 21(6):1245–1248
 9. Shih PJ, Lee CH, Yeh PC, Chen KC (2013) Channel code for reliability enhancement in molecular communication. *IEEE J Sel Areas Commun* 31(2):857–867
 10. Darya AM, Vakani H, Nasir Q (2019) Error control codes for molecular Communication: a survey. In: International conference on communications, signal processing, and their applications (ICCSPA), pp 1–4. IEEE
 11. Muthammal R, Madhane SSR (2013) Design, analysis, and FPGA implementation LDPC codes with BCH codes. In: International conference on current trends in engineering and technology (ICCTET), pp 242–244. IEEE
 12. Lesson MS, Higgins MD (2012) Forward error correction for molecular communications. *Nano Commun Netw* 3(3):161–167
 13. Lesson MS, Higgins MD (2012) Error correction coding for molecular communications. In: IEEE conference on communications (ICC), pp 6172–6176. IEEE
 14. Lu Y, Higgins MD, Lesson MS (2014) Diffusion based molecular communications system enhancement using high order Hamming codes. In: 9th international conference on communication system, networks and digital sign (CSNDSP), pp 438–442. IEEE
 15. Vardhan TV, Neeraja B, Kumar BP, Paidimarry CS (2015) Implementation of turbo codes using Verilog-HDL and estimation of its error correction capability. In: IEEE Asia Pacific conference on postgraduate research in microelectronics and electronics (Prime Asia), pp 75–79. IEEE
 16. Digdarsini D, Mishra D, Mehta S, Ram TVS (2019) FPGA implementation of FEC encoder with BCH & LDPC codes for DVB S2 system. In: 6th international conference on signal processing and integrated networks (SPIN), pp 78–81. IEEE

Power Analyses in AMBA AHB Protocol and Synthesis Over Xilinx ISE



Abhishek Deshwal, Aman Singh, Ashutosh Gupta, P. C. Joshi,
and Chiranjeev Singhal

Abstract The high-performance AHB bus is the advanced microcontroller bus architecture (AMBA) bus used for the microcontroller. It is widely used as a standard for chip design (SoC) connection. In this paper, we present the formation of the AMBA AHB protocol with different functional modes. The AHB protocol architecture is being developed including basic blocks like master, slave, decoder, and arbiter. This high-performance bus has a very high speed of data transfer that uses a huge amount of power. Power consumption is based on a change in the clock's behavior. In this work, a clock net minimization procedure was developed. All of these functions were upgraded to Verilog HDL. Model Sim (simulation software from Mentor Graphics) is utilized to display the design and afterward XPower analyzer (a graphical power calculator tool from Xilinx) is used to calculate the available power and performance.

Keywords AMBA AHB · Dynamic power · Gated clock · Negative latch · SoC

1 Introduction

The advanced high-performance bus (AHB) is an efficient bus for the advanced microcontroller bus architecture (AMBA) family. This bus is used in high-performance clock modules and also serves as a program bus running in the background. It takes into consideration simple usage of different large-scale works maybe working at various frequencies (high recurrence). The AMBA convention is an autonomous innovation since we apply this standard to any scope of utilizations. Empowers the early improvement of numerous processor structures with enormous quantities of controllers and edges. It was worked by ARM Ltd in 1996 and is a

A. Deshwal · A. Singh (✉) · A. Gupta · P. C. Joshi
Department of Electronics and Communication Engineering, Galgotias College of Engineering
and Technology, Greater Noida, India
e-mail: amans6636@gmail.com

C. Singhal
DKOP Labs Pvt Ltd., Kamal Marg, Sector 57, Noida, Uttar Pradesh, India

© Springer Nature Singapore Pte Ltd. 2021
R. Agrawal et al. (eds.), *Advances in Smart Communication and Imaging Systems*,
Lecture Notes in Electrical Engineering 721,
https://doi.org/10.1007/978-981-15-9938-5_64

symbol of it. AMBA is used as an on-chip connection and is utilized to arrange and oversee various functional modules in SoC design. System-on-chip means incorporating all components of an electronic system into one coordinated circuit or chip. The SoC have one or more microcontrollers, a microprocessor, and a DSP, unique memory elements, sensors, digital and analog signal elements, timers, and many more. SoC is widely used in the design of embedded systems because it has many advantages such as small size, high reliability, low memory requirements, and low-cost efficiency.

2 AMBA AHB Different Components

The AMBA protocol primarily comprises of three different buses specifically advanced system bus (ASB), advanced high-performance bus (AHB), and advanced peripheral bus (APB). All these buses have different functions. Buses that work with ASB are often used to carry data at high data rates while advanced peripheral buses are used for low-speed computing devices usually operating at low speeds. Both buses are separated by a bridge that ensures that there is no communication barrier between the low levels in the APB unit or the high AHB processor and ensures that there is no data loss between AHB and APB or APB in the AHB data transmission [1] (Fig. 1).

The AMBA AHB comprises of four fundamental components the AHB master, the AHB slave, the AHB arbiter, and the decoder. At AMBA AHB, there are numerous slaves and numerous masters that are accessible, but only one slave and one slave can cooperate at all times. The decoder is utilized to record the information given to master, and the arbiter provides the bus to the master [2].

1. AHB Master—A master can establish literacy activities by providing address and information management. There are many masters and slaves present, but only one master will be able to communicate with or interact with only one slave.
2. AHB Slave—A slave performs the operation after getting information from its master. Here, the read/write operation is performed which will be given by master.

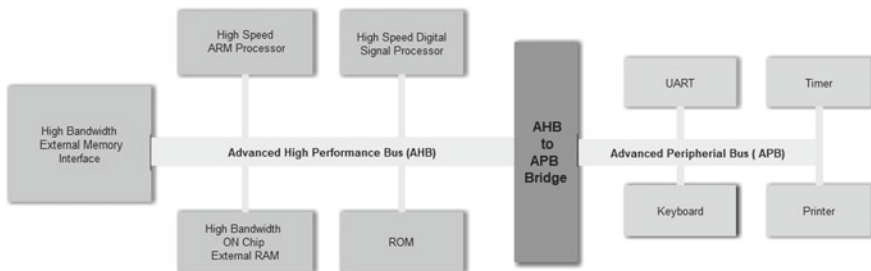


Fig. 1 A typical AMBA based microcontroller

After completion of the operation, this will give an acknowledge signal back to the master which tells that the operation has been done successfully or got failed.

3. AHB Arbiter—If master wants to communicate with the slave, it first interacts with an arbiter which ensures the availability of a bus for communication. If the bus is free, then arbiter grants the request by ‘hgrant’ signal.
4. Decoder—The decoder is utilized to translate the information and signals given by the master and related to a particular slave.

3 Designing of AMBA AHB

In AMBA AHB, there are basically different types of operation for data transfer from master to slave. In simple transfer operation, there is no wait state; hence, ‘hready’ signal is always low (Fig. 2).

In wait state transfer operation, the presence of low ‘hready’ signal bring out the transfer operation in wait state; hence, whenever when the ‘hready’ is low, it will go to the wait State (Fig. 3).

Burst mode operation is used in system-level buses like AHB. It can fetch a large amount of data at a time and then implemented it through the pipelining process. Burst mode eliminated the high impedance state (tri-state) during the transfer of data (Fig. 4).

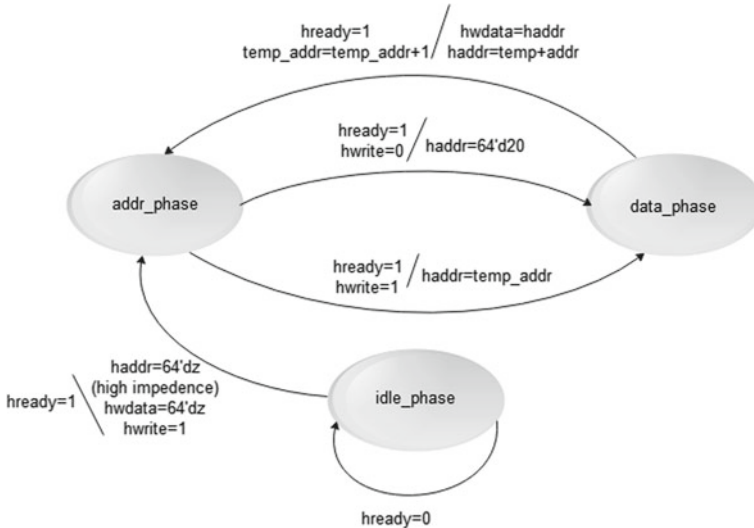


Fig. 2 FSM of simple transfer

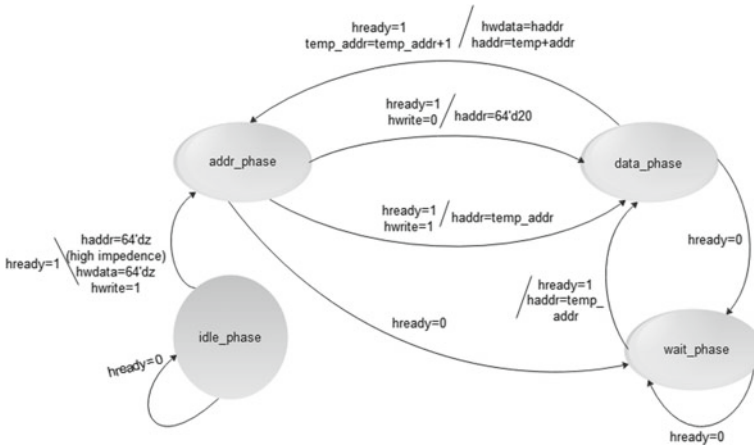


Fig. 3 FSM of transfer with wait state

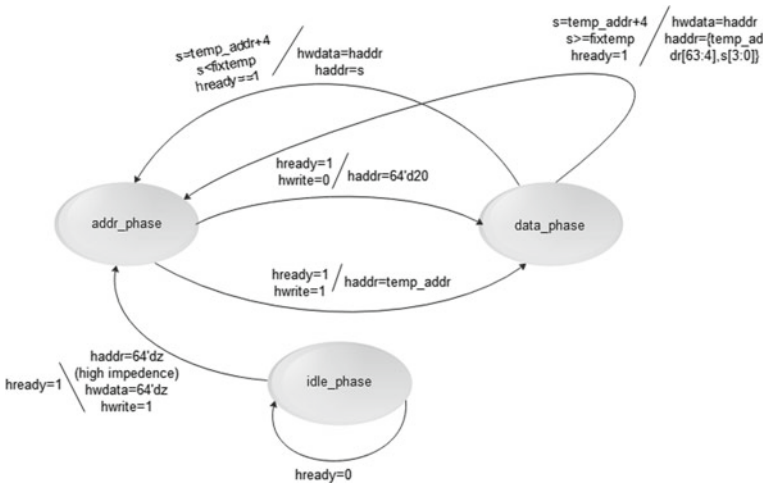


Fig. 4 FSM of burst transfer type operation

4 High Power Dissipation in AHB Based Microcontroller

AMBA AHB is a high-transmission capacity system bus with high information rates. The performance of the standard AMBA based protocol is just a sequential circuit based on a standard clock system. The sequential circuit in the system is the major source of power dissipation in the digital circuit because one of the inputs which are fed into this is the clock, and this clock changes all the time. Reducing dynamic functions requires consideration of signal processing opportunities and other techniques

such as logic optimization, gated clock, and glitches blocking. The total switching power can be reduced by clock gating or stopping some gaps in idle switches.

4.1 Low-Power Design Principle

The power consumption of any circuit is determined by a number of factors, such as frequency f , voltage supply V_{dd} , data function capacitor C , leakage, short circuit current as follows

$$P_{dynamic} = \alpha CV_{dd}^2 f \text{ [3]}$$

$P_{dynamic}$ is also called the switching power and dynamic power. Dynamic power dissipation caused if only if there is a switching function at any point in the CMOS circuitry. The power dissipation is mainly dependent upon the number of times the capacitor is charged and discharged. Therefore, as the frequency of switches increases, so also the power dissipation rate increases. This charging and capacitor output is based on the number of times the clock signal feeds into the circuit.

This switching capacitance can be reduced by clock gating or blocking certain blocks from useless switches. There are different ways to reduce energy consumption based on the assessment of energy consumption. As a clock system, it is recognized as a leading provider of energy conversion algorithms [3].

4.2 Clock Gating Technique

Clock net is responsible for power outages in synchronized digital circuits. In clock gating mode, this clock net is reduced. Clock gating is the principle that deactivates a clock that does not require unwanted switching functionality. In this clock gating method, we use the negative latch support method to reduce power. This negative latch method is used to reduce the switching activity of the clock and hence the power consumption [4, 5].

The idea of a gating clock aims to generate a clock signal by creating a clock signal that allows it to propagate only when a specific function is triggered. The control signal ought to be created based on the structure signal. Present the enabled signal in the structure stage with a clear understanding of the various blocks operating in SoC design. The gated clock runs a low-speed, energy-saving functional block [6] (Fig. 5).

4.3 Applications

Today, AMBA is broadly utilized on a scope of ASIC and SoC parts incorporating applications processors and operating systems utilized in present-day life on mobile

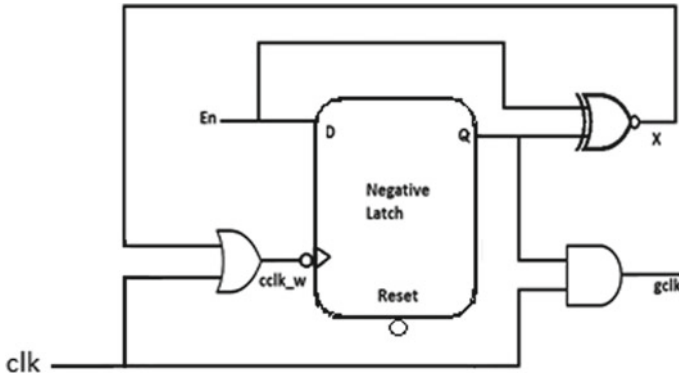


Fig. 5 Negative latch-based clock gating technique

devices such as smartphones. SoC-related problem is what parts or blocks are put on the chip, yet besides how they interconnect. The AMBA AHB is a solution for blocks to interconnect.

It permits the reuse of IP cores and a few peripherals across IC forms, and urge measured framework configuration to improve processor freedom but because of its high bandwidth characteristics, its limitation is that when the transfer data rate is high it will start heating which allows it to consume more external power (from the clock).

5 Simulation and Result Analysis

In Fig. 6, the ‘hready’ signal is utilized to control the number of clock cycles required to finish the transmission. The ‘hwrite’ controls the exchange of information to or from the signal master.

1. High ‘hwrite’ indicates that proper transmission and transmits the data of master to the data bus performing write operation. The signal corresponds to this is ‘hwdata’

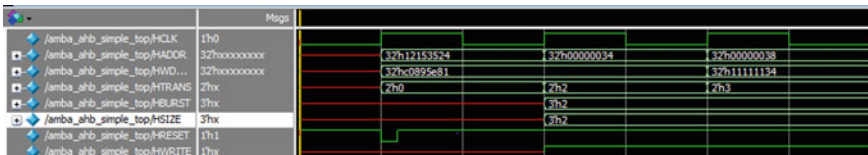


Fig. 6 Simulation of AMBA AHB without clock gating technique

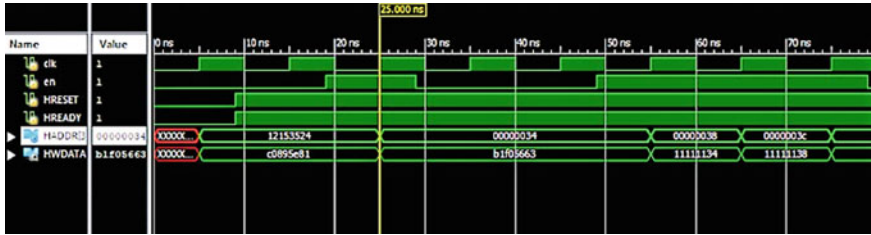


Fig. 7 Simulation of AMBA AHB with clock gating technique

- 2. Low 'hwrite' indicates that the read operation is transmitted and the slave must create information on the data bus performing read operation. The signal corresponds to this is 'hrdata'.

In Fig. 7, the simulation shows that when the enable 'en' signal is high, only then the next data is changed to another state until and unless there is no further activity in the system bus which results in reducing the unnecessary switching in the system bus.

Figure 8a, b describes the proposed clock gated AMBA AHB bus performance. The result of the AMBA AHB system bus with conventional clock technology is compared with the proposed clock gated AMBA AHB system bus at 99 MHz clock frequency and shows that the power usage in the system diminishes from 0.345 to 0.219 if bus is fed with a negative latch-based clock gating strategy. When the frequency is increased to 2000 MHz, the power decreases from 0.472 to 0.280. Power consumption is determined with the assistance of the XPower analyzer of Xilinx ISE Design Suit (Fig. 9).

6 Conclusion

In this paper, the advanced microcontroller bus architecture commonly known as AMBA and its bus AHB, an open source bus protocol and its high-performance buses in designing of low-power devices, has been studied and successfully designed and simulated. Furthermore, AHB which consumes more power due to its clock net behavior is shown with and without clock gating, respectively, and it is found that the power consumption is reduced when we use clock gating instead of a simple clock.

In the present work, we have simulated the AMBA AHB, the result in software has been shown, and in the future, when it will be implemented on the FPGA platform, this can show more accurate and precise results.

a

A	B	C	D	E	F	G	H	I	J	K	L	M	N		
Device			On-Chip	Power (W)	Used	Available	Utilization (%)	Supply Summary			Total	Dynamic	Quiescent		
Family	Zynq-7000	Clocks	0.013	1	--	--	Source			Voltage	Current (A)	Current (A)	Current (A)		
Part	xc7z010	Logic	0.000	65	17600	0	Vccint			1.000	0.039	0.022	0.017		
Package	cg400	Signals	0.004	81	--	--	Vccaux			1.800	0.017	0.006	0.010		
Temp Grade	Commercial	I/Os	0.113	66	230	29	Vcco18			1.800	0.055	0.054	0.001		
Process	Maximum	Leakage	0.214				Vccbram			1.000	0.001	0.000	0.001		
Speed Grade	-3	Total	0.345				Vccpint			1.000	0.078	0.000	0.078		
Environment			Thermal Properties			Effective TjA	Max Ambient	Junction Temp	Vccpaux			1.800	0.027	0.000	0.027
Ambient Temp (C)	25.0	C/W		(C)		(C)	Vcc0_ddr			1.500	0.006	0.000	0.006		
Use custom TjA?	Yes		5.5	83.1	26.9	Vccadc			1.710	0.025	0.000	0.025			
Custom TjA (C/W)	5.5	Supply Power (W)													
Airflow (LFM)	NA	Total	0.345	0.131	0.214										
Heat Sink	High Profile														
Custom TSA (C/W)	NA														
Board Selection	Large (20"x20")														
# of Board Layers	16 or more														
Custom TjB (C/W)	NA														
Board Temperature (C)	NA														

b

A	B	C	D	E	F	G	H	I	J	K	L	M	N		
Device			On-Chip	Power (W)	Used	Available	Utilization (%)	Supply Summary			Total	Dynamic	Quiescent		
Family	Zynq-7000	Clocks	0.001	1	--	--	Source			Voltage	Current (A)	Current (A)	Current (A)		
Part	xc7z010	Logic	0.000	65	17600	0	Vccint			1.000	0.017	0.001	0.016		
Package	cg400	Signals	0.000	81	--	--	Vccaux			1.800	0.011	0.000	0.010		
Temp Grade	Commercial	I/Os	0.006	66	230	29	Vcco18			1.800	0.004	0.003	0.001		
Process	Maximum	Leakage	0.212				Vccbram			1.000	0.001	0.000	0.001		
Speed Grade	-3	Total	0.219				Vccpint			1.000	0.076	0.000	0.076		
Environment			Thermal Properties			Effective TjA	Max Ambient	Junction Temp	Vccpaux			1.800	0.027	0.000	0.027
Ambient Temp (C)	25.0	C/W		(C)		(C)	Vcc0_ddr			1.500	0.006	0.000	0.006		
Use custom TjA?	Yes		5.5	83.8	26.2	Vccadc			1.710	0.025	0.000	0.025			
Custom TjA (C/W)	5.5	Supply Power (W)													
Airflow (LFM)	NA	Total	0.219	0.006	0.212										
Heat Sink	High Profile														
Custom TSA (C/W)	NA														
Board Selection	Large (20"x20")														
# of Board Layers	16 or more														
Custom TjB (C/W)	NA														
Board Temperature (C)	NA														

Fig. 8 a Power analyses of AMBA AHB without clock gating technique. **b** Power analyses of AMBA AHB with clock gating technique

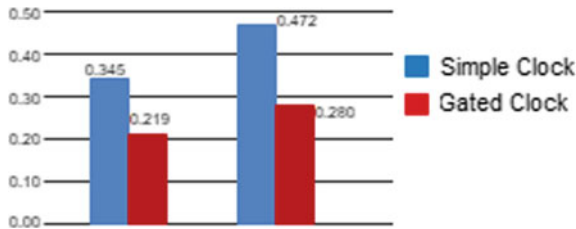


Fig. 9 Power consumption analyses between simple clock and gated clock in the bus

Acknowledgements We would like to thanks Mr. Chiranjeev Singhal and the whole DKOP Labs Pvt Ltd team for supporting and motivating us to write this paper. We would also like thanks Mr. PC Joshi, Assistant Professor of Galgotias College of Engineering and Technology, for mentoring us in the right direction.

References

1. Giridhar Perumalla DPC (2019) Design and verification of AMBA AHB. In: 1st international conference on advanced technologies in intelligent control, environment, computing and communication engineering (ICATIECE)
2. Priyanka KC, Shailesh ML (2017) Decisive analysis of AMBA AHB-APB bridge. India IJIR 3(3), ISSN: 2454-1362. In: Proceedings of 4th international conference on current trends in engineering, science technology and management
3. Zhao P, Wang Z (2010) Power optimization for VLSI circuits and systems. In: 10th IEEE international conference on solid state and integrated circuit
4. Murgai S, A G P K (2006) Design and implementation of low power clock gated 64-bit ALU on ultra scale FPGA s.l. In: American Institute of Physics Advancement of Science and Technology AIP Conference
5. Anand N, Joseph G, Oommen SS (2014) Performance analysis and implementation of clock gating techniques for low power applications. In: International conference of science, engineering and management research, IEEE-32331
6. Lakshmi SV, Vishnu Priya PS, Prema S (2015) Performance comparison of various clock gating techniques. IOSR Journal of VLSI and Signal Processing (IOSR-JVSP) 5(1):15–20. Ver. II (Jan - Feb. 2015)

SPICE Based Design and Implementation of Digital Circuits Using GALEOR Technique



Puneet Kumar Mishra, Amrita Rai, Mayank Rai, and Amiya Prakash

Abstract A low-power VLSI design technique is currently needed for a digital circuit with optimization of a trade-off between power dissipation and delay parameters of circuits. This paper explores a low-power VLSI design methodology, gated leakage transistor (GALEOR) and increases a resistive trail between power supply node and ground node with reducing the leakage current flowing through the circuit. In GALEOR leakage power technique, two gated leakage transistors are inserted in convention CMOS circuit with MOSFET mechanism that utilizes diode by shorting gate terminal with drain terminal. We show the comparative analysis between GALEOR technique and conventional CMOS technique that we perform on basic digital gate circuit with SPICE programming by HSPICE EDA tool.

Keywords CMOS · Delay · GALEOR · Power dissipation · SPICE

1 Introduction

Power dissipation is a significant concern in the design of static CMOS VLSI circuits made with an array of PMOS as pull up device and NMOS as pull down device. Increasing in value of power dissipation will lead to heating phenomenon in the case of digital application of VLSI circuits. If we go for power dissipation concept in VLSI circuits, there are two types of dynamic power dissipation in digital circuits, one is

P. K. Mishra (✉) · A. Rai · M. Rai · A. Prakash

Department of Electronics and Communication Engineering, GL Bajaj Institute of Technology and Management, Greater Noida, India

e-mail: puneetmishra1988@gmail.com

A. Rai

e-mail: amritaskrai@gmail.com

M. Rai

e-mail: mayakraiideal@gmail.com

A. Prakash

e-mail: amiyprakash@gmail.com

© Springer Nature Singapore Pte Ltd. 2021

R. Agrawal et al. (eds.), *Advances in Smart Communication and Imaging Systems*,

Lecture Notes in Electrical Engineering 721,

https://doi.org/10.1007/978-981-15-9938-5_65

unwanted switching activity of load capacitance which generate by generally race around condition of clock application to circuits. Second one is short-circuit power dissipation which occurs due to a current flow between power supply (V_{DD}) and ground (GND) because of finite rise and fall time of clock signal applied at input side of circuits [1, 2]. Other prospective of power dissipation is static power dissipation which will find by MOSFET mechanism/working its self, and there are about six components of leakage current in calculating of static power dissipation for CMOS VLSI circuits with dominant component of sub-threshold leakage current [3]. With technology processes growing toward the deep-submicron system, the feature sizes of the transistors are becoming smaller [4]. The reduction in feature size also forces a reduction in channel length which also decreases the threshold voltage of circuits by leading the cost of leakage current or increasing the value of power dissipation in reference of static power dissipation [4]. Decreasing of threshold voltage will also affect the noise margin and fan-out of switching circuits. In case of dynamic power dissipation, we major concern about short-circuit power dissipation and minimized by increasing a resistive path between power supply and ground [4, 5]. Our motive in this paper is to utilize a power reduction technique in conventional static CMOS circuits and try to increase threshold voltage of circuits and also to increase a resistive path between V_{DD} and GND with optimization of delay and power dissipation product by using 90 nm technology SPICE based simulation of comparative analysis of conventional CMOS and GALEOR based basic digital circuits [5].

1.1 GALEOR Technique

GALEOR technique is basically concentrated on two mechanism, one to increase overall value of threshold voltage of circuits, and second one is increasing a resistive path between V_{DD} and GND [4]. In this technique, the maximum reduction in leakage power is achieved by introducing high threshold voltage transistors, with diode configuration of MOSFET [6] by introducing two gated leakage transistors with high threshold voltage value are inserted below PMOS and above NMOS circuitry of the existing circuit such that gates of the extra inserted transistors are connected to their respective drain regions [4]. The block diagram of GALEOR technique is shown in Fig. 1 [2, 7].

From Fig. 1, GALEOR technique assemble with two transistors: M1, PMOS and M2, NMOS by connecting gate of transistors M1 and M2 with drain terminal of inserting transistors [8]. GALEOR is efficient for both sleep and active state of the circuit with efficient reduction of leakage current. GALEOR reduces leakage power without increasing switching power. It does not require additional circuitry for monitoring the states of the overall circuit. This minimized the short-circuit power dissipation of the additional circuitry which has to be active even when overall circuit is sleep mode. Either one of the two transistors M1 and M2 is always “near its cutoff voltage” for any changes in input combination, without controlling of inserting MOSFETs [8–10].

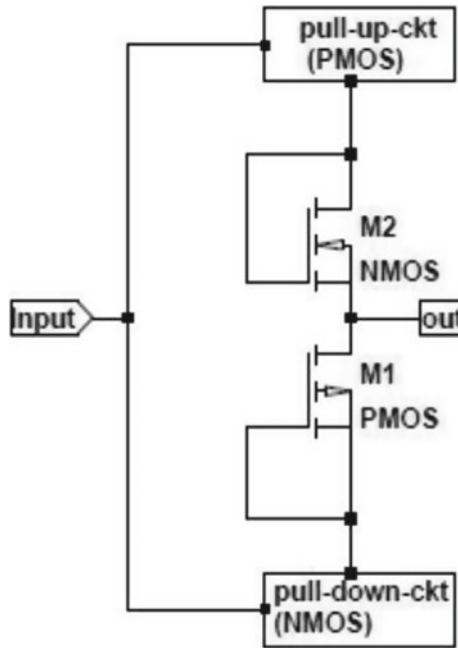


Fig. 1 GALEOR technique [4]

2 Analysis and Results

The GALEOR technique was implemented on the three basic circuits, i.e., NAND, NOR, and NOT (inverter) gates, and the results of conventional CMOS NAND, NOR, and NOT gate circuits were compared and analyzed with GALEOR-implemented NAND, NOR, and NOT gate circuits, respectively.

We conducted the following analysis on the CMOS circuits under study:

- Transient analysis—for calculation of power and delay.
- DC analysis—for calculation of threshold voltage.

2.1 NOT Gate (Inverter) Using CMOS Technique: Transient Response

See Fig. 2.

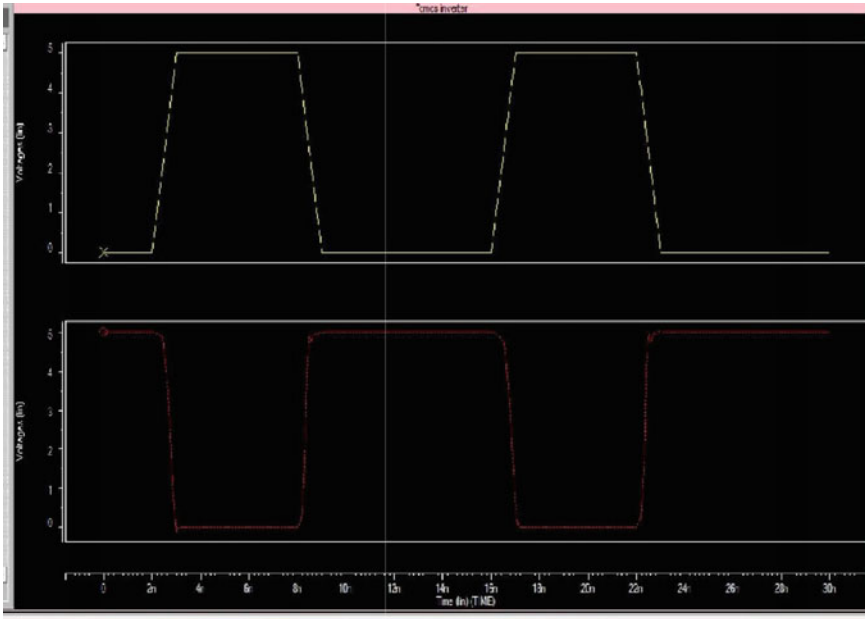


Fig. 2 NOT gate (inverter) using CMOS technique: transient response

2.2 NOT Gate (Inverter) Using CMOS Technique: Leakage Current and Average Power

See Fig. 3.

2.3 NOT Gate (Inverter) Using CMOS Technique: DC Analysis (Transfer Curve) for CMOS Inverter

See Fig. 4.

2.4 NOT Gate (Inverter) Using GALEOR Technique: Transient Response

See Fig. 5.

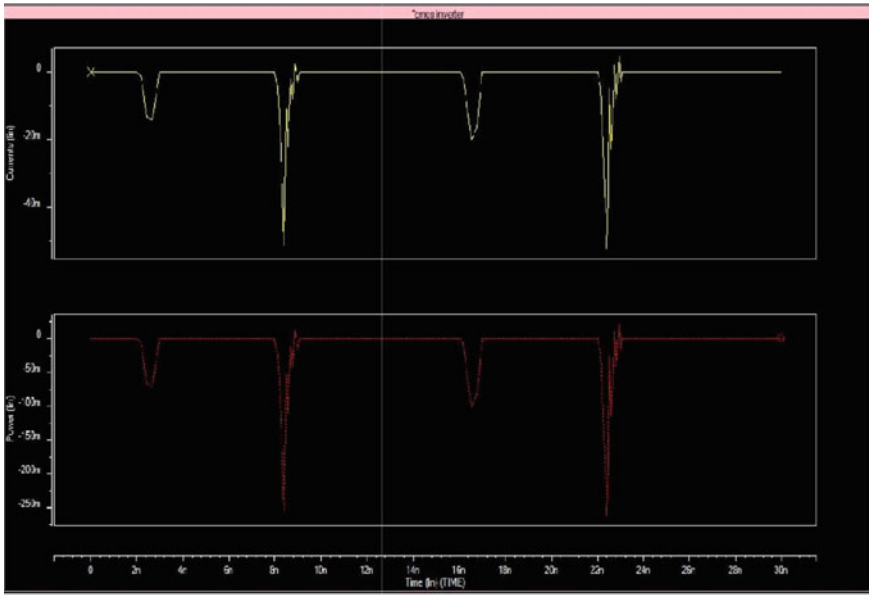


Fig. 3 NOT gate (inverter) using CMOS technique: leakage current and average power

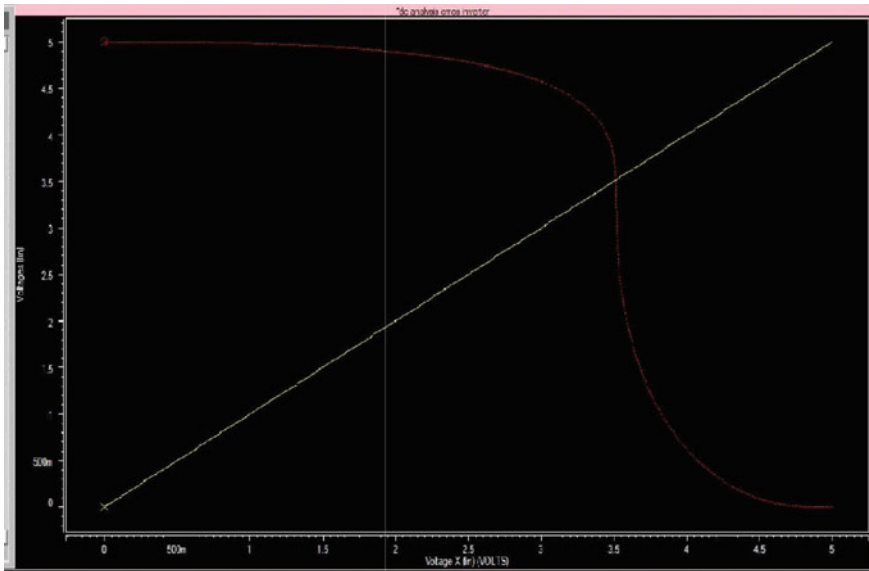


Fig. 4 NOT gate (Inverter) using CMOS technique: DC analysis (transfer curve) for CMOS inverter

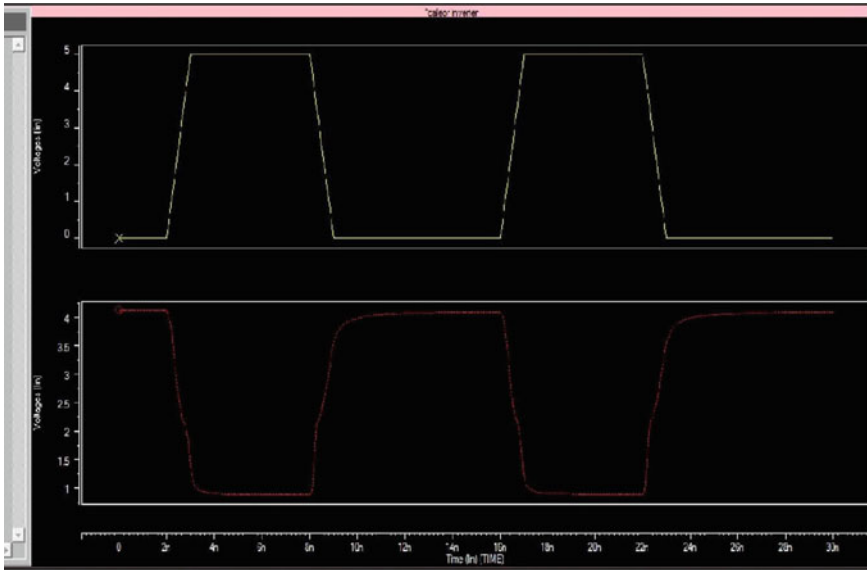


Fig. 5 NOT gate (inverter) using GALEOR technique: transient response

2.5 NOT Gate (Inverter) Using GALEOR Technique: Output Current and Average Power

See Fig. 6.

2.6 NOT Gate (Inverter) Using GALEOR Technique: DC Analysis (Transfer Curve)

See Fig. 7 (Table 1).

3 Conclusion

From paper study, GALEOR technique effectively enhances the threshold voltage of the basic digital circuits and also minimized the power dissipation of circuits by leading the cost of delay on performance of NOT, NAND, and NOR gate with implemented by using static CMOS and GALEOR technique. Through a comparatively study between two techniques, we found where high threshold value is needed, and we utilized GALEOR technique-based logic circuits as compared to conventional CMOS logic circuits.

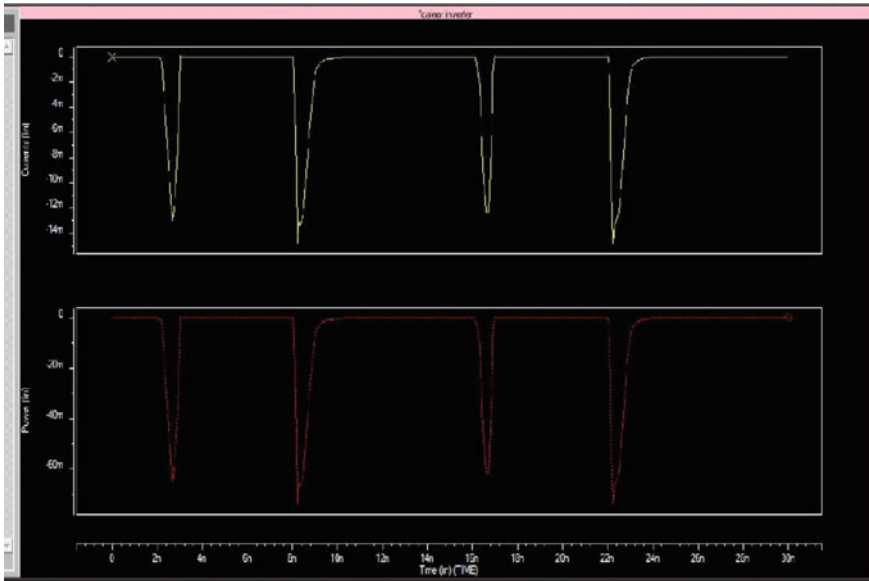


Fig. 6 NOT gate (inverter) using GALEOR technique: output current and average power

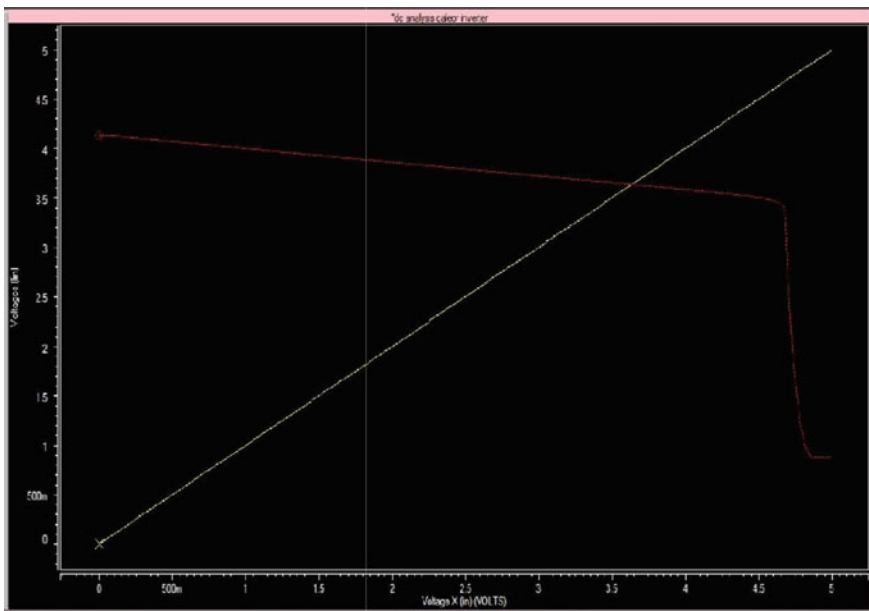


Fig. 7 NOT gate (inverter) using GALEOR technique: DC analysis (transfer curve)

Table 1 Analysis and comparison of GALEOR technique with conventional CMOS circuits

Circuit	VCC (Volt)	I(V _{CC}) (mA)	Power ~P _{avg} (mW)	Threshold voltage, V _{th} (Volt)	T _{PHL} (ns)	T _{PLH} (ns)	Delay (ns)
CMOS inverter	5	51.2	256	3.50	0.23	0.18	0.205
GALEOR inverter	5	14.6	74.1	3.64	0.33	0.24	0.285
CMOS NAND	5	37.5	187	3.97	1.13	0.08	0.605
GALEOR NAND	5	19.2	97.7	4.10	1.27	0.19	0.73
CMOS NOR	5	46.4	232	2.70	0.07	1.07	0.50
GALEOR NOR	5	19.9	99.5	2.73	0.21	0.88	0.545

(continued)

Table 1 (continued)

Circuit	VCC (Volt)	I(V _{CC}) (mA)	Power ~P _{avg} (mW)	Threshold voltage, V _{th} (Volt)	TPHL (ms)	TPLH (ns)	Delay (ns)
Analysis and Comparison of Output Current and Average Power for basic circuits between conventional CMOS and GALEOR technique							
VCC (Volt)	Inverter	Inverter	NAND	NOR	NOR		
I(VCC) (mA)	5	5	5	5	5	5	5
Pavg (mW)	51.2	14.6	37.5	19.2	46.4	19.9	
	256	74.1	187	97.7	232	99.5	

References

1. Weste NHE, Harris D, Banerjee A (2009) CMOS VLSI design, 3rd edn. Pearson
2. Kang S-M, Leblebici Y (1996) CMOS digital integrated circuits, 3rd edn. McGraw-Hill
3. Roy K, Mukhopadhyay S, Mahmoodi H (2003) Leakage current mechanisms and leakage reduction techniques in deep-sub micrometer CMOS circuits. *Proc IEEE* 91(2):305–327
4. Uyemura JP (2001) CMOS logic circuit design. Springer
5. Sharma J, Khandelwal S, Akashe S (2015) Implementation of high performance SRAM cell using transmission gate. In: 2015 fifth international conference on advanced computing and communication technologies
6. Rahman N, Sing BP (2013) Static-noise-margin analysis of conventional 6T SRAM cell at 45nm technology. *Int J Comput Appl* (0975–8887) 66(20):19–23
7. Katrue S, Kudithipudi D (2008) GALEOR: leakage reduction for CMOS circuits, electronics, circuits and systems, ICECS 2008. In: 15th IEEE international conference on 2008, pp 574–577
8. Kim SH, Mooney III VJ (2006) Sleepy keeper: a new approach to low-leakage power VLSI design. In: 2006 IEEE international conference on Very Large Scale Integration, pp 367–372
9. Xue J, Li T, Deng Y, Yu Z (2010) Full-chip leakage analysis for 65nm CMOS technology and beyond, integration. *VLSI J* 43(4):353–364
10. Singhal S, Gaur N, Mehra A, Kumar P (2015) Analysis and comparison of leakage power reduction techniques in CMOS circuits. In: 2015 2nd international conference on signal processing and integrated networks

Efficient Energy Allocation Strategies for Various Cooperative Communication Schemes



Vivek K. Dethe, Om Prakash, and C. V. Ghule

Abstract The issue of ideal vitality allotment and utilize excellent resources for several cooperative transmission protocols is taking attention in existing and advance mobile Ad-hoc constellation. The objective is to accomplish a delay within control and maintaining the average transmit energy limitation with minimum blackout likelihood. To achieve this, we compare the performance of the compress-and-forward (CF), estimate-and-forward (EF), and non-orthogonal amplify-and-forward (NAF) protocols specifically and map these results with the ODF performance. We also proposed a hybrid opportunistic model that selects the best resources to achieve the target rate with the least transmit energy. For conventions utilizing the resources efficiently with vitality imperatives, the instant pace of EF is nearing to NAF for the available link state. The outcome shows that the combination of schemes and protocols can offer postponement constrained limits near the cut-set upper bound.

Keywords Cooperative communication · Amplify-and-forward relaying technique · Transmit diversity · Ad-hoc networks · Orthogonal AF relaying · Channel state information at transmitter/receiver (CSIT/R)

V. K. Dethe (✉)
ECE Department, SJIT University, Jhunjhunu, Rajasthan, India
e-mail: vivekdethe@yahoo.com

O. Prakash
ECE Department, St. Mary's Engineering College, Hyderabad, Telangana, India
e-mail: om4096@gmail.com

C. V. Ghule
ECE Department, Faculty of Engineering Ahmednagar, Adsul Technical Campus, Ahmednagar, Maharashtra, India
e-mail: shekhar.ghule@gmail.com

1 Introduction

In the absence of channel conditions at the sender node, limited efficiency for resource sharing is achieved [5, 11]. However, for instantaneous CSIT, significant gains can be achieved by adapting the channel state under assumptions for analysis. In [3], the ergodic limit of an agreeable framework has investigated under both present moment, and long haul normal all-out transmit vitality limitations. Host-Madsen and Zhang [8] additionally investigate the blackout limit with a transient absolute transmit vitality requirement for both coordinated and offbeat transfers. In [2, 9], resource assignment is considered to advance the ergodic limit under isolated vitality limitations at the source and the transfer node. In [1, 12], blackout execution with a drawn-out normal absolute transmit vitality requirement is researched where full-duplex transfers collaborate independent of the link state; in this manner, no link asset allotment required. In [9], it is presented a sharp ideal vitality allotment plot for the two-source enhance and-forward convention.

Notwithstanding asset designation, when the source and the handoff approach the immediate channel amplitudes, they likewise have a chance to choose a helpful transmission convention [8]. In [7, 10, 13], the possibility of collaboration utilizing decode-and-forward (DF) handing-off has been proposed. In this, the node chooses to decode-and-forward (DF), or direct transmission (DT) contingent and convention are more beneficial in the present link state. This hybrid convention is called orthogonal decode and forward (ODF). The outcomes in [6, 14] show that the opportunity of picking among numerous transmission plans improves both the deferral restricted limit and the base blackout likelihood fundamentally. Separately, the ODF seemed to match the delay limit, while DF and DT only have minimal deferral confined cutoff points. Such plans can be utilized in multiuser disclosure in satellite versatile correspondence structure [15].

2 Proposed Model

A simple cooperative communication system is formed with a one-transmitter node (S), one-receiver (D), and an intermediate node (R), as shown in Fig. 1.

The links between S , D , and R assumed as:

1. An independent link
2. Quasi-static Rayleigh fading

Fig. 1 One-transmitter, one-mid node, one-receiver model

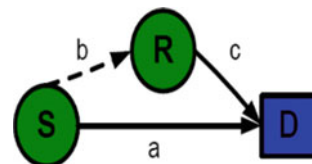


Fig. 2 Two-transmitters one-receiver cooperative transmission system model

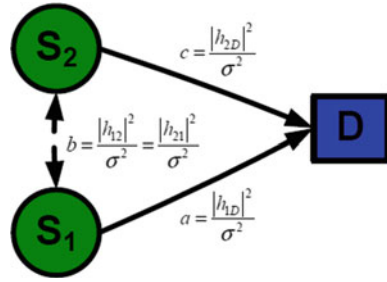
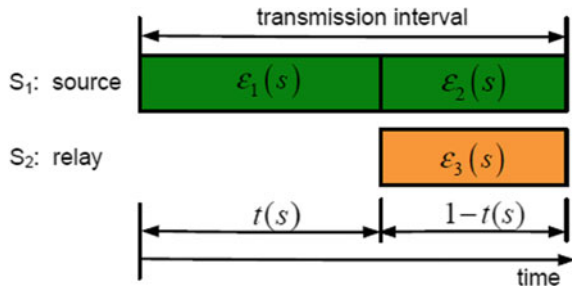


Fig. 3 Half-duplex cooperative conventions



3. Path loss with a zero-mean additive white Gaussian noise
4. Unit variance.
5. Channel coefficients are constant over a block of N symbols.
6. Channel amplitudes $a = |h_1|^2, b = |h_2|^2, c = |h_3|^2$ as in Fig. 2, are exponentially dispersed irregular factors with implies $\lambda a, \lambda b,$ and $\lambda c,$ separately (Fig. 3).

The link sufficiency vector ‘s’ is known at every hub $S, R,$ and at $D,$ while the stage data is accessible just on the beneficiary. The absence of data on the transmitters in the channel stage suggests that the source and the relay cannot be build up. To start with, we attempt to amplify the deferral restricted limit of the framework under a drawn-out normal all-out transmit vitality limitation. The momentary limit with this asset distribution work $E(s)$ at channel state $S.$ With this definition of the condition mentioned above, our objective of limiting blackout likelihood under a drawn-out standard complete transmits vitality requirement, can be composed as

$$P_{out} = \text{Probability} [C(\mathcal{E}(s), s) < R] \tag{1}$$

$\mathcal{E}(s) \in \bar{\Omega}$

3 Hybrid Optimum Energy Allocation with Full CSIT

3.1 Delay-Restricted Limit Investigation

Deferral restricted limit characterizes the most extreme transmission rate free from link condition [4, 7]. This arrangement is valuable for lagging zones, for example, continuous real-time interchanges in communications and live telecasts. However, the link condition parameters are required to guarantee a nonzero transmission rate with invalid blackout likelihood.

Presently, we think about various conventions and dynamically designate the transmit time and vitality among the terminals, given the divert states to boost the restricted postponement limit.

Let $\mathcal{E}(s)$ be the asset allotment capacity, and $C(\mathcal{E}, s)$ be the quick limit of the fundamental participation convention at channel state S . The deferral constrained limit boost issue defined as “maximum $_{\mathcal{E}(s) \in \bar{\Omega}}$ R , such that $C(\mathcal{E}((s), s))$ greater than or equal to R for free states.”

We present specific collaboration conventions for deferral restricted limit as follows:

3.1.1 Non-symmetrical Enhance and Transmit

In this convention [8, 14], the link separated into two equivalent parts, that is $T(S) = 1/2$ for all states. In T_1 , first timeslot, the S transmits a sign to the handoff, and the receiver remains silent during the transfer mode. In T_2 , the second timeslot, the handoff occurs from the first timeslot and retransmits, and the source at the same time transmits new images. The maximum value of coefficients is useful for getting the maximum value of mutual information. Efficiency is achieved in this constellation, only one at a time, i.e., transmitter relay the information or share the time slot for maximization of use of available resources.

3.1.2 Compress and Forward Relaying

The compress-and-forward handing-off presented in paper [9] by which handoff in the first timeslot quantized and packs the received signal and afterward in the second timeslot transmits the compacted signal towards destinations. The source keeps on transmitting dedicated data packets [10]. In this convention, it is not vital to have $t(s) = 1/2$, bringing about greater adaptability contrasted with OAF and NAF.

The limit with regards to CF utilizing resource allotment function $E(s)$ is defined:

$$C(\text{CF})(\mathcal{E}, s) = t(s) \log \left(A + \frac{b\mathcal{E}_1}{1 + \sigma^2 w} \right) + (D) \log(C) \quad (2)$$

where A is an additive factor, and D is a delay. The deferred capacity is obtained by solving the Eq. (2). It improves the performance, but the complexity of the constellation increased at the middle and end parts of the system.

3.1.3 Estimate and Forward Relaying

In this constellation, the transfer signal disregarding the sideband at the receiver and called estimate-and-forward (EF). The momentary limit of EF with vitality portion $E(s)$ at state S is

$$C(\text{EF})(\mathcal{E}(s), s) = t(s) \log\left(A + \frac{b\mathcal{E}_1}{1 + \hat{\sigma}^2 w}\right) + (D) \log(1 + a * \mathcal{E}_2) \quad (3)$$

At the point, when we give delay-constrained limit correlations of various conventions, we will likewise think about a more straightforward adaptation with fixed and equivalent time portion. The final equations derived by setting $T = 1/2$ in conditions (2) and (3). Both the conventions under particular condition; consequently are adaptive.

3.2 Hybrid Opportunistic Optimum Energy Allocation

In the hybrid opportunistic mode, various conventions are utilized at each channel to diminish the delay and target rate achieved at each channel. We remember CF for collaboration conventions. The postponement constrained limit of the hybrid convention and defined as

$$\begin{aligned} &\text{maximum, such that maximum}\{\text{CCF}(\mathcal{E}, s), \text{CDF}(\mathcal{E}, s)\} \text{higher than or equal to } R, \\ &\mathcal{E}(s) \in \overline{\Omega} \\ &\text{for all states.} \end{aligned} \quad (4)$$

3.3 Upper Bound to the Delay-Limited Capacity

We now derive an upper bound (SCB) to the delay-limited capacity by using the usual cut-set bounds for the half-duplex relay. The instantaneous limit at a particular time can be limited above by

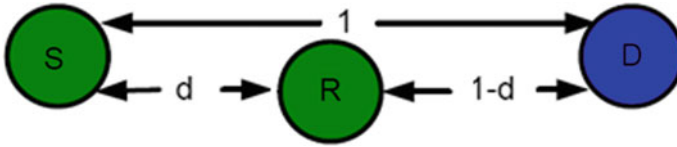


Fig. 4 Simulation model

maximum R such that $C_{CSB}(\mathcal{E}, s)$ more significant than equal to R , for all states.

$$\mathcal{E}(s) \in \bar{\Omega}$$

(5)

The articulation (5) gives an upper bound to the postponement constrained limit since CCSB is an upper bound to the momentary limit at each channel acknowledgment.

3.4 Numerical and Simulation Results

Delay-Limited Capacity Results

The position of R in communication link S and R affected the performance of the link and experimented by using a model in Fig. 4.

We standardize the separation between the S and D and accept that the node situated among S and D . The assumptions made are enumerated above in the proposed model. The numerical and simulation carried out by using Matlab.

Figure 5 shows the deferral restricted limit as a component of the drawn-out normal all-out transmits vitality imperative for various handing-off conventions for a handoff area of $d = 0.5$. The results demonstrate that EF with ideal time allotment can accomplish a restricted postponement limit than CF with the assignment when the handoff is hugely near the receiver or transmitter. When the handoff is near the destination, EF benefits less from the ideal time portion. At the point when the transfer is near the transmitter, NAF performs nearly just as EF with a fixed time assignment. Additionally, the hole among NAF and CF with the ideal time portion is practically free from the handoff area. The outcomes in Fig. 6 affirms that time designation is progressively necessary for CF when the R is near the S or D . It shows that even a basic collaboration technique can improve the exhibition of deferral constrained frameworks. In the low force district, NAF still can be a feasible arrangement as the additions are low for higher complex conventions.

From Fig. 7, when the distance crosses 0.83, the performance of the compress-and-forward scheme is better than the orthogonal decode and forward scheme. In this way, by adaptively picking one of the constellations, the half breed convention is better than both CF and ODF. The pattern is the equivalent in Fig. 8. Without an ideal time assignment, the presentation holes between the CSB and different conventions become bigger compared with the case with the ideal time portion.

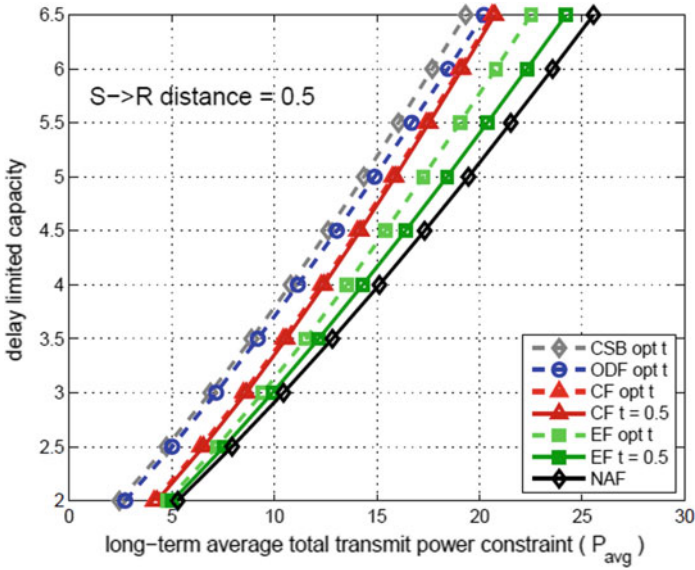


Fig. 5 Capacity versus total average transmit energy $\mathcal{E}_{average}$ when $d = 0.5$

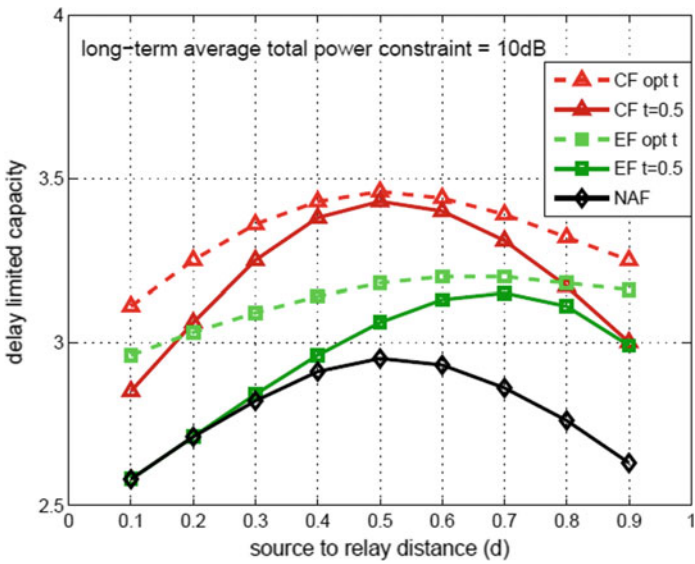


Fig. 6 Capacity versus distance. CF, EF, and NAF protocol with and without optimal time allocation

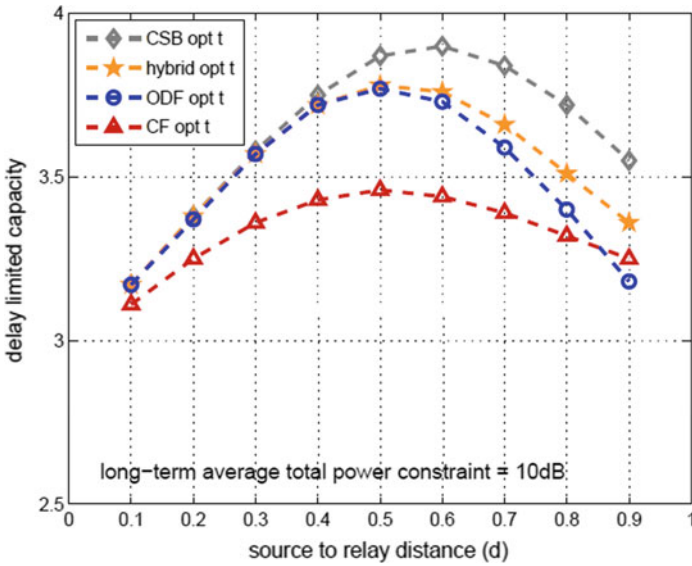


Fig. 7 Capacity versus distance. Hybrid protocol and CSB

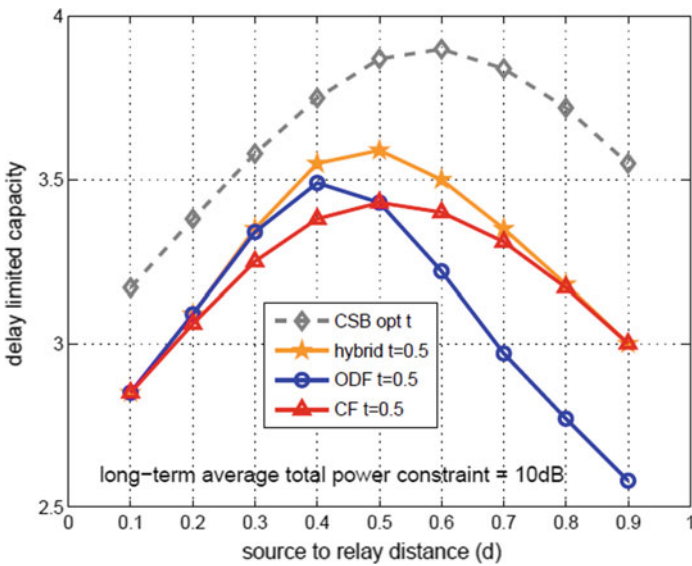


Fig. 8 Capacity versus distance. ODF, CF, Hybrid protocol, and CSB

In all the conventions, ODF is influenced most by the nonattendance of ideal time distribution. We note that CF starts better performing than ODF when distance equals half marks in Fig. 8. For this situation, the benefit of the CF and ODF is significantly progressively self-evident.

4 Conclusion

In this paper, we dissect and think about the postponement restricted limit and blackout likelihood of various cooperative conventions such as compress-and-forward (CF), estimate-and-forward (EF), opportunistic decode-and-forward (ODF), and non-orthogonal amplify-and-forward (NAF) under power constraint and availability of channel amplitudes at source and the relay node. Our results show that, under the condition of optimum resources and energy constraints, EF performance matching with that of NAF. The cross convention offers the unaffected postpone restricted capacity execution, close by blackout likelihood execution since it perpetually chooses the convention with the base all-out transmit power in each channel state. The numerical outcomes show that the mixed convention, in general, is flexible. The postponement constrained capacity of NAF is not close to as high as any of the other helpful conventions. Hence, NAF should have useful in existing as well as futuristic sensible cooperative transmission systems. The Rician, Nakagami channel models could be used for extension of the present study.

References

1. Ahmed E, Gharavi H (2018) Cooperative vehicular networking: a survey. *IEEE Trans Intell Transp Syst* 996–1014
2. Deng Q, Guo L, Dong C et al (2017) High-throughput signal detection based on fast matrix inversion updates for uplink massive multiuser multiple-input multi-output systems. *IET Commun* 2228–2235
3. Doosti-Aref A, Ebrahimzadeh A (2018) Adaptive relay selection and power allocation for OFDM cooperative underwater acoustic systems. *IEEE Trans Mob Comput* 1–15
4. Gao X, Dai L, Han S et al (2017) Reliable beamspace channel estimation for millimeter-wave massive MIMO systems with lens antenna array. *IEEE Trans Wirel Commun* 6010–6021
5. Gao Z, Dai L, Qi C et al (2017) Near-optimal signal detector based on structured compressive sensing for massive SM-MIMO. *IEEE Trans Veh Technol* 1860–1865
6. Gunduz D, Erkip E (2007) Opportunistic cooperation by dynamic resource allocation. *IEEE Trans Wirel Commun* 1446–1454
7. Han G, Dong Z, Zhang J-K, Mu X (2017) Orthogonal binary modulation division for two-user uplink massive MIMO systems with noncoherent ML detection. *IEEE Commun Lett* 294–297
8. Host-Madsen A, Zhang J (2005) Capacity bounds and power allocation for wireless relay channels. *IEEE Trans Inf Theory* 2020–2040
9. Liang Y, Veeravalli V, Poor H (2007) Resource allocation for wireless fading relay channels: max-min solution. *IEEE Trans Inf Theory* 3432–3453
10. Liu ZY, Mao P, Feng L, Liu SM (2018) Energy-efficient incentives resource allocation scheme in cooperative communication system. *Wirel Commun Mob Comput* 1–8

11. Luo J, Blum R, Cimini L et al (2007) Decode-and-forward cooperative diversity with power allocation in wireless networks. *IEEE Trans Wirel Commun* 793–799
12. Qu W, Zhang M, Cheng X, Ju P (2017) Generalized spatial modulation with transmit antenna grouping for massive MIMO. *IEEE Access* 26798–26807
13. Xiao L, Yang P, Xiao Y et al (2017) Efficient compressive sensing detectors for generalized spatial modulation systems. *IEEE Trans Veh Technol* 1284–1298
14. Yang GQ, Shuang W, Ya-Ru H (2019) Deep learning network for multiuser detection in satellite mobile communication system. *Comput Intell Neurosci* 1–11
15. Yang J, Brown DR (2006) The effect of channel state information on optimum energy allocation and energy efficiency of cooperative wireless transmission systems. In: 40th Annual conference on information sciences and systems

Steganography Using Block Pattern Detection in AMBTC Image



Neeraj Kumar and Dinesh Kumar Singh

Abstract In general, AMBTC-based steganography techniques effectively utilize smooth blocks for secret data embedding but keeps complex blocks as it is. It is considered that any modification in the complex blocks may cause a substantiate distortion in an original image. Therefore, conventional techniques do not make any modification in complex blocks. In proposed paper, a technique is disclosed for secret data embedding in complex blocks in addition to smooth blocks. It shows that a cluster of bit-map blocks corresponding to complex blocks of multiple images are formed, and then most frequent 256 bit-map blocks are determined based on histogram analysis. Multiple images can be drawn from any standard image database. The most frequent 256 bit-map are block patterns which are indexed using 8 bits. Now, for secret data embedding, bit-map of each complex block is scanned one-by-one and is compared with the 256 bit-map block patterns. If the bit-map of scanned complex block is matched with any of the 256 block patterns, then first 8 bits of bit-map of scanned complex block is replaced with 8-bit index of matched block pattern and remaining 8 bits of bit-map of scanned complex block are replaced with secret data. Thus, this technique shows a way of embedding secret data in complex blocks using block patterns. Further, for the smooth blocks, present technique utilizes Ou et al. technique which is efficient for secret data embedding in smooth blocks. Results of the proposed scheme show increase in embedding capacity while preserving image quality.

Keywords AMBTC · Image quality · Embedding capacity · Quantization level · Steganography

N. Kumar (✉)
Jamia Millia Islamia University, New Delhi, India
e-mail: neeraj.mohiwal@gmail.com

D. K. Singh
Department of Electronics and Communication Engineering, GL Bajaj Institute of Technology and Management, Greater Noida, India
e-mail: dinesh12dk@gmail.com

1 Introduction

Internet platform is best medium for communicating any information from one end to another end. Using the internet platform, person sitting at any geographic location can transmit or receive the information from the person sitting at different geographic location. However, one of the drawback of the internet platform is that it is a public platform network [1], so security of information cannot be guaranteed. Information can be easily intercepted by any intrusion system in the network. Sometimes information is very sensitive, and it cannot be sent without guaranteeing a secure transmission. Therefore, non-leakage of information should be assured before transmitting the information. Conventional systems provide two ways of secure data transmission. One of the ways is an encryption technique [2] and other is a steganography technique [3]. Steganography is an efficient technique to covertly sending data in the public network. In any steganographic techniques, an image is a best media to be utilize as a cover image. There are two types of steganographic techniques; i.e., reversible steganographic technique and non-reversible steganographic technique are disclosed in literature. Reversible steganographic techniques [4–8] are histogram-expansion (HE) technique, difference-expansion (DE) technique, predication-error-expansion (PEE) technique, and pixel-value-order (PVO). Irreversible steganographic techniques [9–12] are least-significant bit (LSB) updation technique, pixel-value-difference (PVD) technique, and the exploiting modification direction method (EMD) technique. LSB updation-based steganographic technique is primary used by image compression-based steganographic techniques such as block-truncation-coding-based steganographic technique. Block-truncation-coding, in short BTC, is one of the simplest techniques for image compression [18]. In 1979, BTC technique has been introduced by Delp and Mitchell. Because of its simplicity, it is utilized in many compression techniques. Further, in year 1984, AMBTC technique is an improvement over BTC technique is proposed [19]. AMBTC is simpler than BTC technique and preserves image quality. Combination of image compression techniques and steganography techniques has become a new dimension of research [20–29]. In next section, we will discuss related works corresponding to BTC (or AMBTC) compression techniques with secret data embedding.

In rest of the paper, Sects. 2 and 3 show the conventional works corresponding to image compression with steganography techniques. Section 4 shows a set of block patterns. Section 5 shows the proposed technique, and Sect. 6 discloses experimental results. Section 7 discloses the conclusion of the proposed technique.

2 Related Works

There are various BTC or AMBTC-based steganography techniques have been proposed. In our knowledge, in 2006, a first data hiding method on BTC coded data is discussed by Chuang and Chang [20]. After this, in 2008, Hong et al. [21]

suggests a secret data hiding method by selectively exchanging high and low quantization levels, and flipping bit-map corresponding to high and low quantization levels based on secret data bit zero or one. Though it is a good scheme, it has very less embedding capacity. Further, this scheme has a problem when the quantization levels are equal. Chen et al. [22] solves this problem by proposing an enhanced data embedding scheme. It suggests that when quantization levels are equal for a block, then its bit-map is utilized for secret data embedding. This method increases embedding capacity than Hong et al. [21]. Chang et al. in [23] suggests reversible data hiding technique for color images. Raj in [24] introduces an interpolation-based data hiding scheme. All these techniques [20–24] has very less embedding capacity. It is desirable to further increase embedding capacity while also increasing (or at least preserving) image quality. In [25], Ou et al. discloses another improved secret data embedding method, thereby secret data hiding capacity along with image quality improves. The embedding capacity increased by additional secret data hiding by changing the order of quantization levels in addition to the replacing bit-map of smooth blocks by secret data. This scheme is mainly focused on smooth blocks, but it does not utilize bit-map of complex blocks for data embedding. It only discloses one-bit data hiding data in complex block by altering the order of low and high quantization levels. Though, Ou et al. discloses an improved method of secret data embedding in smooth blocks, exploitation of the bit-map of the complex blocks is still needed. Proposed scheme discloses a method of secret data embedding (or hiding) in bit-map of the both smooth and complex blocks. It embeds the data in bit-map of the smooth block by a simple bit replacement strategy in accordance to the Ou et al. For the complex block, proposed technique matches bit-map of the complex block with the one of the 256 block patterns. If any block pattern is matched with the bit-map of complex block, then first 8 bits of bit-map is replaced with 8-bit index of matched block pattern and remaining 8 bits are updated with secret data bits. In this way, complex blocks and smooth blocks both are utilized form secret data hiding in proposed scheme.

3 Ou et al.'s Technique

The Ou et al. discussed a way of secret data embedding based on AMBTC coding. AMBTC trio a_i, b_i, B_i for each i_{th} block is obtained and then difference $d_i = a_i - b_i$ between calculated. If d_i is less than a predetermined threshold, then i_{th} block should be considered as a smooth block, else it should be considered as a complex block. If i_{th} block is smooth block, then 16 bits secret data are embedded into bit-map B_i by simple bit replacement strategy and updated bit-map is now known as \dot{B}_i . Then, image block x_i is formed from the \dot{B}_i , by replacing zero in \dot{B}_i from a_i and by replacing one in \dot{B}_i from b_i . Based on the \dot{B}_i , new \dot{a}_i and \dot{b}_i are calculated.

$$\dot{a}_i = \frac{1}{q} \sum_{x_i \geq \bar{x}} x_i$$

$$\dot{b}_i = \frac{1}{p} \sum_{x_i \leq \bar{x}} x_i$$

Now, $\dot{d}_i = \dot{a}_i - \dot{b}_i$ is calculated. If $\dot{d}_i \leq d_i$, then updated AMBTC trio is \dot{a}_i , \dot{b}_i , and \dot{B}_i and if $\dot{d}_i > d_i$, then updated AMBTC trio is a_i , b_i , and \dot{B}_i .

4 A Cluster of Block Patterns

In Fig. 1, a set of most frequent block patterns are shown. These block patterns are selected based on histogram analysis of bit-maps of complex blocks of multiple images. These multiple images can be from one or more image database. A unique 8-bit index is assigned to each block pattern of the set of block patterns (most frequent 256 block patterns in which 128 block patterns are shown in Fig. 1 and remaining 128 block patterns can be obtaining by flipping the block patterns).

5 Proposed Scheme

Our proposed scheme has two parts, one of the part is encoding and other part is decoding part. The encoding part is executed at transmitter side, and decoding part is executed at receiver side. Encoding part is performed by an encoder which encoded the input cover image using AMBTC technique and further secret data bits are hid into the AMBTC coded cover image. Decoding part is performed by a decoder which decodes the AMBTC encoded image and extracts secret data bits from it.

Encoding and secret data embedding process: Initially, the input cover image is broken into number of image blocks, preferably in $4 * 4$ sized blocks. Each of the blocks is classified into complex blocks and smooth blocks depending upon difference between high and low mean quantization levels of the block. If difference is lower than a predetermined limit (or threshold), then that block is considered to be as a smooth block else it is considered to be as a complex block. If the block is smooth, then its corresponding bit-map is simply replaced by the secret data. For the smooth block, data embedding technique is utilized as per disclosed in Ou et al.'s technique. For the complex block, its corresponding bit-map is tried to match with one of the 256 block patterns. If any block pattern is matched, then 8-bit block pattern index is inserted in to first 8 bits of bit-map and remaining 8 bits are replaced by 8-bits secret data. Further, order of high and low quantization levels are changed to ascending order. However, if no block pattern is matched, then bit-map is not changed but order of high and quantization levels is changed to descending order.

Phase 1: Compression and Data Embedding Method

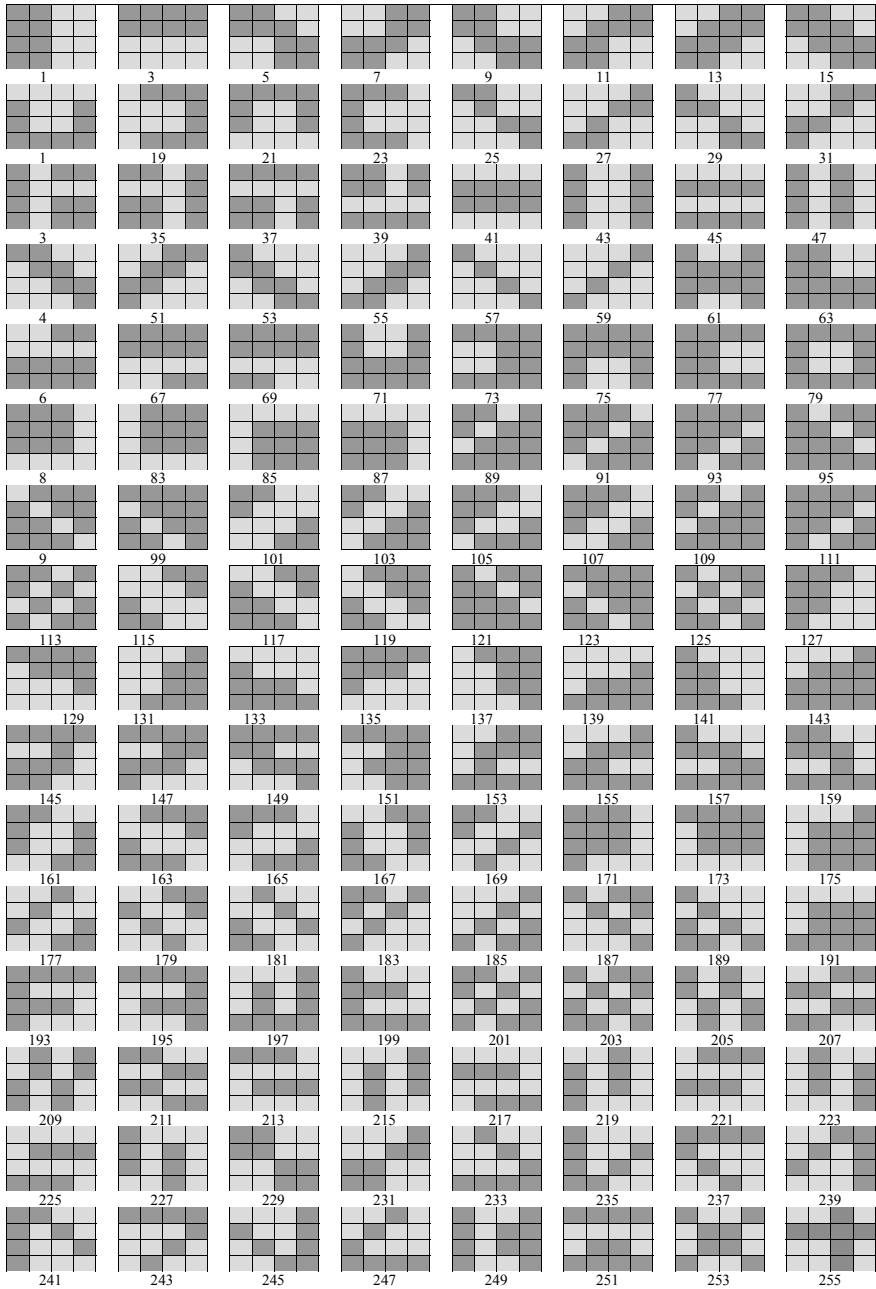


Fig. 1 A set of standard block patterns

Input— I : Original cover image of $M \times M$ pixel size, thr1: Noise Level Threshold, thr2: Block pattern Matching Threshold, S : a stream of secret data bits.

Output—Marked Stego Image I' .

Begin

Step 1: Input the cover image I of size $M \times M$.

Step 2: Break the cover image I into J image blocks of $m \times m$ pixels, where $m = 4$.

Step 3: Estimate the mean gray-level for each of the image blocks as follows:

$$\text{Mean}_j = \frac{\sum_{i=1}^{m \times m} p_i}{m \times m} \quad (1)$$

where p_i representing the i th pixel value of j th block in the image.

Step 4: Estimate high/low quantization levels for each of the image blocks as follows:

$$\text{High}_j = \frac{1}{K_j} \sum_{p_i > \text{Mean}_j}^m p_i \quad (2)$$

$$\text{Low}_j = \frac{1}{16 - K_j} \sum_{p_i \leq \text{Mean}_j}^m p_i \quad (3)$$

here, K_j represent the number of pixels whose gray-level is higher than Mean_j .

Step 5: Construct bit-map B_j for j th block as follows:

- If the pixel value x_i is not less than its respective mean value, mean_j , then the respective bit in the bit-map B_j of the j th block is represented by '1.'
- Else, the pixel is represented by '0.'

Step 6: Estimate difference $\text{Diff}_j = \text{High}_j - \text{Low}_j$.

Step 7: Categorize j th block as a smooth block if $\text{Diff}_j < \text{thr1}$, else j th block is considered as a complex block.

Step 8: If j th block is smooth block, then updates the bit-map B_j with the stream of secret data S , and the modified bit-map is marked as B'_j .

- Substep 8.1: Marked High_j , Low_j and Diff_j as Old High_j , Old Low_j and Old Diff_j .
- Substep 8.2: Repeat step 3 to step 6 to calculate new High_j and Low_j as New High_j and New Low_j .
- Substep 8.3: Calculate New $\text{Diff}_j = \text{New High}_j - \text{New Low}_j$.
- Substep 8.4: If Old $\text{Diff}_j \leq \text{New Diff}_j$, then use $\text{High}'_j = \text{Old High}_j$ and $\text{Low}'_j = \text{Old Low}_j$.
Else use $\text{High}'_j = \text{New High}_j$ and $\text{Low}'_j = \text{New Low}_j$.

Step 9: If j th block is complex block, then scan all the block patterns EB_k of a set of block patterns, where $k = 1, 2, 3, \dots, 0.256$.

- Substep 9.1: For each block pattern EB_k , calculate
- Substep 9.2: Identify minimum value, i.e., Val_k^{\min} from the array of Val_k .
- Substep 9.3: If $Val_k^{\min} < thr2$, then replace initial 8 bits of bit-map B_j by block pattern index of EB_k corresponding to Val_k^{\min} and remaining bits of bit-map B_j are replaced by next bit sequence of secret data S and updated bit-map is marked as B'_j and then keep quantization levels in ascending order as $High'_j = Low_j$ and $Low'_j = High_j$.
Else keep quantization levels in descending order as $High'_j = High_j$ and $Low'_j = Low_j$.

Step 10: Thus, the compressed image block in the form of trios $High'_j$, Low'_j and B'_j is achieved.

Step 11: Repeat step 3 to step 10 for each j th block of all J image blocks.

End

6 Discussion of Proposed Scheme's Results

Now, experimental results of the proposed scheme are discussed with respect to the conventional techniques. Further, a comparative analysis is drawn based on results. The conventional existing techniques which are considered for comparison are such as Chang et al. [23], Raj [24], Keissarian [29], Feng and Lu [30], Dhara and Chanda [31]. For performance comparison, results are taken on different greyscale test images of 512×512 pixel size, namely, Lena, Baboon, Plane, Peppers, Boats, Barb shown in Fig. 2. The performance parameters for comparison secret data hiding capacity and image quality that is defined by PSNR.

6.1 Results of Proposed Technique

Proposed technique is executed on test images which are shown in Fig. 2. In this section, we will discuss performance of the proposed technique with respect to existing techniques Chang et al. [23], Raj [24], Keissarian [29], Feng and Lu [30], Dhara and Chanda [31].

In Table 1, it is shown that techniques utilize type of secret data hiding approach using quantization values and bit-map of image blocks. From the way of showing secret data techniques shown in tabular form—Table 1, it can be deduced that Feng and Lu [30], Dhara and Chanda [31] techniques, embeds data by changing the quantization values but other techniques including proposed technique do not embed data by changing the quantization values. Further, all the techniques except Chang et al. [23] embedded one-bit secret data by altering the order of quantization values. Further, all the techniques except Raj [24] embedded the secret data bits in bit-map of smooth block. At last, only proposed technique utilizes bit-map of complex blocks for secret data hiding and other techniques do not utilize it. This is the advantage of

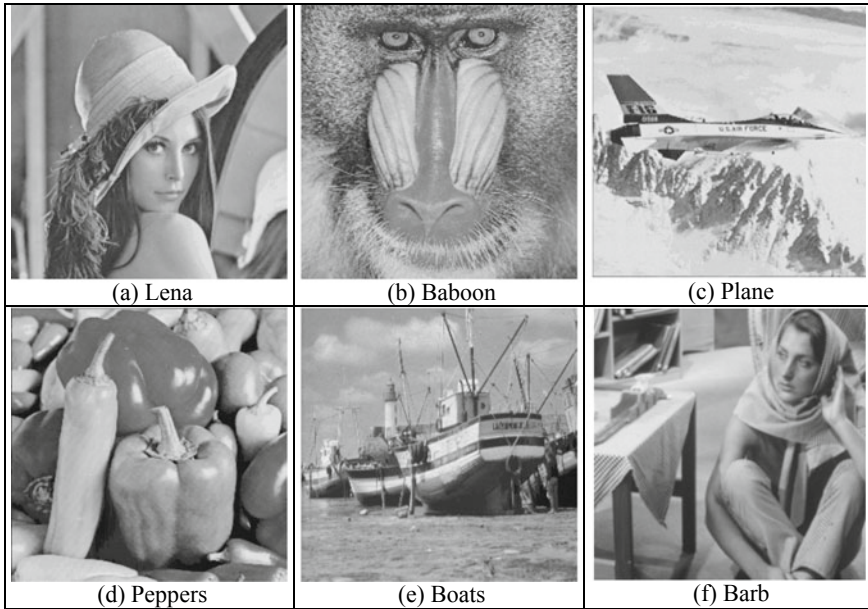


Fig. 2 Cover images

Table 1 Comparison between proposed technique and existing techniques with respect to employed secret data hiding approach

Technique	Quantization values a, b	Order of quantization values	Bitmap of smooth block	Bitmap of complex block
Chang et al. [23]	No	No	Yes	No
Raj [24]	No	Yes	No	No
Keissarian [29]	No	Yes	Yes	No
Feng and Lu [30]	Yes	Yes	Yes	No
Dhara and Chanda [31]	Yes	Yes	Yes	No
Proposed technique	No	Yes	Yes	Yes

proposed technique and same can be seen in performance comparison graphs shown in Fig. 3a–f. Figure 3a–f shows embedding capacity versus PSNR graphs obtained by existing techniques Chang et al. [23], Raj [24], Keissarian [29], Feng and Lu [30], Dhara and Chanda [31] and proposed technique performed on test images.

From the Fig. 3a–f, it is visible that Raj [24] has least embedding capacity but has highest PSNR value. This is because Raj [24] does not change the AMBTC

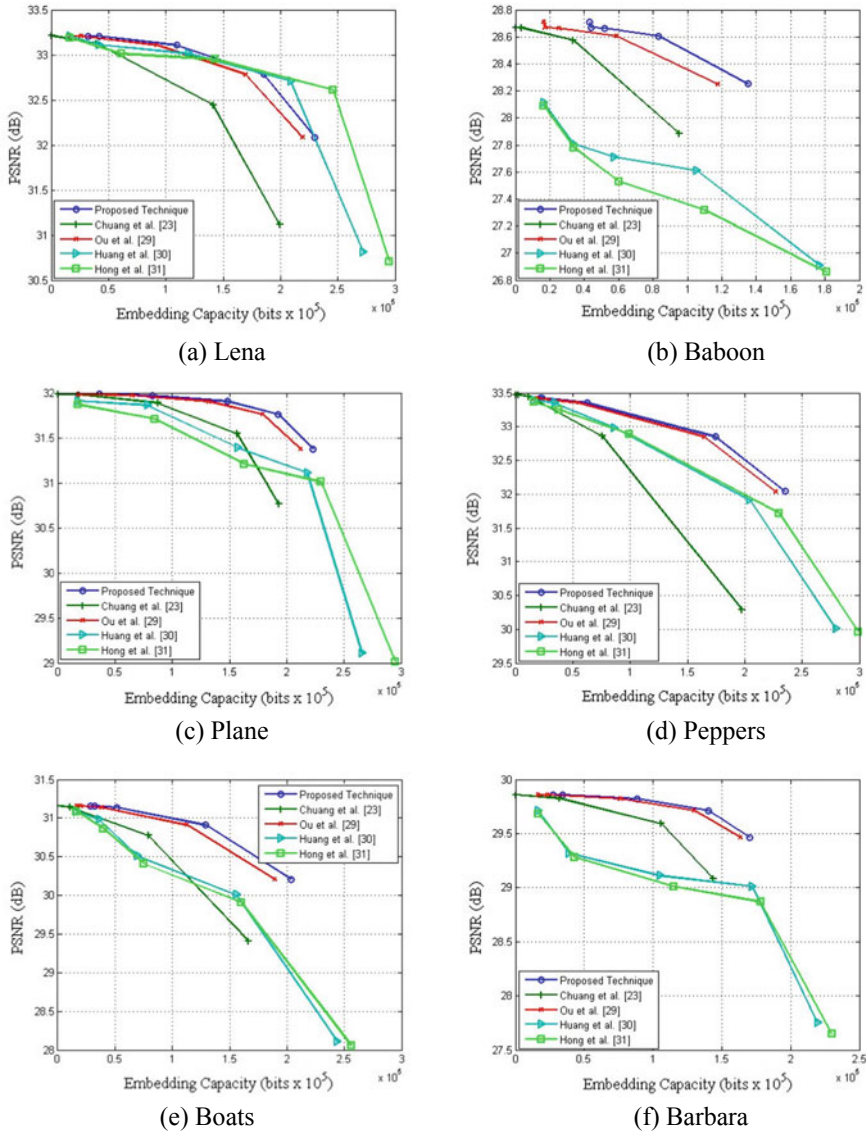


Fig. 3 a–f Comparison PSNR versus embedding capacity results of test images by existing techniques and proposed scheme

coded image while data embedding in AMBTC coded image. It embeds secret data based on changing order of quantization values. So, it has PSNR equal to the standard AMBTC coded image. Proposed scheme has significant data hiding capacity (or embedding capacity) than Chang et al. [23], Raj [24], Keissarian [29] but less embedding capacity than Feng and Lu [30], Dhara and Chanda [31]. Chang et al.

[23] only embeds the data into smooth block while proposed scheme utilize complex blocks along with smooth blocks for secret data bits hiding, so proposed scheme has high embedding capacity than Chang et al. [23]. By comparing with to Keissarian [29], proposed scheme utilizes bit-map of complex blocks for data hiding. So, proposed scheme has greater data hiding capacity than Keissarian [29]. In case of Feng and Lu [30] and Dhara and Chanda [31], these techniques modify the quantization values based on difference between quantization values. The modification is performed to embed additional secret data, therefore these techniques has high embedding capacity. However, because of modification is quantization values, its PSNR values decreases. Proposed scheme have high PSNR value than Feng and Lu [30] and Dhara and Chanda [31] which can be seen in Fig. 3a–f. It is also clearly show that proposed scheme has highest PSNR values among all the techniques for all test images and has same PSNR values as of Keissarian [29]. This is because proposed scheme as well as Keissarian [29] technique recalculate quantization values after secret data replacement. Then, it recalculated quantization values are utilized if it minimizes the distortion. However, such technique is not performed by Chang et al. [23], Feng and Lu [30], and Dhara and Chanda [31] techniques, so they have less PSNR values. From the Fig. 3a–f, it can be also seen than proposed scheme has highest embedding capacity as well as PSNR value in lower range of embedding capacity. In higher range of embedding capacity, proposed scheme has high embedding capacity than Chang et al. [23], Raj [24], and Keissarian [29] but less than Feng and Lu [30] and Dhara and Chanda [31].

7 Conclusion

This method of secret data bits embedding in complex blocks along with smooth blocks is a novel aspect of the proposed scheme. Existing techniques are lack in providing secret data embedding in bit-maps of complex blocks. In the proposed scheme, secret data is embedded by a simple bit replacement strategy in smooth blocks. But in case of complex block, first it is determined that whether the bit-map of the complex block have any block phenomena, which is determined by block pattern matching technique. For this, a closest matching is performed in the bit-map and in a set of block patterns. If any block pattern is determined as closest match, then initial bits of the bit-map is replaced by the block pattern index corresponding to the closest matched block pattern and remaining bits of the bit-map is replaced by the secret data. It shows a good amount of data hiding capacity with an optimum image quality. In future, a set of training block patterns can be identified which can be utilized for the set of block patterns.

References

1. Guo K, Shi L, Ye W, Li X (2014) A survey of internet public opinion mining. In: IEEE International conference on progress in informatics and computing, Shanghai, pp 173–179
2. Dang PP, Chau PM (2000) Image encryption for secure internet multimedia applications. In: 2000 Digest of technical papers. International conference on consumer electronics. Nineteenth in the series (Cat. No.00CH37102), Los Angeles, CA, USA, pp 6–7
3. Lashkari AH, Al Manaf A, Masrom M, Daud SM (2011) A survey on image steganography algorithms and evaluation. In: Digital information processing and communications. Springer, Berlin, pp 406–418
4. Hong W, Chen TS, Chen J (2015) Reversible data hiding using Delaunay triangulation and selective embedment. *Inf Sci* 308(1):140–154
5. Ni Z, Shi Y-Q, Ansari N, Su W (2006) Reversible data hiding. *IEEE Trans Circ Syst Video Technol* 16(3):354–362
6. Shiu CW, Chen YC, Hong W (2015) Encrypted image-based reversible data hiding with public key cryptography from difference expansion. *Signal Process Image Commun* 226–233
7. Tian J (2003) Reversible data embedding using a difference expansion. *IEEE Trans Circ Syst Video Technol* 13(8):890–896
8. Qi Y, Liu L (2017) Reversible watermarking algorithm based on prediction error expansion for color image. In: 2017 32nd Youth academic annual conference of Chinese association of automation (YAC), pp 102–105
9. Cheng SC, Tsai WH (1994) Image compression by moment-preserving edge detection. *Pattern Recogn* 27:1439–1449
10. Hong W (2013) Adaptive image data hiding in edges using patched reference table and pair-wise embedding technique. *Inform Sci* 221(1):473–489
11. Huang YH, Chang CC, Chen YH (2016) Hybrid secret hiding schemes based on absolute moment block truncation coding. *Multimedia Tools Application*
12. Malik A, Sikka G, Verma HK (2016) A high payload data hiding scheme based on modified AMBTC technique. *Multimedia Tools Appl*. <https://doi.org/10.1007/s11042-016-3815-2>
13. Pountain D (1987) Run-length encoding. *Byte* 12(6):317–319
14. Huffman DA (1952) A method for the construction of minimum-redundancy codes. *Proc IRE* 40(9):1098–1101
15. Witten IH, Neal RM, Cleary JG (1987) Arithmetic coding for data compression. *Commun ACM* 30(6):520–540
16. Fisher Y (1994) Fractal image compression. *Fractals* 2(03):347–361
17. DeVore RA, Jawerth B, Lucier BJ (1992) Image compression through wavelet transform coding. *IEEE Trans Inf Theory* 38(2):719–746
18. Delp E, Mitchell O (1979) Image compression using block truncation coding. *IEEE Trans Commun* 27(9):1335–1342
19. Lema MD, Mitchell OR (1984) Absolute moment block truncation coding and its application to color images. *IEEE Trans Commun COM-32(10)*:1148–1157
20. Chuang JC, Chang CC (2006) Using a simple and fast image compression algorithm to hide secret information. *Int J Comput Appl* 28(4):329–333
21. Hong W, Chen TS, Shiu CW (2008) Lossless steganography for AMBTC-compressed images. In: International congress on image and signal processing, vol 2, pp 13–17
22. Chen J, Hong W, Chen TS, Shiu CW (2010) Steganography for BTC compressed images using no distortion technique. *Imaging Sci J* 58(4):177–185
23. Chang CC, Lin CY, Fan YH (2008) Lossless data hiding for color images based on block truncation coding. *Pattern Recogn* 41(7):2347–2357
24. Raj I (2012) Image data hiding in images based on interpolative absolute moment block truncation coding. *Commun Comput Inf Sci* 283:456–463
25. Ou D, Sun W (2015) High payload image steganography with minimum distortion based on absolute moment block truncation coding. *Multimedia Tools Appl* 9117–9139

26. Huang YH, Chang CC, Chen YH (2017) Hybrid secret hiding schemes based on absolute moment block truncation coding. *Multimedia Tools Appl* 76:6159–6174
27. Hong W (2018) Efficient data hiding based on block truncation coding using pixel pair matching technique. *Symmetry* 10:36. <https://doi.org/10.3390/sym10020036>
28. Yang CK, Tsai WH (1995) Improving block truncation coding by line and edge information and adaptive bit-map selection for gray-scale image compression. *Pattern Recogn Lett* 16:67–75
29. Keissarian F (2010) A new predictive image compression scheme using histogram analysis and pattern matching. In: 2010 Second international conference on computer engineering and applications, Bali Island, pp 375–379
30. Feng Y-P, Lu Z-M (2018) An efficient hybrid feature for edge-preserving based on block truncation coding and tree-structured vector quantization with edge orientation classification of bit-maps. *Int J Innov Comput Inf Control* 14:929–946
31. Dhara B, Chanda B (2004) Block truncation coding using pattern fitting. *Pattern Recogn* 37:2131–2139
32. Hu Y-C, Chang C-H (2003) Edge detection using block truncation coding. *Int J Pattern Recogn ArtifIntell* 17:951–966

Analysis of Smart Electricity Grid Framework Unified with Renewably Distributed Generation



Vivek Saxena, Narendra Kumar, Uma Nangia, and Jay Singh

Abstract The electric grid in the developed nations are mature and being strained by functioning circumstances and encounters certainly not intended. Moreover, it is an exclusive in that utilities, and consumption must persist securely poised at every time, reason being there has been no bigger commercialize resolution for energy storage to regulate flexible energy demand. For furtherance, smart grid is an opportunity which embraces with heterogeneous operations and measurement of energy comprising energy demand management, demand response, distributed generation, integration of renewable energy resources, energy storage, and advance metering system to smartly bridge the gap between demand and supply. In this paper a comprehensive assessment of smart grid frame work has been analyzed. Current paper highlights the features, technology, research, economics and challenges for the deployment of secured smart grid power system.

Keywords Smart grid · Energy demand management · Demand response · Distributed generation · Renewable energy sources · Battery storage · Smart devices

1 Introduction

It is essential to integrate the renewable energy resource (RES) with the traditional centralized power generation by considering modern world prospective and ecological apprehensions in electrical power system. Moreover, features of established

V. Saxena (✉)

Department of EN, ABES Engineering College, Ghaziabad, India

e-mail: vvksaxena1234@gmail.com

V. Saxena · N. Kumar · U. Nangia

Department of EE, Delhi Technological University, Delhi, India

J. Singh

Department of EEE, GL Bajaj Institute of Technology & Management, Greater Noida, India

© Springer Nature Singapore Pte Ltd. 2021

R. Agrawal et al. (eds.), *Advances in Smart Communication and Imaging Systems*,

Lecture Notes in Electrical Engineering 721,

https://doi.org/10.1007/978-981-15-9938-5_68

generation; increased expenditure, uncertainties, and lack of consistency can be circumvented with the shrewd opportunity namely smart grid.

The conventional grid works on the following establishment [1]:

- The apparatuses are primarily passive and not governable.
- Moreover, they could not respond rapidly.
- No backup for interrupted duties.
- User demands are overwhelming which could not be fulfilled actively.

It works only to the vicissitudes via regularizing the output of the conventional grid, so that it can maintain equipoise. Unlike above system, smart grid has the advantages, strongly utilization of RES, propagation for power backup, battery-operated electrical vehicles, decentralized generation, advance intelligence, instantaneous monitoring, and approachable atmosphere. In addition to above features, improved management of load profile is also required even the constraints related to the sporadic production of renewable energy are present [2]. It is also noteworthy to decrease the power utilization and maintain a dynamic equilibrium between prosumers despite the presence of intermittent nature of RES [3, 4]. Such type of boundaries can be depleted with the amendment of traditional grid system by smart grid.

1.1 Inspiration and Objective

The analysis offered in this paper is motivated by the contingency of fossil fuel crisis, environmental pollution, depletion of electrical energy, expansion requirement of power system, unfamiliarity to emerging trends in efficient energy consumption, and gradually increasing electricity bill. The aim of this paper is to review and analyze the different aspects of smart grid mechanisms for the advancement of producer and consumer irrespective to its evolution and progression report, techno-economical challenges, possible outcomes, and future scope.

2 Smart Grid

It is an advancement in traditional grid to exploit the advantages for the consumers and as well as producers with the help of effective utilization of resources and smart appliances. It has a potential to serve better in terms of monitoring, analyzing, decision making, controlling, and load management to get stable, reliable, economical, environmental, and intelligent steady operation.

Smart grid technology comprises the data collection, report generation, and optimization processes via two way communication between producers and consumers with the help of advance metering system, energy management server and smart controller [5, 6]. The demand characteristics with the inclusion of local area network

(LAN) is required to implement this technology more effectively in which instantaneous information sharing is required [7]. In [8], authors suggested the four basic physiognomies of modern grid, information, digitalization, automation, and interaction. Moreover controlled methods are also elaborated having a classifications of power electronics-based control method, multi-agent system based control method, advanced fault management control method, and virtual power plant control technology. The risk assessment comparison between conventional grid system and smart grid system has been evaluated with the consideration of self-healing property and intermittent nature of natural resources [9]. It has been also concluded with the risk analysis of the uncertainties of renewable power generation, pre-analysis of energy storage equipment, and user participation. For the integration of RES and its challenges, a three-stage methodology (i.e., building trust, co-construction, and ensuring sustainability) has been proposed with the recommendation of interdisciplinary group formation with the contemplation of their own constraints related to project plan [10]. Consequently, a healthy group formation of the several disciplines can be molded for the mutually approved futuristic approach. A hypothesis has been examined for the financial and environmental challenges present in this scheme, and results from the system approve that authorities must find a common vision with the inclusion of external factors [11].

In continuation, an elaborated literature have been reviewed for the gap between researcher's views to the smart grid optimization and implementation [12]. Authors also presented a comparative weighted analysis having a number of expertise used for cost and pollutant reduction, cause of conflict documentation, and exploration gap.

Integration of advanced communication technologies and standards plays a key role for the enhancement of smart grid effectiveness. Communication technologies have been categorized as, Zigbee, wireless mesh, power line communication, cellular network communication, and digital subscriber lines [13]. The above-mentioned technologies have been categorized on the basis of frequency spectrum (1 MHz to 5.8 GHz), applications (advance metering system, demand response, and home area network), merits, and demerits having same communication requirements like sanctuary, consistency, scalability, and quality of service. This phenomenon has also been shown with different significant technologies as, integrated communication, sensing and measurement, advanced components, advanced control methods, and improved interface with decision support [14]. Authors proposed the shareholders of smart grid structural design namely governmental, industrial, and academia. Smart grid is the pathway for the potential penetration of RES in electricity market to maximize the environmental benefits [15, 16]. This technology is the key tool for providing the efficient energy consumption, negligible intermittency in power supply, and reliable and secured grid system [17–21]. This optimistic approach creates the opportunities for the twenty-first-century electrical power system. In comparison of SCADA and other protection system, smart grid exhibits the properties, fast, safe, dispersed, precise, and intellectual [22]. Additionally, concerns regarding existing power system like less transmission abilities, competitive energy sector, optimized location of apparatus and synchronization between national and scattered generation

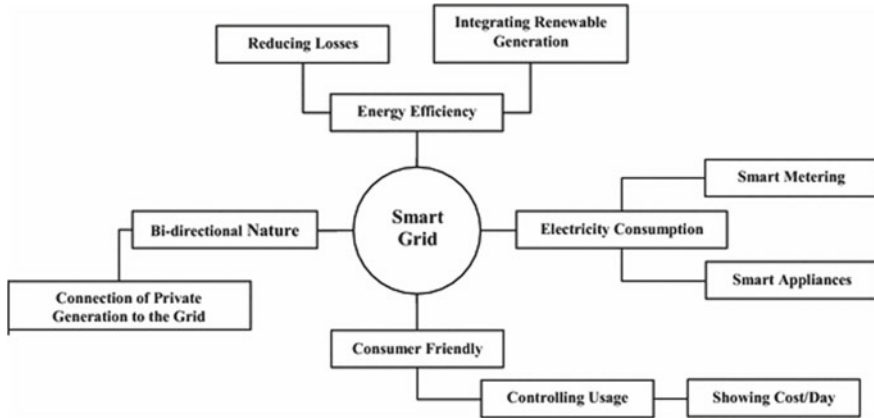


Fig. 1 Smart grid framework [24]

have been highlighted. In [23], authors have been proposed a remedial action for the criticality of smart grid operations by considering observation, data acquisition system, information sharing, optimization and control, battery storage, and smart devices. Framework of smart grid with different participated units from generation to consumption is shown in Fig. 1.

3 Energy Demand Management

In the 1980s, a process was invented on the basis of energy consumption with the deliberation of public interest to transport lower bill of electricity on the basis of their efficient use of energy is known as integrated resource planning. In continuation of this process, a new term was incorporated, i.e., demand-side management (DSM)/energy demand management (EDM) to regulate the energy depletion by plummeting the full day demand, load examining from ultimate hours to bottom hours, and exchange of fuel [25]. Moreover, several smart strategies have been encompassed with EDM which can be highlighted as awareness programs, reimbursements on acquiring the equipment, enticements for producer's well-wishers, price on the basis of consumption and advance controlling of home appliances. Using Monte Carlo simulation, an optimization has been executed for EDM with the essential prerequisite of minimum commotion [26]. In addition to this, the summary indicates the effect of various limitations and rigorous parameters with the inclusion of temperature excursion. Authors demonstrated a binary particle swarm optimization technique for the load management and exemplified the effects of load reduction in different steps and frequent interruption penalties [27]. Load framing techniques are shown in Fig. 2.

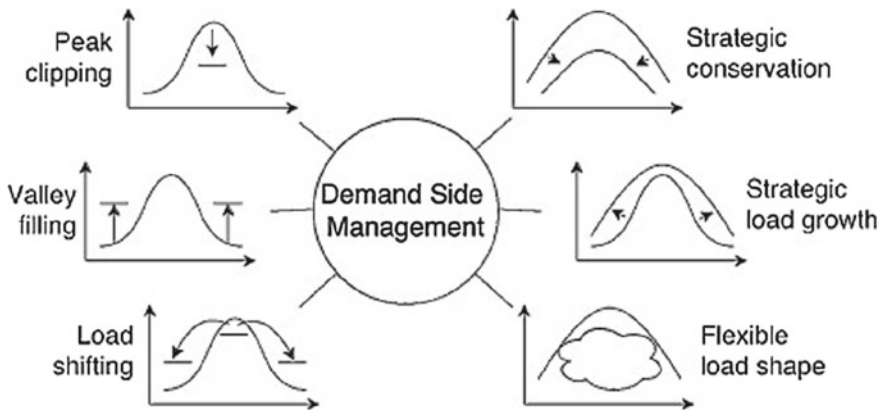


Fig. 2 Load framing techniques [28]

Direct load control method has been adopted in EDM by keeping the effect of information provided by end users and the level of interaction [29–33]. Cost analysis is another important characteristic of load scheduling. Critical-peak pricing for household [34], dynamic pricing for retail market [35], and price responsive demand for regional transmission [36] have been examined in view of EDM and its effect on low-level, medium-level, and high-level users.

For the extraction of maximum benefits at the different level of customer side which aims to the energy saving, cost reduction (capital cost, operating cost, electricity bill, and maintenance cost), pollutant reduction, integration of RES, secured power supply, motivation of individual, improved efficiency, and carrier opportunities, EDM is required to refine the following agendas:

- *Partisan inclination*: This is the first step toward the futuristic approach to incline the authorities. It is necessary because the reliance of producers, distributors, and customers depend on the conviction of selected administration.
- *Guidelines agenda*: Guidelines are essential for the implementation of any successful agenda with in a particular time frame. It will be helpful for preparing the blueprints of EDM in right direction.
- *Objective structure*: For any organization, it is mandatory to prepare objectives in terms of mission and vision on the basis of analytical feedback reports and previous experiences.
- *Grant for EDM programs*: To run the successful operations, it is necessary to have a durable position in financial terms. It plays a significant role for implementation of stable, secured, and advanced results in several segments of handlers.
- *Private contribution*: Involvement on each level is obligatory for the expansion of any project. Contribution of private stakeholders are also imperative for the accomplishment of EDM program, and they must be benefitted as per the pre-decided guidelines.

- *Educational program and development:* Educated employees are the base of this advanced project. They must be technically and professionally expert in their respective areas to set the new standards in EDM.

4 Demand Response

Demand response is a valued characteristic of load demand and used to encounter the energy crisis and inadequate requirement of energy. The demand response or demand curve refers to reducing the energy utilization from consumer side in order to generate electricity bills and incentives on the basis of energy consumption [37], while previously this term was used to elaborate the observations of peak demand reduction for a particular set of hours per year. Additionally, demand response curve can be classified as dispatchable demand response and non-dispatchable demand response. Dispatchable demand response comprises the user agreement to direct control the systematic energy consumption by retailer, while in non-dispatchable demand response, it is controlled by themselves as per the dynamic tariff plan for different hours.

Due to lack of awareness about economic planning of energy consumption, consumers had not been benefitted in conventional power system to shift their loading hours [38]. In [39], authors proposed a significant classification of demand response programs with cost and benefits. Furthermore, a categorization of end users has been given as, manufactures, traders, and residents [40]. All of these customers can contribute for the demand response program at their own interest via decreasing the load or sifting the load to economic hours or using dispersed generations. An assessment of direct load control of electric geyser have been reported in [41]. Subsequently, this method shows that the effectiveness for dropping the load level by shifting the operating hours and mean reduction in consumption of energy per household of between 0.35 and 0.58 kWh/h in the sunrise time and between 0.18 and 0.59 kWh/h in the sunset time has been concluded which contributed the escalation of payback outcome. Penalty can also be imposed on the customers to contravene their responsibility demonstration. This factor has been demonstrated in “interruptible/curtailable program” and “capacity market program” of demand response [42]. The demand buyback is another demand response program in which the load pattern is changed by industrial consumers to get the financial incentives. Distributer and consumer are benefitted and reduce the market clearing price through peak hours with the consideration of constraints of system security and generation [43]. Emergency demand response algorithm has been demonstrated for the emergent expenditure of the system and consists a multiple features, objective to burdened node, sufficient house selection, and boomerang after emergency [44]. Like optimization of demand, optimization of time and cost may be used as an objective function [45].

5 Distributed Generation

Distributed generation (DG) is a vital fragment and back bone of a smart grid power system. It is also known as decentralized or dispersed generation which are placed in the vicinity of end users and different from the traditional centralized generation. DG has numerous advantages, technical, financial, and environmental which can exploit by optimizing its size and location under the progression of DG planning [46–48]. DG planning has a number of driving factors like voltage profile enhancement, power factor optimization, THD reduction, cost reduction, power loss reduction, and pollutant reduction [49–56], but the barriers are also present. These constraints have different cause and effects and subdivided as, technical barrier [57–62], economic barrier [63–69], and socio-political barrier [70–76]. These constraints are also considered during the optimization of DG planning. DGP has multitudinous techniques for the optimization process in which objective function may be single objective or multi-objective and having a stochastic mathematical approach. These optimization techniques can be broadly classified as, basic search methods, nature-inspired methods, and hybrid intelligent algorithms and having their own merits and limitations.

DG planning outline structure has been divided into sequence of design of system configuration, assessment of RES, load profile analysis, system formulation, optimization techniques, and interpretation of results. DG system configuration comprises the number of generating units, size, and source of energy generation. Source of energy generation can be renewable or fossil fuel based system. RES are required to do the pre-analysis due to intermittent nature of natural resources and required the empirical and meteorological data forecasting of distributed area for various technical financial and reliability and security constraints.

6 Role of Renewable Energy

To install a pollution-free and economical energy generation, it is essential to utilize the RES as the adequate sources are going to decay and health hazardous are gradually increasing. For the smart grid implementation, DG planning and amalgamation of RES are essential to extract number of benefitted outcomes for the future point of view. For the contemplation of ecological impact, several parameters have been applied in preceding years. In [77], methodology of cost saving and utilizing the replacement of coal power plant with natural resource of power generation has been suggested. Moreover, environmental benefits and cost factor via DG dissemination has been reported with the comparative analysis of pollutant emission from fossil fuel plant, wind turbine, solar photo voltaic, fuel cell, and natural gas turbine based plants [78]. A fine has been recommended for the pollutant emission [79] while reduced CO₂ emission reported for the optimization of DG allocation [80].

To increase the faith on RES, it is essential to do the pre-assessment because of the source accessibility based on the nature singularities with technical, recurring, and periodic data curve which could not be forecasted with high precision [81, 82]. Solar and wind energy depends on the topographical site-based climatological circumstances. Reaping of agronomic yields, which guides the accessibility of biomass, is dependent of season and affected by the weather conditions [83]. Moreover, farming-dependent energy generation system requires to ensure the uninterrupted feeding stock to deliver secured and reliable energy production. In continuation, tidal-power-based generating plants also had inconstant characteristics but more foreseeable as associated to solar PV system and wind energy because of inferior entropy [84].

Consequently, two techniques have been categorized for solar and wind power resource accessibility, experimental atmospheric data dimension and climatological data prediction [85].

6.1 Experimental Atmospheric Data

Experimental data of solar energy and wind energy could be attained via observation on-site, printed research, weather-related laboratories, private organization, and government administration.

Solar energy parameters can be abridged as, global solar radiation data [86], solar PV array power output [87], average and seasonal annual solar irradiation [88], daily horizontal solar irradiance [89], solar intensity [90], hourly solar radiation [91], and relative frequency of global solar radiation [92]. In continuation, wind speed data characterization as, hourly mean wind speed data [86, 88], monthly average wind speed data [93, 94], daily wind energy data [89], and relative frequency of wind speed [92].

6.2 Climatological Data Prediction

Consistent forecast of climatological data is essential for compensating the subsequent applied constraints that obstruct admittance to empirical reserve calculation [95]:

- Restricted accessibility of amenities and proficiency for meteorological data dimension in definite sections;
- Financial constraint that confines inclusive climate data dimension with great perseverance; and
- Dimension organization failure that interrupts incessant data apprehending for a long period frame (Table 1).

Table 1 Categorization of renewable resource prediction limits with applications [96]

Group	Measurement of prediction limit	Applications
Extreme short period	Few seconds to 1 h	Energy generation clearing price
		Instantaneous grid operation and control
Short period	1 h to several hours	Financial planning of load dispatch
		Secured operation with sensible load pronouncements
Intermediate period	Several hours to 7 days	Unit assurance decisions
		Standby prerequisite decisions
		Generation active/passive mode decisions
Extended period	1 week to 1 year and above	Operative cost optimization
		Planning and management of operation
		Probability study for project of the wind power plant

7 Battery Storage

In generating system, energy storage has been required for the high diffusion of RES due to higher intermittency of solar and wind power [97]. A combination of doubly fed induction generator with a short-range energy stowage device has been considered in order to smoothen the power transients and strengthen the DC bus during wind power generation, thus boosting the competence of low voltage ride through [98]. Authors in [99] have elaborated energy storage techniques based on storage medium like electrical energy, mechanical energy, chemical energy, and thermal energy. Moreover, in [100], electrical energy storage have been sub-categorized as, electrochemical storage, hydrogen-based energy storage, and thermal energy storage. Authors also highlighted the socio-monetary framework and controlling commands in the direction of electrical energy generation. The charging/discharging characteristics elaborated by equations which are consisted in a model of energy storage system, while such model executes the law of energy conservation.

Historic development of energy storage techniques, constraints, and utilization areas has been significantly discovered. Authors in [101, 102] presented a weighted assessment of energy storage technologies on the parameters, technical maturity, power rating and discharge time, storage time, capital cost, cycle efficiency, energy density, cycle life time, and impact on environment. The achievement in academia and trading sectors has been carried out for the various types of energy storage techniques on the basis of pertinent technical and financial data [103]. In continuation, numerous areas have been identified for the comparison of battery storage utilization and could be briefed as, power quality, ride through capabilities, energy management,

load leveling, peak shaving, time shifting, voltage regulation, spinning reserve, fluctuation suppressor, seasonal energy storage, and power backup for telecommunication. Selection of appropriate energy storage system for the integration of renewable energy depends on economic feasibility, life span, efficiency, system capacity, environmental impact, and integrated technical factors [104]. Authors also proposed the necessity of energy storage system in renewable energy generation with the underlining of load dispatch, intermittency of RES, power quality enhancement, technological progression of power electronics, limits of the requirement of power system expansion, and smart grid development.

8 Smart Devices

Another arm of this smart grid structure is smart metering and communication system. The development of smart grid structure is also reliant on great level communication system, observations, and metering processes, thus it ensure the prolonged information subsystem. Due to exchange of bidirectional information, grid and consumers both are responsible for the security and reliability. Wireless and wireline communication system could be used to exchange the information underneath the supervision of cyber security group and physical security group to avoid malfunction [105] because a number of security attacks are happened to disturbing and abolishing the consistent processes [106–108]. A linkage of information exchange have been initiated worldwide to maintain the relation between distributors and end users [109]. Moreover, apprehensions have been elevated regarding the possible effects of radio frequencies exposure on the living things, but it must be as per exposure limit of Federal Communications Commission [110]. The quality of service mechanism and several standards are required to stabile a secured and reliable energy communication system [111]. The task related to the load framework of home equipment like invasive load combination, estimation, and demand response are required on real-time basis. An explicit-duration hidden Markov model with differential observations has been examined from aggregated smart meter data and realization with the help of forward–backward algorithm for heavy load of a household [112]. In [113], authors emphasized on the coordination between electrical and thermal load for the optimized operation in a residential building by the utilization of smart meter communication with the smart controller of grid system. Secured and reliable measurement is not only sufficient parameter for a smart meter, cost is also included. An economic smart meter having sensors, microcontroller, data acquisition system, and display has been proposed and examined with the help of programmable logic controllers and data concentrator [114]. Home load management segments entrenched in smart meter are self-governing mediators between utility and customers to get a coordinated demand response curve by shifting the peak load hours to non-peak hours and got economically better pricing of energy units [115]. A distributed algorithm has been presented for the smart meter operation having optimization of energy generation and storage, shielding the privacy of end user by minimizing the communication [116]. The smart

meter may be owned by distributor or consumer, and a supervisory control approach namely supervisory control and data acquisition (SCADA) with the software and hardware realization is presented by the authors [117].

Consequently, it is very necessary to ensure that minimization of interference in the privacy of consumer to build an authenticity of bidirectional communications. In continuation, with the consideration of privacy of customer and utility requirements, smart meter data has been framed by using communication data theory and a hidden Markov model [118], Lyapunov optimization technique with cost minimization [119], and linkable anonymous credential protocol based on Camenisch–Lysyanskaya (CL) signature [120]. Inspection and maintenance of smart meter is also very essential. Authors proposed an adaptive tree-based algorithm to identify the malicious energy meter in static and dynamic conditions [121].

9 Key Finding

- This paper has reconnoitered the different procedural steps of smart grid framework to meet the energy demand in environmental friendly manner. It is endorsed to examine the effect of diverse manufacturing operations amalgamation on the demand, hours of load intermittency, and efficacy of energy demand management.
- For effective DG planning, optimization process is very significant and its effectiveness and constraints handling. Classic approaches are simple in implementation with high precision but suffer due to slow computation process in single objective. Additionally, artificial intelligence are efficient but undergo due to complex coding and unstable results. Hence, it is recommended to do more research on hybrids approaches of optimization.
- The reliability of DG planning as well smart grid planning could be enhanced by climatological data prediction in comparison with past meteorological data submission, and hence, it is necessary to develop a consistent model for the assessment of RES.
- Energy storage may be affected with the temperature variation, entangling of electrodes, and fuel cell deprivation, so it is recommended to develop a comprehensive hydrogen storage framework with the consideration of charging/discharging cycle.
- Use of smart metering system and bidirectional communication is very sensitive. Reviewed studies have shown that secured reliable information exchange could enhance the popularities of smart grid among political, social, and individuals.

10 Conclusion

It has been concluded that we are the spectator of an innovative era of electricity generation in which experiments and prospects are confronted to reconfigure the

traditional grid into smart grid. The deployment of smart grid power system will help the nations to reduce fuel crisis, efficient energy consumption, reduce pollutant level, increase awareness toward emerging trends, and deplete the gap amid load and generation.

In this paper, the phases of smart grid framework have been analyzed which comprises the energy demand management, demand response, DG, RES, battery storage, and smart devices. Additionally, the benefitted outcomes, challenges, and scopes have been highlighted hence to enlighten the pathway of reliable, secured, stable, dynamic, efficient, environment friendly, and long-tenure energy generation and utilization for the mutual benefits of stakeholders.

References

1. Santacana E, Rackliffe G, Tang L, Feng X (2010) Getting smart. *IEEE Power Energy Mag* 8(2):41–48
2. Ipakchi A, Albuys F (2009) Grid of the future. *IEEE Power Energy Mag* 7(2):52–62
3. Brooks A, Lu E, Reicher D, Spirakis C, Wehl B (2010) Demand dispatch. *IEEE Power Energy Mag* 8(3):20–29
4. Banosa R, Manzano-Agugliarob F, Montoyab FG, Gila C, Alcaydeb A, Gomezc J (2011) Optimization methods applied to renewable and sustainable energy: a review. *Renew Sustain Energy Rev* 15(4):1753–1766
5. Choi IH, Lee JH, Hong SH (2011) Implementation and evaluation of the apparatus for intelligent energy management to apply to the smart grid at home. In: *Proceedings of the 2011 IEEE international instrumentation and measurement technology conference, Binjiang*, pp 1–5
6. Report (2007) Advanced metering for energy supply in Australia. *Energy Futures Australia*
7. Staff Report (2006) Demand response & advanced metering, FERC (<https://www.ferc.gov/legal/staff-reports/demand-response.pdf>)
8. Peng L, Yan GS (2011–12) Clean energy grid-connected technology based on smart grid. *Energy Procedia* 213–218
9. Hou H, Zhou J, Zhang Y, He X (2011) A brief analysis on differences of risk assessment between smart grid and traditional power grid. In: *Proceedings of the 2011 fourth international symposium on knowledge acquisition and modeling, Sanya*, pp 188–191
10. Alvial-Palavicino C, Garrido-Echeverria N, Jimenez-Estevéz G, Reyes L, Palma-Behnke R (2011) A methodology for community engagement in the introduction of renewable based smart micro grid. *Energy Sustain Dev* 15:314–323
11. Agrell PJ, Bogetoft P, Mikkers M (2013) Smart-grid investments, regulation and organization. *Energy Policy* 52:656–666
12. Moretti M, Njakou Djomo S, Azadi H, May K, De Vos K, Van Passel S, Witters N (2017) A systematic review of environmental and economic impacts of smart grids. *Renew Sustain Energy Rev* 68(Part 2):888–898
13. Gungor VC et al (2011) Smart grid technologies: communication technologies and standards. *IEEE Trans Ind Inform* 7(4):529–539
14. Gao J, Xiao Y, Liu J, Liang W, Chen CLP (2012) A survey of communication/networking in smart grids. *Future Gener Comput Syst* 28:391–404
15. Alonso M, Amaris H, Alvarez-Ortega C (2012) Integration of renewable energy sources in smart grids by means of evolutionary optimization algorithms. *Expert Syst Appl* 39(5):5513–5522
16. Markovic DS, Zivkovic D, Branovic I, Popovic R, Cvetkovic D (2013) Smart power grid and cloud computing. *Renew Sustain Energy Rev* 24:566–577

17. Lorena TM, Lochinvar AM (2016) A review of the development of smart grid technologies. *Renew Sustain Energy Rev* 59:710–725
18. Sun DQ et al (2010) The Utilization and Development Strategies of Smart Grid and New Energy. In: Proceedings of the 2010 Asia-Pacific power and energy engineering conference, Chengdu, pp 1–4
19. Mu L, Gao Q (2011) Research on intelligent power consumption in smart grid. In: Proceedings of the 2011 international conference on advanced power system automation and protection, Beijing, pp 1206–1208
20. Batista NC, Melicio R, Matias JCO, Catalao JPS (2013) Photo voltaic and wind energy systems monitoring and building/home energy management using ZigBee devices within a smart grid. *Energy* 49:306–315
21. Chebbo M (2007) EU smart grids framework “Electricity networks of the future 2020 and beyond”. In: 2007 IEEE power engineering society general meeting, Tampa, FL, pp 1–8
22. Amin M, Wollenberg BF (2006) Toward a smart grid: power delivery for the 21st century. *IEEE Power Energy Mag* 4(6):34–41
23. Lin S-Y, Chen J-F (2013) Distributed optimal power flow for smart grid transmission system with renewable energy sources. *Energy* 56(3):184–192
24. Uddin Z, Ahmad A, Qamar A et al (2018) Recent advances of the signal processing techniques in future smart grids. *Human-Centric Comput Inf Sci* 8
25. Masters GM (2004) *Renewable and efficient electric power systems*. Wiley, Hoboken
26. Ramanathan B, Vittal V (2008) A framework for evaluation of advanced direct load control with minimum disruption. *IEEE Trans Power Syst* 23(4):1681–1688
27. Pedrasa MAA, Spooner TD, MacGill IF (2009) Scheduling of demand side resources using binary particle swarm optimization. *IEEE Trans Power Syst* 24(3):1173–11781
28. Gellings CW (1985) The concept of demand-side management for electric utilities. *Proc IEEE* 73(10):1468–1470
29. Gomes A, Antunes CH, Martins AG (2007) A multiple objective approach to direct load control using an interactive evolutionary algorithm. *IEEE Trans Power Syst* 22(3):1004–1011
30. Chu C-M, Jong T-L, Huang Y-W (2005) A direct load control of air-conditioning loads with thermal comfort control. In: Proceedings of the IEEE power engineering society general meeting, vol 1, pp 664–669
31. Weers DD, Shamsedin MA (1987) Testing a new direct load control power line communication system. *IEEE Trans Power Deliv* 2(3):657–660
32. Ruiz N, Cobelo I, Oyarzabal J (2009) A direct load control model for virtual power plant management. *IEEE Trans Power Syst* 24(2):959–966
33. OpenHAN Task Force of the Utility AMI Working Group (2008) Utility AMI 2008 home area network system requirements specification
34. Herter K (2007) Residential implementation of critical-peak pricing of electricity. *Energy Policy* 35:2121–2130
35. Triki C, Violi A (2009) Dynamic pricing of electricity in retail markets. *4OR-A Quart J Oper Res* 7(1):21–36
36. Centolella P (2010) The integration of price responsive demand into regional transmission organization (RTO) wholesale power markets and system operations. *Energy* 35(4):1568–1574
37. Staff Report (2010) National action plan on demand response, FERC (<https://www.ferc.gov/legal/staff-reports/06-17-10-demand-response.pdf>)
38. Kirschen D, Strbac G (2004) *Fundamentals of power system economics*. Wiley, New York
39. Albadi MH, El-Saadany EF (2007) Demand response in electricity markets: an overview. In: 2007 IEEE Power engineering society general meeting, Tampa, FL, pp 1–5
40. Jamshid A, Mohammad-Iman A (2013) Demand response in smart electricity grids equipped with renewable energy sources: a review. *Renew Sustain Energy Rev* 18:64–72
41. Torgeir E (2009) Direct load control of residential water heaters. *Energy Policy* 37(9):3502–3512

42. Aalami HA, Parsa Moghaddam M, Yousefi GR (2010) Demand response modeling considering interruptible/curtailable loads and capacity market programs. *Appl Energy* 87(1):243–250
43. Saebi J, Taheri H, Mohammadi J, Nayer SS (2010) Demand bidding/buyback modeling and its impact on market clearing price. In: *Proceedings of the 2010 IEEE international energy conference*, Manama, pp 791–796
44. Tyagi R, Black JW (2010) Emergency demand response for distribution system contingencies. In: *IEEE PES T&D 2010*, New Orleans, LA, USA, pp 1–4
45. Datchanamorthy S, Kumar S, Ozturk Y, Lee G (2011) Optimal time-of-use pricing for residential load control. In: *Proceedings of the 2011 IEEE international conference on smart grid communications (SmartGridComm)*, Brussels, pp 375–380
46. El-Khattam W, Salama MMA (2004) Distributed generation technologies, definitions and benefits. *Electr Power Syst Res* 71:119–128
47. Chiradeja P, Ramakumar R (2004) An approach to quantify the technical benefits of distributed generation. *IEEE Trans Energy Convers* 19:764–773
48. Pepermans G, Driesen J, Haeseldonckx D, Belmans R, D’Haeseleer W (2005) Distributed generation: definition, benefits and issues. *Energy Policy* 33:787–798
49. Jenkins N (2000) *Institution of electrical E. embedded generation*. Institution of Electrical Engineers, London
50. Barker PP, De Mello RW (2000) Determining the impact of distributed generation on power systems. I. Radial distribution systems. In: *Power engineering society summer meeting*, vol 3. IEEE, pp 1645–1656
51. Edwards FV, Dudgeon GJW, McDonald JR, Leithead WE (2000) Dynamics of distribution networks with distributed generation. In: *Power engineering society summer meeting*, vol 3. IEEE, pp 1032–1037
52. Girgis A, Brahma S (2001) Effect of distributed generation on protective device coordination in distribution system. In: *LESCOPE’01 Large engineering systems conference on power engineering*, pp 115–119
53. Joos G, Ooi BT, McGillis D, Galiana FD, Marceau R (2000) The potential of distributed generation to provide ancillary services. In: *Power engineering society summer meeting*, vol 3. IEEE, pp 1762–1767
54. Masters CL (2002) Voltage rise: the big issue when connecting embedded generation to long 11 kV overhead lines. *Power Eng J* 16:5–12
55. Walling RA, Saint R, Dugan RC, Burke J, Kojovic LA (2008) Summary of distributed resources impact on power delivery systems. *IEEE Trans Power Deliv* 23:1636–1644
56. Willis HL, Scott WG (2000) Distributed power generation: planning and evaluation
57. Manditereza PT, Bansal R (2016) Renewable distributed generation: the hidden challenges—a review from the protection perspective. *Renew Sustain Energy Rev* 58:1457–1465
58. Karimi M, Mokhlis H, Naidu K, Uddin S, Bakar AHA (2016) Photovoltaic penetration issues and impacts in distribution network—a review. *Renew Sustain Energy Rev* 53:594–605
59. Shivashankar S, Mekhilef S, Mokhlis H, Karimi M (2016) Mitigating methods of power fluctuation of photovoltaic (PV) sources—a review. *Renew Sustain Energy Rev* 59:1170–1184
60. Gabash A, Li P (2016) On variable reverse powerflow—part I: active-reactive optimal powerflow with reactive power of wind stations. *Energies* 9:121
61. Qin M, Chan KW, Chung CY, Luo X, Wu T (2016) Optimal planning and operation of energy storage systems in radial networks for wind power integration with reserve support. *IET Gener Transm Distrib* 10:2019–2025
62. Zamani AG, Zakariazadeh A, Jadid S, Kazemi A (2016) Stochastic operational scheduling of distributed energy resources in a large scale virtual power plant. *Renew Sustain Energy Rev* 82:608–620
63. Alam M, Bhattacharyya S (2016) Decentralized renewable hybrid mini-grids for sustainable electrification of the off-grid coastal areas of Bangladesh. *Energies* 9:268
64. Fabbro BD, Valentinčič A, Gubina AF (2016) An adequate required rate of return for grid-connected PV systems. *Sol Energy* 132:73–83

65. Humada AM, Hojabri M, Hamada HM, Samsuri FB, Ahmed MN (2016) Performance evaluation of two PV technologies (c-Si and CIS) for building integrated photovoltaic based on tropical climate condition: a case study in Malaysia. *Energy Build* 119:233–241
66. Ravi Gehlot KP, Dasila NK, Mohanty S, Solar PV (2016) Integrated world super grid (WSG): possibilities, implementation issues and impacts. *J Clean Energy Technol* 4:20–25
67. Herrando M, Markides CN (2016) Hybrid PV and solar-thermal systems for domestic heat and power provision in the UK: techno-economic considerations. *Appl Energy* 161:512–532
68. Afanasyeva S, Saari J, Kalkofen M, Partanen J, Pyrhönen O (2016) Technical, economic and uncertainty modelling of a wind farm project. *Energy Convers Manage* 107:22–33
69. Liu S-Y, Ho Y-F (2016) Wind energy applications for Taiwan buildings: what are the challenges and strategies for small wind energy systems exploitation? *Renew Sustain Energy Rev* 59:39–55
70. Obi M, Bass R (2016) Trends and challenges of grid-connected photovoltaic systems a review. *Renew Sustain Energy Rev* 58:1082–1094
71. Sgarbossa R, Lissandron S, Mattavelli P, Turri R, Cerretti A (2016) Analysis of Delta P Delta Q area of uncontrolled islanding in low-voltage grids with PV generators. *IEEE Trans Ind Appl* 52:2387–2396
72. Bosch C (2015) Securing the smart grid: protecting national security and privacy through mandatory, enforceable interoperability standards. *Fordham Urban Law J* 41:1349–1406
73. Perez-Arriaga IJ (2016) The transmission of the future: the impact of distributed energy resources on the network. *IEEE Power Energy Mag* 14:41–53
74. Ming Z, Shaojie O, Hui S, Yujian G, Qiqi Q (2015) Overall review of distributed energy development in China: status quo, barriers and solutions. *Renew Sustain Energy Rev* 50:1226–1238
75. Ponce P, Polasko K, Molina A (2016) End user perceptions toward smart grid technology: acceptance, adoption, risks, and trust. *Renew Sustain Energy Rev* 60:587–598
76. Kappagantu R, Daniel SA, Venkatesh M (2015) Analysis of rooftop solar PV system implementation barrier in Puducherry Smart Grid Pilot Project. *Procedia Technol* 21:490–497
77. Gao Y, Liu J, Yang J, Liang H, Zhang J (2014) Multi-objective planning of multi-type distributed generation considering timing characteristics and environmental benefits. *Energies* 7(10):6242–6257
78. Sui X (2010) The distribution network reliability and economy study considering the distribution generation. Southwest Jiaotong University, Chengdu
79. Chen M-Y, Cheng S (2012) Multi-objective optimization of the allocation of DG units considering technical, economical and environmental attributes. *Przegląd Elektrotechniczny* 88:233–237
80. Celli G, Mocci S, Pilo F, Soma GG (2008) A multi-objective approach for the optimal distributed generation allocation with environmental constraints. In: *Proceedings of the 10th IEEE international conference on probabilistic methods applied to power systems, PMAPS'08, Rincon*, pp 1–8
81. Izadyar N, Ong HC, Chong WT, Leong KY (2016) Resource assessment of the renewable energy potential for a remote area: a review. *Renew Sustain Energy Rev* 62:908–923
82. Milligan M, Donohoo P, O'Malley M (2012) Stochastic methods for planning and operating power system with large amounts of wind and solar power. In: *Proceedings of the transmission networks for offshore wind power plants conference*. National Renewable Energy Laboratory (NREL), Lisbon, Portugal
83. Stenek V, Connell R (2011) Ghana oil palm development company full report. climate risk and business agribusiness. International Finance Corporation (IFC), Pennsylvania Ave. NW, Washington, DC
84. Kim IC, Lee NJ, Wata J, Hyun BS, Lee YH (2016) Experiments on the magnetic coupling in a small scale counter rotating marine current turbine. *Mater Sci Eng* 129
85. Zhou W, Lou C, Li Z, Hu L, Yang H (2010) Current status of research on optimum sizing of stand-alone hybrid solar-wind power generation systems. *Appl Energy* 87:380–389

86. Busaidi ASA, Kazem HA, Al-Badi AH, Khan MF (2016). A review of optimum sizing of hybrid PV-wind renewable energy systems in Oman. *Renew Sustain Energy Rev* 53:185–193
87. Chen CL (2008) Optimal wind–thermal generating unit commitment. *IEEE Trans Energy Convers* 88(1):273–280
88. Maheri A (2014) A critical evaluation of deterministic methods in size optimisation of reliable and cost effective standalone hybrid renewable energy systems. *Reliab Eng Syst Saf* 130:159–174
89. Diaf S, Notton G, Belhamel M, Haddadi M, Louche A (2008) Design and techno-economical optimization for hybrid PV/wind system under various meteorological conditions. *Appl Energy* 85:968–987
90. Ho WS, Hashim H, Lim JS (2014) Integrated biomass and solar town concept for a smart eco-village in Iskandar Malaysia (IM). *Renew Energy* 69:190–201
91. Wang J, Yang Y, Mao T, Sui J, Jin H (2015) Life cycle assessment (LCA) optimization of solar-assisted hybrid CCHP system. *Appl Energy* 146:38–52
92. Merei G, Berger C, Sauer DU (2013) Optimization of an off-grid hybrid PV-wind- diesel system with different battery technologies using genetic algorithm. *Sol Energy* 97:460–473
93. Al-Badi AH, Bourdoucen H (2012) Feasibility analysis of renewable hybrid energy supply options for Masirah Island. *Int J Sustain Eng* 5:244–251
94. Al-Badi AH (2011) Hybrid (solar and wind) energy system for Al Hallaniyat Island electrification. *Int J Sustain Energy* 30:212–222
95. Ayodele TR, Ogunjuyigbe ASO (2015) Prediction of monthly average global solar radiation based on statistical distribution of clearness index. *Energy* 1–10
96. Chang W-Y (2014) A literature review of wind forecasting methods. *J Power Energy Eng* 2:161–168
97. Hossain MS, Madlool NA, Rahim NA, Selvaraj J, Pandey AK, Faheem KA (2016) Role of smart grid in renewable energy: an overview. *Renew Sustain Energy Rev* 60:1168–1184
98. Abbey C, Joos G (2007) Super capacitor energy storage for wind energy applications. *IEEE Trans Ind Appl* 88(3):769–776
99. Mahlia TMI, Saktisahdan TJ, Jannifar A, Hasan MH, Matseelar HSC (2014) A review of available methods and development on energy storage: technology update. *Renew Sustain Energy Rev* 33:532–545
100. Kyriakopoulos Grigorios L, Garyfallos A (2016) Electrical energy storage systems in electricity generation: energy policies, innovative technologies, and regulatory regimes. *Renew Sustain Energy Rev* 56:1044–1067
101. Haisheng C, Ngoc CT, Wei Y, Chunqing T, Yongliang L, Yulong D (2009) Progress in electrical energy storage system: a critical review. *Prog Nat Sci* 19(3):291–312
102. Kousksou T, Bruel P, Jamil A, El Rhafiki T, Zeraoui Y (2014) Energy storage: applications and challenges. *Sol Energy Mater Sol Cells* 120:59–80
103. Xing L, Jihong W, Mark D, Jonathan C (2015) Overview of current development in electrical energy storage technologies and the application potential in power system operation. *Appl Energy* 137:511–536
104. Mohammed YS, Mohd WM, Nouruddeen B (2014) Energy storage systems for renewable energy power sector integration and mitigation of intermittency. *Renew Sustain Energy Rev* 35:499–514
105. Yasin K (2016) A survey on smart metering and smart grid communication. *Renew Sustain Energy Rev* 57:302–318
106. Bou-Harb E, Fachkha C, Pourzandi M, Debbabi M, Assi C (2013) Communication security for smart grid distribution networks. *IEEE Commun Mag* 51:42–49
107. Yilin M, Kim TH-H, Brancik K, Dickinson D, Heejo L et al (2012) Cyber–physical security of a smart grid infrastructure. *Proc IEEE* 100:195–209
108. Ericsson GN (2010) Cyber security and power system communication—essential parts of a smart grid infrastructure. *IEEE Trans Power Deliv* 25:1501–1507
109. Brown RE (2008) Impact of Smart Grid on distribution system design. In: *Proceedings of the 2008 IEEE power and energy society general meeting—conversion and delivery of electrical energy in the 21st century*, Pittsburgh, PA, pp 1–4

110. Smart meters and smart meter systems: a metering industry perspective, an EEI-AEIC-UTC white paper, Edison Electric Institute (EEI) (2011)
111. Gungar VC, Sahin D, Kocak T, Erguit S, Buccella C, Cecati C, Hancke GP (2011) Smart grid technologies: communication technologies and standards. *IEEE Trans Industr Inf* 7(4):529–539
112. Zhenyu G, Wang ZJ, Kashani A (2015) Home appliance load modeling from aggregated smart meter data. *IEEE Trans Power Syst* 30:254–262
113. Tasdighi M, Ghasemi H, Rahimi-Kian A (2014) Residential micro grid scheduling based on smart meters data and temperature dependent thermal load modeling. *IEEE Trans Smart Grid* 5:349–357
114. Aurilio G, Gallo D, Landi C, Luiso M, Graditi G (2014) A low cost smart meter network for a smart utility. In: *Proceedings of the 2014 IEEE international instrumentation and measurement technology conference (I2MTC) proceedings, Montevideo*, pp 380–385
115. Safdarian A, Fotuhi-Firuzabad M, Lehtonen M (2014) A distributed algorithm for managing residential demand response in smart grids. *IEEE Trans Industr Inf* 10(4):2385–2393
116. Atzeni I, Ordonez LG, Scutari G, Palomar DP, Fonollosa JR (2013) Demand-side management via distributed energy generation and storage optimization. *IEEE Trans Smart Grid* 4(2):866–876
117. Pereira R, Figueiredo J, Melicio R, Mendes VMF, Martins J, Quadrado JC (2015) Consumer energy management system with integration of smart meters. *Energy Rep* 22–29
118. Sankar L, Rajagopalan SR, Mohajer S, Poor HV (2013) Smart meter privacy: a theoretical framework. *IEEE Trans Smart Grid* 4(2):837–846
119. Lei Y, Xu C, Junshan Z, Poor HV (2015) Cost-effective and privacy-preserving energy management for smart meters. *IEEE Trans Smart Grid* 6:486–495
120. Feng D, Fangguo Z, Xiangguo C (2015) A privacy-preserving smart metering scheme using linkable anonymous credential. *IEEE Trans Smart Grid* 6:461–467
121. Zhifeng X, Yang X, Du DH (2013) Exploring Malicious meter inspection in neighborhood area smart grids. *IEEE Trans Smart Grid* 4:214–226